Lecture Notes in Electrical Engineering 1102

Xuzhu Dong
Li Cai *Editors*

The Proceedings of 2023 4th International Symposium on Insulation and Discharge Computation for Power Equipment (IDCOMPU2023)

Volume III

Springer

Lecture Notes in Electrical Engineering

Volume 1102

Series Editors

Leopoldo Angrisani, Department of Electrical and Information Technologies Engineering, University of Napoli Federico II, Napoli, Italy
Marco Arteaga, Departament de Control y Robótica, Universidad Nacional Autónoma de México, Coyoacán, Mexico
Samarjit Chakraborty, Fakultät für Elektrotechnik und Informationstechnik, TU München, München, Germany
Jiming Chen, Zhejiang University, Hangzhou, Zhejiang, China
Shanben Chen, School of Materials Science and Engineering, Shanghai Jiao Tong University, Shanghai, China
Tan Kay Chen, Department of Electrical and Computer Engineering, National University of Singapore, Singapore, Singapore
Rüdiger Dillmann, University of Karlsruhe (TH) IAIM, Karlsruhe, Baden-Württemberg, Germany
Haibin Duan, Beijing University of Aeronautics and Astronautics, Beijing, China
Gianluigi Ferrari, Dipartimento di Ingegneria dell'Informazione, Sede Scientifica Università degli Studi di Parma, Parma, Italy
Manuel Ferre, Centre for Automation and Robotics CAR (UPM-CSIC), Universidad Politécnica de Madrid, Madrid, Spain
Faryar Jabbari, Department of Mechanical and Aerospace Engineering, University of California, Irvine, CA, USA
Limin Jia, State Key Laboratory of Rail Traffic Control and Safety, Beijing Jiaotong University, Beijing, China
Janusz Kacprzyk, Intelligent Systems Laboratory, Systems Research Institute, Polish Academy of Sciences, Warsaw, Poland
Alaa Khamis, Department of Mechatronics Engineering, German University in Egypt El Tagamoa El Khames, New Cairo City, Egypt
Torsten Kroeger, Intrinsic Innovation, Mountain View, CA, USA
Yong Li, College of Electrical and Information Engineering, Hunan University, Changsha, Hunan, China
Qilian Liang, Department of Electrical Engineering, University of Texas at Arlington, Arlington, TX, USA
Ferran Martín, Departament d'Enginyeria Electrònica, Universitat Autònoma de Barcelona, Bellaterra, Barcelona, Spain
Tan Cher Ming, College of Engineering, Nanyang Technological University, Singapore, Singapore
Wolfgang Minker, Institute of Information Technology, University of Ulm, Ulm, Germany
Pradeep Misra, Department of Electrical Engineering, Wright State University, Dayton, OH, USA
Subhas Mukhopadhyay, School of Engineering, Macquarie University, NSW, Australia
Cun-Zheng Ning, Department of Electrical Engineering, Arizona State University, Tempe, AZ, USA
Toyoaki Nishida, Department of Intelligence Science and Technology, Kyoto University, Kyoto, Japan
Luca Oneto, Department of Informatics, Bioengineering, Robotics and Systems Engineering, University of Genova, Genova, Genova, Italy
Bijaya Ketan Panigrahi, Department of Electrical Engineering, Indian Institute of Technology Delhi, New Delhi, Delhi, India
Federica Pascucci, Department di Ingegneria, Università degli Studi Roma Tre, Roma, Italy
Yong Qin, State Key Laboratory of Rail Traffic Control and Safety, Beijing Jiaotong University, Beijing, China
Gan Woon Seng, School of Electrical and Electronic Engineering, Nanyang Technological University, Singapore, Singapore
Joachim Speidel, Institute of Telecommunications, University of Stuttgart, Stuttgart, Germany
Germano Veiga, FEUP Campus, INESC Porto, Porto, Portugal
Haitao Wu, Academy of Opto-electronics, Chinese Academy of Sciences, Haidian District Beijing, China
Walter Zamboni, Department of Computer Engineering, Electrical Engineering and Applied Mathematics, DIEM—Università degli studi di Salerno, Fisciano, Salerno, Italy
Junjie James Zhang, Charlotte, NC, USA
Kay Chen Tan, Department of Computing, Hong Kong Polytechnic University, Kowloon Tong, Hong Kong

The book series *Lecture Notes in Electrical Engineering* (LNEE) publishes the latest developments in Electrical Engineering—quickly, informally and in high quality. While original research reported in proceedings and monographs has traditionally formed the core of LNEE, we also encourage authors to submit books devoted to supporting student education and professional training in the various fields and applications areas of electrical engineering. The series cover classical and emerging topics concerning:

- Communication Engineering, Information Theory and Networks
- Electronics Engineering and Microelectronics
- Signal, Image and Speech Processing
- Wireless and Mobile Communication
- Circuits and Systems
- Energy Systems, Power Electronics and Electrical Machines
- Electro-optical Engineering
- Instrumentation Engineering
- Avionics Engineering
- Control Systems
- Internet-of-Things and Cybersecurity
- Biomedical Devices, MEMS and NEMS

For general information about this book series, comments or suggestions, please contact leontina.dicecco@springer.com.

To submit a proposal or request further information, please contact the Publishing Editor in your country:

China

Jasmine Dou, Editor (jasmine.dou@springer.com)

India, Japan, Rest of Asia

Swati Meherishi, Editorial Director (Swati.Meherishi@springer.com)

Southeast Asia, Australia, New Zealand

Ramesh Nath Premnath, Editor (ramesh.premnath@springernature.com)

USA, Canada

Michael Luby, Senior Editor (michael.luby@springer.com)

All other Countries

Leontina Di Cecco, Senior Editor (leontina.dicecco@springer.com)

**** This series is indexed by EI Compendex and Scopus databases. ****

Xuzhu Dong · Li Cai
Editors

The Proceedings of 2023 4th International Symposium on Insulation and Discharge Computation for Power Equipment (IDCOMPU2023)

Volume III

Springer

Editors
Xuzhu Dong
School of Electrical Engineering
and Automation
Wuhan University
Wuhan, China

Li Cai
School of Electrical Engineering
and Automation
Wuhan University
Wuhan, China

ISSN 1876-1100 ISSN 1876-1119 (electronic)
Lecture Notes in Electrical Engineering
ISBN 978-981-99-7404-7 ISBN 978-981-99-7405-4 (eBook)
https://doi.org/10.1007/978-981-99-7405-4

© Beijing Paike Culture Commu. Co., Ltd. 2024

This work is subject to copyright. All rights are solely and exclusively licensed by the Publisher, whether the whole or part of the material is concerned, specifically the rights of translation, reprinting, reuse of illustrations, recitation, broadcasting, reproduction on microfilms or in any other physical way, and transmission or information storage and retrieval, electronic adaptation, computer software, or by similar or dissimilar methodology now known or hereafter developed.
The use of general descriptive names, registered names, trademarks, service marks, etc. in this publication does not imply, even in the absence of a specific statement, that such names are exempt from the relevant protective laws and regulations and therefore free for general use.
The publisher, the authors, and the editors are safe to assume that the advice and information in this book are believed to be true and accurate at the date of publication. Neither the publisher nor the authors or the editors give a warranty, expressed or implied, with respect to the material contained herein or for any errors or omissions that may have been made. The publisher remains neutral with regard to jurisdictional claims in published maps and institutional affiliations.

This Springer imprint is published by the registered company Springer Nature Singapore Pte Ltd.
The registered company address is: 152 Beach Road, #21-01/04 Gateway East, Singapore 189721, Singapore

Paper in this product is recyclable.

Contents

Simulation and Experimental Study of Temporary Grounding Potential Distribution in Power Engineering

Yuanjun Pan, Zhenfei Li, Dilong Shen, Liejiang Huang, Haipeng Tian, Jianwei Zhang, and Qingchen Wang

Abstract Focusing on the problems of high grounding resistance and surface potential in the temporary grounding of the current outdoor power engineering construction, it is easy to cause electric shock safety of construction workers. In this paper, CDEGS simulation calculation software is utilized to establish the grounding dispersion model of horizontal bare copper stranded grounding conductor, calculate the grounding resistance value and surface potential distribution characteristics of temporary grounding device under different laying lengths and soil resistance conditions, and compare and analyze the grounding dispersion characteristics of horizontal bare copper stranded and common vertical grounding pile. In view of the actual outdoor construction conditions of power engineering, a calculation model for the dispersion of temporary grounding device was established. At the same time, the dispersion characteristics of grounding conductor under the mixed geomorphic condition of cement road surface and soil were calculated. Through the simulation calculation results, proved by single dimension and the structure of vertical grounding pile as the risk of temporary grounding device, the laying suggestions of grounding device under the actual construction conditions of temporary grounding are given. The relevant research conclusions can provide reference for the construction safety of temporary grounding scene in power engineering.

Keywords Electric power construction · Temporary grounding · Grounding resistance · Surface potential distribution · Vertical grounding pile

Y. Pan · D. Shen · L. Huang
Hangzhou Xinmei Complete Electric Appliance Manufacturing Co., LTD, Hangzhou 310000, China

Z. Li (✉) · H. Tian · J. Zhang · Q. Wang
School of Electrical and Electronic Engineering, Shandong University of Technology, Zibo 255000, China
e-mail: lizhenfei0105@126.com

© Beijing Paike Culture Commu. Co., Ltd. 2024

X. Dong and L. Cai (eds.), *The Proceedings of 2023 4th International Symposium on Insulation and Discharge Computation for Power Equipment (IDCOMPU2023)*, Lecture Notes in Electrical Engineering 1102, https://doi.org/10.1007/978-981-99-7405-4_1

1 Introduction

Temporary power supply devices are usually used in outdoor construction of power engineering, such as mobile emergency power supply vehicles, diesel generators, energy storage power supplies, etc., to provide power supply for field measuring and mechanized operations [1–3]. Due to the special combination of mobile power supply system, it is impossible to have large fixed grounding grid conditions like conventional substation, which makes it difficult to meet the requirements of lightning proof grounding, anti-static grounding and neutral point working grounding in outdoor construction of power system [4, 5]. At present, two kinds of grounding methods are usually used in outdoor construction work outside the station: one is to connect the nearby plant grounding grid, the building wall lightning rod, the steel pipe tower body or the cement rod cable. When there is no fixed grounding device at the construction point, the construction worker usually uses mobile grounding devices such as artificial grounding piles and grounding modules [6, 7]. With the continuous construction of new power systems, the randomness and mobility requirements of power construction operations are gradually increasing, and the application scenarios for mobile grounding devices are increasing.

At present, the research on mobile grounding devices mainly focuses on the potential distribution and electric shock safety of temporary grounding devices: Reference [8] pointed out through experiments that when the vertical grounding pile has a soil resistivity of about 30Ω·m and a short-circuit current of 48.1A, the surface step voltage exceeds the safety limit of 80 V.When the ground current exceeds 100A, the safety distance within 8 m specified in GB 26,860–2011 may be underestimated, and there are certain safety hazards. Reference [9] used simulation calculation software to analyze the fault principle of overhead line live mistakenly hanging the ground wire or missing the ground wire closing power transmission, and discussed the early warning function of outdoor construction grounding. For a long time, mobile substations in China usually use metal grounding piles (commonly known as ground nails), ion grounding rods, metal grounding grids and other grounding devices, which have the disadvantages of inconvenient transportation and installation, high grounding resistance, short service life, high cost and maintenance cost [10, 11]. It brings potential risks of step voltage and touch voltage to power operators and pedestrians near mobile substations.

This paper aims at the problems of high grounding resistance, high surface potential gradient and high potential amplitude in the temporary grounding of the current outdoor power engineering construction operation. The grounding current dispersion characteristics of the current temporary grounding device are compared and analyzed, and the optimal layout of the temporary grounding device construction in power engineering is proposed.

2 Simulation Calculation of Horizontal Dimension Dispersion Characteristics

Horizontal and vertical laying methods are generally used in outdoor power maintenance projects when temporary grounding devices are buried. Horizontal dimension and vertical dimension dispersion have great influence on the efficiency of grounding body dispersion. To compare the grounding current dispersion characteristics of vertical grounding pile and horizontal grounding cable, the horizontal grounding cable is set up in CDEGS simulation software. The grounding conductor is bare copper strand, the width is 2 cm, the thickness is 4 mm, and the length of a single horizontal grounding body is 20 m. The frequency of ground current is set to 50 Hz (mainly to simulate the working grounding under power frequency current). The soil type is uniform soil condition. In order to simulate the soil of different soils, the soil resistivity is set as 50Ω·m, 250Ω·m, 500Ω·m, 1000Ω·m and 1500Ω·m respectively. The bare copper strand is buried shallowly in the soil laying (the corresponding construction site is covered by thin soil layer), and the equivalent buried depth is 5 cm. In the simulation calculation, one, two, three and four bare copper strand grounding cable models are set respectively. The ground current is 1A and the soil resistivity is 50 ~ 1500Ω·m. The simulation of the power frequency grounding resistance of each model under different soil resistivity is shown in Table 1.

The boundary condition of soil resistivity is set to 50Ω·m in the simulation calculation model, and the amplitude of ground current is 0.5 ~ 100A. The touch voltage and step voltage of each model under different ground current are simulated and calculated as shown in Table 2.

From Table 2, it can be seen that as the amplitude of the ground current increases gradually, the step voltage increases in multiples. When the soil resistivity is 50Ω·m, the ground step voltage amplitude is 554.97 V. At this time, the step voltage exceeds the safety threshold. With the increase of the length of the grounding cable, the volume of the soil medium participating in the conduction increases significantly, and the step voltage decreases accordingly.

Table 1 Power frequency grounding resistance of horizontal grounding cable under different soil resistivity

Soil resistivity(Ω·m)	1 grounding cable	2 grounding cable	3 grounding cable	4 grounding cable
50Ω·m	3.555	2.072	1.511	1.217
250Ω·m	17.722	10.257	7.4	5.876
500Ω·m	35.43	20.487	14.76	11.7
1000Ω·m	70.847	40.947	29.48	23.346
1500Ω·m	106.263	61.408	44.201	34.993

Table 2 Step voltage of different incoming current

Type of grounding device	Step voltage/V				
	0.5A	1A	10A	50A	100A
1 grounding cable	2.78	5.55	55.50	277.49	554.97
2 grounding cable	1.54	3.07	30.72	153.59	307.18
3 grounding cable	1.09	2.18	21.82	109.10	218.19
4 grounding cable	0.94	1.87	18.70	93.50	187.00

Table 3 Power frequency grounding resistance of vertical grounding pile under different soil resistivity

Number	Grounding resistance/Ω				
	50Ω·m	250Ω·m	500Ω·m	1000Ω·m	1500Ω·m
One	38.302	191.496	382.988	765.973	1148.958
Two	22.092	107.595	213.490	424.857	636.102
Three	16.184	78.523	155.681	309.686	463.605
Four	12.997	63.003	124.895	248.438	371.914

3 Simulation Calculation of Vertical Dimension Dispersion Characteristics

Aiming at the simulation calculation of the grounding current dispersion characteristics of the traditional metal temporary vertical grounding pile, different vertical grounding pile models are established by CDEGS. Set 1 ~ 4 metal grounding pile models, the grounding current is 1A, and the soil resistivity is 50 ~ 1500Ω·m. The power frequency grounding resistance of the vertical direct ground pile under different soil resistivity are calculated as shown in Table 3.

4 Simulation Calculation of Dispersing Current Optimization of Temporary Grounding Device

In order to study the influence of different laying directions of grounding cable on the grounding characteristics of grounding cable under uniform soil resistivity, the grounding cable models in different directions are established in the simulation software. The single-direction, two-direction, three-direction and four-direction grounding cable models (vertical laying in each direction) are set, the grounding current is 1A, and the soil resistivity is 50 ~ 1500Ω·m. The power frequency grounding resistance under different soil resistivity is calculated as shown in Table 4.

According to the calculation results shown in Table 4, the power frequency grounding resistance of each model increases with the increase of soil resistivity,

Table 4 Power frequency grounding resistance of different laying directions

Type	Power frequency grounding resistance/Ω				
	50Ω·m	250Ω·m	500Ω·m	1000Ω·m	1500Ω·m
Unidirectional	3.548	17.722	35.430	70.847	106.263
Bidirectional	2.035	10.141	20.273	40.535	60.797
Three-dimensional	1.571	7.829	15.651	31.296	46.941
Four-directional	1.307	6.516	13.026	26.048	39.070

and the power frequency grounding resistance of the grounding cable laid in four directions is the smallest. By comparing the vertical and horizontal unidirectional laying methods, it can be seen that when the soil resistivity is low, there is little difference in the power frequency grounding resistance between the multi-direction laying bare copper stranded wire grounding cable and the single-direction laying bare copper stranded wire grounding cable.

Considering that power construction often faces a more complex soil environment, a non-uniform soil calculation model of soil and cement mixed is established in CDEGS. The potential distribution of grounding cables with different lengths in the soil is shown in Fig. 1.

It can be seen from the calculation results of Fig. 1 that due to the high resistivity of the cement ground, the horizontal grounding cable is directly laid on the cement ground, and its grounding resistance often reaches tens or even hundreds of ohms. At this time, even if the leakage current with a small amplitude still has an electric shock risk to the operation and maintenance personnel. In contrast, burying some horizontal grounding cables in the soil layer of cement pavement can play a significant role in reducing the resistance of grounding resistance. Further analysis of the ‘ soil–cement

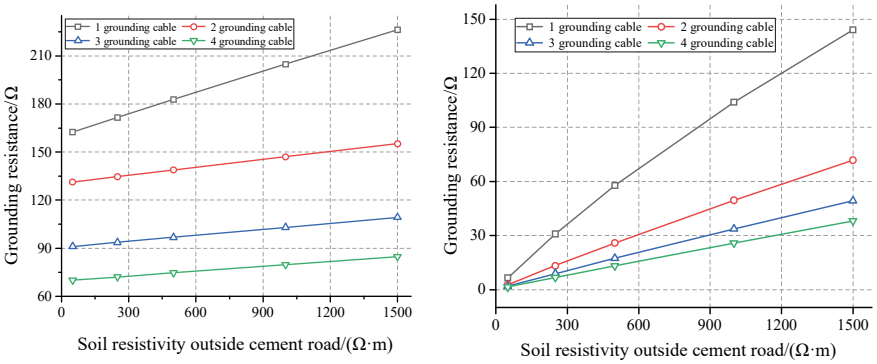

(a) Grounding resistance value under the condition of cement laying

(b) Grounding resistance value under the condition of 'soil-cement' mixed landform

Fig. 1 Calculation results of grounding resistance under mixed geomorphic conditions

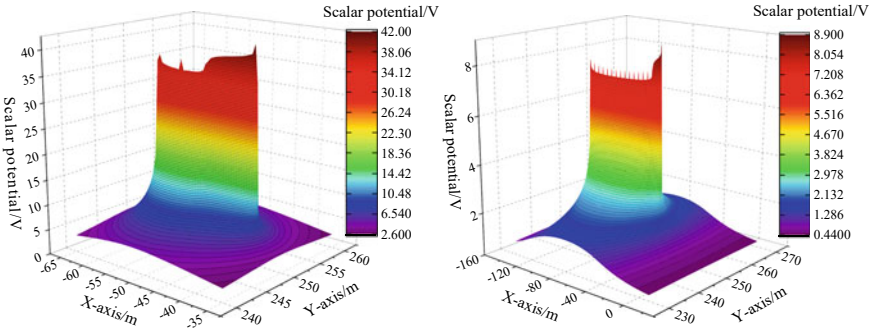

(a) Potential distribution of single grounding cable laying in soil

(b) Potential distribution of four grounding cables in soil

Fig. 2 Potential distribution in "soil–cement" mixed landform

' mixed landform conditions, the affecting law of the length of the grounding body in the low resistivity soil on the surface potential is shown in Fig. 2.

Comparing the simulation results of Fig. 2, it can be seen that the longer the grounding body laid in the soil, the higher the reduction efficiency of the ground potential. Due to the high resistivity of cement pavement, the current in the grounding cable is difficult to penetrate into the soil below the 30 cm cement medium layer, which makes the potential distribution on the pavement higher. Under the same conditions, when four grounding cables are used in the soil, the potential value at the grounding current point of the cement ground is reduced from a maximum of 42 V to 8.9 V.

5 Simulation Experiment

In order to further verify the simulation test results of grounding characteristics of different numbers of vertical grounding electrode, the open flat soil area is selected for grounding simulation test to verify the grounding resistance values of different numbers of vertical grounding bodies and their combinations. The ZC-8 ground shaking table and the Megger DET2 electronic grounding resistance tester was used to measure the 'apparent' grounding resistance Rs, and the soil resistivity ρ of the measuring site was further calculated according to Eq. (1):

$$\rho = 4\pi a R / \left(1 + \frac{2a}{\sqrt{a^2 + 4b^2}} - \frac{a}{\sqrt{a^2 + b^2}}\right) \tag{1}$$

In Eq. (1): ρ is soil resistivity (Ω·m); R is the measured resistance (Ω); a is the test electrode distance (m); b is the depth of the test electrode into the ground (m). When the depth of the test electrode into the ground b does not exceed 0.2a, it can

be assumed that $b = 0$, the calculation formula can be simplified as follows:

$$\rho = 2\pi a R \tag{2}$$

The soil resistivity measurement results under different probe spacing are shown in Table 5.

Because the soil quality of the grounding simulation test site is relatively uniform, the measurement results are in good agreement, and the measurement average soil resistivity ρ of the simulation test site is 96.76Ω·m. At the same time, according to the distribution methods shown in Fig. 3(a), the position of 1# ~ 4# vertical grounding piles is arranged. The vertical grounding piles are round steel with a length of 1.1 m (buried depth of 1.0 m) and a diameter of 24 mm, and different grounding piles are connected by wires with insulating layer.

According to the simulation results of the combination model of different numbers of temporary grounding piles in this paper, the grounding resistance values of different numbers of temporary grounding piles are measured by the three-pole method (the distance between the voltage pole and the current pole is 62 m and 100 m from the 1# vertical grounding pile respectively). The spacing d of the grounding piles is 2 m ~ 10 m, and the soil resistivity measurement results under different probe spacing are shown in Table 6 and Table 7.

From the R_j measurement results of different numbers of grounding piles shown in Table 6, it can be seen that when the number of grounding bodies increases, the overall grounding resistance of temporary vertical grounding piles decreases significantly, and the decrease tends to be moderate. From the measurement results of R_j of grounding piles with different spacing in Table 7, it can be seen that when the number of vertical grounding piles is fixed, increasing the spacing of vertical grounding piles is beneficial to reduce the grounding resistance value, and with the increase of the spacing of grounding piles, the shielding effect between adjacent grounding bodies decreases, which is beneficial to the balanced current dispersion of grounding bodies and improves the current dispersion efficiency of each grounding pile.

Table 5 Measurement results of soil resistivity ρ at different probe spacing

Wiring direction	Probe spacing(m)				
	5	10	15	20	25
Direction A	2.74	1.40	0.99	0.72	0.57
Direction B	2.90	1.48	1.05	0.75	0.59
Direction C	3.32	1.67	1.18	0.86	0.67
R_s average value	2.98	1.52	1.08	0.78	0.61
ρ average val-ue	93.68	95.31	101.34	97.56	95.93

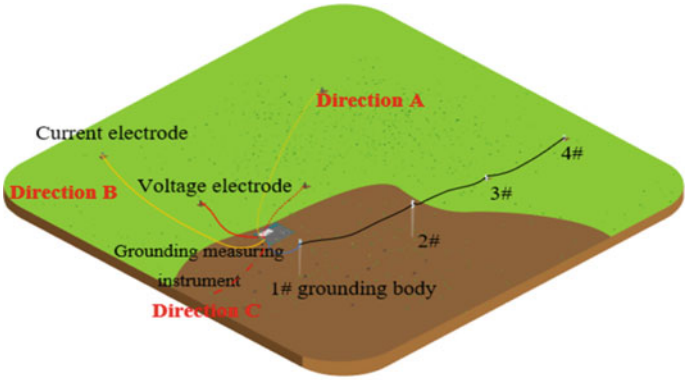

(a) Vertical grounding pile distribution

(b) Grounding simulation test layout

Fig. 3 Simulation test of different number of temporary grounding piles

Table 6 Measurement results of different number of grounding piles R_j (Ω, $d = 2$ m)

grounding mode	Direction A	Direction B	Direction C	Average value
1#	65.2	68.4	71.2	68.27
1# ~ 2#	37.8	39.6	41.2	39.55
1# ~ 2# ~ 3#	28.0	29.5	31.0	29.51
1# ~ 2# ~ 3# ~ 4#	22.2	23.2	24.1	23.15

Table 7 Measurement results of grounding pile R_j with different spacing (Ω, $N = 4$)

Measurement solutions	Grounding pile spacing (m)				
	2	4	6	8	10
Direction A	22.2	14.7	12.0	9.6	7.7
Direction B	24.5	15.5	12.1	10.2	7.9
Direction C	24.7	16.1	12.9	10.8	8.4
R_j Average value	23.79	15.44	12.33	10.18	8.02

6 Conclusion

This paper analyzes the dispersing characteristics of the temporary grounding device in the power engineering construction operation, and puts forward the optimal arrangement of the temporary grounding construction. The conclusions include:

1) When the temporary grounding device uses bare copper stranded wire for grounding dispersion in the horizontal dimension, the grounding resistance decreases with the increase of the length of the grounding cable. The common vertical grounding pile has low current dissipation efficiency. When the leakage current amplitude of the temporary power supply system is high, the risk of electric shock caused by the ground surface potential is high, which should be used in conjunction with the horizontal grounding cable.
2) When the horizontal grounding cable is laid in multiple directions, the grounding current divergence density is more uniform and the ground surface potential gradient is lower, which is beneficial to improve the grounding safety. When the construction point is located in the mixed landform of cement pavement and soil, the laying length of the grounding body should be reasonably arranged, and the horizontal grounding cable body in the soil has higher dispersion efficiency, which is more conducive to reducing the electric shock risk of construction workers.
3) The grounding simulation test verifies that the combination of multiple vertical grounding piles in power engineering is beneficial to reduce the grounding resistance. The grounding resistance value is related to the soil resistivity of the construction point, the number of grounding bodies and the arrangement mode.

Acknowledgements This work is supported by Technology project of Hangzhou Electric Power Equipment Manufacturing Co., LTD(XJZYY-2021089).

References

1. Zhou N, Zhang S, Wang X (2021) Comprehensive Safety Check Analysis of Substation Grounding Grid. Insulators and Surge Arresters 03:119–124 (in Chinese)
2. IEEE Guide for Temporary Protective Grounding Systems Used in Substations," in IEEE Std 1246–2020 (Revision of IEEE Std 1246–2011) , vol., no., pp.1–70, 19 Feb. 2021.
3. B. Rittong and S. Sirisumrannukul, ", Assessment of Voltage Sag and Temporary Overvoltage for Neutral Grounding Resistance in Distribution System,, " (2019) IEEE PES GTD Grand International Conference and Exposition Asia (GTD Asia). Bangkok, Thailand 2019:796–801
4. Chen K, Sun C, Tang Y.: Research on neutral grounding mode and technology of leakage protection in mine low-voltage electric network. Power System Protection and Control 2010. (in Chinese)
5. X. Li, J. Zhang, J. Song and X. Han, "Design of security management system based on RFID temporary grounding wire borrowing," 2019 IEEE 3rd Advanced Information Management, Communicates, Electronic and Automation Control Conference (IMCEC), Chongqing, China, 2019, pp 832–836

6. A. B. Poda, C. M. Riley, J. Perkel, R. N. Hampton, S. Patel and T. Lancaster, “A Simulation Model to Analyze Current Split Distribution of Multiple Temporary Protective Grounds (TPGs),” 2019 IEEE Power & Energy Society General Meeting (PESGM), Atlanta, GA, USA, 2019, pp 1–5
7. Yu M, Wang K, Zhou F.: Step Voltage Test and Simulation for 10 kV Distribution Grid Based on Artificial Short-circuit. High Voltage Apparatus 53(02), 147–153 (2017). (in Chinese)
8. Ma Y, Wang K, Zhou F. Step Voltage Test and Simulation for 10 kV Distribution Grid Based on Artificial Short-circuit[J]. High Voltage Apparatus, 2017,53(02):147-153. (in Chinese)
9. Hu X, Zhang L (2017) Development of a New Type of Power Short Grounding Wire for Preventing Misoperation. Journal of Shanghai University of Electric Power 33(5):430–433 (in Chinese)
10. Wang X, Dong X, Li W.: Study on Personal Safety Factors Related to Wind Farm Grounding System. Insulators and Surge Arresters 04, 1–8+25 (2022). (in Chinese)
11. Xiong W, Mao X, Li J (2019) Influence of small resistance grounding mode on personal safety and research of intelligent resistance grounding mode. Power System Protection and Control 47(14):166–172 (in Chinese)

Study on Lightning Dispersion and Breakdown Protection of Corrosion Protection Layer in Soil Adjacent to Buried Metal Pipeline

Xiaole Su, Xianqin Qiao, Wei Liu, Zhipeng Jiang, Can Qiu, Jie Xiong, and Ju Sun

Abstract Transmission lines in the vicinity of natural gas pipelines are vulnerable to lightning strikes during operation. High amplitude lightning currents expose buried natural gas pipelines to shock potentials of a certain amplitude. In this paper, the safety protection of the intersection of natural gas pipelines and power lines has attracted extensive attention. This paper uses ATP-EMTP software to calculate the characteristics of the current waveform and the influencing factors of the pylons near the natural gas pipeline, establishes a three-dimensional finite element model of the pressure resistance of the natural gas pipeline electrode and the anticorrosion layer, and illustrates the mechanism of the generation of the difference between the pipeline electrode potential and the anticorrosion layer potential. Secondly, the effects of lightning current amplitude, soil conditions and pipeline distance on the impact potential of natural gas pipelines are analysed through simulations, and a lightning impact protection method for natural gas pipelines based on the vertical dimensional scattered current of piles is proposed. Finally, the practical application effect and technical economy are verified through simulation examples and engineering application simulation tests. The conclusions of this paper can provide references for the design, construction and safe operation and maintenance of natural gas pipelines.

Keywords Natural gas pipelines · Adjacent crossings · Lightning strikes · Corrosion protection · Pipeline protection

X. Su · W. Liu · Z. Jiang · C. Qiu · J. Xiong · J. Sun
State Grid Hubei Power Supply Limited Company Ezhou Power Supply Company, Ezhou 436000, China

X. Qiao (✉)
Electrical and Electronic Engineering College, Shandong University of Technology, Zibo 255000, China
e-mail: qiao19980821@163.com

© Beijing Paike Culture Commu. Co., Ltd. 2024

X. Dong and L. Cai (eds.), *The Proceedings of 2023 4th International Symposium on Insulation and Discharge Computation for Power Equipment (IDCOMPU2023)*, Lecture Notes in Electrical Engineering 1102, https://doi.org/10.1007/978-981-99-7405-4_2

1 Introduction

As international demand for natural gas resources becomes more pressing, natural gas energy and electricity are becoming important factors in the international situation. Inevitably, electricity and natural gas transmission lines are faced with proximity and cross-over conditions in the form of "two lines, one place". Both the power and natural gas industries are paying more and more attention to the safe and stable operation of the two energy transmission lines in the case of "two lines and one place" crossings [1]. There are significant differences between the existing power transmission and distribution lines and natural gas energy transmission, with the former mainly using an overhead line structure in non-urban areas, while natural gas pipelines are usually buried in the underground soil. Both the power and natural gas industries are paying more attention to the safe and stable operation of the two types of energy transmission lines in the case of "two lines and a place" crossing each other [2, 3]. Some EMC protection measures have been applied on a pilot basis in the "two lines, one ground" cross-adjacent project. In addition to the impact of power lines on gas pipelines under normal operating conditions, some studies have found that incoming currents along towers after lightning strikes on power lines may create some risk of overvoltage to adjacent pipelines. Nagat et al. [4] used the ATP program to calculate the induced voltage of pipelines under normal and fault conditions and proposed a grounding system to suppress the induced voltage, and verified the effectiveness of this measure through tests. Amauri et al. [5] developed a transient circuit model based on frequency-dependent parameters for predicting the transient electromagnetic disturbance effects caused by lightning strikes. Ossama et al. [6] calculated the induced voltage of the pipe in a MATLAB program based on the "Distributed Source Analysis" method, and the calculated results were in good agreement with the actual measured induced voltage. The paper [7] used software to simulate the situation when a 500 km 1000 kV double transmission line with the same tower was struck by lightning, and verified the characteristics of the pipeline overvoltage distribution at a "tower-line" spacing of 50 m for a 100 kA lightning current striking the tower through simulation. The literature [8] suggests that the protective measures of installing drainage strips and changing the structure of the tower grounding device can reduce the lightning overvoltage of the pipeline corrosion layer. Huang Wanli et al. conducted theoretical calculations for the transient potential of the Haixi-Tala 750 kV transmission line in the Ulan section and the adjacent buried natural gas pipeline [9], where the pipeline potential reached 4.3 kV for a single-phase ground fault and 12.9 kV for a broken line ground fault. In, literature [10] analysed the potential risk of pipeline lightning strikes in the case of "two lines and one ground" crossed and adjacent to each other by using the simulation software CDEGS to analyse the soil resistivity frequency variation characteristics. but from a practical engineering application point of view the method requires a large amount of excavation and backfilling works. The above research shows that in order to avoid the problem of lightning overvoltage in the case of power lines and natural gas pipelines

"two lines and one ground" crossed adjacent to each other, the natural gas industry and the power sector have high application value.

This paper analyses the mechanism and influencing factors of natural gas pipeline overvoltage through simulation modelling, which can provide theoretical reference for the maintenance of the actual natural gas pipeline corrosion layer.

2 Lightning Strike Dispersion Modelling and Calculation

High-voltage overhead lines in power systems are often set up with a single or double lightning line to prevent the natural connection of lightning clouds bypassing the lightning line to discharge the overhead conductors. Lightning flow shunt process as shown in Fig. 1, Ib1 and Ib2 for both sides of the lightning line shunt lightning flow component, Ia is hit by the tower tower and its grounding device installed to shunt the lightning flow component.

Power lines adjacent to the natural gas pipeline corrosion layer overvoltage protection in addition to the normal operation of the line coupling voltage, the main concern along the tower into the soil of lightning current on the impact of overvoltage potential. In order to quantitatively analyse the influence of direct lightning on the pipeline overvoltage of the neighbouring power line, the ATP-EMTP electromagnetic transient analysis software, which is commonly used in the power industry, is used to establish a simulation model of lightning overvoltage in the case of power lines and natural gas pipelines “two lines and one ground” crossed and adjacent to each other.

3 Simulation Models and Parameters

Considering that the grounding resistance of towers in the power industry is generally maintained within 10 Ω and the proportion of lightning line shunt is small, the study generally considers that the resistive coupling component in the case of lightning strikes is the main factor.

This paper uses COMSOL Multiphysics finite element simulation software to establish a model for calculating the lightning overvoltage in the case of a power line and a natural gas pipeline with "two lines and a ground" crossed and adjacent to each other as shown in Fig. 2. The finite element simulation can calculate the potential, current and electric field components at any point in the soil medium, and can solve for the withstand voltage on the pipeline grid and the insulation and corrosion layer. In the simulation model, the distance between the tower and the gas pipeline is taken as $d_{pg1} = 40$ m, and the vertical distance between the extension end of the Φ12 mm galvanised steel grounding grid and the pipeline is d_{pg2}. The standard lightning current waveform with a wavefront and half-wave duration of 2.6/50 μs recommended by the power industry test regulations is used, and the standard lightning current double exponential function waveform is created in COMSOL

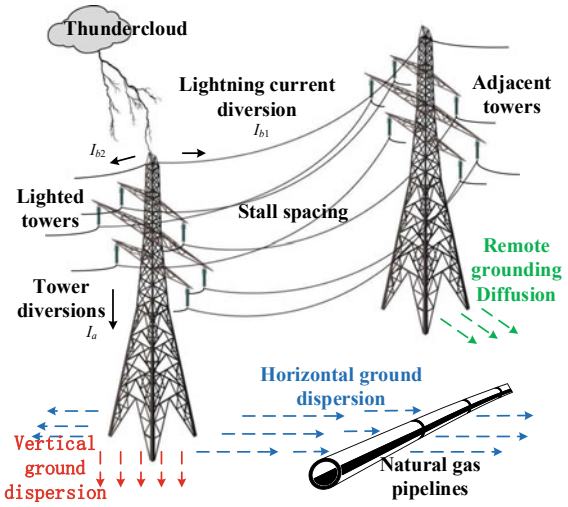

(a) Lightning current dissipation paths

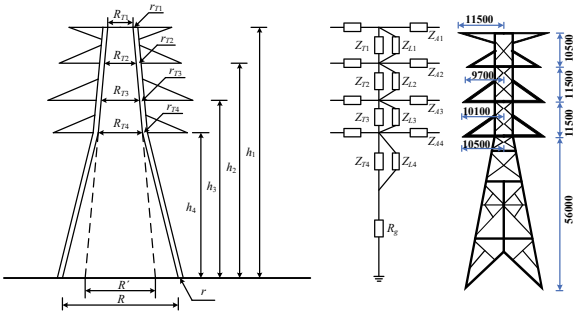

(b) ATP-EMTP tower calculation model and parameters

Fig. 1 Power line lightning dispersion with calculated parameters

Multiphysics software as follows

$$i(t) = 1.0474 I_{\mathrm{m}}\left(e^{-14790.18t} - e^{-1877833t}\right) \tag{1}$$

In addition, according to the general construction specification of electric power and natural gas pipeline, the simulation set pole tower galvanized steel grounding conductor and the burial depth of the pipeline are taken as 0.8 m and 1.5 m respectively, the edge and extension of the grounding grid are taken as $l_{\mathrm{g1}} = 16$ m, $l_{\mathrm{g2}} = 20$ m, respectively. The length of the pipe l_{p} is 500 m, the outer diameter Φ530 mm, the wall thickness of the pipe 13 mm. The pipe anticorrosion layer is 3 layers of polyethylene material (3LPE), the thickness of the insulation anticorrosion layer is taken as 3 mm, the surface resistivity ρ_{F} is 10^5 Ω-m. The potential distribution characteristics of the adjacent natural gas pipeline and the influence law can be obtained through simulation calculation.

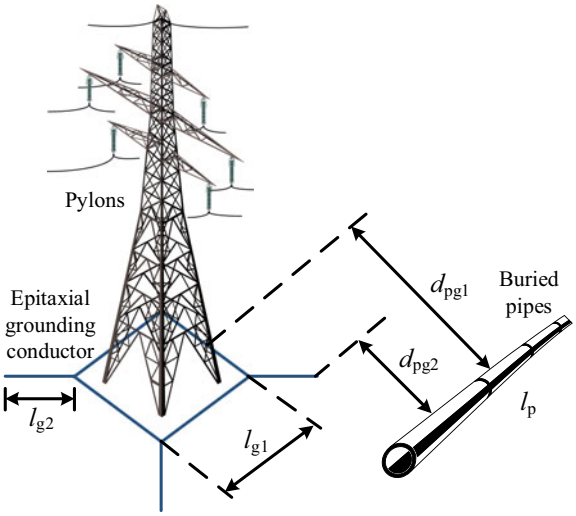

Fig. 2 Finite element calculation model for "two lines and a ground"

4 Soil Vertical Dispersion Optimization

In this paper, we propose a method to optimise the grounding and dispersion structure of the spiral pile base, to ensure that the effective grounding and dispersion of the tower and the grounding resistance of the tower do not exceed the limit, to significantly reduce the dispersion of the natural gas pipeline side, and to reduce the withstand voltage value of the pipeline body and the anti-corrosion layer, the basic structure of which is shown in Fig. 3.

The horizontal structure of the pole tower earthing network in Fig. 3a is the same as in Fig. 2, with the difference being the addition of a spiral earthing structure

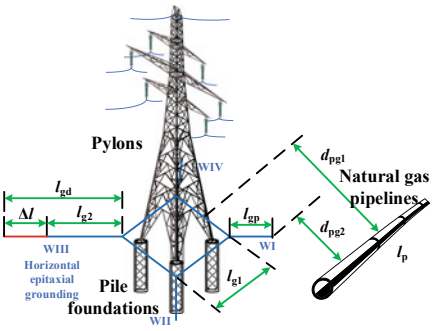

(a) Horizontal and vertical grounding grid simulation parameters

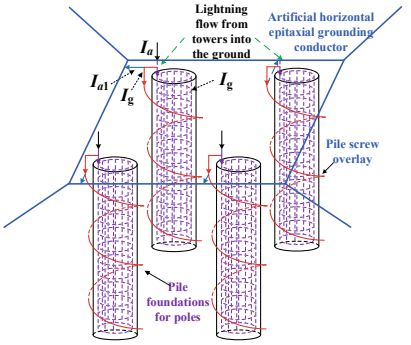

(b) Horizontal and vertical grounded diffusion structures for towers

Fig. 3 Schematic diagram of the epitaxial grounding grid renewal

on the outside of the concrete pile base of the pole tower, which can be made of conventional galvanised steel, copper-clad steel metal material or flexible graphite composite earthing material, of which the latter is easier to spiral lay due to its flexible material properties. The purpose of using a spiral structure is to increase the effective current dispersion volume of the earthing grid in the vertical dimension, with the steel skeleton within the pile base encapsulated in the concrete medium acting as a lesser grounding dispersion. The lightning current I_a in Fig. 8 is dispersed to the soil medium by the grounding grid at three locations: the horizontal component of the boxed extended ray grounding grid I_{a1} in the horizontal dimension, the component of the reinforcement skeleton I_t in the vertical dimension and the component of the external spiral grounding grid I_g in the vertical dimension. The "diversion" effect on the adjacent gas pipeline varies accordingly. It is envisaged that increasing the I_t and I_g components in the vertical dimension will reduce the amplitude of the lightning current on the adjacent gas pipeline.

In order to analyse the effect and influence factors of the external material of the concrete pile foundation of the pole tower, consistent with Fig. 2 and the horizontal grounding dispersion calculation model, the incoming mine current component amplitude is 60 kA, the length of the box grounding grid $l_{g1} = 15$ m, the length of the external grounding grid l_{g2} is 10 m. In the four pile pits of the pole tower are single column pile foundation, the height of a single pile foundation is 15 m, the radius is 0.6 m, the concrete resistivity is 1×10^4 Ω-m. Simulations were carried out for the full pile foundation, the upper 2/3 of the pile foundation and the upper 1/3 of the pile foundation in turn, and compared with the case without external application. The effect of the external application area of the spiral vertical grounding grid on the current density in the vertical dimension of the soil for a soil resistivity ρ of 500 Ω-m is shown in Fig. 4.

By the current density distribution can be seen, pile foundation external grounding grid current density is much higher than the concrete pile foundation reinforcement skeleton dissipation density, and with the increase of external material, spiral grounding grid dissipation effect is more obvious, external spiral grounding grid can effectively solve the concrete resistivity is too high, steel can not through the concrete

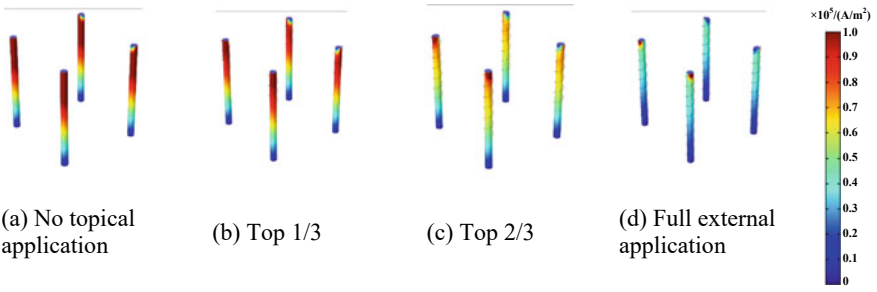

Fig. 4 Effect of external area on current density distribution

medium dissipation problem, which for reducing the lightning current component on the adjacent natural gas pipeline play a better This is a good “shunting” effect.

5 Conclusion

The main findings of the study on the formation mechanism and protection strategies for lightning overvoltages in natural gas pipelines adjacent to power lines include: (1) pipe adjacent to the tower lightning strike through the tower tower and double side lightning line dispersion, the smaller the tower gear distance and grounding resistance shunt coefficient is greater.

natural gas pipeline adjacent to the tower pile steel conductor is limited by the concrete resistivity and small dissipation density, the use of pile spiral external grounding structure can increase the vertical dimension of the dissipation density, reduce the power line in the pipeline side of the lightning strike dissipation component, can take into account the power line lightning trip and pipeline overvoltage impact potential over the limit, reduce the amount of land acquisition and construction work.

The findings of this paper can provide a reference for the design, selection of materials and safe and protective operation of power lines and natural gas pipelines.

Acknowledgements This work is supported by State Grid Hubei Electric Power Co., LTD. Science and Technology Project (5215F0220001/SGHBEZ00FCJS2200282/3).

References

1. LI R.: Study on the Safety Impact of Transmission Line on Oil and Gas Pipeline Operation Based on CDEGS. Insulators and Surge Arresters, 2020(05):171–175. (in Chinese)
2. WU b.: Influence of AC Drainage Facility on Cathodic Protection Power Switch-Off Potential Test Results of Buried Pipeline. Corrosion and Protection, 2022,43(09):88–92. (in Chinese)
3. Lucca G (2020) AC interference from a faulty power line on nearby buried pipelines: influence of the surface layer soil. IET Sci Meas Technol 14(2):225–232
4. Nagat MK, Dein EAZ, Mohamed M (2015) Mitigation of induced voltages and AC corrosion effects on buried gas pipeline near to OHTL under normal and fault conditions. Electric Power Systems Research 127:297–306
5. Amauri GMB, Caio MM, Felipe VL (2021) Transient electromagnetic interferences between a power line and a pipeline due to a lightning discharge: An EMTP-based approach. Electric Power Systems Research 197:107321
6. Ossama EG, Dein EAZ, Mostafa AHEG (2013) Effect of electromagnetic field of overhead transmission lines on the metallic gas pipe-lines. Electric Power Systems Research 103:129–136
7. WAN B Q, XIE C H, ZHANG X W, WU X and FAN L.: Influence of lightning strike to UHV AC double-circuit tower on oil or gas pipelines. High Voltage Engineering, 2009, 35(8): 1812–1817. (in Chinese)

8. WANG X Y, AN Y Z, HU Y C, XIANG Z, HUANG T and HUANG S J.: Protection Effect of Oil and Gas Pipeline Insulation Layer Based on Low-Inductive Graphite Composite Grounding Material. Corrosion and Protection, 2022,43(04):33–39. (in Chinese)
9. Huang WL, Zhou SH, Sun CM, Mo BY, Han ML, Kang J et al (2021) Research on Electromagnetic Interference of AC Transmission Line to Adjacent Buried Pipeline Under Transient States. Proceedings of the CSEE 41(S1):275–285 (in Chinese)
10. Kou XS, Li C, Li YJ, Wen XS, Lu HL, Zhang K et al (2022) Influencing Factors and Protective Measures of Induced Voltage of Buried Pipeline When Lightning Strikes Transmission Tower. Insulators and Surge Arresters 04:99–105 (in Chinese)

Study on Dispersion Characteristics and Drag Reduction Efficiency of Transmission Line Tower Fractal Epitaxial Grounding

Qihao Liu, Jianfei Yang, Chao Zhang, Daohuan Liu, Ningxin Wang, Chenglong Cao, and Jungan Zhang

Abstract Reducing the grounding resistance of transmission line tower is helpful to reduce lightning trip and ensure the safe operation of power system. In response to the problems of difficult construction and high grounding resistance in traditional grounding grid forms in mountainous and complex terrain areas, fractal theory is introduced to propose a resistance reduction scheme for laying fractal epitaxial grounding grids on transmission line towers. The finite element simulation software is used to establish the fractal epitaxial grounding grid model with flexible graphite as the material. The effects of angle, fractal dimension, fractal layers on its grounding characteristics are studied. Then various typical epitaxial grounding grid models were established and the grounding characteristics were compared. The calculation results show that proper angle, lower fractal dimension and lower fractal layers are helpful to improve the grounding resistance reduction effect of fractal epitaxial grounding grid, and the resistance reduction effect shows different trends with the change of soil resistivity. The proposed fractal epitaxial grounding grid laying scheme can provide a reference for the design of transmission line tower grounding grids in mountainous areas and other areas with high difficulty in traditional epitaxial grounding grid laying.

Keywords Grounding grid · Fractal theory · Flexible graphite · Fractal dimension · Grounding resistance

Q. Liu · C. Zhang · D. Liu · N. Wang · C. Cao · J. Zhang
State Grid Huantai Power Supply Company, Shandong Electric Power Corporation, Zibo 255000, China
e-mail: 519371920@qq.com

J. Yang (✉)
School of Electrical and Electronic Engineering, Shandong University of Technology, Zibo 255000, China
e-mail: yangjf5277@163.com

© Beijing Paike Culture Commu. Co., Ltd. 2024

X. Dong and L. Cai (eds.), *The Proceedings of 2023 4th International Symposium on Insulation and Discharge Computation for Power Equipment (IDCOMPU2023)*, Lecture Notes in Electrical Engineering 1102, https://doi.org/10.1007/978-981-99-7405-4_3

1 Introduction

Lightning strikes are the main cause of tripping accidents on transmission lines, which have adverse effects on the safe and stable operation of the power system. The grounding device aims to reduce the grounding resistance of the tower, reduce the increase in grounding potential, and protect personal and equipment safety by timely dispersing lightning current to the ground [1]. As a result, the research on grounding schemes for transmission line towers is of great significance.

At present, the research of reducing grounding resistance of grounding grid mainly focuses on the study of grounding grid forms and grounding materials [2–5]. Flexible graphite grounding materials with good corrosion resistance, flexibility and conductivity have been developed and widely employed in recent years [6–8]. In view of the problem of resistance reduction of transmission line tower grounding grid, this paper proposes a fractal epitaxial grounding grid based on flexible graphite material, and studies the influence of angle, fractal dimension, and fractal layer factors on the grounding grid drag reduction efficiency and dispersion characteristics, providing relevant reference for the design and construction of tower grounding grid under complex terrain conditions.

2 Fractal Theory and Model Establishment

2.1 Fractal Theory

The spatial structure of traditional geometry has a high degree of symmetry, while nature has a large number of complex shapes and structures that cannot be described through traditional geometry, such as river branches and lightning shapes. The theory of fractal geometry helps to describe these complex phenomena. Fractal is a geometric form that is similar to the whole in some form, has scale invariance and self-similarity [9]. Therefore, fractal geometry is a large class of irregular or unsmooth sets and functions that can not be described by traditional Euclidean geometric methods and calculus methods [10]. At present, fractal theory has been widely applied in fields such as engineering technology and natural sciences [11, 12]. In order to express the self-similarity of fractals, an important concept in fractal geometry is called dimension. For example, increasing the length of each side of a cube by 3 times results in a large cube that is comparable to 3^3 original little cubes. If the fractal dimension is D and a figure is transformed by l times, N figures similar to the original figure can be obtained, then Formula (1) can be obtained:

$$N = l^D \tag{1}$$

Formula (1) can be used to calculate the fractal dimension D, as illustrated in Formula (2):

$$D = \frac{\ln N}{\ln l} \tag{2}$$

Note that for fractal geometry, the fractal dimension D is not limited to integers.

2.2 Model Establishment

To study the influence of different factors on the performance of dispersion characteristics and drag reduction efficiency of fractal epitaxial grounding grid, the simulation model of fractal epitaxial grounding grid for transmission line towers with different layers was established in finite element simulation software. The grounding material is made of flexible graphite, with a diameter of 28 mm and a resistivity of 3.25×10^{-5} Ω m, with a relative permeability of 1. The main grounding grid has a side length of $l = 12$ m, a down lead length of $h = 0.8$ m, a buried depth of 0.8 m, and a total epitaxial lead length of 120 m. For fractal epitaxial grounding grids with different layers, the main epitaxial length is denoted as L_0, the first layer fractal epitaxial lead length is denoted as $L_1^{(i)}$ (i = 1, 2), the second layer fractal epitaxial lead length is denoted as $L_2^{(i)}$ (i = 1, 2, 3, 4), and the third layer fractal epitaxial lead length is denoted as $L_3^{(i)}$ (i = 1, … , 8). The fractal angles of each layer are α.The structure of fractal epitaxial grounding grid models with different layers is shown in Fig. 1.

As indicated in Formula (3), a 2.6/50 μs standard lightning current with an amplitude of 10 kA is injected into grounding grid, and the lightning current function uses the double exponential function model expression [13].

$$I(t) = 11{,}157 \times (e^{-15{,}900t} - \mathrm{e}^{-712{,}000t}) \tag{3}$$

In Formula (3): I is the equivalent value of lightning current, A; t is the time, μs. Considering soil spark discharge, the time-varying soil resistivity should vary with the intensity of the electric field [14, 15].

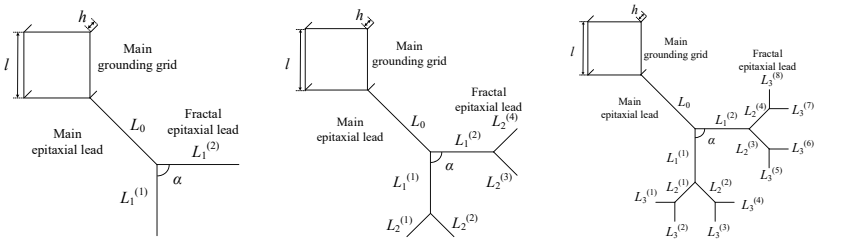

(a) One layer fractal epitaxial grounding grid (b) Two layers fractal epitaxial grounding grid (c) Three layers fractal epitaxial grounding grid

Fig. 1 Fractal epitaxial grounding grid model structure with different layers

3 Calculation and Analysis of Grounding Characteristics of Fractal Epitaxial Grounding Grid

3.1 The Influence of Angle on Grounding Characteristics

As shown in Formula (4), the total current I_z flowing into the grounding grid and the current I_{wy} flowing into the epitaxial lead are defined as the shunt coefficient η to characterize the influence of different factors on the dispersion characteristics of fractal epitaxial grounding grid.

$$\eta = \frac{I_{wy}}{I_z} \times 100\% \tag{4}$$

In Formula (4), I_z is the total current injected into the transmission line tower grounding grid, A; I_{wy} is the current flowing into the epitaxial lead, A.

We have established a grounding grid as shown in Fig. 1a. We set $L_0 = 60$ m, ${L_1}^{(1)} = {L_1}^{(2)} = 30$ m, so the total length is 120 m. Set the angles α as 30°, 60°, 90°, 120°, 150°, and 180°. At the same time, the initial soil resistivity ρ_0 was set to vary between 200 and 1800 Ω m. The percentage decrease in grounding resistance of a quadrilateral grounding grid with epitaxial leads compared to a quadrilateral grounding grid without epitaxial leads is called drag reduction efficiency. The drag reduction efficiency and shunt coefficient of grounding grid at different angles is obtained by simulation calculation, as shown in Fig. 2.

It can be seen from Fig. 2a that the drag reduction efficiency exhibits a tendency of initially increasing and then decreasing as the angle increases due to the influence of the shielding effect when the soil resistivity remains constant. It can be seen from Fig. 2b that as the soil resistivity increases, the shunt coefficient of the grounding grid under different fractal angles increases gradually and tends to be flat. Under the

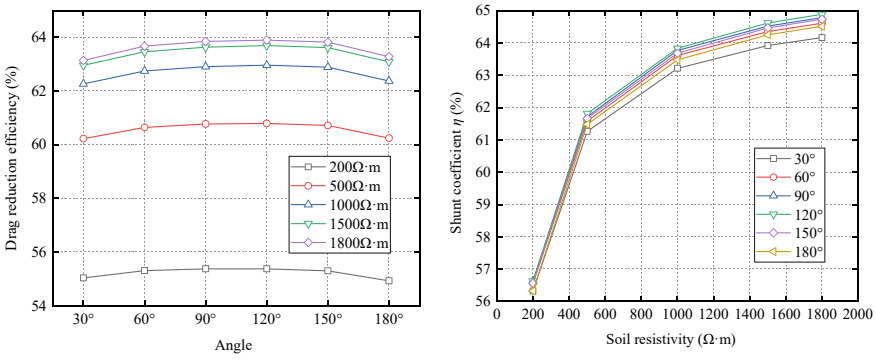

(a) Drag reduction efficiency (b) Shunt coefficient

Fig. 2 Drag reduction efficiency and shunt coefficient under different angle conditions

same soil resistivity, the shunt coefficient of the fractal epitaxial grounding grid first increases and then decreases with the increase of the angle. As the angle increases, the shielding effect decreases gradually. When the angle reaches 120°, the shunt coefficient is the largest, at this time the shielding effect is the smallest, and the grounding electrode has the best dispersion effect. As the angle continues to increase, due to the enhanced shielding effect between the main epitaxial lead L_0 and the fractal epitaxial leads $L_1{}^{(1)}$ and $L_1{}^{(2)}$, the shunt coefficient of the grounding electrode decreases gradually.

3.2 *The Influence of Fractal Dimension on Grounding Characteristics*

In order to study the influence of different fractal dimensions on the grounding characteristics of the fractal epitaxial grounding grid, fractal epitaxial grounding grid models as shown in Fig. 1b were established in the finite element simulation software. Each fractal obtains 2 graphics similar to the original graphics, and the length of the epitaxial lead of each layer of fractal is 1/R of the length of the epitaxial lead of the previous layer of fractal, that is:

$$\frac{L_0}{L_1^{(1)}} = \frac{L_0}{L_1^{(2)}} = \frac{L_1^{(1)}}{L_2^{(1)}} = \frac{L_1^{(1)}}{L_2^{(2)}} = \frac{L_1^{(2)}}{L_2^{(3)}} = \frac{L_1^{(2)}}{L_2^{(4)}} = R \tag{5}$$

Define the fractal dimension as D, then the fractal dimension D is as follows:

$$D = \frac{\ln 2}{\ln R} \tag{6}$$

The total length of the epitaxial lead is set to be 120 m, and the angle α of each layer is 90°. Taking R as 2, 3, 4, 5 respectively, the corresponding fractal dimensions D are 1, 0.631, 0.5, 0.431 respectively. Under the condition that the initial soil resistivity ρ_0 is 200–1800 Ω m, the drag reduction efficiency and shunt coefficient of the fractal epitaxial grounding grid is calculated respectively, as shown in Fig. 3.

It can be seen from Fig. 3a that when the soil resistivity exceeds 500 Ω m, the drag reduction efficiency gradually increases with the decrease of the fractal dimension, and the drag reduction efficiency is the highest when the fractal dimension is 0.431. When the soil resistivity is 1800 Ω m, the drag reduction efficiency is 63.97% under the condition of fractal dimension 0.431. It can be seen from Fig. 3b that under the condition of high soil resistivity, the fractal epitaxial grounding grid with a fractal dimension of 0.431 has the best shunting effect. When the soil resistivity is 1800 Ω m, The maximum shunt coefficient is 64.82%. For areas with high soil resistivity, the fractal dimension of the fractal epitaxial grounding grid should be appropriately reduced to improve the effect of dispersing and reducing resistance of the grounding electrode.

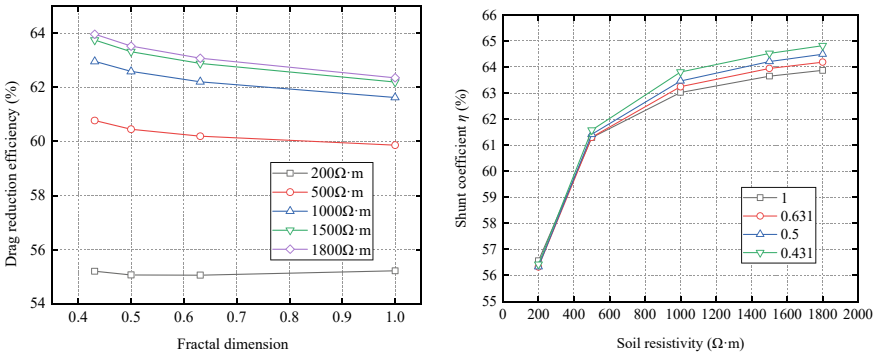

(a) Drag reduction efficiency (b) Shunt coefficient

Fig. 3 Drag reduction efficiency and shunt coefficient under different fractal dimensions

3.3 The Influence of Fractal Layers on Grounding Characteristics

To study the effect of the number of layers on the fractal epitaxial grounding grid, we have established one layer, two layers, and three layers fractal epitaxial grounding grid models, as shown in Fig. 1a–c. The total length of the epitaxial leads is 120 m, the angle α is 90°, and the fractal dimension D is 0.5. When the initial soil resistivity ρ_0 is 200, 500, 1000, 1500, 1800 Ω m, the drag reduction efficiency and shunt coefficient is shown in Fig. 4.

As shown in Fig. 4a when the soil resistivity is constant, the drag reduction efficiency gradually declines as the number of fractal layers rises. When the number of fractal layers is high, the shielding effect between the grounding electrodes increases, so the drag reduction efficiency gradually decreases with the increase of the number of

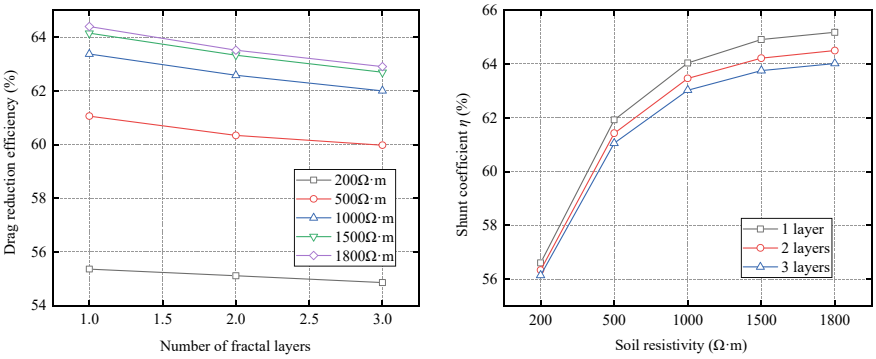

(a) Drag reduction efficiency (b) Shunt coefficient

Fig. 4 Drag reduction efficiency and shunt coefficient under different fractal layers

fractal layers. It can be seen from Fig. 4b that under the same soil resistivity condition, the shunt coefficient of the fractal epitaxial grounding grid decreases gradually with the increase of the number of fractal epitaxial lead layers. With the increase of soil resistivity, the divergence of shunt coefficient between different fractal layers grounding grid gradually increases.

4 Comparison Between Fractal Epitaxial Grounding Grid and Typical Grounding Grid

In this section, different transmission line tower grounding grid models were established. They are respectively named as quadrilateral with four corner epitaxia lead grounding grid, quadrilateral with single epitaxia lead and needle structure grounding grid, and quadrilateral with four corner epitaxia lead and needle structure grounding grid, and are denoted as forms I, II, and III, as shown in Fig. 5a–c. Their grounding resistances are denoted as R_{I}, R_{II} and R_{III}, respectively. At the same time, a binary tree fractal epitaxial grounding grid model with 2 layers was established. It is recorded as form IV, as shown in Fig. 5d, and its grounding resistance is recorded as R_{IV}. The parameters of the main grounding grid are the same as those of the grounding grid in Fig. 1. For the form I grounding grid, $L = 30$ m. For the form II grounding grid, $L = 60$ m, $L_{\mathrm{zc}} = 4$ m and $d = 3.75$ m. For the form III grounding grid, $L = 20$ m, $L_{\mathrm{zc}} = 2.5$ m and $d = 4$ m. For the form IV fractal epitaxial grounding grid, the angles α are all 90°, the number of fractal layers is 2, the fractal dimension is 0.387. The total length of the epitaxial leads of all grounding grids is 120 m.

The drag reduction efficiency of each grounding grid under different epitaxial lead forms is shown in Fig. 6 through simulation calculation.

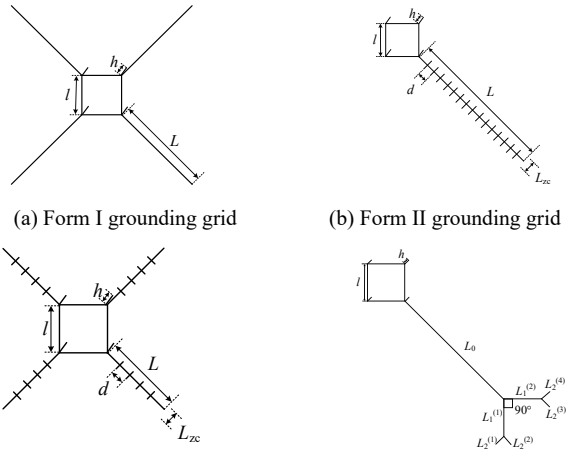

(a) Form I grounding grid

(b) Form II grounding grid

(c) Form III grounding grid

(d) Form IV grounding grid

Fig. 5 Schematic diagram of the grounding grid under different epitaxial lead forms

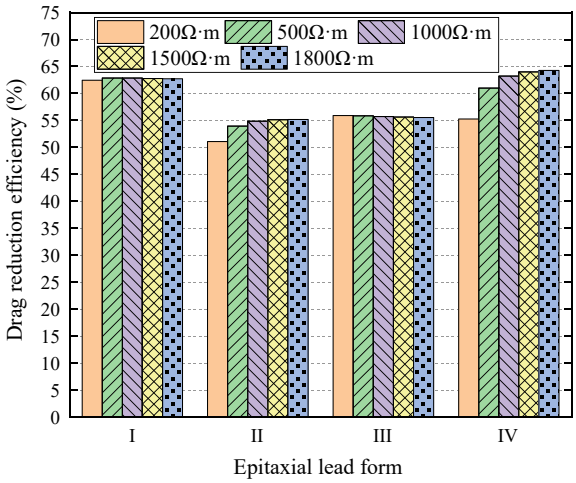

Fig. 6 Drag reduction efficiency under different epitaxial lead forms

As can be seen from the calculation results in Fig. 6, for form IV fractal epitaxial grounding grid, when the soil resistivity increases from 200 to 1800 Ω m, the drag reduction efficiency increases from 55.23 to 64.24%.When the soil resistivity is higher than 1000 Ω m, the drag reduction efficiency of form IV fractal epitaxial grounding grid has the highest among the four kinds of epitaxial grounding grid. Therefore, compared to traditional epitaxial grounding grids, fractal epitaxial grounding grid have superior drag reduction efficiency under high soil resistivity conditions. It is especially suitable for complex terrain areas such as mountainous areas with high soil resistivity and obstacles.

5 Conclusion

This research proposes a fractal epitaxial grounding grid laying method based on flexible graphite grounding material and fractal theory. Under the impact of the shielding effect, the ability of fractal epitaxial grounding grid to lower grounding resistance initially increases and subsequently diminishes with angle. The effect of decreasing the grounding resistance of the fractal epitaxial grounding grid increases with decreasing fractal dimension and decreases with increasing fractal layer number when the total length of the epitaxial leads is the same. In areas with high soil resistivity, the drag reduction efficiency of fractal epitaxial grounding grid is superior than that of traditional epitaxial grounding grid under the same length of epitaxial lead.

Therefore, in complex terrain areas where traditional epitaxial grounding grid is difficult to lay, such as mountainous areas with high soil resistivity, fractal epitaxial grounding grid can be flexibly selected to reduce the grounding resistance of transmission line tower.

Acknowledgements This research is supported by State Grid Shandong Electric Power Company Science and Technology Project (SGSDZBHTYJJS2200211).

References

1. Zhang B, He J, Zeng R (2015) State of art and prospect of grounding technology in power system. Voltage Eng 41(08):2569–2582 (in Chinese)
2. Li J, Jiang J, Li L (2013) Simulation and experiment study on resistance-reducing mechanism of grounding device with spicules. Power Syst Technol 37(01):211–217 (in Chinese)
3. Deng C, Zhao X, Qiu L et al (2015) Research on distribution of diffusing current and reducing resistance measures of tower grounding electrodes in impulse current condition. Insulators and Surge Arresters 267(05):128–133 (in Chinese)
4. Zhang C, Gan Y, Zou J et al (2017) Influences of spark effect and spark thorn on impulse grounding resistance of graphite grounding body. Water Resources and Power 35(06):178–181 (in Chinese)
5. Lian X, Hu Y, An B et al (2021) Current dispersion characteristic and material se-lection of extended auxiliary grounding grid for towers adjacent slopes. Insulators and Surge Arresters 299(01), 22–28+37 (in Chinese)
6. Hu Y, Ruan J, Gong R et al (2014) Flexible graphite composite electrical grounding material and its application in tower grounding grid of power transmission system. Power Syst Technol 38(10):2851–2857 (in Chinese)
7. Huang D, Chen J, Gu S et al (2018) Characteristics of flexible graphite grounding material and its application in lightning protection. High Voltage Eng 44(06):1766–1773 (in Chinese)
8. Yan W, An Y, Hu Y et al (2021) Research on cylinder Flexible Graphite Earth Electrode (FGEE) used to reduce tower earth resistance. Electric Power Syst Res 196(3):107268
9. Dong J, Gao Y (2002) Discussion on fractal in lightning. Journal of Beijing University of Posts and Telecommunications 25(03):46–49 (in Chinese)
10. Chen W, Wang W, Xia Q (2013) Research on multifractal characteristics of leakage current for contamination discharge of insulators. Trans China Electrotech Soc 28(01):50–56 (in Chinese)
11. Duan Q, An J, Mao H et al (2021) Review about the application of fractal theory in the research of packaging materials. Materials 14(4):860
12. Ma J, Liu D, Chen Y (2016) Random fractal characters and length uncertainty of the continental coastline of China. J Earth Syst Sci 125:1615–1621
13. Sun J, Hu Y, Li X el al (2021) Overvoltage protection of gas pipelines based on distributed auxiliary dispersion grounding grid. Southern Power System Technology 15(01), 54–60. (in Chinese)
14. Yuan T, Li J, Sima W et al (2011) Effect analysis about impulse-current dispersal regularity of grounding device under transient ionization phenomenon of soil. High Voltage Eng 37(7):1606–1613 (in Chinese)
15. Mousa M (1994) The soil ionization gradient associated with discharge of high currents into concentrated electrodes. IEEE Trans Power Delivery 9(3):1669–1677

Research on Resistance Reduction Method of Transmission Line Tower Epitaxial Grounding Based on Slope Soil Nailing Wall

Dawei Song, Ziping Liu, Yang Li, Xiying Liu, Zongjie Liu, and Muran Liu

Abstract Aiming at the problem of high grounding resistance of transmission line tower along the steep slope of the road, this paper proposes a method of reducing the resistance of the steel mesh in the soil nailing wall supported in the steep slope terrain, and builds the tower grounding grid and soil nailing wall along the steep slope terrain. The model compares and analyzes the changes of grounding parameters such as grounding resistance and step voltage before and after connecting the soil nailing wall, and analyzes the influence of the number of connecting wires, connection position, connection material and tower grounding grid position on the grounding resistance of the tower grounding grid. The simulation results show that the resistance reduction effect of the soil nailing wall on the tower grounding grid can reach 19.3–73.4%, and the maximum step voltage of the soil surface where the grounding grid is located is not more than 6 kV, which verifies the feasibility of the soil nailing wall scattered current resistance reduction method. The more the number of connecting wires, the smaller the low resistance, but the resistance reduction efficiency reaches 56.3% when the number of connecting wires is 4, which tends to be saturated. The more dispersed the connection position, the smaller the tower grounding resistance; the resistance reduction efficiency of the connecting wires using the new graphite composite material is 9.04% higher than that of the galvanized steel. The grounding grid is set on the slope and can have lower grounding resistance.

Keywords Grounding resistance · Transmission line · Soil nail wall

D. Song · Y. Li · X. Liu · Z. Liu · M. Liu
State Grid Huantai Power Supply Company, Shandong Electric Power Corporation, Zibo 255000, China

Z. Liu (✉)
School of Electrical and Electronic Engineering, Shandong University of Technology, Zibo 255000, China
e-mail: lzpperking06@sina.com; 364773948@qq.com

© Beijing Paike Culture Commu. Co., Ltd. 2024

X. Dong and L. Cai (eds.), *The Proceedings of 2023 4th International Symposium on Insulation and Discharge Computation for Power Equipment (IDCOMPU2023)*, Lecture Notes in Electrical Engineering 1102, https://doi.org/10.1007/978-981-99-7405-4_4

1 Introduction

Transmission line pylon grounding grid is a basic lightning protection facility that affects the lightning resistance level of the line [1]. Under the condition, high soil resistivity is difficult to reach the standard. Therefore, it is a basic measure to reduce the ground resistance of tower grounding grid to prevent lightning flashover fault of transmission line. In practical projects, pylons and towers of transmission lines are often erected around public buildings such as highways, slopes and embankments. Due to the limitations of construction conditions such as landforms and public transportation roads, the design and construction of pylons and towers along roads still face the following problems: rolling terrain and complex terrain, poor soil conditions and high soil resistivity for pylons and towers construction; The construction area of the tower along the road is limited, which is not conducive to the laying of the ground grid or large ground electrode. After the pylon grounding grid runs for a long time, some problems such as corrosion and human damage occur to the local grounding electrode, and the pylon grounding grid along the road is not easy to be replaced and maintained frequently. Therefore, there is still a lack of effective construction scheme for tower grounding resistance reduction under the condition of limited epitaxial construction area along roads and embankment slopes [2].

In recent years, scholars at home and abroad have made a lot of research on the problem of high ground resistance of pole tower in mountainous areas. In order to improve the lightning resistance level of the line and reduce the grounding resistance of the tower grounding grid, literature [3] proposed to carry out the epitaxial way to reduce the grounding resistance on the basis of the tower grounding grid, and believed that the epitaxial lead itself also had different effects on the loose flow. Considering the influence of the area, direction and number of connecting wires on the drag reduction effect of the pole tower grounding grid, literature [4] proposes a method to reduce the drag of transmission line tower grounding by increasing the length, area and number of connecting wires of the auxiliary grounding grid. For the case of high soil resistivity, literature [5] believes that the resistance can be reduced by increasing the area of grounding grid, extensional grounding or deep well grounding, etc. Miao Haoming et al. verified the dispersion characteristics of grounding devices in different soil areas under the action of continuous impact by simulation calculation, and proposed the selection of grounding materials. Zhou Lixing et al. used the EMTP-ATP simulation software to calculate the impact characteristics of the grounding device of the tower in double-layer soil. The moment of lightning strike, the end of the grounding electrode would rapidly heat up and ionize the soil [6], and the spark discharge effect could reduce the impact grounding impedance of the tower grounding grid. Gao Xiaojing et al. calculated the ground dispersion characteristics of concrete pile foundation of tower and pole, and proposed a method to reduce the natural grounding resistance of pile foundation under the condition of limited construction area [7]. In addition, it is mentioned in literature [8] that reinforcement frame is adopted for soil nailing wall of slope protection under terrain conditions such as roads and embankments, which can play a role in fixing soil layer of slope

and simulating landslide collapse construction. Considering that the pole and tower grounding resistance reduction of adjacent transmission lines under terrain conditions such as roads and embankments requires long distance extension, the slope protection soil nailing wall steel frame under terrain conditions such as roads and embankments can provide a scattering channel for the ground flow of adjacent pylons and towers, extend the tower grounding grid to the slope soil nailing wall steel frame, and achieve an effective increase in the area of the tower grounding grid and thus reduce the tower grounding resistance. This method can reduce the cost of tower grounding construction and avoid slope damage caused by large-scale equipment transportation construction. It has high engineering practical value.

Aiming at the problem of grounding resistance reduction of adjacent tower and tower under the condition of limited construction area such as road and river bank, this paper established a simulation model of grounding net and soil nail-wall under steep slope terrain, analyzed the influence law of grounding resistance reduction efficiency of tower and tower, such as the location of tower grounding net, the number of connecting wires and material parameters, and verified the feasibility of using road soil nail-wall for grounding resistance reduction of tower and tower. Relevant research conclusions can provide a feasible reference for the design and operation of power lines near slope protection land walls such as roads and embankments.

2 Analysis of the Influence of Different Factors on the Effect of Soil Nail Wall Assisted Resistance Reduction

2.1 Analysis of the Influence of the Number of Connection Lines

Soil nail wall as an epitaxial grounding grid, the number of connection lines between it and the pole tower grounding grid, will affect the size of the grounding resistance of the grounding grid. In order to investigate the influence of the number of connecting wires between soil nail wall and tower grounding grid on the grounding resistance, set the number of connecting wires as 1 ~ 5, respectively, and establish the transmission line tower epitaxial grounding resistance reduction model as shown in Fig. 1.

According to the different simulation calculation models shown in Fig. 1, the simulation calculations were carried out under the conditions of soil resistivity of 100 Ω-m, 300 Ω-m, 500 Ω-m, 700 Ω-m, and 900 Ω-m, respectively, and the results of the grounding resistance data of the pole tower grounding grid under the conditions of different numbers of connecting wires were obtained as shown in Fig. 2, and the conditions of soil resistivity of 100 Ω-m were used as an example to observe.

The simulation calculation results in Fig. 2 and show that increasing the connection lines between the grounding grid of the tower and the inner grid of the soil nail wall can enhance the resistance reduction effect of the inner grid of the soil nail wall

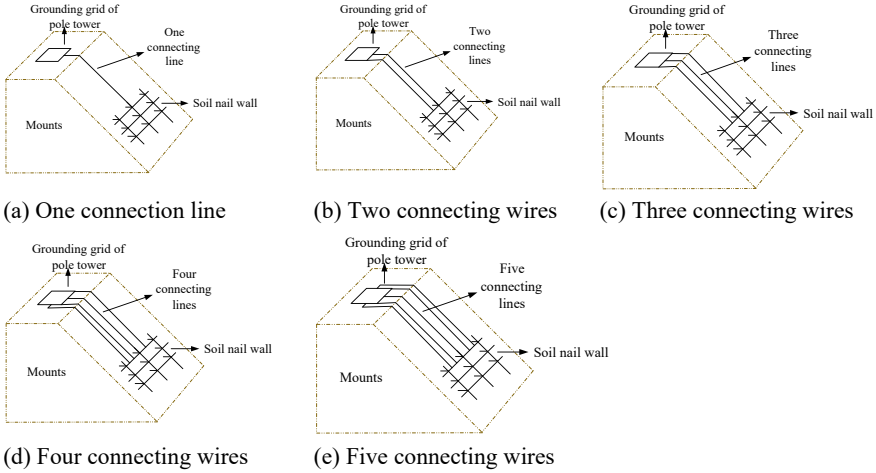

Fig. 1 Grounding grid model with different number of connection lines

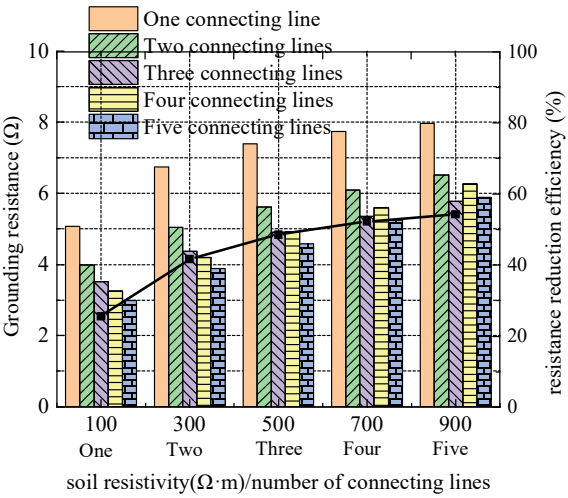

Fig. 2 The relationship between grounding resistance and soil resistance, number of connecting conductor

on the grounding grid of the tower, which can reach 25–55%. However, with the increase of soil resistivity, this positive correlation between "resistance reduction effect and the number of connecting wires" gradually weakened, and the number of 4 reached the saturation state, the shunt coefficient reached 54.32%, and the number of external leads continued to increase instead of making the grounding resistance reduced. Analysis is due to the influence of shielding effect, the more grounding conductors per unit area, the stronger the shielding effect, so that the effective dissipation area can be used is smaller. In the project if the use of soil nail wall grid or other auxiliary grounding grid for resistance reduction processing, the

use of 1–2 grounding conductors to connect the soil nail wall and tower grounding grid.

2.2 *Analysis of the Influence of Connection Position*

The soil nail wall, as an extension of the grounding grid of the pole tower, is excited by the connection line, and the end of the connection line is the excitation point of the soil nail wall. Therefore, to investigate the influence of different excitation points on the grounding resistance, three connection lines are used to connect the edge of the inner grid of the soil nail wall, three centralized connections to the edge of the inner grid of the soil nail wall, and three centralized connections to the center of the inner grid of the soil nail wall, and the model shown in Fig. 3 is established.

Simulations were performed for the three models in Fig. 3 under the soil resistivity conditions of 100, 300, 500, 700, and 900 Ω-m. Through simulation, the results of grounding resistance of the pole tower grounding grid under different connection positions are shown in Fig. 4.

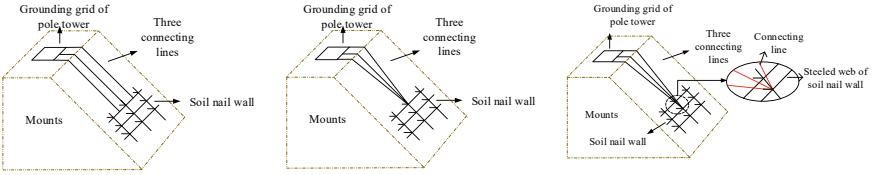

(a) Dispersion connection border

(b) Centralized connection border

(c) Centralized connection center

Fig. 3 Grounding grid models with different connection positions

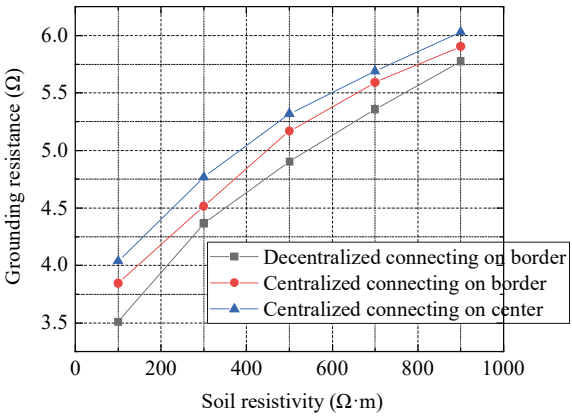

Fig. 4 The relationship between grounding resistance and connecting position

Comprehensive Fig. 4, simulation calculation results can be seen: comparing the connection line scattered connection soil nail wall and connection line concentrated in a point connection soil nail wall, in any soil resistivity conditions, the grounding resistance of the scattered connection are less than the grounding resistance of the tower grounding grid after two centralized connection methods under the same conditions. Therefore, in the actual project, when using multiple connecting wires to connect the grounding grid of the tower with the soil nail wall, each connecting wire should be dispersed. connection points and make each connection line keep a certain distance between them, reduce the conductor shielding effect, improve the grounding conductor's dissipation, and make the pole tower grounding resistance lower.

2.3 *Analysis of the Influence of the Connection Lines Material*

Galvanized steel due to its poor corrosion resistance, in the steep slope along the road and other terrain, it is difficult to ensure a long time of operation without damage [9–11]. As a metal less active copper and non-metallic material new graphite composites, with high corrosion resistance, excellent mechanical structure and good current dissipation, while avoiding rapid temperature rise, have become the optional material for today's grounding conductors.

In order to investigate the influence of different materials of connecting wires on the grounding resistance of the pole tower under the same conditions, the above three materials were chosen as the connecting wire materials, and the connection of soil nail wall and pole tower grounding grid with three connecting wires scattered connection was simulated under the soil resistivity conditions of different soil resistivity. Through simulation, the results of grounding resistance of the pole tower grounding grid under different connecting wire materials are shown in Fig. 5.

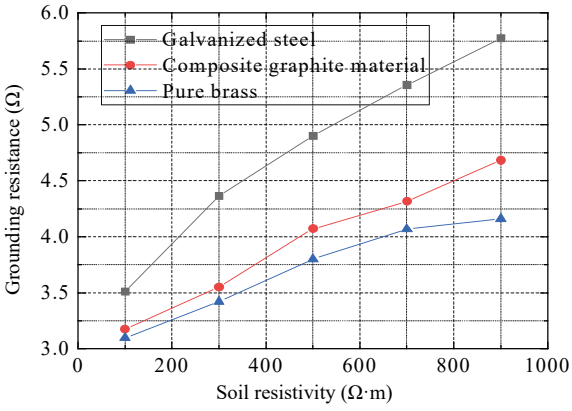

Fig. 5 The relationship between grounding resistance and connecting conductor material

Combined with the simulation calculation results in Fig. 5, it can be seen that under the same conditions, the connection wire made of copper and new graphite composite material is more conducive to the dissipation and resistance reduction of the pole tower grounding grid than the connection wire made of galvanized steel, in which the connection wire made of copper is lower than the grounding resistance of the pole tower grounding grid made of the connection wire made of new graphite composite material. However, the simulation results of the shunt coefficient show that the shunt coefficient of the new graphite composite grounding conductor can reach 62.01%, while copper is 57.44%, both higher than 53.13% of galvanized steel. The reason: the relative permeability of copper and new graphite composite materials is lower, the shielding effect is less, the current amplitude flowing into the grounding conductor is larger, and thus the shunt coefficient is high. And the new graphite composite grounding conductor shunt coefficient is greater than the copper counter-current coefficient, but the tower grounding resistance is greater, because the relative resistivity of the new graphite composite material is larger, much higher than copper, lightning flow at the connection line of the new graphite composite material is weaker than the copper material, while the effect of the soil nail wall to reach saturation, resulting in the use of the connection line with the new graphite composite material tower grounding grid The grounding resistance is slightly higher than that of copper. Therefore, new graphite composite material or copper can be used as the connecting wire material in actual projects.

2.4 Analysis of the Influence of the Location of the Pole Tower Grounding Grid

In some steep slopes due to construction difficulty, distance and other reasons, the grounding grid of the pole tower will be buried at the slope of the steep slope. The grounding grid at the slope is different from the grounding grid at the top of the slope because of the position, inclination angle, distance, etc. Therefore, in order to investigate the influence of the tower position on the grounding resistance, the grounding grid at the top of the slope and the slope are set as shown in Fig. 6.

Under the soil resistivity conditions of 100, 300, 500, 700, and 900 Ω-m, the pole tower grounding grid at the two locations of the slope top and slope shown in Fig. 6 are simulated and calculated respectively. Through simulation, the grounding resistance results of the pole tower grounding grid under the conditions of two different locations are shown in Fig. 7.

Under the same conditions, the grounding resistance of the pole tower grounding grid located on the slope is lower than that of the pole tower grounding grid located at the top of the slope.

After calculation can be obtained, the position in the slope top, the pole tower grounding grid connection line shunt coefficient is 53.13%, is located in the slope when it reaches 63.32%, much higher than the slope top position. Analysis of the

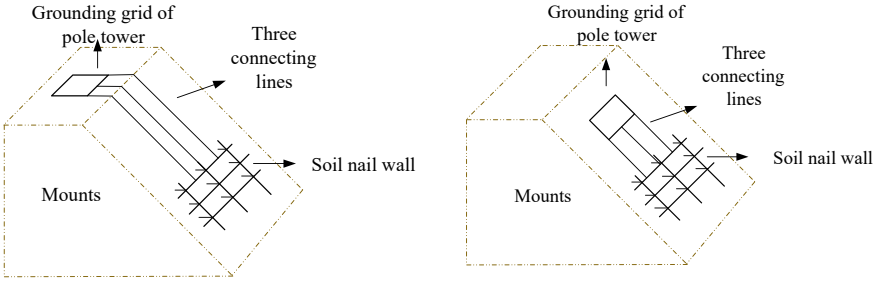

(a) grounding grid at the top of the slope (b) grounding grid on the slope

Fig. 6 Model of the grounding grid of the pole tower at different locations

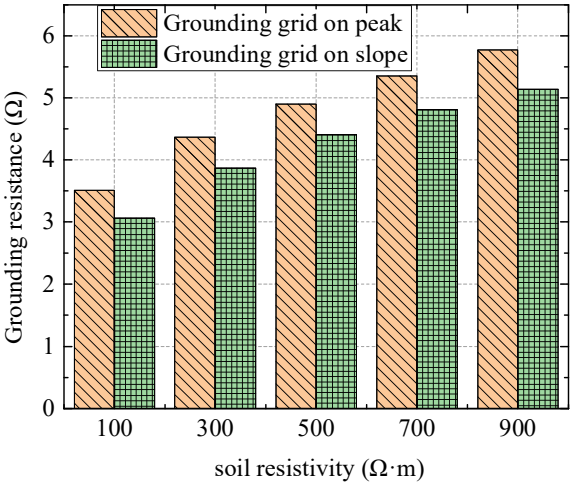

Fig. 7 The relationship between grounding resistance and position of grounding grid

reason: the slope of the tower grounding grid is closer to the soil nail wall, lightning flow more balanced dispersion to a wider area of the reinforcement grid of the soil nail wall; and the slope of the top of the tower grounding grid connection line is longer, part of the current in the conduction process of the connection line scattered flow makes lightning flow to the soil nail wall scattered flow is limited, making the shunt coefficient relatively small. Therefore, in the project, under the condition that construction conditions allow, the grounding grid can be set in the slope of the soil layer relatively close to the soil nail wall, in order to reduce the grounding resistance of the pole tower grounding grid.

3 Conclusion

This paper simulates and calculates the effect of soil nail wall on the grounding resistance and stride voltage of the pole tower grounding grid under steep slope conditions, and compares the effect of four factors, namely the number of connection wires, the connection position, the connection material and the location of the pole tower grounding grid, on the grounding resistance of the pole tower grounding grid. The following conclusions were obtained:

(1) Under the condition of steep slope, soil nail wall has obvious resistance reduction effect on the grounding grid of the pole tower, and the higher the resistance reduction ratio with the increase of soil resistivity. At the soil resistivity of 100 Ω-m, the resistance reduction ratio reaches 19.3%; at the soil resistivity of 900 Ω-m, the resistance reduction can reach 73.4%. Meanwhile, the simulation distribution of voltage across the step verifies the reasonableness of soil nail wall in terms of safety.

(2) compare and analyze the influence of each factor on the grounding resistance of the pole tower grounding grid, it can be learned that: the more the number of connecting wires of the soil nail wall and the pole tower grounding grid, the higher the resistance reduction effect, but the shunt coefficient saturates when the connecting wires reach 3–4, in the project generally use 3–4 can; the connecting wires adopt the connection method of dispersed connecting box to reduce resistance more obviously, the shunt coefficient is higher (53.13%); compared with Compared with the pole tower grounding grid set at the top of the steep slope, the grounding grid set at the slope has a lower grounding resistance.

(3) The new graphite composite material and copper can be a good material for connection wire because of the good corrosion and heat resistance of the new graphite composite material, although the resistance reduction efficiency is only 9–10% compared to galvanized steel as the connection wire material.

Acknowledgements This work is supported by State Grid Shandong Electric Power Company Science and Technology Project (520606220003)

References

1. Shengxing Z, Xiaoqiang X, Xiaobo W (2020) Application of graphite cable flexible grounding electrode in power transmission lines. Shandong Electric Power Technol 47(05):41–45 (2020) (in Chinese)
2. Guanlei D, Peng G, Songlin L et al (2023) Influence of grounding network form on the extrapolation resistance reduction of pole tower grounding network in near water source area. Electric Porcelain Lightning Arrester 311(01):106–115 (2023) (in Chinese)
3. Shen Z, Xue F, Wang SF et al (2022) Research on reducing the risk of electric shock around transmission towers by using inclined shaft grounding body. Smart Power 50(12):26–33 (in Chinese)

4. Yang X, Wang YF, Tang G, et al (2022) Study on the application of coupled ground line in 10 kV overhead line. High Voltage Electrical 58(12):92–101+108 (2022) (in Chinese)
5. Hao-Ming M, Wei S, Wen C et al (2022) Study on the dissipation characteristics of grounding devices in different soil regions under the action of continuous impact. Power Grid Clean Energy 38(11):71–79+87 (2022) (in Chinese)
6. Zhou LH, Luo LZ, Liu YB et al (2022) Simulation study on the impact characteristics of pole tower grounding device in double-layered soil based on ATP-Draw. J Electric Power Sci Technol 37(05):191–197 (in Chinese)
7. Gao X, Yuanchao H, Zhipeng J et al (2021) Research on grounding dissipation and structural optimization of concrete pile foundation of transmission towers. Electroceramic Lightning Arrester 303(05):115–122 (in Chinese)
8. Minyun H, Weijie O, Qianhao C et al (2021) A fine-scale numerical simulation study on the working characteristics of composite soil nail walls. J Zhejiang Univ Technol 49(04):442–448 (2021) (in Chinese)
9. Freddy MSS, Flavio AQP, Hernán P, Guillén C et al (2018) Soil treatment to reduce grounding resistance by applying low-resistivity material (LRM) and chemical ground electrode in different grounding systems configurations. In: IEEE international autumn meeting on power, electronics and computing (ROPEC)
10. Khan Y, Malik NH, Al-Arainy AA et al (2011) Efficient use of low resistivity material for grounding resistance reduction in high soil resistivity areas. In: Tencon IEEE region 10 conference. IEEE
11. Jing M, Wen X, Cai H et al (2020) Research on earth resistivity measuring and modeling of HVDC deep-well grounding electrode sites. IEEE 8:1–1. Access

A Novel Detection Method for Interface Defect Development of High-Speed Train Cable Terminal

Yujing Tang, Yuqi Xu, Guoqiang Gao, Kai Liu, Kui Chen, and Guangning Wu

Abstract As the weak link of the cable assembly, the internal insulation structure of the cable terminal is complex, the installation requirements are high, and the operating environment is complex, which is prone to external interference and insulation failure. However, the existing detection means of the cable terminal of the rolling stock is complicated, expensive, vulnerable to field noise interference and inefficient detection. In this study, a new method for diagnosis of cable termination insulation status by measuring the field strength along the cable termination surface is proposed. The characteristics of axial electric field distribution of defective cable terminals are studied by using multi-physical field simulation method to realize the degree of axial development of faulty cable terminal. The electric field sensor was used to measure the surface field intensity distribution of cable terminals with different degrees of interface defects, and the electric field intensity distribution law of cable terminals with different degrees of defects is obtained. The distribution of the interquartile range and variance of the electric field intensity along the cable terminal is analyzed. The results show that the greater the interface defect, the greater the interquartile range and variance of the electric field intensity along the cable terminal. Therefore, the development degree of interface defects can be judged by testing the surface electric field intensity of cable terminal.

Keywords Cable terminal · Fault detection · Simulation · Internal defects · Electric field · Interquartile range · Variance

1 Introduction

High-voltage cable and its terminal of the high-speed electric multiple units (EMU) are the key equipment for train's power supply. It is mainly used to connect the high-voltage equipment of EMU and power transmission. Its safety is crucial to ensure

Y. Tang · Y. Xu · G. Gao · K. Liu (✉) · K. Chen · G. Wu
School of Electrical Engineering, Southwest Jiaotong University, Chengdu 611756, China
e-mail: 1129757680@qq.com

© Beijing Paike Culture Commu. Co., Ltd. 2024

X. Dong and L. Cai (eds.), *The Proceedings of 2023 4th International Symposium on Insulation and Discharge Computation for Power Equipment (IDCOMPU2023)*, Lecture Notes in Electrical Engineering 1102, https://doi.org/10.1007/978-981-99-7405-4_5

the safe and stable operation of EMU [1, 2]. The research data shows that the cable terminal is the weak link of the cable assembly [3, 4], and its failure rate over 70% [5]. Therefore, effectively and accurately grasping the insulation state of cable terminal is an important means to ensure the safe and reliable operation of EMU cable terminal.

Partial discharge detection is a commonly used electrical detection method. Partial discharge is often accompanied by sound, light, electromagnetic heat and other phenomena [6]. According to different characteristic signals, partial discharge detection methods are divided into pulse current method [7, 8], high frequency pulse current method [9, 10], ultra-high frequency method [11, 12]. However, partial discharge signal detection is susceptible to sensor sensitivity, field noise, external electromagnetic interference, signal attenuation and other factors. And how to extract and separate the information that can characterize the cable insulation state from the complex working condition environment is a problem faced by the current partial discharge insulation state detection. Therefore, it is very important to put forward new detection methods to improve the reliability of cable terminal operation, reduce the failure rate of EMU and ensure the safe operation of EMU.

In this paper, the multi-physical field simulation method was used to study the axial electric field distribution characteristics of the defective cable terminal, and the axial distribution location of the fault cable terminal was. realized. The electric field sensor is used to measure the surface field intensity distribution of cable terminals with different degrees of interface defects, and the electric field intensity distribution law of cable terminals with different degrees of defects is obtained. It provides the possibility for online diagnosis of cable terminal in the future.

2 Case Analysis

High-voltage cable terminal failure accident occurred frequently in a certain type of EMU in China. The faulty cable is shown in Fig. 1. The faulty cable terminal was disassembled and dissected on site. Through dissection, it was found that there were obvious traces of power generation between main insulation of the cable terminal and long strain control tube, as shown in the red dashed box in Fig. 1.

The cracking of the insulating sheath is the cause of the internal surface breakdown of the shed, and the air gap defect between the layers inside the shed is the main reason for the breakdown of the inner surface. When the air gap fault at the cable terminal interface, it will cause partial discharge inside the cable terminal. During the long-term operation of the EMU, the insulation degradation will be accelerated of the cable terminal, and eventually insulation failure, which will affect the safety of the EMU. safe and stable operation.

Fig. 1 The faulty cable terminal of high-speed train

3 Simulation Study

The finite element method is used to simulate the cable termination, which is mainly based on Maxwell's system of equations to construct the model and choose the static electric field to solve, Maxwell's system of equations is calculated as follows [13].

$$\nabla \times H = J + \frac{\partial D}{\partial t} \tag{1}$$

$$\nabla \times E = 0 \tag{2}$$

$$\nabla \cdot B = 0 \tag{3}$$

$$\nabla \cdot D = \rho \tag{4}$$

where H is the magnetic field strength, E is the electric field strength, J is the full current density, D is the electric induction strength; B is the magnetic induction strength. At the same time each linear material medium of the cable terminal needs to satisfy the following intrinsic relationship [13].

$$D = \varepsilon E \tag{5}$$

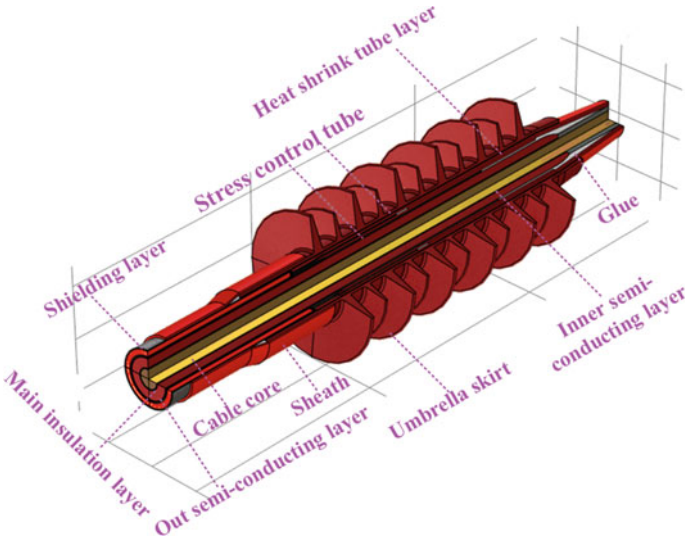

Fig. 2 Three-dimensional structure of cable terminal

$$J = (\sigma + j\omega\varepsilon)E \tag{5}$$

where ε is the dielectric constant, σ is the electrical conductivity, B is the magnetic induction, ω is the magnetic permeability, and is the angular frequency.

Based on the actual model structure of the on-board high-voltage cable terminal, the cable terminal model diagram was constructed using COMSOL simulation software, and the model was built according to the actual terminal scale of 1:1, and the cable terminal model was constructed as shown in Fig. 2.

4 Simulation Results

In this paper, the length of the first layer of the high voltage cable terminal is defined as l, and its length is 260 mm. The air gap length is used to describe the degree of defects. Defects are constructed in the main insulation and the first layer of stress tube. The defect lengths l' are 0.55 and 100%l, respectively. In order to simulate the actual discharge effect inside the cable terminal, carbon marks were used to replace air gap defects. Figure 3 is the schematic diagram of the cable terminal defect model.

Figure 4 and Table 1 statistics of the electric field intensity results inside the defective cable terminal. When there is no defect inside the cable terminal, the maximum electric field intensity inside it is mainly at the location where the three phases of the main insulation, the outer semi-conducting layer and the long stress control tube are combined, such as at the location of the red circle in Fig. 4. As the voltage level

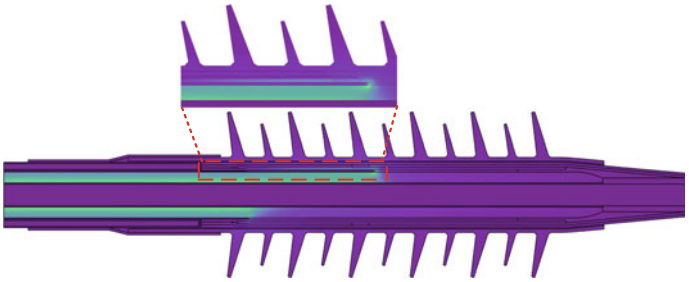

Fig. 3 Schematic diagram of carbon mark defect at cable terminal interface

increases, the intensity of its internal distortion electric field gradually increases. When there is a defect between the main insulation and the long control tube inside the cable terminal, the maximum distortion position inside the cable terminal appears at the defective end position. With the increase of defects, the electric field strength of internal distortion of the cable gradually increases at the same voltage level.

In the cable terminal large umbrella skirt surface 2 mm set air domain, along the main insulation and the first layer should control the tube interface between the carbon trace vertical direction at the electric field strength marked as E_0, cable terminal electric field strength starting test electric field position and cut-off position as shown in Fig. 5.

In order to clarify the relationship between the degree of defect development at the cable termination interface and the electric field tested along the surface, the electric field intensity values tested at different locations were processed in this study, and

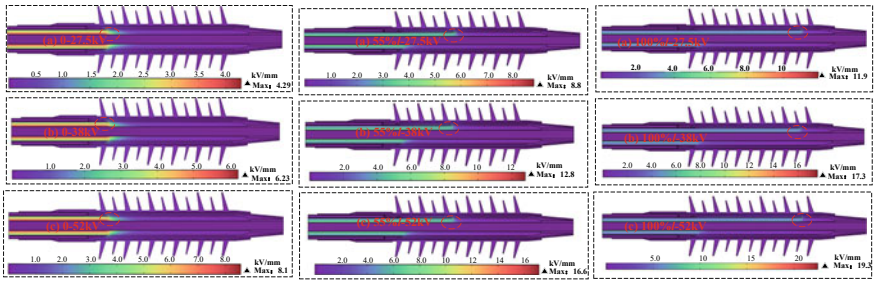

Fig. 4 Electric field strength inside the cable terminal

Table 1 Electric field intensity statistics inside the cable terminal

	10 kV	20 kV
0 (kV/mm)	1.65	3.12
55%l (kV/mm)	3.34	6.4
100%l (kV/mm)	4.33	8.67

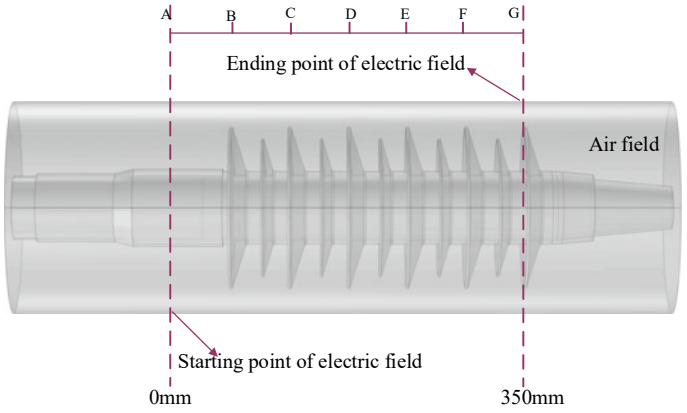

Fig. 5 Cable terminal simulation electric field test location

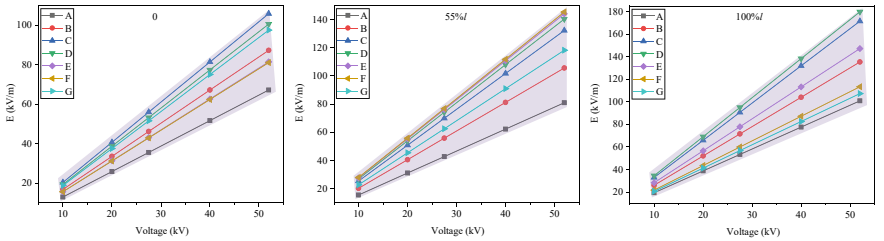

Fig. 6 Statistics of electric field strength of defective cable terminals under different voltage levels

the degree of defect development at the cable termination interface was expressed using the parameters of *Interquartile Range* (IR) and *Variance.*

The Interquartile Range [14] is the difference between the 3rd quartile and the 1st quartile, also known as the internal distance or quartile spacing, and is denoted by Q_r. The IR is calculated as $Q_r = Q_3 - Q_1$. The quartiles reflect the degree of dispersion of the middle 50% of the data. The smaller the value, the more centralized the data in the middle. The smaller the value, the more concentrated the data in the middle, the larger the value, the more dispersed the data in the middle. Q_1 and Q_3 are calculated by the formula:

$$\mathrm{Q}_1 = L + \frac{\frac{n+1}{4} - F}{f} i \tag{7}$$

$$\mathrm{Q}_3 = L + \frac{\frac{3(n+1)}{4} - F}{f} i \tag{8}$$

where, L is the lower bound of the group in which the *IR*, F is the cumulative frequency, f is the frequency, and i is the width of the group.

In statistics, variance is used to calculate the difference between each variable and the population mean. Variance describes the degree of dispersion of the value of a random variable to its mathematical expectation. The calculation formula is as follows:

$$S^2 = \frac{\sum (X - \overline{X})^2}{n - 1} \tag{9}$$

where S^2 represents the sample variance, X is the variable, $\overline{X}$ is the sample mean, and n is the number of samples.

The statistical results of *IR* of electric field strength at the cable terminal were shown in Fig. 7.

$$y = ax + b \tag{10}$$

where y is the *IR* of field intensity, x is the voltage level, a is the slope, and b is the intercept. As can be seen from Fig. 7, with the increase of interface defects, the IR of electric field intensity also increases, resulting in greater dispersion of electric field intensity at different locations. The larger the defect, the greater the IR slope of the electric field intensity. When the interface defect increased from 20 to 100%l, the IR slope of electric field intensity increased from 0.34 to 1.01.

Figure 8 shows the variance of electric field intensity. The variance of electric field intensity measured at different voltages meets the following fitting formula:

$$y = y_0 + A_1 e^{x/t_1} \tag{11}$$

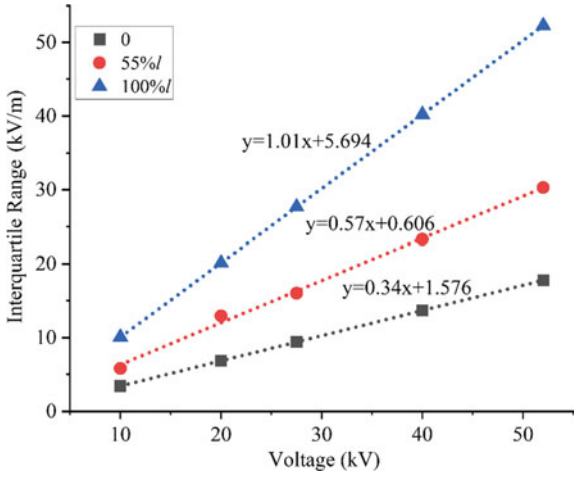

Fig. 7 Interquartile range of simulation

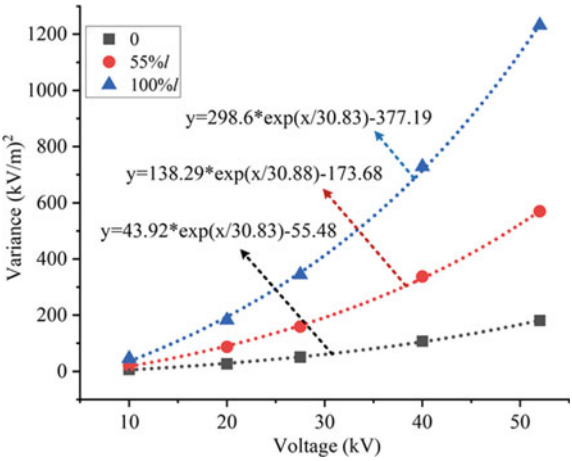

Fig. 8 Electric field strength variance statistics of simulation

where y_0 refers to the offset, A_1 refers to the preexponential, and t_1 refers to the relaxation time.

It can be seen from the statistical results that as the interface defects gradually increase, the variance of the electric field strength of the cable terminal also gradually increases. The larger the defect, the larger the pre-exponential factor of the electric field intensity variance at different positions, and the absolute value of the electric field intensity variance offset gradually increases. When the interface defect of the cable terminal is 100%l, the pre-exponential factor and the absolute value of the offset of the fitting parameters of the electric field intensity variance are 298.6 and 377.19, respectively. Compared with the defect-free cable terminal, the absolute value of the pre-exponential factor and the offset of the electric field intensity variance increased by about 85.3% and 85.29%, respectively. However, the relaxation time changes irregularly with the increase of interface defects.

5 Experiments and Test Results

In this paper, different lengths of air gap defective cable terminal are prepared, and the length of the first layer of stress control tube inside the high voltage cable terminal is defined as l. The air gap length was used to describe the degree of defects, and the defect lengths l' are 0, 55, 100%l. Use a carbon pen to draw a line from point A according to the predetermined defect length (hereinafter referred to as "carbon mark"). Make sure the carbon marks are clear and the width is not less than 1mm. A wire with a diameter of 2 mm is pre-buried next to the carbon trace. The prefabricated defective cable terminal is shown in Fig. 9.

The schematic diagram of the sensor test arrangement is shown in Fig. 10.

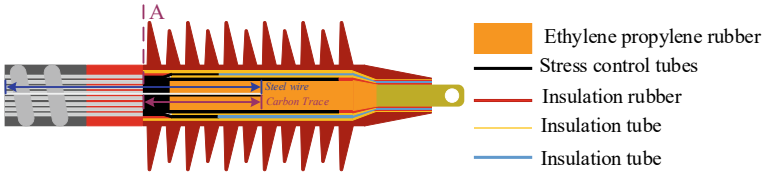

Fig. 9 Prefabricated defect cable terminal schematic diagram

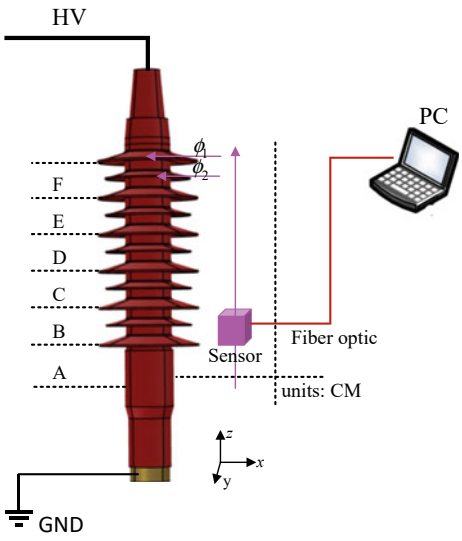

Fig. 10 Schematic diagram of electric field sensor arrangement along the cable terminal surface

The result of testing the cable termination strength quadrature difference value by test is shown in Fig. 11. The linear relationship between the test electric field strength quartile difference value and voltage is good. The larger the defect is, the larger the slope of the test field strength quartile difference is. When the interface defect increases from 20 to 100%l, the slope of the electric field strength quadrature difference increases from 0.076 to 0.679, which is consistent with the simulation results.

Figure 12 shows the statistics of the electric field strength variance of the cable termination test, and the trend is consistent with the simulation results. From the statistical results, it can be seen that with the gradual increase of interface defects, the variance of electric field strength at cable terminals also gradually increases. The variance fitting parameters of the cable termination specimens with 0, 55 and 100%l are 2.76, 62.86 and 109.42; the absolute values of the variance fitting parameters offset were 3.33, 85.51 and 126.71, respectively. the larger the defect, the larger the variance fitting factors of the electric field strength at different locations, and the absolute values of the electric field strength variance offset also increased gradually.

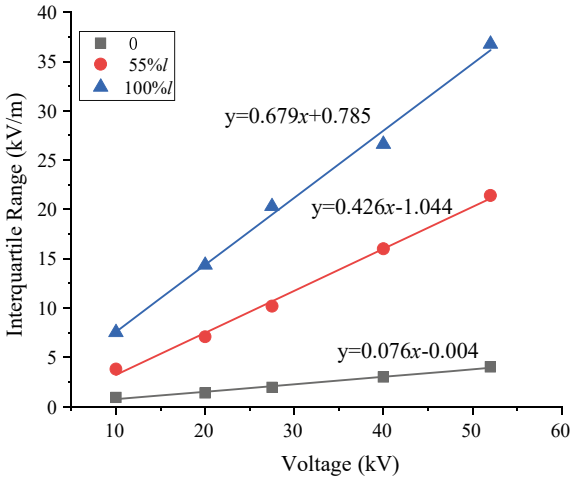

Fig. 11 The interquartile range of experiment

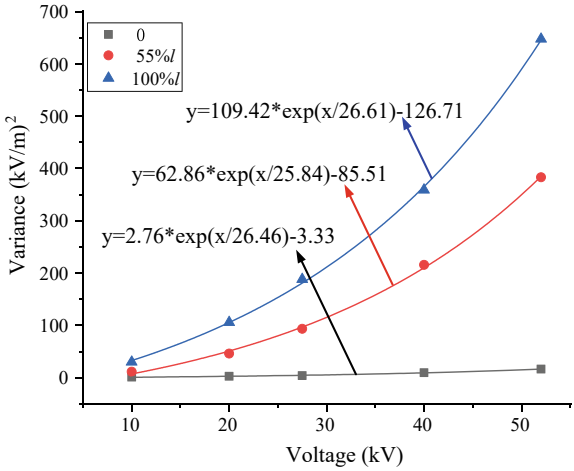

Fig. 12 The variance of experiment

The simulation and experimental test results are consistent. By testing the electric field strength along the umbrella skirt of the cable terminal, the development degree of internal defects in the cable terminal can be effectively reflected. Compared with traditional cable terminal fault detection methods, this method is simple to test and has strong anti-interference ability.

6 Conclusion

The following conclusions are obtained:

(1) With the increase of voltage level, the electric field intensity along the surface of the cable terminal also gradually increases, and the linear relationship between electric field intensity and voltage level is good. As the interface air gap defects are larger, the electric field strength dispersion of cable terminals at different axial positions is obviously inconsistent. The larger the interface air gap defects, the greater the interquartile range and variance of the electric field strength at different locations, the greater the electric field strength dispersion.
(2) By arranging multiple sensors along the surface of the cable terminal, the internal fault of the cable terminal can be detected quickly and effectively, effectively improving the sensitivity of cable terminal insulation fault detection; therefore, the reasonable arrangement of electric field sensors can be used for the detection of internal defects of the cable terminal, determining the degree of development of internal defects of the cable terminal and assisting in deciding whether the cable terminal needs to be replaced.

Acknowledgments This work is supported by National Natural Science Foundation of China (U1966602) and Excellent Young Scientists Fund of China (51922090).

References

1. Bai L, Zhou L, Li L, Chen Y, Guo L (2019) Partial discharge of cable termination on EMU of China high-speed railway below zero degrees centigrade. IET Sci Meas Technol 13(6):912–921
2. Zhou L, Zhu S, Bai L, Liu Y, Zhu L, Guo L (2019) Influence of stress tubes interface on partial discharge of vehicle cable terminal at low temperatures. High Voltage Eng 45(4):1266–1273
3. Mazzanti G, Marzinotto M (2017) Advanced electro-thermal life and reliability model for high voltage cable systems including accessories. IEEE Electr Insul Mag 3(33):17–25
4. Lai Q, Chen J, Hu L, Cao J, Xie Y, Guo D, Liu G, Wang P, Zhu N (2020) Investigation of tail pipe breakdown incident for 110 kV cable termination and proposal of fault prevention. Eng Fail Anal 108:104353
5. Du B, Han T (2014) Tree characteristics in silicone rubber/SiO_2 nanocomposites under low temperature. IEEE Trans Diel Electron Ind 21(2):503–510
6. Nie YJ, Zhao XP, Li ST (2020) Research progress in condition monitoring and insulation diagnosis of XLPE cable. High Voltage Eng 464:1361–1371
7. Chou CJ, Chen CH (2018) Measurement and analysis of partial discharge of high and medium voltage power equipment. In: 2018 7th International symposium on next generation electronics (ISNE), Taipei, Taiwan
8. Bai LL, Zhou LJ, Cao WD, Che XY, Xing LM, Li LN (2020) Characteristics of partial discharge in air gap defects in EPR cable termination under −40 °C condition. High Voltage Eng 4610:3605–3614
9. Álvarez F, Garnacho F, Ortego J, Sánchez-Urán M (2015) Application of HFCT and UHF sensors in on-line partial discharge measurements for insulation diagnosis of high voltage equipment. Sensors (Basel, Switzerland) 15:7360–7387

10. Yii CC, Rohani MNKH, Isa M, Hassan SIS (2017) Multi-end PD location algorithm using segmented correlation and trimmed mean data filtering techniques for mv underground cable. IEEE Trans Dielectr Electr Insul 24:92–98
11. Ma S, Chen M, Wu J, Wang Y, Jia B, Jiang Y (2019) High-voltage circuit breaker fault diagnosis using a hybrid feature transformation approach based on random forest and stacked autoencoder. IEEE Trans Ind Electron 66:9777–9788
12. Dey D, Chatterjee B, Dalai S (2018) A deep learning framework using convolution neural network for classification of impulse fault patterns in transformers with increased accuracy. IEEE Trans Dielectr Electr Insul 24(6):3894–3897
13. Hayt AJ Jr, William H, Buck JAS (2018) Buck engineering electromagnetics. Xi'an Jiaotong University Press, Xi'an
14. Zhao TH, Zhang Y, Wang JX (2021) Load outlier identification method based on spatial density clustering and abnormal data domain. Autom Electric Power Syst 45

A 3D Modeling Method for Substations Based on Oblique Photography

Cong Hu, Fuhua Xie, Li Cai, Xin Yang, Jianguo Wang, and Yadong Fan

Abstract Substation is the key part to ensure the normal operation of power system. A real, accurate and highly scalable 3D realistic simulation model of substation is the realistic basis for building a digital and intelligent power system, virtual reality simulation training system and augmented reality field-aided analysis system. In this paper, a simple and effective method for 3D modeling of substations is proposed. Acquisition of image data in two aerial shots. First, the image data is collected above the substation through oblique photography, and then the UAV is flown manually to collect close electrical equipment image data in the substation. The image data obtained from both times are imported into ContextCapture separately, and the high-density point cloud is obtained by aerial triangulation separately, and then the two high-density point clouds are fused to reconstruct a high-quality 3D model of the substation. The result proves that, compared with the conventional oblique photography method, the 3D model of substation built by the proposed method is completer and more accurate, and the model of electrical equipment has fewer defects, which meets the requirements in practical applications.

Keywords Oblique photography · 3D modeling · Substation

C. Hu · X. Yang
Foshan Power Supply Bureau, Guangdong Power Grid Co., Foshan, China

F. Xie · L. Cai · J. Wang · Y. Fan
Engineering Research Center of Ministry of Education for Lightning Protection and Grounding Technology, School of Electrical Engineering and Automation, Wuhan University, Wuhan, China

F. Xie · L. Cai (✉) · J. Wang · Y. Fan
School of Electrical Engineering and Automation, Wuhan University, Wuhan, China
e-mail: 2580968099@qq.com

© Beijing Paike Culture Commu. Co., Ltd. 2024

X. Dong and L. Cai (eds.), *The Proceedings of 2023 4th International Symposium on Insulation and Discharge Computation for Power Equipment (IDCOMPU2023)*, Lecture Notes in Electrical Engineering 1102, https://doi.org/10.1007/978-981-99-7405-4_6

1 Introduction

In recent years, the construction of smart grids has been gradually promoted. Smart grid can make the power system more visualized, simulated and refined operation, which is more conducive to the safe operation and health monitoring of the power system [1]. As the hub of the power system, the substation not only has the function of distributing power supply but also controls the voltage rise and fall. It is an important part of the robust operation of smart grids to ensure the operational safety of substations [2]. The 3D digital technology has the characteristics of visualization, simulation and refinement, which is very suitable for the new substation maintenance needs, but first of all, it is necessary to get the substation 3D model.

The oblique photogrammetry aerial survey process obtains image data from vertical and multiple oblique angles of the photographed object, and after 3D reconstruction, generates a realistic 3D model with a high degree of reproduction of the real scene. The American company Pictometry was the first company in the world to study oblique photogrammetry technology. Its Pictometry image processing software [3] can realize the functions of image contour extraction, measurement and texture mapping, so that the image has three-dimensional information, and the research results have been widely used. The French company Acute 3D developed its own Smart 3D software [4], which is by far the best 3D modeling software in the world, and was later acquired by Bentley and renamed ContextCapture. Today, oblique photography is used in mapping [5], power inspection [6], agriculture and forestry [7], and digital city construction [8].

Commonly used substation 3D modeling is mainly done by using substation geometric features, substation image data, and LIDAR distance measurement. Romero et al. [9] built a 3D model of substation based on existing actual pictures in paper or digital format using 3D software such as AutoCAD, VRML, etc. Yan et al. [10] built a 2D solid library and a 2D image library based on the actual scene photos of the substation, and then used modeling tools to build the substation equipment and the surrounding environment. Sun et al. [11] segmented the equipment from the 2D images, then matched the equipment with similar contours with the 3D equipment database, and then constructed a 3D model by computing the mapping data. Suo et al. [12] proposed a 3D reconstruction method based on dynamic clustering algorithm. The dynamic cluster center array was first established to divide different shapes of the same device, then extract and match the information, and finally complete the 3D model construction with the 3D model library. Duanmu [13] et al. used a coarse-grained culling algorithm based on CPU and GPU batch processing technology to improve the rendering efficiency of 3D model data based on the construction of a 3D model of a substation using 3ds Max. Based on the Unity3D platform and MySQL database, a 3D visualization management platform for substation equipment was designed and developed.

In this paper, a method is proposed to reconstruct a refined 3D model of the substation. At the time of data acquisition, the image data of multiple views above the substation are first obtained by oblique photography method, and then the image

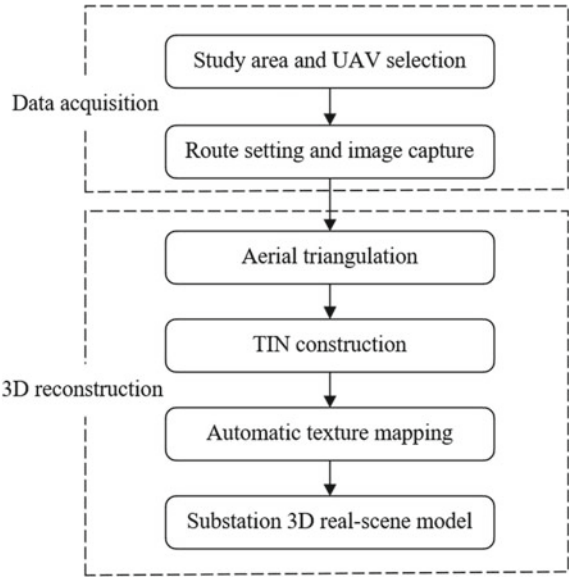

Fig. 1 The 3D modeling flowchart

data of the electrical equipment in the substation captured by the UAV near the ground are collected. Then, the two images are imported into ContextCapture, and aerial triangulation is performed separately to obtain a high-density point cloud. After fusing the two high-density point clouds, the TIN model is constructed and then a white body model is generated, and finally a high-quality 3D model of the substation is obtained through texture mapping. The 3D modeling flow chart is shown in Fig. 1.

2 Data Acquisition

2.1 Study Area and UAV Selection

The study area of this paper is a small substation in the School of Electricity and Automation of Wuhan University, which includes electrical equipment such as insulators, current transformers, voltage transformers and lightning arresters. The area of the substation is about 300 square meters, and the highest point is about 12 m. The overview of the substation is shown in Fig. 2.

Mapping UAVs for oblique photography require higher flight standards, with limits in terms of payload, cruise speed, practical lift, endurance, safety and wind resistance rating. In this paper, the DJI Phantom 4 RTK, a small multi-rotor high-precision aerial survey UAV for low-altitude photogrammetry applications, is selected as the UAV flight platform to acquire image data. It has a centimeter-level navigation and positioning system and a high-performance imaging system, and

Fig. 2 The overview of the substation

carries an RTK module to ensure image accuracy, so it can eliminate the need to set up image control points and improve operational efficiency.

2.2 Route Design and Image Acquisition

The aerial photography schematic is shown in Fig. 3. Route 1 refers to the oblique photography route, and its main parameters are to select the appropriate flight altitude, forward overlap and side overlap. The flight altitude needs to be set according to the ground resolution required by the task and the performance of the camera, and the calculation formula is as follows:

$$H = \frac{f \times GSD}{\alpha} \tag{1}$$

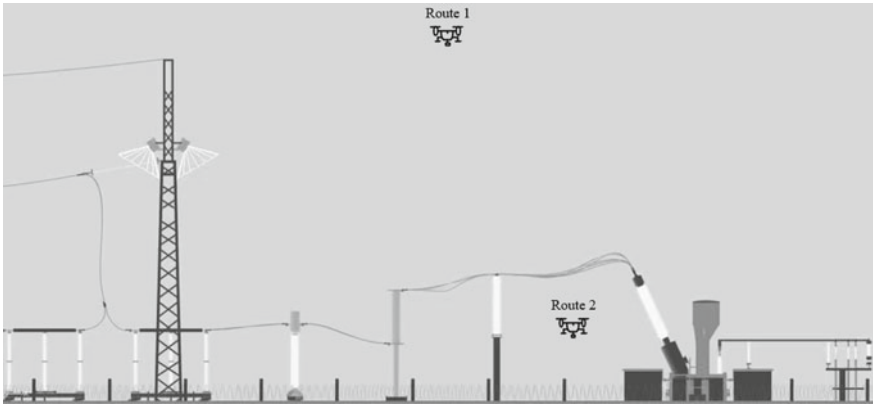

Fig. 3 The aerial photography schematic

Table 1 The parameters of aerial photography

Parameter	Value
Flight altitude	40 m
Forward overlap	80%
Side overlap	80%
Pitch angle of the cloud platform	45°
Main route angle	0°
GSD	1.10 cm/pixel

Where, H is the height of the UAV relative to the mean elevation; GSD is the image spatial resolution; f is the camera focal length; α is the image element size. When the flight altitude is set to 40m, the GSD reaches 1.10cm/pixel, which meets the modeling accuracy requirement.

Where, H is the height of the UAV relative to the mean elevation; GSD is the image spatial resolution; f is the camera focal length; α is the image element size. When the flight altitude is set to 40 m, the GSD reaches 1.10 cm/pixel, which meets the modeling accuracy requirement.

In the UAV oblique photography, both the forward overlap and the side overlap are recommended to be above 60%. Considering that the substation studied in this paper is surrounded by buildings and the electrical equipment in the substation is at a relatively compact distance, there is the problem of mutual occlusion, so both the forward overlap and the side overlap are set to 80%. The pitch angle of the cloud platform is set to 45°, which can reduce the image dead angle. The parameters of aerial photography are shown in Table 1. The final time is 6 min, and 131 oblique photography images are obtained.

Route 2 refers to the images of electrical equipment taken by the UAV near the ground. We obtained the close range image data of electrical equipment by using the UAV at flight heights of 1m, 5m, and 13m, maintaining an overlap rate of about 60%. It takes 9min to get 64 images of electrical equipment in substations.

3 3D Reconstruction

After checking and confirming that all the acquired image data are OK, the image data obtained twice are imported into ContextCapture separately for 3D reconstruction.

3.1 Aerial Triangulation

The most important aspect of aerial triangulation is how to mix and level the orthographic and oblique images. The obtained feature points are then used to match the

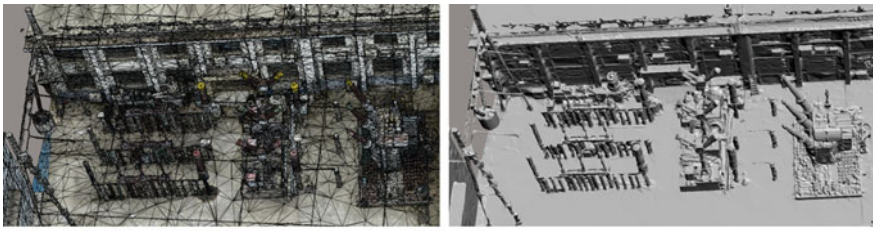

Fig. 4 **a** TIN model, **b** white body model

same name points in multiple views, and then the spatial position of each image and the pose angle of the image are solved in reverse to determine the relationship between the images. After the completion of the null-three encryption, the position density of the null-three points, the image pair position of each image and the azimuth angle of the range covered by the images are solved. At the same time, by establishing the coordinate files of connection points and control points, it is possible to realize the iterative calculation of the level difference of the multi-view image self-calibration area network, and finally get the level difference results that meet the accuracy requirements through repeated joint solving.

3.2 Triangulated Irregular Network Construction

Aerial triangulation is followed by dense matching of multi-vision images to obtain high-density 3D point cloud data. Then the 3D point cloud data is transformed into a triangulated irregular network (TIN) model, and the TIN model is encapsulated, which will generate a white model of the 3D model. The TIN model as well as the white body model are shown in Fig. 4.

3.3 Texture Mapping

Because the oblique images captured by the UAV have precise coordinate information, the correspondence between each triangular surface sheet in the TIN model and the image can be calculated, and the corresponding texture information is aligned with the triangular surface sheets in the TIN model. After the TIN model is constructed, the texture mapping is performed using the 2D images with higher resolution to generate a realistic 3D model.

3.4 3D Model of Substation

The 3D model of the substation obtained by the method used in this paper is shown in Fig. 5. The 3D model of the substation obtained by the traditional oblique photography method is shown in Fig. 6. Comparing these two figures, it can be seen that the 3D models built by both methods are relatively complete in general. However, in terms of details, the 3D model of electrical equipment built by the proposed method in this paper is more complete and basically free of defects. The 3D model of electrical equipment obtained by the traditional oblique photography method has problems such as distortion and deformation, especially the insulator strings are missing very obviously. Therefore, the method proposed in this paper can effectively improve the quality and accuracy of the 3D model.

Fig. 5 The 3D model built by the method proposed in this paper. **a** 3D model of the substation; **b** 3D model of electrical equipment

Fig. 6 The 3D model built by the traditional oblique photography method. **a** 3D model of the substation; **b** 3D model of electrical equipment

4 Conclusion

In this paper, a method for fine-grained 3D modeling of substations is proposed. On the basis of oblique photography, the images of electrical equipment obtained from near-ground photography by UAV are added for 3D modeling. Although the method used in this paper takes longer time than the single oblique photography, the accuracy of the obtained 3D model is very high. The 3D model of the substation is complete and the defects of the electrical equipment are small, so it can provide an effective 3D model of the substation for the visualization system of the substation.

Acknowledgements This study was supported by the technology project of Southern Power Grid Corporation (Project No. 030600KK52220016).

References

1. Butt OM, Zulqarnain M, Butt TM (2021) Recent advancement in smart grid technology: future prospects in the electrical power network. Ain Shams Eng J 12(1):687–695
2. Basahel AM (2021) Safety leadership, safety attitudes, safety knowledge and motivation toward safety-related behaviors in electrical substation construction projects. Int J Environ Res Public Health 18(8):4196
3. Saito K, Spence R, Booth E et al (2010) Damage assessment of Port au Prince using Pictometry. In: 8th international workshop on remote sensing for disaster management. Tokyo 2010, p 30
4. Ren J, Chen X, Zheng Z (2019) Future prospects of UAV tilt photogrammetry technology. In: IOP conference series: materials science and engineering, vol 612, no 3. IOP Publishing, p 032023
5. Huang C, Zhang H, Zhao J (2020) High-efficiency determination of coastline by combination of tidal level and coastal zone DEM from UAV tilt photogrammetry. Remote Sens 12(14):2189
6. Liang LH, Yang ZG, Wang YG et al (2022) Accuracy analysis of oblique photogrammetry measurement in 3D modeling of power line selection design. J Phys Conf Ser 2400(1):012013
7. Wu J, Wen S, Lan Y et al (2022) Estimation of cotton canopy parameters based on unmanned aerial vehicle (UAV) oblique photography. Plant Methods 18(1):129
8. Jie S, Zhixin LI, Wenyuan Z (2019) Recent progress in large-scale 3D city modeling. Acta Geodaetica et Cartographica Sinica 48(12):1523
9. Romero G, Maroto J, Felez J et al (2008) Virtual reality applied to a full simulator of electrical substations. Electr Power Syst Res 78(3):409–417
10. Yan G, Zhang L, Wang Y (2010) Research and implementation of the auto-generating system of three-dimensional substation simulation scene. In: 2010 IEEE International conference on intelligent computing and intelligent systems, vol 3. IEEE, pp 768–771
11. Sun L, Suo X, Liu Y, et al (2016) 3D modeling of transformer substation based on mapping and 2D images. Math Probl Eng 2016
12. Suo X, Hou C, Sun L et al (2017) 3D reconstruction optimization algorithm based on dynamic clustering in transformer substation. J Comput Theor Nanosci 14(1):248–251
13. Duanmu X, Lan G, Chen K, et al (2022) 3D Visual Management of Substation Based on Unity3D. In: 2022 4th International academic exchange conference on science and technology innovation (IAECST). IEEE, pp 427–431

Simulation Study on Motion of Metal Particles During Translation of Flat Plate Electrode

Lu Peile, Yan Yingjie, Liu Yadong, Jiang Xiuchen, and Deng Jun

Abstract A two-dimensional flat plate electrode advection model is established, and the SST k-ω turbulence model is selected to study the insulating oil motion according to the plate motion. The N-S equation of the impinging oil flow is constructed by the Eulerian method, and the kinetic equation of the metal particles is constructed by the Lagrangian method, and they are coupled by the interaction forces for the solid–liquid two-phase flow. The simulation is carried out to obtain the flow state of insulating oil when the flat plate is moving and the motion of metal particles under multiple forces. It has been found that during the translation of flat electrodes, the particles also develop a "small bridges", which may cause breakdown.

Keywords Turbulence · Solid–liquid two-phase flow · Metal particles

1 Introduction

In the process of high-voltage power transmission, the reliable operation of electrical equipment is the key to ensuring the safety of the power grid. Insulating oil, as the most commonly used liquid insulating medium in electrical equipment, closely

L. Peile
College of Smart Energy, Shanghai Jiao Tong University, Shanghai 200240, China

Y. Yingjie · L. Yadong (✉) · J. Xiuchen
Department of Electrical Engineering, Shanghai Jiao Tong University, Shanghai 200240, China
e-mail: lyd@sjtu.edu.cn

Y. Yingjie
e-mail: yanyingjie@sjtu.edu.cn

J. Xiuchen
e-mail: xcjiang@sjtu.edu.cn

D. Jun
Maintenance and Test Center, Ultra High Voltage Company of South Grid, Guangzhou 510000, China

© Beijing Paike Culture Commu. Co., Ltd. 2024

X. Dong and L. Cai (eds.), *The Proceedings of 2023 4th International Symposium on Insulation and Discharge Computation for Power Equipment (IDCOMPU2023)*, Lecture Notes in Electrical Engineering 1102, https://doi.org/10.1007/978-981-99-7405-4_7

influences the insulating performance of electrical equipment. Metal particles, as one of the most common impurities in the most insulating oil, can seriously reduce the quality of the insulating oil and damage the insulating properties of electrical equipment, bringing harm to the electrical equipment and the power grid. The main reason is that the movement and accumulation of metal particles with good electrical conductivity can cause distortions in the internal electric field of the equipment, triggering partial discharges or even breakdown [1]. The main sources of particles in insulating oils are external particles originally contained in the oil and internal particles generated by vibration and friction during the installation and maintenance of the equipment [2, 3]. Although the insulating oil is filtered before entering electrical equipment such as transformers to reduce the concentration of impurities in the oil, some metallic and non-metallic particles remain. It is mainly metal parts that vibrate and rub against each other inside the equipment, so the majority of particles are metal.

At present, domestic and international research on the motion of particles in insulating oils inside equipment has focused on the motion of particles in static or low-flowing insulating oils. For static insulating oil, S. Birlasekaran from Australia has studied the motion of metal spheres between parallel flat plate electrodes in a DC field [4], scholars from the University of Genoa, Italy have investigated the motion of metal particles between sphere-plane electrodes in DC and AC fields respectively [5, 6], while C. Choi and others have studied the motion of metal particles between flat plate electrodes in uniform and non-uniform electric fields [7], R. Sarathi of the Indian Institute of Technology studied the motion of metal particles between flat plate electrodes under composite voltages [8]. On the basis of this study, Wang Youyuan and others from Chongqing University in China studied the motion of metal particles between flat plate electrodes, needle-plate electrodes and double-ball electrodes at different ratios of composite voltages [9]. For insulating oil with low flow rate, Tang Ju et al. from Chongqing University investigated the motion of metal particles between flat plates under laminar flow of insulating oil with AC and DC electric field and AC-DC composite electric field [10–13]. Based on the existing research, it can be seen that for static insulating oil, the electric field plays a dominant role in the motion of the metal particles, including the electric field force effect on the charged metal particles and the dielectrophoretic force effect of the non-uniform electric field as the driving force of the particle motion, while the fluid traction force of the insulating oil on the particles is presented as resistance. For insulating oil flowing at low flow rates, as the direction of flow is generally perpendicular to the direction of the electric field, the forces on the metal particles in the electric field direction and the laws of motion are similar to those in the case of static insulating oil, while in the direction of insulating oil flow, the fluid provides the driving force for the particles and the particles move in the same direction as the fluid, with the final motion of the particles resulting from the superposition of the states in both directions.

In electrical equipment, however, in addition to static and low-flow laminar flow states, there is the possibility of turbulence in the insulating oil. In the case of an on-load tap-changer, for example, the contact movement, up to 5–8 m/s, during switching action results in a complex movement of metal particles under the action

of the impinging oil flow and the electric field. In this paper, a simulation is carried out with a flat electrode model to study the movement of metal particles in this case. The simulation allows the motion of the metal particles to be digitized and facilitates the study of the internal motion mechanism and the external influences [14].

2 Simulation Model

In this paper, a two-dimensional simulation model is established using the translation of the flat plate electrodes to imitate the motion of the switch contacts. At the initial moment, the gap between the two flat plates is zero, and the flat plates are subjected to a uniform acceleration followed by a uniform deceleration with the same acceleration magnitude, and the motion lasts for 12 m illiseconds, resulting in a distance of 60 mm between the two flat plate electrodes (Fig. 1).

2.1 Insulation Oil Flow Model

The insulating oil, as a continuous phase, needs to be studied using the Eulerian method, and because of the fast movement of the switch contacts and the complex internal structure, the SST k-ω model is chosen to simulate the fluid motion. According to the Reynolds time-averaged equation:

$$v_0 = \overline{v_0} + v_0' \tag{1}$$

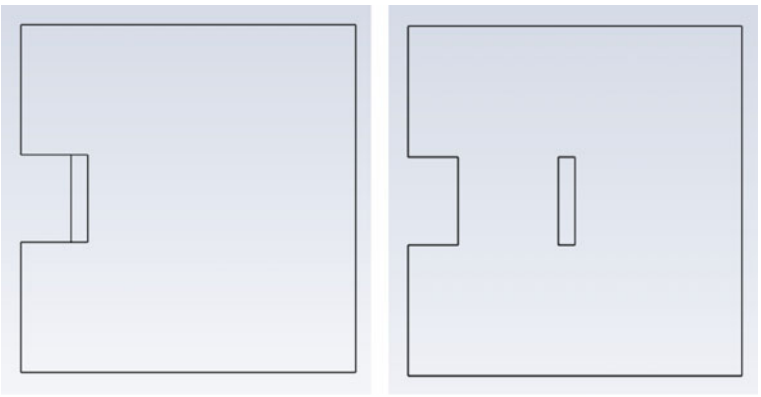

(a) Initial moment (b) Ending moment.

Fig. 1 Schematic diagram of flat plate flat motion

the N-S equation of the turbulence model obtained is:

$$\rho\frac{\partial\overline{v_0}}{\partial t}+\rho(\overline{v_0}\cdot\nabla)\overline{v_0}=\rho g-\nabla\overline{p}+\mu\nabla^2\overline{v_0}+R+S \tag{2}$$

while the Reynolds stress is:

$$R=R(v_0') \tag{3}$$

where ρ is the fluid density, v_0 is the fluid velocity, p is the fluid pressure, R is the Reynolds stress, S is the external force.

2.2 Metal Particle Motion Mode

Since the concentration of metal particles in the insulating oil is small enough to be studied as a discrete phase, the Lagrangian method is used to analyze the forces on individual metal particles, and the kinetic equation of the particles during fluid motion is:

$$\frac{4}{3}\pi R^3\rho_p\frac{dv_p}{dt}=F_G+F_{Bu}+F_D+F_{Am}+F_{Mn}+F_{Sf}+F_p \tag{4}$$

where ρ_p, v_p and R are the density, velocity and radius of the particle, F_G, F_{Bu}, F_D, F_{Am}, F_{Mn}, F_{Sf}, F_p are the gravitational force, buoyancy force, fluid drag force, virtual mass force, Magnus lift force, Saffman force and pressure gradient force on the particle.

Besides, since it is a flat plate electrode, it can be considered as a uniform electric field in the middle, so the dielectric swimming force is not considered. And for the charged particles, the electric field force is:

$$F_E=Eq \tag{5}$$

The charge of charged metal particles comes from the charge transfer when the metal particles collide with the electrode and the value is:

$$q=\frac{2\pi^3\varepsilon R^2E_0}{3} \tag{6}$$

Then the kinetic equation of the charged metal particles is:

$$\frac{4}{3}\pi R^3\rho_p\frac{dv_p}{dt}=F_G+F_{Bu}+F_D+F_{Am}+F_{Mn}+F_{Sf}+F_p+F_E \tag{7}$$

2.3 Solid–liquid Two-Phase Flow Model

The motion model of metal particles in insulating oil can be studied by the solid–liquid two-phase flow model. The external forces S on the insulating oil in Eq. (2) are the force of the moving flat plate and the reaction force of the metal particles on the fluid, whose magnitude is related to the velocity of the metal particles; the external forces F_D, F_{Am}, F_{Mn}, F_{Sf}, F_p on the metal particles in Eq. (4) are related to the fluid velocity of the insulating oil. Thus the solid and liquid phases are coupled by interaction forces and the results are presented by the velocity.

3 Simulation Results

Ansys Fluent was used to simulate the motion of metal particles subjected to both fluid forces and electric field forces when a flat plate electrode is translating.

3.1 Simulation Results of Fluid Motion

The motion of the flat plate was carried out for 12 ms and the simulation lasted 20ms, with a uniform acceleration followed by a uniform deceleration of the same magnitude, and the results were selected for analysis at 3, 6, 9, 12, 15 and 18 ms (Fig. 2).

From the velocity vector diagram of the insulating oil fluid, it can be seen that during the motion of the flat plate, the motion of both sides of the middle axis of the plate is symmetrical, and the insulating oil shows the motion of vortex. In the initial stage of movement, the gap between the flat plate is small, only a symmetrical pair of vortex, with the expansion of the gap between the flat plate, a new pair of vortex on one side of the stationary plate in the opposite direction to the original vortex.

3.2 Simulation Results of Metal Particles Motion

Similarly the positions of the metal particles at 3, 6, 9, 12, 15 and 18 ms were selected for analysis (Fig. 3).

As can be seen from the trajectory of the metal particles, the direction of motion of the metal particles is essentially the same as the direction of velocity of the fluid, so initially, the metal particles enter the inter-plate gap from the side close to the stationary plate. As the motion of the fluid is symmetrical about the central axis, the velocities in the vertical direction are of the same magnitude and in opposite directions at the central position, while in the horizontal direction the velocities are

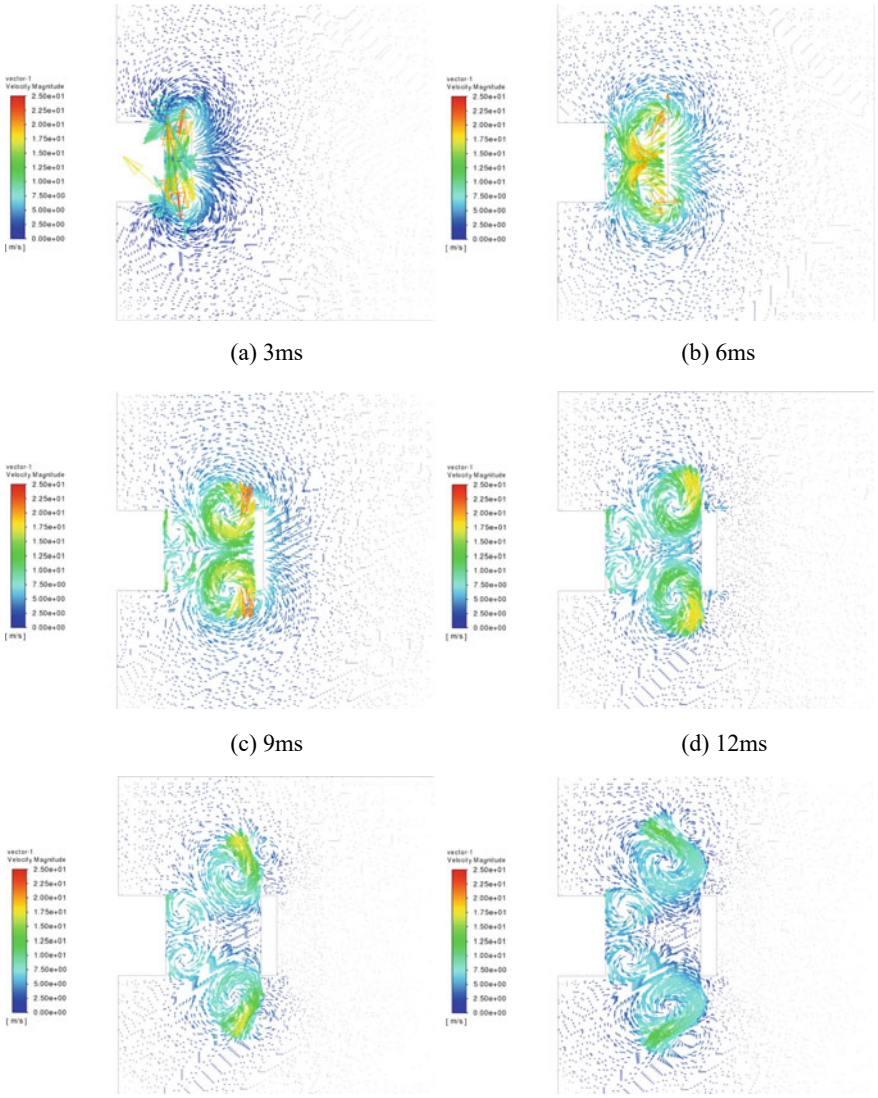

(a) 3ms (b) 6ms

(c) 9ms (d) 12ms

(e) 15ms (f) 18ms

Fig. 2 Fluid velocity vector diagram

of the same magnitude and in the same direction. The metal particles therefore create a 'bridge' of particles at the central axis. As the velocity of the metal particles is much less than the fluid velocity, the 'bridge' of metal particles does not cross the gap until after the plate has finished moving.

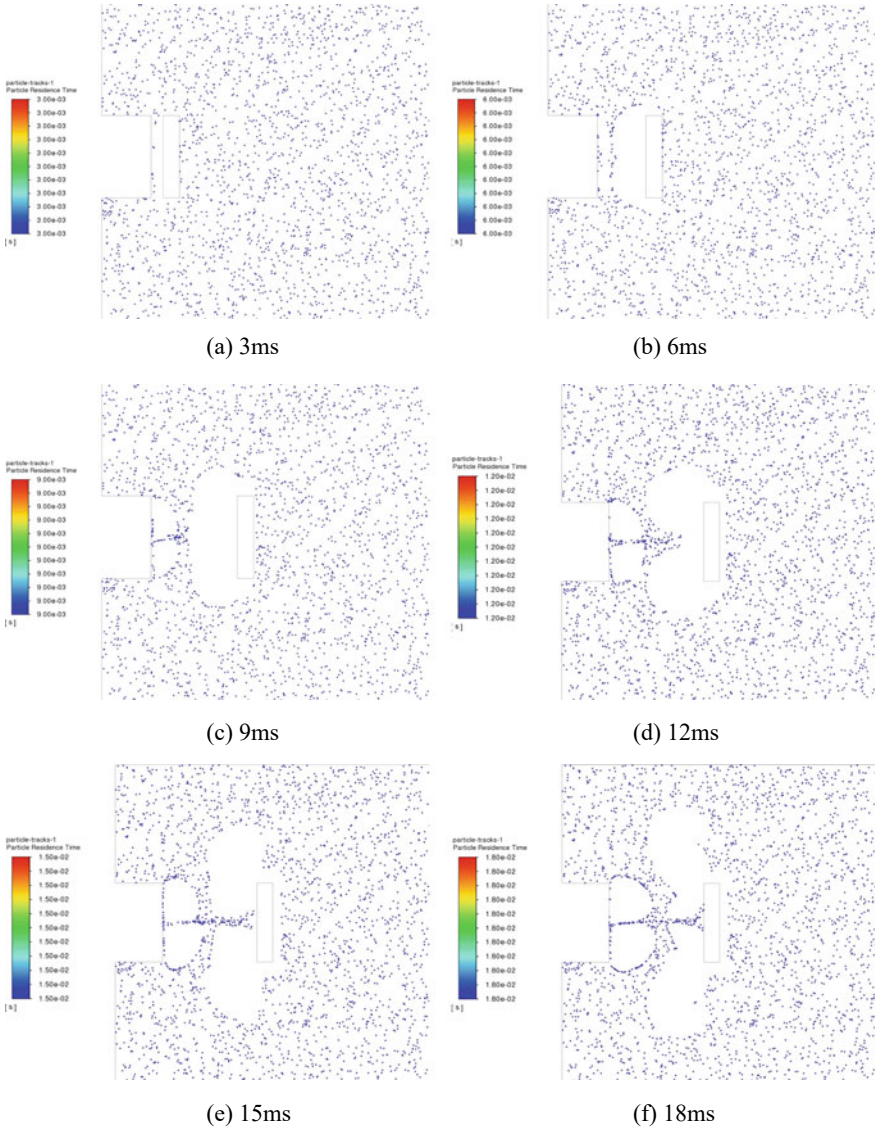

(a) 3ms (b) 6ms

(c) 9ms (d) 12ms

(e) 15ms (f) 18ms

Fig. 3 Metal particle trajectory

4 Conclusion

In this paper, the motion of metal particles in the turbulent state of insulating oil is investigated by constructing a two-dimensional flat plate electrode translation model. According to the solid–liquid two-phase flow, the Eulerian method is used to describe the continuous-phase insulating oil and the Lagrangian method to describe

the discrete metal particles, and the kinetic equations are constructed respectively and coupled. The velocity distribution of the insulating oil and the trajectory of the metal particles are obtained by simulation when the flat plate is moving, and it is found that the metal particles form a “small bridge” under the influence of fluid.

References

1. Hao J et al (2019) Influence of particle properties on DC breakdown characteristics of mineral oil and its difference reason analysis. Trans China Electrotechnical Soc 34(24):5270–5281 (in Chinese)
2. Wang S et al (1988) The effect of content of particle on the dielectric property of transformer oil. High Voltage Eng 1988(03):5–9 (in Chinese)
3. Zhang G et al (2022) Study on fiber impurity particles in liquid insulation of converter transformer. High Voltage Eng 48(11):4297–4305 (in Chinese)
4. Birlasekaran S (1991) The measurement of charge on single particles in transformer oil. IEEE Trans Electr Insul 26(6):1094–1103
5. Denegri GB et al (1977) Field-enhanced motion of impurity particles in fluid dielectrics under linear conditions. IEEE Trans Electr Insul 12(2):114–124
6. Molinari G, Viviani A (1978) Analytical evaluation of electro-dielectrophoretic forces acting on spherical impurity particles in dielectric fluids. J Electrost 5(SEP):343–354
7. Asano K, Choi C, Kamiya M et al (2000) The behavior of a spherical particle under non-uniform electricfield in silicone oil. In: 2000 Annual report conference on electrical insulation and dielectric phenomena, Victoria, Canada, 2000, pp 72–76
8. Sarathi R, Sundarsan RVNV, Roy S (2000) Motion of a particle in the transformer oil under composite voltages. In: The 11th National power systems conference (NPSC 2000) Bangalore, India, 2000, pp 125–129
9. Wang Y et al (2018) Distribution of copper particle in insulating oil and its influence on breakdown strength of insulating oil under combined AC and DC voltage. Trans China Electrotechnical Soc 33(23):5581–5590 (in Chinese)
10. Ma S et al (2015) Simulation study on distribution and influence factors of metal particles in traction transformer. High Voltage Eng 41(11):3628–3634 (in Chinese)
11. Yao Y et al (2021) Motion behaviors and partial discharge characteristics of metallic particles in moving transformer oil under AC/DC COMPOSITE Voltage. Trans China Electrotechnical Soc 36(15):3101–3112 (in Chinese)
12. Cheng L et al (2018) Discharge process and its mechanism analysis in flowing liquid dielectric containing metal particles at different temperatures. High Voltage Eng 44(9):2917–2925 (in Chinese)
13. Luo X et al (2020) Motion behaviors of metallic particles in moving transformer oil under uniform DC electric fields. High Voltage Eng 46(3):824–831 (in Chinese)
14. Liu Y et al (2021) Key technology and application prospect of digital twin in power equipment industry. High Voltage Eng 47(5):1539–1554 (in Chinese)

The Effect of the Number of Wire Electrodes on the Performance of Wire Plate Electrostatic Precipitators

Xinxin Yang, Dongxuan Zhang, Chenlei Han, Feng Liu, and Zhi Fang

Abstract Electrostatic precipitators, which are frequently used in industry, use corona discharge to remove particles from dust air. This article uses COMSOL simulation software to conduct numerical simulation on wire plate electrostatic precipitators, exploring the multiple physical characteristics of electrostatic precipitators with different numbers of wire electrodes, and delving into the collection mechanism and phenomenon of particles in electrostatic precipitators. The simulation results show that the space charge produced by the discharge of the wire plate electrode has the highest density near the discharge electrode and gets weaker in all directions. As the quantity of wire electrodes grows, the lateral flow velocity of the airflow in the entire channel decreases, and the removal efficiency of each particle size also gradually increases. By studying the removal efficiency of particles with different radii, it is found that particles at the submicron level have the lowest removal efficiency. Based on the simulation, experiments are conducted on the wire plate electrostatic precipitator to study the voltage and current characteristics and dust removal effect of the electrostatic precipitator under different numbers of wire electrodes. The experimental results demonstrate that as the number of wire electrodes increases, the peak current increases and the dust removal effect improves, achieving good consistency with the numerical simulation results.

Keywords Electrostatic precipitator · Corona discharge · Wire electrodes · Dust removal effect

X. Yang · D. Zhang · F. Liu (✉) · Z. Fang
College of Electrical Engineering and Control Science, Nanjing Tech University, Nanjing 211816, China
e-mail: f.liu_1@hotmail.com

C. Han
Nanjing Power Supply Company, State Grid Jiangsu Electric Power Co., Ltd, Nanjing 210000, China

© Beijing Paike Culture Commu. Co., Ltd. 2024

X. Dong and L. Cai (eds.), *The Proceedings of 2023 4th International Symposium on Insulation and Discharge Computation for Power Equipment (IDCOMPU2023)*, Lecture Notes in Electrical Engineering 1102, https://doi.org/10.1007/978-981-99-7405-4_8

1 Introduction

With the economy and technology developing so quickly in recent years, the total global energy consumption and pollutant emissions have sharply increased. Air pollution, especially particulate pollution, has caused serious harm to human health and the living environment, so it is of great significance to develop effective dust removal technology. Therefore, it is crucial to create efficient dust removal technology. Among various gas filtration and separation technologies [1], electrostatic precipitators have the characteristics of high dust collection efficiency, low energy consumption, low maintenance cost, and small pressure loss. They are widely used for smoke and dust control, especially in industrial waste gas emissions. The principle of an electrostatic precipitator is to ionize the surrounding air molecules by applying a high voltage between the dust collector and the discharge electrode to form a corona discharge, which generates a huge quantity of electrons and ions. When the dust particles in the air enter the electrostatic precipitator and are charged near the discharge electrode, the charged dust particles change their trajectory under the action of the electric field force and start to move in the direction of the dust collector, which is captured by the plate used to gather dust. The overall removal rate of electrostatic precipitators can reach over 99%. For submicron particles, due to the small particle size carrying less charge, the efficiency is as low as 70–80% [2, 3], and the dust removal effect is not ideal.

To increase the effectiveness of dust removal of electrostatic precipitators, many scholars have conducted research. Kılıç et al. [4] concluded by a combination of experimental and numerical modeling that the effectiveness of particle collecting of all diameters increases with increasing wire diameter. Choi et al. [5] examined the impact of wire electrode arrangement on the characteristics of electrostatic precipitators. For low voltage conditions, the wire electrodes' stacked arrangement caused a turbulence effect and therefore the collection efficiency increased more than the series arrangement. However, under high voltage conditions, the collection efficiency decreased. Chen et al. [6] developed a model in mathematics of an electrostatic precipitator and simulated the occurrence of electrostatic shielding in a wire-plate electrostatic precipitator, and the results showed that increasing the number of discharge electrodes within a particular range can improve the effectiveness of dust removal of an electrostatic precipitator. Khaled and Eldein [7] proposed that a laboratory model of an electrostatic precipitator's corona voltage and current parameters are impacted by the discharge. According to the experimental findings, when the number of discharge wires grows, the corona current also increases noticeably. From the study, it is clear that the number of wire electrodes is one of the crucial parameters impacting the ability of electrostatic precipitators to remove dust.

This paper takes the wire plate electrostatic precipitator as the research object and uses COMSOL simulation software to carry out two-dimensional numerical simulation for electrostatic precipitators with a different number of wire electrodes. It contrasts and evaluates the electrostatic precipitator's flow field velocity distribution as well as the path taken by particles as they pass between the plates. Then, based on

the simulation, experiments are conducted on the wire plate electrostatic precipitator to study its voltage and current characteristics and dust removal effect with a different number of wire electrodes, verifying the accuracy of the simulation model.

2 Numerical Simulation and Result Analysis

The foundation of numerical simulation is modeling. We analyze the physical characteristics and dust removal effect of the dust collector with different numbers of wire electrodes through the model and simulation results, understand the actual experimental situation, and optimize the structural parameters.

2.1 Simulation Module

Electric Field Model The electric field of the wire plate electrostatic precipitator is non-uniform. The generated electrostatic field can be described by Poisson and current continuity equations. The ionic charge density and electric field intensity distribution can be estimated using the following formulae [8–11]:

$$\nabla^2 V = -\frac{\rho}{\varepsilon_0} \tag{1}$$

$$\nabla \cdot \vec{J} = S; \quad \vec{J} = Z_q \mu_i \vec{E} + \rho \vec{u} \tag{2}$$

$$\mu_i \left(\frac{\rho}{\varepsilon_0} - \nabla V \cdot \nabla \rho \right) + \rho \nabla V \cdot \nabla \mu_i + \nabla \rho \cdot \vec{u} = S \tag{3}$$

where, $\vec{J}$ denotes current density; ρ denotes space charge density; S denotes current source; Z_q denotes charge number; $\vec{E}$ table denotes electric field strength; V denotes electric potential; μ_i denotes ionic mobility; $\vec{u}$ denotes fluid velocity vector; ε_0 denotes vacuum dielectric constant.

The strength of the corona electric field is given by Pick's law [12]:

$$E_0 = 3 \times 10^6 \delta \left(1 + \frac{0.0308}{\sqrt{\delta r_i}} \right) \tag{4}$$

Flow Field Model Inside the electrostatic precipitator, the gas flow is seen as incompressible and stable turbulence. The k-ε turbulence model has good convergence. The following are the equations for the conservation of mass and momentum:

$$\nabla \cdot \vec{u} = 0 \tag{5}$$

$$\rho(\vec{u}\cdot\nabla)\vec{u} = \nabla\cdot[-\vec{p}I + \mu(\nabla\vec{u} + (\vec{u}))^T] + F_{EHD} \tag{6}$$

where, μ denotes the dynamic viscosity; ρ denotes the fluid density; P denotes the pressure; F_{EHD} denotes the electrohydrodynamic force, $F_{EHD} = \rho\vec{q}E$.

Particle Charging Model The charge accumulation model of particles is as follows:

$$\tau_c \frac{dZ}{dt} = \begin{cases} R_f + f_a, \ (|v_e| \le |v_s|) \\ R_d f_a, (|v_e| > |v_s|) \end{cases} \tag{7}$$

$$R_f = \frac{v_s}{4\varepsilon_0}\left(1 - \frac{v_e}{v_s}\right)^2; \quad R_d = \frac{v_e - v_s}{\exp(v_e - v_s) - 1} \tag{8}$$

$$f_a = \frac{1}{\begin{cases} (w_e + 0.475)^{0.575} \\ 1, w_e < 0.525 \end{cases}}, w_e \ge 0.525 \tag{9}$$

where, τ_c denotes the characteristic charging constant; R_f and R_d denote the charge rate parameters of field charge and diffusion charge, respectively; f_a denote the function connecting diffusion charge and field charge.

Particle Tracking Model In electrostatic precipitators, the movement of particles is mainly affected by drag and electric field forces. Newton's second law is applied to describe the momentum equation of the particle phase.

The momentum equation is as follows:

$$m_p = \frac{d\overrightarrow{u_p}}{dt} = \vec{F}t; \quad \frac{d\vec{q}}{dt} = \vec{u} \tag{10}$$

where, $\vec{F}t = \vec{F}d + \vec{F}_e$; $\vec{F}_d = \frac{1}{8}\pi C_d \rho_g d_p^2 |\vec{u} - \overrightarrow{u_p}|(\vec{u} - u_p)$; $\vec{F}_e = e\vec{Z}E$.

$$C_d = \max\left[\frac{24}{C_e \mathrm{Re}_p}(1 + 0.15\mathrm{Re}_p^{0.687}), 0.44\right] \tag{11}$$

where, Z denotes the amount of charge accumulated by each particle; C_d denotes the drag coefficient; m_p denotes the mass of particles; u_p denotes particle velocity; Re_p denotes the particle Reynolds number.

2.2 Simulation Results

The geometric model is built using 2D modeling. The double plate electrodes inside the dust collector are equally spaced on both sides of the wire electrode array and

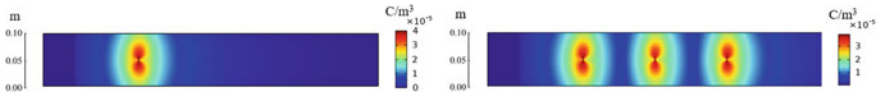

(a) 1 wire electrode (b) 3 wire electrodes

Fig. 1 Space charge density distribution at different numbers of wire electrodes

are used not only as grounding electrodes but also as dust collection electrodes. The wire electrodes are connected to 20 kV DC high voltage. The inlet flow rate is fixed at 1 m/s.

Space Charge Density Distribution The distribution of space charge density at different numbers of wire electrodes is shown in Fig. 1. The charge generated by the discharge of the wire plate electrode is mainly concentrated on both sides of the wire electrode, and the density of space charge is highest near the wire electrode, and gets weaker and weaker away from the wire electrode. When the particles flow through the wire electrodes, the charge accumulates rapidly near the electrodes and moves toward the dust collection plate when the electrostatic force is at work. As the number of wire electrodes increases, the charge density increases accordingly, and most of the particles are more likely to accumulate charge during the flow and spread towards the dust collector plate on both sides and are successfully captured.

Effect of the Number of Wire Electrodes on the Velocity of the Flow Field The velocity distribution of the flow field at varying amounts of wire electrodes is shown in Fig. 2. It can be found that there is a very obvious low wind speed area behind each electrode, while high-speed locations appear on each of the electrodes' sides. When the number of electrodes increases, the high-speed zone also increases accordingly, the transverse flow velocity of airflow in the whole channel decreases, and the residence time of particles in the reaction zone is prolonged, which is more easily captured by the dust-collecting pole under the action of ionic wind.

The Influence of the Number of Wire Electrodes on the Dust Removal Effect As shown in Fig. 3, the diffusion of particles to the two plate electrodes and the quantity of particles caught by the dust collecting plate both increase as the number of wire electrodes rises. From the particle motion trajectory, it can be concluded that the amplitude of each particle diffusion gradually decreases, which is due to the fact that the distance between the particle stream and the wire electrodes increases after each

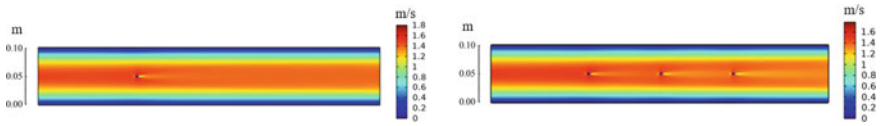

(a) 1 wire electrode (b) 3 wire electrodes

Fig. 2 Velocity distribution of flow field at different numbers of wire electrodes

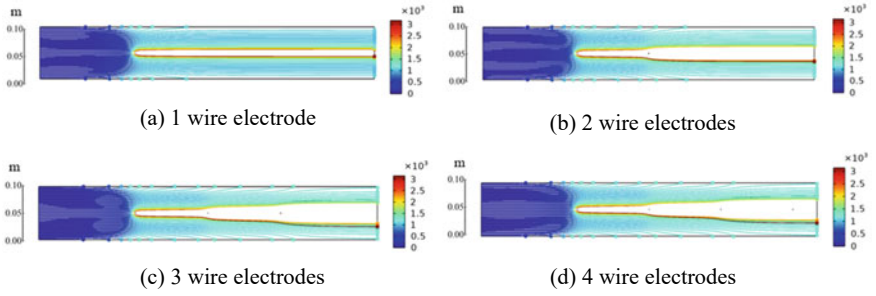

(a) 1 wire electrode (b) 2 wire electrodes

(c) 3 wire electrodes (d) 4 wire electrodes

Fig. 3 Trajectory distribution of 2 μm diameter particles at different numbers of wire electrodes

diffusion, and the ability of the particles to be charged and the electric field force on the particles after being charged will be weakened accordingly, and the amplitude of each particle diffusion decreases. By comparison, it can be seen that the dust removal effect of one and two-wire electrodes is significantly weaker than that of three and four-wire electrodes, and most of the particles are not captured by the dust collection poles, but escape in the original direction of motion after several diffusions, so the more the number of wire electrodes, the better the dust removal effect.

As shown in Fig. 4, when there are four wire electrodes, particles of various sizes can be collected with more efficiency than when there are fewer wire electrodes. When there are more electrodes, the probability of particles being fully charged gradually increases, and it is furthermore simpler to migrate toward the plate electrode under the influence of the electric field force. The collection efficiency of particles of different particle sizes decreases and then increases for different numbers of wire electrodes. The particle collecting efficiency is at its lowest when the particle radius is around 0.2 μm. The accumulated charge number of particles is positively correlated with the particle radius. When the particle radius is too small, the accumulated charge number of particles is less, but it is easier to adhere to the dust collection plate because the traction force is also smaller, thus the collection efficiency of small radius particles is higher. Large-radius particles accumulate more charges during the flow process and are more likely to move towards the dust collection plate under the electrostatic force, resulting in the same high particle collection efficiency.

3 Experiments and Results Analysis

3.1 Experimental Setup and Test Methods

The wire electrodes of the same radius in the wire plate electrostatic precipitator are fixed at equal intervals, and the multi-wire electrodes are placed parallel to the plate electrodes. The specification of the plate electrode is 100 mm × 100 mm stainless

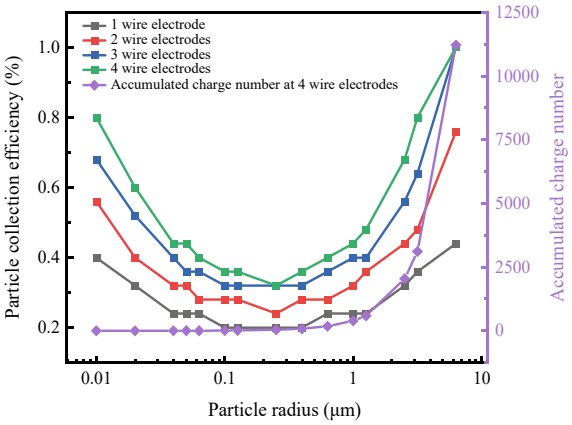

Fig. 4 Particle collection efficiency for different particle radii at different numbers of wire electrodes and cumulative charge of particles with different radii at 4 wire electrodes

steel plate as a ground electrode and dust collection pole, and the wire electrode at the high voltage end is tungsten wire with 10 mm spacing between wire and plate placed to get high dust removal efficiency. The whole reactor is placed inside the closed acrylic box.

In this experiment, high-voltage probes, current coils, and oscilloscopes are used to measure the discharge characteristic images and corresponding voltage and current values. The method of lighting a fixed time moxibustion smoke stick is used to ensure that the initial particle number is at the same level, and the particle level in the reaction box after 220s of stable operation of the dust collector is detected by a particle counter to compare the dust removal effect of different numbers of wire electrodes. After each experiment, the particles inside the reaction box are blown out by a fan to bring the particle number inside the box back to the normal level.

3.2 Experimental Results

Electrical Characteristics and Dust Removal Effect The peak current variation with voltage for different numbers of wire electrodes is shown in Fig. 5a. The experimental environment will have an impact on the data acquisition, resulting in some errors in the experimental results, but the overall trend is within a reasonable range. The overall current peak increases with the rising voltage, and the larger the current peak, the more intense the discharge. For the same voltage applied, the current peak increases as the number of wire electrodes increases, which is mainly due to the increased electric field between adjacent wire electrodes and between the dust collection pole and the wire electrodes.

This experiment mainly compares the particles with particle size greater than or equal to 1.0 μm at different numbers of wire electrodes, so that the dust removal results can be observed more intuitively. According to the comparison of the removal

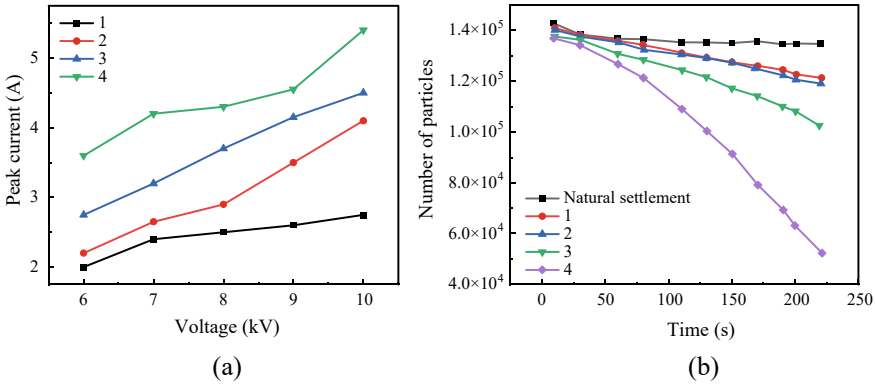

Fig. 5 Variation of peak current with voltage for different numbers of wire electrodes and comparison of the removal effect of particles larger than 1.0 μm with different numbers of wire electrodes

effect of particles with particle size greater than 1.0 μm at different numbers of wire electrodes in Fig. 5b, the more wire electrodes there are, the better the electrodes' ability to remove dust, which is consistent with the earlier simulation results. And the dust removal rate increases slightly with time.

4 Conclusion

(1) The simulation results show that the high-density area of charge grows in proportion to the number of wire electrodes, and most particles are more likely to accumulate charges during the flow process. The high-speed zone in the flow field also increases accordingly, and the maximum wind speed gradually decreases. The transverse flow velocity of the entire channel decreases, and the dwelling time of particles in the reaction zone is extended, making it easier for them to be captured by the dust collector under the action of ion wind.

(2) The efficacy of dust removal increases with the number of wire electrodes. The particle collecting efficiency of different particle sizes first declined and subsequently increased under the number of various wire electrodes. The particle collecting efficiency is at its lowest when the particle radius is around 0.2 μm.

(3) The outcomes of the trial indicate that as the number of wire electrodes increases, the peak current also increases, the discharge intensity becomes stronger, and the dust removal effect becomes better, which is consistent with the simulation results.

References

1. Zhou W, Jiang R, Sun Y et al (2021) Study on multi-physical field characteristics of electrostatic precipitator with different collecting electrodes. Powder Technol 381:412–420
2. Dong M, Zhou F, Zhang Y et al (2018) Numerical study on fine-particle charging and transport behaviour in electrostatic precipitators. Powder Technol 330:210–218
3. Zhuang Y, Kim YJ, Lee TG et al (2000) Experimental and theoretical studies of ultra-fine particle behavior in electrostatic precipitators. J Electrostat 48(3–4):245–260
4. Kılıç M, Mutlu M, Altun AF (2022) Numerical simulation and analytical evaluation of the collection efficiency of the particles in a gas by the wire-plate electrostatic precipitators. Appl Sci 12(13):6401(2022)
5. Choi HY, Park YG, Ha MY (2020) Numerical study on the effect of staggered wire electrodes in an electrostatic precipitator. J Mech Sci Technol 34:3303–3310
6. Chen B, Li S, Guo Y et al (2022) Research on electrostatic shielding characteristics of electrostatic precipitator. J Air Waste Manag Assoc 72(4):331–345
7. Khaled U, Eldein AZ (2013) Experimental study of V-I characteristics of wire–plate electrostatic precipitators under clean air conditions. J Electrostat 71(3):228–234
8. Arif S, Branken DJ, Everson RC et al (2016) CFD modeling of particle charging and collection in electrostatic precipitators. J Electrostat 84:10–22
9. Cagnoni D, Agostini F, Christen T et al (2013) Multiphysics simulation of corona discharge induced ionic wind. J Appl Phys 114(23):233301
10. Adamiak K, Atten P (2004) Simulation of corona discharge in point–plane configuration. J Electrostat 61(2):85–98
11. Wang Y, Gao W, Zhang H et al (2019) Insights into the role of ionic wind in honeycomb electrostatic precipitators. J Aerosol Sci 133:83–95
12. Zhu Y, Gao M, Chen M et al (2019) Numerical simulation of capture process of fine particles in electrostatic precipitators under consideration of electrohydrodynamics flow. Powder Technol 354:653–675

The Effect of Inflation Pressure on the Dielectric Recovery Strength of SF_6 Circuit Breakers

Shijin Xu, Wei Luo, Guoli Wang, Chao Gao, Fusheng Zhou, Yao Zheng, Ruodong Huang, and Ran Zhou

Abstract SF_6 gas is widely used in high-voltage power equipment due to its excellent arc extinguishing performance. During the process of breaking fault current in a circuit breaker, the thermal electrical breakdown problem in the post arc phase is significant. This article is based on a 252 kV high-voltage circuit breaker model, combined with the real gas model of SF_6 gas and the valve plate motion model, and uses the thermal critical breakdown field strength (E_{cr}) of SF_6 to study the calculation method of the recovery strength of the post arc medium. The critical breakdown field strength data under different charging pressures are simulated. The results indicate that increasing pressure Increasing pressure will lead to the decrease of E_a/E_{cr}, and the dielectric recovery strength will increase versus. The research results of this article are of great significance for the optimization design of high-voltage circuit breakers.

Keywords CFD analysis · Dielectric recovery strength · SF_6

1 Introduction

High voltage SF_6 circuit breakers are the key equipment in the power system [1]. During the process of breaking fault current in a circuit breaker, the thermal electrical breakdown problem in the post arc phase is significant. Therefore, in-depth analysis of the thermal re-breakdown mechanism of the circuit breaker has important significance for the maintenance of the circuit breaker.

In recent years, extensive research has been conducted on the simulation of the interruption process of high-voltage SF_6 circuit breakers. A two-dimensional magnetohydrodynamic (MHD) arc model was established for the arc burning stage to study

S. Xu · W. Luo
China Southern Power Grid Co., Ltd, Guangzhou, China

G. Wang · C. Gao · F. Zhou · Y. Zheng · R. Huang · R. Zhou (✉)
CSG Electric Power Research Institute, Guangzhou, China
e-mail: 1009926964@qq.com

© Beijing Paike Culture Commu. Co., Ltd. 2024

X. Dong and L. Cai (eds.), *The Proceedings of 2023 4th International Symposium on Insulation and Discharge Computation for Power Equipment (IDCOMPU2023)*, Lecture Notes in Electrical Engineering 1102, https://doi.org/10.1007/978-981-99-7405-4_9

the complex physical processes inside the arc extinguishing chamber during the disconnection process of high-voltage gas circuit breakers [2, 3]. *Yan* et al. used the MHD model to study the arc behavior of arc extinguishing chambers with different principles, and compared it with the measurement results of arc voltage in air compressor circuit breakers and air pressure in the expansion chamber of self-energy expansion circuit breakers, verifying the effectiveness and feasibility of the MHD model [4, 5]. After the current crosses zero point, the temperature of the gas medium between the contacts rapidly cools from tens of thousands of K during the arc stage to thousands or even hundreds of K, so it can withstand a certain recovery voltage. However, when the recovery voltage is greater than the critical strength of the medium, heavy breakdown may occur. Many scholars have also conducted corresponding research on the electrical breakdown characteristics of SF_6 gas within a certain temperature range [6–8]. Literature [8] provides the calculation results of the equivalent critical breakdown field strength of SF_6 gas under different pressure and temperature ranges. On this basis, Seeger further studied the breakdown characteristics of high-voltage gas circuit breakers by combining arc MHD simulation with electrical breakdown characteristics analysis [6].

This article establishes a magneto-hydro-dynamic model of a 252 kV self-blasted circuit breaker. The dielectric recovery was evaluated, and the recovery of the medium under different inflation pressures was compared. The research results of this article are of great significance for the optimization design of high-voltage circuit breakers.

2 Simulation Models and Calculation Methods

2.1 Arc Model

Computational fluid dynamics (CFD) analysis has been widely used since the last century, especially in the field of design and manufacturing of high-voltage switchgear. During the process of circuit breaker short circuit current breaking, there are complex arc plasma physical phenomena in the surrounding airflow field. This article uses a two-dimensional MHD arc model to simulate the motion of the arc during the breaking process of a circuit breaker. This includes physical processes such as thermal convection, thermal radiation, electromagnetic fields, and nozzle material erosion. Describe the arc behavior based on the basic form of the Navier Stokes equation with added source terms:

$$\frac{\partial \rho \phi}{\partial t} + \nabla(\rho \phi \vec{v}) - \nabla(\Gamma \nabla \phi) = S_\phi \tag{1}$$

where, ρ is the mass density, Φ is a dependent variable that varies with the type of equation: mass conservation, momentum conservation, energy conservation, and component transport equation. S_Φ is the source item.

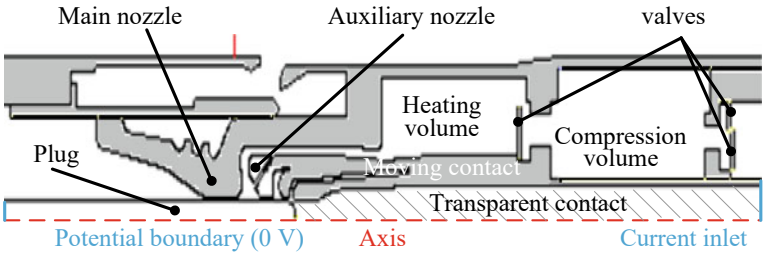

Fig. 1 High voltage circuit breaker calculation model and boundary condition settings

2.2 Calculation Model for High Voltage Circuit Breakers

The simulation in this article is based on a 252 kV level self-blasted circuit breaker model. Due to the symmetrical structural characteristics of the arc extinguishing chamber, the model used in the calculation is half of the circuit breaker profile. Figure 1 shows the physical model of the circuit breaker. Considering that the self-energy SF6 circuit breaker has a hollow arc contact structure, a "transparent contact" is introduced in the model to prevent arc deviation. The maximum stroke of the moving parts is 166 mm. When opening, the distance between the dynamic and static arc contacts is 78 mm, and the average speed during the movement of the mechanism is 5.5 m/s.

Import ANSYS FLUENT for magnetic fluid simulation, with boundary and initial conditions set as:

(1) The interior of the switch is filled with SF_6 gas;
(2) The effective value of the set short-circuit current is 35 kA, the frequency is 50 Hz, and the arc is ignited for half a cycle;
(3) The initial inflation pressure is 0.6 MPa and 0.7 MPa, and the pressure outlet boundary is shown in the figure;

2.3 Valve Plate Motion Model

The action of the valve is mainly determined by the force difference on the two sides of the valve. When the air pressure in the chamber increases, the force on the side of the valve will increase. If the force driving the valve to open is F_k and the force driving the valve to close is F_g, the percentage P_F of the difference in force on the two sides of the valve can be expressed as:

$$P_F = \frac{F_k - F_g}{F_k} \times 100\% \tag{2}$$

Considering the influence of factors such as friction and pressure fluctuations on the valve, a threshold of ± 2% has been introduced to prevent the valve from oscillating back and forth. The action criteria of the valve are:

When $P_F > 2\%$, the force driving the valve to open is greater. If the valve is in a closed state at this time, the valve will open, otherwise it will not act. If the pressure relief valve is already in an open state, it will tend to move in the direction of larger opening scale;

When $P_F < -2\%$, the force driving the valve to close is greater. If the valve is in an open state at this time, the valve will close, otherwise it will not act. If the opening scale of the relief valve is large, the relief valve will tend to move in the direction of the smaller opening scale;

When $-2\% \leq P_F \leq 2\%$, the valve does not operate, i.e. it remains in its current state.

2.4 SF_6 Thermal Critical Breakdown Field Strength

Due to the large amount of heat generated during the arc stage, the temperature increases, leading to gas decomposition. The critical breakdown field strength of gases is related to the types of particles, collision ionization, adsorption, and recombination processes. The electron energy distribution of weakly ionized gases will deviate from the Maxwellian and Druyvesteyn distributions. By solving the Boltzmann equation with two approximations, the electron energy distribution function (EEDF), reduced ionization reaction coefficient, and reduced adsorption reaction coefficient of the hot gas can be obtained. The reduced critical breakdown field strength $(E/N)_{cr}$ of the gas at different temperatures can be determined. Finally, the product of $(E/N)_{cr}$ and particle number N can be used to obtain the critical breakdown field strength E_{cr} of the hot gas. Figure 2 shows E_{cr} under different pressures between 300 and 3000 K. E_{cr} is a function of temperature and pressure.

2.5 Calculation Method for Recovery Strength of Post Arc Dielectric

Taking the pressure and temperature distribution in the arc extinguishing chamber at the end of the thermal recovery phase as the initial state of the electrical recovery phase, the E_{cr} of each point in the arc extinguishing chamber is obtained by linear interpolation of the critical breakdown field strength data table, and the electric field strength E_a of each point in the arc extinguishing chamber is calculated according to the applied voltage U_a. By comparing the value of E_a/E_{cr} and 1, it is determined that breakdown occurs in the arc extinguishing chamber, i.e. in the area where $E_a/E_{cr} > 1$ occurs. In addition, taking the weakest point between fractures, i.e. the maximum $E_a/$

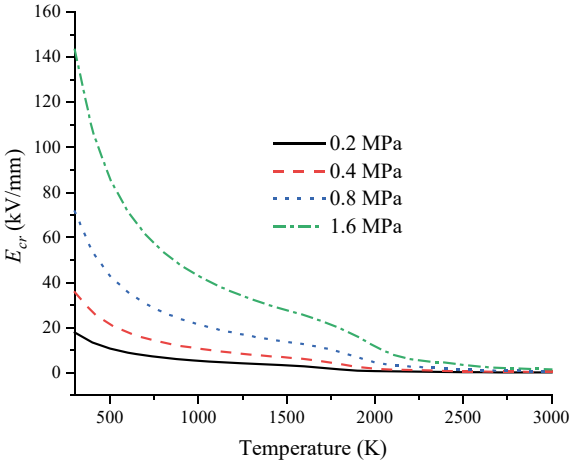

Fig. 2 The Ecr of pure SF6 at 300 K ~ 3000 K for different gas pressure

E_{cr} value, as the reference value, the calculation formula for the critical breakdown voltage Ucr that the circuit breaker can withstand at different times after arc is:

$$U_{\mathrm{cr}} = U_{\mathrm{a}}/(E_{\mathrm{a}}/E_{\mathrm{cr}})_{\max} \tag{3}$$

The above evaluation method is based on the weakest point between ports, and the obtained critical breakdown voltage is much greater than the actual critical breakdown voltage. However, the critical breakdown field strength of each point in the arc extinguishing chamber obtained through temperature and pressure interpolation still has certain reference significance for the recovery of post arc dielectric strength.

3 Calculation Results of Electric Breakdown Characteristics

As shown in Fig. 3, the distribution diagram of temperature and pressure inside the arc extinguishing chamber at the moment of maximum contact rebound under different inflation pressures when the 252 kV circuit breaker breaks the short circuit current. The temperature has dropped to below 500 K after cooling for 12 ms. It can be seen that changing the pressure will affect the temperature distribution inside the arc extinguishing chamber. Increasing the pressure is conducive to the cooling of the arc extinguishing chamber. The lower the internal temperature of the arc extinguishing chamber. By comparing the pressure distribution, it can be seen that the curves of the pressure cloud map distribution are almost consistent.

Figure 4 shows the comparison of E_{cr} and E_a and E_a/E_{cr} distribution at different filled pressure when the contact bounces back to the maximum. It can be observed that the critical breakdown field strength in the nozzle area between the arc contacts

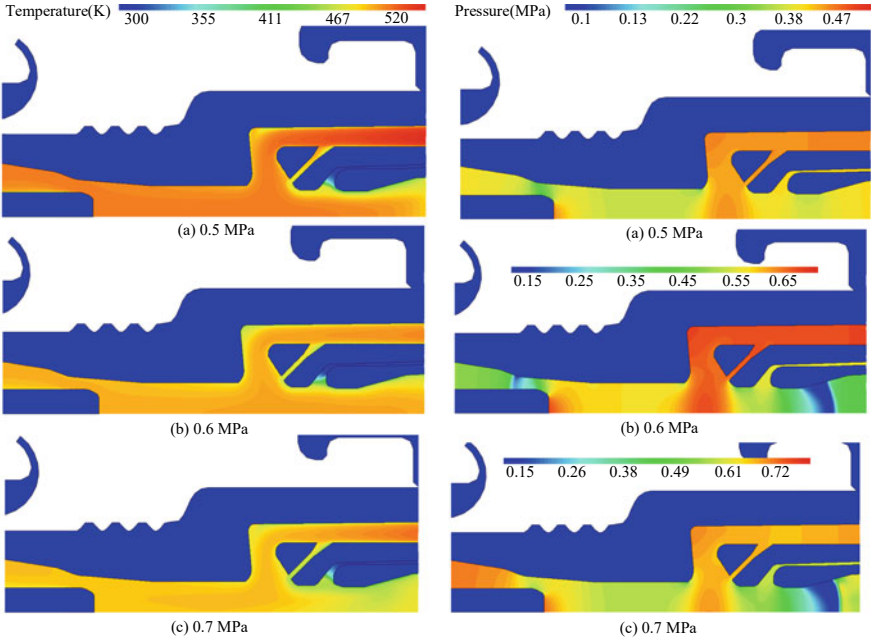

Fig. 3 Comparison of temperature and pressure distribution at different short-circuit currents and maximum contact rebound

gradually increases with the increase of pressure. The distribution of the critical breakdown field strength is consistent with the distribution of temperature and pressure (Fig. 3). The distribution of field strength is similar in several cases, with higher field strength near the end of the arc contact and lower field strength inside the nozzle throat and moving arc contact. Under different pressures, E_a/E_{cr} will decrease with increasing pressure. The distribution of E_a is approximately the same under different pressures, and increasing pressure will lead to an increase in E_{cr}. Therefore, after increasing pressure, E_a/E_{cr} will decrease, and the dielectric recovery strength will also decrease.

Figure 5 shows the variation curve of dielectric recovery strength under different pressures. Near the current zero zone, the arc gradually contracts as the current decreases, and the gas flowing out of the expansion chamber quickly cools the hot gas near the nozzle area. Therefore, the strength of the arc gap medium increases rapidly after the current passes zero. As the rebound process of the circuit breaker begins, around 2.5 ms after zero, the recovery strength of the medium will reach a peak value. The rebound process will increase the background field strength between the contacts and increase the probability of breakdown, The recovery strength of the medium decreases and increases correspondingly with the increase and decrease of rebound. At the same time, the rebound of the contact causes fluctuations in the internal pressure of the arc extinguishing chamber, resulting in fluctuations in the dielectric recovery strength. At 40 ms, the rebound stage ends, and at this time, the dielectric

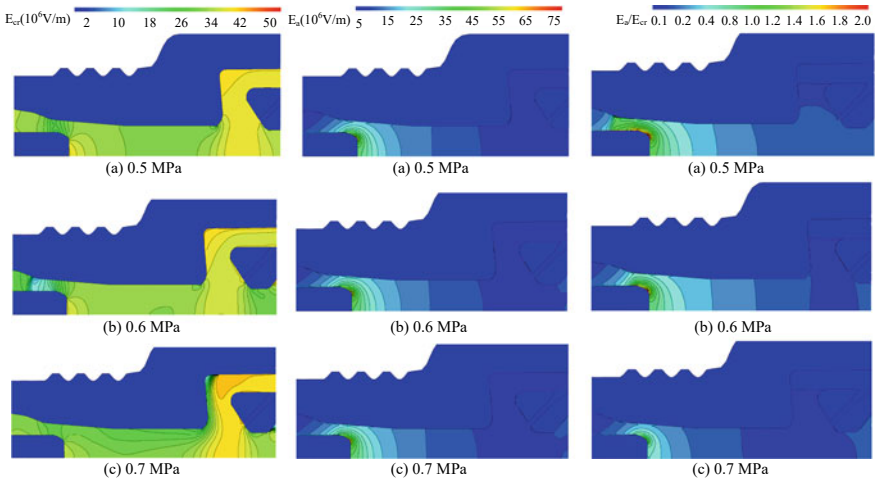

Fig. 4 Comparison of E_{cr} and E_a and E_a/E_{cr} distribution at different filled pressure when the contact bounces back to the maximum

recovery strength inside the arc extinguishing chamber remains almost unchanged. As the pressure increases, the fluctuation of the medium recovery strength during the rebound stage gradually increases. After lowering the atmospheric pressure by one atmosphere, the recovery strength of the quasi cold medium decreases by 31.7%; After increasing by one atmospheric pressure, the recovery strength of the quasi cold medium increases by 27.4%.

Fig. 5 Strength recovery curve of arc gap medium under different pressure

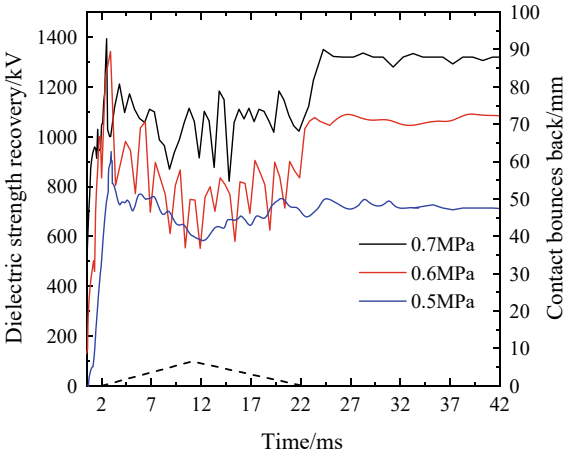

4 Conclusion

This article is based on the 252 kV high-voltage circuit breaker model to study the influence of the filled pressure on the dielectric recovery strength. The following conclusions are obtained:

(1) Regardless of the pressure, the temperature inside the arc extinguishing chamber drops to around 500 K in the post arc stage. Increasing the pressure is beneficial for the cooling of the arc extinguishing chamber and will lead to the decrease of E_a/E_{cr}, and the dielectric recovery strength will increase versus.
(2) Lowering the pressure by one atmosphere will lead to decreases of 34.7% of the recovery strength of the quasi cold condition, and increasing by one atmospheric pressure will lead to increasing by 14.6%.

Acknowledgements This manuscript is sponsored by the Science and Technology Project of China Southern Power Grid SEPRI-K225015.

References

1. Bizjak G, Zunko P, Povh D (2004) Combined model of SF_6 circuit breaker for use in digital simulation programs. IEEE Trans Power Delivery. https://doi.org/10.1109/TPWRD.2003.820218
2. Guo Z, Liu S, Pu Y, Zhang B, Jia S (2019) Study of the arc interruption performance of CO_2 gas in high-voltage circuit breaker. IEEE Trans Plasma Sci 47(5):2742–2751. https://doi.org/10.1109/TPS.2019.2904981
3. Guo Z, Li X, Zhang Y, Guo X, Xiong J (2017) Investigation on the influence of gas pressure on CO_2 arc characteristics in high-voltage gas circuit breakers. Plasma Phys Technol 4(1):95–98. https://doi.org/10.14311/ppt.2017.1.95
4. Jin LZ, Yan JD (2000) Investigation of the effects of pressure ratios on arc behavior in a supersonic nozzle. IEEE Trans Plasma Sci 28(5):1725–1734. https://doi.org/10.1109/27.901260
5. Jin LZ, Yan JD, Murphy AB, Hall W, Fang MTC (2002) Computational investigation of arc behavior in an auto-expansion circuit breaker contaminated by ablated nozzle vapor. Plasma Sci IEEE Trans 30(2):706–719. https://doi.org/10.1109/TPS.2002.1024273
6. Seeger M, Schwinne M, Bini R, Mahdizadeh N, Votteler T (2012) Dielectric recovery in a high-voltage circuit breaker in SF_6. J Phys D Appl Phys 45(39):395204. https://doi.org/10.1088/0022-3727/45/39/395204
7. Yan JD, Fang M (1997) Dielectric breakdown of a residual SF_6 plasma at 3000 k under diatomic equilibrium. IEEE Trans Dielectr Electr Insul 4(1):114–119. https://doi.org/10.1109/94.590878
8. Li X, Zhao H, Jia S (2012) Dielectric breakdown properties of SF_6–N_2 mixtures in the temperature range 300–3000K. J Phys D-Appl Phys 44(45):20–2134. https://doi.org/10.1088/0022-3727/45/44/445202

Investigation on Very Fast Transient Overvoltage Caused by Incomplete Separation of Air-Insulated Switches

Yongjie Zhang, Yong Xu, Ming Gao, Ji Sheng, Danhua Chen, Jie Yuan, and Wentao Yang

Abstract The air-insulated isolation switch has the ability to interrupt small capacitive currents, but it does not have the function of extinguishing arcs. In the event of incomplete Break of Three-Phase, severe arcs can occur, and the capacitive voltage and arc current on the power side will produce a large pulse wave, which poses a great threat to the equipment insulation. Based on the actual spatial structure and electrical characteristics of the substation, each component underwent reasonable equivalence processing. Using ATP-EMTP simulation, the situation of gap discharge in the isolation switch during incomplete Break was analyzed. The transitory process of repeated breakdown of the gap was studied, and the causes of accidents caused by incomplete Break of Three-Phase were summarized. Measures and ideas for suppressing transitory overvoltage were proposed. The results indicate that incomplete Break of the isolating switch can cause a significant decrease in insulation voltage at the disconnection gap, and long-term intermittent repetitive discharge can cause high-frequency oscillations that generate rapid overvoltage with amplitudes and steepness higher than normal values. This phenomenon can easily cause damage to adjacent equipment insulation, resulting in huge hazards. In large power systems, most cases of incomplete Break of Three-Phase switch are caused by long-term overvoltage shocks that lead to equipment insulation breakdown. Appropriate line lengths and reducing residual charges can help to reduce overvoltage.

Keywords Air-insulated substation · Incomplete separation · Disconnect switch · Very fast transient overvoltage · Electromagnetic transient program

Y. Zhang · Y. Xu · M. Gao · J. Sheng
STATE Grid Yangzhou Power Supply Company, Yangzhou 225001, China

D. Chen (✉) · J. Yuan · W. Yang
College of Electrical and Information Engineering, Hunan University, Changsha 410082, China
e-mail: danielchen@hnu.edu.cn

J. Yuan
e-mail: yuanjie@hnu.edu.cn

W. Yang
e-mail: yangwt@hnu.edu.cn

© Beijing Paike Culture Commu. Co., Ltd. 2024

X. Dong and L. Cai (eds.), *The Proceedings of 2023 4th International Symposium on Insulation and Discharge Computation for Power Equipment (IDCOMPU2023)*, Lecture Notes in Electrical Engineering 1102, https://doi.org/10.1007/978-981-99-7405-4_10

1 Introduction

With the continuous construction and expansion of power grids, high-voltage AC air-insulated isolation switches are widely used in power systems because of their small footprint, high reliability and low cost. The isolation switch has no arc extinguishing function and generally does not undertake the function of short-circuit and load currents, but as it is usually connected to lightning arresters, transformers, no-load transformers et cetera, the isolation switch needs to have a certain small current disconnection capability [1–5]. The electromagnetic transient issues such as overvoltage and overcurrent caused by operating isolation switches are becoming increasingly serious, and the number of accidents they trigger is gradually increasing [6].

Currently, research on the ultra-fast transient overvoltage is mainly focused on GIS disconnect switches (DSes) [6–12]. Research on air-insulated DS is relatively few, and there is currently no research on the incomplete disconnection conditions of air-insulated DS. Kai [6] investigates the ultra-fast transient overvoltage induced by CBs under incomplete breaking conditions, but there is a significant difference between the overvoltage induced by CB breakdowns under GIS conditions and those under air isolation switch conditions. Though [13] proposed a breaking model for air-insulated isolating switches, it did not consider the impact of incomplete three-phase breaking on overvoltage. In the long process of arc discharge, weather and other physical factors, as well as the coupling effect between fault phase and non-fault phase, may lead to multiple reignitions of the arc caused by small currents. Therefore, its simulation model is difficult to achieve ideal results.

This paper selects the air-insulated isolating switch of a 220 kV substation in Jiangsu as the research object. The electromagnetic transient program (EMTP) is used to compute the overvoltage of the air-insulated disconnect switch under incomplete breaking conditions; the effects of parameters such as transformer incoming line length and residual charge are discussed.

2 Description of Failure Caused by Incomplete Separation of DS

A conventional substation in Jiangsu has 220 kV bus operation as shown in Fig. 1, and its operation status before the fault is described below. 220 kV A substation has two 220/110/10 kV main transformers. According to the dispatching command, all equipment connected to bus I needs to be transferred to bus II, and No. 4616 switch is changed to run on 220 kV bus I, through bus couple 2610 and 4616 switch to 4616 line impact, after the impact is normal, the dispatching order is executed to turn 220 kV female switch to cold standby, the accident process as shown in Table 1.

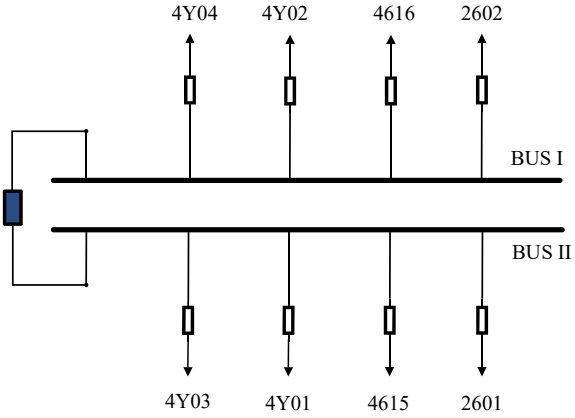

Fig. 1 Single-line diagram of 220 kV substation

Table 1 SOE of the fault

Time	Event
2020.9.16 20:45	Switch 2610 splitter
2020.9.16 21:00	Disconnect switch 26,101 incomplete separation
2020.9.16 21:49	Current transformer B phase explosion

On September 16, 2020, the No. 2610 CB, as illustrated in Fig. 1, was switched to standby state and the console SOE signal showed that No. 2610 switch was tripped at 20:45:10, confirming that the 220 kV switch was disconnected at 20:45.

While separating the busbar I DS 26,101 at around 21:00, phases B and C DSes were not in place, and the contacts were only separated by about 10 cm. After the manual operation was invalid, the isolation switch was in discharge state, and the DS was divided as shown in Fig. 2.

At 21:49, an explosion occurred in the 220 kV busbar No. 2610 branch together, 220 kV busbar protection I busbar differential action, all switches of 220 kV busbar are tripped, loss of power of No.1 main transformer, total loss of load 35,000 kW, affecting a total of 6820 users.

According to the investigation and failure analysis, 220 kV busbar 2610 current transformer B-phase short-circuit fault, resulting in busbar protection tripping, the cause of the fault is 26101 isolation switch is not in place to generate arc, small current arc by external influences in the long time discharge process constantly reignited to generate overvoltage, a longer impact leads to the insulation breakdown of current transformer.

Fig. 2 Photo of DS under incomplete isolating state in the field

3 Mathematical Model

According to the actual spatial structure and operation mode of the substation line, appropriate line branches are selected to model the isolation switch overvoltage model, and the 220 kV bus operation mode of the substation is shown in Fig. 3.

The establishment of a proper equivalent model and the selection of appropriate parameters will have an important impact on the simulation results. Each phase in the three-phase incomplete division process has differences, and the influence of factors such as inter-phase coupling needs to be considered, so a three-phase independent division and closing model of the disconnecting switch should be established. In the modeling of substation air-insulated switches, the parameter selection of components needs to be taken into account the influence of multiple relationships such as size, shape and mutual position on the parameters, mainly considering those factors that have a greater impact on the results, such as transformers, busbars, overhead lines, CBs, DSes, PTs, etc. Factors such as grounding cutter, bushing and arrester that have less impact on the simulation can be ignored [14]. Transformer equivalent inlet capacitance is 2500 pF, equivalent inductance is 25 pF, AC voltage source provides stable excitation of transformer voltage level [15, 16]. The busbar is equated with a parametric model with a wave speed of light and a wave impedance of 350 Ω. The overhead line is equated with a distributed parametric model with a wave speed of light and a wave impedance of 300 Ω. The potential transformer can be represented by the equivalent capacitance to ground. The disconnecting switch can be equated

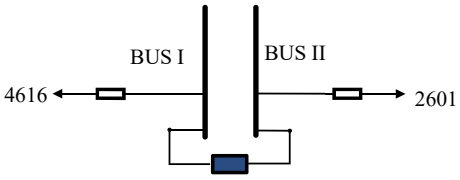

Fig. 3 Single-line diagram of 220 kV substation under study

Table 2 Main parameters for substation

Parameter	Value	Unit
Transformer	2500	pF
Busbar	350	Ω
Overhead line	300	Ω
Circuit breaker opening status	450	pF
Circuit breaker closing status	Equivalent to part of the busbar	pF
DS opening status	150	pF
DS closing status	80	pF
PT	200	pF
Wavespeed	3 × 108	m/s

to the ground capacitance in the divide-and-close state, and can be equated to the series model of inductance and resistance in the arc-burning state. The CB and in the closed state can be equated as a part of the overhead line, and in the split state the switch break can be replaced by a series capacitance. The distance between the transformer and the isolating cutter is 20 m, the length of the double-ended busbar is 50 m, and the length between the rest of the components is 5 m (Table 2; Fig. 4).

4 Simulations Study

This simulation sets the first closing at the peak of phase B, which makes the maximum overvoltage generated, and the overvoltage magnitude on its main equipment is shown in Table 3.

As can be seen from Table 3, while operating the DS, the transformer, the DS, the CB and the busbar has different peak values. The overvoltage amplitude at busbar I is the largest and the overvoltage amplitude at the transformer side is the smallest, The overvoltage at the value of transformer side is much smaller than t others. the maximum value of overvoltage at each point is smaller than the lightning surge withstand voltage of 2.32 p.u. [17], the overvoltage of the transformer is also less than the rated withstand voltage of the winding 2.0 p.u. [18–20]. So, the CT in the accident between the middle of the DS and CB is not directly pierced by the overvoltage, and Fig. 5 shows the overvoltage waveforms on both sides of DS.

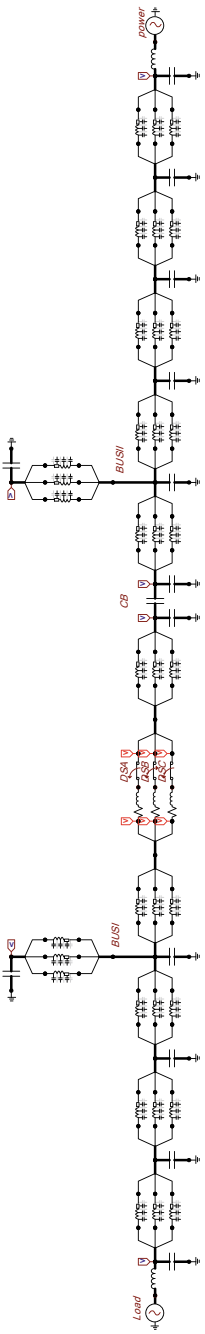

Fig. 4 Circuit diagram for simulation under DS incomplete breaking overvoltage model

Table 3 Overvoltages of power equipment within substation

Main test components	Peak value	Peak value (p.u.)
Transformer	442	1.42
Load side of DS	600	1.93
Power side of DS	602	1.94
CB	510	1.61
Busbar I terminal	670	2.15
Busbar II terminal	639	2.05
Load side	601	1.93

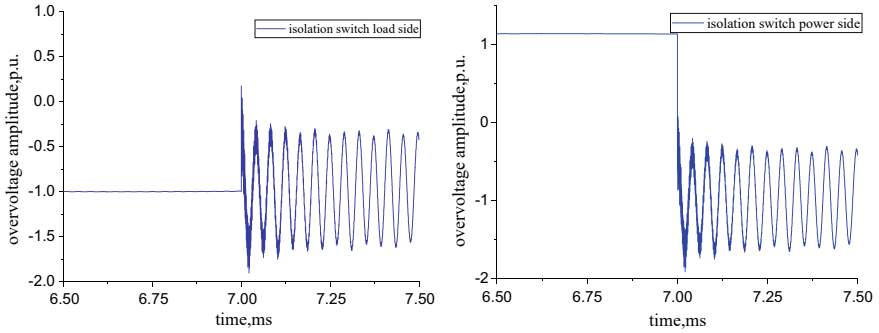

Fig. 5 Waveform of overvoltage around the DS. **a** Load side of DS; **b** Load side of power

5 Results and Discussion

5.1 Influence of Main Transformer Inlet Line

Branch circuit length is one of the main factors affecting overvoltage, in some cases, a small change in bus length can cause a large change in node voltage [21], Considering the different spatial structure of each substation, the length of the main transformer inlet to the transformer also varies greatly. Integrating the spatial structure of several substations, six different lengths were selected for simulation, and the parameters were obtained as shown in Table 4.

As the length of the main transformer inlet line increases, within the length range of 5–20 m, the change law of overvoltage magnitude of each device has obvious differences, mainly divided into 3 categories, busbar, load-side equipment and power-side equipment. In the bus end position, with the length increase, the overvoltage amplitude shows an overall decreasing trend, for the isolated switch load side equipment, its overvoltage has an obvious decreasing trend with the increase of the main transformer inlet length, while for the isolated switch power side equipment, its overvoltage basically does not change, only the transformer outlet voltage increases, but

Table 4 Effect of main transformer inlet line length on the equipment overvoltage (p.u.)

Main test equipments	5 m	10 m	15 m	20 m	25 m	30 m
Transformer	1.42	1.44	1.45	1.45	1.43	1.44
Load side of DS	2.29	2.14	2.18	1.88	1.93	2.03
Power side of DS	1.93	1.94	1.92	1.93	2.32	2.27
Terminal of busbar I	2.57	2.56	2.51	2.18	2.64	2.73
Terminal of busbar II	2.28	1.96	2.05	2.05	2.49	2.51
Load side	2.29	2.14	2.03	1.95	2.29	2.40

the increase magnitude is very small and can be considered to remain unchanged. As the inlet length of the main transformer continues to increase, the overvoltage of equipment at other locations besides the transformer has a tendency to increase significantly, while the overvoltage at the transformer decreases slightly, but it basically considered to remain unchanged. The reason for this phenomenon is that due to the short wavefront time of overvoltage, it propagates in the form of traveling waves within the overhead line. Complex refraction and reflection phenomena occur at the wave impedance mutation, and the branch length determines the overvoltage after folding and reflection, and the subsequent generation of overvoltage superimposed to enhance or weaken the overvoltage amplitude. Due to the extremely fast propagation speed and short wavelength of the traveling wave, a small change in the branch length will have a great impact on the overvoltage waveform. Figure 6 shows the overvoltage waveform when the main transformer feed line length is 5 and 20 m.

From Fig. 6, it can be seen that the overvoltage generated at the isolation switch at the main transformer feed line length of 5 m is much higher than that at the feed line length of 20 m. Therefore, choosing a suitable branch length will help suppress overvoltages at the equipment within the substation.

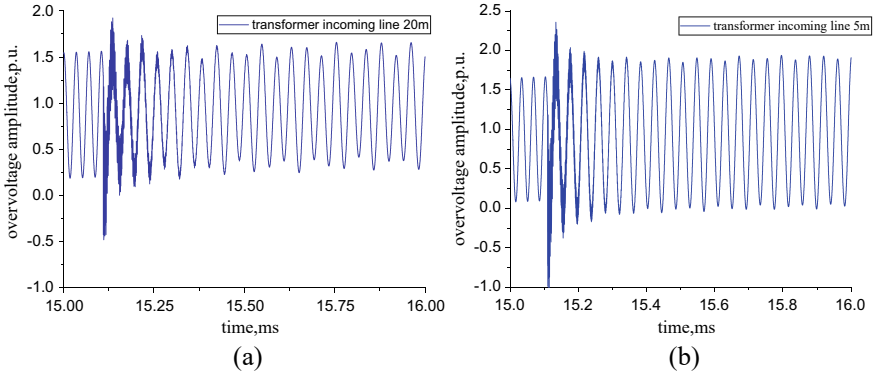

Fig. 6 Overvoltage waveforms at the DS. **a** Inlet line length of main transformer is 20 m. **b** Inlet line length of main transformer is 5 m

5.2 *Influence of Residual Charge*

After the isolation switch gap is broken, due to the small current passing through the isolation switch gap, resulting in different magnitudes of residual charge on the load side of the isolation switch after the arc is broken. In order to study the effect of different residual charges on the overvoltage of each device, five groups of residual charges are selected for simulation in this paper, which are 0, −0.25, −0.5, −0.75, −1.0 times the voltage value (Table 5).

As can be seen from Fig. 7, as the residual voltage of the line rises, the overvoltage magnitude of each device is also increasing, where the overvoltage of the transformer reacts more slowly to the residual voltage, while the maximum overvoltage at the disconnector switch break reacts more violently to the magnitude of the residual voltage, which shows that the overvoltage at the disconnector switch break rises faster under the same residual voltage change, while the characteristics of the bus overvoltage are in the middle of the transformer and the DS. This shows that the residual charge has a greater influence on the overvoltage at the disconnector switch.

Table 5 Overv Effect of residual charge on overvoltage

Residual voltage (p.u.)	DS	Transformer	Busbar I	Busbar II
0	1.07	1.12	1.48	1.68
−0.25	1.64	1.25	1.23	1.81
−0.5	1.85	1.29	1.70	2.02
−0.75	2.08	1.38	2.18	2.06
−1.0	2.21	1.43	2.15	2.12

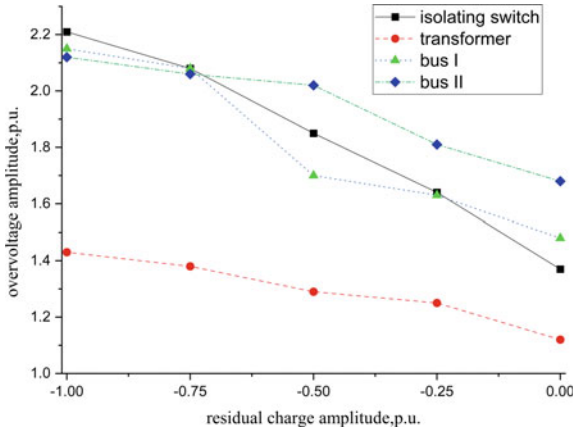

Fig. 7 Effect of residual charge on overvoltage

6 Introduction

The conclusions are as follows:

- The simulation data found that even in the most serious case of overvoltage, the overvoltage of the equipment at each location did not exceed the set value of insulation breakdown, and the disconnecting switch three phases incompletely divided to the final explosion of the current transformer for a longer period of time, so the possibility of direct destruction of insulation by overvoltage is ruled out. But the data show that the overvoltage generated at the isolation switch is large, in a complex external environment, small current discharge process for a long time, must be accompanied by the reignition of the isolation switch gap arc, overvoltage will impact the adjacent equipment again and again, continuous discharge will also lead to the surrounding temperature rise, and compared to other equipment, the current transformer nearest to the isolation switch and more fragile, again and again the overvoltage impact and temperature rise The insulation of the current transformer is gradually aging, and eventually the insulation is destroyed, which leads to more serious accidents.
- The length of the main transformer inlet line has different degrees of influence on the overvoltage at each location of the substation, among which the overvoltage at the exit of the transformer is the smallest, and the overall influence on the equipment at other locations shows a trend of first decreasing and then increasing. Therefore, choosing the appropriate length of the main transformer inlet line has a certain role in reducing the overvoltage generated by the incomplete separation of the three phases of the disconnecting switch.
- The residual charge has an overall positive correlation to the overvoltage generated by the substation. As the residual charge increases, the greater the overvoltage generated by each device in the case of incomplete three-phase separation of the disconnecting switch. Rapid removal of residual charge is of some significance to eliminate this type of overvoltage.

References

1. Xinyin (2009) Electrical part of power plant. Electric Power Press, Beijing: China (in Chinese)
2. Wei SHI, Yuchang QIU (2006) ZHANG qiaogen foundation of high voltage engineering. Machine Press, Beijing, China (in Chinese)
3. Zhang YAN (2002) ZHU Deheng High voltage insulation technology. Electric Power Press, Beijing, China (in Chinese)
4. Jiali Q, Jierong Z (1999) Switching capacitor current and small inductance current of high voltage switch. China Electric Power Press, Beijing (in Chinese)
5. Pu Z (2021) Simulation and analysis of fast transient overvoltage in UHV GIS. Electric Power Press, Beijing: China (in Chinese)
6. Kai D (2018) Research on extra fast transient overvoltage induced by incomplete breaking of circuit breakers. Chongqing University, Chongqing, China (in Chinese)

7. Qi W (2022) Study on the effect of disconnect switch division and no-load busbar on VFTO. Electro Technical Materials, China (in Chinese)
8. Zhenhua L, Xingrui L, Yue T, Xiaoxue C (2023) Simulation and characterization of VFTO and VFTC based on dynamic reignition arc model. Power System Protection and Control, China (in Chinese)
9. Yinbiao S, Bin H, Jiming L et al (2013) Influence of the switching speed of the disconnector on very fast transient overvoltage. IEEE Trans on Power Del 28(4):2080–2084
10. Haseeb MA, Thomas MJ (2017) Computation of very fast tran-sient overvoltages (VFTO) in a 1000 kV gas insulated substation. In: IEEE PES Asia-Pacific Power and energy engineering conference. Bangalore, India
11. Pathak N, Bhatti TS (2015) Ibraheem study of very fast transient over voltages and mitigation techniques of a gas insulated substation. In: International conference on circuit Kumaracoil, India
12. Huamao Z, Shaofeng D, Chengrong L et al (20141) A novel arc model for very fast transient overvoltage simulation in a 252-kV gas-insulated switchgear. IEEE Trans on Plasma Sci
13. Chunqiang S, Zhendong K, Bo L, Liang W, Shulei X, Nana D, Chunjie W (2023) ATP-EMTP based arc model for air-insulated disconnect switch breaking. High Volt Electr ,59(01):8–16. https://doi.org/10.13296/j.100109.hva (in Chinese)
14. Yuhong H (2018) Analysis of photovoltaic grid-connected system under weak power grid. Chong-qing: Chongqing University, Chongqing: China (in Chinese)
15. Zhiguo L, You W, Yi-qian L (2018) A vector angle compensation method study of finite control set model predictive control based on photovoltaic grid inverter. Power Syst Tech 42(2):548–554 (in Chinese)
16. Feng Z, Tao Y, Shi-chun L et al (2019) Research on grid-connected/is-landed smooth transition of microgrid based on general-ized control algorithm of energy storage. Proc CSEE 39(10):2840–2853 (in Chinese)
17. Guangrun X (2018) Overvoltage of power system. Electric Power Press, Beijing: China (2018) (in Chinese)
18. Kunyu S (2018) VFTO simulation considering time-varyingcapacitive effect of isolation switch. Wuhan: Huazhong Universty of Science and Technology, Wuhan China (in Chinese)
19. Kunyu S, Chun L (2018) Simulation of isolation switch VFTO process considering time-varying gap capacitance. Power Syst Tech 42(9):3078–3085. Wuhan China (in Chinese)
20. Guangfan L, Xiaoning W, Peng L et al (2018) Research on insulation level and test of 1000 kV UHV power trans-former. Power Syst Tech 32(3):1–62008 China (in Chinese)
21. Dedong LIU (2015) The research of very fast transient overvoltage in GIS. East China Jiaotong University, Nanchang, China (in Chinese)

The Prediction of the Dielectric Breakdown Properties of 6% C_4F_7N–94% CO_2 Mixtures at 300–4000 K and 0.1–3.2 MPa

Yunkun Deng, Ke Wang, and Yuyang Yao

Abstract SF_6 is a greenhouse gas, therefore, we need to find a SF_6 substitute environment gases as an insulation and arc-quenching medium is an urgent for electrical engineer. C_4F_7N is a promising environmentally friendly insulating gas, while its boil temperature is high, therefore, CO_2 was added as a buffer gas. The dielectric strength of 6% C_4F_7N–94% CO_2 mixtures were evaluated at different pressure and temperature 0.1–3.2 MPa, and 300–4000 K. Firstly, the equilibrium compositions of 6% C_4F_7N–94% CO_2 mixtures at different gas pressures and temperatures up to 4000 K were calculated by the method of minimizing the Gibbs free energy. By Boltzmann equation analysis, the electron energy distribution function was obtained by the composition data. Finally, the critical reduced electric field ($(E/N)_{cr}$) of hot 6% C_4F_7N–94% CO_2 mixtures was determined, at which the rate of ionization is equal to attachment. The results show that in the gas temperature has an influence on 6% C_4F_7N–94% CO_2 mixing. The overall trend was that it first decreased with the increase of temperature, then rised, and finally falld. Further, the effect of barometric pressure on the $(E/N)_{cr}$ was also evident after 2000 K. The calculated results provided basic data for the post-arc breakdown of 6% C_4F_7N–94% CO_2, and have guiding significance for the engineering application of 6% C_4F_7N–94% CO_2.

Keywords Environmentally friendly insulating gas · Minimizing the Gibbs free energy · Boltzmann equation

Y. Deng · K. Wang
Yunnan Electric Power Research Institute Yunnan Power Grid Co. Ltd, Kunming, China

Y. Yao (✉)
State Key Laboratory of Electrical Insulation and Power Equipment, Xi'an Jiaotong University, Xi'an 710049, China
e-mail: 1319845528@qq.com

© Beijing Paike Culture Commu. Co., Ltd. 2024

X. Dong and L. Cai (eds.), *The Proceedings of 2023 4th International Symposium on Insulation and Discharge Computation for Power Equipment (IDCOMPU2023)*, Lecture Notes in Electrical Engineering 1102, https://doi.org/10.1007/978-981-99-7405-4_11

1 Introduction

SF_6 is mainly used for transmission and distribution equipment insulation and arc extinguishing in the power industry [1]. But given that SF_6 has an atmospheric lifetime of 3200 years (CO_2: 300–1000 years), in addtion, its global warming potential (GWP) is 23,500 times greater than CO_2 [2]. Therefore, the realization of SF_6 free has become an important issue to be solved urgently for the green development of power grid. At present, the research on SF_6 alternative gases mainly focuses on traditional gases, SF_6 mixed gases and new environmental gases. Among them, new environment-friendly gases include CF_3I, C–C_4F8, C_4F_7N, $C_5F_{10}O$ and so on [3–6].

C_4F_7N has twice the insulation strength of SF_6 and its GWP is 2100 [7]. Its liquefaction temperature is about − 4.7 °C, which is high, and the buffer gas is usually injected to meet the requirements of minimum operating temperature in engineering equipment, therefore, it is considered to be the most potential SF_6 alternative gas. Zhang et al. studied the breakdown strength and partial discharge characteristics of the C_4F_7N/CO_2 mixtures at alternating current voltages, and compared it with SF_6 [8]. Li et al. performed a breakdown experiment on C_4F_7N/N_2 gas mixture and measured the decomposition products using spherical electrodes at alternating current voltage [9]. The results shown that the main products were CF_4, C_2F_6, C_3F_8, CF_3CN, C_2F_4, C_3F_6 and C_2F_5CN after thirty times of breakdowns and the CF_4, C_2F_6 and CF_3CN contents were the highest. Li et al. analyzed the saturated vapor pressure characteristics of C_4F_7N-CO_2 mixtures based on the Antoine constants and the Antoine equation [10]. Then they discussed the application conditions at limits of environment temperature. Moreover, Zhang et al. first evaluated the electron neutral collision cross section of C_4F_7N. The set was verified by systematic comparison of Boltzmann equation analysis and experimental measurements of pure C_4F_7N, C_4F_7N/N_2 and C_4F_7N/Ar mixtures [11]. Under partial discharge (PD) and spark discharge conditions, the experimental values of decomposition products of C_4F_7N/CO_2 and $C_5F_{10}O$/air mixtures were also first presented by them. Then, ab initio molecular dynamics simulations of typical decomposition products were performed. In addition, the reliability of ab initio molecular dynamics simulation method in simulating electron induced ionization was verified [12]. GE, ABB and other companies have developed C_4F_7N as insulation medium in GIL, GIS and other products, and realized engineering application in Europe [13].

The dielectric properties of 6% C_4F_7N–94% CO_2 mixtures at 0.1–3.2 MPa and 300–4000 K were studied. First, by using the minimizing the Gibbs free energy, the equilibrium compositions of 6% C_4F_7N–94% CO_2 mixtures under different thermal states and gas pressure were calculated. By solving two-term Boltzmann equations, the electron energy distribution function (EEDF) was obtained. The value of the critical reduced electric field strength $(E/N)_{cr}$ was the electric field value corresponding to the reduced effective ionization coefficient $\alpha_{eff}/N = 0$. Finally, the $(E/N)_{cr}$ of 6% C_4F_7N–94% CO_2 mixture was determine. The calculated results provided basic data for the post-arc breakdown of 6% C_4F_7N–94% CO_2, and have guiding significance for the engineering application of 6% C_4F_7N–94% CO_2.

2 The Method of Calculation

Since the increase of gas temperature will lead to great variations in the total particle number density and gas composition, the dielectric breakdown methods of cold and hot gases are very different. The insulation properties of 6% C_4F_7N–94% CO_2 mixtures are evaluated by calculating the $(E/N)_{cr}$. The value of the$(E/N)_{cr}$ is the electric field (E/N) value corresponding to the effective ionization coefficient equals to zero. This means that the number of electrons produced by the collision ionization is balanced by the number of electrons lost by the collision attachment reaction. EEDF is important for obtaining ionization and attachment coefficients [14]. In this paper, Boltzmann equation is simplified by 2-term spherical harmonic approximation.

By minimizing the Gibbs free energy [15], the equilibrium composition of 6% C_4F_7N–94% CO_2 mixture at 0.1–3.2 MPa and 300–4000 K is calculated. The change of the composition of the 6% C_4F_7N–94% CO_2 mixture as gas temperature at different gas pressures is shown in Fig. 1. Ten speices in 6% C_4F_7N–94% CO_2 mixtures are found, which concentrations are over 10^{-6}, at the temperature range of 300–4000 K. There are CO_2, CO, CF_4, N_2, O_2, O, F, CF_2, NO and F_2, and is no C_4F_7N in the calculated component, which is due to the small amount of C_4F_7N, which will be quickly decomposed or react with other products. Among them, a large amount of CO, CF_4 and N_2 will be generated. Below 2000 K, the contents of CO_2, CO and N_2 are almost unchanged, and the content of CF_4 slowly declines with the increase of temperature. And, at this point, the content of these four gases does not change with the pressure. After 1500 K, F is decomposed, and the content of F also increases rapidly with the increase of temperature. Moreover, at the same temperature, the content of F decreases with the increase of air pressure. After 3000 K, the content is almost unchanged and does not change with the change of air pressure. At about 2000 K, O_2, O, CF_2, NO and F_2 increased with the increase of temperature. The content of O_2 is almost constant after 3000 K and does not change with the change of air pressure. When the temperature reaches a certain level, the contents of CF_2 and F_2 begin to decline. The change of components with temperature is very important for the calculation of the $(E/N)_{cr}$.

Solving the Boltzmann equation requires cross sections of all components in 6% C_4F_7N–94% CO_2 mixtures. Cross sections for all components (CO_2, CO, CF_4, N_2, O_2, O, F, CF_2, NO and F_2) are taken from the Lxcat website [16].

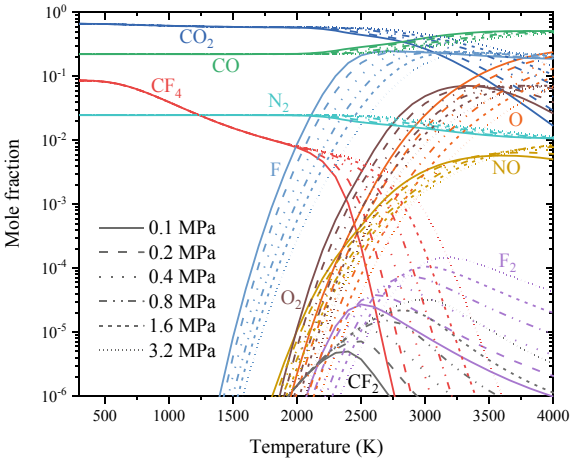

Fig. 1 Mole fractions of 6% C_4F_7N–94% CO_2 mixture with gas temperature at 0.1–3.2 MPa

3 Results and Discussion

3.1 α_{eff} and the $(E/N)_{cr}$ in 6% C_4F_7N–94% CO_2 Mixture at Room Temperature

As the electron kinetics model is adopted, the calculated $(E/N)_{cr}$ is independent of pressure, and the displayed α_{eff} is also independent of pressure. The α_{eff} of 6% C_4F_7N–94% CO_2 at room temperature is shown in Fig. 2. At lower field strengths (< 40 Td), α_{eff} is almost zero. At 40–80 Td, α_{eff} is less than 0 and decreases as E/N increases. At larger electric field, α_{eff} increases with E/N increasing. Moreover, when $E/N = 99.71$ Td, $\alpha_{eff} = 0$, which is the $(E/N)_{cr}$ of 6% C_4F_7N–94% CO_2 at room temperature.

3.2 α_{eff} and the $(E/N)_{cr}$ in 6% C_4F_7N–94% CO_2 Mixtures at High Temperature

Figure 3 shows that α_{eff} of in 6% C_4F_7N–94% CO_2 mixture at 1.6 Mpa and different gas temperatures. The overall trend of α_{eff} is almost constant at lower E/N, then decreasing and then increasing. At 1000–2000 K, the value of α_{eff} increases with the increase of temperature when the E/N is higher, so the $(E/N)_{cr}$ decreases with the increase of temperature. When the temperature is between 3000 and 4000 K, α_{eff} at 3000 K is less than that at 4000 K before 80 Td. And the $(E/N)_{cr}$ for 3000 K is less than that of 4000 K.

α_{eff} of in 6% C_4F_7N–94% CO_2 mixture at 3000 K and different gas pressures is shown in Fig. 4. As the electric field becomes larger, α_{eff} first drops and then rises.

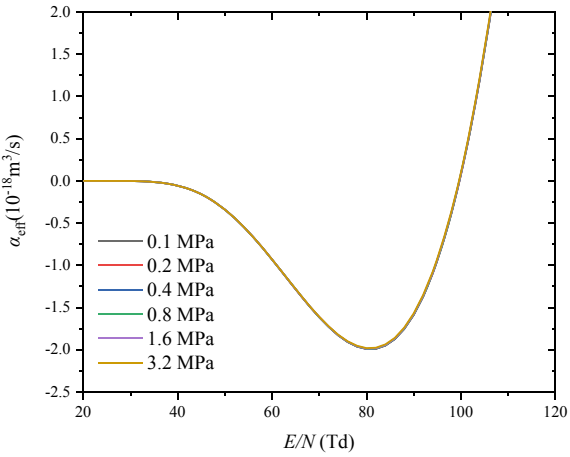

Fig. 2 α_{eff} of in 6% C_4F_7N–94% CO_2 mixture at room temperature and different gas pressures

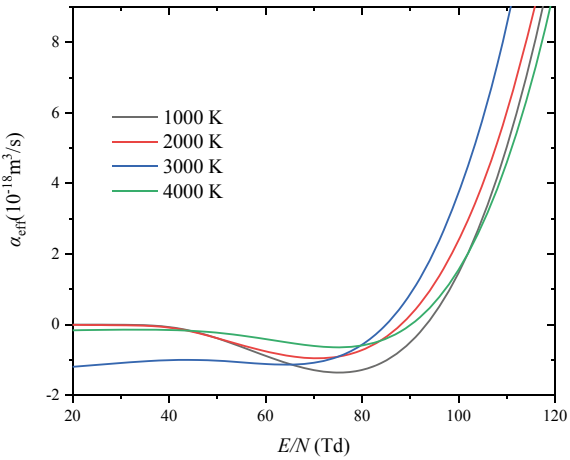

Fig. 3 The α_{eff} of in 6% C_4F_7N–94% CO_2 mixture at 1.6 MPa and different gas temperatures

α_{eff} decreases with increasing air pressure before 80 Td. After 80 Td, α_{eff} increases with increased air pressure. At 3000 K, the $(E/N)_{cr}$ varies between 80 and 90 Td, but with little regularity. This is due to the different ionization and attachment rates of the decomposition products in C_4F_7N-CO_2 mixture.

Except for 3.2 MPa, the overall trend of the $(E/N)_{cr}$ under other gas pressure is roughly the same, first decreasing, then increasing, and then decreasing with the increase of temperature. Before 2000 K, $(E/N)_{cr}$ does not change with the change of gas pressure, but decreases slowly with the increase of temperature. After 2000 K, $(E/N)_{cr}$ first decreases, then increases and then decreases with the increase of temperature. With the increase of pressure, the variation trend of $(E/N)_{cr}$ with temperature slows down, and the temperature at the inflection point of $(E/N)_{cr}$ rising and falling

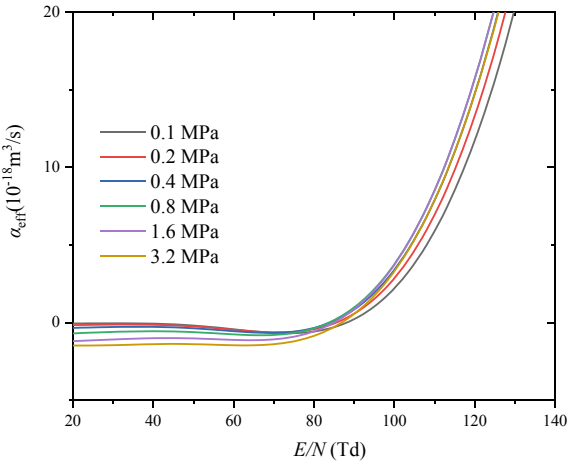

Fig. 4 Effective ionization coefficient α_{eff} of in 6% C_4F_7N–94% CO_2 mixture at different gas pressures and 3000 K

increases. When the pressure is 3.2 MPa, it is completely consistent with other pressure values and trends before 2000 K. With the further increase of temperature, it first continues to decline until the temperature reaches 3000 K, then rises, then falls and rises again. These trends are mainly caused by the formation of O_2, CF_2, F_2 and NO at 2000 K, and the rapid decline of F_2 and CF_2 at 2500–3000 K (Fig. 2).

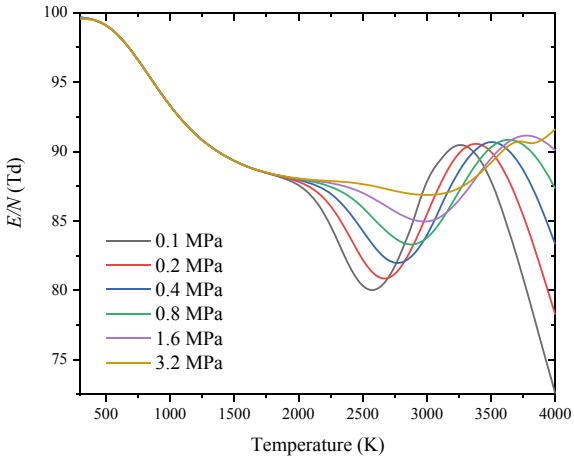

Fig. 5 $(E/N)_{cr}$ in hot 6% C_4F_7N–94% CO_2 mixtures at 0.1–3.2 MPa

4 Conclusions

The dielectric breakdown properties of 6% C_4F_7N–94% CO_2 mixtures at 0.1–3.2 MPa and 300–4000 K were studied in this paper. By using the minimizing the Gibbs free energy, the equilibrium compositions of 6% C_4F_7N–94% CO_2 mixtures under different thermal states and gas pressure were calculated. Then, by solving two-term Boltzmann equations, the EEDF was obtained. The value of the $(E/N)_{cr}$ was the electric field value corresponding to the $(\alpha\text{-}\eta)/N = 0$. Except for 3.2 MPa, the overall trend of the $(E/N)_{cr}$ under other gas pressure is roughly the same, first decreasing, then increasing, and then decreasing with the increase of temperature. Finally, the $(E/N)_{cr}$ of 6% C_4F_7N–94% CO_2 mixture was determine. The calculated results provided basic data for the post-arc breakdown of 6% C_4F_7N–94% CO_2, and have guiding significance for the engineering application of 6% C_4F_7N–94% CO_2.

Acknowledgements This manuscript is sponsored by the Science and Technology Project of China Southern Power Grid (YNKJXM20220051).

References

1. Tang N, Xiong J, Zhou Y, Wang K, Zhang B, Li X, Sun D (2021) Insulation performance of environmental-friendly gas HFO-1336mzz (E) and its mixtures. Trans China Electrotechnical Soc 36(13)
2. Li X, Zhao H, Murphy A (2018) SF_6-alternative gases for application in gas-insulated switchgear. J Phys D Appl Phys 51:153001
3. Li X, Zhao H, Jia S, Murphy A (2013) Study of the dielectric breakdown properties of hot SF_6–CF_4 mixtures at 0.01–1.6 MPa. J Appl Phys 114(5):053302
4. Zhou B, Tan D, Xue J, Cai F, Xiao D (2019) Lighting impulse withstand performance of CF_3I–N_2 gas mixture for 252 kV GIL insulation. IEEE Trans Dielectr Electr Insul 26(4):1190–1196
5. Liu X, Wang J, Wang Y, Zhang Z, Xiao D (2007) Analysis of the insulation characteristics of c-C_4F_8/CO_2 gas mixtures by the Monte Carlo method. J Phys D Appl Phys 41(1):015206
6. Rabie M, Franck C (2018) Assessment of eco-friendly gases for electrical insulation to replace the most potent industrial greenhouse gas SF_6. Environ Sci Technol 52(2):369–380
7. Chachereau A, Hösl A, Franck CM (2018) Electrical insulation properties of the perfluoronitrile C_4F_7N. J Phys D Appl Phys 51(49):495201
8. Zhang B, Chen L, Li X, Guo Z, Pu Y (2020) Evaluating the dielectric strength of promising SF_6 alternatives by DFT calculations and DC breakdown tests. IEEE Trans Dielectr Electr Insul 27(4):1187–1194
9. Yi L, Zhang X, Chen Q, Fu M, Zhuo R, Xiao S, Chen D, Tang J (2018) Study on the dielectric properties of C_4F_7N/N_2 mixture under highly non-uniform electric field. IEEE Access 6:42868–42876
10. Li X, Deng Y, Jiang X, Zhao H, Zhuo R, Wang D, Fu M (2017) Insulation performance and application of environment friendly gases mixtures of C_4F_7N and $C_5F_{10}O$ with CO_2. High Voltage Eng 43(3):708–714
11. Zhang B, Hao M, Yao Y, Xiong J, Li X, Murphy A, Sinha N, Antony B, Ambalampitiya H (2023) Determination and assessment of acomplete and self-consistentelectron-neutral collision cross-sectionset for the C_4F_7N molecule. J Phys D Appl Phys 56:134001

12. Zhang B, Hao M, Xiong J, Li X, Koopman J (2023) Ab initiomolecular dynamics calculations onelectron ionization induced fragmentationsof C_4F_7N and $C_5F_{10}O$ for understanding theirdecompositions under discharge conditions. Phys Chem Chem Phys 25:7540
13. Zhang B, Uzelac N, Cao Y (2018) Fluoronitrile/CO_2 mixture as an eco-friendly alternative to SF_6 formedium voltage switchgears. IEEE Trans Dielectr Electr Insul 25(4):1340–1350
14. Yousfi M, Robin-Jouan P, Kanzari Z (2005) IEEE Trans Dielectr Electr Insul 12:1192–1200
15. Zhang J, Yan J, Murphy AB, Hall W, Fang MTC (2002) Computational investigation of arc behavior in an auto-expansion circuit breaker contaminated by ablated nozzle vapor. IEEE Trans Plasma Sci 30:706
16. Lxcat https://nl.lxcat.net/data/set_processes.php. Last accessed 11 Apr 2023

Study on Arc Extinguishing Capability of HFO-1336mzz(E)/CO_2 as SF_6 Substitute Gas

Nian Tang, Dongwei Sun, Yongyan Zhou, and Kai Wang

Abstract SF_6 gas is mostly used in medium and high voltage power equipment due to its great insulation and arc extinguishing performance. However, large amounts of SF_6 gas can have a serious greenhouse effect. This article studies the arc extinguishing performance of HFO-1336mzz (E)/CO_2 mixture to evaluate its feasibility as an environmentally friendly gas to replace SF_6 in medium voltage switchgear. Based on the theory of local thermodynamic equilibrium, the physical parameters of HFO-1336mzz(E)/CO_2 were calculated by Gibbs energy minimization method, which provided important data support for the basic input parameters of simulation for arc burning simulation. Two-dimensional magnetohydrodynamic simulation model was established, and the load current breaking process was simulated under the pneumatic load switch structure. The temperature field distribution in the arc extinguishing room of HFO-1336mzz(E)/CO_2 and SF_6 gas were compared during the arc burning process. The results provide a key reference for the application of HFO-1336mzz(E)/CO_2 as arc extinguishing medium in medium voltage switchgear.

Keywords HFO-1336mzz(E)/CO_2 · Arc extinguishing performance · Magnetohydrodynamic · Physical parameter

1 Introduction

SF_6 was widely used in various switchgear since the 1960s due to its excellent arc extinguishing performance, insulation performance, self-recovery, thermal conductivity and stability, greatly promoting the development and application of high-voltage electrical equipment [1, 2]. In the field of medium voltage equipment, SF_6

N. Tang · D. Sun · Y. Zhou
Electirc Power Research Insitute of Guangdong Power Grid Co. Ltd., Guangzhou 510080, China

K. Wang (✉)
State Key Laboratory of Electrical Insulation and Power Equipment, Xi'an Jiaotong University, Xi'an, China
e-mail: wk0729@stu.xjtu.edu.cn

© Beijing Paike Culture Commu. Co., Ltd. 2024

X. Dong and L. Cai (eds.), *The Proceedings of 2023 4th International Symposium on Insulation and Discharge Computation for Power Equipment (IDCOMPU2023)*, Lecture Notes in Electrical Engineering 1102, https://doi.org/10.1007/978-981-99-7405-4_12

has gradually replaced the power equipment with compressed air or high pressure nitrogen as the insulating medium. Because of its superior insulation performance, using it as an insulating medium can reduce the charging pressure of medium voltage equipment and reduce the volume of equipment, in line with the miniaturization of power equipment, safe and reliable technology and use requirements.

However, the widely used SF_6 gas not only promotes the development of related industries, but also brings serious environmental problems. The Global Warming Potential (GWP) of SF_6 is about 25,200 times that of CO_2, and its atmospheric life is over 3000 years. In the Kyoto Protocol signed by over 100 countries in 1997, SF_6 is clearly stipulated as one of the six greenhouse gases that are limited in emission [3, 4]. Under the Protocol, governments of all countries are required to formulate and carry out a series of SF_6 emission policies, but SF_6 gas is still continuously discharged into the atmosphere.

In the past few decades, a series of emission reduction measures for SF_6 gas have been adopted in the power industry, such as gas recovery and gas leak detection. But these measures can not fundamentally avoid the SF_6 gas application in power equipment. Therefore, finding gas media with electrical performance and safety and environmental protection close to SF_6 is a recent hot topic. Research on SF_6 substitute gas at home and abroad has not been interrupted. Alternative gases that have been proposed include conventional gases (dry air, CO_2, N_2, etc.) and their mixtures with SF_6 [5–7], fluorocarbon compounds and their halogenates (c-C_4F_8, CF_3I, etc.) [8–10], other fluorine-containing compounds (C_4F_7N, $C_5F_{10}O$, HFO-1234ze(E), HFO-1336mzz(Z), etc.) [11–14]. However, these alternative gases have their own advantages and disadvantages.

This paper proposes high insulation gas HFO-1336mzz (E) as a substitute gas for SF_6 for medium voltage switchgear. At present, HFO-1336mzz(E) is mainly studied as a new type of heat pump working medium and refrigerant. The GWP value of this gas was 18, and Ozone Depletion Potential was 0, indicating low toxicity. At the same time, its atmospheric life is about a few days to a few weeks, good environmental performance. However, the liquefaction temperature of HFO-1336mzz(E) is relatively high, about 7.58 °C, and buffer gas has to be added in practical application [15, 16]. This paper selects CO_2 as the buffer gas. Preliminary study shows that HFO-1336mzz(E) gas mixture can achieve the insulation level comparable to SF_6, suitable for medium voltage switchgear. At present, some researchers have carried out preliminary studies on the insulation properties of HFO-1336mzz(E) gas mixture. However, the arc extinguishing performance of HFO-1336mzz(E) gas and its mixture remains to be further verified. Therefore, this paper carries out a systematic simulation study on the arc extinguishing performance of SF_6 and HFO-1336mzz(E)/CO_2 mixture in 12 kV load switch.

2 Simulation Model

As a kind of switch equipment with simple structure, convenient installation and maintenance, safe and reliable, and reasonable economic and technical indexes, medium voltage load switch has been widely used in 10–35 kV power supply system, especially in the urban distribution network. Load switch is a kind of switching appliance with simple arc extinguishing device, which can close, break and carry normal load of line or specified overload current, and has certain short-circuit closing capacity. According to different arc extinguishing medium or mode, load switches are mainly divided into gas production type, pressure type, vacuum type and SF_6 type. The four kinds of load switches have different structures and different performance. In this paper, the pneumatic load switch with strong arc extinguishing performance is selected, which has an obvious disconnect point. Its working principle is to compress the gas in the arc extinguishing chamber through the relative motion between the piston and the cylinder in the gas chamber when the contacts are separated, so that the pressure of the gas increases gradually. The gas is blown out by the arc in the process of gas flow in the nozzle. The performance of breaking small current is good, and the arc extinguishing effect is stable. In this paper, the pneumatic load switch structure with strong arc extinguishing performance is selected as the simulation research object. Pneumatic load switch is composed of moving arc contact, static arc contact, nozzle, pneumatic type, piston and so on. The nozzle material is PTFE.

Figure 1 shows the simulation model of load switch. The arc extinguishing media studied are SF_6 and HFO-1336mzz(E)/CO_2. The inflation pressure is 0.1 and 0.12 MPa, the outlet pressure is set as the aeration pressure of the chamber, and the ambient temperature is 300 K.

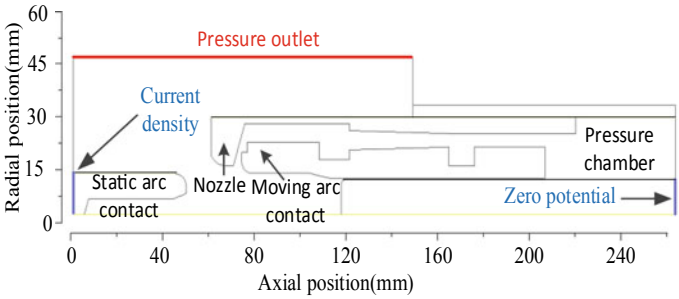

Fig. 1 Simulation model of the load switch

3 Physical Parameter

Physical parameters are the key data reflecting gas properties. Understanding the physical parameters of gas is beneficial to systematically compare the inherent microscopic properties of gas medium, and qualitatively evaluate the arc extinguishing ability of medium from the microscopic point of view. Since the physical parameters of arc plasma at high temperature are difficult to be directly measured by experiments, based on the theory of local thermodynamic equilibrium, the plasma components of SF_6 and HFO-1336mzz(E)/CO_2 in the range of 300–30,000 K are calculated by Gibbs free energy minimization method. Furthermore, the physical properties of arc plasma are calculated, including thermodynamic properties and transport coefficients. The calculated physical parameters, as the basic input parameters of arc magnetohydrodynamic simulation, provide important data support for arc ignition simulation.

Figure 2 shows the comparison of physical parameters between HFO-1336mzz(E)/CO_2 and SF_6 at 0.1 MPa. At temperatures above 5000 K, the density of SF_6 is higher than the mass density of the HFO-1336mzz(E) gas mixture, due to the fact that the mass of S atoms is higher than the mass of C and O. The change of enthalpy with temperature is related to density, and the higher the density, the lower the enthalpy. The thermal conductivity in the arc reflects the ability of the arc to transfer the energy from the arc core area to the edge area and the outside of the arc. Higher thermal conductivity in the arc burning stage can accelerate the energy dissipation rate, which is conducive to the recovery of the strength of the post-arc medium. In general, the thermal conductivity of HFO-1336mzz(E) gas mixture is higher than that of SF_6 in the temperature range of 2500 K to 20,000 K, so it can be considered that HFO-1336mzz(E) gas mixture has better thermal conductivity during arc burning. In the temperature range below 10,000 K, the conductivity of HFO-1336mzz(E) gas mixture is slightly lower than SF_6, but above 10,000 K, the conductivity of HFO-1336mzz(E) gas mixture is higher than SF_6. This indicates that HFO-1336mzz(E) gas mixture has lower electrical conductivity in the post-arc stage. If analyzed only from the perspective of electrical conductivity, HFO-1336mzz(E) gas mixture is more conducive to the establishment of gap insulation strength and less prone to post-arc breakdown than SF_6 in the post-arc stage. The viscosity coefficient of the gas mixture has a peak value with little difference from SF_6, but the peak value corresponds to different temperatures, and the gas mixture peaks at lower temperatures.

Therefore, HFO-1336mzz(E) gas mixture should have a certain degree of arc extinguishing ability, and only from the conductivity, thermal conductivity parameters, HFO-1336mzz(E) gas mixture should have better energy dissipation ability in the recovery stage of post-arc medium. However, the behavior of arc plasma is very complex and difficult to predict. It is not accurate to evaluate the specific arc extinguishing ability of gas mixture only based on the calculated physical parameters. Therefore, it is necessary to further combine the actual switch structure and

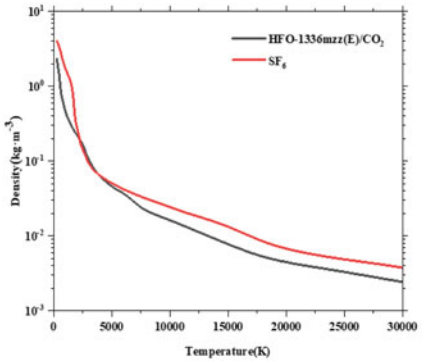

(a) Density

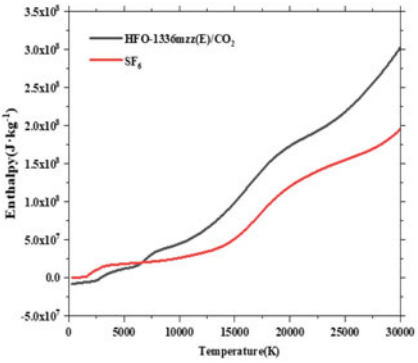

(b) Enthalpy

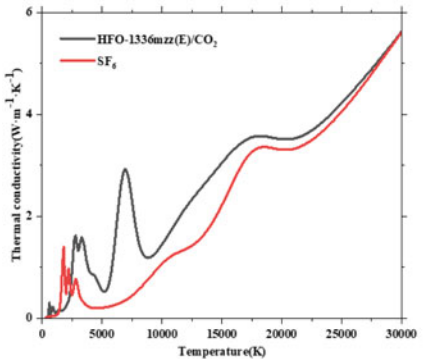

(c) Thermal conductivity

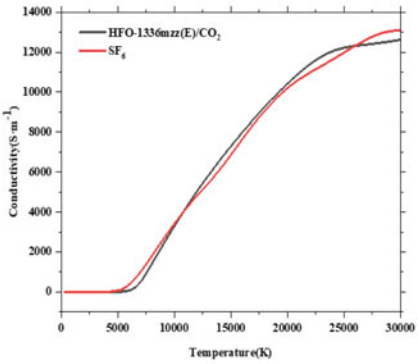

(d) Conductivity

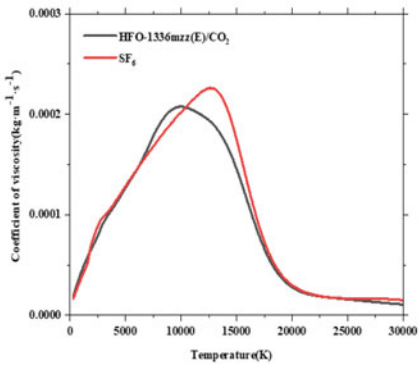

(e) Coefficient of viscosity

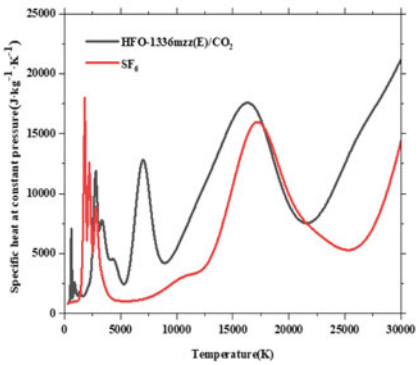

(f) Specific heat at constant pressure

Fig. 2 Comparison of physical parameters between SF_6 and HFO-1336mzz(E)/CO_2 mixture

the related governing equations in the arc development process to carry out more comprehensive simulation calculation of arc burning.

4 Simulation Result Analysis

Figure 3 shows the arc temperature distribution of SF_6 and mixed gas during arc ignition. When the arc burning reaches 1 ms, the contact spacing gradually expands. At this time, the load current is 523.7 A, and the arc begins to expand. At the same time, it can be observed that the high-temperature gas of the mixed gas arc further expands outward, but the radius of SF_6 arc is not much different. It is worth noting that the highest temperature of mixed gas arc is 13,800 K, lower than the highest temperature of SF_6 gas arc 15,400 K, which indicates that SF_6 gas arc combustion is more intense. When the arc is fired to 4 ms, the current increases to A peak of 890.9 A. At this stage, the energy injected into the arc increases significantly, and the arc will rapidly expand and further extend into the gas region. Although the current increases, the arc temperature remains basically unchanged. When the nozzle and movable contact continue to move, the gas is compressed, so the gas will continue to blow from the pressure chamber towards the arc core. At the same time, it can be seen that the axial diffusion rate of the mixed gas arc is greater than SF_6, indicating that the energy dissipation rate of the mixed gas is stronger. The arc temperature is still SF_6 with a maximum of 16,900 K. When the arc burning reaches 8 ms, the current attenuates to 275.3 A, the input energy of arc decreases, and the arc is in a weakened state of contraction. In addition, the compression effect of the mixed gas arc is more obvious, the high temperature area of the arc is more concentrated near the axis, and the arc becomes thinner and longer. The arc temperature is also lowered. The arc temperature of the mixed gas is only 14,400 K, which is 1400 K lower than SF_6, which is conducive to avoiding arc reignition.

5 Conclusion

This paper studies the arc extinguishing characteristics of HFO-1336mzz(E)/CO_2 as the extinguishing medium in 12 kV load switch, and compares it with SF_6. According to the arc temperature distribution, when the axial diffusion rate of HFO-1336mzz(E)/CO_2 arc is greater than SF_6 and the current is faster than zero, the arc temperature of HFO-1336mzz(E) /CO_2 arc is 1400 K lower than SF_6, which is conducive to avoiding arc reignition. It can be concluded that HFO-1336mzz(E)/CO_2 can be used as an environmental protection gas arc extinguishing medium in 12 kV load switch.

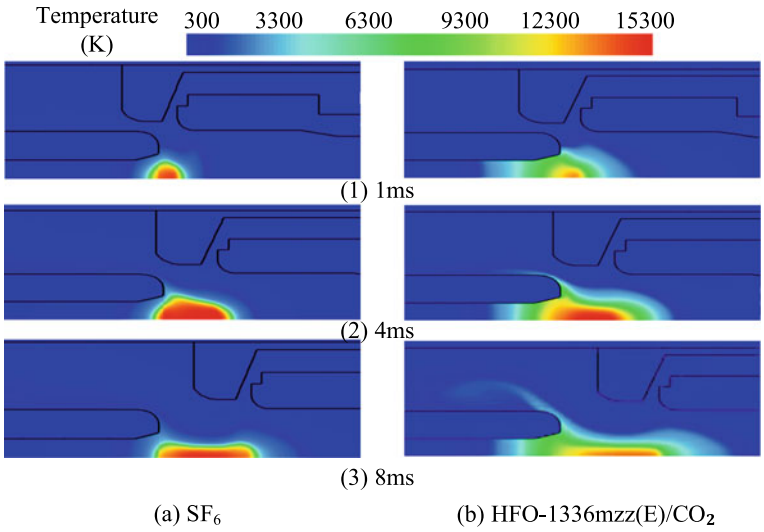

Fig. 3 Distribution of arc temperature during arcing period in SF_6 and HFO-1336mzz(E)/CO_2 mixture

Acknowledgements This work was supported by the National Natural Science Foundation of China (52277162, 51825702), the Science and Technology Project of China Southern Power Grid(GDKJXM20220361), and Shaanxi Provincial Science and Technology Plan Project (2022TD-59)

References

1. Li X, Zhao H (2016) Review of research progress in SF_6 substitute gases. High Voltage Eng 42(6):1695–1701 (in Chinese)
2. Rabie M, Franck CM (2018) Assessment of eco-friendly gases for electrical insulation to replace the most potent industrial greenhouse gas SF_6. Environ Sci Technol 52(2):369–380
3. Zhang B, Wang K et al (2023) Insulation Characteristics of HFO-1336mzz(E) and its mixtures as eco-friendly alternatives to SF_6 for medium-voltage switchgears. IEEE Trans Dielectr Electr Insul 30(2):536–545
4. Zhang B, Yao Y et al (2022) Study of the dielectric breakdown strength of CO_2–O_2 mixtures by considering ion kinetics in a spatial–temporal growth avalanche model. J Appl Phys 132(9):093302
5. Guo Z, Liu S et al (2019) Study of the arc interruption performance of CO_2 gas in high-voltage circuit breakers. IEEE Trans Plasma Sci 47(5):5742–2751
6. Stoa-Aanensen NS, Runde M, Jonsson E (2016) Empirical relationships between air-load break switch parameters and interrupting performance. IEEE Trans Power Delivery 31(1):278–285
7. Wada J, Ueta G, Okabe S (2013) Evaluation of breakdown characteristics of CO_2 gas for non-standard lightning impulse waveforms-breakdown characteristics in the presence of bias voltages under non-uniform electric field. IEEE Trans Dielectr Electr Insul 20(1):112–121
8. Chen L, Widger P, Kamarudin MS et al (2016) CF_3I Gas mixtures: breakdown characteristics and potential for electrical insulation. IEEE Trans Power Delivery 32(2):1089–1097

9. de Urquijo J, Juárez AM, Basurto E et al (2007) Electron impact ionization and attachment, drift velocities and longitudinal diffusion in CF_3I and CF_3I–N_2 mixtures. J Phys D Appl Phys 40:2205–2209
10. Katagiri H, Kasuya H (2008) Investigation of the performance of CF_3I gas as a possible substitute for SF_6. IEEE Trans Dielectr Electr Insul 15(5):1424–1429
11. Zhang B, Xiong J et al (2022) Pulsed Townsend measurement of electron swarm parameters in C_4F_7N-CO_2 and C_4F_7N–N_2 mixtures as eco-friendly insulation gas. J Appl Phys 131(3):033304
12. Hao M, Zhang B et al (2022) Electron swarm parameters and dielectric strength of C_5F_{10O} and its mixtures with CO_2 and dry air. J Phys D: Appl Phys 55(12):125205
13. Hösl A, Pachin J, Eguz E et al (2020) Positive synergy of SF_6 and HFO1234ze(E). IEEE Trans Dielectr Electr Insul 27(1):322–324
14. Nechmi HE, Beroual A, Girodet A et al (2016) Fluoronitriles/CO_2 gas mixture as promising substitute to SF_6 for insulation in high voltage applications. IEEE Trans Dielectr Electr Insul 23(5):2587–2593
15. Xiao S, Han P, Li Y (2021) Insulation performance and electrical field sensitivity properties of HFO-1336mzz(E)/CO_2: a new eco-friendly gas insulating medium. IEEE Trans Dielectr Electr Insul 28(6):1938–1948
16. Katsuyuki T, Junichi I, Konstantinos K (2017) Thermodynamic properties of HFO-1336mzz(E) (trans−1,1,1,4,4,4−hexafluoro−2−butene) at saturation conditions. Int J Refrig 82:283–287

Calculation of Thermodynamic Properties and Transport Coefficients of C_4F_7N–PTFE Mixtures

Yunkun Deng, Ke Wang, and Guanyu Wang

Abstract The thermodynamic properties and transport coefficients of C_4F_7N–PTFE gas mixtures in the temperature range from 300 to 30,000 K and the pressure range from 0.1 to 1.6 MPa are calculated. Special attention is paid to the effects of different PTFE ratios and gas pressures on the physical properties of C_4F_7N–PTFE mixed gases. The composition of arc plasma particles was determined based on the principle of minimizing Gibbs free energy, and the thermodynamic parameters and transport coefficients were determined by standard thermodynamic equations and Chapman-Enskog theory. It can be concluded that the addition of PTFE will have a certain degree of impact on the specific heat at constant pressure and thermal conductivity of the mixture. However, due to the compositional similarity between C_4F_7N and PTFE elements, a small amount of PTFE is not expected to result in significant changes to the performance of the plasma. Elevating the gas pressure can lead to an augmentation of the transport coefficients, particularly within the domain of elevated temperatures. The calculation results provide basic data for the simulation of plasmas using magnetohydrodynamics arc models, also provide a reference for the design of environmentally-friendly high-voltage circuit breakers; some examples are presented.

Keywords Thermodynamic properties · Transport coefficients · C_4F_7N · PTFE · Environmentally-friendly circuit breakers · Arc

Y. Deng · K. Wang
Electric Power Research Institute of Yunnan Power Grid Co., Ltd., Kunming 650217, Yunnan, China

G. Wang (✉)
State Key Laboratory of Electrical Insulation and Power Equipment, Xi'an Jiaotong University, Xi'an 710049, China
e-mail: wangguanyu@stu.xjtu.edu.cn

© Beijing Paike Culture Commu. Co., Ltd. 2024

X. Dong and L. Cai (eds.), *The Proceedings of 2023 4th International Symposium on Insulation and Discharge Computation for Power Equipment (IDCOMPU2023)*, Lecture Notes in Electrical Engineering 1102, https://doi.org/10.1007/978-981-99-7405-4_13

1 Introduction

C_4F_7N is under investigation as a promising SF_6 environmentally friendly substitute gas and is widely utilized in high-voltage circuit breakers owing to its excellent insulation and arc-extinguishing properties. C_4F_7N has a significantly lower global warming potential (GWP) than SF_6 and a suitable liquefaction temperature [1], making it an excellent choice for environmentally friendly substitute gases. In addition, compared with CO_2 and N_2, C_4F_7N has better arc interruption characteristics. In the low temperature and pressure range, the presence of C_4F_7N can increase the dielectric strength of CO_2 by more than half [2]. Therefore, studying the thermodynamic parameters and transport coefficients of C_4F_7N in the arc combustion process is essential.

When the self-powered circuit breaker is opened, PTFE vapor inevitably generated from the ablating nozzle material will alter the composition [3], thermodynamic properties, and transport coefficients of the arc plasma to a certain extent. To accurately evaluate the properties of gas mixtures and understand plasma behavior, it is essential to calculate the thermodynamic parameters and transport coefficients of C_4F_7N -PTFE mixed gases. In addition, plasma thermophysical parameters are essential input parameters for macroscopic magnetohydrodynamic (MHD) simulations of arc plasmas, which will also provide guidance for the design and manufacturing of environmentally friendly self-energizing expanding circuit breaker.

Previous research on the parameters of C_4F_7N gas has mostly focused on pure C_4F_7N and C_4F_7N-CO_2 binary mixtures. Chen et al. [4] used the Gibbs free energy minimization method to calculate the composition of C_4F_7N arc plasma under the assumptions of local thermodynamic equilibrium (LTE) and non-local chemical equilibrium (NLCE), and established a complete chemical decomposition pathway. Zhang et al. [5] derived the saturated vapor pressure of C_4F_7N-CO_2 mixture gas using the gas–liquid equilibrium law, and calculated the physical properties of the mixture such as compressibility factor, specific heat at constant pressure, and viscosity based on the Peng Robinson (P-R) equation of state, Joback group contribution method, and Thodos method. Zhang et al. [6] also calculated the equilibrium composition, thermodynamic properties, and transport coefficients of C_4F_7N-CO_2 thermal plasma at 300K-30kK, and analyzed the effect of pressure and CO_2 mixing ratio on the results, providing basic parameters for the magnetohydrodynamic (MHD) simulation of arc plasma.

In fact, the conditions in practical applications are highly complex. For example, in high-voltage circuit breakers, vapors generated from the arcing erosion of contacts and nozzles will mix with the arc extinguishing medium to form more complex gas mixtures. We have already calculated the thermodynamic properties and transport characteristics of the SF_6-PTFE-Cu ternary mixture generated from the nozzle erosion [7]. The results show that the addition of PTFE has a significant impact on the physical property parameters of SF_6, while a small amount of Cu vapor has little effect except for the electrical conductivity in the low-temperature region. However, research on environmentally friendly gas insulation media is still insufficient, and the

properties of such mixtures are not fully understood. To address this issue, we studied the thermodynamic properties and transport coefficients of C_4F_7N-PTFE mixtures in this paper.

2 Calculation Principle and Method

The composition of thermal plasmas under local thermodynamic equilibrium (LTE) was calculated by the method of minimizing Gibbs free energy. The effect of solid phase on the calculation of transport coefficients and thermodynamic parameters in the low-temperature range was not considered in our calculations, due to the restrictions imposed by the MHD simulation modeling. The mass conservation law, Dalton's law of partial pressures, and the quasi-neutrality condition were used as constraints to determine the particle composition that minimizes the Gibbs free energy of the system. The system's Gibbs free energy can be expressed as follows:

$$G = \sum_{i=1}^{N} n_i \mu_i \tag{1}$$

$$\mu_i = \mu_i^0 + RT \ln(n_i / \sum_{j=1}^{N} n_j) + RT \ln(p/p^0) \tag{2}$$

In the equation, n_i represents the particle number density of species i, μ_i represents the chemical potential of species i, μ_i^0 represents the standard chemical potential of species i, R is the ideal gas constant, T is the plasma temperature, p is the gas pressure and p^0 is the reference pressure, and N is the total number of particle species.

Due to the additional effect of the electrostatic interaction between charged particles, it is assumed that the average electrostatic energy of electrons is much smaller than their thermal energy. It is also assumed that there are many of charged particles in the Debye sphere. According to the Debye–Huckel correction, the Gibbs free energy will be correspondingly reduced [8]:

$$g_h = -\sum_{j=1}^{N} N_j \left(eZ_j\right)^2 / (8\pi \varepsilon_0 \lambda_D) \tag{3}$$

Dalton's law of partial pressures should be corrected to:

$$P + kT / \left(24\pi \lambda_D^3\right) = \sum_{i=1}^{w_{max}^g} n_i kT \tag{4}$$

The charge number of ion j is denoted as Z_j, ε_0 is the vacuum permittivity, λ_D is the Debye length, and k is the Boltzmann constant. The thermodynamic functions used to calculate the standard chemical potentials of the particles are often theoretically calculated using standard statistical mechanics methods for thermodynamic data such as particle rotational constants, fundamental vibrational frequencies, electron excitation energies, and formation enthalpies. These functions are then fitted to temperature-dependent standard functions using the least-squares method in the NASA chemical equilibrium code CEA. Upon determining the particle composition of the plasma, the thermodynamic properties such as density, enthalpy, and specific heat can be computed using established thermodynamic functions [9]. Specifically, they can be expressed as:

$$\rho = \sum_{i=1}^{N} n_i m_i \tag{5}$$

$$h = \frac{1}{\rho} \sum_{i=1}^{N} n_i m_i h_i \tag{6}$$

$$C_p = \frac{\partial h}{\partial T}|_{p=const} \tag{7}$$

3 Comparison and Analysis of Calculation Results

3.1 Plasma Composition

This section mainly calculates the plasma composition of C_4F_7N-PTFE mixed gas within the temperature range spanning from 300 K to 30,000 K. The main species considered in the calculation are shown in Table 1.

Figure 1 illustrates the variation of mole fraction of each species in 70% C_4F_7N-30% PTFE thermal plasma at 0.8 MPa with temperature from 300 to 30,000 K. In the lower temperature range of 300 to 5000 K, ionization reactions are weak, and the dissociation of C_4F_7N and PTFE molecules is the dominant process, resulting in a low concentration of charged ions in the plasma. The primary ionization strength significantly increases above 5000, and at about 9000 K, carbon atoms undergo

Table 1 Particle components of C_4F_7N-PTFE mixture

Particle type	Main species considered in plasma
Neutral	CF, CF_2, CF_3, CF_4, CN, C_2N, C_4N_2, C, F, N, C_2, C_3, N_2
Charged	C^+, C^{2+}, F^+, F^{2+}, N^+, N^{2+}, e

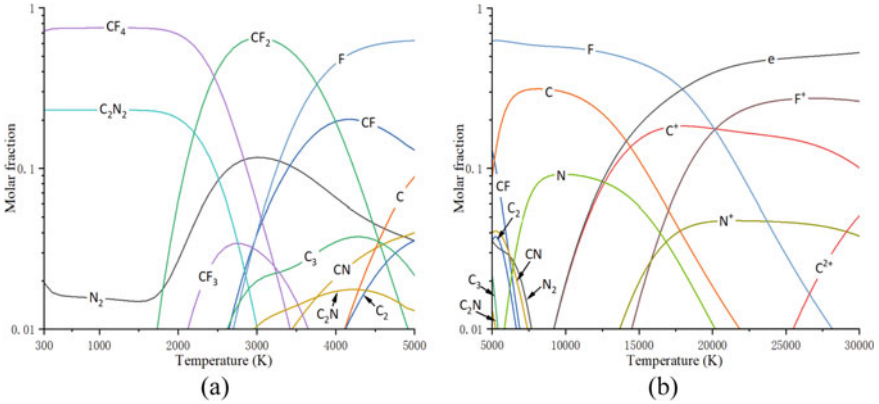

Fig. 1 Composition of C_4F_7N-PTFE mixture (C_4F_7N: PTFE = 7:3) as a function of temperature at 0.8 MPa, within the temperature ranges **a** from 300 to 5000 K, and **b** 5000 K to 30,000 K

intense ionization, resulting in a rapid increase in the number density of C^+ ions in the space. The significant ionization of nitrogen and fluorine atoms occurs at about 13,700 K and 14,500 K, respectively, due to the difference in their first ionization energies. At approximately 25,000 K, carbon atoms undergo intense second-order ionization, and the number of C^{2+} ions in the space significantly increases. With increasing temperature, molecular thermal motion and ionization reaction intensity become stronger, thus the behavior of electrons becomes evident at about 9000 K, and their number density continues to increase with increasing temperature.

The calculation results of the mole fraction of each species in the plasma do not correspond to the standard 70% C_4F_7N-30%PTFE mixture at 300K, which is due to the limitation of the algorithm principle. When calculating the plasma composition based on the principle of minimizing Gibbs free energy, only the possible particles in the system and their combinations that can exist in the specified temperature and pressure with the minimum Gibbs free energy are considered. Therefore, the calculation results in the low-temperature region correspond to the composition of the substance after the arc combustion, which is the result of the recombination of the high-temperature decomposition products of C_4F_7N-PTFE, and matches the post-arc analysis process.

3.2 Thermodynamic Properties

Effects caused by gas pressure. The partial thermodynamic properties of the C_4F_7N-PTFE mixture at different pressures are shown in Fig. 2. According to the gas state equation, an elevation in pressure results in an augmentation of the particle number per unit volume, resulting in an increase in the mass density of the plasma at all temperatures. In addition, according to the Le Chatelier's principle, ionization

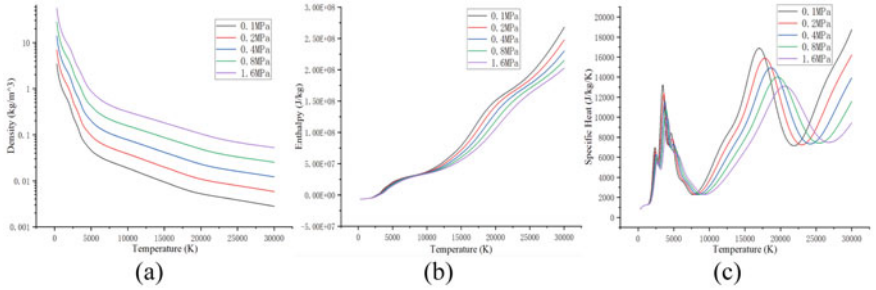

Fig. 2 Thermodynamic properties of C_4F_7N-PTFE mixture (C_4F_7N: PTFE = 7:3) as a function of temperature at 0.1–1.6 MPa, **a** Density **b** Enthalpy **c** Specific Heat

and dissociation reactions are suppressed as pressure increases, and heavy particles appear at higher temperatures. Figure 2 further illustrates the specific heat and enthalpy at constant pressure of the C4F7N-PTFE mixture under varying pressures. As the gas pressure increases, the peak of the specific heat related to ionization and dissociation reactions moves to higher temperatures and the peak value gradually decreases. This further corroborates that raising the gas pressure at a specific temperature can mitigate ionization and dissociation reactions.

Effects caused by PTFE. The partial thermodynamic properties of C_4F_7N-PTFE mixtures at 8 atm under different mixing ratios are shown in Fig. 3. Since the atomic composition of C_4F_7N is similar to that of PTFE, the proportion of PTFE has little effect on the density and enthalpy of the mixture. In the mixture, the peak values of the specific heat at constant pressure are observed approximately around 2600, 3900, and 5200 K, corresponding to the decomposition of CF4, CF2, and CF molecules, respectively. The differences in the specific heat at constant pressure of the mixture at different PTFE contents around 3900, 5200, and 8000 K are mainly related to the decomposition and recombination of CN, C_2N, and N_2 molecules. The physical and chemical reactions in the mixture are dominated by the ionization and recombination of C and F atoms, so the trends in the thermodynamic properties of the plasma under different mixing ratios are roughly the same.

3.3 Transport Properties

Effects caused by gas pressure. The partial transport coefficients of the C_4F_7N-PTFE mixture at different pressures are shown in Fig. 4. Within the high-temperature range, an elevation in pressure leads to an augmentation of the plasma conductivity. This phenomenon arises due to the positive correlation between the conductivity of the mixture and the electron number density. At high temperatures, the C_4F_7N-PTFE mixture is intensely ionized, and higher pressure results in a greater electron number

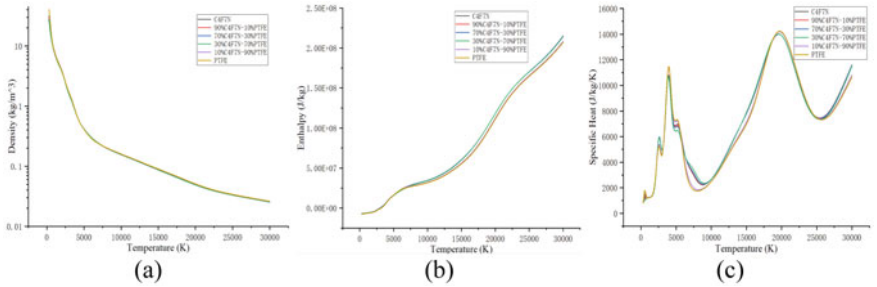

Fig. 3 Thermodynamic properties of C_4F_7N-PTFE mixture with different mixing ratios at 0.8 MPa, **a** Density **b** Enthalpy **c** Specific Heat

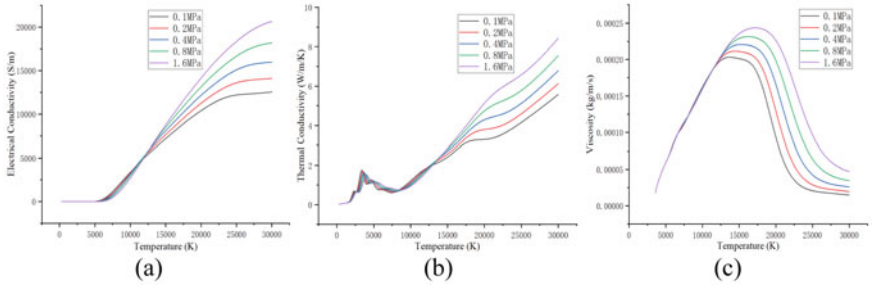

Fig. 4 Transport properties of C_4F_7N-PTFE mixture (C_4F_7N: PTFE = 7:3) as a function of temperature at 0.1–1.6 MPa, **a** Electrical Conductivity **b** Thermal Conductivity **c** Viscosity

density, which in turn increases the plasma conductivity. However, at low temperatures, increasing pressure suppresses the ionization reaction, leading to a decrease in the corresponding electron number density. Therefore, at low temperatures, the conductivity of the mixture decreases with increasing pressure.

Regarding the thermal conductivity of the C4F7N-PTFE mixture, an increase in pressure results in a shift of the thermal conductivity peak towards higher temperatures, accompanied by a decrease in the absolute value of the peak. This is consistent with the variation pattern of the mixture's specific heat capacity at constant pressure and is related to the effect of pressure on ionization and dissociation reactions. Additionally, Fig. 4 also shows the viscosity coefficient of the mixture at different pressures. At temperatures above approximately 12,000 K, the viscosity coefficient exhibits a significant increase with rising pressure. This phenomenon is attributed to the reduction in particle ionization degree caused by the elevated pressure, which subsequently impacts the Coulomb collisions among charged particles. The cross section of Coulomb collisions is significantly greater than that of collisions between neutral particles. Therefore, the viscosity increases with decreasing ionization degree, i.e., it increases with increasing pressure.

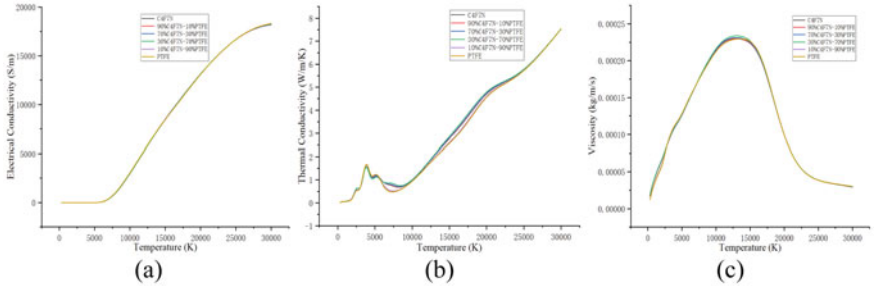

Fig. 5 Transport properties of C_4F_7N-PTFE mixture with different mixing ratios at 0.1–1.6 MPa, **a** Electrical Conductivity **b** Thermal Conductivity **c** Viscosity

Effects caused by PTFE. The partial transport coefficients of C_4F_7N-PTFE mixtures at 8 atm for various mixing ratios are presented in Fig. 5. The electrical conductivity of the plasma mainly depends on the electron number density. Since the ionization energy of C atoms is relatively low and the N content in the mixture is relatively low, the ionization reaction of the mixture is mainly dominated by C and F atoms, and the PTFE content has little effect on the electrical conductivity of the C_4F_7N-PTFE mixture. The differences in thermal conductivity around 8000 K correspond to the decomposition of CN and N_2 and the generation of N atoms. Meanwhile, due to the similarity in the number density of charged particles, the collision integral results of Coulomb interactions are also similar, and the viscosity coefficient of the mixture is also less affected by the PTFE content.

4 Discussion

The computational accuracy of thermodynamic properties and transport coefficients for low-temperature plasmas is currently insufficient. At low plasma temperatures, the inter-particle collisions are insufficient, and the efficiency of energy transfer between electrons and heavy particles is low, leading to the breakdown of the assumption of thermodynamic equilibrium (LTE). In situations where the collisions between electrons and heavy particles are insufficient, they acquire different temperatures, and the principle of minimum Gibbs free energy no longer applies. In future work, we will consider non-equilibrium thermodynamics and double-temperature plasma models to obtain more accurate results.

In addition, some researchers have shown that solid deposition can affect certain properties of low-temperature plasmas [10]. Although the theoretical calculation of transport coefficients is not significantly affected by solid particles, this is still an area that can be improved for obtaining more accurate theoretical calculations.

5 Conclusion

This paper calculates the thermodynamic properties and transport coefficients of C_4F_7N-PTFE mixtures, and studies the effects of different pressures and PTFE mixing ratios on these parameters. The results show that due to the similarity in atomic composition between C_4F_7N and PTFE, the PTFE mixing ratio has a small influence on the physical properties parameters, except for specific heat and thermal conductivity. The thermal conductivity and specific heat of the plasma are mainly related to the dissociation and ionization reactions of the mixture, and are affected to some extent by the presence of N-containing particles. Furthermore, the gas pressure exerts a notable influence on the transport coefficients and thermodynamic parameters of the mixture, particularly at elevated temperatures. At lower temperatures, the electrical conductivity of the plasma decreases with increasing pressure, indicating that higher gas pressure is beneficial for extinguishing the arc in high-voltage circuit breakers.

The thermodynamic properties and transport coefficients of the plasma are essential input parameters for the macroscopic magnetohydrodynamic (MHD) model of the arc. The calculated results of this study will provide basic data for MHD simulations of the arc, and further guide the design and manufacture of C_4F_7N environmentally friendly gas circuit breakers.

Acknowledgements This manuscript is sponsored by the Science and Technology Project of China Southern Power Grid (YNKJXM20220051).

References

1. Boychev B (2021) Recovery and regeneration of alternative gases for insulation in gas-filled electricity facilities. In: 13th electrical engineering faculty conference (BulEF). IEEE, Varna, pp 1–3
2. Zheng Y, Zhou W, Li H et al (2020) Experimental and calculation study on insulation strength of C_4F_7N/CO_2 at low temperature. IEEE Trans Dielectr Electr Insul 27(4):1102–1109
3. Sato M, Horinouchi K, Hiza S et al (2019) Ablated mass of PTFE nozzle due to high-current SF6 arc exposure: formulation of ablated mass. Elect Eng Jap 208(3–4):29–38
4. Chen L, Zhang B, Xiong J et al (2019) Decomposition mechanism and kinetics of iso-C4 perfluoronitrile (C_4F_7N) plasmas. J Appl Phys 126(16):163303
5. Zhang Z, Lin X, Li X et al (2019) Calculation of thermodynamic physical properties of C_4F_7N-CO_2 Mixed Gas. In: IEEE 20th international conference on dielectric liquids (ICDL). IEEE, Roma, pp 1–4
6. Lisong Z, Mingtian Y, Lei P et al (2019) Thermodynamic properties and transport coefficients of C_4F_7N/CO_2 thermal plasma as an alternative to SF_6. In: 2019 IEEE Pulsed power and plasma science (PPPS). IEEE, Orlando, pp 1–4
7. Wang Z, Wang S, Li Q et al (2022) Calculation of thermodynamic properties and transport coefficients of SF_6-PTFE-Cu mixtures. In: 2022 IEEE international conference on high voltage engineering and applications (ICHVE). IEEE, Chongqing (2022), pp 1–4
8. Kovitya P (1985) Physical-properties of high-pressure plasmas of hydrogen and copper in the temperature-range 5000–60000k. IEEE Trans Plasma Sci 13(6):587–594

9. Li X, Guo X, Murphy AB et al (2017) Calculation of thermodynamic properties and transport coefficients of $C_5F_{10}O$-CO_2 thermal plasmas. J Appl Phys 122(14):143302
10. Wang WZ, Wu Y, Rong MZ et al (2012) Theoretical computation of thermophysical properties of high-temperature F_2, CF_4, C_2F_2, C_2F_4, C_2F_6, C_3F_6 and C_3F_8 plasmas. J Phys D: Appl Phys 45(28):285201

A Physics-Informed Neural Network Model for Temperature Inversion of Axisymmetric Gas Discharge Channel

Zhenyu Liu, Lilang Xiao, Shen Chen, Yubin Huang, Hengxin He, and Weijiang Chen

Abstract The accurate measurement of gas discharge channel temperature is of great significance for the study of lightning physics. How to accurately solve the Abel equation and reduce the impact of noise accumulation is the key to the accurate inversion of the temperature. Physics-Informed Neural Networks (PINN) have shown promising future by combining the data driving nature of neural network with physical information guidance. In this paper, the schlieren image dataset is generated by assuming temperature distribution and simulations. With the dataset, the model is developed by training a PINN guided by inverse Abel transform, where the input is a schlieren image and the output is the distribution of relative gas destiny. After training, the results show that the accuracy of the proposed PINN method is close to that of other numerical algorithms, while PINN shows a significant improvement in computation speed. Moreover, compared with other methods, the accuracy of the PINN method remains stable under varying levels of noise, indicating its robustness, while the traditional methods are significantly affected by noise. The results of this paper indicate that PINN is more efficient in temperature inversion fields and more resistant to the effects of noise than previous methods, providing strong support for gas discharge temperature inversion.

Z. Liu · L. Xiao · S. Chen · Y. Huang · H. He (✉) · W. Chen
State Key Laboratory of Advanced Electromagnetic Engineering and Technology, Huazhong University of Science and Technology, Wuhan, China
e-mail: hengxin_he@hust.edu.cn

Z. Liu
e-mail: hust_lzy@hust.edu.cn

L. Xiao
e-mail: d202180692@hust.edu.cn

S. Chen
e-mail: d202280715@hust.edu.cn

Y. Huang
e-mail: huang_yubin@hust.edu.cn

© Beijing Paike Culture Commu. Co., Ltd. 2024

X. Dong and L. Cai (eds.), *The Proceedings of 2023 4th International Symposium on Insulation and Discharge Computation for Power Equipment (IDCOMPU2023)*, Lecture Notes in Electrical Engineering 1102, https://doi.org/10.1007/978-981-99-7405-4_14

Keywords Temperature inversion · PINN · Inverse Abel transform · Noise resistance

1 Introduction

Insulation coordination is important for high-voltage transmission lines, which determines the safety and cost-effectiveness. The study of gas gap discharge characteristics is a key issue in ensuring the safe and economic operation of power systems. In the process of gas discharge, temperature is a characteristic parameter that helps to reveal the mechanism of long air gap discharge. Therefore, the accurate measurement of temperature distribution in the discharge channel is of great significance for improving models for air gap discharges [1]. However, the inversion of temperature in the gas discharge channel still faces challenges. On the one hand, the accuracy of traditional methods is greatly affected by noise accumulation in the process of Abel integral [2]. On the other hand, the processing speed of traditional methods is slow, and the computational cost is not negligible when a large amount of calculation is required.

In recent years, neural network methods have been widely used in the field of physics due to their good performance and excellent robustness [3]. However, problems such as false output and low training efficiency still exist in traditional neural network due to the lack of constraints [4]. Hence, Raissi M tried to incorporate prior information to the network for constraints, which is called physical informed neural network (PINN), and applied it to the solution of various nonlinear partial differential equations, showing enormous potential of PINN [5]. PINN exhibits substantial advantages in solving physical equations, making it a promising approach for temperature inversion in gas discharge channel.

To address these issues, this paper develops an axisymmetric gas discharge channel temperature inversion model based on the PINN, which can not only reduce the cost of temperature inversion, but also has excellent noise resistance performance.

2 Methodology

2.1 Dataset

As mentioned in the previous analysis, obtaining schlieren images through experiments is not only time-consuming, but also difficult to simulate different discharge scenarios. In order to train a PINN model, simulations were made to generate different schlieren images, which not only reduced the cost of dataset establishment, but also ensured the diversity of temperature distribution in dataset. Figure 1 shows the process of generating the dataset.

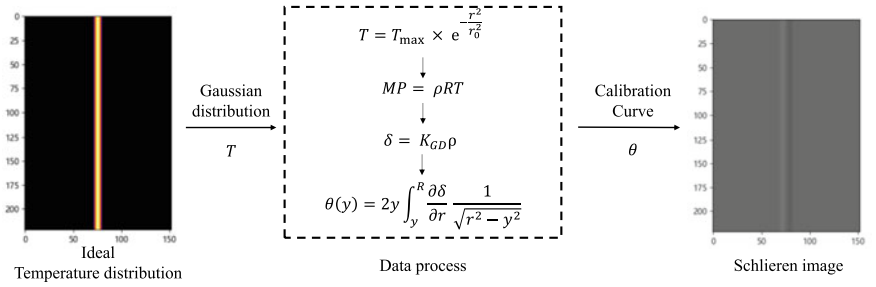

Fig. 1 The process of Schlieren dataset generation

Based on literature [6], it is assumed that the temperature in the discharge channel follows a Gaussian distribution, with T_{max} and r_0 being the maximum temperature and the thermal radius of the discharge channel, respectively. By modifying the parameters $T_{\max}$ and r_0 and combining the ideal gas equation, various gas density distributions can be simulated. Then connect the gas density and the refractive index difference through the Gladstone-Dale formula [7]. As the Gladstone-Dale coefficient, K_{GD} is calculated as 2.2597×10^{-4} [8]. Then δ is subjected to Abel inversion to obtain the distribution of deflection angle difference in the region. Based on Cheng's experimental setup [8], The calibration curve relating image grayscale values to kerf width is established, successfully converting the deflection angles to grayscale distribution of the discharge channel, generating grayscale images.

With above processing, the training dataset was generated, consisting of 2000 schlieren images with varying grayscale distributions. The resolution was 222×152 pixels [8], with the electrode part removed. The temperature varies between 1000 and 2000 K and the radius varies between 0.1 and 0.9 mm.

2.2 PINN Network

On the basis of traditional neural networks, PINN introduced prior knowledge to guide the training, avoiding unrealistic results [9], and it has shown good performance in various fields such as physics and mathematics [10, 11]. In this paper, we optimize PINN with FNN as the backbone by incorporating batch normalization (BN) layers after each linear layer. This reduces the instability of parameter updates and improves the network's generalization performance by introducing noise during the training process. Meanwhile, to ensure that the outputs satisfy the physical rule, we introduce the Abel equation in the loss function to guide the training process, thus constructing the PINN model. The improved model structure is shown in Fig. 2.

The input image is processed through multiple neuron combinations, normalization by BN layer, and non-linear transformations by activation functions in PINN. Afterwards, the network computes the error through the loss function, which includes weighted sums of physical consistency loss L_{Abel} and boundary loss L_{bound}, in order

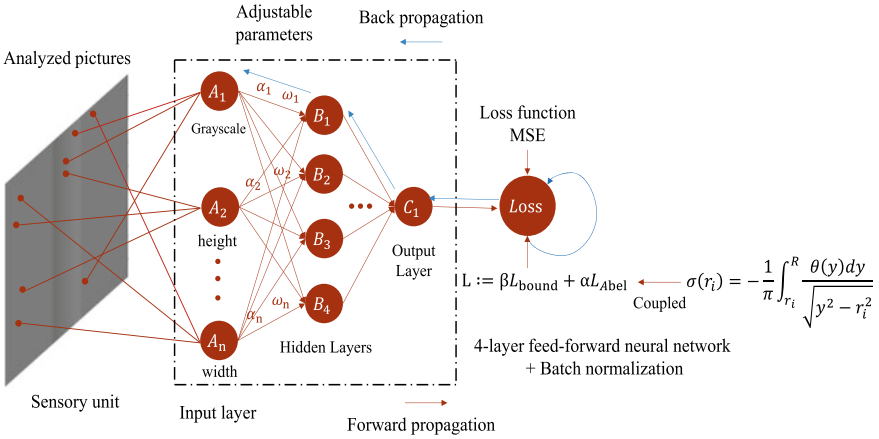

Fig. 2 The network structure of PINN

to ensure the accuracy of the inversion process.

$$Loss_{\text{all}} = \alpha \bullet L_{\text{Abel}} + \beta \bullet L_{\text{bound}} \tag{1}$$

The image was segmented into internal and boundary regions using grayscale-based edge detection. The L_{Abel} and L_{bound} are calculated for internal and boundary regions, respectively. The internal region was constrained by inverse Abel transform, while the boundary region is constrained by the Dirichlet boundary condition, with a relative gas density of 1. To balance the loss magnitudes and focus on the central region, α and β are set and determined through multiple parameter pre-experiments, with $\alpha = 0.9$ and $\beta = 0.1$.

2.3 Train

The model was deployed on a Tesla A16 graphics card, and the training framework used is PyTorch 1.9.1. The hyperparameters required for training are shown in Table 1.

Table 1 Hyperparameters list

Hyperparameter	Value
Batch size	16
Epoch	2000
Loss function	MSE + Abel
Optimizer	Adam
Learning rate	0.001 step decay

During the training process, 16 sets of data were input to the model for each iteration, and the model was trained through 2000 iterations of forward computation and backward propagation. The MSE loss function was used, which was based on the Abel equation and boundary conditions. We chose the Adam optimization algorithm to train the model, with an initial learning rate of 0.001, which decayed by a factor of 0.75 every 50 iterations. With BN layer and Abel equation introduced, PINN achieved high inversion accuracy, reaching convergence after around 750 iterations, with an overall average accuracy of approximately 93.5%.

3 Results

3.1 Performance Under Noise-Free Condition

To evaluate the performance of the PINN model, we compared its results with those obtained from traditional numerical methods. The calculations of the two-point method and three-point method in this paper was based on Xu's approach [2], while the Fourier–Hankel method followed Chehouani et al. [12]. Since there were no specific details available in literature, we employed the adaptive Gaussian-Kronrod quadrature method for numerical integration to sum the results discretely in this paper. The relative accuracy (RA) and coefficient of determination (R2) were chosen as the evaluation metrics for precision, while computation time was used to assess efficiency. The performance of each method is summarized in Table 2, and the comparative results of temperature inversion for a single row without noise are shown in Fig. 3.

According to Table 2 and Fig. 3, The accuracy of the PINN model on the test set was 93.5%, which is close to that of other numerical algorithms. Furthermore, PINN demonstrates significantly higher efficiency than previous methods, with a processing time of only 0.34 s per image, indicating a competitive advantage in large-scale data processing.

Table 2 Comparison between PINN and traditional methods

Method metrics	PINN	Two point	Three point	Fourier–Hankel
RA (%)	93.5	99.04	98.2	98.7
R-square	0.9828	0.9998	0.9986	0.9994
Time (s)	0.35	53.56	8.78	39.21

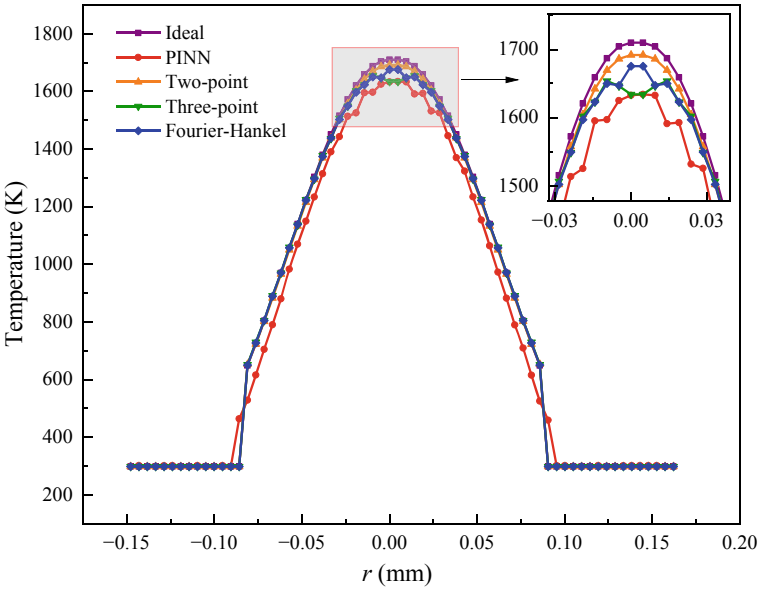

Fig. 3 Inversion results under noise-free condition

3.2 Performance in Various Noise Condition

In this section, we analyze the noise resistance performance of PINN compared to traditional methods using Lv's method [13]. Gaussian noise is used as the noise signal, and the RA and R2 are chosen to evaluate the performance of noise resistance. Meanwhile, the decibel value of the noise is used to measure and control the impact of noise on accuracy. Considering the practical scenario, the decibel values representing the magnitude of noise in the input data are [0, 14, 20], and 10 sets of experiments are conducted at each noise level to obtain an average result, thereby reducing the randomness of the noise. Table 3 presents the performance of different methods under various noise levels, while Fig. 4 displays the temperature outputs of different algorithms under various noise levels.

Table 3 Performance comparison under noisy conditions

Method noise	PINN		Two-point		Three-point		Fourier–Hankel	
Metrics	RA (%)	R^2	RA (%)	R^2	RA (%)	R^2	RA (%)	R^2
Noise-free	93.5	0.9828	99.1	0.9998	98.2	0.9986	98.7	0.9994
Noise-14 dB	91.4	0.9847	−4.41	−2.9E7	−165	−3.1E7	67.6	−4.1E4
Noise-20 dB	84.5	0.9812	−5.1	−1.8E6	−888	−7.5E5	−921	−1.2E5

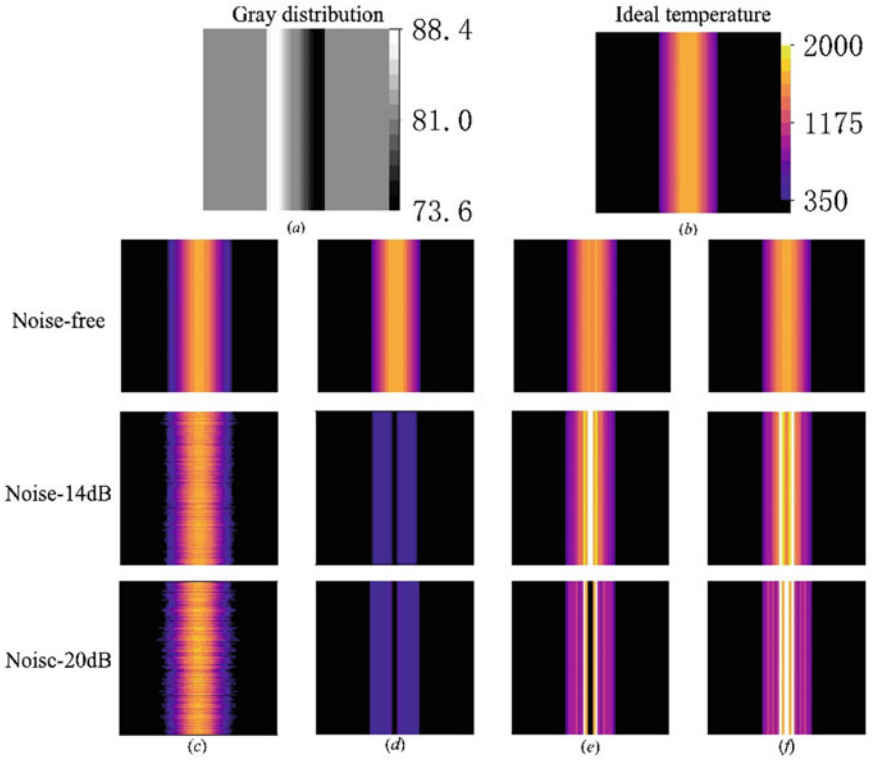

Fig. 4 Temperature output of different methods under various noise levels. **a** Grayscale distribution of the test image. **b** Ideal temperature distribution of the test image. **c** Outputs of PINN. **d** Outputs of Two-point method. **e** Outputs of Three-point method. **f** Outputs of Fourier–Hankel method

As can be seen from Table 3 and Fig. 4, with the noise level increasing, the accuracy of traditional algorithms continuously decreases. Under the noise level of 14 dB, the accuracy of the two-point method and the three-point method turned negative, indicating that their outputs significantly deviate from the ideal values, as the FHK method maintaining an accuracy of 68%. Under the noise level of 20 dB, the accuracy of the conventional method has all turned negative, indicating significant errors. In contrast, PINN demonstrates overall low sensitivity to noise, with an average accuracy of over 85%. PINN exhibits strong robustness compared to other traditional methods when taking noise into consideration.

4 Conclusion

In this paper, a PINN model was proposed for temperature inversion of gas discharge schlieren images. The model was trained on a dataset of 2000 schlieren images generated based on simulations. Under noise-free condition, the accuracy of the PINN model on the test set was 93.5%, which is close to that of other numerical algorithms, and it is 25 times faster than traditional methods. This paper also compares the robustness of PINN with traditional methods, and the results showed that PINN exhibited lower sensitivity to noise and superior noise resistance compared to previous methods. In the following research, the performance of the PINN model can be further improved by refining the design of loss function and dataset.

Acknowledgements This work is supported by the National Natural Science Foundation of China (51977090).

References

1. Chen WJ, Zeng R, He HX (2013) Research progress on long air gap discharge. High Volt Eng 39(06):1281–1295 (in Chinese)
2. Xu L (2018) Study on diagnostic of gas temperature field in atmospheric pressure DC glow discharge plasma. Chongqing University (in Chinese)
3. Chai J, Zeng H, Li A et al (2021) Deep learning in computer vision: a critical review of emerging techniques and application scenarios[J]. Mach Learn Applicat 6:100134
4. Zhang C, Bengio S, Hardt M et al (2021) Understanding deep learning (still) requires rethinking generalization[J]. Commun ACM 64(3):107–115
5. Raissi M, Perdikaris P, Karniadakis GE (2019) Physics-informed neural networks: a deep learning framework for solving forward and inverse problems involving nonlinear partial differential equations[J]. J Comput Phys 378:686–707
6. Zhao XG (2017) Study on streamer characteristics in long air gap under positive impulse voltage. Huazhong University of Science and Technology (in Chinese)
7. Allen CW (1976) Astrophysical quantities (3rd edition) [M]. Athlone, London, p 92
8. Cheng C, He H, Luo B, et al. Temperature measurements of long sparks in air using time-resolved moiré deflectometry[J]. J Phys D: Appl Phys 55(26):265201
9. Cuomo S, Di Cola VS, Giampaolo F et al (2022) Scientific machine learning through physics–informed neural networks: where we are and what's next[J]. J Sci Comput 92(3):88
10. Mao Z, Jagtap AD, Karniadakis GE (2020) Physics-informed neural networks for high-speed flows[J]. Comput Methods Appl Mech Eng 360:112789
11. Cai S, Wang Z, Wang S et al (2021) Physics-informed neural networks for heat transfer problems[J]. J Heat Transfer 143(6)
12. Chehouani H, El Fagrich M (2013) Adaptation of the Fourier-Hankel method for deflection tomographic reconstruction of axisymmetric field[J]. Appl Opt 52(3):439–448
13. Lv X, Bi G, Wang C, Xing M (2011) Lv's distribution: principle, implementation, properties, and performance. IEEE Trans Sign Process 59(8):3576–3591

Lightning Risk Assessment of 330 kV Transmission Line Under Icing Conditions in Qinghai Area

Haiping Zhang, Mingliang Liu, Jun Zhang, Jing Tong, Feng Li, Xinghai Fu, and Minghui Jia

Abstract Icing and lightning strikes are the main causes of transmission line faults. Currently, the lightning strike risk assessment methods are too singular. The impact of icing on the electrical performance of the line is not comprehensively considered, resulting in assessment results that cannot reflect the actual lightning strike risk of iced-up lines. Therefore, a lightning risk assessment method considering icing factors is proposed. The method establishes an icing thickness calculation model based on the weighing method and uses the electromagnetic transient analysis software (Electro Magnetic Transient Program, EMTP) to write a preliminary flashover criterion module for icing insulators. In order to more accurately calculate actual line shielding, an improved electrical geometry model considering lightning incident angle and ground slope is established. Finally, the lightning strike tripping rate is calculated using the above model, and the towers are assessed for risk level based on risk classification standards. This evaluation method can provide a new reference scheme for the design of risk assessment systems for transmission lines in China.

Keywords Lightning strike · Icing · Flashover voltage · Tripping rate · Risk Assessment

H. Zhang (✉) · M. Liu · X. Fu
Huanghua Power Supply Company, State Grid Qinghai Electric Power Company, Jianzha 811200, China
e-mail: 859541891@qq.com

J. Zhang · J. Tong · F. Li
Qinghai Power Transmission Transfer Engineering Co., Ltd, Xining 810000, China

M. Jia
State Grid Qinghai Extra High Voltage Company, Xining 810000, China

© Beijing Paike Culture Commu. Co., Ltd. 2024

X. Dong and L. Cai (eds.), *The Proceedings of 2023 4th International Symposium on Insulation and Discharge Computation for Power Equipment (IDCOMPU2023)*, Lecture Notes in Electrical Engineering 1102, https://doi.org/10.1007/978-981-99-7405-4_15

1 Introduction

High-voltage transmission lines will inevitably pass through some harsh climatic and geographical environments. resulting in a sharp increase in the frequency of natural disasters such as icing and lightning strikes, which seriously threatens the safe and reliable operation of the power grid [1]. Domestic and foreign scholars' research on lightning risk mostly focuses on the influence of lightning parameters, line structure and topography. there is little research on the lightning risk of lines under icing conditions. Therefore, it is significant to carry out research on lightning risk assessment of iced lines.

The lightning trip risk assessment and lightning protection of transmission lines in mountainous wind farms is proposed [2]. Based on the improved Dempster-Shafer theory [3], proposed a lightning fault risk assessment for overhead transmission lines [4]. proposed a dynamic simulation method of power system considering transmission line icing and insulator flashover in extreme weather. The collapse of transmission tower-line system induced by ice shedding is analyzed in detail [5]. A full-level evaluation system of power grid-line-tower section-tower is established, tower sections and towers for lightning protection transformation [6]. Proposed an optimization analysis method for directly obtaining lightning strike parameters and optimized the existing lightning risk assessment methods [7]. Proposed a lightning risk assessment method for transmission lines based on multi-dimensional correlation information fusion [8]. Established a time-varying failure rate model of transmission lines and a time model considering ice-melting devices [9]. According to the meteorological forecast, micro-topography information and the temporal and spatial evolution of ice disaster, the ice thickness of the line is predicted [10].

In this paper, combined with the influence of icing and lightning strike on the electrical performance of the line, a lightning risk assessment method for icing lines is proposed. Firstly, based on the weighing method, the calculation model of icing line thickness is established. Through the icing insulator string and the actual line parameters, the flashover criterion module of icing insulator string is written by using the MODELS of EMTP. In order to improve the calculation accuracy of actual line shielding failure, an improved electrical geometric model considering lightning incident angle and ground inclination angle is established. Finally, based on the above model, the quantitative analysis of the influence of icing and lightning strike on transmission lines is realized. The research can provide reference for the design of transmission line risk assessment system.

2 Calculation of Lightning Icing Line Related Parameters

2.1 Icing Thickness Calculation Model

In this paper, combined with the engineering practice, the calculation of the ice thickness of the line is simplified. According to the relationship between the factors such as the tension F of the suspension insulator strings, the self-weight G_i of the insulator string and the fitting and the wind deflection angle, the vertical load G_v of the conductor in the vertical span of the straight tower, the calculation formula is as follows:

$$G_v = \frac{F}{\sqrt{1 + \mathrm{tg}\mu^2 + \mathrm{tg}\alpha^2}} - G_i \tag{1}$$

where, μ represents wind deflection angle. G_i is the net weight of insulator string and fittings. α represents deflection angle of suspension insulator strings.

The concept of equivalent length and simplified the calculation method of ice thickness was adopted in the article. That is, the icing load is equivalent to the equivalent length of the transmission line. the calculation formula is as follows:

$$l_{\mathrm{eq}} = \frac{G_{v0}}{q_0 n} \tag{2}$$

where, q_0 is the weight per unit length of the wire. n is the number of wire splitting. G_{v0} can be obtained by using the tension of the overhanging string in the absence of ice according to Formula (1). Based on the above parameters, the unit length ice load q and the equivalent ice thickness b can be obtained, the calculation formula is as follows:

$$q = \frac{G_v}{l_{\mathrm{eq}} n} - q_0 \tag{3}$$

$$b = \sqrt{\frac{q}{\pi \rho g} + \left(\frac{D}{2}\right)^2} - \frac{D}{2} \tag{4}$$

where, ρ represents the icing density, d represents the wire diameter.

2.2 Leader Model of Iced Insulator

The leader model of iced insulator is established in this paper, and the icing correction coefficient k_0 is introduced to correct the leader development speed, and k_1 is introduced to correct the average streamer field strength.

The long air gap discharge process mainly includes three steps: streamer initiation, continuous leader initiation and breakdown.

Considering the influence of icing on the insulator string, the correction coefficient k_0 is introduced to correct the leader development coefficient k, that is, $k_2 = k_0 \times k$. The calculation formula of revised leader development rate as follows:

$$v_z' = k_2 U(t)(\frac{U(t)}{L-l} - E_0) \tag{5}$$

According to ECI recommendation, insulator flashover voltage can be expressed as $U_{50\%} = E_l \times L$. Considering the influence of icing on the average field strength of insulator streamer, the correction coefficient k_1 is introduced, the streamer average field strength calculation formula is as follows:

$$U_{50\%}' = k_1 E_l L = E_{l0} L \tag{6}$$

where, k_1 is the correction coefficient, which is related to the icing degree and structure of the insulator. E_l is the average field strength of streamer.

The continuous leader should develop forward, and the streamer of the leader head should take precedence over the leader development. Therefore, the leader initiation threshold E_0 can be equivalent to E_{l0}.

3 Calculation of Lightning Icing Line Related Parameters

3.1 Counterattack Trip Rate

The counterattack tripping rate of the transmission line, the calculation formula is as follows:

$$P_f = N_1 \eta g P \tag{7}$$

where, P_f is the counterattack trip-out rate converted to 40 thunderstorm days and 100 km length, times/100 km·a. N_1 is the number of lightning strikes on the line, times/100 km·a, η is the arc-establishing rate. P is the probability that the amplitude of lightning current is greater than the lightning withstand level of counterattack.

3.2 Shielding Failure Trip-Out Rate

In this paper, an improved electrical geometry model considering lightning incidence angle and ground inclination angle is established based on the icing line, so that the

calculation of shielding failure trip-out rate is more in line with the actual line. The calculation of striking distance is the basis of electrical geometric model, and the size of striking distance is determined by the amplitude of lightning current. The size of striking distance calculation formula is as follows:

$$r_s = 6.72I^{0.65} \tag{8}$$

$$r_g = \begin{cases} 3.6 + 0.17\ln(43 - h) & h \geq 40\text{m} \\ 5.5 \times I^{0.65} & h \leq 40\text{m} \end{cases} \tag{9}$$

where, r_s is the striking distance between the conductor and the lightning conductor, r_g is the distance to ground, h is the average height of the wire to the ground.

The probability distribution of the spatial position flashover of the phase conductor, the calculation formula is as follows:

$$P_\alpha = \int_{I_{\min}}^{I_{\max}} xf(I)\mathrm{d}I \tag{10}$$

where, $I_{\min}$ is the minimum lightning current amplitude of the line without flashover, $I_{\max}$ is the maximum lightning current amplitude of shielding failure.

The shielding failure tripping rate, the calculation formula is as follows:

$$P_r = N_1 \eta P_\alpha \tag{11}$$

where, P_r is the shielding failure trip rate, times/100 km·a, N_1 is the number of lightning strikes.

3.3 Lightning Risk Classification Standard

Based on the derived calculation formula of line counterattack and shielding failure trip-out rate, this paper classifies the risk levels of counterattack and shielding failure of transmission lines into grades A, B, C and D, and the classification criteria are shown in Tab. 1.

Table 1 Lightning hazard risk classification standard

Risk level	A	B	C	D
Circling stroke	$P_\mathrm{r} < 2.503$	$2.503 \leq P_\mathrm{r} < 3.758$	$3.758 \leq P_\mathrm{r} < 5.012$	$P_\mathrm{r} \geq 5.012$
Counter attack	$P_f < 1.140$	$1.140 \leq P_f < 2.188$	$2.188 \leq P_f < 3.237$	$P_f \geq 2.356$

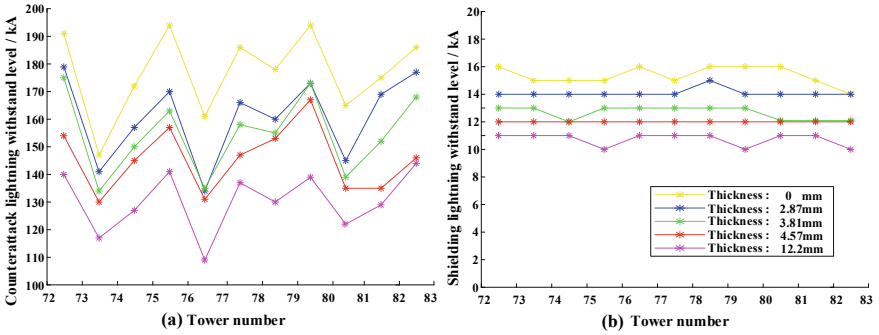

Fig. 1 Lightning withstand level, **a** counterattack lightning withstand level, **b** shielding lightning withstand level

4 Case Study

In this paper, a 330 kV transmission line is taken as an example to evaluate the lightning protection performance of iced transmission lines according to the above risk assessment method.

4.1 Analysis of Risk Assessment Results

The lightning withstand level of the line under different icing degrees and non-icing conditions is analyzed and calculated. The calculation results are shown in Fig. 1.

According to Fig. 1, The lightning withstand level of line shielding failure and counterattack gradually decreases with the increase of line icing thickness. The lightning withstand level of counterattack and shielding failure of the 79th base tower decreased obviously, which decreased by 55 and 6 kA respectively. Except for the 73-base tower, the lightning withstand level of other towers is reduced by more than 40 kA. The lightning withstand level of shielding failure decreases by about 5 kA.

Based on the calculation results of lightning withstand level and the calculation methods of counterattack and shielding failure, the shielding failure and counterattack tripping rates of transmission lines under different icing degrees are calculated. The results are shown in Fig. 2.

According to Fig. 2, The counterattack and shielding failure trip-out rate of the line gradually increase with the increase of ice thickness. The back stroke and shielding failure trip-out rate of the 76th base tower have the greatest influence, which are increased by 3.1831 and 3.2837 times/100 km·a, respectively. Except for the 82# tower, the reverse (shielding) stroke trip-out rates of the other towers are increased by 1–2 times/100 km·a. Therefore, it can be concluded that the influence of icing on the lightning risk of transmission lines is important.

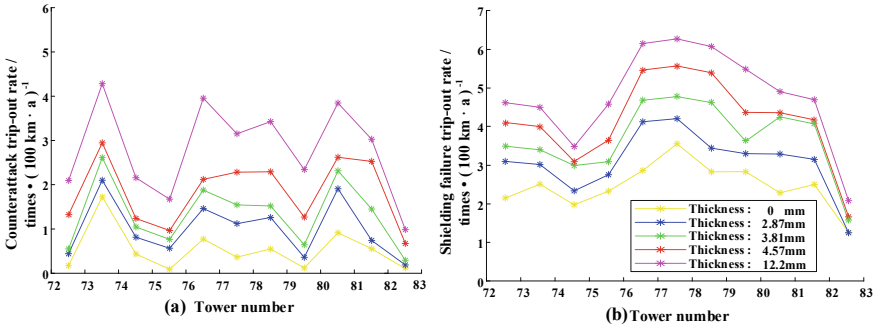

Fig. 2 Lightning trip-out rate. **a** counterattack trip rate, **b** shielding failure trip-out rate

Based on the calculation results of counterattack and shielding failure trip-out rate, and according to the classification standard of lightning risk level of the line, the risk level of the tower in the line section is counted. The statistical results are shown in Fig. 3.

According to the statistical analysis results of Fig. 3, the risk level of the line tower gradually increases with the increase of the icing thickness. Taking the counterattack as an example, when the line is not covered by ice, the number of A-level risk towers of the line is 10 bases, and the B-level is 1 base. When the icing thickness of the line reaches 12.2 mm, there is only one base left for the A-level risk tower, the number of B-level risk towers rises to 3 bases, and the number of C-level and D-level risk towers rises to 3 bases and 4 bases.

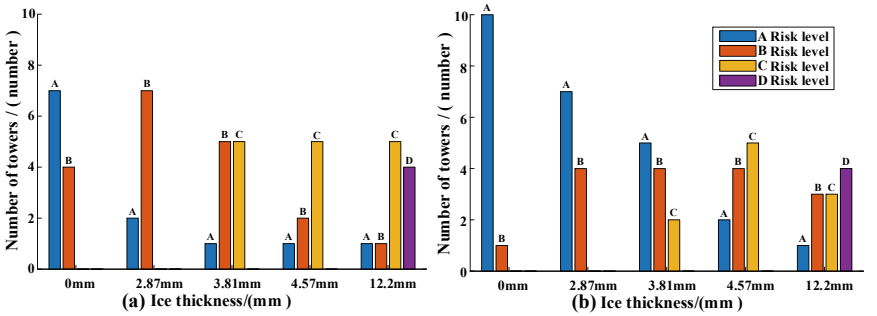

Fig. 3 Tower risk level statistics. **a** Counterattack tower risk statistics. **b** Risk statistics of tower failure

5 Conclusion

(1) Considering the influence of icing and other factors on the flashover voltage of insulator string, the leader model of iced insulator is modified by introducing a correction coefficient. The value of correction coefficient k_0 is greater than 1, and the value of correction coefficient k_1 is related to flashover voltage and insulator string length.
(2) When the icing thickness increases to 12.2 mm, the lightning withstand level of line counterattack and shielding failure decreases by more than 40 and 5 kA, respectively. The line counterattack and shielding failure tripping rates are increased by 1–2 times/100 km•a, respectively.
(3) About 90% of the tower counterattack and shielding failure risk levels in the icing line increase with the increase of icing thickness.

References

1. Li P, Ruan JJ, Huang DC (2018) Influence factors analysis of the conductor-plane gap breakdown characteristic under simulation forest fire condition. Transact China Electrotechn Soc 33(01):195–201 (in Chinese)
2. Yang Y, Wang S, Wang SF et al (2021) Lightning trip-out risk assessment and differential lightning protection of 35 kV transmission lines in mountain wind farm. In: 8th international conference on power and energy systems engineering (CPESE), pp 581–588
3. Liu J, Jia BY, Zhang ZM, Wang ZM et al (2022) Lightning failure risk assessment of overhead transmission lines based on modified dempster-shafer theory. Energies 15(07):2538
4. Chen LZ, Shi XH, Peng B et al (2018) Dynamic simulation of power systems considering transmission lines icing and insulators flashover in extreme weather. IEEE Access 10(01):39656–39664
5. Li JX, Wang BA, Sun J, Wang SH et al (2021) Collapse analysis of a transmission tower-line system induced by ice shedding. Front Phys 09(01):32–48
6. Zhao C, Chen JH, Wang J et al (2011) Research on technology of lightning disaster risk assessment for power system. High Volt Eng 37(12):3012–3021 (in Chinese)
7. Chen JH, Zhao C, Wang J et al (2015) Optimal lightning risk assessment method of transmission line based on direct acquisition of lightning stroke parameter. High Volt Eng 41(01):14–20 (in Chinese)
8. Xie CZ, Bai JF, Wang HB et al (2018) Lightning risk assessment of transmission lines based on multidimensional related information fusion. Proceed CSEE 38(21):6233–6244 (in Chinese)
9. Yan MY, Zhou ZY, Wen JY et al (2016) Assessment method for power grid icing risk based on short-term icing forecasting. Automat Electric Pow Syst 40(21):168–175 (in Chinese)
10. Xie YY, Xue YS, Wen FS et al (2013) Space-time evaluation for impact of ice disaster on transmission line fault probability. Automat Electric Pow Syst 37(18):32–41 (in Chinese)

Arc Radiation Characteristics of CO_2–O_2 Mixtures at 0.1–0.8 MPa and 300–30,000 K

Ke Wang, Yunkun Deng, and Junwei Deng

Abstract For high-voltage circuit breakers, it is necessary and urgent to explore SF_6 alternative gases that are environmentally friendly. CO_2 and its mixtures have been widely studied as eco-friendly insulation and arc-quenching media, but how to achieve large-capacity breaking to make it applicable to higher voltage levels is still a pressing issue. Radiation plays a crucial role in the energy dissipation process of the arc, especially under high-current conditions. Therefore, studying the radiation characteristics is beneficial for a better understanding of the breaking capacity of the arc-quenching medium. In this paper, the plasma composition of the CO_2–O_2 mixture at local thermodynamic equilibrium (LTE) is calculated using the minimization of Gibbs free energy. The radiation characteristics of the 70%CO_2–30%O_2 mixture over a pressure range of 0.1–0.8 MPa and a temperature range of 300–30,000 K are evaluated. It is found that increasing the pressure increases the number density of the gas, thus increasing the net emission coefficient. The radiation emitted by the 70%CO_2–30%O_2 mixture in the arc center is strongly absorbed within 1 mm, and the net emission coefficient of 70%CO_2–30%O_2 is higher than that of SF6 at the same pressure.

Keywords High-voltage circuit breakers · CO_2–O_2 mixtures · Arc radiation · Net emission coefficient

K. Wang · Y. Deng
Electric Power Research Institute of Yunnan Power Grid Co., Ltd, Kunming 650217, China

J. Deng (✉)
State Key Laboratory of Electrical Insulation and Power Equipment, Xi'an Jiaotong University, Xi'an 710049, China
e-mail: zhangby@xjtu.edu.cn

© Beijing Paike Culture Commu. Co., Ltd. 2024

X. Dong and L. Cai (eds.), *The Proceedings of 2023 4th International Symposium on Insulation and Discharge Computation for Power Equipment (IDCOMPU2023)*, Lecture Notes in Electrical Engineering 1102, https://doi.org/10.1007/978-981-99-7405-4_16

1 Introduction

High-voltage circuit breakers are one of the most important and critical switchgears in the power system, playing a vital role in ensuring the safe, reliable, and stable operation of the transmission and distribution system. SF_6 is widely used as an insulation and arc-quenching medium in high-voltage circuit breakers [1]. However, SF_6 is a potent greenhouse gas and its use is restricted to a certain extent. Therefore, finding an environmentally friendly and high-performance SF_6 substitute gas is an urgent issue. Due to its low greenhouse effect, strong arc-quenching ability, and low cost, CO_2 has a high feasibility for the development and optimization of environmentally friendly high-voltage circuit breakers [2, 3]. In order to increase the voltage level and breaking capacity of circuit breakers and provide a reference for the research and optimization design of environmentally friendly high-voltage circuit breakers, it is necessary to carry out corresponding theoretical and experimental research around CO_2 and its mixed gases [4]. shows that adding a small amount of O_2 to CO_2 can significantly improve its thermal breaking performance, and at the same time eliminate the influence of carbon deposition to a certain extent. Therefore, this paper mainly studies the radiation characteristics of CO_2–O_2 mixed gas.

The arc behavior during current interruption in high-voltage circuit breakers is a complex process involving multiple physical fields. Experiments are costly and time-consuming, but with the improvement of arc models, simulation predictions of arc characteristics have become possible. The temperature of the arc plasma can reach several tens of thousands of degrees, and radiation is a very important way of energy dissipation. When simulating and analyzing arc plasma, the effect of radiation must be considered, and precise radiation coefficients are a prerequisite for reliable arc simulation. However, radiation and absorption processes in arc plasma are very complicated, with a wide range of spectral lines, so solving the radiation transport equation accurately requires a large amount of time and the computational cost is unacceptable.

At present, the calculation methods of plasma radiation characteristics mainly include net emission coefficient (NEC) method, partial characteristic method (MPC), P1 method and discrete ordinated method (DO). The MPC method assumes that in the integral of the radiation transport equation, the temperature change between the radiation source point and any point on the radiation path is always linear, because the local characteristic function used for calculation is related to the temperature and distance between two points, Therefore, it can also effectively consider the self-absorption of central radiation energy by the edge region [5]. The P1 model assumes that the plasma is a gray body, and solves the radiation transport equation into an elliptic equation, which can well deal with the influence of the plasma edge region and the vessel wall on the radiation [6]. However, because it deals with more than one equation, the calculation time is greatly increased. The DO model is based on discretizing the directional variation of radiant intensity, and the problem is solved by solving the radiative transfer equations for a set of discrete directions covering the entire 4π solid angle. Since the DO model can easily handle the incident scattering

term, it outperforms other methods in computing scattered radiation problems, and it has better accuracy [7]. The NEC method proposed by Lowke [8] has been widely used as a simplified model for efficient calculation of radiation, which avoids solving the radiative transport equation. This method assumes that the arc is an isothermal and uniform sphere, which represents how much energy the plasma actually radiates outward. Fang et al. [9] compared the application of these three radiation models in circuit breaker arc plasma simulation, and pointed out that in most cases, the NEC method can effectively estimate the radiation characteristics of the central region of arc plasma.

The calculation in this paper is based on the assumption of LTE, the pressure range is 0.1–0.8MPa, and the temperature range is 300–30,000 K. First, the Gibbs free energy is minimized to calculate the plasma composition of 30%CO_2–70%O_2, and the line emission coefficient and continuous emission coefficient are calculated in the full spectrum range of the arc, and then the net emission coefficient of the mixed gas is obtained. Finally, the radiative properties of CO_2–O_2 mixed gas are evaluated. This study provides a basis for a deep understanding of the energy dissipation mechanism and arc extinguishing properties for CO_2–O_2.

2 Calculation Method

2.1 Plasma Composition

Computing the plasma composition is the first step in solving the radiation properties. The calculation of plasma composition in this paper is based on the assumption of local thermodynamic equilibrium (LTE), that is, electrons and heavy particles have the same temperature. Therefore, the composition of the plasma depends only on temperature and pressure. The ion components of the arc plasma need to satisfy the minimum Gibbs free energy, quasi-electric neutrality conditions, stoichiometric equilibrium conditions, and Dalton's law of partial pressure at the same time. This is a typical problem of constrained optimization in applied mathematics. For the convenience of solving, Lagrangian multipliers are usually used to convert the constrained optimization problem into an unconstrained problem, and then the Newton–Raphson iterative method is used to solve it.

Assuming that there are N kinds of particles in the plasma system, the Gibbs free energy can be expressed as [10]:

$$G = \sum_{i=1}^{N} n_i \mu_i \tag{1}$$

where, G is the Gibbs free energy, N is the species number of the particle, n_i is the particle number density.

The minimum Gibbs free energy method to solve the plasma particle composition must obtain the standard Gibbs free energy of each particle. The standard Gibbs free energy of a given particle can be calculated from the fitting coefficients obtained by fitting the thermodynamic parameters by the least square method.

2.2 NEC Method

In the arc plasma, various particles are in excited states or ionized states. At this time, if the energy state of electrons changes, radiation will be generated to the outside. In the high temperature region, radiation is the most important way of energy dissipation of the arc. It can be seen that the radiation will affect the properties of the plasma, so it is necessary to study the radiation characteristics.

The NEC refers to the difference between the radiation energy per unit volume and unit solid angle and the self-absorption energy at a certain position of the isotropic and isothermal plasma, which characterizes the actual outward radiation energy of the plasma. To obtain the NEC, the internal emission and absorption mechanisms of the arc plasma must be understood. Due to the very wide frequency domain range of the arc, an accurate spectral description is necessary [11].

In this work, the atomic line spectrum and continuum spectrum are considered, and the main calculation particles of radiation include: C, O, C^+, O^+, C^{++}, O^{++}, C^{+++}. NEC is obtained by line-by-line calculation.

3 Results and Discussion

3.1 Plasma Composition

Figure 1 shows the composition of 70% CO_2–30% O_2 arc plasma as a function of temperature under different pressures, and the mixing ratio refers to the initial ratio of gas mass fraction. As shown in the figure, around 2500 K CO_2 decomposes to produce CO and O_2. Therefore, the O_2 will increase slightly at this time. Subsequently, O_2 and CO begin to decompose around 4000 K and 4300 K successively, forming O atoms.

and C atoms. When the temperature is higher than 12,000 K, the molecules in the components have basically disappeared, and the plasma is mainly composed of atoms and ions. Since the content of O element in the 70% CO_2–30% O_2 mixture is greater than that of C element, although the ionization potential of C atoms is lower, the proportion of O^+ is higher than that of C^+ at high temperatures. C^{2+} ions appear earlier and have a higher proportion than O^{2+} ions at high temperatures.

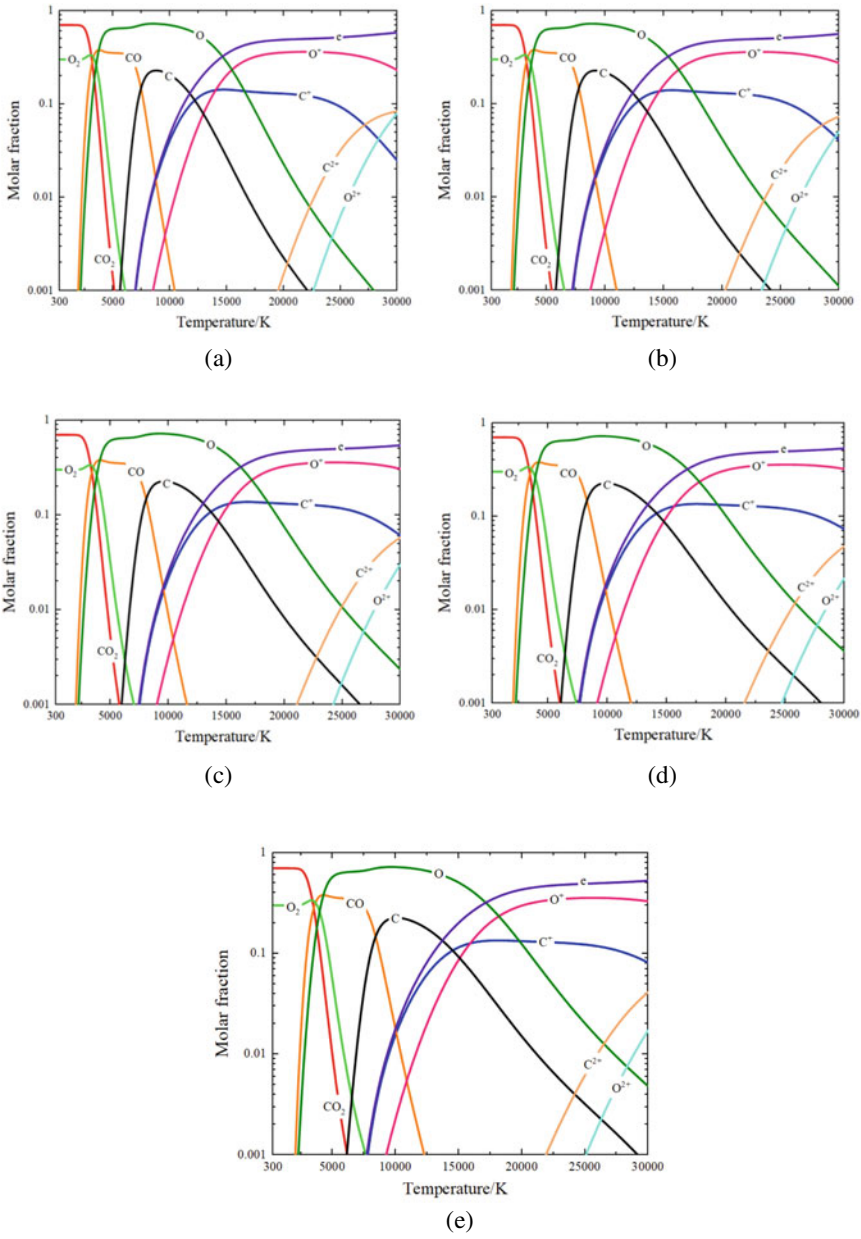

Fig. 1 Composition of 70%CO_2–30%O_2 mixture as a function of temperature. **a** P = 0.1 MPa, **b** P = 0.2 MPa, **c** P = 0.4 MPa, **d** P = 0.6 MPa, **e** P = 0.8 MPa

In this work, we mainly focus on the radiation characteristics of the arc at high temperature, so the plasma composition at high temperature directly affects the calculation results of the NECs. It is evident from Fig. 1 that increasing the pressure leads to an increase in the temperature at which dissociation and ionization occur. Therefore, an increase in pressure also changes the radiation properties, which will be discussed in the next section.

3.2 NEC Results

Figure 2 shows the NEC of 70% CO_2–30% O_2 at different pressures under optically thin conditions. The pressure is higher and the radiation is stronger. The most intuitive explanation is that the increase in pressure leads to an increase in particle number density. The change is more significant at high temperature, at 30,000 K, the NEC of 0.8MPa is an order of magnitude higher than the NEC of 0.1 MPa.

The effect of arc radius on NEC is illustrated in Fig. 3. A radius equal to 0 indicates that the arc is an optically thin plasma, and a radius not equal to 0 indicates that the attenuation of radiation during propagation is considered. The arc shape is considered as a sphere.

The NEC decreases sharply with the increase of the arc radius, which is mainly due to the strong self-absorption of the line spectrum. It can be seen that when R = 1mm, the NEC is only about 10% of that when R = 0mm, which means that most of the emissions from the central area of the arc are absorbed within 1mm. This

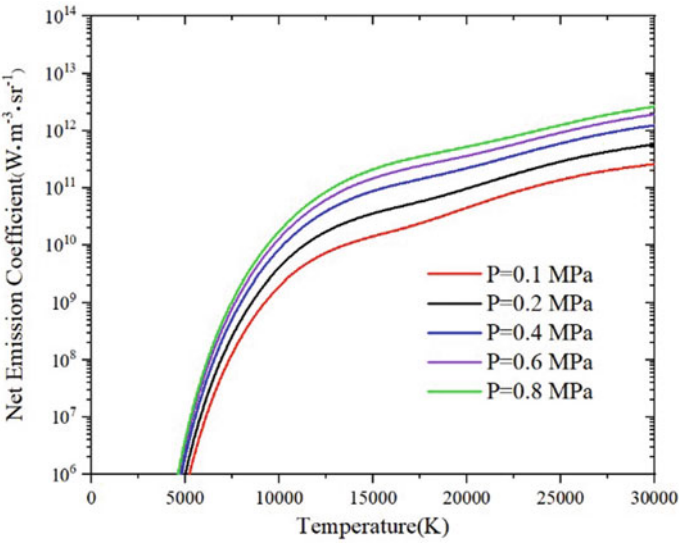

Fig. 2 NEC of 70%CO_2–30%O_2 mixture at different pressures (R = 0 mm)

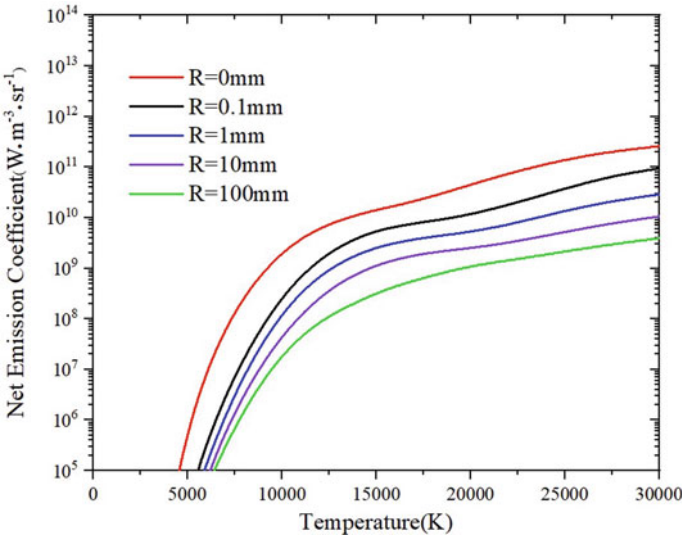

Fig. 3 NEC of 70%CO_2–30%O_2 mixture with different arc radii at 0.1 MPa

is similar to previous research conclusions of other gases. Figure 3 only shows the NEC of 70% CO_2–30%O_2 with different radii at 0.1 MPa. Of course, the degree of self-absorption of NEC coefficients is different at different pressures, but the overall trend is very similar, so results for each pressure are no longer shown.

The purpose of this paper is to evaluate its arc extinguishing ability through the radiation characteristics of 70% CO_2–30%O_2, and analyze the feasibility of using 70% CO_2–30%O_2 as an arc extinguishing medium to replace SF_6. Figure 4 compares the NEC coefficients of 70% CO_2–30%O_2 and pure SF_6, and the NEC of 70% CO_2–30%O_2 mixture holds the lead in the temperature range from 7500 to 30000 K. It can be considered that 70% CO_2–30%O_2 has a stronger radiation emission capability under optically thin conditions. At high temperatures, 70% CO_2–30%O_2 arc energy dissipation will be faster than SF_6, which is beneficial to arc extinguishing.

It is worth noting that radiation is a complex physical process. The NEC method is an excellent method to quickly evaluate the arc radiation in the high temperature area, but it cannot be well evaluated for the arc edge area, so the radiation process in the low temperature area needs more complex methods. In addition, there are many factors affecting the arc extinguishing characteristics, which require a comprehensive and objective evaluation.

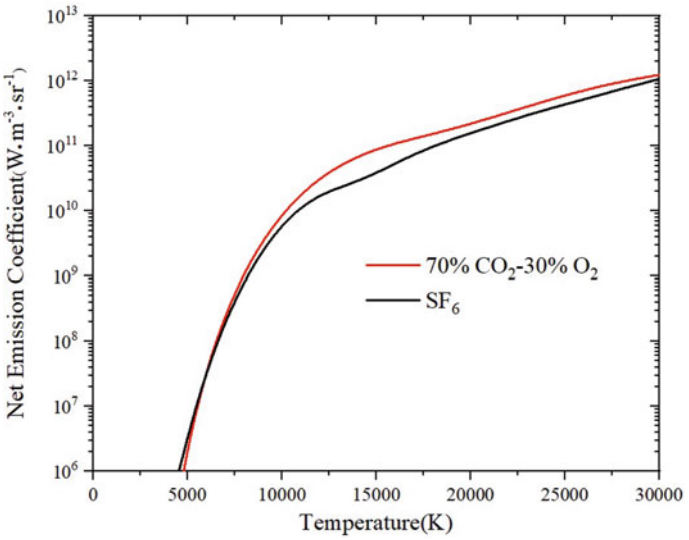

Fig. 4 NEC of 70%CO_2–30%O_2 mixture and SF_6 at 0.4 MPa

4 Conclusion

Based on LTE assumptions, this paper calculates the 0.1–0.8 MPa, 300–30,000 K 70% CO_2–30%O_2 plasma composition and NEC. The increase in pressure increases the number density of the gas, which in turn increases the radiation of the gas. Most of the energy emitted from the high temperature area of the arc center is self-absorbed within 1 mm. Compared with SF_6, 70% CO_2–30%O_2 has stronger radiation emission at 0.4 MPa, which is beneficial for arc quenching. The results of this paper provide a reference for the research on the radiation characteristics and arc extinguishing ability of 70% CO_2–30%O_2 mixture.

References

1. Beroual A, Haddad AM (2017) Recent advances in the quest for a new insulation gas with a low impact on the environment to replace sulfur hexafluoride (SF_6) gas in high-voltage power network applications. Energies 10(8):1216
2. Rokunohe T, Yagihashi Y, Aoyagi K et al (2007) Development of SF_6-free 72.5 kV GIS. IEEE Transact Power Deliv 22(3):1869–1876
3. Stoller PC, Seeger M, Iordanidis AA et al (2013) CO_2 as an arc interruption medium in gas circuit breakers. IEEE Trans Plasma Sci 41(8):2359–2369
4. Uchii T, Majina A, Koshizuka T et al (2010) Thermal interruption capabilities of CO_2 gas and CO_2-based gas mixtures. In: 18th international conference on gas discharges and their applications (GD 2010), pp 78–81

5. Aubrecht V, Lowke JJ (1994) Calculations of radiation transfer in SF_6 plasmas using the method of partial characteristics. J Phys D Appl Phys 27(10):2066–2073
6. Nordborg H, Iordanidis AA (2008) Self-consistent radiation based modelling of electric arcs: I. Efficient radiation approximations. J Phy D Appl Phys 41(13):135205
7. Jamaluddin AS, Smith PJ (1988) Predicting radiative transfer in rectangular enclosures using the discrete ordinates method. Combust Sci Technol 59(4–6):321–340
8. Lowke JJ (1969) A relaxation method of calculating arc temperature profiles applied to discharges in sodium vapor. J Quant Spectrosc Radiat Transfer 9(6):839–854
9. Dixon CM, Yan JD, Fang MTC (2004) A comparison of three radiation models for the calculation of nozzle arcs. J Phys D Appl Phys 37(23):3309–3318
10. Guo XX, Li XW, Murphy AB et al (2017) Calculation of thermodynamic properties and transport coefficients of CO_2-O_2-Cu mixtures. J Phys D Appl Phys 50(34):345203
11. Sevast'yanenko VG (1979) Radiation transfer in a real spectrum. J Eng Phys Thermophys 36(2):138–148

Arc Interruption Performance of SF_6/N_2 Gas and Dielectric Recovery in Disconnector

Weihong Yang, Zhoujing Wang, Dibo Wang, Qiulin Chen, Sicheng Zhao, and Ran Zhuo

Abstract SF_6 as a gas medium for power switchgear, has outstanding performance on arc suppression and insulation. However, because of the strong greenhouse effect, it is limited to use recently. SF_6/N_2 mixture is an effective alternative in high voltage power switchgear, which not only reduce the emission of SF_6 but also lower the gas liquefaction temperature. Based on a 220 kV disconnector, this paper built a magneto-hydro-dynamic (MHD) model to simulate the arc burning process. The electric field distribution and the critical breakdown voltage within 100 us after current zero (CZ) were calculated to evaluate the arc interruption performance of the SF_6/N_2 mixture. The model established in this paper is effective and referable in arc simulation and dielectric recovery assessment. The research results in this thesis are significant to the application of SF6/N2 mixture in disconnectors.

Keywords SF_6/N_2 mixture · Disconnector · Critical breakdown voltage · Dielectric recovery

1 Introduction

SF_6 as a gas medium for power switchgear, has outstanding performance on arc suppression and insulation [1]. But for its strong greenhouse effect, the electrical industry urgently needs to find an environmentally friendly substitute gas. Researchers have conducted extensive and in-depth research in the field of SF_6 alternative gases over the years. At present, the widely studied and applied SF_6 alternative gases can be divided into four categories. The first is natural conventional gases [2], which are cheap and do little harm to the environment. But their arc interruption

W. Yang · D. Wang · Q. Chen · S. Zhao · R. Zhuo
CSG Electric Power Research Institute, Guangzhou, China

Z. Wang (✉)
State Key Laboratory of Electrical Insulation and Power Equipment, Xi'an Jiaotong University, Xi'an, China
e-mail: wangzhoujing@stu.xjtu.edu.cn

© Beijing Paike Culture Commu. Co., Ltd. 2024

X. Dong and L. Cai (eds.), *The Proceedings of 2023 4th International Symposium on Insulation and Discharge Computation for Power Equipment (IDCOMPU2023)*, Lecture Notes in Electrical Engineering 1102, https://doi.org/10.1007/978-981-99-7405-4_17

and insulation performance are insufficient. The other two are new environmentally friendly gases such as fluorocarbons and new fluoride, which are still being explored [3–5]. And the last category is the SF_6 mixture [6]. This category of gas can solve the problem of SF_6 liquefaction that can occur in cold regions and also helps reduce SF_6 use, which has great important engineering significance. One of the most studied gases is the mixture of SF_6 and N_2 [7, 8].

Researchers have done a lot of research on the breakdown characteristics of the SF_6/N_2 mixture. Christophorou et al. [9, 10] studied the breakdown characteristics of SF_6/N_2 mixture under different electrode structures and found an excellent synergistic effect of them. Lu et al. [11] conducted frequency breakdown tests and lighting impulse tests to 30% SF_6/N_2 mixture at a temperature range from −30 to 20 °C based on a 126 kV GIS partial discharge test platform. The results showed that in low temperatures about −30–−10 °C, the frequency breakdown voltage was significantly influenced by the mixing ratio of SF_6; as in the higher temperature of 0–20 °C, the influence became inconspicuous. Dmitry and Laxminarayan [12] built a two-dimensional axisymmetric fluid model and coupled it with the comprehensive mechanism of plasma chemical reactions, to figure out the influence of the SF_6 fraction in the SF_6/N_2 mixture on the breakdown voltage. It was observed that the breakdown voltage increased by 7–43% when adding only 1% SF_6 to N_2 depending on the voltage rise time. All the studies mentioned above were carried out on the single electrode structure or simplified electrode model. Therefore, studying the arc-suppressing performance of SF_6/N_2 mixed gas on specific electric high voltage power switchgear is essential and has great engineering practical research significance.

This thesis aims to evaluate the arc suppressing property of SF_6/N_2 mixture. Firstly, a magneto-hydro-dynamic (MHD) model of a 220 kV disconnector structure was built up to simulate the arc burning process. Secondly, the electric breakdown in the arc extinguishing room after arc was evaluated. The probability of electrical breakdown in each region of the arc extinguishing room was predicted through the temperature, pressure, and the actual electric field distribution of the mixture, meanwhile, the critical breakdown voltage of the SF_6/N_2 mixture was calculated. The results revealed the breakdown probability and arc reigniting after current zero (CZ), and effectively evaluate the arc interruption performance of the SF_6/N_2 mixture. The model established in this paper is effective and referable in arc simulation and dielectric recovery assessment. The research results in this thesis are significant to the application of SF_6/N_2 mixture in disconnectors.

2 Simulation Model and Calculation Method

In this section, a two-dimension MHD model is built based on ANSYS FLUENT, which is software to simulate the interaction of multiple physical fields during arc burning process [13]. Then the method to calculate the critical breakdown field strength of the mixture and the method of evaluating the electric breakdown in the arc extinguishing room after arc is presented.

2.1 MHD Model

In the process of current interrupting simulation, the arc is regarded as a special fluid, and the arc plasma is considered to be electrically neutral, which is in the state of Local Thermodynamic Equilibrium (LTE) and Local Chemical Equilibrium (LCE). The effect of a thin sheath near the electrode is ignored. The dynamic development of arc and surrounding airflow field is described using the Navier–Stokes equations that reflect the conservation of mass, momentum, and energy, electromagnetic field equations, radiation model, and turbulence model [14].

2.2 The Geometric Model of Disconnector

The geometric model is based on a 220 kV disconnector. It is axisymmetric including half of the disconnector structure, so as to simplify the calculation. Figure 1 shows the disconnector model as the moving contact has moved for 9 ms. Along the axis, there is an evaluation line L1, which is used to calculate the critical breakdown voltage.

The boundary and initial conditions of the model are set as follows:

1. The IRMS and frequency of current is 1.6 kA, 50 Hz. The maximum value of the transient recovery voltage (TRV) is 73 kV.
2. The inflation pressure is 0.6 MPa, the upper part of the chamber is set as the pressure outlet, and the ambient temperature is 300 K. And the separation speed of contact is 5 m/s.
3. There are three proportions of mixture filled in the switch: pure SF_6,28%SF_6 + 72%N_2, and 40%SF_6 + 60%N_2.

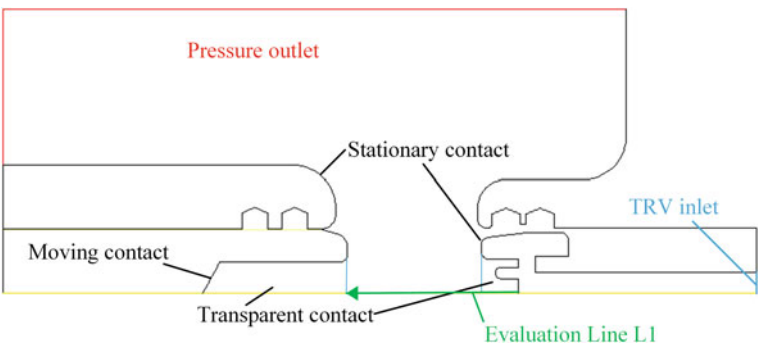

Fig. 1 Geometric model of the disconnector

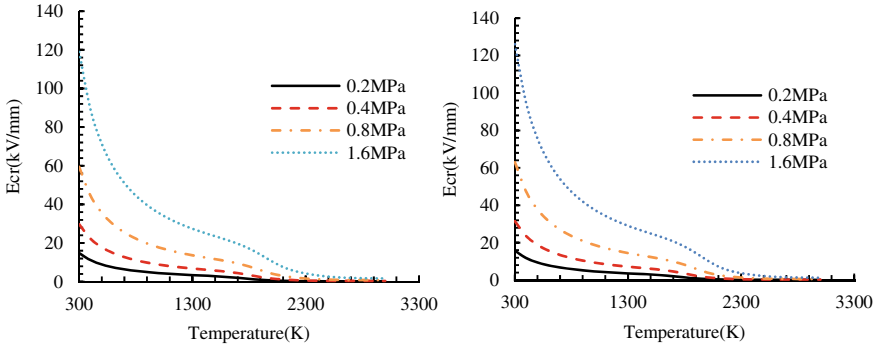

Fig. 2 The E_{cr} of SF_6/N_2 gas at different temperatures and pressure

2.3 Calculation of Critical Breakdown Field Strength

During the arc burning process, the gas will decompose and change its properties because of the high temperature and fluctuating pressure. To assess the dielectric strength recovery after arc, The critical breakdown electric field strength E_{cr} at high temperatures is calculated. For the mixture, the collision cross sections are acquired using the semi-classical Deutsch-Märk (DM) method. Then, the collision cross sections and gas components are used to calculate E_{cr} at different temperatures and pressures by solving the Boltzmann equation [15]. Figure 2 shows the E_{cr} of two proportions of mixture. The E_{cr} is the function of temperature and pressure, inversely correlated with temperature and positively correlated with pressure.

2.4 Evaluation of the Dielectric Strength Performance of Gas Mixture

To estimate the electrical breakdown of the gas mixture in the arc extinguishing room, the real electrical field distribution and the airflow field are considered. Figure 3 shows that the electrical field E_a is determined by the transient recovery voltage (TRV) after arc. The distribution of temperature and pressure field in the chamber influences the critical breakdown field E_{cr}. It is supposed that the gas gap is likely to break down when the critical breakdown field is smaller than the background field. Therefore, the ratio of E_a to E_{cr} represents the probability of electric breakdown in this area.

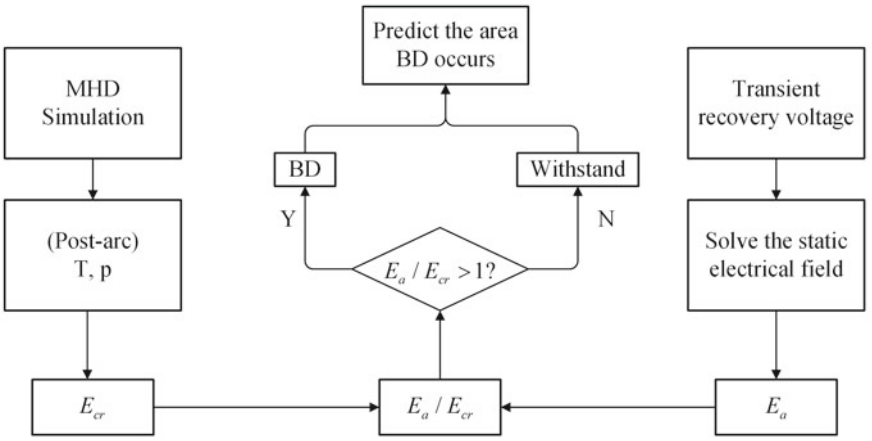

Fig. 3 The evaluation method of electrical breakdown

3 Simulation Results and Analysis

In this section, the post-arc electrical breakdown simulation of the disconnector is carried out after the CZ. After that, the distribution of the physical field and the critical breakdown voltage for three proportions of SF_6/N_2 mixture are analyzed.

3.1 The Distribution of the Physical Field

Figure 4 shows the temperature contour and E_a/E_{cr} contour of the disconnector in three proportions of SF_6/N_2 mixture at 100 us after arc. It can be found that the temperature of gas is low at this time, as the highest temperature of the three gases is within 3000 K. Therefore, it is helpful for the recovery of dielectric insulation strength. When analyzing the distribution of the E_a/E_{cr}, it is similar in all three cases. The maximum value of E_a/E_{cr} appears at the edge of the contact, because of the large electric field caused by the unsmooth structure. For 28% SF_6/N_2, the maximum value of it is 0.7, which is less than 1, so the arc is less likely to be re-struck. Although the highest temperature appears at the bottom of the static contact which can lead to the lowest E_{cr}, as E_a is much lower, the E_a/E_{cr} value is small. At last, it can be concluded that in the same position, the higher the SF_6 concentration is, the smaller the E_a/E_{cr} value is.

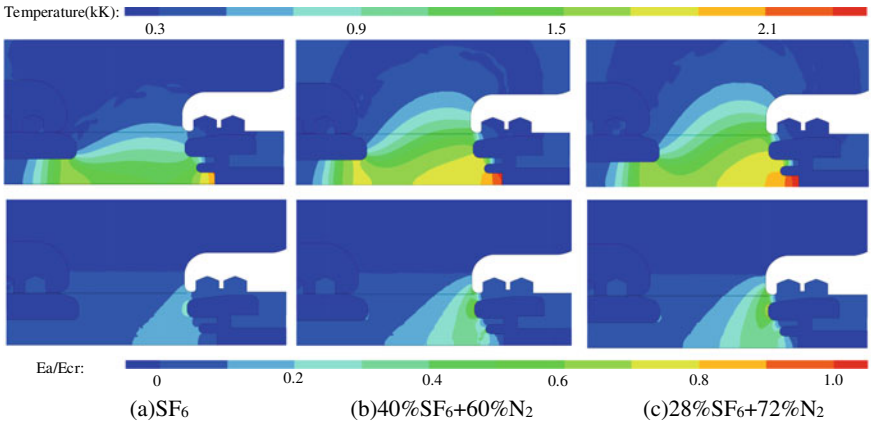

Fig. 4 Temperature and E_a/E_{cr} distribution at 100 μs after CZ

3.2 The Calculation of Critical Breakdown Voltage

The critical breakdown voltage along the selected path (shown in Fig. 1) is calculated and shown in Fig. 5. With the decrease of the temperature and the fluctuation of the pressure in the arc extinguishing room, the critical BD voltages all fluctuate in a small amplitude, and show an upward trend overall time. The initial critical BD voltages of 28% SF_6/N_2 and 40% SF_6/N_2 mixture are 275.5 and 300 kV, about 56.0 and 61.0% compared to SF_6, but still higher than the TRV, the maximum value of which is set as 73 kV. Meanwhile, the presence of N_2 in the mixed gas also increases the fluctuation of the critical BD voltages and affects the recovery of dielectric strength. It is indicated that in the first 30 μs, the critical breakdown voltage of the two SF_6/N_2 mixtures fluctuated sharply, and the value was very close. After 30 μs, the critical breakdown voltage began to stabilize and because of the effect of SF_6, the critical breakdown voltage of 40% SF_6/N_2 was slightly higher than 28% SF_6/N_2.

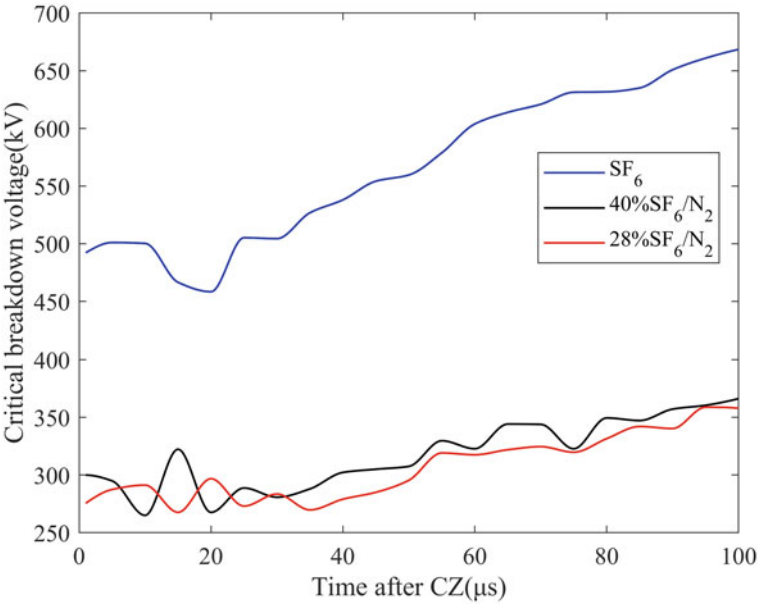

Fig. 5 The critical breakdown voltage along the selected path

4 Conclusion

To evaluate the arc suppressing property of SF_6/N_2 mixture, the MHD model was built based on the 220 kV disconnector. The arcing process of SF_6 gas and SF_6/N_2 mixture is simulated and the critical breakdown field strength is calculated as the precondition to evaluate the dielectric recovery performance of SF_6 and SF_6/N_2 mixture. The following conclusions were drawn:

1. The critical breakdown field strength of SF_6/N_2 mixture is calculated, which decreases when temperature increases and pressure decreases. At the same time, the rise of SF_6 ratio in the mixture increases the critical breakdown field strength.
2. The critical breakdown voltage of $28\%SF_6/N_2$ and $40\%SF_6/N_2$ mixture under 0.6 MPa after current zero is predicted and compared to pure SF_6. The calculated critical breakdown voltage is lower than SF_6, but it is much higher than the maximum of TRV, without the risk of breakdown.

Therefore, SF_6/N_2 mixture has perfect arc suppressing performance and can be used as the substitution for SF_6 in the power switchgear. The simulation results in this thesis are helpful to the application of SF_6/N_2 mixture in disconnectors and have high engineering significance.

Acknowledgements This work was supported by the Science and Technology Program of Guizhou Power Grid Co. Ltd. (GZKJXM20220057).

References

1. Guo Z, Li X, Su H et al (2017) Interrupting characteristics of paralleled SF_6 circuit breakers with a highly coupled split reactor. In IEEE Transactions on components, packaging and manufacturing technology 7(5):768–776
2. Seeger M, Avaheden J, Pancheshnyi S et al (2017) Streamer parameters and breakdown in CO_2. J Phys D: Appl Phys 50(1):5207
3. Zhang B, Zhou R, Wang K et al (2023) Arc interruption performance of C_4F_7N-CO_2 mixture in a 126 kV disconnector. IEEE Transact Pow Deliv 38(2):1197–1207
4. Lin X, Zhang J, Xu J et al (2022) Dynamic dielectric strength of C_3F_7CN/CO_2 and C_3F_7CN/N_2 mixtures in high voltage circuit breakers. IEEE Transact Power Deliv 37(5):4032–4041
5. Alonso ML, Alonso RM, Lombraña JI et al (2021) Exploring the Decomposition Products of 1,3,3,3-Tetrafluoropropene and Perfluoro-(3-methylbutan-2-one) mixtures in medium-voltage electrical switchgear as alternatives to SF_6. ACS Omega 6(33):21534–21542
6. Ou X, Wang L, Liu J et al (2020) Numerical simulation of streamer discharge development processes with multi-component SF6 mixed gas. Phys Plasmas 27:073504
7. Geng J, Yang J, Shu T et al (2023) Stability of breakdown phenomenon in N_2, SF_6, and their mixture under impulse voltages. AIP Adv 13:035033
8. Wang L, Ou X, Zheng Y et al (2019) Numerical simulations of the SF_6-N_2 mixed gas streamer discharge development process. AIP Adv 9:055320
9. Christophorou LG, Olthoff JK, VanBrunt RJ (1997) Sulfur hexafluoride and the electric power industry. IEEE Electric Insulat Magaz 13(5):20–24
10. Christophorou LG, Olthoff JK, Green DS (1997) Gases for electrical insulation and arc interruption: possible present and future alternatives to pure SF6. NIST Techn Note 1425:1–44
11. Lu G, Su Z, Xu O et al (2016) Experimental study on performance of SF_6+N_2 mixed gas insulation. In: 2016 international conference on mechatronics, manufacturing and materials engineering (MMME 2016),63,03017
12. Dmitry L, Laxminarayan LR (2023) Computational analysis of electrical breakdown of SF_6/N_2 mixtures. J Appl Phy133:053301
13. Guo Z, Liu S, Pu Y et al (2019) Study of the arc interruption performance of CO_2 gas in high-voltage circuit breaker. IEEE Transact Plasma Sci 47(5):2742–2751
14. Jiang X, Li X, Zhao H et al (2013) Analysis of the dielectric breakdown characteristics for a 252-kV gas circuit breaker. IEEE Transact Pow Deliv 28(3):1592–1599
15. Zhao H, Li X, Jia S et al (2013) Dielectric breakdown properties of SF_6–N_2 mixtures at 0.01–1.6 MPa and 300–3000 K. J Appl Phys 113:143301

Analysis of Fluid Velocity and Temperature Variation Characteristics in Boundary Layer of Transformer Wall

Shaonan Chen, Qianyi Chen, Kewen Li, Qingfa Chen, and Shifeng Ou

Abstract It is one of the important research contents to understand the fluid velocity and temperature variation characteristics of the boundary layer on the transformer wall in order to analyze the heat dissipation characteristics of the transformer. In this paper, a simplified analysis model of the boundary layer on the transformer wall is established, and the effects of flow velocity, temperature, ambient temperature and ambient convection heat transfer coefficient on the distribution of the fluid temperature boundary layer and velocity boundary layer on the transformer wall are simulated and analyzed. The simulation results show that the main influencing factors of the velocity boundary layer are the inflow temperature and velocity, and the temperature boundary layer is affected by the inflow temperature and velocity as well as the external environment. Given the external ambient temperature and convective heat transfer conditions, as well as the transformer load rate, the temperature and flow velocity of the near wall streamline point can be derived from the transformer shell temperature by combining the results of multiple physical field calculations.

Keywords Oil immersed transformer · Temperature fluid field · Boundary layer · Streamline temperature

1 Introduction

Transformer is one of the important equipment that constitutes the transmission and distribution network of the power system [1]. Transformers play an important role in voltage transformation, energy distribution, and transfer in the system, and their

S. Chen · Q. Chen (✉) · K. Li · Q. Chen · S. Ou
Electric Power Research Institute of Guangxi Power Grid CO., LTD, Nanning 530023, Guangxi, China
e-mail: 345310737@qq.com

S. Chen · K. Li · S. Ou
Guangxi Key Laboratory of Intelligent Control and Maintenance of Power Equipment, Electric Power Research Institute of Guangxi Power Grid CO., LTD, Nanning 530023, Guangxi, China

© Beijing Paike Culture Commu. Co., Ltd. 2024

X. Dong and L. Cai (eds.), *The Proceedings of 2023 4th International Symposium on Insulation and Discharge Computation for Power Equipment (IDCOMPU2023)*, Lecture Notes in Electrical Engineering 1102, https://doi.org/10.1007/978-981-99-7405-4_18

safe and stable operation is of great significance for ensuring the reliability of power supply [2]. In order to accurately obtain the internal temperature field distribution of transformers and provide guidance for the structural optimization of transformers, many scholars and production units have gradually applied numerical calculation methods to the calculation of transformer temperature fluid fields [3–5]. It is one of the important research contents to understand the fluid velocity and temperature variation characteristics of the boundary layer on the transformer wall in order to analyze the heat dissipation characteristics of the transformer. In this paper, a simplified analysis model of the boundary layer on the transformer wall is established, and the effects of flow velocity, temperature, ambient temperature and ambient convection heat transfer coefficient on the distribution of the fluid temperature boundary layer and velocity boundary layer on the transformer wall are simulated and analyzed. The research results of this article can provide a certain reference for the multi physical field inversion detection of transformer winding hot spot temperature.

2 Simplified Analysis Model of Boundary Layer on Transformer Wall

2.1 Simplified Analysis Model

The established boundary layer analysis model for the velocity and temperature of the transformer wall is shown in Fig. 1. The wall flow solid interface is a smooth flat plate, and the fluid inlet velocity is evenly distributed in the vertical inlet direction.

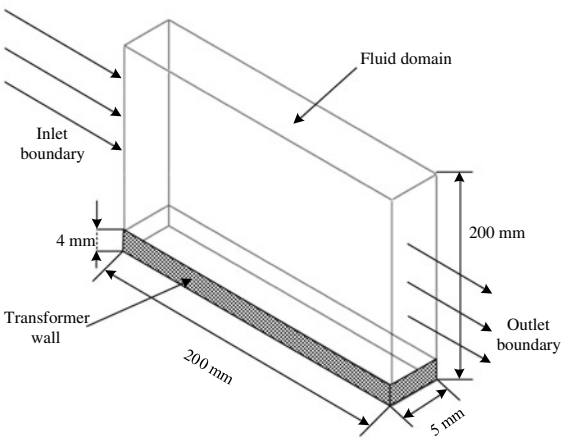

Fig. 1 Analytical model of transformer wall boundary layer of velocity and temperature

2.2 Temperature Fluid Field Control Equation

The mathematical model for the flow and heat transfer of heat dissipating media in a fluid field is established on the basis of the law of conservation of mass, Newton's second law (law of conservation of momentum), and the first law of thermodynamics (law of conservation of energy). The equation expressions for these three laws are as follows [6–8]:

$$\nabla \cdot \boldsymbol{v} = 0 \tag{1}$$

$$\frac{\partial(\rho v)}{\partial t} + \rho \boldsymbol{v} \cdot \nabla \boldsymbol{v} = \rho f - \nabla \boldsymbol{p} + \mu \nabla^2 \boldsymbol{v} \tag{2}$$

$$\frac{\partial(\rho e)}{\partial t} + \nabla \cdot (\rho e \boldsymbol{v}) = \rho \boldsymbol{q} + \nabla(k \nabla T) - \boldsymbol{p} \nabla v + S \tag{3}$$

where, ρ is the fluid density; v is the fluid velocity; f stands for the fluid volume force; p represents the pressure; μ is the dynamic viscosity; k is the thermal conductivity; q indicates the heat source per volume inside the transformer; e is the internal energy of the fluid; T represents the temperature; S represents the part of fluid mechanical energy converted into heat energy under the action of fluid viscous and internal heat source of fluid.

2.3 Boundary Conditions

Inlet boundary conditions: At the inlet of the fluid field, given boundary conditions such as inlet velocity, pressure, and temperature, which are usually set as constants, can be expressed as [9, 10]:

$$\boldsymbol{v}|_{in} = C \quad \text{or} \quad \boldsymbol{P}|_{in} = C \quad \text{or} \quad T|_{in} = C \tag{4}$$

where, C is a known constant.

In this article, the set inlet boundary condition is that the inlet flow velocity and temperature are constants.

Outlet boundary conditions: At the outlet of the fluid field, given boundary conditions such as outlet velocity, pressure, and outlet conditions, usually constant or vector gradient of velocity and temperature is zero, which can be expressed as:

$$\boldsymbol{v}|_{out} = C \quad \text{or} \quad \boldsymbol{P}|_{out} = C \quad \text{or} \quad T|_{out} = C \tag{5}$$

$$\left.\frac{\partial \boldsymbol{v}}{\partial n}\right|_{out} = 0, \qquad \left.\frac{\partial T}{\partial n}\right|_{out} = 0 \tag{6}$$

In this article, the set outlet boundary condition is that the outlet pressure is constant, which is equal to atmospheric pressure.

The boundary condition of the wall flow solid interface: no slip wall, i.e. the fluid velocity at the interface is 0;

Boundary conditions of the external interface of the wall: specify the ambient temperature and external heat transfer convective coefficient;

Boundary conditions outside the fluid domain: free slip wall boundary conditions, with no heat exchange with the outside world.

2.4 Material Parameters

Transformer oil is the main cooling medium inside the transformer. Its thermodynamic parameters include density, specific heat capacity, thermal conductivity, viscosity, etc.

The density and specific heat capacity determine the ability to store heat, and the thermal conductivity represents the ability of transformer oil to transfer heat. The viscosity is generated by the internal friction of transformer oil, so when the fluid flows, the viscosity will produce a certain mechanical energy loss, which will interfere with the shape and flow rate of the fluid, so the viscosity has a great impact on the cooling effect of transformer oil. These thermodynamic parameters are greatly affected by temperature, so in order to more accurately describe the parameters of transformer oil, this paper selects the fitting formula that introduces temperature T as a variable.

The thermodynamic parameters of transformer oil are shown in Table 1. T in the table is the temperature of transformer oil, in °C.

The relationship between viscosity of transformer oil and temperature is as follows [11]:

$$\mu(T) = \exp(B)T^{-A} \tag{7}$$

In the equation, A = 9.55 ± 0.23, B = 50.24 ± 1.33, μ Is the dynamic viscosity of transformer kg/ms, T is the temperature of transformer oil, and the unit is K.

The wall material of transformer oil tank is cold-rolled steel plate, and relevant material parameters are shown in Table 2:

Table 1 Thermodynamic parameters of transformer oil

Parameters	Value
Density ($kg \bullet m^{-3}$)	880
Specific heat capacity ($J \bullet kg^{-1} \bullet K^{-1}$)	$1433 + 5.233\ T$
Thermal conductivity ($W \bullet m^{-1} \bullet K^{-1}$)	0.105

Table 2 Thermodynamic parameters of transformer wall

Thermal conductivity/ ($W \bullet m^{-1} \bullet K^{-1}$)	Density/($kg \bullet m^{-3}$)	Thermal conductivity/($J \bullet kg^{-1} \bullet K^{-1}$)
60.5	7854	485

3 Distribution of Temperature and Fluid Field in Boundary Layer of Transformer Wall

3.1 Classification of Fluid Boundary Layer

The fluid boundary layer can be further divided into velocity boundary layer and temperature boundary layer. The flow boundary layer is defined as the thin layer of fluid whose velocity changes significantly in the direction perpendicular to the wall. When a fluid flows through a solid wall, due to the non-slip characteristics of fluid molecules in the wall layer, the flow velocity of the near wall fluid will gradually change from zero velocity at the wall to flow velocity in the direction perpendicular to the wall under the action of fluid viscous force. The fluid outside of $u = 0.99u_{\infty}$ can be considered unaffected by fluid viscosity and is called the mainstream region. The region within $u = 0.99u_{\infty}$ has obvious velocity gradient, which is called the boundary layer region.

When the fluid flows through the flat plate and the temperature t_w of the flat plate is not equal to the temperature t_{∞} of the inlet fluid, a thin layer with significantly changed temperature can also be formed above the wall, which is often called the thermal boundary layer. When the temperature difference between the wall and the fluid reaches 0.99 times of the temperature difference between the wall and the inlet fluid, that is $(t_w - t)/(t_w - t_{\infty}) = 0.99$, this position is the outer edge of the boundary layer, and the distance from this point to the wall is the thickness of the thermal boundary layer, recorded as $\delta_t(x)$.

3.2 Impact of Inlet Flow Velocity

The ambient temperature is 20 °C, the heat transfer convective coefficient is 20 W/(m^2K), the fluid inlet temperature is 50 °C, and the wall boundary layer thickness and wall temperature difference at different inlet speeds (0.01m/s, 0.02 m/s, 0.04 m/s, 0.1 m/s, 0.2 m/s, 0.5 m/s, 1 m/s) are shown in Fig. 2.

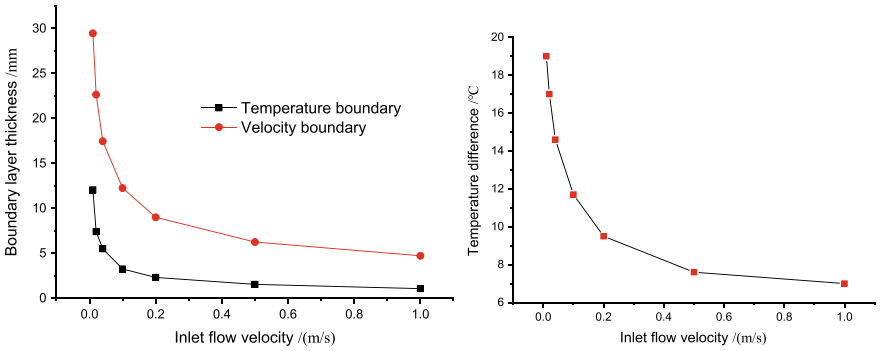

Fig. 2 Impact of inlet flow velocity

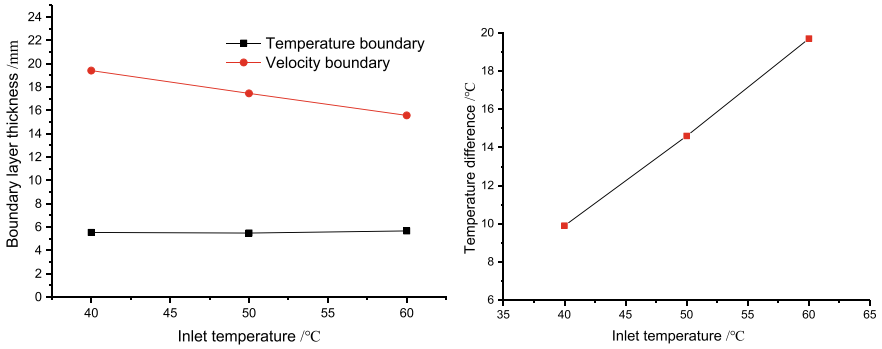

Fig. 3 Impact of inlet flow temperature

3.3 Impact of Inlet Flow Temperature

The ambient temperature is 20 °C, the heat transfer convective coefficient is 20 W/(m^2K), and the inflow velocity is 0.04 m/s. The wall boundary layer thickness and wall temperature difference under different inflow temperatures (40, 50, 60 °C) are shown in the Fig. 3.

3.4 Impact of External Ambient Temperature

The convection heat transfer coefficient of the external environment is 20 W/(m^2K), the inlet temperature is 50 °C, and the inlet speed is 0.04 m/s. The wall boundary layer thickness and wall temperature difference under different ambient temperatures (10, 15, 20, 25, 40 °C) are shown in Fig. 4.

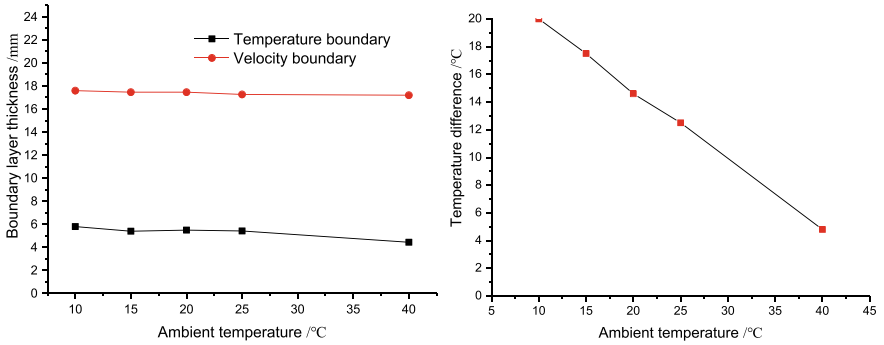

Fig. 4 Impact of external ambient temperature

3.5 Impact of External Heat Transfer Convective Coefficient

The ambient temperature is 20 °C, the inlet velocity is 0.04 m/s, the inlet temperature is 50 °C, and the wall boundary layer thickness and wall temperature difference under different heat transfer convective coefficients (10W/(m^{2}K), 20W/(m^{2}K), 40W/(m^{2}K)) are shown in Fig. 5.

The temperature and velocity distribution of the model boundary layer under the conditions of 50 °C fluid temperature, 0.04 m/s fluid velocity, 25 °C ambient temperature, and 20 W/(m^{2}K) ambient heat transfer convective coefficient are shown in Figs. 6 and 7.

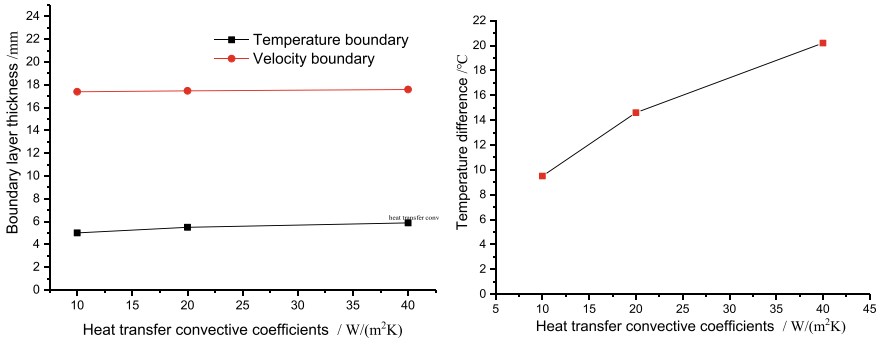

Fig. 5 Impact of external heat transfer convective coefficient

Fig. 6 Cloud chart of wall temperature distribution

Fig. 7 Cloud chart of wall velocity distribution

4 Conclusion

The main conclusions can be drawn as follows:

(1) The thickness of the wall velocity boundary layer is related to the fluid inlet velocity and temperature. The higher the velocity, the thinner the velocity boundary layer, the higher the inlet temperature, and the thinner the velocity boundary layer; The thickness of velocity boundary layer is less affected by ambient temperature and external convection heat transfer coefficient;

(2) The thickness of the wall temperature boundary layer is greatly affected by the inlet flow velocity, and the greater the velocity, the thinner the temperature boundary layer; The thickness of temperature boundary layer is less affected

by the inflow temperature, ambient temperature and external convection heat transfer coefficient;

(3) The higher the inflow velocity, the smaller the temperature difference on the boundary layer wall, the higher the inflow temperature, the larger the temperature difference on the boundary layer wall, the higher the external ambient temperature, the smaller the temperature difference on the boundary layer wall, the higher the external convection heat transfer coefficient, and the larger the temperature difference on the boundary layer wall;

(4) Based on the above analysis, the velocity boundary layer is mainly affected by the inlet temperature and velocity, and the temperature boundary layer is affected by the inlet temperature and velocity as well as the external environment;

(5) Given the external ambient temperature and convective heat transfer conditions, as well as the transformer load rate, the temperature and flow velocity of the near wall streamline point can be derived from the transformer shell temperature by combining the results of multiple physical field calculations.

Acknowledgements This paper is supported by Science and Technology Project of Guangxi Power Grid CO under project number **GXKJXM20220126**.

References

1. Rommel DP, Di Maio D, Tinga T (2021) Transformer hot spot temperature prediction based on basic operator information. Int J Electr Power Energy Syst 124:1–15
2. Thummala P, Schneider H, Zhang Z et al (2016) Investigation of transformer winding architectures for high-voltage (2.5 kV) capacitor charging and discharging applications. IEEE Trans Pow Electron 31(8):5786–5796
3. Torriano F, Campelo H, Quintel AM et al (2018) Numerical and experimental thermofluid investigation of different disc-type power transformer winding arrangements. Int J Heat Fluid FL 69:62–72
4. Mohamed MMS, Diaa-Eldin AM, Muhammad D et al (2020) Thermal performance of transformers filled with environmentally friendly oils under various loading conditions. Int J Electr Power Energy Syst 118:1–10
5. Zhang X, Wang ZD, Liu Q (2017) Prediction of pressure drop and flow distribution in disc-type transformer windings in an OD cooling model. IEEE Trans Power Deliv 32(4):1655–1664
6. Zhang X, Wang ZD, Liu Q et al (2018) Numerical investigation of oil flow and temperature distributions for ON transformer windings. Appl Therm Eng 130:1–9
7. Córdoba PA, Silin N, Dari E (2015) Natural convection in a cubical cavity filled with a fluid showing temperature-dependent viscosity. Int J Therm Sci 98:255–265
8. Córdoba PA, Dari E, Silin N (2019) A 3D numerical model of an ONAN distribution transformer. Appl Therm Eng 148:897–906
9. Habbachi F, Oueslati FS, Bennacer R et al (2013) Simulation of heat transfer and fluid flow in 3D porous media in non-equilibrium. In: 2015 World Symposium on Mechatronics Engineering & Applied Physics (WSMEAP), Sousse, pp 1–12
10. Çengel YA (2008) Introduction to thermodynamics and heat transfer. McGraw-Hill, USA
11. Ruan JJ, Deng YQ, Huang DC et al (2020) HST calculation of a 10 kV oil-immersed transformer with 3D coupled-field method. IET Electr Power App 14(5):921–928

Study on Magnetic Leakage Device Parameters Suitable for Crimping Defects of Carbon Fiber Composite Core Conductor

Yongli Liao, Bo Feng, Bo Gong, Ruihai Li, Wei Zhang, and Xiaofei Xia

Abstract Carbon fiber composite core conductor has the advantages of high conductivity, low line loss and obvious energy saving effect. It is one of the ideal schemes for capacity improvement of transmission corridors. However, at present, there is a lack of effective methods for the quality inspection of carbon fiber composite core. To solve the above problems, based on the theory of magnetic leakage detection, this paper uses magnetic film coated carbon fiber core to build a three-dimensional simulation model of crimping fittings, and analyzes the effects of exciter size, magnetic pole spacing of magnetic leakage device and radial air gap on magnetic leakage signals. The optimal parameters obtained are: Permanent magnet size L1 is 15 mm, pole distance L2 is 50 mm and gap distance M is 2 mm. Finally, the influence of fracture width of magnetic composite core conductor on magnetic leakage signal is analyzed through the above parameters of magnetic leakage device. The results show that, in the axial component of the MFL signal, the magnetic induction intensity increases first and then decreases, and the MFL signal reaches its maximum when d = 4 mm. The radial component increases with the increase of fracture width.

Y. Liao (✉) · B. Gong · R. Li
Electric Power Research Institute, China Southern Power Grid Co., Ltd, Guangzhou, Guangdong, China
e-mail: liaoyl02@163.com

B. Gong
e-mail: gongbo@csg.cn

R. Li
e-mail: lirh@csg.cn

B. Feng · W. Zhang · X. Xia
Electric Power Research Institute, Guagnxi Power Grid Co., Ltd, Nanning, Guangxi, China
e-mail: fengb.sy@gx.csg.cn

W. Zhang
e-mail: zhangw.sy@gx.csg.cn

X. Xia
e-mail: xiaxf.sy@gx.csg.cn

© Beijing Paike Culture Commu. Co., Ltd. 2024

X. Dong and L. Cai (eds.), *The Proceedings of 2023 4th International Symposium on Insulation and Discharge Computation for Power Equipment (IDCOMPU2023)*, Lecture Notes in Electrical Engineering 1102, https://doi.org/10.1007/978-981-99-7405-4_19

Keywords Magnetic flux leakage detection · Composite core conductor · Exciter parameters · Finite element

1 Introduction

With the continuous increase of power demand and power grid scale, carbon fiber composite core conductor has gradually replaced steel core Al stranded wire in overhead transmission lines due to its advantages of large transmission capacity, high conductivity, high temperature resistance and high strength in some areas with large power demand and lack of power transmission corridors [1–3]. At the same time, it is necessary to crimp carbon fiber composite core conductor, and tensioning clip during overhead transmission line erection. Due to the unstable construction environment of high-altitude operation and human factors, the crimping of tools is easy to cause damage to composite core conductor [4, 5]. Therefore, in order to avoid wire breaking accidents caused by wire crimping quality and ensure the safe operation of transmission lines, an accurate and rapid nondestructive detection method is urgently needed.

In order to intuitively and clearly understand the crimping quality of power lines, most scholars adopt X-ray detection method. Zhang et al. [6], from Hebei Institute of Electrical Science and Technology, analyzed the crimping quality of the tensioning clamp and connecting pipe by using X-ray method and combining with the structural characteristics of the tensioning clamp. However, it only studied the tensioning clamp and connecting pipe, but did not go further. On this basis, Wang et al. [7] from Shandong University, used X-ray machine to detect the wire and obtained the core diagram inside the aluminum layer. However, because the effect of aluminum layer and steel core in the pictures is not obvious, it is impossible to judge the defects. Xu et al. [8] added special developer to epoxy resin to enhance the contrast effect between aluminum layer and steel core. However, due to the influence on the mechanical properties of transmission wires, it is not suitable for practical engineering applications. Based on the above research, there is no effective method for nondestructive testing of compacting quality of carbon fiber composite core. Steel core aluminum stranded wire and carbon fiber composite core conductor are very similar in structure, and magnetic leakage detection technology is most commonly used for steel core [9]. The development of magnetic flux leakage detection technology has been very mature at home and abroad. It not only has low detection environment requirements, good detection effect, but also has high reliability. At present, many scholars have made remarkable achievements in theoretical model research of magnetic leakage [10, 11], excitation structure research [12, 13] and magnetic leakage signal analysis [14]. However, as the carbon fiber core itself does not possess magnetism, targeted improvements are needed.

In this paper, based on the magnetic flux leakage detection method, the magnetic film coated carbon fiber composite core rod was used to establish a 3D simulation model of the metal crimping of the magnetic film coated core rod. The magnetic

flux leakage signal under different permanent magnet sizes under normal and broken conditions was compared. Under the optimal permanent magnet size, the effects of magnetic pole spacing, radial air gap and defect size on the magnetic leakage signal of defects were compared. The research results of this paper can provide an optimal exciter size for the magnetic leakage detection of carbon fiber composite core crimping defects. By using this exciter to detect the fracture core rod, the fracture degree can be judged according to its magnetic leakage signal rule.

2 Finite Element Theory of Magnetic Flux Leakage Detection

The principle of magnetic leakage detection is that the object is locally magnetized to saturation state by adding an external magnetic field source, and then the magnetic sensitive element obtains the magnetic leakage field signal to judge whether there is damage. Since the carbon fiber wire core itself is not magnetic, a magnetic coating method is proposed in this paper. The flexible film material with high permeability is coated on the surface of the composite carbon core. Due to its good followability, when defects occur in the carbon core, the state of the magnetic film at the corresponding position will also change and be captured by the magnetic leakage detection device. The principle is shown in Fig. 1. When the magnetic carbon fiber composite core has no defects, most of the magnetic force lines will pass through the magnetic film. When the magnetic carbon fiber composite core breaks, the magnetic force line will be distorted at the fracture because the reluctance of the air is greater than that of the magnetic carbon fiber composite core, and the magnetic sensitive element will pick up the magnetic leakage signal in the air here to realize the detection and positioning of the crimping defect of the carbon fiber composite core.

In practical engineering application, the portability and reliability of the magnetic flux leakage detection device are the key factors for its application in different complex environments. Due to its advantages of high coercivity and no power supply,

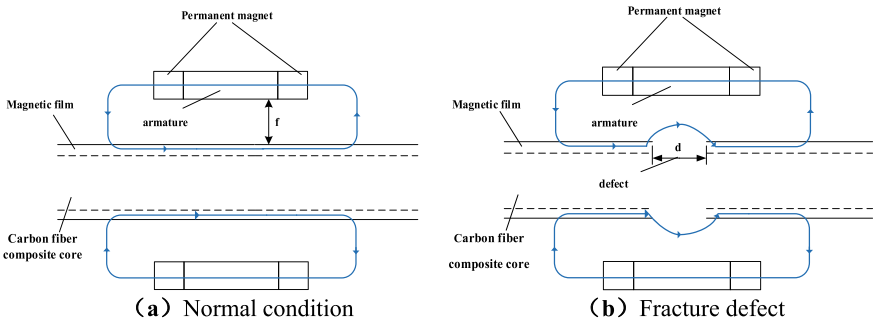

Fig. 1 Schematic diagram of magnetic leakage principle

permanent magnet is used as the magnetic field source of this magnetic leakage detection model. The model selected is NdFe35. The closed magnetic circuit is composed of armature, permanent magnet, air, steel anchor, aluminum liner and magnetic carbon fiber composite core. The problem of magnetic field solving boils down to the solution of magnetic vector potential A. Magnetic vector potential A is defined as follows:

$$\boldsymbol{B} = \nabla \times \boldsymbol{A} \tag{1}$$

According to Stokes formula:

$$\int_S \boldsymbol{B} \cdot d\boldsymbol{S} = \int_S (\nabla \times \boldsymbol{A}) \cdot d\boldsymbol{S} = \Phi \tag{2}$$

Type: $\boldsymbol{B}$ for the magnetic induction intensity, $\boldsymbol{S}$ per unit area, Φ for flux.

3 Simulation Model

According to the actual size parameters of crimping fittings, the simulation model was established, and the structure of the three-dimensional simulation model for magnetic leakage detection was shown in Fig. 2. The steel anchor is a regular hexagon after crimping, and its outer circle radius is 11 mm, thickness is 1.475 mm and length is 180 mm. Aluminum liner outer radius 6.3mm, wall thickness 4.1 mm; The thickness of magnetic film is 0.1 mm; The radius of the carbon fiber core rod is 4.15 mm. Considering that better magnetic leakage signal can be obtained, the probe shoe slot is dug at the center of the armature of the exciting device. At the same time, in order to avoid the magnetic leakage detection device in the process of movement, the magnetic sensor and the crimping device collision damage. The magnetic sensor will be placed inside the boot slot, 7.5 mm away from the upper surface of the magnetic film. Parameters of the finite element model are shown in Table 1.

In order to ensure that the magnetic carbon fiber composite core can be uniformly magnetized in the magnetic leakage detection area, the excitation device adopts a

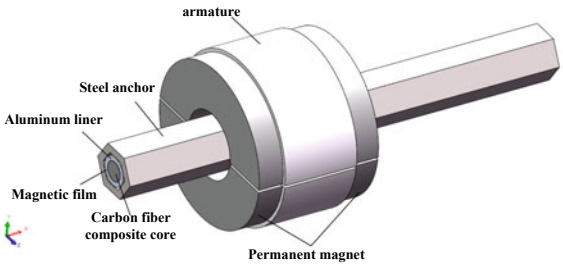

Fig. 2 Simulation model structure diagram

Table 1 Simulation model parameter table

Parameter name	Parameter type
Steel anchor	Stainless steel
Aluminum liner	Aluminum
Magnetic film	Iron-nickel alloy
Carbon fiber composite core	Carbon fiber
Permanent magnet	NdFe35
Armature	Iron

double-circuit structure. The excitation device is composed of permanent magnet and armature, among which four permanent magnets have the same parameters, with an external radius of 29 mm and a thickness of 15 mm. The outer radius of armature is 30.5 mm and the thickness is 18 mm. The outer radius of the armature inner probe shoe slot is 16.5 mm, the depth is 4 mm and the length is 8 mm. The side view of the crimped hardware model is shown in Fig. 3.

This simulation model uses permanent magnet as excitation, so it is necessary to set the magnetizing direction of permanent magnet. In this simulation model, the magnetization direction of permanent magnet is the negative direction of X axis, and the magnetization direction of magnetic carbon fiber composite core is along the positive direction of X axis. The simulated boundary condition is magnetic insulation. Set this parameter to an air zone with a radius of 50 mm and a length of 200 mm.

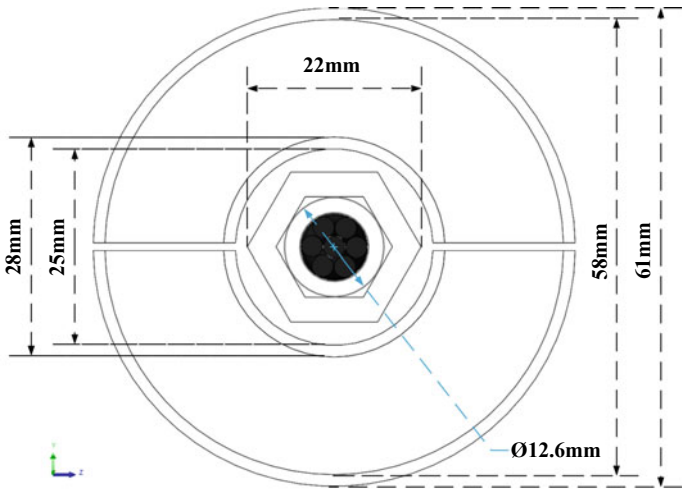

Fig. 3 Side view of crimped hardware

4 Simulation Analysis

4.1 Permanent Magnet Size Selection

Considering the small size of the actual crimping model, the size of the permanent magnet in the magnetic leakage detection device should not be too large. Otherwise, the magnetic flux leakage detection device cannot detect the head and end of the crimped fittings. In this paper, three different sizes of exciter are first constructed, in which L1 represents the permanent magnet size, L2 represents the magnetic pole distance and M represents the radial air gap, as shown in Fig. 4. Then, the magnetic induction intensity at the center of armature under normal and broken carbon fiber composite core working conditions is calculated through finite element simulation. Different exciter sizes are shown in Table 2.

In order to explore the law of magnetization effect of exciter of different sizes on magnetic thin films, the amplitude B_{mag} of magnetic induction intensity of armature central part under two working conditions of normal and broken core was extracted, and the changes of B_{mag} with the size of exciter under two working conditions were plotted, as shown in Fig. 5. It can be seen that, with the change of exciter size, the magnetic induction B_{mag} at the center of the armature increases in both normal and fracture conditions. However, compared with the fracture condition, the increase trend of magnetic induction intensity under normal condition is relatively gentle, and the variation of magnetic induction intensity amplitude is no more than 0.0045 T. Under normal circumstances, the magnetic induction intensity of the center part of exciter 3 armature is 0.0091 T. Therefore, exciter 3 is the most suitable for the exciter size of this simulation model, and its permanent magnet size L1 is 15 mm.

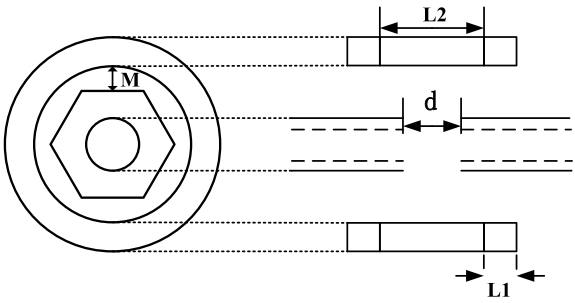

Fig. 4 Exciter parameter diagram

Table 2 Exciter parameter list

No.	L1 (mm)	L2 (mm)	M (mm)
Exciter 1	5	30	3
Exciter 2	10	30	3
Exciter 3	15	30	3

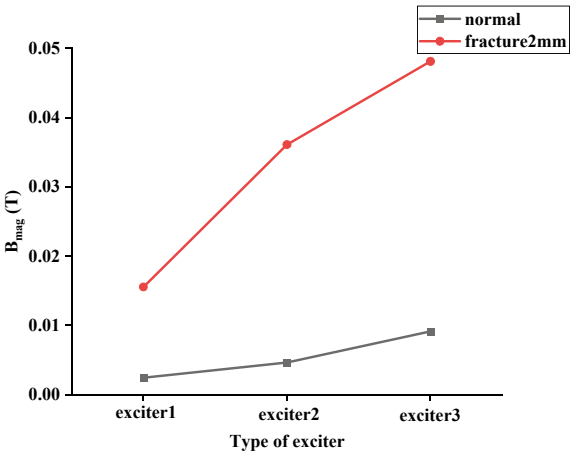

Fig. 5 Variation of magnetic induction intensity with exciter size under different working conditions

4.2 Influence of Magnetic Pole Spacing and Radial Air Gap

Through the above analysis of exciter size, the maximum magnetic leakage signal is determined when L1 is 15 mm. On this basis, the distance between the magnetic poles of two permanent magnets L2 and the radial distance M between the permanent magnet and the outer circle of the regular hexagon are further explored. The effects of L2 and M on magnetic leakage signal were analyzed using the amplitude B_{mag} of magnetic induction intensity at the armature center under normal and broken carbon fiber composite core conditions. The parameters of L2 and M under different working conditions are shown in Table 3.

In order to further optimize the key parameters of the exciter, the changes of B_{mag} with magnetic pole distance L2 at different air gap M under normal and fracture conditions of 2 mm were plotted, as shown in Figs. 6 and 7. As can be seen from the figure, under normal conditions, with the increase of the distance between magnetic poles under the same air gap, the amplitude B_{mag} of magnetic induction intensity

Table 3 L2 and M parameter tables

No.	L2 (mm)	M (mm)	No.	L2 (mm)	M (mm)
1	30	1	9	50	1
2	30	2	10	50	2
3	30	3	11	50	3
4	30	4	12	50	4
5	40	1	13	60	1
6	40	2	14	60	2
7	40	3	15	60	3
8	40	4	16	60	4

at the center of the armature showed an overall trend of rising. However, when the magnetic pole spacing is 50mm, B_{mag} first increases and then decreases with the increase of the air gap M. For the selected parameter range, the magnetic induction intensity varies less than 0.00266T with different pole spacing. When the magnetic carbon fiber composite core is broken by 2 mm, the amplitude B_{mag} of magnetic induction intensity at the center of the armature decreases with the increase of the air gap M at the same magnetic pole distance. With the same air gap distance, B_{mag} decreases with the increase of magnetic pole distance L2. This is because the increase of the air gap M will lead to the enhancement of the background magnetic field around the magnetic sensitive element, thus reducing the sensitivity of detection.

According to the requirements of the actual magnetic leakage detection device, increasing the magnetic pole distance L2 will not significantly change the magnetic

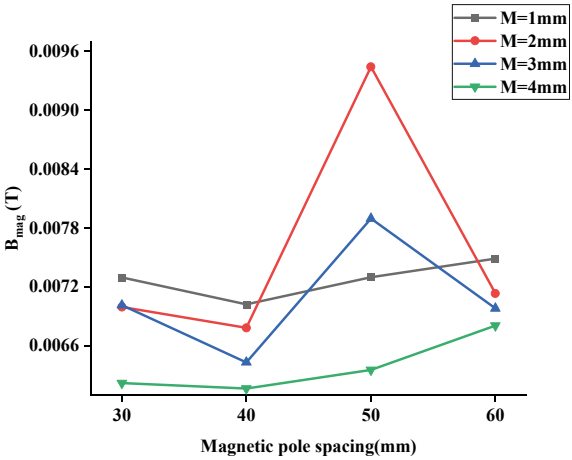

Fig. 6 Magnetic intensity varies with pole spacing at different M under normal conditions

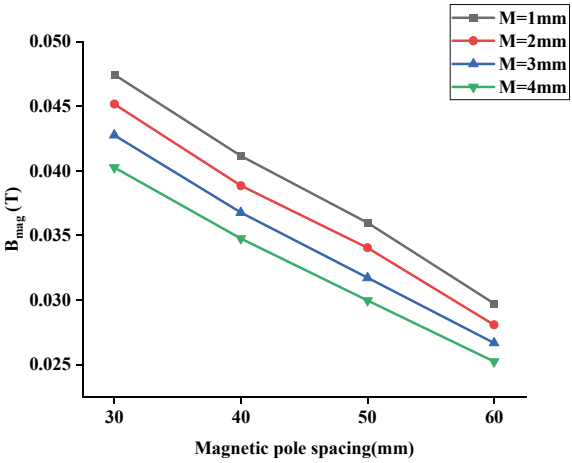

Fig. 7 Magnetic intensity variation with pole spacing at different M at fracture

leakage signal, but can reduce the magnetic field intensity of the magneto-air field, so as to improve the detection accuracy. Based on the above analysis, the magnetic pole distance L2 and air gap distance M of the magnetic leakage detection device adopted in this study are 50 mm and 2 mm respectively.

4.3 Case Verification

Through the above research and analysis, after determining the size and key parameters of the magnetic leakage detection device, the influence rule of the fracture width of the magnetic carbon fiber composite core on the magnetic leakage signal was explored, and the analysis was carried out from the axial component (along the axis of the core) and the radial component (pointing outward from the center of the core). The lifting value of the magnetic leakage detection device is set at 7.5 mm. As shown in Fig. 8, the B_x curve presents an approximate symmetry at the fracture center of the magnetic core rod. In the axial component of magnetic leakage signal, the magnetic induction intensity at the center of the armature increases first and then decreases with the increasing of the breaking width of the magnetic carbon fiber composite core. Among them, the magnetic leakage signal value is the largest when $d = 4$ mm. The reason is when the carbon fiber composite core just began to break, due to the huge difference in permeability between the air and the magnetic film, resulting in serious distortion of the magnetic field line. However, as the fracture width continues to increase, the proportion of air at the defect becomes larger and larger, and the material parameters become more uniform, reducing the degree of axial distortion, ultimately leading to a trend of increasing and then decreasing the axial signal. In Fig. 9, on the radial component of the magnetic flux leakage signal, as the fracture width increases, the magnetic induction intensity at the center of the armature increases, but the difference of change is relatively small. The B_y curve exhibits odd symmetry at the fracture center of the magnetic core rod.

5 Conclusion

In this paper, the flexible film material with high permeability is coated on the surface of the composite carbon core. Finite element simulation is used to study the parameters of a magnetic flux leakage detection device applicable to the crimping defects of carbon fiber composite core, and the influence of the exciter size and the key parameters of magnetic flux leakage detection device on magnetic flux leakage signals is explored. The following conclusions are reached:

- According to the actual crimping model, the magnetic leakage signal amplitudes of the three exciter parameters under normal and fracture conditions are compared, and the optimal permanent magnet size is determined to be 15 mm.

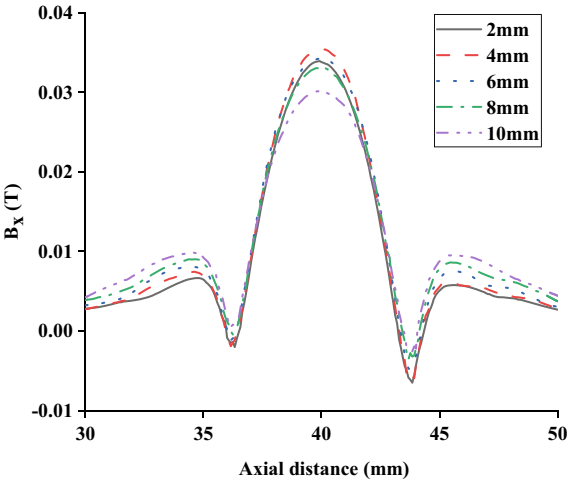

Fig. 8 Axial component of magnetic leakage signal with different fracture width

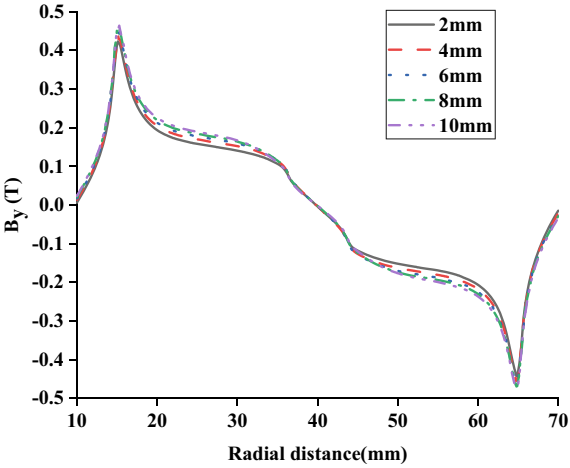

Fig. 9 Radial component of magnetic leakage signal with different fracture width

- On the basis of the above permanent magnet size, the influence of magnetic pole spacing and radial air gap on magnetic leakage signal is further analyzed. Combined with the actual testing situation, it is determined that the magnetic leakage signal accuracy is higher when the magnetic pole spacing is 50 mm and the gap distance is 2 mm.
- According to the parameters of the designed MFL detection device, the influence rule of fracture width on MFL signal was analyzed. It was found that the axial component first increased and then decreased with the increase of fracture width, and the MFL signal reached its maximum when d = 4 mm. In the radial component, the magnetic leakage signal increases with the increase of fracture width.

References

1. He ZW, Chen X, Wang QL, Zhang Z (2010) Research and application overview of ACCC conductor in China. Electr Power Constr 31(04):90–93. (in Chinese)
2. Wu J, Hui F, Huang X et al (2017) An online MFL sensing method for steel pipe based on the magnetic guiding effect. Sensors 12:2911
3. Zhao H, Liu J, Tang J et al (2023) A MFL mechanism-based self-supervised method for defect detection with limited labeled samples. IEEE Trans Instrum Meas 72:1–10
4. Yu GH, Deng YK (2019) Review on development of carbon fiber composite conductor. Hot Working Technol 48(20):1–5+9. (in Chinese)
5. Gao R, Cheng XK, Fan BR (2020) Discuss the necessity of applying X-ray to detect the defects of tensile lines in transmission lines. China Plant Eng 21:181–182 (in Chinese)
6. Zhang ZM, Jia BY, Wu HL (2016) Application of X-ray detection device in overhead transmission line compression type-fitting quality inspection. Hebei Electr Power 35(04):43–46 (in Chinese)
7. Wang YW, Zhu B, Cao WW (2014) Development and application of non-destructive testing technology on ACCC. Chem Anal Meterage 23(05):72–74 (in Chinese)
8. Xu ZW, Lu GL, Zhu B (2020) Application of X-Ray detection in carbon fiber conductor of transmission line. Heilongjiang Electr Power 42(03):215–217. (in Chinese)
9. Yi X, Lei Y, Sida W, Dengke L et al (2019) Study on nondestructive testing methods for crimping quality of steel Cored aluminum strand. IOP Conf Ser: Earth Environ Sci 295(3)
10. Jiang X, Sun C, Xia Y et al (2011) Optimal design of MFL sensor for detecting broken steel strands in overhead power line. In: Optimal design of MFL sensor for detecting broken steel strands in overhead power line, vol 121, pp 301–315
11. Alexander N, Vorontsov, Dmitry A, Slesarev, Vasily V et al (2014) Electromagnetic inspection and diagnostics of steel ropes: technology, effectiveness and problems. Mater Eval 72:1019–1027
12. Rao G, Kang Y, Yang S (2001) Inspection of high-voltage transmission lines using eddy current and magnetic flux leakage methods. Insight Non-Destr Test Condition Monit 43(5):307–309
13. Chen J, Feng Q, Wang F et al (2012) Research on burst tests of pipeline with spiral weld defects. In: Proceedings of the biennial international pipeline conference, vol 3, pp 53–60
14. Ken M (2022) MFL inspection of small diameter, previously Unpiggable, pipelines-lessons learned. In: 34th Pipeline pigging and integrity management, pp 503–522

Simulation of Arc Breaking in a 550 kV 80 kA SF_6 Circuit Breaker

Guoli Wang, Weihua Zhong, Chao Gao, Fusheng Zhou, Yun Yang, Jiaming Xiong, Xipeng Chen, Lei Jia, and Shizhe Chen

Abstract As the structure of power grid becomes increasingly complex and the capacity keeps increasing, the short-circuit current endurance of existing switching devices can no longer meet the needs of the development of power grid. The rated short-circuit current of 550 kV circuit breakers needs to be increased from 63 to 80 kA, which puts forward more stringent requirements on the breaking capacity of circuit breakers. In this paper, based on the magnetohydrodynamic model of arc burning in the arc extinguishing chamber of the circuit breaker, a 550 kV SF_6 auto-expansion circuit breaker was simulated for 9 ms under the working condition of 80 kA short-circuit current breaking. The distribution of temperature field, pressure field and electromagnetic field in the arc extinguishing chamber during the breaking process was obtained, together with the characteristic of the hot flow field. Through the comprehensive analysis of temperature field, pressure field and boundary conditions, this paper describes the arc burning process of circuit breaker in the arc extinguishing chamber, and accurately analyzes the physical process of circuit breaker when it breaks off, which provides some reference value for the optimization design of circuit breaker structure.

Keywords Auto-expansion circuit breaker · Magnetohydrodynamics · Arc simulation · Temperature · Pressure

G. Wang · C. Gao · F. Zhou · Y. Yang · J. Xiong · X. Chen · L. Jia · S. Chen (✉)
CSG Electric Power Research Institute, Guangzhou, China
e-mail: francis_0205@163.com

G. Wang
e-mail: wanggl@csg.cn

W. Zhong
China Southern Power Grid Co., Ltd, Guangzhou, China

© Beijing Paike Culture Commu. Co., Ltd. 2024

X. Dong and L. Cai (eds.), *The Proceedings of 2023 4th International Symposium on Insulation and Discharge Computation for Power Equipment (IDCOMPU2023)*, Lecture Notes in Electrical Engineering 1102, https://doi.org/10.1007/978-981-99-7405-4_20

1 Introduction

With the continuous expansion of power grid scale in our country, the level of short circuit current is increasing year by year. Excessive short circuit current can harm the safe and stable operation of power system and electrical equipment [1]. The current short-circuit current endurance capacity of the existing 500 kV main grid frame can no longer meet the needs of power grid development. It is urgent to develop a large-capacity switching device with large capacity, high reliability, and considering the renovation of old station and new project. Modern electric power transmission and distribution networks rely on SF_6 AC high-voltage circuit breaker technology because of the remarkable arc quenching properties and dielectric insulation of this gas [2, 3], which is of great significance to the reliable operation of power system [4]. The large-capacity 550 kV GIS with 8000 A current flow and 80 kA break capacity is the most advanced technical solution with high economic reliability and wide application scenarios. In view of this, it is of great significance to study 550 kV 80 kA SF_6 circuit breaker.

As the rated short circuit current of the 550 kV SF_6 circuit breaker is increased to 80 kA, a series of problems are brought, such as extremely high energy of the arc extinguishing chamber, extreme pressure gradient, higher medium recovery requirements and more serious nozzle ablation. It is necessary to carry out in-depth theoretical research on the electromagnetic-thermal-fluid-mechanical coupling process and the key mechanism affecting the breaking performance. Through arc simulation, the typical distribution characteristics of airflow field, temperature field, pressure field and electromagnetic field in the short-circuit breaking process can be obtained, and the key parameters affecting the breaking of circuit breakers can be defined.

Based on the established two-dimensional axisymetrical model of circuit breaker, the breaking process of the 550 kV auto-expansion circuit breaker at 80 kA short circuit was simulated, and the temperature and pressure distribution of the arc extinguishing chamber in the process of arc burning was obtained. The analysis of the physical quantity and boundary conditions lays a theoretical foundation for the optimal design of circuit breaker [5].

2 Circuit Breaker Simulation Model

2.1 Simulation Structure Model and Boundary Conditions

The 550 kV auto-expansion high-voltage SF_6 circuit breaker calculation structure model is composed of dynamic arc contact, static arc contact, nozzle, expansion chamber, pressure chamber, cooling chamber and valve structure. The nozzle material is PTFE. Since the circuit breaker is a two-dimensional axisymetrical model, the flow hole is equivalent by using the principle of constant flow to ensure the accuracy of calculation. The specific parameters of the circuit breaker are as follows:

(1) The effective value of rated short-circuit current is 80,000 A, frequency is 50 Hz, and the standard sinusoidal current is 1 ms at the moment of arc-starting;
(2) In the calculation, the initial radial velocity and axial velocity of the flow field are 0 m/s, the initial temperature is 300 K, and the inflation pressure is 0.6 MPa;
(3) The average motion speed of the mechanism in the process of motion is 6.5 m/s.

In the calculation process, the initial pressure is consistent with the inflation pressure, the end of the dynamic arc contact is set as the flux, namely the second type of boundary, the current density is applied, the end of the static arc contact is set as the potential value, namely the first type of boundary condition, the potential is 0. The static contact is set as a static component, and the dynamic arc contact and nozzle are set as moving components. Transparent contact is introduced to compensate arc axis deviation caused by hollow structure [6]. The fluid–solid coupling method is used to calculate the electric field. The region of dynamic and static arc contacts and the region of flow field are solved jointly.

2.2 Arc MHD Model

The arc is regarded as a conducting compressible fluid and follows the three principles of mass conservation, momentum conservation and energy conservation [7]. It is considered that the arc is in a neutral state and in local thermodynamic equilibrium and local chemical equilibrium [8]. The Navier–Stokes equations with source terms are used to describe the arc, and the governing equations of MHD arc simulation can be formed by coupling the electric field equation and the magnetic field equation.

(1) The standard form of the Navier–Stokes equation

$$\frac{\partial(\rho\phi)}{\partial t} + \nabla \cdot (\rho\phi \overrightarrow{V}) - \nabla \cdot (\Gamma \nabla\phi) = S_\phi$$

(2) Conservation of mass

$$\frac{\partial\rho}{\partial t} + \nabla(\rho \cdot \overrightarrow{V}) = 0$$

(3) Conservation of momentum

Axial momentum is conserved

$$\frac{\partial(\rho w)}{\partial t} + \nabla(\rho \vec{V} w) = -\frac{\partial p}{\partial z} + \nabla \cdot ((\mu_l + \mu_t)\nabla w) + J_r B_\theta + \nabla \cdot \overline{\overline{\tau}}$$

Conservation of radial momentum

$$\frac{\partial(\rho v)}{\partial t} + \nabla(\rho \vec{V} v) = -\frac{\partial p}{\partial r} + \nabla \cdot ((\mu_l + \mu_t)\nabla v) + J_z B_\theta + \nabla \cdot \overline{\overline{\tau}}$$

(4) Conservation of energy

$$\frac{\partial(\rho H)}{\partial t} + \nabla(\rho \vec{V} H) = \nabla \cdot \left(\left(\frac{\lambda_l + \lambda_t}{c_p} \right) \nabla H \right) + \sigma E^2 - q + \nabla \cdot \left(\overline{\overline{\tau}} \cdot \overrightarrow{V} \right)$$

(5) Electromagnetic field equation

$$B_\theta = \frac{\mu_0}{r} \int_0^R J_z r dr$$

$$\nabla \cdot (\sigma \nabla \varphi) = 0$$

where, ρ—density, kg/m^3; ϕ—a physical quantity to be solved; $\overrightarrow{V}$—velocity vector; t—time/s; Γ—diffusion coefficient; S_ϕ—source; w—axial velocity component/m·s^{-1}; p—air pressure/Pa; μ_l—laminar viscosity coefficient/kg·m-1·s^{-1}; μ_t—turbulent viscosity coefficient/kg·m^{-1}·s^{-1}; J_r—radial current density/A·m^{-2}; B_θ—circumferential component of magnetic field/A·m^{-1}; $\nabla \cdot \overline{\overline{\tau}}$—viscous term; v—radial velocity component/m·s^{-1}; J_z—axial current density/A·m^{-2}; H—enthalpy/J·kg-1; λ_l—laminar thermal conductivity W·m^{-1}·K^{-1}; λ_t—turbulent thermal conductivity/W·m^{-1}·K^{-1}; c_p—specific heat at constant pressure/J·kg^{-1}·K^{-1}; σ—electrical conductivity/S·m^{-1}; E—electric field intensity/V·m^{-1}; q—radiation source term/J·m^{-3}; $\nabla \cdot \left(\overline{\overline{\tau}} \cdot \overrightarrow{V} \right)$—viscous dissipation term; μ_0—vacuum permeability/H·m^{-1}; R—arc radius/m; φ—potential/V.

In this paper, the k-ε turbulence model in ANSYS FLUENT is used to describe the momentum and energy exchange between mass points under turbulent flow. The viscosity μ_t and thermal conductivity λ_t in the above equation can be calculated according to the k-ε turbulence model. The NEC method of net emission coefficient can provide relatively accurate results in arc plasmas dominated by axial flow [9], which is based on net emission coefficient. It is applied to consider the thermal radiation of arc [10], as shown in Fig. 1.

The travel curve of the simulation input is shown in Fig. 2.

3 Simulation Results and Analysis

In this paper, according to the breaking current and the burning time, the dynamic changing process of the hot flow field in the process of arc burning is simulated and calculated, and the changing characteristics of the pressure field and temperature field in different positions of the circuit breaker in the process of arc burning are obtained. According to the variation characteristics of the airflow field and the state of the arc

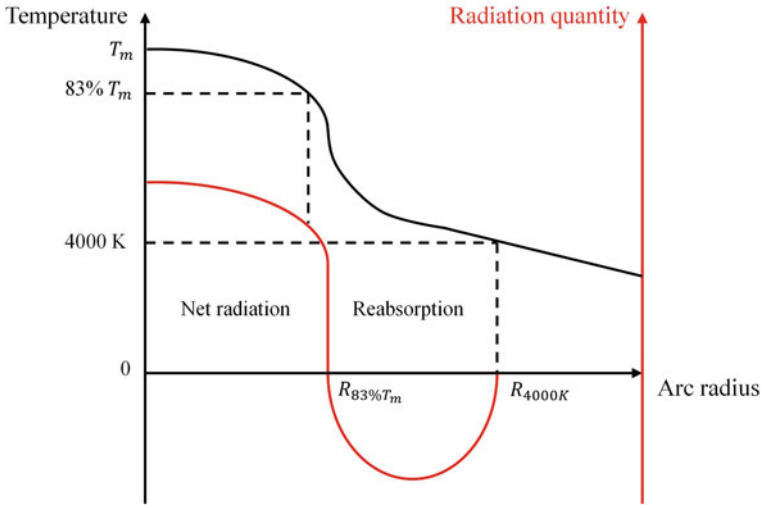

Fig. 1 Arc radiation model based on net radiation coefficient

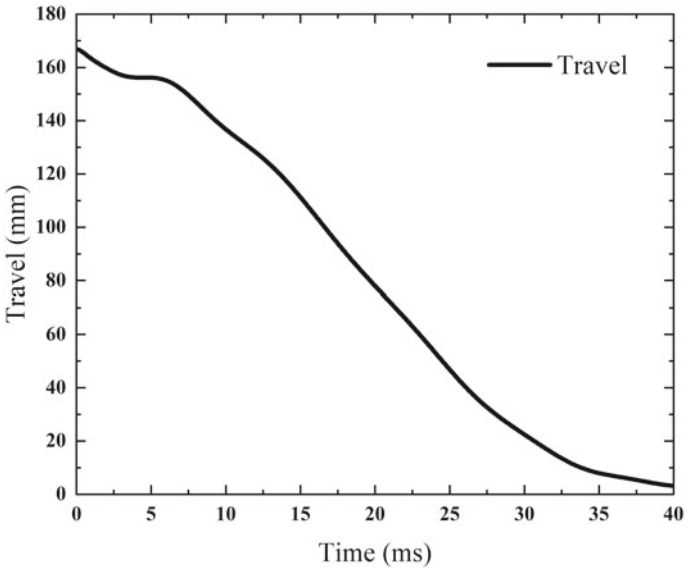

Fig. 2 Simulation input travel curve

extinguishing chamber before the current crossing, the performance of the 550 kV circuit breaker breaking 80 kA short circuit current is evaluated, which provides some reference for the improvement and optimization of the arc extinguishing chamber.

The simulation arc burning time is 9 ms, t is the contact movement time, *i* is the current value. During the whole arc burning period, the maximum temperature of the arc is over 30,000 K and the maximum pressure is 1.87 MPa. Arc burning experienced four processes of enhancement, intensity, attenuation and extinction respectively. The ablation of nozzle and electrode and the influence of non-thermochemical equilibrium state are not considered in the simulation.

3.1 Variation Characteristics of Temperature Field

Figure 3 shows the arc burning process.

At 0 ms, since the initial phase of the current is 1ms, the current is 34.94 kA. The arc radius is small. Most of the air flows along the arc through the contact gap. The arc cooling effect is weak, resulting in higher arc core temperature, exceeding 25,000 K.

At 2 ms, the current continues to increase, leading more intense arc burning. The arc radius is equal to the throat of the nozzle, which plays a certain hindering role on the airflow, making the airflow basically unable to flow to the downstream of the nozzle.

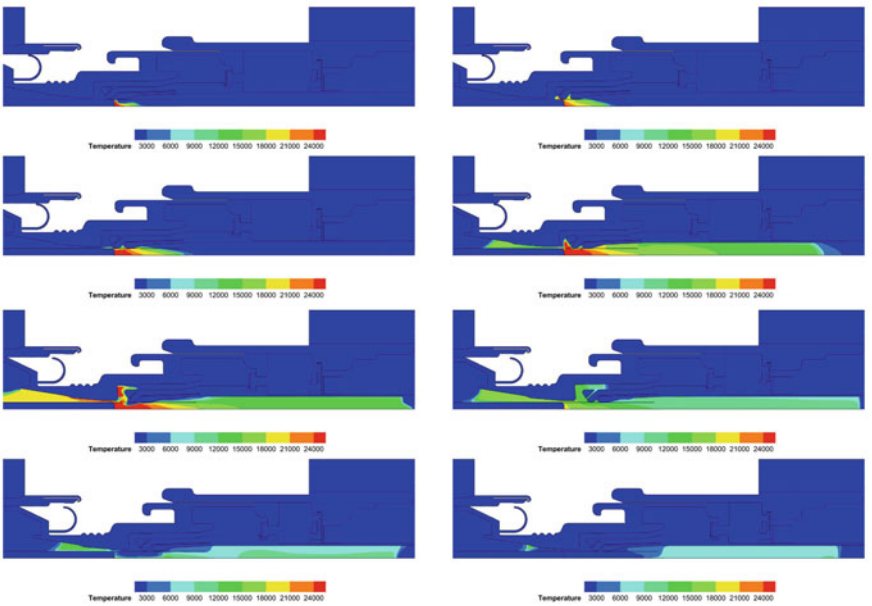

Fig. 3 Dynamic distribution diagram of arc temperature of circuit breaker during arc burning (K)

At 4 ms, the current reaches the peak and the arc core temperature reaches the highest at 30,230 K. The arc burns intensely and its high energy drives the high-temperature gas to spread to the expansion chamber.

At 6 ms, the current decreases to 91.48 kA after passing the peak value. The static contact is in the nozzle expansion position, making a small part of hot gas flow downstream to the nozzle. A part of high temperature gas still rushes to the expansion chamber, but the temperature decreases due to the effect of air blowing.

At 9.0 ms, the current passed through zero for the first time. Weak energy injection and strong cooling effect made the arc unable to maintain the original state and finally extinguished.

3.2 Variation Characteristics of Pressure Field

Figure 4 shows the dynamic distribution of pressure in part of the circuit breaker during arc burning. As can be seen from the figure, the gas pressure in the area where the arc exists is higher.

At 0 ms, the pressure distribution outside the arc is less affected by the arc. The maximum pressure in the arc area is 1.05 MPa, and the upstream pressure of the nozzle is 0.8 MPa.

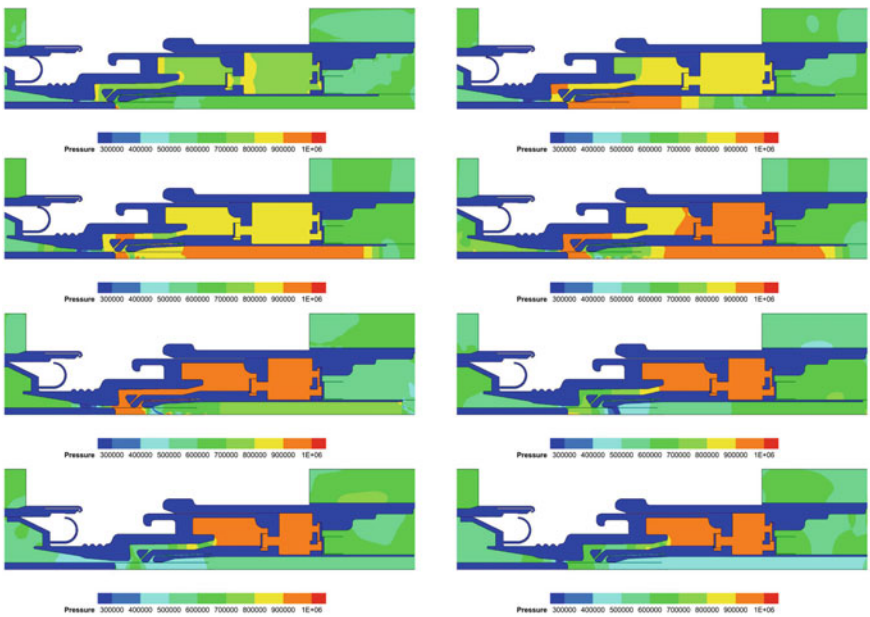

Fig. 4 Dynamic distribution diagram of arc pressure of circuit breaker during arc burning (Pa)

With the gradual compression of the cylinder and the expansion of the arc area, the pressure in the nozzle area gradually increases, among which the pressure at the top of the static arc contact is the largest, increasing from 1.18 MPa to 1.87 MPa.

At 4 ms, the arc burning is the most intense. The dynamic arc contact hollow inner tube is surrounded by a large amount of hot gas, with the minimum pressure at 0.91 MPa.

After 8.8 ms, the arc tends to be extinguished, and the flow field is almost not affected by the arc. The maximum gas pressure appears in the upstream of the cylinder and nozzle. The hot gas of the cylinder makes the pressure much higher than that of the cold state due to the violent arc ignition.

4 Conclusion

Based on the arc burning MHD model, the simulation model of SF_6 circuit breaker arc extinguishing process is established. For the 550 kV auto-expansion circuit breaker whose short circuit current is 80 kA, the arc quenching process of the circuit breaker is simulated. The key flow field parameters such as temperature and pressure are obtained, which can provide certain guidance for the product design. More reference value is offered to the determination of the subsequent optimization scheme.

Acknowledgements This manuscript is sponsored by the Science and Technology Project of China Southern Power Grid SEPRI-K225015.

References

1. Song Y, Lin S, Zhou T et al (2023) Simulation of airflow field and breaking capacity of 550 kV fast circuit breaker. High Voltage 1–9 (2023). (in Chinese)
2. Hermosillo V, Gregoire C, Vancell D et al (2018) Performance evaluation of CO_2/Fluoronitrile mixture at high short circuit current level in GIS and DEAD-Tank high-voltage circuit breakers. CIGRE Session
3. Jiang X, Jia S, Li X et al (2012) Simulation and analysis of cold flow field characteristics in SF_6 circuit breakers with UDRGM. Chin J Electr Eng 32(7):167–173 (in Chinese)
4. Mu J, Guo J, Li X et al (2012) Review of the numerical ion method for the interruption capability of SF_6 circuit breaker. High Voltage Apparatus 48(3):104–107 (in Chinese)
5. Zhang H et al (2021) Simulation analysis of 550 kV 80 kA SF_6 gas circuit Breaker's interrupting capability in T100a test. In: 2021 3rd Asia energy and electrical engineering symposium, Chengdu, China, pp 235–238
6. Yan J, Fang MTC, Hall W (1999) The development of PC based cad tools for auto-expansion circuit breaker design. IEEE Trans Power Delivery 14(1):176–181
7. Jiang X, Zhao H, Jia S et al (2013) Analysis of the dielectric breakdown characteristics for a 252-kV gas circuit breaker. IEEE Trans Power Deliv 28(3):1592–1599
8. Zhang B, Zhou R, Hao M et al (2022) Research on the application of C_4F_7N gas mixture in a 40.5 kV circuit breaker: part I. Simulation and evaluation of arc extinguishing performance. Chin J Electr Eng 1–12 (2022). (in Chinese)

9. Wang Z, Zhou R, Li Q et al (2022) Study on the dielectric recovery performance of high voltage SF_6 circuit breaker. In: IEEE international conference on high voltage engineering and applications, pp 1–4
10. Zhang J, Fang MTC, Newland DB (1987) Theoretical investigation of a 2 kA DC nitrogen arc in a supersonic nozzle. J Phys D Appl Phys 20(3):368

Simulation and Design of Electric Field Distribution for the Incoming Conductor Between 330 kV Terminal Tower and 750 kV Substation

Yuelin Fan, Peng Liu, Wei Shen, Wen Han, Chuang Liu, Jun Zhang, and Zongren Peng

Abstract During the field research of a 750 kV substation, corona discharge was found on the incoming conductors between the 330 kV terminal tower and the portal frame. To improve the corona discharge situation, the electric field of the incoming conductors was studied. A three-dimensional electric field simulation model of the incoming conductors between the 330 kV terminal tower and the portal frame in the 750 kV substation was established by using COMSOL Multiphysics, then surface electric field distribution of the incoming conductors was calculated. The impact of three factors—the width of the terminal tower cross-arm, the distance between the terminal tower and the portal frame, and the diameter of the incoming conductor—on the maximum electric field strength of the conductors was analyzed. The results showed that increasing the terminal tower cross-arm, increasing the distance between the terminal tower and the portal frame, and increasing the diameter of conductors can all reduce the surface electric field strength. The influence of increasing the diameter on electric field strength is significant. As the diameter increases from 26.6 to 33.6 mm and 36.2 mm, the maximum field strength decreases by 22.1% and 26.7%, respectively. The calculation results can provide the design basis for the incoming conductor layout and selection of 750 kV substations.

Keywords 750 kV substation · Incoming conductor · Electric field strength

Y. Fan · P. Liu (✉) · C. Liu · J. Zhang · Z. Peng
State Key Laboratory of Electrical Insulation and Power Equipment, Xi'an Jiaotong University, Xi'an, Shaanxi, China
e-mail: pengliu@mail.xjtu.edu.cn

Z. Peng
e-mail: pengzr@mail.edu.cn

W. Shen · W. Han
State Grid Shaanxi Electric Power Company Limited Electric Power Research Institute, Xi'an, Shaanxi, China
e-mail: adonies@126.com

© Beijing Paike Culture Commu. Co., Ltd. 2024

X. Dong and L. Cai (eds.), *The Proceedings of 2023 4th International Symposium on Insulation and Discharge Computation for Power Equipment (IDCOMPU2023)*, Lecture Notes in Electrical Engineering 1102, https://doi.org/10.1007/978-981-99-7405-4_21

1 Introduction

750 kV transmission and transformation project is an important component of China's ultra-high voltage (UHV) and extra-high voltage (EHV) transmission network. Its safe and stable operation is of great significance for the China's power transmission network. As the direct carrier of electric energy, conductor is an important part of the transmission line, which has a significant impact on the energy transmission, transmission performance, and environmental issues (such as corona discharge and noise). With the rapid development of UHV and EHV, the voltage level of transmission lines continues to increase. Then the corona discharge problem of conductors becomes more prominent [1–7]. One effective method to suppress corona discharge is to control the conductor's surface electric field strength, which requires reasonable arrangement and selection of the conductor.

At present, there has been a considerable amount of researches on the electric field distribution of transmission lines [8–11]. Reference [12] analyzed the influence of the geometric parameters of UHV transmission lines on the electric field strength and corona characteristics, which introduced the basic design principles of split conductors. Huang Zixuan established three-dimensional transmission line models using the simulation charge method to calculate the electric field strength [13]. Yu Jufeng calculated the surface electric field strength of UHV transmission lines under different arrangements [14]. Zhang Yemao et al. conducted electromagnetic research on the inverted triangle arrangement in UHV single-circuit transmission lines and determined seven optimal conductor structures [15]. On the other hand, the researches on the electric field distribution of conductors in substations are also relatively abundant. Zheng Haitao et al. considered different splitting numbers and splitting distances to analyze the surface electric field distribution of substation internal conductors using finite element software [16]. Reference [17] established a calculation model for the conductors in a 750 kV substation and determined the optimal structure of four split conductors through optimization calculation. However, there are still few reports on the electric field distribution of incoming conductors of substations.

When the transmission lines enter a substation, the conductors are arranged in a staggered manner and the electromagnetic environment becomes more complex. Moreover, it has been observed that corona discharge occurs on the surface of the incoming conductors which is connected between a 330 kV terminal tower and portal frame of a 750 kV substation. Therefore, it is necessary to conduct an study on the electric field distribution of incoming conductors of substations.

In this paper, a three-dimensional electric field calculation model was established for the incoming conductors between the 330 kV terminal tower and 750 kV substation by using COMSOL Multiphysics, and the electric field distribution of the conductors was simulated and analyzed. Based on the calculated results and the observation situation of corona discharge, the characteristics of the electric field distribution were analyzed. The factors that affect the surface electric field strength of the conductors were studied. Then the suggestions for improving the surface electric field distribution of the incoming conductors were proposed. This research can

provide support and reference for the surface electric field regulation and design of the incoming conductors of substations.

2 Simulation Model and Electric Field Calculation

2.1 Model Building

Based on the design drawing and overall dimensions of the 750 kV substation, a three-dimensional simulation model is established (as shown in Fig. 1). In order to save computing resources and simplify the calculation, only parts between the portal frame and the terminal tower is retained. Moreover, due to the shielding effect of the portal frame, the equipment that has little effect on the electric field distribution between the terminal tower and the portal frame can be deleted. The simplified computational model is in Fig. 2.

The simulation model uses the double-circuit transmission line on the same tower. The terminal tower is 45 m, with a cross-arm spacing of 10 m. In the portal frame, the distance between the insulators of the conductors is 10 m, and the distance between the three-phase conductors of each circuit is 8 m. The type of conductor is a two split conductor. From the terminal tower to the portal frame, the conductors changes from the vertical arrangement to the horizontal arrangement sequentially.

Fig. 1 Picture of incoming conductors of the 750 kV substation

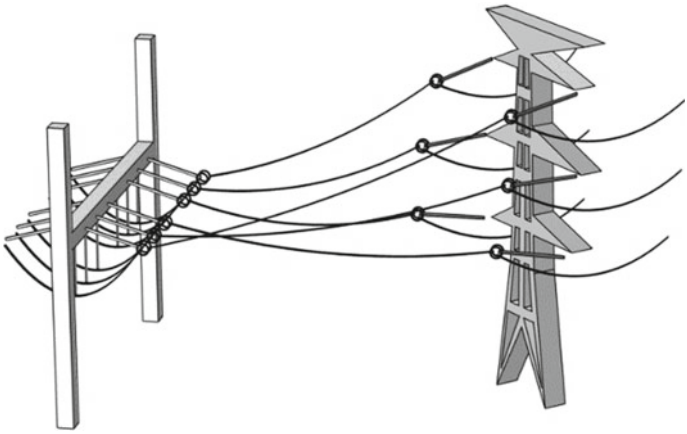

Fig. 2 Simulation model of incoming conductors of the 750 kV substation

2.2 Electric Field Calculation

In the simulation, the environmental factors are set to the ideal environment and it is assumed that all metallic surfaces are clean and dry. When subjecting the B-phase conductor to the highest operational phase voltage $U_m = 1.1 \times 750 \times \sqrt{2} \div \sqrt{3} = 653.2\,\text{kV}$, the other two phase conductors are subjected to a voltage of $-\frac{1}{2}U_m$. The low voltage conductors, such as the portal frame, are grounded, while the conductors with unknown potential are set to a floating potential.

The incoming conductors in the model are the two-split conductor. Among them, the three-phase conductors for Circuit I are named as A1, B1, and C1. Similarly, A2, B2, and C2 are named to the Circuit II conductors. The conductors of each phase is the two-split conductor. So the sub-conductor positioned closer to the inner side of the two circuits is caller the inner conductor, while that positioned closer to the outer side is called the outer conductor. The details are shown in Fig. 3.

The field strength of the entire model was computed. Figure 4 displays the calculated results of the electric field strength on the surface of the C1 conductor. It is evident that the maximum field strength value is 2.73 kV/mm. The shielding effect between the two split conductors results in a significantly higher field strength on the outer side compared to the inner side. This observation suggests that corona discharge predominantly transpires on the outer side of the conductors. This result is the same as the actual observation shown in Fig. 5. Therefore, this paper mainly focuses on the analysis and comparison of the field strength on the outer side of each conductor.

Comparing the calculated electric field strength of the incoming conductors in Fig. 6, it can be seen that the distribution of the field strength on the outer side surface of conductors is similar for each phase under different voltage peak conditions. The field strength is relatively small at both ends of the conductors due to the shielding

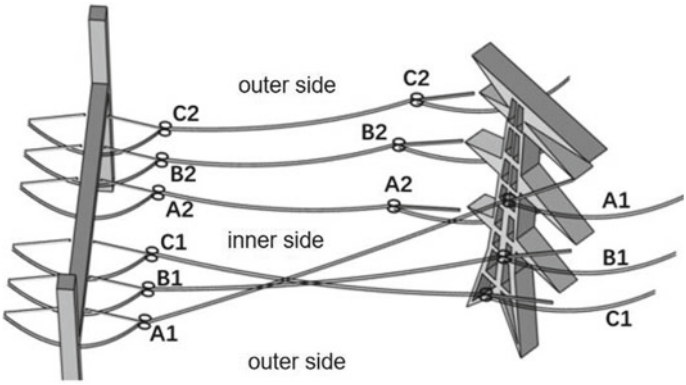

Fig. 3 Phase distribution of incoming conductors

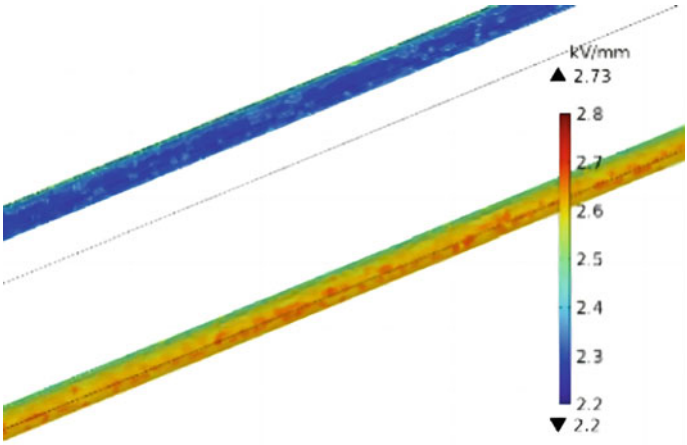

Fig. 4 Electric field distribution on C1 conductor surface

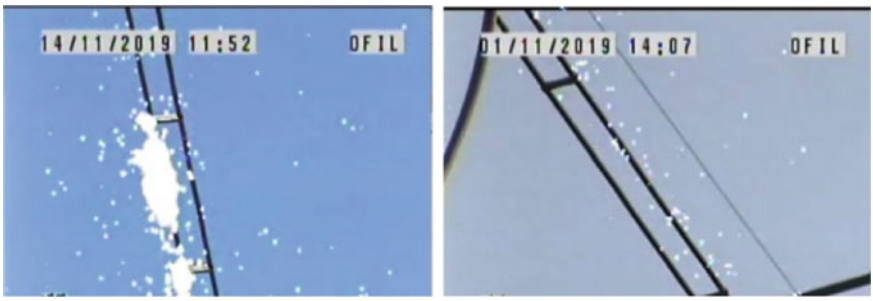

Fig. 5 Observation of corona discharge on incoming conductors

effect of the shielding ring. When the length of the conductor exceeds the shielding range, the field strength of the wire increases rapidly. The field strength in the middle of the conductor is basically unchanged, with a slight increase. This is due to the change in the arrangement of the incoming conductors from the terminal tower to the portal frame. The phase spacing between the conductors is reduced from 10 to 8 m, which leads to an increase in the field strength.

By comparing the maximum electric field strength of the inner and outer sub-conductors of each phase's conductors, as presented in Table 1, it is evident that the field strength on the inner sub-conductors of each phase is lower than that on the outer sub-conductors. This discrepancy can be attributed to the shielding effect between the conductors.

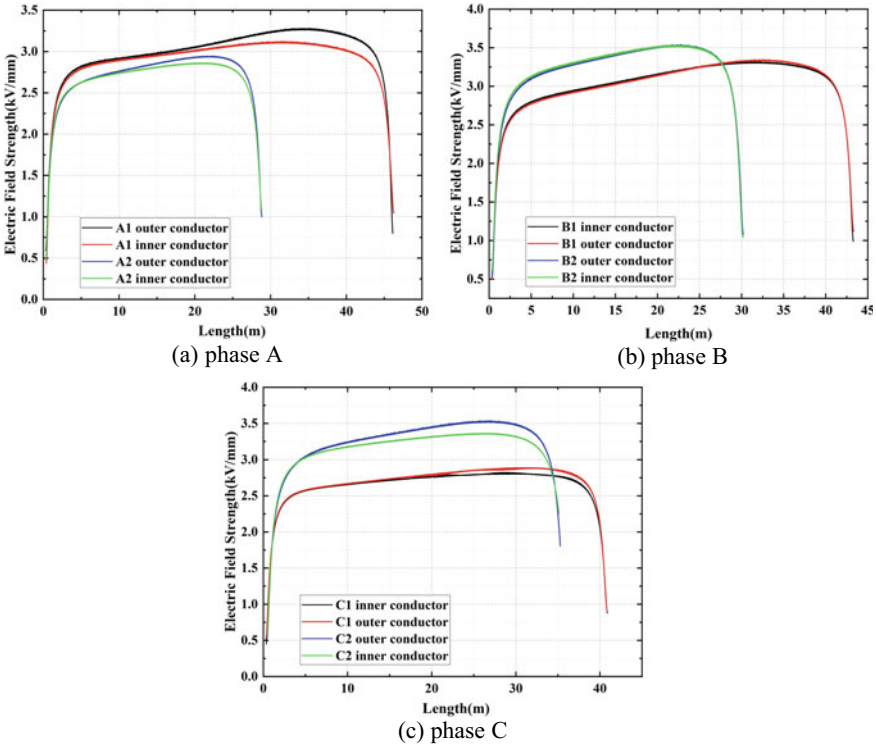

(a) phase A (b) phase B

(c) phase C

Fig. 6 Field strength on the outer side surface of conductors at the different peak voltage

Table 1 Maximum electric field on the outer side surface of incoming conductors (kV/mm)

	Circuit I		Circuit II	
	Inner conductor	Outer conductor	Inner conductor	Outer conductor
Phase A	3.23	3.36	2.88	3.00
Phase B	3.35	3.36	3.56	3.70
Phase C	2.82	2.90	3.39	3.63

3 Impact of Different Factors on the Surface Electric Field Strength of Incoming Conductors

Based on the analysis of the simulation results, this paper proposes three different design schemes to enhance the electric field strength on the incoming conductors. These schemes involve modifying the width of the terminal tower cross-arm, the distance between the terminal tower and the portal frame, and the diameter of the conductors. The objective is to improve the electric field strength based on the findings from the analysis.

3.1 Impact of Terminal Tower Width on the Electric Field Strength

See Fig. 7.

By simulating the changes in the field strength of incoming conductors through increasing the cross-arm width of terminal tower by 2 and 4 m respectively, the maximum field strength on the conductors were calculated and presented in Table 2.

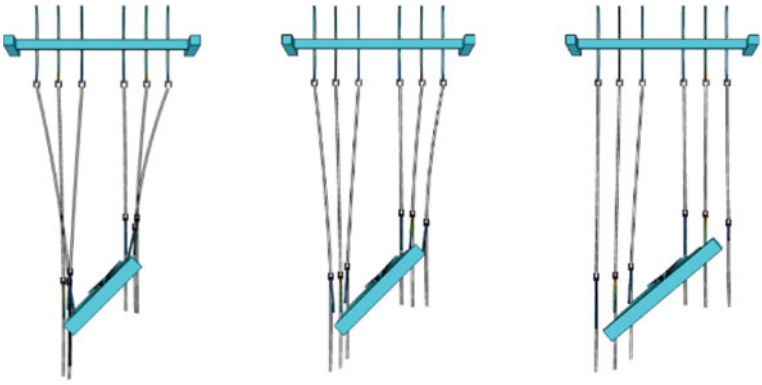

(a) Initial scheme (b) Widened by 2m (c) Widened by 4m

Fig. 7 Model structure of changing the cross-arm

Table 2 Maximum electric field on the outer side surface of incoming conductors (kV/mm)

	Initial scheme	Widened by 2 m	Widened by 4 m
A1 inner conductor	3.36	3.19	3.16
A1 outer conductor	3.23	3.03	2.96
A2 inner conductor	2.88	2.87	2.87
A2 outer conductor	3.00	2.99	2.83
B1 inner conductor	3.36	3.26	3.18
B1 outer conductor	3.36	3.24	3.15
B2 inner conductor	3.56	3.48	3.49
B2 outer conductor	3.70	3.60	3.35
C1 inner conductor	2.82	2.81	2.76
C1 outer conductor	2.90	2.83	2.80
C2 inner conductor	3.63	3.50	3.38
C2 outer conductor	3.39	3.31	3.31

Table 2 indicates that widening the terminal tower cross-arm can reduce the maximum field strength of each phase conductor. When the terminal tower is widened by 2 m, the maximum field strength of conductors is cumulatively reduced by 2.7%. When the terminal tower cross-arm is widened by 4 m, the maximum field strength of conductors is cumulatively reduced by 4.9%. This is because as the cross-arm width of the terminal tower increases, the spacing between the conductors increases, which reduces the surface field strength. In addition, the increase in cross-arm width also expands the shielding range of the terminal tower, further reducing the surface field strength on the conductors.

3.2 Impact of the Distance Between the Terminal Tower and the Portal Frame on the Electric Field Strength

See Fig. 8.

By increasing the distance by 10 m and 20 m respectively, the changes in field strength of the incoming conductors were simulated and the maximum field strength on the conductors were presented in Table 3.

Table 3 indicates that when the distance increases, the maximum field strength of the conductors decreases. When the distance increases by 10 m, the maximum field strength of conductors is cumulatively reduced by 4.9%, and when the distance increases by 20 m, the maximum field strength is cumulatively reduced by 7.1%. This is because as the distance between increases, the electric field distribution between the tower and the portal frame becomes more uniform, leading to a reduction in the maximum field strength.

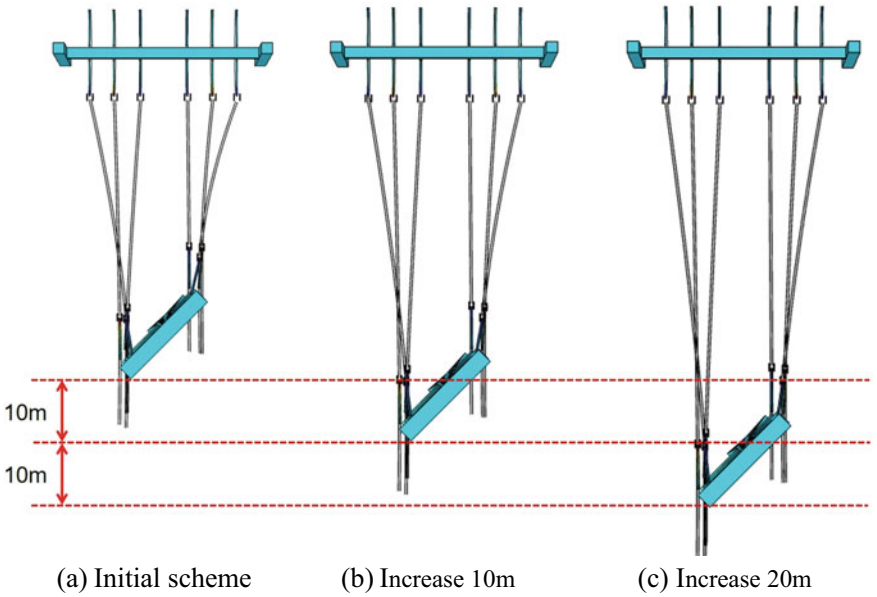

Fig. 8 Model structure of the distance between the terminal tower and the portal frame

Table 3 Maximum electric field on the outer side surface of incoming conductors (kV/mm)

	Initial scheme	Distance increased by 10 m	Distance increased by 20 m
A1 inner conductor	3.36	3.18	3.08
A1 outer conductor	3.23	2.98	2.91
A2 inner conductor	2.88	2.83	2.82
A2 outer conductor	3.00	2.92	2.90
B1 inner conductor	3.36	3.28	3.23
B1 outer conductor	3.36	3.28	3.26
B2 inner conductor	3.56	3.34	3.26
B2 outer conductor	3.70	3.33	3.23
C1 inner conductor	2.82	2.81	2.79
C1 outer conductor	2.90	2.90	2.82
C2 inner conductor	3.63	3.31	3.07
C2 outer conductor	3.39	3.09	3.03

Table 4 Maximum electric field on the outer side surface of incoming conductors (kV/mm)

	Initial scheme	Distance between the tower and the portal frame increased by 10 m		
Diameter/mm	26.6	26.6	33.6	36.2
A1 inner conductor	3.36	3.18	3.19	3.16
A1 outer conductor	3.23	2.98	3.03	2.96
A2 inner conductor	2.88	2.83	2.90	2.90
A2 outer conductor	3.00	2.92	2.99	2.83
B1 inner conductor	3.36	3.28	3.26	3.18
B1 outer conductor	3.36	3.28	3.24	3.15
B2 inner conductor	3.56	3.34	3.48	3.49
B2 outer conductor	3.70	3.33	3.60	3.35
C1 inner conductor	2.82	2.81	2.91	2.86
C1 outer conductor	2.90	2.90	2.83	2.80
C2 inner conductor	3.63	3.31	3.50	3.38
C2 outer conductor	3.39	3.09	3.31	3.31

3.3 Impact of the Diameter of the Conductors on the Electric Field Strength

After increasing the distance between the tower and the portal frame by 10 m, the maximum surface field strength of the incoming conductors were calculated for two different conductor diameters: 33.6 and 36.2 mm. The results are presented in Table 4.

The results presented in Table 4 demonstrate that when the distance between the terminal tower and the portal frame is increased by 10 m, the maximum field strength of conductors cumulatively decreases only by 4.9%. Furthermore, as the conductor diameter increases from 26.6 mm to 33.6 mm, the maximum field strength cumulatively decreases by 22.1%, and when the conductor diameter further increases to 36.2 mm, the maximum field strength cumulatively decreases by 26.7%. The increase in conductor diameter leads to a more uniform distribution of the electric field on the surface of the conductor, resulting in a significant reduction in the maximum electric field strength.

4 Conclusion

This article presents a three-dimensional modeling and electric field simulation analysis of the double-split incoming conductors between the portal frame and the terminal tower of the 750 kV substation. The study analyzed the relationship between the surface electric field distribution of the incoming conductors and three factors.

Corresponding design suggestions were proposed to improve the surface electric field distribution of the incoming conductors. The specific conclusions are as follows:

(a) The electric field strength on the outer side surface of the incoming conductor is significantly higher than that on the inner side surface, so corona discharge often occurs on the outer side surface of the conductors.
(b) Widening the width of the terminal tower cross-arm, increasing the distance between the terminal tower and the gantry, and increasing the conductor's diameter can all effectively reduce the surface electric field strength of the incoming conductor. When the terminal tower cross-arm is widened by 2 m and 4 m, the maximum field strength decreased cumulatively by 2.7% and 4.9%, respectively. When the distance between the terminal tower and the portal frame was increased by 10 m and 20 m, the maximum field strength decreased cumulatively by 4.9 and 7.1%. As the diameter increases from 26.6 mm to 33.6 mm and 36.2 mm, the maximum field strength decreases cumulatively by 22.1 and 26.7%. Adjusting the diameter of the conductor has the best overall effect.
(c) Considering the practical design of substations and transmission lines, these methods which are increasing the distance between the terminal tower and the portal frame, increasing the width of the terminal tower, and increasing the diameter of the conductor are useful to achieve the corona prevention and noise reduction for incoming conductors and to ensure the reliability and economy of the power system operation.

Acknowledgements This work was supported by the 2022 Power Grid operation Inspection Technical Service Project of State Grid Shaanxi Institute of Electric Science and Technology SGSNKY00SPJS2201853.

References

1. Yi LD, Lv SR (2006) Research and application of construction key technologies for 750 kV transmission and transformation demonstration project. Power Syst Technol 30(3):51–56 (in Chinese)
2. Shao FY (2007) Electromagnetic environment of 1000 kV ultra-high voltage transmission lines. Power Syst Technol 31(22):1–6 (in Chinese)
3. Huang SL, Liu YP, Chen SS, He WL, Wan BQ, Xu LH, Li YJ (2019) Corona loss characteristics of bundle conductors in UHV AC transmission lines at 2200 m Altitude. Electric Power Syst Res
4. Pei CM, Wu XW, Hu S et al (2016) Characteristic and distribution law of audible noise in 750 kV substations. High Voltage Apparatus 52(1):101–105 (in Chinese)
5. Kolcio N, DiPlacido J (1977) Apple grove 750 KV project—two year statistical analysis of audible noise from conductors at 775 KV and ambient noise data. Dietrich F.M.IEEE Trans Power Apparatus Syst 1977(2)
6. Balametov AB, Khalilov ED, Isaeva TM (2018) Modeling the EHV transmission-line mode in light of actual corona losses. Russ Electr Eng 2018(2)
7. EPRI (198) Transmission line reference book-345kV and above. EPRI, California

8. Chen MX, Lan S (2022) Surface electric field strength analysis of sub-conductor in UHV Transmission. Energy Environ 173(04):56–60 (in Chinese)
9. Zhang HB, Wu HT, Hu Q (2022) Review on audible noise of overhead transmission lines. High Voltage Electr Apparatus 58(05):1–6. 10.13296 (in Chinese)
10. Tang K, Xu SC, Liu YB (2020) Transmission lines of large span across the engineering cable type research. Electric Power Surv Des 142(7): 28 and 33. 10.13500 (in Chinese)
11. Song CM, Huang SL, LIU YP, Comparative analysis of corona loss of different types of conductors in 750 k V four-loop transmission project. Sci Technol Eng 202, 22(27):11975–11982 (in Chinese)
12. Zeng QY (2007) Research on electrical and corona characteristics of UHV transmission lines. Power Syst Technol 264(19):1–8 (in Chinese)
13. Huang ZX (2013) Research on prediction and calculation of electromagnetic environment of UHV transmission lines. Zhengzhou University, Zhengzhou, pp 74–75 (in Chinese)
14. Yu JF (2009) Calculation of surface electric field strength of UHV transmission lines under different arrangement forms. North China Electric Power University (Hebei), Baoding, 50 (in Chinese)
15. Zhang YM, Zhang GZ, Wan BQ et al (2011) Study on electromagnetic environment of 1000 kV AC single loop compact transmission lines. High Voltage Eng 37(8):7 (in Chinese)
16. Zheng HT, Jia YH, Zhang XW et al (2017) Numerical analysis of surface electric field distribution of Busbars in 750 kV substations. Proc CSEE 29(1):123–127 (in Chinese)
17. Ma AQ, Chen J, Ma W (2016) Structural Optimization of Splitting Conductors in 750 kV Substations Based on APDL. Proc CSEE 28(8):85–90 (in Chinese)

Research on X Ray Live Work of UHV Transmission Line by Helicopter

Jun Wang, Nan Wang, Shuai Li, Guangkai Yu, Yong Peng, Songyuan Cao, and Yuli Wang

Abstract In this paper, an X ray device used in UHV helicopter live work is developed, and its electrical performance, mechanical performance and X ray detection function are tested. The results show that the feature of the device meet requirements of live operation on site. In addition, the suspension method are used for field work, which solves the problems of inconvenient of X ray live test of UHV transmission lines.

Keywords Ultra-high voltage · Connecting hardware · Helicopter · X ray · Live working

1 Introduction

The events of disconnection at the self-voltage nozzle of transmission lines have occurred from time to time. Now, X ray test technology has a large number of applications in transmission line for high-resolution penetrating detection of line and fittings, so as to detect hidden defects in real time and quickly and prevent dis-connection accidents, which has very important practical significance [1–5]. However, on the one hand, the application of existing X ray detection technology mainly depends on power outage detection. If large-scale detection is carried out, the power outage time of the line will be greatly prolonged, and the economy is low. Live detection

Project funding: The Fundamental Research Funds for Project of State Grid Corporation of China (5500-202220144A-1-1-ZN).

J. Wang · N. Wang · S. Li
State Grid Electric Power Space Technology Company Limited, Beijing 100000, China

G. Yu · Y. Peng · Y. Wang (✉)
China Electric Power Research Institute, Wuhan 430074, China
e-mail: 1910654759@qq.com

S. Cao
State Grid Anhui Electric Power Co. Ltd, Hefei 230041, China

© Beijing Paike Culture Commu. Co., Ltd. 2024

X. Dong and L. Cai (eds.), *The Proceedings of 2023 4th International Symposium on Insulation and Discharge Computation for Power Equipment (IDCOMPU2023)*, Lecture Notes in Electrical Engineering 1102, https://doi.org/10.1007/978-981-99-7405-4_22

has only been applied in a small range on 110/220 kV lines, and some units have carried out live detection pilots on 750 kV lines [6–8]. On the other hand, when X ray inspection of connecting fittings is carried out on EHV transmission lines, due to the large tower height and many operating points, the traditional tower climbing inspection method has the problems of high labor intensity, low efficiency and high risk, which is difficult to meet the actual operation and maintenance requirements of EHV trans-mission lines. Using helicopter to carry out X ray live detection can not only complete the operation in the live environment of the line, but also greatly improve the detection efficiency and reduce the operation risk, which has strong practical significance [9–13].

In order to make it safe and feasible for helicopters to carry out X ray detection, in this paper, a set of X ray detection system based on live working of helicopters was successfully developed, and passed the electrical performance, mechanical performance and communication performance tests. Combined with the operation flow of X ray inspection and the operation characteristics of helicopter suspension method, the flight test schemes of helicopter suspension method are analyzed and formed, and the practical demonstration is completed in flight training, forming a complete and detailed operation flow. The project results are planned to be demonstrated and applied in ultra-high voltage transmission lines, and can be further popularized in power systems after the technology application is mature.

2 Design of X Ray Live Detection Device for 1 Helicopter

2.1 Overall Structure of the Device

In this paper, a helicopter live X ray test system is proposed based on XRS-3 X ray machine, which is mainly composed of (1) X ray machine, (2) X ray receiver, (3) equipotential supporter, (4) operation PAD, (5) wireless router, as shown in Figs. 1 and 2. In this paper, the tablet computer is used as the control terminal, as shown in the following figure.

2.2 Equipotential Detection Tooling

During the live working, to maintain the electric potential of the online testing device all the time, avoid spark dis-charge with small gap, and consider the convenience of installing and adjusting the position after on-line, an equipotential supporter is proposed, and it contains: X ray receiver shield, pulley, lightweight conductive rod and X ray machine shield. Its structural diagram is as follows (Fig. 2).

(a) X ray Machine

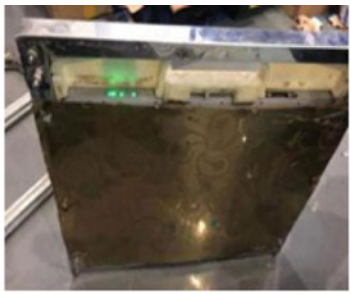

(b) X ray receiver

(c) Equipotential supporter

(d) Operation PAD

(e) Wireless router

Fig. 1 Helicopter live X ray detection system

2.3 Equipotential Control Terminal

The portable control terminal mainly realizes the functions of ray emission and image acquisition, and adopts wireless control. It is proposed to use tablet computers instead of notebook computers, and fix it with metal brackets, to prevent the EMI during live work (Fig. 3).

3 Performance Test of X Ray Live Detection Device for 2 Helicopter

3.1 Electrical Performance Test

Equipotential function test and arc discharge immunity test of X ray live work system proposed above were conducted in the environmental climate hall of UHV AC test base. the test layout is as follows (Fig. 4).

Place all equipment on the remote operating insulation testing device. Boosting the voltage to a specified voltage which is equal to the UHV rated phase voltage. Adjust

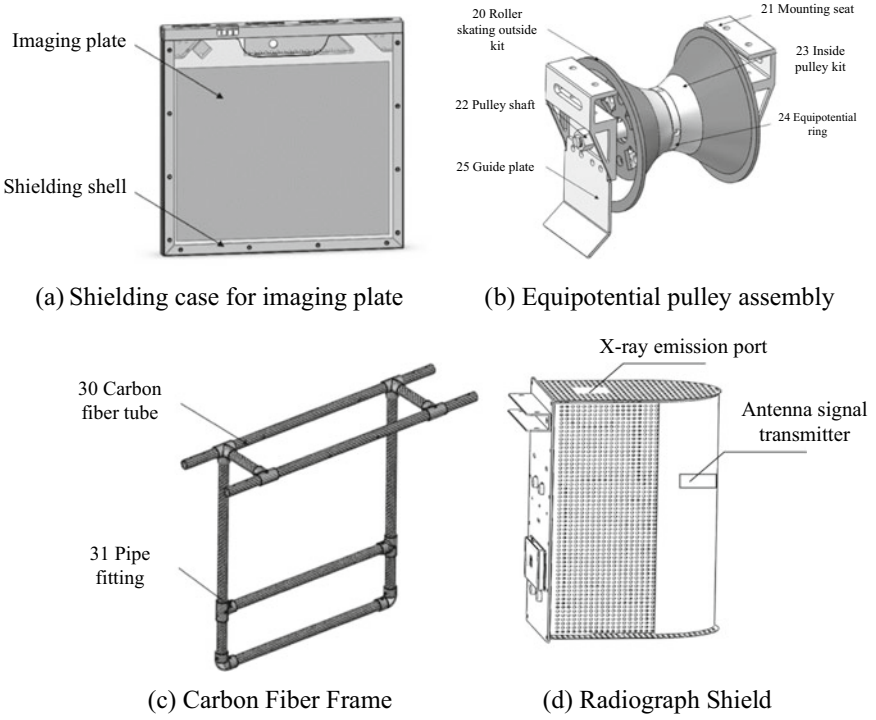

(a) Shielding case for imaging plate (b) Equipotential pulley assembly

(c) Carbon Fiber Frame (d) Radiograph Shield

Fig. 2 Schematic diagram of equipotential detection tooling structure

Fig. 3 Flat panel control terminal and protective housing

the height of the insulating platform to cause arc discharge between the measured object and the wire, and observe the effect of arc discharge on the X-ray device.

The AC voltage test results are shown in Table 1.

The discharge arc in the test is shown in Fig. 5:

From the experiment, X ray imaging can be carried out on the test hardware samples to observe the crimping of clamps, and the imaging quality is clear. It is obvious that the X ray live work system is able to suffer the EMI in live working environment of 1000 kV AC and below, mainly due to high-frequency conduction

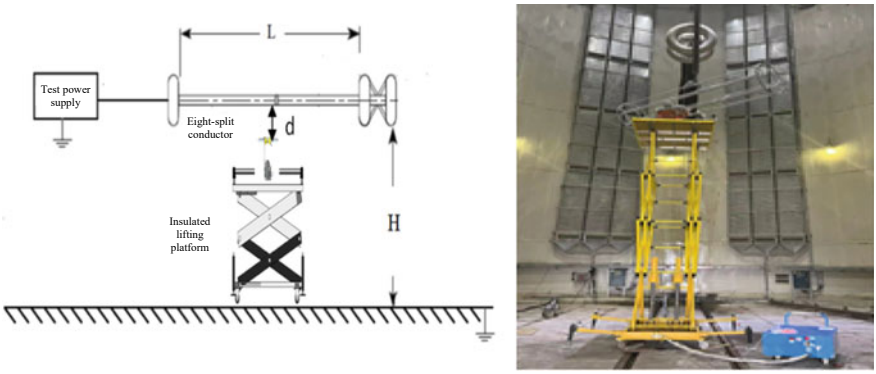

Fig. 4 Test layout

Table 1 AC voltage live test results

Test voltage (kV)	Discharge distance cm	Test result
400	0	Work normally in the test
	18	
	25	
	33 (critical discharge distance)	
500	0 (equipotential)	Work normally in the test
	10	
	22	
	38 (critical discharge distance)	
635	0 (equipotential)	Work normally in the test
	48	
	77	
	89 (critical discharge distance)	

current and electromagnetic radiation interference generated by arc discharge in the process of entering and leaving equipotential.

3.2 Mechanical Property Test

The total weight of the whole on-line device is 22 kg. In order to verify the bearing capacity of equipotential tooling support, 50 kg standard counter-weight is used for 5 min static load test. The results show that the support can bear 500N tension without deformation or damage (Fig. 6).

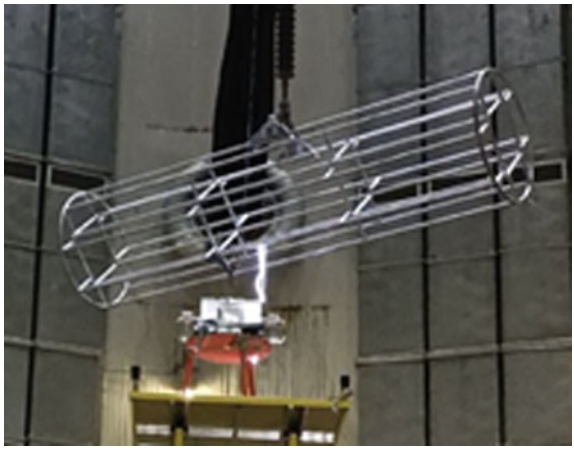

Fig. 5 Arc discharge test of 635 kV AC

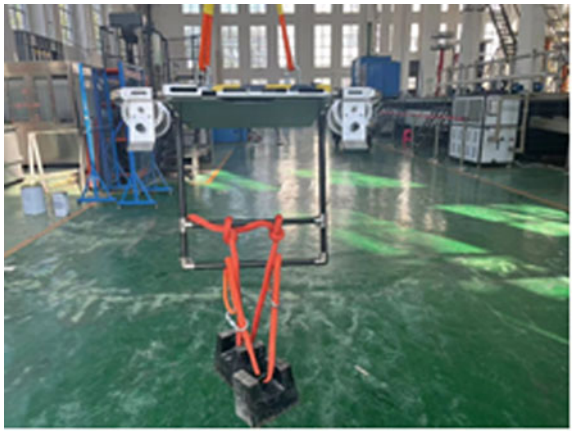

Fig. 6 Mechanical static load test of equipotential tooling support

3.3 X Ray Shooting Test of Ultra-High Voltage Clamp

In this paper, XRS-3 pulse ray machine is selected. In order to ensure the penetrating effect of X ray test system, the sample of tension clamp (NY-1250/100) of 1250 mm^2 large wire diameter wire on 1100 kV line was selected, and the photographing experiment was carried out (20/30/40/60 pulses) respectively. The photographing effect met the requirements of field use. Between 2–20 pulses, the image definition was slightly different with the in-crease of pulse number, and when the pulse number reached 20, the image quality was basically not affected (Fig. 7).

Fig. 7 Test layout and imaging diagram of NY-1250/100 tension clamp sample

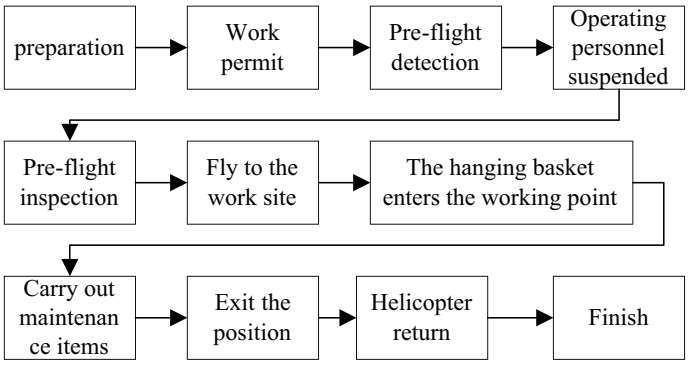

Fig. 8 Operation flow chart of helicopter hanging basket method

4 Field Application

4.1 Helicopter Suspension Operation

The suspension method is mainly applicable to UHV lines, 6-split and 8-split conductor lines, mainly 1000, 800 and 1100 kV. 750 kV lines can be selected for EHV lines. The helicopter trans-ports two operators and tools to the operation position at the same time through a special hanging basket, and all of them are installed and operated by online personnel to carry out inspection operations, without the need for the helicopter to hover for a long time.

The operation flow are shown in Figs. 8 and 9.

4.2 Operation Efficiency Analysis

We set up a training unit to carry out X ray on-line special training in Xiantao Training Base. A total of 4 qualified opera-tors carried out the whole-process hanging basket method and sling method on-line operation for 5 days, 15 sorties and 9 h, and took

Fig. 9 Field application picture

dozens of photos of tension clamps. The main difference between sling method and hanging basket method lies in the different ways of going on and going out, which has been introduced in detail above, and the working flow on the conductor is the same.

During this training, the operator recorded in detail the time nodes such as personnel and equipment on-line, equipment installation and photo shooting. After many flight test analysis, the total time for completing the operation of one-phase 8 split conductors is about 70 min. See the following table for the time distribution of each step in the whole on-line operation process. It can be seen from the data in the table that the measurement time of 8 sub-conductors accounts for about 47.8% of the total operation time, and the proportion of 3-phase conductors in the total operation time is about 60%. With the improvement of the proficiency of operators, the efficiency of disassembling and installing equipment among each sub-conductors will gradually improve. However, due to the influence of site and line distance in actual line operation, there is great uncertainty in the time of take-off and take-off, and the proportion of online operation time to total operation time may be greatly reduced, so the impact of simply improving online operation efficiency on overall operation efficiency will be very limited. Therefore, to improve the efficiency of helicopter X ray inspection operation, it is necessary to comprehensively consider various aspects and continuously optimize the operation process from all aspects.

5 Conclusion

- A helicopter live X ray test system is proposed based on XRS-3 X ray machine, which is mainly composed of X ray machine, X ray receiver, equipotential supporter, operation PAD, wireless router;

- The electrical performance, mechanical performance, communication performance and X ray detection function of the helicopter X ray live work system are tested, and the results show that the feature of the device meet the requirements of live operation on site;
- The suspension method are used for field operation, which solves the problems of inconvenient of X ray live test of UHV transmission lines.

References

1. Di W, Chunhui M, Zhenbang F (2021) Defect statistics in strain clamps of three-span transmission lines based on radiographic testing. Nondestructive Testing 043(007):71–73 (in Chinese)
2. Yu C (2018) Detection and application analysis of tension clamp of high voltage transmission line by X ray. Sci Technol Wind (34):1 (in Chinese)
3. Xiaopan S (2016) Analysis on live detection technology of porcelain insulators for UHV AC transmission lines. Telecom World: Second Half 3:2 (in Chinese)
4. Guan W, Liang L, He Y (2017) Systematic research and application of X ray nondestructive testing technology in condition detection of transmission lines. Electron World (16):1 (in Chinese)
5. Ouyang K, Cao X, Qu G et al (2020) Live detection technology of tension-resistant clamp quality for transmission lines. Hunan Electr Power 40(6):4 (in Chinese)
6. Zheng X, Jia R, Aisikaer et al (2021) Component identification and default detection in transmission lines based on deep learning. J Intell Fuzzy Syst: Appl Eng Technol (2):40
7. Gao Haipeng, Hao Binbin, Ye Dapeng. Study on live working technology of helicopter sling method for UHVDC transmission lines [J]. Ningxia Electric Power, 2022 (3): 6. (in Chinese)
8. Yulin G, Hong C (1996) X ray nondestructive testing of steel cord conveyor belt [J]. Coal Mine Electromechanical 4:2 (in Chinese)
9. Li Ming, Hu Zhipeng, Hu Hongwei. Study on phase-in potential mode in live working of helicopter platform on 500kV AC line [J]. Big Tech, 2013, 000 (034): 124-125. (in Chinese)
10. Zheng X, Jia R, Aisikaer, et al. Component identification and default detection in transmission lines based on deep learning [J]. Journal of Intelligent & Fuzzy Systems: Applications in Engineering and Technology, 2021 (2): 40.
11. Du Yong, Liu Tie, Tu Ming, Qin Shaoxian. Application of live working by helicopter platform method in EHV transmission lines [J]. Hubei Electric Power, 2012, 036 (004): 36-38. (in Chinese)
12. Hao H, Da C, Yongchun W (2010) Safety distance evaluation of helicopter live working. Hubei Electric Power 034(005):33–35 (in Chinese)
13. SHUAI L, NAN W, GUANGKAI Y, et al. Research on X-ray Detection Technology for Connection Fittings of UHV Transmission Lines based on helicopter live work; proceedings of the 5th International Conference on Electronics and Electrical Engineering Technology, EEET 2022, December 2, 2022 - December 4, 2022, Beijing, China, F, 2022 [C]. Institute of Electrical and Electronics Engineers Inc.

Study on Charge Accumulation Characteristics of Tri-post Insulators Under Temperature Gradient Field

Xinyuan He, Yan Shi, Wei Shi, Junran Jia, and Xiaolong Li

Abstract The insulator of DC gas-insulated transmission line (DC-GIL) will accumulate surface charge under the action of thermal-electric coupling field, which will cause local electric field distortion and make insulator flashover along the surface. In this paper, the actual GIL model is used for simulation. Based on the 3D horizontally mounted GIL model, the surface charge accumulation characteristics of transient DC GIL tri-post insulators under the action of thermal-electric coupling field are studied by COMSOL finite element simulation software. The results show that the surface charge density and the electric field intensity increase by 168 and 19.37% when the temperature gradient is considered at the same position on the belly of the tri-post insulator. Therefore, the distribution of surface charge and electric field under the action of temperature gradient field should be considered when designing and optimizing GIL tri-post insulators.

Keywords DC gas insulated transmission line · Tri-post insulator · Themal-electrical coupling

1 Introduction

With the construction of hydropower stations, trans-river transmission lines and urban integrated pipeline corridors, gas-insulated transmission lines have been widely used in power systems for their advantages of low loss, low environmental impact and high reliability [1–3]. Currently, GIL equipment has been widely used in AC power grid,

X. He · J. Jia · X. Li (✉)
Shenyang University of Technology, Shenyang 110870, China
e-mail: xiaolongli@sut.edu.cn

Y. Shi
State Grid Shandong Electric Power Company, Jinan 250001, China

W. Shi
Shandong Electric Power Research Institute, Jinan 250003, China

© Beijing Paike Culture Commu. Co., Ltd. 2024

X. Dong and L. Cai (eds.), *The Proceedings of 2023 4th International Symposium on Insulation and Discharge Computation for Power Equipment (IDCOMPU2023)*, Lecture Notes in Electrical Engineering 1102, https://doi.org/10.1007/978-981-99-7405-4_23

while its application in DC power grid is rarely reported [4]. The main reason is that under the action of DC voltage, GIL will produce surface charge accumulation on the surface of the insulator, and the accumulation of charge will cause local electric field distortion, resulting in the decrease of insulator flashover voltage [5].

Therefore, many scholars have conducted in-depth research on the characteristics of insulator surface charge accumulation under the action of temperature gradient. Winter et al. [6] considered the influence of temperature on the conductivity of insulating materials. The research shows that when the temperature of the insulating material is greater than 278 K, the dominant way of charge accumulation is through the body conduction of the insulating material, but the influence of convection and radiation on the interior of GIL is not considered in this study. Zhou et al. [7] studied the surface charge distribution under different temperature gradients and considered the influence of convection and radiation within GIL. The research shows that the surface charge accumulation of insulators is aggravated when temperature gradient exists.

The emphasis of the above work is to analyze the surface charge accumulation and electric field distribution of basin insulators under temperature gradient. In the actual operation of GIL, not only basin insulators but also tri-post insulators are used. Because of the geometry of the tri-post insulators, the electric field distribution of the tri-post insulator is more uneven than that of the basin insulator. The uneven distribution of electric field will lead to uneven distribution of charge on the surface of the three post insulators. Therefore, the existing research on basin insulators cannot be directly applied to the evaluation of the insulation of tri-post insulators.

In order to solve the above problems, a ± 500 kV three-dimensional tri-post insulators insulator simulation model is established in this paper. The surface charge and electric field distribution of a tri-post insulator in the presence of temperature gradient are studied. The research results can provide reference for the insulation evaluation of DC-GIL in long-term operation.

2 The Construction of Simulation Model

2.1 Geometric Model

In order to study the surface charge distribution of a tri-post insulator with temperature gradient, a three-dimensional geometric model is established. As shown in Fig. 1.

2.2 Principle of Heat Transfer

In this paper, the effects of convection, radiation and heat conduction on the interior of GIL are considered. The heat conduction is:

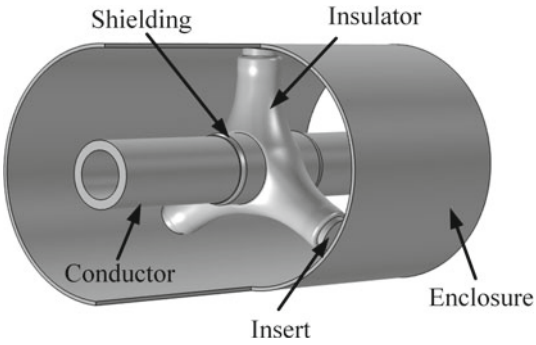

Fig. 1 GIL geometric model

$$pC_p \frac{\partial T}{\partial t} + \nabla \cdot (\boldsymbol{q} + \boldsymbol{q_r}) = Q \tag{1}$$

$$\boldsymbol{q} = -\kappa \nabla T \tag{2}$$

where: ρ is density; C_p is the specific heat capacity at constant pressure; $\boldsymbol{q}$ is the conduction heat flux; $\boldsymbol{q_r}$ is radiant heat flow; κ is thermal conductivity; T is the absolute temperature; Q is the extra heat source, which is zero for insulators and gases.

The effects of radiation between the high voltage guide rod and the insulator, between the insulator and the metal shell, and between the metal shell and the atmosphere are considered. As follows:

$$e_b(T) = n_r^2 \sigma_{SB} T^4 \tag{3}$$

$$q_r = \varepsilon_{se}[G - e_b(T)] \tag{4}$$

where, $e_b(T)$ is the radiated power of all wavelengths; nr is the refractive index; σ_{SB} is Stefan-Boltzmann constant; q_r is net inward radiant heat flux; ε_{se} is the surface emissivity; G is the incoming radiation heat flow.

Convection is a very important heat transfer mode in GIL, and Navier–Stokes equation is used to deal with convection in this model. The specific content of heat transfer can be referred to our previous research [8].

2.3 Charge Accumulation Principle

The current density in the insulating gas is shown below

$$\boldsymbol{J_G} = \frac{\partial \boldsymbol{D}}{\partial t} + e\boldsymbol{E}\left(n^+ b^+ + n^- b^-\right) - egrad\left(D^+ n^+ - D^- n^-\right) \tag{5}$$

where, ∂D/∂t is displacement current density; e is the primary charge; $\boldsymbol{E}$ is electric field intensity; n^+ and n^- are positive and negative ion concentrations respectively; b^+ and b^- are positive and negative ion mobility; D^+ and D^- are the diffusion rate of positive and negative ions.

The transport equation of ions is shown in Eqs. (6) and (7)

$$\frac{\partial n^+}{\partial t} = \frac{\partial n_{\mathrm{IP}}}{\partial t} - n^+ k_r n^- - b^+ \nabla \cdot \left(n^+ \boldsymbol{E}\right) + D^+ \nabla^2 n^+ \tag{6}$$

$$\frac{\partial n^-}{\partial t} = \frac{\partial n_{\mathrm{IP}}}{\partial t} - n^- k_r n^+ + b^- \nabla \cdot \left(n^- \boldsymbol{E}\right) + D^- \nabla^2 n^- \tag{7}$$

where, $\partial n_{\mathrm{IP}}/\partial t$ is the production rate, and its value can be obtained from [9]. k_r is the composite coefficient, whose value can be obtained from [10].

The relation between electric field and potential is shown in Eq. (8), the relationship between electric potential and positive and negative ions is expressed by Poisson equation

$$\boldsymbol{E} = -\nabla \varphi \tag{8}$$

$$\nabla^2 \varphi = -\frac{\rho}{\varepsilon} = -\frac{e\left(n^+ - n^-\right)}{\varepsilon} \tag{9}$$

where, ε is the dielectric constant.

The current density in an insulator can be expressed as:

$$\boldsymbol{J_I} = \frac{\partial \boldsymbol{D}}{\partial t} + \sigma_I(T)\boldsymbol{E} \tag{10}$$

where, $\sigma_I(T)$ is the bulk conductivity of the solid insulating material, whose value can be obtained from [11].

The charge on insulator surface is mainly conducted by the bulk conduction of insulating material, the gas conduction of insulating gas and the surface conduction of insulator surface. Therefore, the charge accumulation process at the gas–solid interface is represented by Eq. (11)

$$\frac{\partial \rho_s}{\partial t} = \boldsymbol{J_{In}} - \boldsymbol{J_{Gn}} - \nabla \cdot (\sigma_s \boldsymbol{E_t}) \tag{11}$$

where, ρ_s is surface charge density; $\boldsymbol{J_{In}}$ is the normal current density of the insulating material; $\boldsymbol{J_{Gn}}$ is the normal current density of the insulating gas; σ_s is the surface conductivity of the insulating material, and its value can be obtained from [11]. $\boldsymbol{E_t}$ is the surface tangential electric field.

2.4 Boundary Condition

The high voltage electrode and the ground electrode are arranged according to the first type of boundary conditions.

$$\varphi_{HV} = U \tag{12}$$

$$\varphi_{GND} = 0 \tag{13}$$

where, φ_{HV} is the potential of the guide bar; φ_{GND} is the potential of the grounding shell; U is the DC voltage applied; In this paper, $U = +500$ kV.

The boundary conditions of Eq. (6) and (7) of ion transport equation are defined according to the direction of current:

On the boundary of current outflow, the first type of boundary condition is set for the concentration of positive ions, and the second type of boundary condition is set for the concentration gradient of negative ions.

On the boundary of current inflow, the first type of boundary condition is set for the concentration of negative ions, and the second type of boundary condition is set for the concentration gradient of positive ions.

2.5 Model Verification

To ensure the correctness of the model, the experimental data in the paper of Winter et al. [6] were compared.

Figure 2 shows the comparison results between the simulated values and the experimental measured values at different times. By comparing with the experimental measured values, the simulated values have a good consistency with the experimental measured values.

3 Simulation Results and Analysis

3.1 Temperature Distribution of Insulators and Pipes

In this paper, the load current is 5000 A, SF_6 pressure is 0.5 MPa, and the ambient temperature is 20 °C. Steady-state temperature distribution of GIL pipeline and tri-post insulators is shown in Fig. 3.

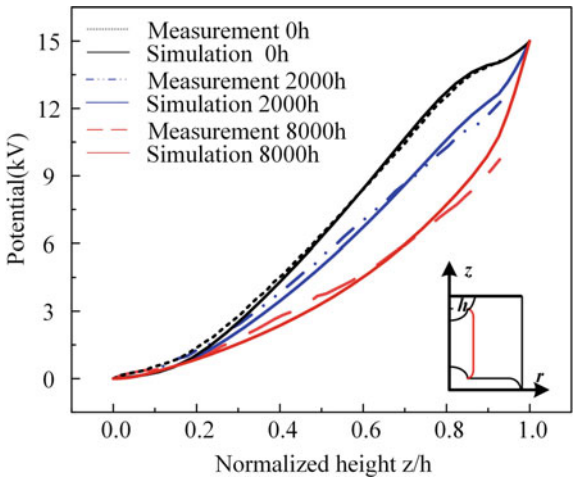

Fig. 2 Comparison of simulation calculated values with experimental measured values in [6]

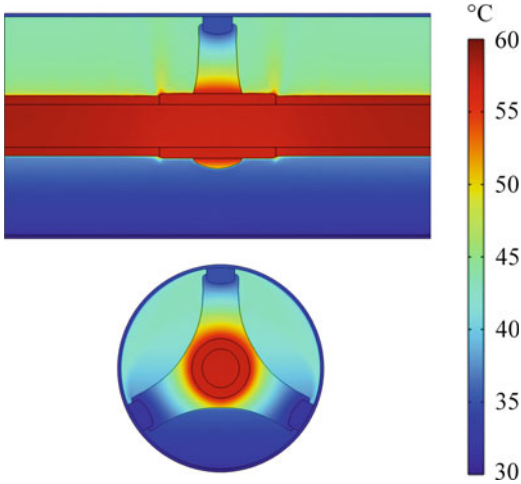

Fig. 3 Temperature distribution of GIL pipes and tri-post insulators

3.2 Accumulation Effect of Temperature Gradient on Insulator Surface Charge Accumulation

In this section, the surface charge distribution of a tri-post insulator under the action of a temperature gradient field is studied. The process of insulator charge accumulation is obtained under the load current of 5000 A and SF_6 pressure of 0.5 MPa. Taking no temperature gradient as the basis, the transient accumulation process of surface charge accumulation under the action of no temperature gradient field is compared, as shown in Fig. 4. The results were compared for 10, 50, 100, 1000, 8000 and

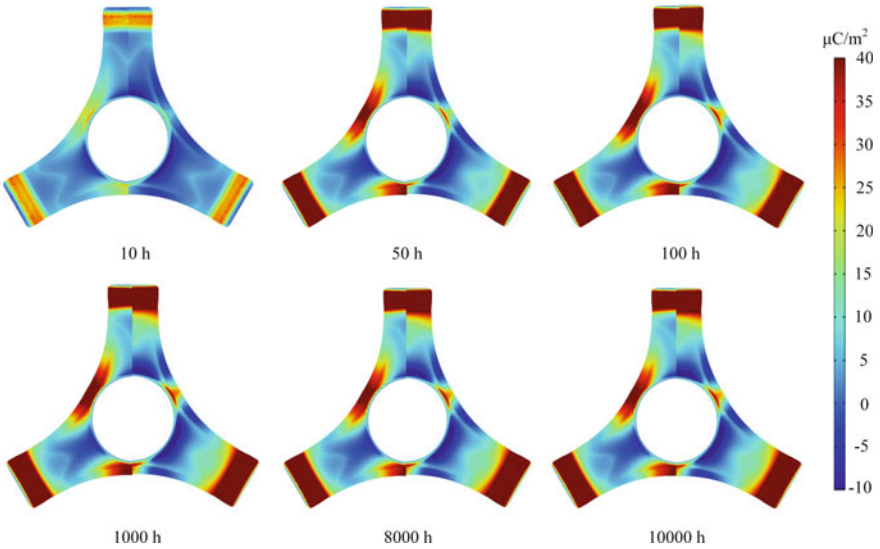

Fig. 4 Transient surface charge accumulation in a tri-post insulator

10,000 h. The left half of the figure indicates that there is a temperature gradient, and the right half indicates that there is no temperature gradient.

As shown in Fig. 4, when the influence of temperature gradient on surface charge is considered, the speed of charge accumulation is faster than that without consideration of temperature gradient, and the amount of charge accumulated under consideration of temperature gradient is also more than that without consideration of temperature gradient at the same time.

3.3 Surface Charge and Tangential Electric Field Distribution of Tri-post Insulators Under Temperature Gradient Field

The temperature distribution of the GIL pipe and insulator has been obtained in the previous subsection. In this section, the distribution of charge and electric field intensity on the surface of the tri-post insulator interface is compared when there is no temperature gradient. The ambient temperature without temperature gradient is set to 20 °C and SF_6 pressure to 0.5 MPa.

As shown in Fig. 5a, a large amount of positive charge accumulates on the surface of the tri-post insulator, and a small amount of negative charge accumulates near the ground housing. The charge density is higher in the presence of a temperature gradient than in the absence of a temperature gradient. When the temperature gradient is not considered, the surface charge density is 8.23 $\mu C/m^2$ with distance of about

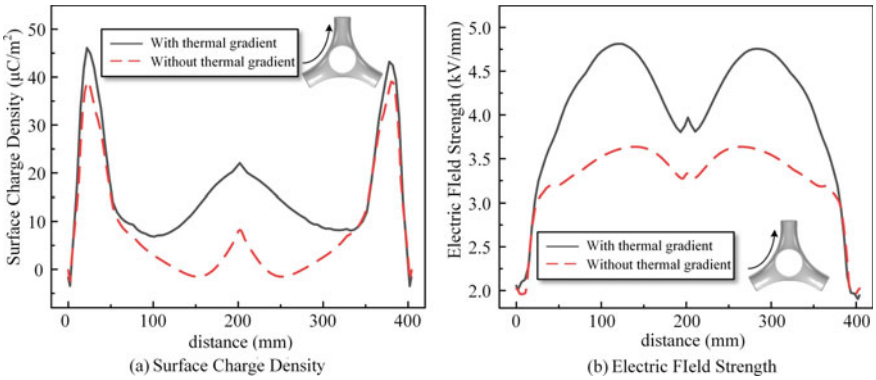

Fig. 5 Surface charge density and electric field distribution of insulator with or without temperature gradient in steady state

202 mm, and the peak surface charge density is 22.07 $\mu C/m^2$ at the same position with temperature gradient considered, which increases by 168%.

The actual working condition of GIL shows that surface flashover is a very easy fault for tri-post insulators, and the surface flashover voltage of insulators is closely related to tangential electric field intensity. As shown in Fig. 5b, compared with the condition without temperature gradient, tangential electric field intensity is higher in the condition with temperature gradient than in the condition without temperature gradient. When the temperature gradient is not taken into account, the tangential electric field intensity of distance of 202 mm is 2.22 kV/mm; when the temperature gradient is taken into account, the tangential electric field intensity of the same position is 2.64 kV/mm, increasing by 19.37%.

In conclusion, when the temperature gradient is considered, the surface charge density and tangential electric field intensity of the insulator are both higher than that when the temperature gradient is not considered. In addition, a large amount of charge accumulates at the position of the tri-post insulator near the guide bar, which will cause the electric field distortion at the position of the insulator near the guide bar. Therefore, it is necessary to consider the influence of surface charge and electric field distribution on temperature gradient in the optimal design of tri-post insulator structure.

4 Conclusion

In this paper, a DC GIL surface charge accumulation model was built. By comparing with the experimental data in the Winter paper, the simulation values were in good agreement with the experimental results, thus verifying the accuracy of the simulation model. The surface charge distribution of DC-GIL tri-post insulators under temperature gradient field was studied, and the amount of charge accumulated was

more than that without considering the temperature gradient. A large amount of positive charge accumulates on the surface of the tri-post insulator, and a small amount of negative charge accumulates near the ground housing.

When the temperature gradient is not considered, the surface charge density is 8.23 $\mu C/m^2$ with distance of 202 mm and 22.07 $\mu C/m^2$ with temperature gradient at the same position, which increases by 168%. The electric field intensity of 202 mm distance is 2.22 kV/mm, and the tangential electric field intensity of 2.64 kV/mm at the same position is increased by 19.37% when the temperature gradient is considered.

Acknowledgements This research is funded by the State Grid Company Headquarters Science and Technology Project "Research on Key Technology of GIS Internal Multispectral Optical Imaging Based on Optical Fiber Transmission" (5500-202216134A-1-1-ZN).

References

1. Li G et al (2020) Research progress of environment-friendly gas insulated pipe technology. Trans China Electrotech Soc 35(1):18 (in Chinese)
2. Zhang C, Zhang B, Li M et al (2023) Research review on key insulation technologies of high voltage direct current GIL equipment. High Voltage Technol 49(03):920–936 (in Chinese)
3. Xing YQ, Liu L, Xu Y, Yang Y, Li CY (2021) Defects and failure types of solid insulation in gas insulated switchgear: in situ study and case analysis. High Volt
4. Tenzer M, Koch H, Imamovic D (2016) Underground transmission lines for high power AC and DC transmission. In: 2016 IEEE/PES transmission and distribution conference and exposition (T&D). IEEE, 2016
5. Okabe S (2007) Phenomena and mechanism of electric charges on spacers in gas insulated switchgears. IEEE Trans Dielectr Electr Insul 14(1):46–52
6. Winter A, Kindersberger J (2014) Transient field distribution in gas-solid insulation systems under DC voltages. IEEE Trans Dielectr Electr Insul 21(1):116–128
7. Zhou HY, Ma GM, Li CR, Shi C, Qin SC (2017) Impact of temperature on surface charges accumulation on insulators in SF6-filled DC-GIL. IEEE Trans Dielectr Electr Insul 24(1):601–610
8. Chen G, Tu Y, Wang C, Cheng Y, Jiang H, Zhou H, Jin H (2018) Analysis on temperature distribution and current-carrying capacity of GIL filled with fluoronitriles-CO_2 gas mixture. J Electr Eng Technol 13(6):2402–2411
9. Kindersberger J, Wiegart N, Boggs SA (1985) Ion production rates in SF6 and the relevance thereof to gas-insulated switchgear. In: Conference on electrical insulation & dielectric phenomena-annual report 1985. IEEE
10. Morrow R (1986) A survey of the electron and ion transport properties of SF6. IEEE Trans Plasma Sci 14(3):234–239
11. Yan SY (2022) Study on the effect of electrothermal complex field on insulator surface charge accumulation in SF6. Shenyang University of Technology, Shenyang, pp 21–27, 2022 (in Chinese)

Study on Charge Accumulation Characteristics of Basin Insulators with Polarity Reversal

Xinyuan He, Yan Shi, Jie Li, Junran Jia, and Xiaolong Li

Abstract The insulator of a DC gas-insulated transmission line (DC-GIL) will accumulate surface charge under the action of polarity reversal, leading to the risk of flashover. In this paper, the actual GIL model was used for simulation. Based on the 3D horizontally mounted GIL model, COMSOL finite element simulation software was used to study the surface charge accumulation characteristics of DC GIL basin insulators under the action of polarity reversal. In order to prove the correctness of the mathematical model, the same model as A. Winter et al. was established and compared with the experimental data to verify the correctness of the mathematical model in this paper. The results show that the surface charge density of the insulator is almost constant during the voltage polarity reversal process. When the reversal time is 60 s, the surface electric field intensity of the convex surface of the basin insulator increases by 23.7% and that of the concave surface increases by 33.2% compared with the steady state before and after reversal. As a result, flashover is more likely to be triggered during voltage polarity reversal.

Keywords DC gas insulated transmission line · Basin insulator · Polarity reversal

1 Introduction

Gas insulated transmission line (GIL) has been widely used in power system because of its advantages of large transmission capacity, low unit loss and small footprint [1]. Insulators are the most core part of GIL but also the most vulnerable part.

X. He · J. Jia · X. Li (✉)
Shenyang University of Technology, Shenyang 110870, China
e-mail: xiaolongli@sut.edu.cn

Y. Shi
State Grid Shandong Electric Power Company, Jinan 250001, China

J. Li
Shandong Electric Power Research Institute, Jinan 250003, China

© Beijing Paike Culture Commu. Co., Ltd. 2024

X. Dong and L. Cai (eds.), *The Proceedings of 2023 4th International Symposium on Insulation and Discharge Computation for Power Equipment (IDCOMPU2023)*, Lecture Notes in Electrical Engineering 1102, https://doi.org/10.1007/978-981-99-7405-4_24

Ensuring the long-term stable operation of the insulator also ensures the long-term stability of the GIL [2]. The electric field distribution of insulators is affected by the surface charge distribution, and the amount of surface charge accumulation directly affects the insulation level of GIL. In recent years, many scholars have studied the characteristic of charge accumulation indicated by GIL. Among them, Winter [3] and Straumann [4] et al. show through simulation and calculation that the process of surface charge accumulation on insulators will last for thousands of hours. However, in the actual measurement, the voltage duration applied to the guide bar is very short. Therefore, when exploring the influence of surface charge accumulation on GIL insulators, simulation calculation has more advantages than actual measurement.

There are many factors that determine the flashover voltage of a basin insulator, such as the shape and structure of the insulator, the enhancement of local electric field strength, or the pollution of the insulator surface, etc. [5]. However, insulator surface flashover caused by electric field distortion has been restricting the development of GIL. In HVDC transmission systems, it is necessary to reverse the polarity of the DC voltage in the GIL for necessary maintenance and testing. Therefore, polarity reversal is a common operation in engineering practice [6]. A study has shown that voltage polarity reversal has no effect on the breakdown characteristics of insulators [7]. Another study shows that the breakdown characteristics of insulators will be affected after the voltage polarity reversal [8]. At present, the effect of GIL polarity reversal on the surface charge accumulation of insulators is still controversial.

Taking ± 200 kV basin insulator as the research object, a 3D simulation model is established in this paper. The surface charge and tangential electric field intensity distribution of insulator under polarity reversal operation are studied. The research results provide a reference for the insulation performance of DC GIL insulators during long-term operation.

2 The Construction of Simulation Model

2.1 Geometric Model

In order to study the surface charge distribution under polarity reversal, a 3D geometric model is established. See Fig. 1.

2.2 Charge Accumulation Principle

The current density in the insulating gas is shown below

$$\boldsymbol{J_G} = \frac{\partial \boldsymbol{D}}{\partial t} + e\boldsymbol{E}\left(n^+ b^+ + n^- b^-\right) - egrad\left(D^+ n^+ - D^- n^-\right) \tag{1}$$

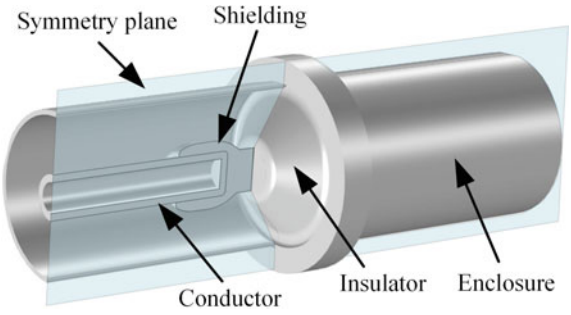

Fig. 1 GIL geometric model

where, ∂D/∂t is displacement current density; e is the primary charge; $\boldsymbol{E}$ is electric field intensity; n^+ and n^- are positive and negative ion density; b^+ and b^- are positive and negative ion mobility; D^+ and D^- are the diffusion rate of positive and negative ions.

The transport equation of ions is shown in Eqs. (2) and (3)

$$\frac{\partial n^+}{\partial t} = \frac{\partial n_{IP}}{\partial t} - n^+ k_r n^- - b^+ \nabla \cdot \left(n^+ \boldsymbol{E}\right) + D^+ \nabla^2 n^+ \tag{2}$$

$$\frac{\partial n^-}{\partial t} = \frac{\partial n_{IP}}{\partial t} - n^- k_r n^+ + b^- \nabla \cdot \left(n^- \boldsymbol{E}\right) + D^- \nabla^2 n^- \tag{3}$$

where, $\partial n_{IP}/\partial t$ is the production rate, and its value can be obtained from [9]. k_r is the composite coefficient, whose value can be obtained from [10].

The relation between electric field and potential is shown in Eq. (4), the relationship between electric potential and positive and negative ions is expressed by Poisson equation

$$\boldsymbol{E} = -\nabla\varphi \tag{4}$$

$$\nabla^2\varphi = -\frac{\rho}{\varepsilon} = -\frac{e\left(n^+ - n^-\right)}{\varepsilon} \tag{5}$$

where, ε is the dielectric constant.

The current density in an insulator can be expressed as:

$$\boldsymbol{J_I} = \frac{\partial \boldsymbol{D}}{\partial t} + \sigma_I \boldsymbol{E} \tag{6}$$

where, σ_I is the bulk conductivity of the solid insulating material, whose value can be obtained from [11].

The charge on insulator surface is mainly conducted by the bulk conduction of insulating material, the gas conduction of insulating gas and the surface conduction of insulator surface. Therefore, the charge accumulation process at the gas–solid

interface is represented by Eq. (7)

$$\frac{\partial \rho_s}{\partial t} = \boldsymbol{J_{In}} - \boldsymbol{J_{Gn}} - \nabla \cdot (\sigma_s \boldsymbol{E_t}) \tag{7}$$

where, ρ_s is surface charge density; $\boldsymbol{J_{In}}$ is the normal current density of the insulating material; $\boldsymbol{J_{Gn}}$ is the normal current density of the insulating gas; σ_s is the surface conductivity of the insulating material, and its value can be obtained from [11]. $\boldsymbol{E_t}$ is the surface tangential electric field.

2.3 Boundary Condition

The high voltage electrode and the ground electrode are arranged according to the first type of boundary conditions.

$$\varphi_{HV} = U \tag{8}$$

$$\varphi_{GND} = 0 \tag{9}$$

where, φ_{HV} is the potential of the guide bar; φ_{GND} is the potential of the grounding shell; U is the DC voltage applied; In this paper, $U = +200$ kV.

When the voltage waveform diagram shown in Fig. 2 is applied to the high voltage conductor, the corresponding boundary conditions need to be adjusted during the polarity reversal process.

The boundary conditions of Eqs. (2) and (3) of ion transport equation are defined according to the direction of current.

On the boundary of current outflow, the first kind of boundary conditions is set for the concentration of positive ions, and the second kind of boundary conditions is set for the concentration gradient of negative ions.

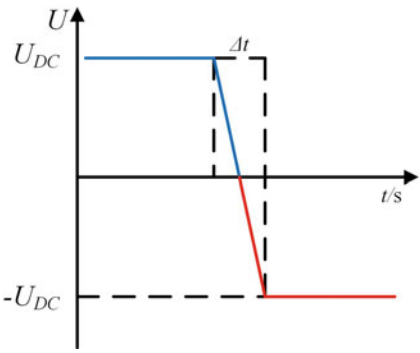

Fig. 2 Voltage waveform under polarity reversal

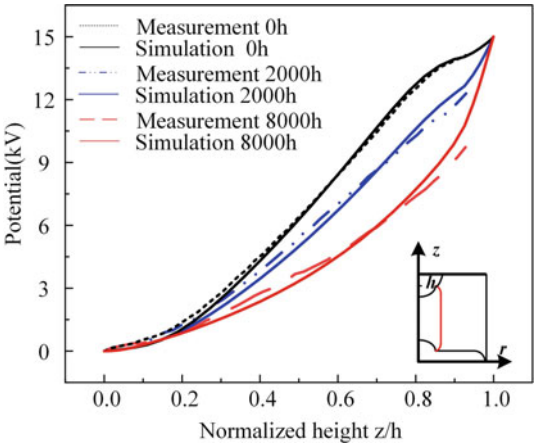

Fig. 3 Comparison of simulation calculated values with experimental measured values in [3]

On the boundary of current inflow, the first kind of boundary conditions is set for the concentration of negative ions, and the second kind of boundary conditions is set for the concentration gradient of positive ions.

2.4 Model Verification

In order to ensure the correctness of the model of GIL surface charge accumulation, the experimental data in the paper of Winter et al. [3] were compared.

Figure 3 shows the comparison results between the simulated values and the experimental measured values at different times. By comparing with the experimental measured values, the simulated values have a good consistency with the experimental measured values.

3 Simulation Results and Analysis

3.1 Surface Charge Accumulation Under Polarity Reversal

Under the voltage waveform in Fig. 2, the precompression time is 1000 h, and the inversion time is $\Delta t = 60$ s. The surface charge density of the concave-convex surface of an insulator in the polarity reversal process is shown in Fig. 4. Defined distance 0 represents the connection point between the shell and the insulator.

As can be seen from Fig. 4a, under the effect of polarity reversal voltage waveform, a large amount of positive charge was accumulated on the convex surface of GIL insulator near the shell before reversal, while a small amount of negative charge was

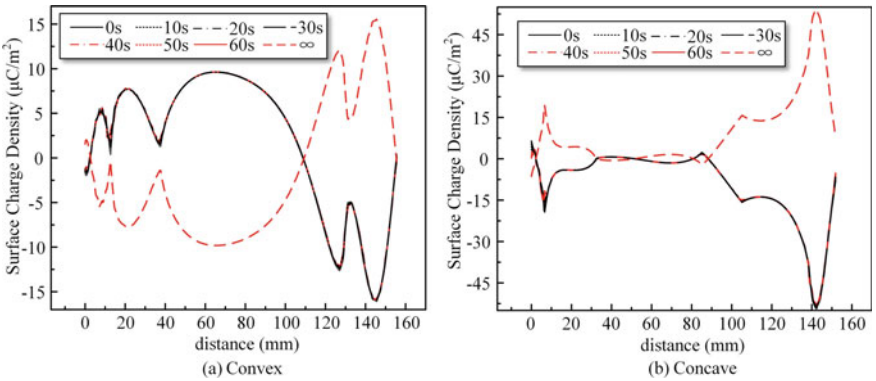

Fig. 4 Surface charge density of concave and convex surface of basin insulator

accumulated near the guide bar. The accumulated surface charge basically remained unchanged in the process of polarity reversal, and reached another steady state after polarity reversal. A convex insulator carries the same amount of charge as the steady state before the reversal but the polarity of the charge is reversed.

As can be seen from Fig. 4b, the amount of charge that reaches the steady state after the inversion of the concave insulator is the same as that before the inversion (0 s), but the polarity of the accumulated charge is opposite.

3.2 Electric Field Distribution of Insulator Along Surface

The long-term GIL actual operation experience shows that the flashover along the surface of the insulator is the most common fault [12], and the flashover voltage along the surface is related to the tangential electric field along the insulator. Therefore, in this paper, the tangential electric field along the surface of the concave and convex surface of the GIL insulator under the influence of the surface charge is calculated under the polarity reversal waveform, as shown in Fig. 5.

As shown in Fig. 5, tangential electric field of insulator along the convex surface gradually increases during the polarity reversal process, while steady-state value of tangential electric field before and after the reversal is almost the same. When the reversal time is 60 s, for the convex surface of the insulator, it can be seen from Fig. 5a that the tangential electric field intensity reaches its maximum value at 2.40 kV/mm when the distance is about 108 mm. The tangential field strength of the same position in the stable state before and after inversion is 1.94 kV/mm, which increases by 23.7%. For the concave surface of the insulator, it can be seen from Fig. 5b that the maximum tangential electric field occurs at the distance of about 97 mm, and its value is 2.85 kV/mm. The tangential field strength at the same position in the stable state before and after inversion is 2.14 kV/mm, which increases by 33.2%. As

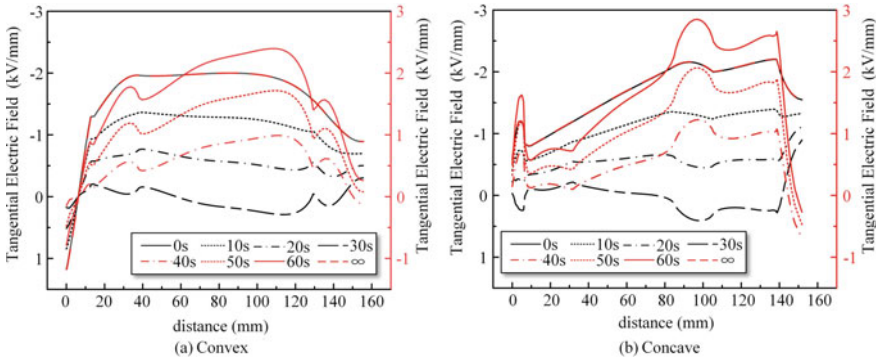

Fig. 5 Tangential electric field strength of concave-convex insulator

a result, flashover is more likely to occur after a polarity reversal. The reason for this phenomenon is that before the polarity reversal operation, most of the surface charge on the insulator is positive.

3.3 Surface Electric Field Distribution Under Different Pre-applied Voltage Time

As the surface flashover voltage is related to the tangential field strength along the surface, it is the most likely time for flashover to occur when the reversal time is 60 s. Therefore, the influence of different pre-applied voltage (PVT) on tangential field strength along the concave and convex surfaces was compared, as shown in Fig. 6.

It can be seen from Fig. 6a that the maximum tangential electric field increases with the increase of the pre-applied voltage, which is 10 h. Compared with 60 s before the

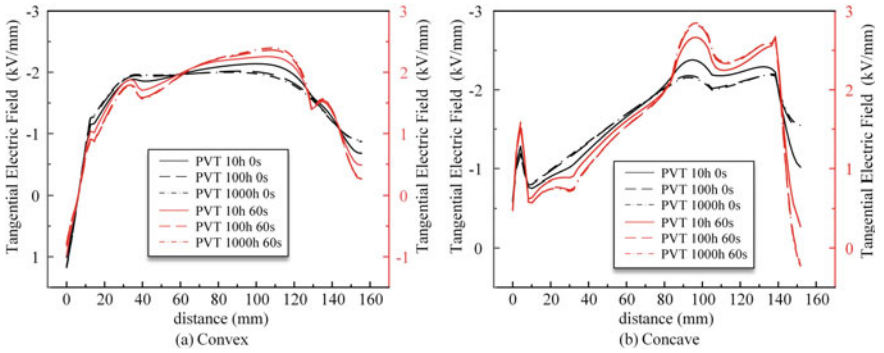

Fig. 6 Tangential electric field intensity of insulator concave-convex surface under different pre-applied voltage time

reversal of the convex surface, the maximum tangential electric field in the stable state increases from 2.14 kV/mm to 2.26 kV/mm, with an increase of 5.61%. Similarly, the concave surface increased from 2.38 kV/mm to 2.72 kV/mm, an increase of 14.29%. When the pre-applied voltage time is 100 h, the maximum tangential field strength in the stable state before convex reversal increases from 2.19 kV/mm to 2.36 kV/mm by 7.76% compared with the reversal time of 60 s. Similarly, the concave surface increased from 2.19 kV/mm to 2.82 kV/mm, an increase of 28.77%. The pre-applied voltage time was 1000 h, and the maximum tangential field strength increased from 2 kV/mm to 2.40 kV/mm in numerical value by 20% compared with 60 s in stable state before convex reversal. Similarly, the concave surface increased from 2.2 kV/mm to 2.85 kV/mm, an increase of 29.55%.Therefore, with the increase of pre-applied voltage time, the maximum tangential electric field on the insulator surface also increases.

4 Conclusion

In this paper, a DC GIL surface charge accumulation model was built. By comparing with the experimental data in the Winter paper, the simulation values were in good agreement with the experimental results, thus verifying the accuracy of the simulation model. The surface charge distribution of DC GIL insulator under polarity reversal operation is analyzed. During the reversal time of 60 s, the amount of surface charge on the concave-convex surface of the insulator basically remained unchanged, and the amount of charge on the concave and convex surfaces of the insulator is basically the same but the polarity is opposite when the insulator reaches steady state before and after inversion.

In the process of voltage polarity reversal, the stable tangential field intensity before and after reversal is almost equal. When the reversal time is 60 s, for the convex surface of the insulator, the distance is about 108 mm, and the tangential electric field intensity reaches the maximum value of 2.40 kV/mm, while the tangential electric field at the same position in the stable state before and after reversal is 1.94 kV/mm, which increases by 23.7%. The maximum tangential electric field occurs when the concave distance of the insulator is about 97 mm, and its value is 2.85 kV/mm The tangential electric field at the same position in the stable state before and after inversion is 2.14 kV/mm, which increases by 33.2%. The tangential field strength is also affected by different pre-applied voltage time, and the tangential field strength increases with the increase of pre-applied voltage time.

Acknowledgements This research was supported by the Science and Technology Special Project of State Grid Corporation Headquarters “Research on Key Technologies of GIS Internal Multispectral Optical Imaging Based on Optical Fiber Transmission” (5500-202216134A-1-1-ZN).

References

1. Koch H (2014) Gas insulated transmission lines (GIL). John Wiley and Sons, Chichester, UK, pp 4–5
2. Xing YQ et al (2021) Metal particle induced spacer surface charging phenomena in direct current gas-insulated transmission lines. J Phys D, Appl Phys 54(34), Art. No. 34LT03
3. Winter A, Kindersberger J (2014) Transient field distribution in gas-solid insulation systems under DC voltages. IEEE Trans Dielectr Electr Insul 21(1):116–128
4. Straumann U, Schüller M, Franck CM (2012) Theoretical investigation of HVDC disc spacer charging in SF6 gas insulated systems. IEEE Trans Dielectr Electr Insul 19(6):2196–2205
5. Sundararajan R, Gorur RS (1994) Effect of insulator profiles on DC flashover voltage under polluted conditions. A study using a dynamic arc model. IEEE Trans Dielectr Electr Insul 1:124–132
6. Du BX, Ran ZY, Li J, Liang HC, Yao H (2020) Fluorinated epoxy insulator with interfacial conductivity graded material for HVDC gaseous insulated pipeline. IEEE Trans Dielectr Electr Insul 27(4):1305–1312
7. Luo Y, Tang J, Pan C, Pan Z, Li Y, Cui Z (2020) Dynamics of surface charge and electric field distributions on basin-type insulator in GIS/GIL due to voltage polarity reversal. High Voltage 5(2):151–159
8. Nakanishi K, Yoshioka A, Arahata Y, Shibuya Y (1983) Surface charging on epoxy spacer At DC stress in compressed SF6 gas. IEEE Trans Power App Syst, PAS-102(12):3919–3927
9. Kindersberger J, Wiegart N, Boggs SA (1985) Ion production rates in SF6 and the relevance thereof to gas-insulated switchgear. In: Conference on electrical insulation & dielectric phenomena—annual report 1985. IEEE
10. Morrow R (1986) A survey of the electron and ion transport properties of SF6. IEEE Trans Plasma Sci 14(3):234–239
11. Yan SY (2022) Study on the effect of electrothermal complex field on insulator surface charge accumulation in SF6. Shenyang University of Technology, Shenyang, pp 21–27 (in Chinese)
12. Yan Z, Zhu DH (2002) High voltage insulation technology. China Electric Power Press, Beijing

Compressive Strength Analysis of Capacitor Metal Shell

Weihua Zhong, Qingjiang Li, and Jungang Wang

Abstract Aiming at the bulging deformation phenomenon during the operation of the capacitor, the finite element simulation software is used to analyze the compressive strength of the capacitor metal shell from two aspects of deformation and stress value. Considering the geometric nonlinearity and material nonlinearity of the structure, the response law of the shell under different internal pressures is explored. It is found that the deformation of the wide side of the capacitor shell is the most significant, and the deformation on the shell surface decreases from the middle area to the periphery. The stress near the area of corner angle of the shell is more concentrated. The simulation results are consistent with the deformation trend of the shell in the actual air charging test, which verifies the accuracy of the calculation model. This paper has practical guiding significance for the structural optimization design of capacitors.

Keywords Capacitor metal shell · Compressive strength · Finite element simulation · Stress analysis

1 Introduction

There are many kinds of power capacitors [1, 2], which play an important role in reactive power compensation [3], harmonic filtering [4], and power quality improvement in power system [5–7]. The shell is one of the most important parts of the capacitor [8]. From the inside of the capacitor, when the partial discharge or short circuit fault

W. Zhong (✉) · Q. Li · J. Wang
China Southern Power Grid Co., Ltd., Guangzhou 510663, Guangdong, China
e-mail: zhongwh@csg.com

Q. Li
e-mail: liqj@csg.com

J. Wang
e-mail: wangjg@csg.com

© Beijing Paike Culture Commu. Co., Ltd. 2024

X. Dong and L. Cai (eds.), *The Proceedings of 2023 4th International Symposium on Insulation and Discharge Computation for Power Equipment (IDCOMPU2023)*, Lecture Notes in Electrical Engineering 1102, https://doi.org/10.1007/978-981-99-7405-4_25

occurs during the operation of the capacitor, the insulating medium deteriorates and decomposes to produce a large amount of gas, resulting in an increase in the internal pressure of the sealed capacitor, which cause the obvious bulging deformation of the capacitor shell [9, 10]. When the internal pressure reaches a high value, it will lead to the failure of the strength or stability of the shell. In severe cases, it will cause the capacitor burst or even catch fire, damaging the surrounding electrical equipment [11, 12]. From the outside of the capacitor, the shell, as the first line of defense to protect the internal components of the capacitor from external shocks, should have sufficient sealing and mechanical strength.

Based on the above reasons, it is vital to study the compressive strength characteristics of the capacitor shell. In this paper, the response characteristics of the capacitor shell under different static loads are analyzed by applying a static constant internal pressure to the capacitor shell. Considering the strength check of the pressure shell from two aspects of deformation and stress distribution, it can provide reference for the structural design, safety evaluation and failure analysis of the capacitor.

2 Calculation Method and Principle

2.1 Calculation Method

In order to study the compressive strength characteristics of the sealed metal shell of the capacitor, a three-dimensional calculation model is established according to the structure of the actual capacitor shell, and the material parameters are given. The static normal pressure is applied to the inner surface of the shell to solve the deformation and stress distribution of the shell under different internal pressures. The specific calculation process is shown in Fig. 1.

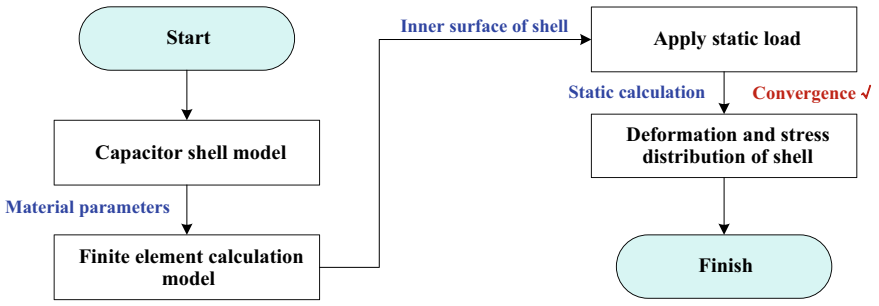

Fig. 1 Calculation flow chart

2.2 Calculation Principle

Under the action of internal pressure, the capacitor shell will exceed the yield strength of the material itself and produce large deformation. This process includes two kinds of nonlinear structural analysis problems: geometric nonlinearity and material nonlinearity, that is, the stiffness matrix $[k]$ in the dynamic equation of the equilibrium state will change due to the change of displacement [13, 14]. Incremental method can be used to obtain the tangential stiffness of the structural elements at each moment, so that the stress of the shell at any moment can be understood.

The principle of virtual work is valid for any type of nonlinear problem [15], that is, the virtual work done by the node force on the nodal virtual displacement should be equal to the virtual strain energy of the element, so the virtual work equation is expressed as:

$$\int_V \left\{\varepsilon^*\right\}^T \{\sigma\} dV - \left\{u^{e*}\right\}^T \left\{F^e\right\} = 0 \tag{1}$$

where, $\{u^{e^*}\}$ is the virtual displacement vector, $\{\varepsilon^*\}$ is the virtual strain $\{\sigma\}$ is the real stress of the shell element e, and $[F^e]$ is the force vector.

The geometric equation is satisfied between the virtual strain and the virtual displacement of the corresponding node:

$$\left\{\varepsilon^*\right\} = [B]\left\{u^{e*}\right\} = ([B_0] + [B_L])\left\{u^{e*}\right\} \tag{2}$$

where, $[B]$ is the strain matrix, which is composed of two parts: the part $[B_0]$ independent of the node displacement and the part $[B_L]$ related to the node displacement.

After the shell element enters the plastic deformation stage, its stress–strain relationship no longer satisfies the generalized Hooke's law, but is determined by the elastic–plastic matrix. The expression is:

$$d\{\sigma\} = \left[D_{ep}\right] d\{\varepsilon\} = \left([D] - \left[D_p\right]\right) d\{\varepsilon\} \tag{3}$$

where, $[D]$ is the elastic matrix, $[D_p]$ is the plastic matrix, and $[D_{ep}]$ is the elastic–plastic matrix.

The element strain matrix $[B]$ and stress $\{\sigma\}$ are both functions of displacement. Substituting Eqs. (2) and (3) into the differential form of Eq. (1), the element stiffness equation with incremental form can be obtained as follows:

$$\begin{cases} [k_T] d\{u^e\} = d\{F^e\} \\ [k_T] = [k_\sigma] + [k_0] + [k_L] - [k_R] \end{cases} \tag{4}$$

where, $[k_T]$ is the tangent stiffness matrix of the shell element, which represents the instantaneous stiffness of the element at a certain deformation position. $[k_\sigma]$ is the

initial stress stiffness matrix. $[k_0]$ is the main tangent stiffness matrix independent of the element node displacement. $[k_L]$ is the initial displacement stiffness matrix. $[k_R]$ is the load correction matrix of the element.

3 Calculation Model and Parameter Setting

3.1 Calculation Model and Mesh Generation

According to the actual capacitor structure, the shell model is established as shown in Fig. 2a. In the modeling process, the model is simplified as follows: (1) Ignore the pressure relief valve at the top of the shell and the external outlet casing; (2) Ignore small structures such as anchor bolts used to meet the installation requirements.

The bottom surface of the capacitor shell is 685 mm long and 175 mm wide, and the overall height is 920 mm. The thickness of the shell cover and the shell bottom is 3 mm, and the thickness of the other surrounding shell walls is 2 mm. Meshing the built capacitor shell model. Since the thickness of the shell is only 2 or 3 mm, and the maximum longitudinal size of the capacitor is as high as 920 mm, the difference between the vertical and horizontal dimensions is huge. Therefore, if the tetrahedral mesh is used for free subdivision, the number of overall meshes will be too much, which greatly increases the calculation time. For a model of the same size, the hexahedral mesh division can greatly reduce the number of element nodes. Therefore, the hexahedral mesh division is carried out for the shell model, and three-layer mesh element in the thickness direction is ensured. While reducing the number of meshes, the calculation efficiency can be improved, and the stress change in the thickness direction of the shell is considered. The overall meshing and local details of the shell are shown in Fig. 2b. The total number of mesh elements of the capacitor shell is 363,507.

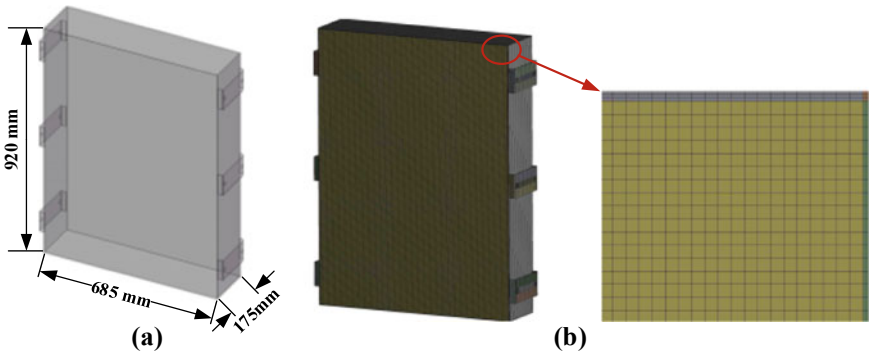

Fig. 2 Calculation model and mesh generation of capacitor shell

3.2 Material Parameter

The capacitor shell is made of stainless steel sheet, and the specific parameters of the material are shown in Table 1. Since 304 stainless steel is a plastic metal, when the stress is greater than the yield strength, plastic deformation that cannot be restored will occur. At this time, the relationship between stress and strain is no longer linear, as shown in Fig. 3a. The bilinear isotropic hardening model is proposed to simulate the nonlinear properties of the material, that is, the stress–strain relationship of the material is characterized by two lines. It is considered that the stress and strain of the material are proportional to the elastic modulus before yielding, and proportional to the tangent modulus after reaching the yield strength, as shown in Fig. 3b.

4 Calculation Results and Analysis

A wide side with the size of 685 × 920 mm on the capacitor shell is fixed constraint and the internal pressure of the shell is set to change in the range of 0–90 kPa. The maximum deformation of the shell and the maximum equivalent stress varying with the internal pressure are shown in Fig. 4. It can be seen from Fig. 4 that with the increase of internal pressure, the deformation of the shell increases obviously. while

Table 1 Material parameter

Material	Parameter	Value
304 Stainless steel	Density (g/cm^3)	7.75
	Elastic modulus (GPa)	193
	Tangent modulus (GPa)	1.8
	Poisson ratio	0.31
	Yield strength (MPa)	210

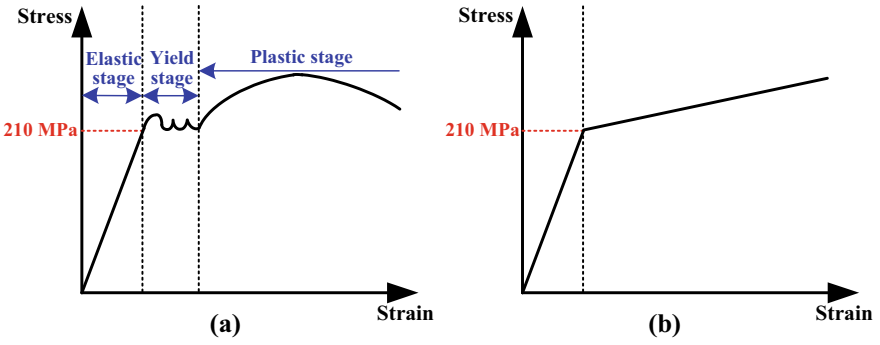

Fig. 3 Bilinear isotropic hardening material model

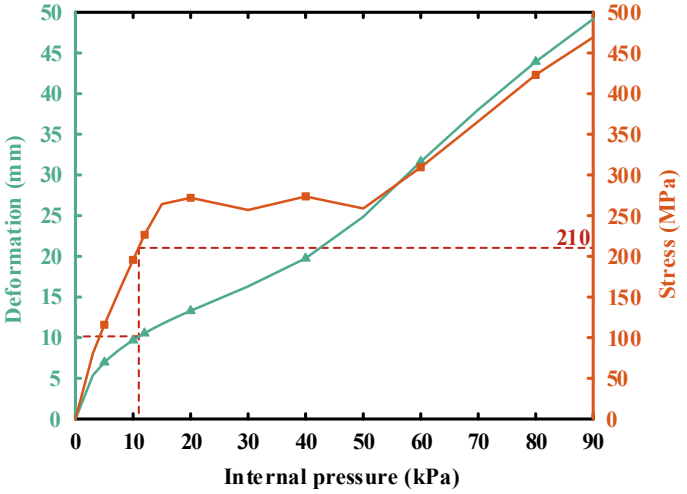

Fig. 4 The maximum deformation and equivalent stress change curve of the shell

the stress increases first, then fluctuates slightly, and then continues to increase. When the internal pressure is 11 kPa, the maximum deformation of the shell is 10.11 mm, and the maximum stress is 211.10 MPa. At this time, the maximum stress on the shell is close to the yield strength of the stainless steel material of 210 MPa.

Further analysis shows that when the internal pressure is less than 11 kPa, the deformation on the capacitor shell is elastic deformation. That is, after the internal pressure disappears completely, the shell can return to its original shape. As the internal pressure is between 11 and 55 kPa, the deformation of the shell still shows a significant increasing trend, while the stress value fluctuates slightly, indicating that the shell is in the yield stage, also known as the elastic–plastic deformation stage. After the internal pressure is removed at this stage, the deformation of the shell can only be partially restored, and some residual plastic deformation will still be retained. And some areas of the shell regain the ability to resist deformation and begin to produce uniform plastic deformation when the internal pressure exceeds 55 kPa.

According to Fig. 4, the deformation growth rate of the shell in the elastic stage is about 0.48 mm/kPa, which is 0.64 mm/kPa in the plastic stage. Since the elastic modulus represents the difficulty level of the elastic deformation of the material, under the action of a certain force, the larger the elastic modulus, the smaller the elastic deformation. Furthermore, as can be observed from Fig. 3, the stress–strain relationship of the material in the plastic stage varies in proportion to the tangential modulus, while the tangential modulus is smaller than the elastic modulus value. In other words, the material is more prone to deformation in the plastic stage, so the deformation growth rate of the shell in the plastic stage is higher than that in the elastic stage.

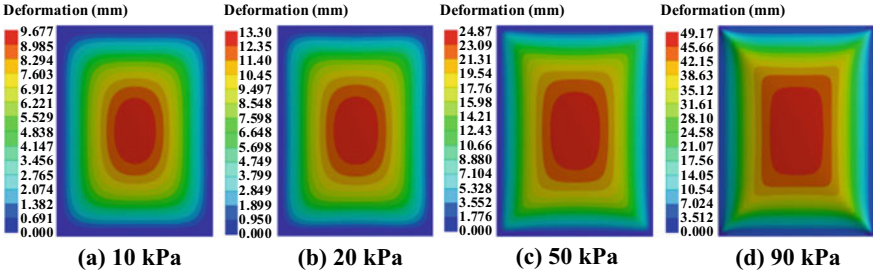

Fig. 5 Deformation distribution of the shell

4.1 Deformation Analysis

The deformation distribution of the shell is shown in Fig. 5 when the internal pressure is 10 kPa, 20 kPa, 50 kPa and 90 kPa respectively.

It can be known from Fig. 5 that when the shell is subjected to different internal pressures, it shows bulging deformation, and the maximum deformation is located on the other wide side opposite to the fixed surface. In addition, the deformation of the middle region of the shell surface is the most significant, especially the bulging, and the deformation decreases from the middle to the periphery. With the increase of internal pressure, the deformation of the shell tends to increase, while the qualitative regularity of the deformation distribution does not alter, and the range of deformation on the shell is expanding.

4.2 Stress Analysis

The equivalent stress distribution of the shell is shown in Fig. 6 when the internal pressure is 10 kPa, 20 kPa, 50 kPa and 90 kPa respectively.

From Fig. 6, it can be noticed that the stress on the corners of the inner shell of the capacitor is the most concentrated under the action of any internal pressure. With

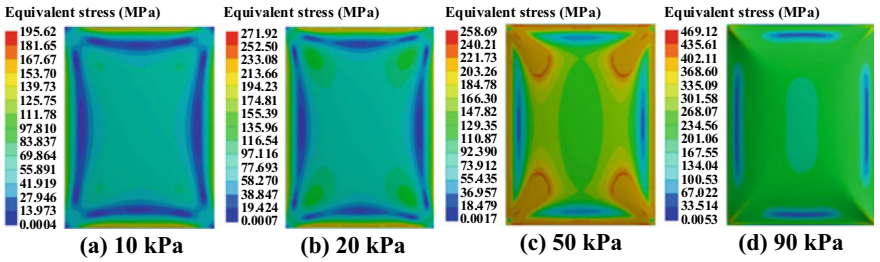

Fig. 6 Equivalent stress distribution of the shell

the increase of internal pressure, the stress of the region near the four right angles on the shell surface increases significantly. And the maximum stress of the whole shell is located on the edge of the inner shell surface near the right-angle area. Further analysis shows that the bulging deformation occurs when the shell is subjected to internal pressure, and the angular area around the shell is in a tensile state due to the large deformation of the middle part of the shell surface. Meanwhile, due to the geometric shape, the stress area is small, so it is easy to produce the phenomenon of stress concentration.

4.3 Experimental Verification

The air charging test of the capacitor shell shown in Fig. 2 is carried out as shown in Fig. 7. There is an air inlet for gas access on the top of the shell cover, and the pressure regulating valve can be adjusted to set different sizes of internal pressure. It can be found from Fig. 7 that after the sealed capacitor shell is filled with a certain pressure of gas, obvious bulging deformation occurs on the wide side of the shell, which is consistent with the finite element analysis results, and verifies the accuracy of the simulation model.

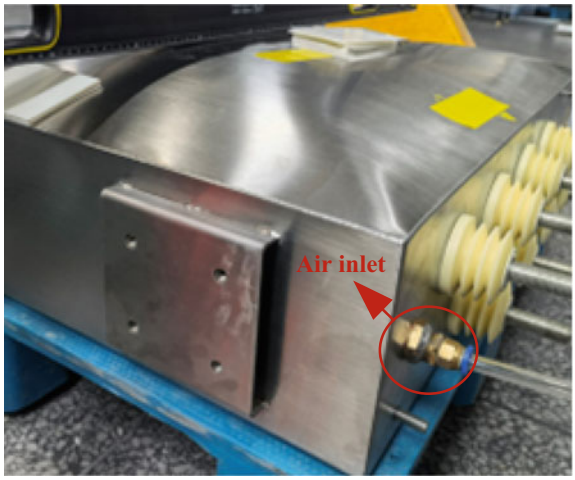

Fig. 7 Air charging test of the capacitor shell

5 Conclusion

In this paper, the finite element software is used to carry out static mechanical simulation of the capacitor metal shell, and the influence of different internal pressures on the deformation and stress of the shell is explored. The following conclusions can be drawn:

- Under the action of internal pressure, the capacitor shell will occur obvious bulging deformation. And the deformation in the middle areas of the shell surface is larger, which is smaller in the surrounding areas. It is consistent with the experimental deformation trend. In addition, with the increase of internal pressure, the deformation on the shell surface will also increase, and the range of deformation will continue to expand.
- When the shell is subjected to internal pressure, the stress in the angular area of the inner shell surface is the largest, which will enter the plastic stage first. And the plastic deformation begins to be produced in the stress concentration area on the shell while the internal pressure exceeds 11 kPa.
- The accuracy of the calculation model is verified by experiments, and the position of the maximum stress point on the shell is given, which provides a certain reference value for the optimization of capacitor structure.

References

1. Ho J, Jow TR, Boggs S (2010) Historical introduction to capacitor technology. IEEE Electr Insul Mag 26(1):20–25
2. Peters A (1996) Power capacitors-new developments. In: IEE Colloquium on capacitors and inductors for power electronics. IET, London, UK, pp 3/1
3. Basmanov VG, Kalinina EA, Kholmanskikh VM (2018) Selecting optimum stage switching interval for capacitor unit as way to increase efficiency of reactive power regulation. In: 2018 International conference on industrial engineering, applications and manufacturing (ICIEAM). IEEE, Moscow, Russia, pp. 1–6
4. Daut I, Bahaudin RC, Hadzer CM et al (2008) Investigation on the effect of shunt capacitor and shunt filter on harmonic in distribution system. In: 2008 IEEE 2nd International power and energy conference. IEEE, Johor Bahru, Malaysia, pp 684–688
5. Zhao ZY, Davari P, Lu WG et al (2021) An overview of condition monitoring techniques for capacitors in DC-link applications. IEEE Trans Power Electron 36(4):3692–3716
6. Li P, Xiong SP, Li WQ et al (2022) Electromagnetic radiation characteristics of potential transfer arc during live working on 1000 kV AC transmission line tension tower. High Voltage Eng 48(11):4628–4637 (in Chinese)
7. Goodarzi A, Allahbakhshi M, Tajdinian M (2020) Multi-criteria protection scheme for online element failure detection in shunt capacitor banks. IET Gener Transm Distrib 14(19):4152–4163
8. Velazquez-Salazar A, Gnonhoue OG, David E et al (2022) Dry-type high voltage capacitors. In: 2022 IEEE 4th international conference on dielectrics (ICD). IEEE, Palermo, Italy, pp 41–44
9. Wang SC, Bai HW, Liu YC (2022) Research on common faults, causes and preventive measures of power capacitor. Mech Res Appl 35(3):112–115 (in Chinese)

10. Wang ZH, Chen T, Xian RC et al (2020) Analysis of common faults and preventive measures for power capacitors. Power Capacitor React Power Compensation 41(2):42–46 (in Chinese)
11. Chen YH, Li H, Lin FC et al (2011) Effect of interlayer air on performance of dry-type metalized film capacitor in DC, AC and pulsed applications. IEEE Trans Dielectr Electr Insul 18(4):1301–1306
12. Mohanty R, Pradhan AK (2021) Time-Domain protection and fault location of wye-connected shunt capacitor banks using superimposed current and differential voltage. IEEE Trans Power Deliv 36(6):3486–3495
13. Wei GT, Jin Y, Wu LZ (2020) Geometric and material nonlinearities of sandwich beams under static loads. ACTA Mech Sinica 36(1):97–106
14. Chernyshenko IS, Storozhuk EA, Rudenko IB (2008) Elastoplastic state of flexible spherical shells with a reinforced elliptic hole. Int Appl Mech 44(12):1397–1404
15. Cindra JL (2008) An outline concerning the history of the concept of virtual work and its applications. Rev Bras Ensino Fis 30(3)

Analysis of Electromagnetic Wave Characteristics of PD in Transformer

Wenzhi Chang, Tingyu Gao, Fei Du, Shuai Yuan, and Guangzhen Wang

Abstract Ultra-high frequency (UHF) technology is a partial discharge (PD) test technology based on spatial electromagnetic field coupling. It can detect the partial discharge of equipment by detecting the electromagnetic wave signal radiated by PD. It has strong anti-interference ability and high detection sensitivity. Due to the complex internal structure of the transformer, various metal structures may affect the propagation of radiated electromagnetic waves. Therefore, it was necessary to investigated the propagation law of electromagnetic waves inside the transformer. In this article, a simplified model of transformer's internal structure was established. The Gaussian current source was used to simulate the PD source. Moreover, the finite difference time domain (FDTD) method was used to simulate the propagation characteristics of the ultra-high frequency electromagnetic wave inside the transformer. The results showed that the electromagnetic wave was seriously distorted during the propagation of the iron core, the high and low voltage windings, and the signal amplitude attenuation was serious. Increasing the amplitude of the pulse current, the peak value of the radiation length increased. And it still had the same attenuation law after passing through the obstacle.

Keywords Transformers · PD · UHF · Electromagnetic · FDTD

W. Chang · T. Gao (✉) · F. Du · S. Yuan · G. Wang
China Electric Power Research Institute, Haidian District, Beijing 100192, China
e-mail: 18831292879@163.com

W. Chang
e-mail: changwenzhi@epri.sgcc.com.cn

F. Du
e-mail: dufei@epri.sgcc.com.cn

S. Yuan
e-mail: yuanshuai@epri.sgcc.com.cn

G. Wang
e-mail: wangguangzhen@epri.sgcc.com.cn

© Beijing Paike Culture Commu. Co., Ltd. 2024

X. Dong and L. Cai (eds.), *The Proceedings of 2023 4th International Symposium on Insulation and Discharge Computation for Power Equipment (IDCOMPU2023)*, Lecture Notes in Electrical Engineering 1102, https://doi.org/10.1007/978-981-99-7405-4_26

1 Introduction

Power transformer was a key component of power system and played a very important role in the safe and stable operation of power grid. As more and more transformers approach their life expectancy, it was very important to detect their insulation state. Partial discharge (PD) was one of the main causes of insulation failure. Therefore, PD detection was a sensitive and effective method to evaluate power transformers.

Ultra-high Frequency (UHF) technology realized the detection of PD by detecting the electromagnetic wave signal. It had strong anti-interference ability and high detection sensitivity. As a PD test technology based on spatial electromagnetic field coupling, it could realize the real PD online detection, and could locate the PD fault source [1–11]. Due to the complex internal structure of the transformer, the electromagnetic wave signal was affected by the core, winding, box body and oil-paper insulation medium during the propagation process, resulting in changes in the amplitude, energy, spectrum and propagation time of the UHF signal. Therefore, it was necessary to investigate the propagation characteristics of electromagnetic waves in transformers.

References [12] and [13] used the Finite Difference Time Domain (FDTD) method to simulate the propagation of UHF signal of PD in Gas Insulated Switchgear (GIS), and obtained relevant conclusions. Due to the internal structure of the transformer was much more complex than the coaxial waveguide structure of GIS, the analysis method was not applicable to the transformers. In [14], the propagation characteristics of UHF signal in transformer were studied by means of actual measurement, and good results were obtained. However, the random influence of interference in actual measurement was relatively large, which had influence on the accuracy of the results.

The propagation loss of UHF electromagnetic wave in the oil-paper composite insulation medium inside the transformer was very small, which could be approximated as lossless propagation [10]. In this article, the actual core winding structure was reasonably simplified, and a computer model conforming to the actual structural characteristics was established and explored the attenuation and distortion of UHF signal by transformer structural components.

2 Propagation Characteristics of Electromagnetic Wave of PD

PD signal could be regarded as an electromagnetic wave signal emitted by power supply. When PD occurred in the insulating medium, the generated current pulse excited electromagnetic radiation, which followed the Maxwell electromagnetic field basic equation. Dynamic vector potential and dynamic scalar potential were introduced to analyze the time-varying electromagnetic field generated by PD. At this time, the basic equations were transformed into dynamic potential equations.

$$\nabla^2 \vec{A} = -\mu \vec{\delta_C} + \nabla\left(\mu\varepsilon \frac{\partial \varphi}{\partial t}\right) + \nabla\left(\nabla \cdot \vec{A}\right) + \mu\varepsilon \frac{\partial^2 \vec{A}}{\partial t^2} \tag{1}$$

$$\nabla^2 \varphi + \nabla \cdot \frac{\partial \vec{A}}{\partial t} = -\frac{\rho}{\varepsilon} \tag{2}$$

where $\vec{A}$ was dynamic vector, Wbm^{-1}; φ was dynamic scalar, V; μ was magnetic permeability of medium, ε was dielectric constant of medium; $\vec{\delta_C}$ was current density, $\mathrm{A/m}^2$; ρ was excitation source, $\mathrm{C/m}^3$. (1) represented the relationship between the dynamic potential and the excitation source ρ and the current density $\vec{\delta_C}$.

3 Principle of FDTD

The FDTD for solving electromagnetic field problems was based on the finite-difference discretization of Maxwell's curl equations in the time and space domains. The central finite-difference scheme with two-order accuracy was used to approximately replace the original differential equation. The parameters of the FDTD method were given by the spatial grid. Only the medium parameters of the corresponding spatial points were given, the complex electromagnetic structure could be simulated.

Mesh generation was the key problem of FDTD. Yee proposed to use a grid structure with half a step difference in space and time domains. The current electric and magnetic field values were obtained by using the magnetic and electric field values of the previous moment through a leap-frog step, and this process was calculated throughout the whole space at each moment, so the solution of the electric and magnetic field values changing with time in the whole space domain could be obtained [8].

When applying this method, it was not necessary to solve the Green's function of the problem. By using pulse source as excitation, combined with Fourier transform, only one calculation was needed to obtain the response of various effective frequencies contained in the pulse. Compared with the frequency domain method, it would save a lot of calculation time. Therefore, the FDTD method was more suitable for the analysis of the PD electromagnetic wave propagation process inside the transformer than other methods.

4 Simulation Model Design

Large power transformer had high voltage level, large capacity and complex structure. In order to meet the needs of computer simulation, its structure must be simplified. The body structure of the double-layer winding of the core outer sleeve with relatively

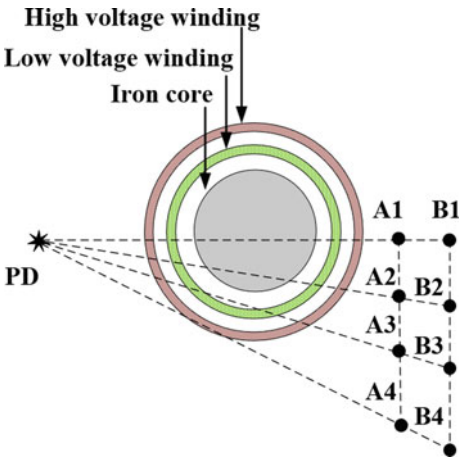

Fig. 1 The model cross-sections and observation points

simple structure was selected as the simulation prototype, and some factors that had no significant effect on the propagation of electromagnetic wave were ignored (such as insulation cardboard and insulation oil, winding and core production process, etc.). The conductive solid cylinder was used to simulate the transformer core, and the concentric double-layer spiral coil structure was used to simulate the low–high voltage winding of the transformer. And the number of low voltage winding turns was small, the pitch was large; the number of turns of the high-voltage winding was large and the pitch was small [9]. The simulation model was shown in Fig. 1.

The simulation parameter: the core was an ideal conductor cylinder of Φ60 * 90 cm; the inner coil size was Φ 35 * 50 cm, the wire diameter was 2 cm, and the turn spacing was 0.8 cm; the outer spiral coil size was Φ 40 * 50 cm, the wire diameter was 1.2 cm, and the turn spacing was 0.4 cm; line current source was 2 cm long, located outside the winding; gaussian pulse current excitation; subdivision grid: 0.5 × 0.5 × 0.5 cm; time step: 9.629 ps; the highest frequency used in the simulation was 6 GHz.

When PD occurred in the transformer, discharge signals of different frequencies were generated, and the frequency of the ultra-high frequency signal could reach 2 GHz. In the simulation, Gaussian pulse was used to simulate the actual PD signal. The PD source could be simulated by a line current source, and the line current source could be equivalent to a series of element currents. For transient electromagnetic field signals, Gaussian signals could be used to simulate actual PD signals. The time domain signals of Gaussian pulse currents with different pulse widths and amplitudes were shown in Fig. 2.

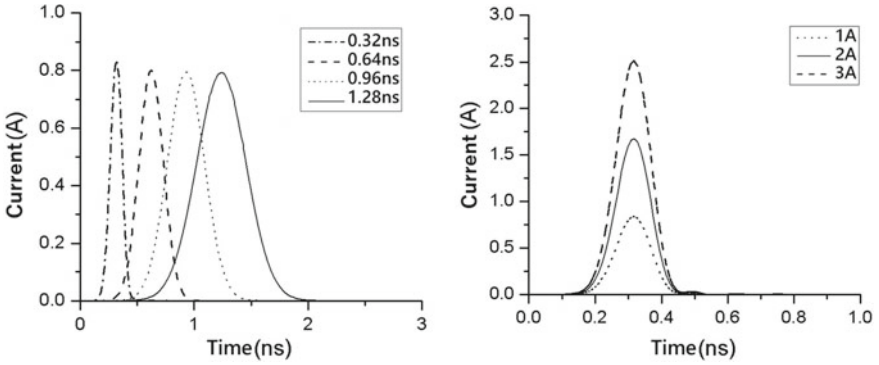

(a) Gauss current element with different pulse widths.

(b) Gauss current element with different amplitudes.

Fig. 2 Time domain waveforms of Gauss pulse function

5 Analysis of Simulation Results

Some electromagnetic waves were reflected on the surface of the core, and some of the reflected waves were diffracted on the surface and propagate to the shadow area. The other part was folded and reflected back and forth between the core and the winding, leading to an increase in the intensity of the radiation field between the core and the winding, and the signal waveform was seriously distorted. Different colors in the image represented different radiation field intensity. The time domain waveform and spectrum of the radiation field at the B_2 observation point were shown in Fig. 3.

A series of refraction, reflection and diffraction phenomena would occur when the electromagnetic wave passed through the core, the high and low voltage winding

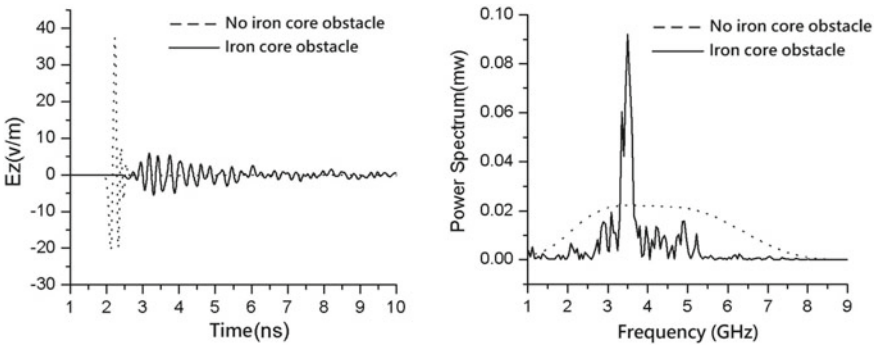

(a) Time domain waveforms

(b) Spectrums

Fig. 3 The effects on time domain waveforms and frequency spectrums by core and windings structure

structure. In the process of diffraction, the proportional relationship determined the characteristics of the diffraction. In order to investigate the influence of core and winding structure size on the propagation characteristics, the propagation law of radiated electromagnetic wave signals excited by different pulse width current elements in core and windings structures was compared and analyzed. The Gaussian pulse current element with pulse different width and amplitude of 1 A was taken as the excitation, and the other simulation parameters were the same. The time domain waveforms of the current elements corresponding to the three pulse widths were shown in Fig. 2a. The radiation field waveform at the observation point A_4 was shown in Fig. 4.

It could be clearly seen in Fig. 4 that as the pulse width of the pulse current element increases, the radiated electromagnetic field became weaker and weaker, but the difference in the waveform of the electromagnetic wave radiation field at the same observation point with or without the core winding structure became smaller and smaller. After the electromagnetic wave excited by the 1.28 ns pulse width current source passed through the core winding structure, its waveform was basically

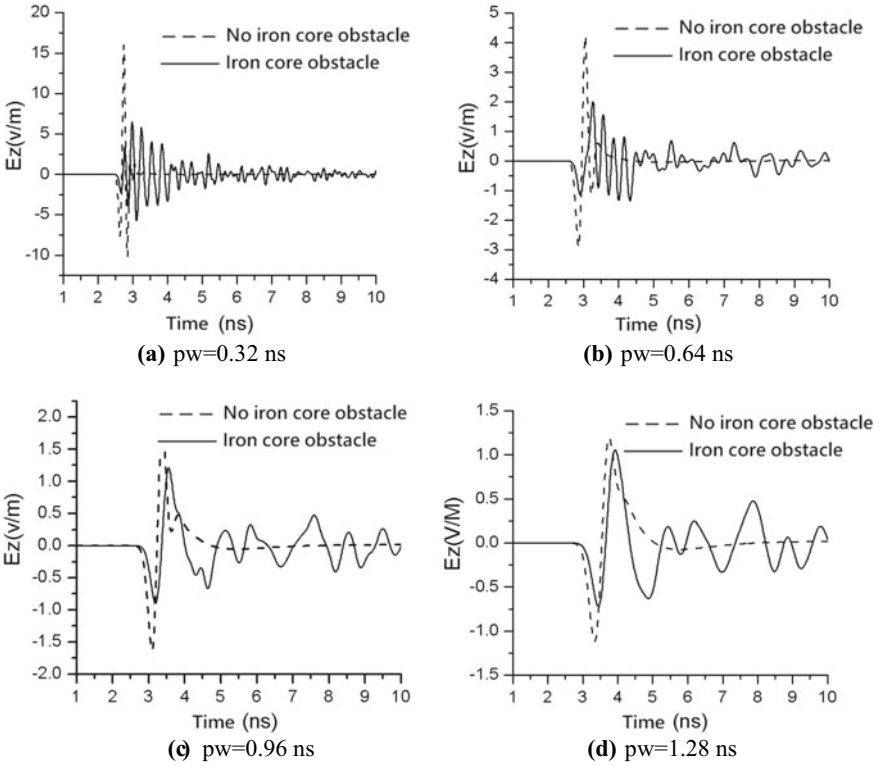

Fig. 4 The propagation of electromagnetic incited by different pw pulse current element cross core and windings structure (observation point A_4)

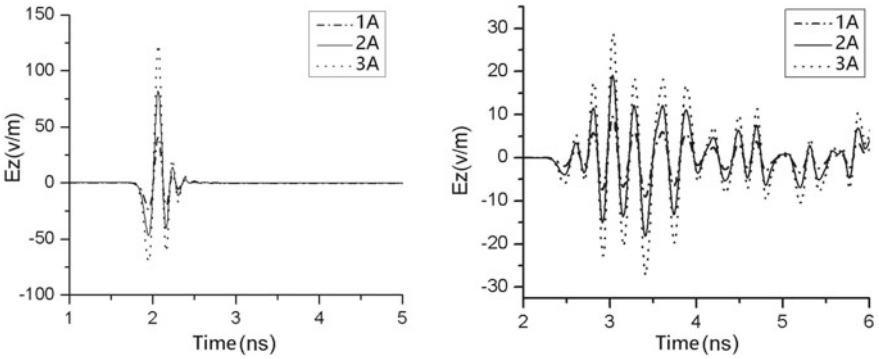

(a) Without core and windings structure **(b)** With core and windings structure

Fig. 5 Time domain waveforms of electromagnetic radiation with different amplitudes whether core and windings structure is existences

consistent with the waveform without the core winding structure, and the amplitude decreased very little. It could be seen that with the same amplitude, the larger the pulse width, the smaller the radiation field intensity excited by the current source. As the pulse width increased, the wavelength wave increased, and the diffraction effect on the obstacle was enhanced. After passing through the core and the high and low voltage winding structure, the waveform was closer to the case without the core winding structure.

In order to study the influence of the amplitude on the radiated electromagnetic wave signal, the radiation field was simulated when the amplitude was 1 A, 2 A, and 3 A, respectively. The pulse width of the current source was 0.32 ns. The time domain waveform of the pulse current element was shown in Fig. 2b, and the other simulation parameters were set the same.

Figure 5 showed the signal waveform at the A_1 observation point. It could be seen that the pulse width of the current element was the same, and the amplitude of the current was changed. The amplitude of the radiation field was proportional to the amplitude of the pulse current element, but the propagation characteristics did not change when passing through the obstacle.

6 Conclusion

In this article, the FDTD was used to simulate and analyzed the propagation characteristics of UHF electromagnetic waves inside the transformer. The following conclusions were drawn:

(1) The pulse current generated by PD of transformer could excite UHF electromagnetic wave. The pulse width and amplitude of pulse current had great influence on the radiation characteristics of electromagnetic wave.

(2) A series of phenomena such as reflection, refraction and diffraction of UHF electromagnetic waves occurred in the core, high and low voltage winding structures, resulting in serious distortion of the waveform of electromagnetic waves and serious attenuation of signal amplitude.
(3) When the pulse width of the pulse current element increased, the amplitude of the radiation field decreases, but the diffraction ability of the radiated electromagnetic wave to the obstacle was enhanced, and the waveform after passing through the obstacle was closer to that without the obstacle.
(4) Increasing the amplitude of the pulse current, the peak value of the radiation field increased, but the change rule after passing through the obstacle was the same.

Acknowledgements This project was supported by China Electric Power Research Institute Research and Development Project "Development of highly reliable intelligent sensing device in complex electromagnetic and meteorological environment" (GY83-21-018).

References

1. Judd MD (2011) Experience with UHF partial discharge detection and location in power transformers. In: 2011 Electrical insulation conference (EIC). IEEE, pp 201–205
2. Dukanac D (2018) Application of UHF method for partial discharge source location in power transformers. IEEE Trans Dielectr Electr Insul 25(6):2266–2278
3. Ariannik M, Azirani MA, Werle P et al (2019) UHF measurement in power transformers: an algorithm to optimize accuracy of arrival time detection and PD localization. IEEE Trans Power Delivery 34(4):1530–1539
4. YIN Kuilong, REN Sheyi, REN Wei. Study on the generation mechanism and transmission characteristics of ultra-high frequency electromagnetic waves in partial discharge of power transformers. Electr Technol 537(03):117–119 (in Chinese)
5. Uwiringiyimana JP, Khayam U, Montanari GC (2022) Design and implementation of ultra-wide band antenna for partial discharge detection in high voltage power equipment. IEEE Access 10:10983–10994
6. Salah WS, Gad AH, Attia MA et al (2022) Design of a compact ultra-high frequency antenna for partial discharge detection in oil immersed power transformers. Ain Shams Eng J 13(2):101568
7. Riba JR (2022) Application of image sensors to detect and locate electrical discharges: a review. Sensors 22(15):5886
8. Jiang J, Chen J, Li J et al (2021) Partial discharge detection and diagnosis of transformer bushing based on UHF method. IEEE Sens J 21(15):16798–16806
9. Shahsavarian T, Pan Y, Zhang Z et al (2021) A review of knowledge-based defect identification via PRPD patterns in high voltage apparatus. IEEE Access 9:77705–77728
10. Tang Z (2006) The methods of partial discharge power UHF to position of power transformer. The Doctoral Dissertation of North China Electric Power University, Beijing (in Chinese)
11. Judd MD, Yang L, Craddock IJ (2005) A study of signal propagation using the time-domain finite-deference method of the locating partial discharge using UHF measurement. In: XIVth International symposium on high voltage engineering proceeding, Tsinghua University, Beijing, China
12. Li X, Li C, Li Y, Wang W, Li H (2005) An analysis to FDTD method for the dissemination of GIS partial discharge. Electr Mech (in Chinese)

13. Huang X, Kang S, Li H, Zhang Y (2006) Simulation study on the characteristics of ultra-high frequency electromagnetic wave in GIS. High Voltage Eng 32(10):32–35 (in Chinese)
14. Thiviyanathan VA, Ker PJ, Leong YS et al (2022) Power transformer insulation system: a review on the reactions, fault detection, challenges and future prospects. Alexandria Eng J

Analysis of Chaotic Behaviors of Partial Discharge Using Plasma Dynamic Model

Dezhao Wu, Yangchun Cheng, and Ziqi Yang

Abstract The traditional researches on the chaos of partial discharge (PD) use the simplified description of a single discharge process, but ignore the plasma dynamic process of PD, and due to the randomness of discharge process, it is difficult to accurately describe the essential characteristics of the PD. Based on the principle of plasma dynamics and COMSOL Multiphysics simulation software, a plasma dynamic model of PD under flat electrode was built in this paper. The space–time evolution process of particles in the air gap during partial discharge are described by using this model, and the motion trajectories of electrons, positive ions and negative ions and the variation of electric field in the air gap during PD are described. Based on this, the formation mechanism of the chaotic behaviors of PD is explained. The results show that the PD in the air gap of insulating materials has obvious chaotic characteristics. The feedback mechanism between spatial charge density and electric field is an important factor affecting the chaotic behaviors of PD. This conclusion lays a foundation for further research on the causing reason of chaotic behaviors of PD.

Keywords Partial discharge · Plasma dynamics · Chaotic behaviors

1 Introduction

In the process of using insulating materials, due to the aging of materials, air gap defects will occur inside them. Due to the existence of a small air gap, a local high field strength area appears inside the insulating material. When the high field strength

D. Wu (✉) · Y. Cheng · Z. Yang
Beijing Key Laboratory of High Voltage and EMC, North China Electric Power University, Beijing, China
e-mail: 2191793951@qq.com

Y. Cheng
e-mail: chych@ncepu.edu.cn

Z. Yang
e-mail: 120212201439@ncepu.edu.cn

© Beijing Paike Culture Commu. Co., Ltd. 2024

X. Dong and L. Cai (eds.), *The Proceedings of 2023 4th International Symposium on Insulation and Discharge Computation for Power Equipment (IDCOMPU2023)*, Lecture Notes in Electrical Engineering 1102, https://doi.org/10.1007/978-981-99-7405-4_27

area reaches the discharge condition, it will cause partial breakdown of the insulating medium. This partial breakdown is called partial discharge (PD). The internal air gap of insulating material is one of the main causing reasons of PD in power equipment. For power equipment, PD in air gaps is an important factor in the evaluation of insulation degradation. The measurement and identification of PD signals is the main means of insulation monitoring and diagnosis of power equipment.

Traditional PD signal measurement methods are based on the random process of PD, and use statistical analysis methods to develop a variety of statistical spectra such as PD pulse phase statistical spectra (PRPD) and a series of characteristic parameters such as skewness and steepness. However, the accuracy of these methods is still not ideal. The existing research shows that PD is not a completely random process, and some characteristics show that PD has chaotic characteristics [1, 2]. Now the study on the chaotic behaviors of PD in air gaps is mainly based on the description of experimental phenomena or the simplified description of single discharge process [3–5]. The causing reason of PD chaotic behaviors is not yet clear. The numerical simulation of PD by using plasma fluid model is an effective method to study the chaotic mechanism of PD in air gaps. This method is widely used in the study of atmospheric dielectric barrier discharge (DBD), and successfully reveals the complex time nonlinear behaviors and chaotic behaviors in atmospheric DBD [6, 7]. Analogous to atmospheric dielectric barrier discharge, this paper establishes a simulation model of PD in air gap based on plasma fluid equation, analyzes the chaotic behaviors of PD current pulse, and finds out the causes of PD chaotic mechanism by observing the changes of various particles and spatial electric field in air gap with time.

2 Simulation Model

2.1 Geometry

In reference [8], a one-dimensional plasma fluid model of air gap is established by COMSOL Multiphysics software, which is used to simulate the PD process of spherical air gap in insulating material under flat electrode. As shown in Fig. 1, the thickness of the outer insulating material is 3.5 mm, the material property is set as insulating oil, the relative dielectric constant is 2.4, the radius of the internal spherical air gap is 1.5 mm, the internal medium is air, the pressure is 1.013×10^5 Pa, and the temperature is 300 K. The left side of the plate electrode is added with a frequency $f = 50$ kHz sinusoidal AC power supply, and the right side is grounded.

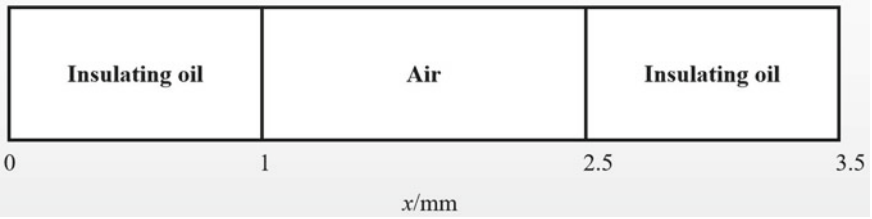

Fig. 1 Model geometry

2.2 Model Control Equation

The spatial distribution of electron concentration and electron energy density is obtained by solving the drift diffusion equation of electron concentration and electron energy density [9].

$$\frac{\partial}{\partial t}(n_e) + \nabla \cdot \mathbf{\Gamma_e} = R_e \tag{1}$$

$$\frac{\partial}{\partial t}(n_\varepsilon) + \nabla \cdot \mathbf{\Gamma}_\varepsilon + E \cdot \mathbf{\Gamma_e} = R_\varepsilon \tag{2}$$

$$\mathbf{\Gamma_e} = -n_e(\boldsymbol{\mu}_\mathbf{e} \cdot \mathbf{E}) - D_e \cdot \nabla n_e \tag{3}$$

$$\mathbf{\Gamma_\varepsilon} = -n_\varepsilon\left(\boldsymbol{\mu}_\boldsymbol{\varepsilon} \cdot \mathbf{E}\right) - D_\varepsilon \cdot \nabla n_\varepsilon \tag{4}$$

where n_e is used to describe the electron concentration and n_ε is used to describe the electron energy density. $\mathbf{\Gamma}_\mathrm{e}$ and $\mathbf{\Gamma}_\varepsilon$ are electron concentration flux and electron energy density flux, respectively. μ_e represents electron mobility and D_e represents electron diffusion coefficient. They conform to the Einstein relationship:

$$D_e = \mu_e T_e \tag{5}$$

T_e is the average electron temperature.

R_e and R_ε are the source terms of electron concentration and electron energy density. The electron source term describes the change of electron concentration during plasma chemical dynamics, and the electron energy density source term describes the energy loss caused by inelastic collision. R_e and R_ε can be calculated by the following formula:

$$R_e = \sum_{j=1}^{M} x_j k_j N_n n_e \tag{6}$$

$$R_\varepsilon = \sum_{j=1}^{P} x_j k_j N_n n_e \Delta\varepsilon_j \tag{7}$$

P is the number of electron-neutral particle inelastic collision reactions, M is the number of chemical reactions that can cause changes in electron concentration, x_j is the molar fraction of the target substance of reaction j, k_j is used to describe the rate coefficient of reaction j, and N_n is used to describe the total neutral particle number density. $\Delta\varepsilon_j$ is used to describe the energy loss of reaction j.

For non-electronic substances, the multi-component diffusion equation is used to solve the mass fraction of various substances:

$$\rho\frac{\partial}{\partial t}(w_k) + \rho(\mathbf{u}\cdot\nabla)w_k = \nabla\cdot\mathbf{j_k} + R_k \tag{8}$$

Here ρ describes the density of non-electron matter mixture, ω_k is cited to describe the mass fraction of the kth heavy matter, S_k is the source term of the kth heavy matter, and j_k is the flux vector of the kth heavy matter.

The distribution of electric field inside the air gap is described by Poisson equation:

$$E = -\nabla V \tag{9}$$

$$-\nabla\cdot(\varepsilon_0\varepsilon_r\nabla V) = \rho_v \tag{10}$$

ρ_v is the density of spatial charge.

2.3 Boundary Condition

On the air gap wall, electrons will collide with the air gap surface and cause losses, and the secondary emission effect of the air gap surface will supplement the electrons [10]. The boundary conditions of electron concentration flux and electron energy density flux on the air gap wall are:

$$\mathbf{n}\cdot\mathbf{\Gamma_e} = \frac{1}{2}v_{e,th}n_e - \sum_p \gamma_p\left(\mathbf{\Gamma_p}\cdot\mathbf{n}\right) \tag{11}$$

$$\mathbf{n}\cdot\mathbf{\Gamma_\varepsilon} = \frac{5}{6}v_{e,th}n_\varepsilon - \sum_p \varepsilon_p\gamma_p\left(\mathbf{\Gamma_p}\cdot\mathbf{n}\right) \tag{12}$$

The first term of Eq. 11 is the electron concentration flux flowing to the wall, the second term on the right is the electron gain caused by the secondary emission effect, and γ_p is used to describe the secondary emission coefficient. The first term in Eq. 12 is used to describe the electron energy density flux, the second term is the

secondary emission energy flow, ε_p is the secondary electron average energy, $\mathbf{\Gamma_p}$ is used to describe the ion flux on the surface of the air gap wall, $v_{e,\,th}$ is used to describe the electron thermal velocity, and the calculation formula is:

$$v_{e,th} = \sqrt{\frac{8T_e}{\pi m_e}} \tag{13}$$

m_e is the electronic mass.

For heavy particles, the ions will be lost during the surface reaction, and the boundary conditions are:

$$\mathbf{n} \cdot \mathbf{j_k} = M_k R_{sk} + M_k c_k z_k \mu_k (\mathbf{E} \cdot \mathbf{n}) \tag{14}$$

j_k, M_k, R_{sk}, z_k and c_k represent the flux, molar mass, surface reaction rate, particle charge number and mass fraction of k heavy substances, respectively.

The surface charge accumulation on the air gap wall is characterized by the following boundary conditions:

$$\mathrm{n} \cdot (\mathbf{D}_1 - \mathbf{D}_2) = \sigma_\mathrm{s} \tag{15}$$

$$\frac{d\sigma_s}{dt} = n \cdot J_i + n \cdot J_e \tag{16}$$

3 Results and Analysis

3.1 Characterization of Chaotic Behaviors of PD in Air Gap

The initial electron concentration in the air is set to be $2 \times 10^3/\mathrm{m}^3$, the initial positive ion density and the initial negative ion density are both $1 \times 10^3/\mathrm{m}^3$. The simulation condition $f = 50$ kHz and the air pressure is set to be 1.013×10^5 Pa. The PD current pulse in the air gap under different applied voltages are shown in the Fig. 2. Figure a–c shows the variation of discharge current pulse and applied voltage in three discharge cycles.

As shown in the figure, under the high frequency uniform electric field, the PD in the air gap is a multi-peak discharge, that is, each semi-period discharge has two or more current pulses [11]. In the same half cycle discharge process, the amplitude of the first discharge after polarity reversal is the largest. In different discharge cycles, the peak value of PD current pulse in each cycle is also quite different. It can be seen that the discharge current pulse value is not constant. In different periods, the discharge current pulse exhibits fluctuating characteristics and even chaotic characteristics. Taking the PD of air gap under the condition of $V_m = 25$kV and $f = 50$ kHz as an

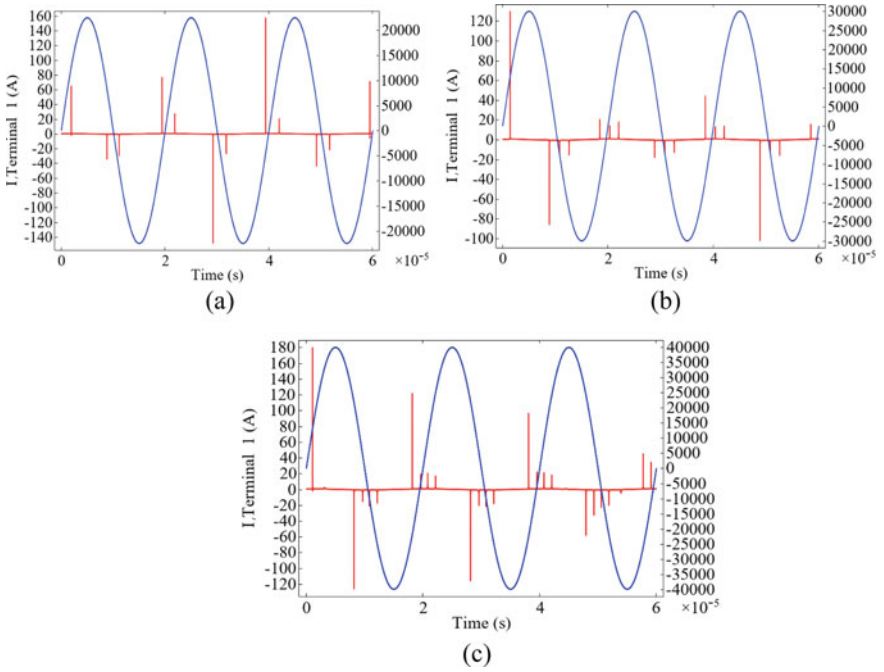

Fig. 2 The PD current pulse in the air gap. The applied voltages of Fig **a–c** are $V_m = 25$ kV, $V_m = 30$ kV, $V_m = 40$ kV, respectively

example, Fig. 3 shows the multi-period current pulse distribution diagram. The value is the average value of the whole space. The discharge waveform loses the common period repeatability and becomes a chaotic discharge.

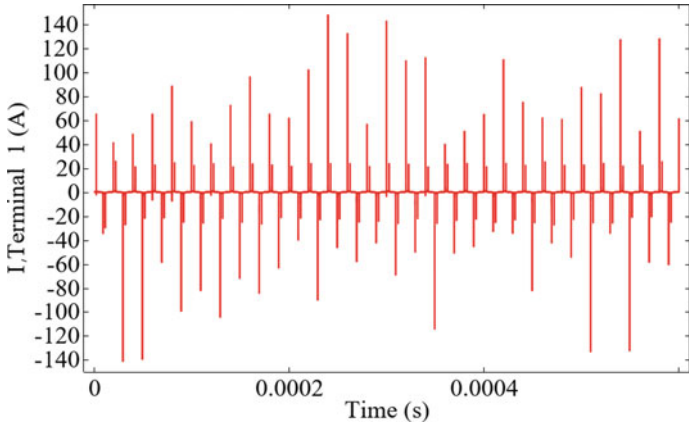

Fig. 3 Multi period current pulse distribution

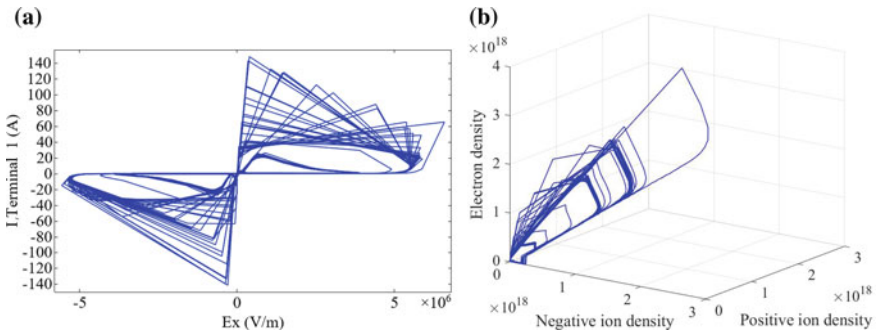

Fig. 4 PD attractor diagram. **a** Is the phase space trajectory of three kinds of space particles, **b** is the phase space trajectory of voltage and current

The attractor is used to describe the trajectory of the phase space point, which can qualitatively analyze the chaotic behavior of the system. When the attractor presents a non-periodic disordered steady-state motion pattern, the attractor is a singular attractor, and the corresponding nonlinear system has a chaotic process. According to the control equation, the average values of electric field and space current in the space are selected to form a two-dimensional phase space, and the average density values of electrons, positive ions and negative ions in the space are selected to form a three-dimensional phase space. The two-dimensional and three-dimensional attractors of PD in air gap are constructed respectively, as shown in Fig. 4a and b. From Fig. 4, it can be seen that the attractor presents a non-periodic disordered steady-state motion pattern, and its trajectory has self-similarity, so the obtained attractor is a singular attractor, which also verifies the chaotic behaviors of PD.

3.2 The Spatial Evolution of Particles in the Same Semi-period Discharge

Figure 5 is the space–time evolution diagram of electrons and positive ions in a discharge period. For each semi-period PD, the current pulse of the first discharge is always the largest. For the negative semi-period discharge of the first period, before the discharge occurs, after the polarity reversal from positive discharge to negative discharge, the right surface is the anode, and the electrons in the space begin to move to the right dielectric surface. At the same time, the electric field of the cathode surface in the air gap is lower than that of the anode due to the electron aggregation on the cathode surface. After the electric field on the cathode surface reaches the initial field strength, electron avalanche begins to appear, and the particle concentration in the space continues to increase. At the beginning, the electric field is small, and the particle concentration changes slowly. As the applied electric field becomes

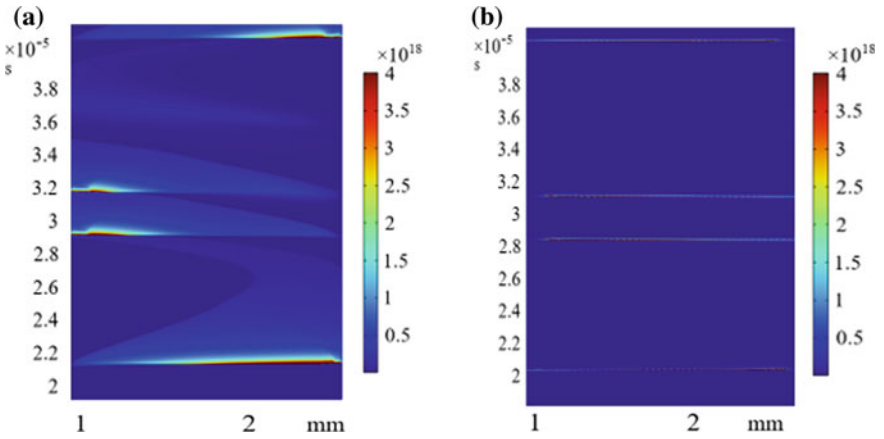

Fig. 5 The space–time evolution diagram of electrons and positive ions in a discharge cycle. Fig. **a** is positive ion. Fig. **b** is electron

larger and larger, the particle concentration increases more and more, and finally reaches the peak. When the number of electron avalanches in the anode reaches the peak, the electron avalanches rapidly develop from the anode to the cathode. In this process, strong ionization occurs, and the peak values of electron density and ion density increase rapidly. After that, due to the inhibition from the reverse electric field generated by the accumulation of surface charges on the dielectric plate, the electron avalanche velocity gradually decreases. At this time, the positive ions move slowly to the cathode [12, 13]. It can be seen that the high frequency partial discharge in the air gap will undergo a process from Townsend discharge to streamer state.

Due to the short time interval between the two discharges in the same half cycle, the plasma channel formed by the first discharge in space has not been completely dissipated before the second discharge, which hinders the formation and development of the electron avalanche, so that the number of electron avalanches in the second discharge is less than that in the first discharge. Similarly, due to the high charge density in the space, the conductivity decreases, and the space electric field at the second discharge is also lower than that at the first discharge [14, 15].

3.3 Feedback Mechanism Between Spatial Charge and Electric Field in Partial Discharge

In the process of partial discharge from positive semi-period discharge to negative semi-period discharge, polarity reversal occurs, and the direction of charge movement in space changes. Similarly, the polarity reversal occurs at the moment the negative semi-period turns to the positive semi-period discharge, and the direction of motion of the spatial charge changes again. In the process of polarity reversal, the

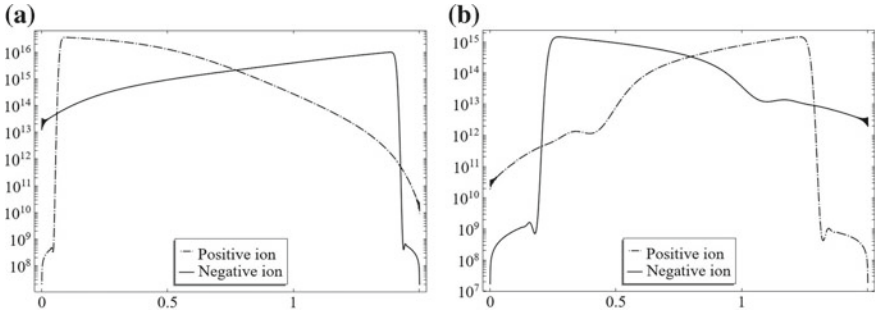

Fig. 6 The concentration distribution of positive and negative ions in space when positive semi-period discharge is converted to negative semi-period discharge and negative semi-period discharge is converted to positive semi-period discharge with two polarity reversals. **a** Negative semi-period discharge is converted to positive semi-period discharge, **b** positive semi-period discharge is converted to negative semi-period discharge

undissipated space particles may affect the first discharge after polarity reversal [16, 17]. Figure 6 is the concentration distribution of positive and negative ions in space when positive semi-period discharge is converted to negative semi-period discharge and negative semi-period discharge is converted to positive semi-period discharge with two polarity reversals. It can be seen that the existence of a large number of negative ions near the cathode will hinder the formation of the next discharge electron avalanche. Therefore, the discharge will occur at higher field strength.

According to the definition of chaotic system and the characteristics of partial discharge, the process of partial discharge satisfies the basic conditions of generating chaotic characteristics, namely nonlinear and feedback properties. For the nonlinear properties, first of all, it can be known from the control equation that the nonlinearity of the applied voltage and the change of the ion concentration in the space are also nonlinear, and the discharge leads to the nonlinear change of the electric field inside the air gap. The feedback property is mainly reflected in the feedback between the spatial charge left by the discharge and its internal field strength. For the discharge with reversed polarity, the negative ions remaining in the previous half cycle accumulate on the discharge surface, which increases the discharge field strength. At this time, the spatial charge has a positive feedback effect on the discharge field strength [18]. For the discharge of the same half period, at the beginning of the discharge, the previous discharge current pulse has not completely disappeared, and all kinds of particles in the space have not completely dissipated, that is, the initial particle concentration in the space during the discharge is higher than that of the previous discharge, and the corresponding discharge field strength will also decrease. At this time, the spatial charge is a negative feedback effect on the discharge field strength. Under the action of power frequency voltage, the positive feedback and negative feedback of partial discharge will continue to alternate, which is an important factor that led to the chaotic behaviors of partial discharge in air gap under power frequency voltage.

4 Conclusion

(1) Under the action of high frequency electric field, taking $V_m = 25$ kV, $V_m = 30$k V, $V_m = 40$k V applied voltage, the partial discharge current pulse of air gap is uneven multi-peak discharge, and the phase space trajectory of space particles and voltage and current conforms to the characteristics of singular attractor, indicating that the partial discharge of air gap under the action of high frequency electric field is a chaotic process.
(2) By observing the evolution process of air gap electrons, positive ions, negative ions and electric field in space during the discharge process, it is shown that the partial discharge of air gap under high frequency electric field will undergo a process from Townsend discharge to streamer state.
(3) At the moment the polarity is reversed, the spatial charge has a positive feedback effect on the discharge field strength; in the same half cycle discharge, the spatial charge has a negative feedback effect on the discharge field strength. The alternation of positive and negative feedback effects is an important factor that affect the chaos of partial discharge.

Acknowledgements This work was supported by a project of National Natural Science Foundation of China (51977076).

References

1. Dissado LA (1997) Propagation of electrical tree structures in solid polymeric insulation comment and reply[J]. IEEE Trans Dielectr Electr Insul 5(3):458–460
2. Yongfen L, Ping H, Yanming L (2010) Chaotic characteristics of partial discharges time series in oil-paper insulation with applications to pattern recognition. J Xi 'an Jiaotong Univer 44(12):55–60 (in Chinese)
3. Shuai C (2019) Study on chaotic characteristics of partial discharge of electrical treeing in oil-paper insulation. North China Electric Power University, Beijing (in Chinese)
4. Liu Z, Cheng Y, Wei S, Wang B, Cheng Z, Peng L (2022) Analysis of chaotic characteristics of partial discharge in solid insulating material voids. In: 2022 IEEE international conference on high voltage engineering and applications (ICHVE), Chongqing, China, 2022, pp 1–4. https://doi.org/10.1109/ICHVE53725.2022.9961499
5. Ke W, Ruijin L, Shengxun Z, Jun G, Lijun Y, Jiaming Y (2013) Chaotic characteristic of partial discharge during electrical degradation of oil—impregnated paper. vol 39(12). pp 3075–3081, High Voltage Technology (in Chinese)
6. Zhang J, Wang Y, Wang D (2013) Numerical simulation of torus breakdown to chaos in an atmospheric-pressure dielectric barrier discharge. Phys Plasmas 20. https://doi.org/10.1063/1.4819722
7. Xiaotong L (2022) Numerical investigation on the temporal nonlinear behaviors in helium dielectric barrier discharges at atmospheric pressure. Shandong University, Shandong (in Chinese)
8. George C, Thanarat T, Paul L (2018) Simulating partial discharge activity in a cylindrical void using a model of plasma dynamics. J Phys D: Appl Phys 52. https://doi.org/10.1088/1361-6463/aaedf0

9. Feng G (2020) Numerical simulation and characteristic study on partial discharge in a dry air cavity with a plasma fluid model. South China University of Technology. https://doi.org/10.27151/d.cnki.ghnlu.2020.003202(inChinese)
10. Pan C, Meng Y, Wu K, Han Z, Qin K, Cheng YH (2011) Simulation of partial discharge sequences using fluid equations. J Phys D Appl Phys 44:255201. https://doi.org/10.1088/0022-3727/44/25/255201
11. Zhang YH, Ning WJ, Dai D (2018) Numerical investigation on the dynamics and evolution mechanisms of multiple-current-pulse behavior in homogeneous helium dielectric Barrier discharges at atmospheric pressure. AIP Adv 8(3):035008
12. Zhou Kai W, Guangning GB et al (2008) Space charge effects on partial discharge activities under pulse voltage. J Electri Technol 23(10):11–17 (in Chinese)
13. Anbang S, Tianxu L, Shurong Y, etc (2022) One-dimensional particle simulation of characteristics of dielectric barrier discharge in atmospheric pressure argon. J Nanchang Univer (Science Edition) 46(01):16–23+31. https://doi.org/10.13764/j.cnki.ncd l.2022.01.007 (in Chinese)
14. Zhao Z, Wei X, Guan R, Zhu B, Nie H, Yao Y (2022) Study on discharge characteristics of low-temperature subatmospheric air streamer under square wave voltage. IEEE Trans Plasma Sci 50(9):2786–2795. https://doi.org/10.1109/TPS.2022.3188756
15. Xinxin W, Chengrong L (2011) Review of homogenous dielectric barrier discharge in nitrogen at atmospheric pressure. High Voltage Technol 37(6):1405–1415 (in Chinese)
16. Seenivasagam L, Maheswari RV, Subburaj P (2013) Modelling of partial discharge behaviour in a cavity within the solid dielectrics. In: 2013 International conference on circuits, power and computing technologies (ICCPCT), Nagercoil, India, 2013, pp 618–624. https://doi.org/10.1109/ICCPCT.2013.6528834
17. Luigi T, Gian M (2010) Advanced modeling of electron avalanche process in polymeric dielectric voids: simulations and experimental validation. J Appl Phys 108. https://doi.org/10.1063/1.3359713
18. Gutfleisch F, Niemeyer L (1995) Measurement and simulation of PD in epoxy voids. IEEE Trans Dielectr Electr Insul 2(5):729–743. https://doi.org/10.1109/94.469970

Discharge Characteristics of DBD with Contact Electrodes at Atmospheric Pressure in Quiescent Air

Jin Haosheng, Liu Shiyun, Liang Hengrui, Shi Yaqin, Mei Danhua, and Fang Zhi

Abstract Dielectric barrier discharge (DBD) has been widely concerned due to its stability and non-corrosive electrode structure. In this study, a mesh-like DBD reactor with wire-to-wire cross-contact electrodes is proposed. Coated high-voltage electrodes with dielectric barriers in directed contact with the ground electrodes facilitate the generation of a wide range of non-thermal plasma at lower voltages. The performance of the designed plasma reactor has been investigated in terms of its electrical, optical, thermal properties and ozone generation capabilities. It is shown that the discharge first occurs in the gap at the contact point, which produces initial electrons and then diffuses into the surrounding air gap, leading to the formation of a certain discharge region. Increasing the magnitude of the applied voltage and the number of contact points increases the discharge intensity, discharge power, emission intensity of active particles and ozone concentration. Decreasing the mesh size d favors ozone formation, and the highest ozone yield of 240 ppm can be achieved with a mesh size d of 4 mm.

Keywords Dielectric barrier discharges · Wire-to-wire cross electrode · Discharge characteristics · Ozone generation

1 Introduction

Non-thermal plasma has received increased attention as a promising technology for versatile applications in environmental, material, food and biological fields [1–5]. For better industrial application performance large area plasma are required [6]. Dielectric barrier discharges (DBDs), also regarded as silent discharges or barrier

J. Haosheng · L. Shiyun (✉) · L. Hengrui · S. Yaqin · M. Danhua · F. Zhi
School of Electrical Engineering and Control Science, Nanjing Tech University, Nanjing 211816, China
e-mail: shiyunliulisza@163.com

L. Shiyun
School of Electrical Engineering Southeast University, Nanjing 210096, China

© Beijing Paike Culture Commu. Co., Ltd. 2024

X. Dong and L. Cai (eds.), *The Proceedings of 2023 4th International Symposium on Insulation and Discharge Computation for Power Equipment (IDCOMPU2023)*, Lecture Notes in Electrical Engineering 1102, https://doi.org/10.1007/978-981-99-7405-4_28

discharge attract growing interest in different applications since it offers high electron density and a large volume stable discharge in atmospheric pressure [1, 7]. The application performance of DBD strongly depends on the discharge characteristics, which can be easily tuned by the electrodes arrangement. There are a number of existing configurations of DBD, including volume discharge (coaxial cylindrical and parallel plate discharge), surface discharge and coplanar discharge [8]. Compared with the conventional volumetric DBDs, surface discharge shows more potential since it offers more available treatment space over the plasma zone, which allows some active species (e.g.,O_3) to accumulate without destructing by the plasma channels [1, 9]. However, typical surface DBD plasma sources are limited by relatively high energy consumption for large areas.

Glow discharge is characterized by stable, low temperature and large-volume, while its difficult to avoid the transition from glow to arc and sustenance of a large-volume plasma discharge mode [10]. The proper arrangement of DBDs could generate a diffuse plasma, which has the advantage of large-area production of glow discharge and the dielectric material used in the DBDs avoid the discharge transition from glow to arc [11]. Mesh electrodes have been employed to obtain the diffused DBD in various gas conditions [12]. In this study, a mesh-like DBD reactor with wire-to-wire contact electrodes is developed to generate more widespread plasma discharges with relatively low energy consumption and high activity. The discharge characteristics are evaluated in terms of the applied voltage and mesh size. Furthermore, an ozone monitor is used to investigate the capability of the designed reactor for ozone generation.

2 Experimental Setup

Figure 1 shows the structure of the plasma reactor and the corresponding diagnostic system for discharge characteristics. The discharge apparatus consists of several wire-to-wire cross-contact electrodes forming a mesh-like structure with dimensions of 50 mm × 50 mm. The electrodes have an outer diameter of 1.4 mm and consist of a 1.1 mm diameter copper rod and a 0.15 mm thickness dielectric material PTFE. The mesh size d is set to 4, 8 and 12 mm, respectively. The developed mesh-like plasma reactor is connected to a laboratory homemade microsecond pulse power supply with a maximum peak voltage of 20 kV and a pulse reputation frequency in the range of 0–5 kHz. The applied voltage is measured by a high voltage probe (Tektronix P615A) while the discharge current is recorded by a current monitor (Pearson 4100). An external capacitor (10 nF) is inserted between the induction electrode and grounded point, through a differential voltage probe(Pintech N1070A) to obtain the charge generated in the discharge process. All the electrical signals are saved by a four-channel digital oscilloscope (Tektronix TDS2014B). The discharge images are captured by a Canon EOS6D digital camera with an exposure time of 1/4 and an ISO of 25,600. The emission spectrum of the plasma discharge is measured using the Ocean Optics HR4000CG spectrometer with a resolution of 0.75 nm.

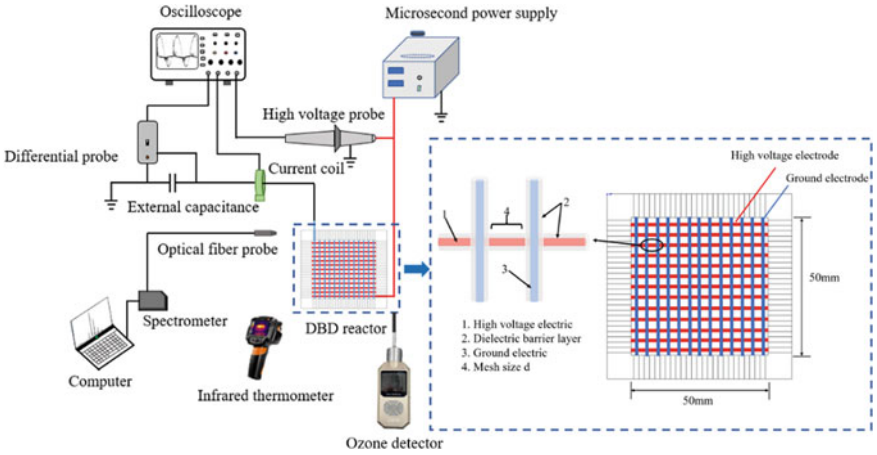

Fig. 1 The experimental setup of the wire-to-wire cross contact electrode configuration

Moreover, the surface temperature of the reactor during the discharge is collected by an infrared thermometer (FOTRIC 325 Pro).

3 Results and Discussion

3.1 Electrical Characteristics of Discharge

Figure 2 shows the typical voltage and current waveforms and discharge image of the wire-to-wire cross contact electrodes with different mesh size (d), where U_t and i_t are the applied voltage and the total current, respectively. As demonstrated in Fig. 2, the rising and falling edges of the pulse voltage contain multiple current pulses that oscillate with a period of about 370 ns. During the discharge process, when the applied voltage across the electrodes reaches a certain value, the breakdown field strength is formed in the externally applied electric E_a and leads to the formation of the discharge. Under the effect of E_a the charged particles would do directional movement in the discharge space while the electrons accumulate on the surface of the dielectric material at the high electrode, eventually forming an electric field E_c with an opposite direction of the E_a. When the difference between the external applied electric field E_a and the strengths of E_c is less than the strength of breakdown field, the discharge terminate. Once the difference between the E_a and E_c exceeds the breakdown field again, the discharge could occurs again [13]. At the rising and falling edges of the pulse voltage, the strength of the external electric field E_a increases monotonically with time and the several discharges can be observed during this stage, so that the discharge current appears as many short pulses. Literatures also reported similar results [11].

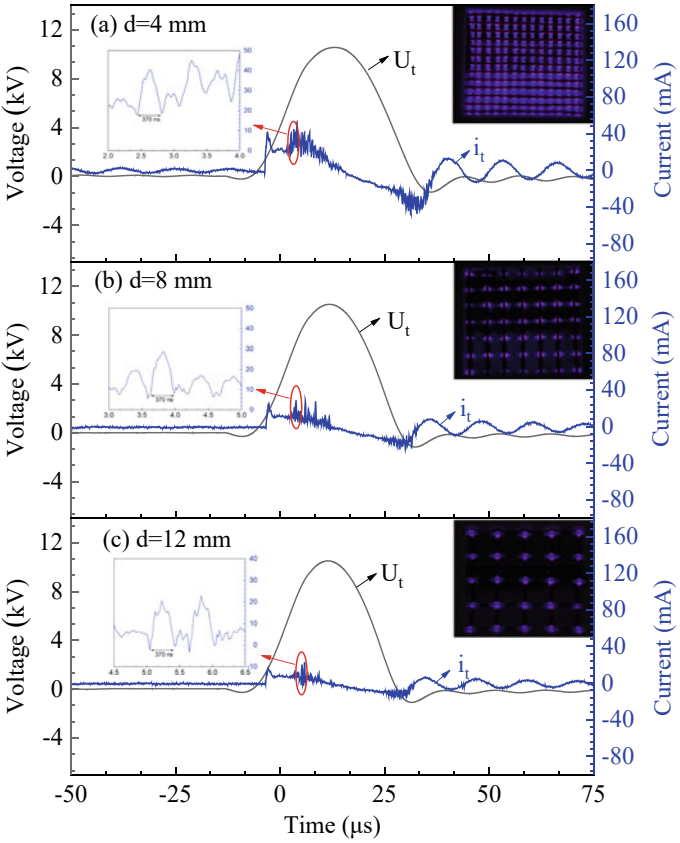

Fig. 2 Typical discharge waveforms and images of the mesh structure electrode with different mesh size d (applied voltage: 10 kV, frequency: 1.5 kHz)

It is worthy to note that the initial discharge voltage of the proposed electrodes almost at the same level regardless the changes in the mesh size d. However, the amplitude and number of the discharge current pulse remarkably reduced with the increases of mesh size d. This phenomenon might be attributed to the changes of the number of contact points, which is significantly reduced from 169 to 25 when the mesh size d increases from 4 to 12 mm. Each contact point would occurs discharge and contributes to the discharge current during the discharge process, therefore the magnitude of the discharge current pulse increased with the decreases in mesh size d. As can be seen from the discharge images that the discharge is occurred at each single contact point and gradually expends to the surrounding space, resulting in a three-dimensional discharge space with a shape of cube. Compared to a large mesh size d, the discharge can be developed to the full surface of the proposed reactor with a narrow mesh size d. At a same time, the discharge density and intensity are significantly weaker when the mesh size d is increased, which matches perfectly with

the discharge current waveform. This result suggests that decreasing the mesh size d can generate the non-thermal plasma discharges in a large area with good stability and discharge strength.

For more detailed analysis, an equivalent circuit of the wire-to-wire cross contact electrodes is established to evaluate its physical properties such as power consumption and transferred charge. Based on previous studies, the discharge process of a DBD can be simulated by an RC circuit as shown in Fig. 3, where C_d, C_g and C_m represent the equivalent capacitance of the dielectric layers, the capacitance of the air gap and the measured capacitance, respectively. R_g stands an equivalent resistance of the discharge path [14]. Therefore, for the proposed electrodes, the applied voltage U_t consists of the voltage across the dielectric barrier and the voltage across the air gap, similarly the measured current I_t can be divided into the displacement current I_d and the conduction current I_g. Through the above voltage and current, the instantaneous values of total power (P_t), power deposited on the dielectric layer (P_d) and the air gap also noted as discharge power (P_g) and the corresponding average values could be determined ($\overline{Pt}$, $\overline{Pg}$, $\overline{Pd}$). The energy efficiency (η) of the mesh-liked cross electrode DBD reactor is determined by the ratio of the average discharge power and the average total power, as described by Eq. 1. The detailed descriptions of the calculation procedure of the above-mentioned parameter can be found in our previous studies [15–17]. The transferred charge (Q_{trans}) in the single pulse of applied voltage is calculated by integrating the instantaneous conduction current over the duration of the discharge pulse (see Eq. 2).

$$\eta = \frac{\overline{Pg}}{\overline{Pt}} \times 100\% \tag{1}$$

$$Q_{trans} = \int_0^{t=T} I_g(t)\,dt \tag{2}$$

Figure 4 shows the variations in the power consumption and transferred charge of the proposed DBD reactor with various mesh size d. It is clear that narrow the mesh size d significantly enhanced the discharge intensity, the average discharge power almost quadrupled when the mesh size d changes from 12 to 4 mm (from 0.6 W to 2.3 W). Similarly, decreasing the mesh size d results in an exponential growth of the transferred charge. For a mesh-like structure reactor with a fixed reactor size, decreasing the mesh size d would increase the number of contact points and form more discharge points, leading to intense discharge current pulses and favoring an increase in discharge power and transferred charge. The voltage on the dielectric layer is proportional to the capacitance of the dielectric layer, which depends on the contact point. Increasing the number of contact points leads to an increase in capacitance since two dielectric layers are involved, resulting in an enhancement of the voltage across the dielectric layer and therefore more power deposited on the

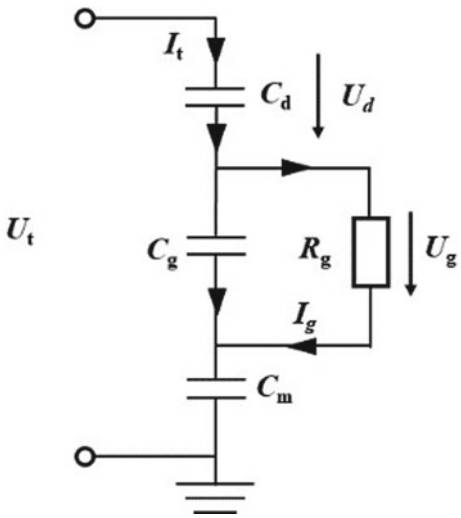

Fig. 3 The equivalent circuit of the proposed DBD reactor

dielectric layer. As a result, the average power deposited on the dielectric layer rises from 1.6 W to 3.9 W for mesh sizes ranging from 12 to 4 mm.

To further analyze the effect of the mesh size on the discharge characteristics, the spatial electric field distribution is analyzed by using the COMSOL simulation software. Figure 5 shows the spatial distribution of the electric field at the applied voltage of 10 kV for the proposed reactor with different mesh sizes. Obviously, the strongest electric field is located at the contact point with a value of 2.5×10^7 V/m, which decreases exponentially with increasing horizontal distance X from the contact point. It is interesting to note that the mesh size d has no appreciable effect on the maximum strength of the electric field, it only affects the number of discharge points. The discharge first occurs at the contact point and generates initial

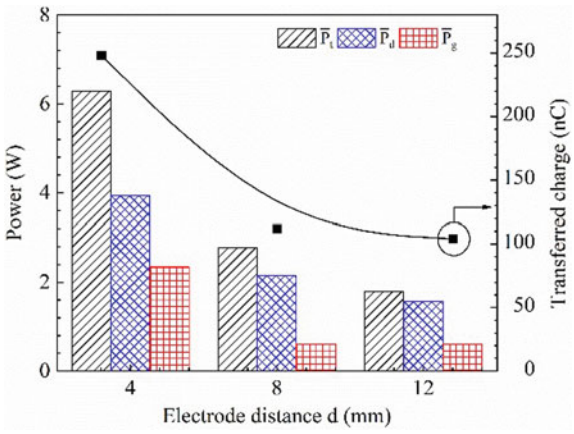

Fig. 4 The variation of power consumption and transferred charge at with different mesh size

electrons, which then diffuse into the gas space, resulting in a cubic 3D discharge space. Figure 6 presents the variation of strength of electric field along the horizontal axis in order to further characterize the electric field distribution with different mesh size d. It is observed that decreasing the mesh size d from 12 to 4 mm, the value of lowest electric filed is continuously increased from 25 to around 80 kV/cm, while the maximal strength of electric field is almost same, indicating that decreasing the mesh size is favored to stable the variation of electric field. Moreover, as the mesh size decreases, leading to an increase in the number of contact points, the interaction of the electric field between any two adjacent points is strengthened, thus facilitating the development of discharges.

Figure 7 presents the power consumption, transferred charge and discharge images of a mesh-like cross contact electrode DBD reactor with a mesh size of 4 mm at different applied voltages with a frequency of 1.5 kHz. It is clear that the energy consumption of the DBD reactor increases with the applied voltage. Specifically, the value of $\overline{Pg}$ and $\overline{Pt}$ are in the range of 1.0–5.6 W and 2.2–8.6 W, respectively when the applied voltage varies from 7 to 11 kV. Both energy efficiency and energy consumption tend to increase with the applied voltage. The transferred charge increases almost linearly with the applied voltage, reaching a maximum value of 302 nC at the applied voltage of 11 kV. Similar conclusions have been reported in previously work [15, 16]. The applied voltage shows a considerable effect on the discharge properties, especially for the discharge area and intensity. As can be seen from Fig. 7c, the

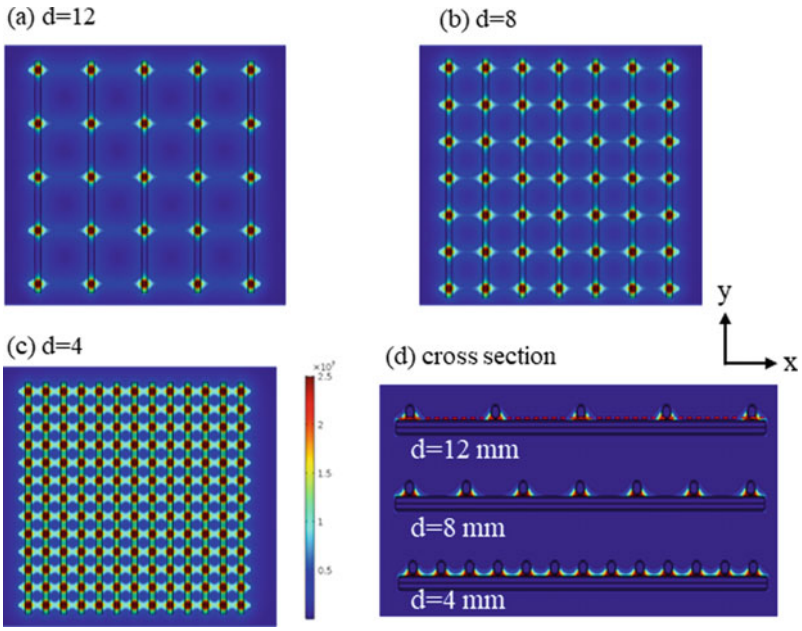

Fig. 5 Spatial distribution of the electric field for the mesh-like structure DBD reactor with different mesh size

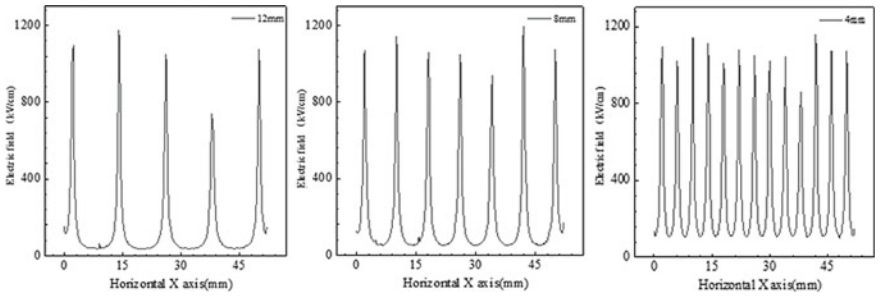

Fig. 6 The variation of electric field along the horizontal distance X with different mesh size

discharge only occurred at the contact point when the applied voltage at a lower level. Increasing the magnitude of the applied voltage expands the discharge into the surrounding space, leading to a wider discharge, which can be attributed to an increase in the discharge power, resulting in a large discharge area and high discharge intensity.

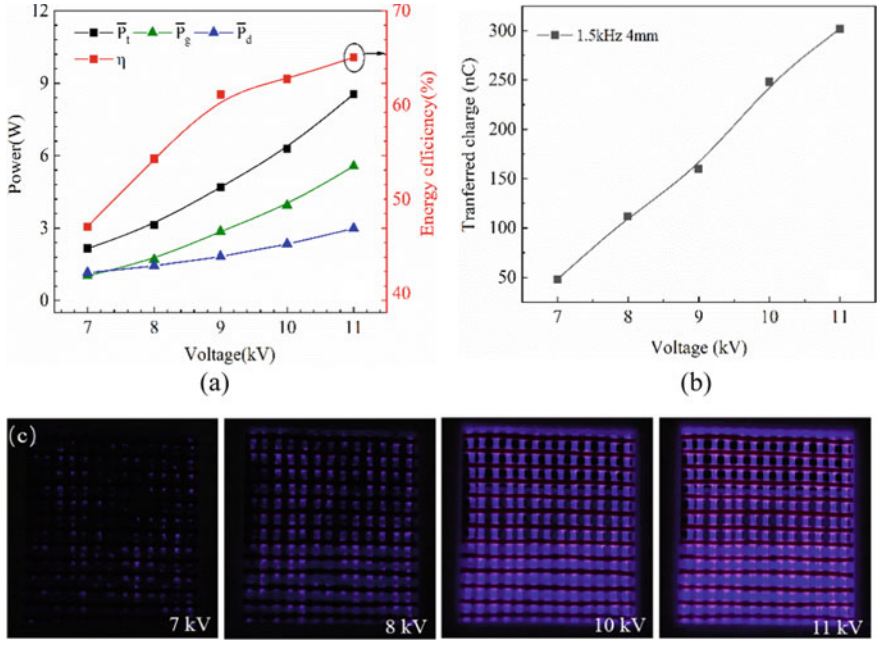

Fig. 7 The effect of applied voltage on **a** power consumption, **b** transferred charge and **c** discharge images

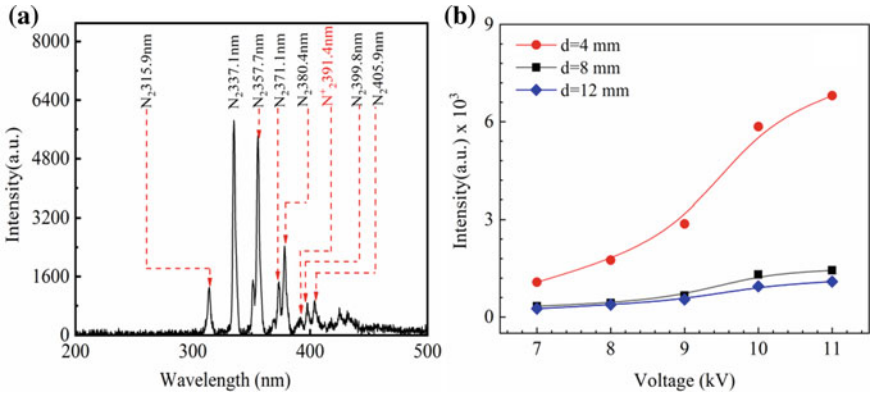

Fig. 8 **a** Typical emission spectra in range of 250–500 and **b** the influence of applied voltage on the emission intensity at 337.1 nm

3.2 Optical Emission Spectrum Diagnosis

The typical optical emission spectra (OES) of the proposed DBD reactor with mesh size d of 4 mm in the wavelength range of 250–500 nm is shown in Fig. 8 under the operation condition of applied voltage 10 kV and pulse repetition frequency 1.5 kHz. It is clearly that the spectral dominated by various vibrational transition bands in $N_2(C^3\ \Pi_u - B^3\ \Pi_g)$second positive system and the first negative system band of N_2^+ ($B^2\ \Sigma_u^+ - X^2\ \Sigma_g^+$), which correspond to the excitation energy of 6.17 eV and 11.03 eV, respectively [18]. This result confirms that the proposed reactor can generate abundant energetic electrons to excite the working gas and generate a variety of reactive species. The emission intensity of the excited state of nitrogen at 337.1 nm is the strongest, therefore its evolution at different applied voltages is also obtained to investigate its effect. From Fig. 7b, the emission intensity gradually rises with the increased applied voltage regardless of the mesh size d and lower the mesh size d contributes to obtain a higher emission intensity at the same applied voltage. The reason for this phenomenon is that the discharge power becomes stronger with the narrow mesh size d, whereas the value of discharge power is proportional to the applied voltage. Thus, increasing the applied voltage or decreasing the mesh size d favors the formation of more active species.

3.3 Operation Temperature

Figure 9 shows the temperature profile and the variation of the surface temperature of the mesh-liked structure DBD reactor as a function of operation time. The discharge conditions are selected with the stable and intense discharge, which are more preferred to the practical operation conditions (applied voltage 10 kV, frequency

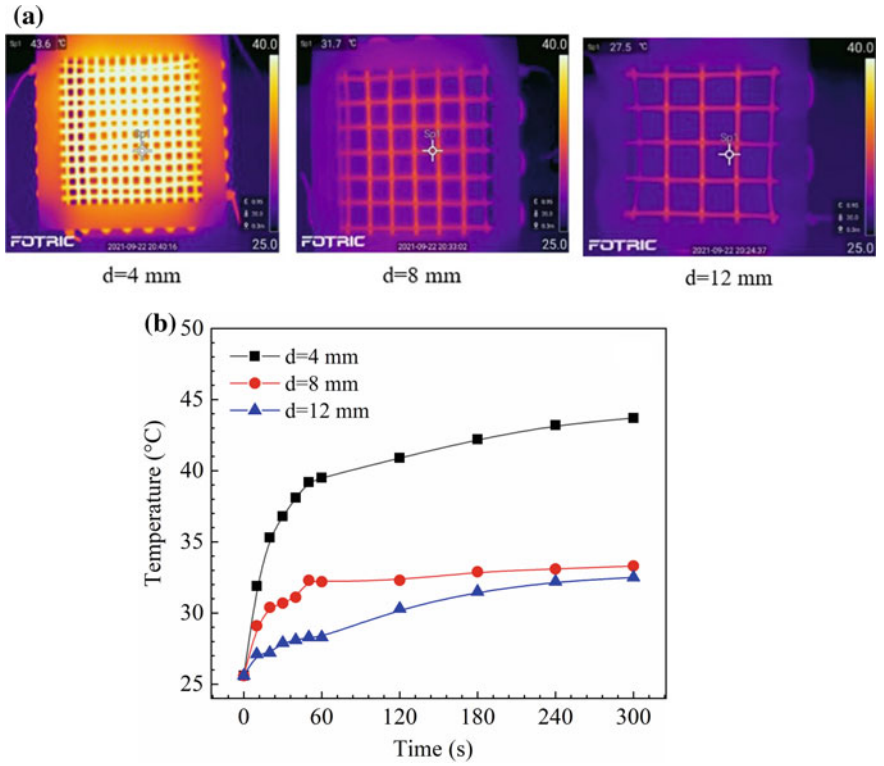

Fig. 9 **a** The temperature profiles and **b** the variations of surface temperature of the proposed DBD reactors as a function of operation time

1.5 kHz). The surface temperature of the reactor suddenly climbs in the first 60 s and gradually increases with the operation time regardless of the mesh size d. Moreover, decreasing the mesh size d significantly enhances the surface temperature of the reactor and the highest temperature of the mesh size d follows the order of 4 mm > 8 mm > 12 mm. This agrees with the properties of the power consumption given in Fig. 4, which shows that the narrowest electrode distance has the largest total power.

3.4 Ozone Concentration

The mesh-like DBD reactor is capable of generating a widespread non-thermal plasma, therefore, it has great potential for many applications such as indoor purification, waste gas treatment, bleaching and air sterilization. Ozone shows positive effects in applications since its strong oxidizing capability and non-residual pollution property [19]. Hereby, the capability of the proposed DBD reactor for ozone generation is evaluated by using the ozone monitor (Pulitong, PLT3000-O3, China).

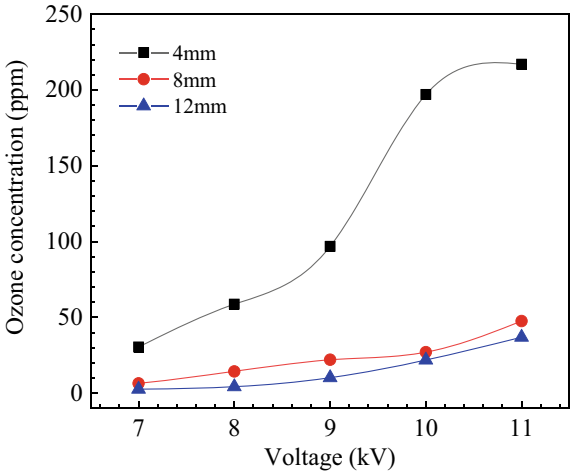

Fig. 10 The effect of applied voltage on ozone concentration

Figure 10 shows the influence of the applied voltage and the mesh size d on ozone concentration. Evidently, increasing the applied voltage is found to increase the ozone concentration. Ozone could be generation through the reaction between atomic and molecular oxygen based on the basic mechanism [20]. In air environment, increasing the applied voltage would deliver more energy into the reactor to trigger the reaction of oxygen dissociation, leading to the formation of atomic oxygen O. Therefore, a higher applied voltage is favorable to the formation of O and an increase of ozone concentration can be achieved (R1–R2). Xie et al. reported a similar result that the improvement of applied voltage favors the yield of ozone [21]. Notably, the ozone concentration decrease with the increase of the mesh size d and the ozone concentration of these electrodes follows the order 4 mm > 8 mm > 12 mm. This phenomenon can be attributed to the lower discharge power when the mesh size d varies from 4 to 12 mm. The maximum ozone concentration of 240 ppm is reached at the applied voltage of 11 kV and the frequency of 1.5 kHz.

$$O_2 + e \rightarrow O + O + e \tag{3}$$

$$O + O_2 + M \rightarrow O_3 + M \tag{4}$$

4 Conclusion

In this paper, a mesh-like DBD reactor with wire-to-wire cross contact electrode is proposed. The discharge characteristics of the proposed reactor in air are evaluated in terms of different applied voltages and mesh sizes. Increasing the applied voltage

could significantly enhance the discharge power, discharge area and transfer charge, leading to an increase in the discharge intensity and the emission intensity of the active species. Based on the analysis of the spatial electric field distribution, the highest electric field is generated at the contact point and decreasing the mesh size d is preferred to stabilize the electric field variability. The temperature of the reactor during discharge is inversely proportional to the mesh size d, indicating the large values of the mesh size d correspond to lower reactor temperatures. The maximum ozone yield of 240 ppm could be achieved with the applied voltage of 10 kV, the frequency of 1.5 kHz and the mesh size d of 4 mm.

References

1. Abdelaziz AA et al. (2017) Plasma Sources Sci Technol 25:035012
2. Hu XR et al (2023) Chemosphere 329:138651
3. Mei D et al (2023) Chem Eng J 462:142044
4. Zhu X et al (2022) ACS Appl Mater Interfaces 14:49094
5. Tanaka H et al. (2017) Rev Mod Phys 1
6. Nayak G et al (2017) Plasma Sources Sci Technol 26:035001
7. Xu H et al (2021) Plasma Sources Sci Technol 30:8
8. Gibalov VI, Pietsch GJ (2012) Plasma Sources Sci Technol 21:024010
9. Malik MA et al (2015) Plasma Chem Plasma Process 35:697
10. Yuan X et al (2006) Vacuum 80:1199
11. Liu S et al (2023) Vacuum 209:111793
12. Martin S et al (2004) Surf Coat Technol 177–178:693
13. Liu W et al (2018) Plasma Sci Technol 20:035401
14. El-Zein A et al (2020) IEEE Trans Plasma Sci 48:1022
15. Wang Q et al (2018) Plasma Sci Technol 20:035404
16. Duan G et al (2021) IEEE Trans Plasma Sci 49:1173
17. Liu F et al (2021) J Appl Phys 129:033302
18. Liu S et al (2017) Chem Eng J 307:793
19. Kim S-J et al (2020) J Korean Phys Soc 77:572
20. Jodzis S, Barczyński T (2018) Ozone Sci Eng 41:69
21. Xie S et al (2019) Plasma Sci Technol 21:055505

Experimental Analysis of Corona Discharge Characteristics and Acoustic Characteristics of Negative Needle-Plate with Different Pressures

Yang Zhou, Wangling He, Jiqiu Liu, Duo Lv, Zheyuan Gan, Yanzhao Wang, Baoquan Wan, and Hongyu Wei

Abstract The generation of corona discharge and audible noise during the operation of UHV transmission lines is a crucial aspect that should be taken into account when selecting and erecting these lines. In order to study the corona discharge characteristics and audible noise (AN) characteristics in complex environments, especially under different pressures, a climate tank test platform with artificially adjustable air pressure was built in this paper, and the corona discharge characteristics of negative DC needle-plate and its audible noise were measured in an anechoic shielding room. The corona current pulse and AN data in the pressure range of 101.3–78.9 kPa were obtained, and the variation law and correlation between them were analyzed. The findings presented in this paper can offer significant experimental data support to the investigation of corona discharge and audible noise characteristics in complicated environments.

Keywords Needle-plate discharge · Corona discharge · Pulse characteristics · Audible noise

1 Introduction

In the actual operation of overhead transmission lines, the electromagnetic environment caused by corona discharge has always been a key issue to be considered in the erection and selection of transmission lines. Audible noise (AN) is one of the

Y. Zhou (✉) · W. He · H. Wei
North China Electric Power University, Baoding 071000, China
e-mail: zhouyang227@ncepu.edu.cn

J. Liu · D. Lv
State Grid Corporation of China, Beijing 100000, China

Z. Gan · Y. Wang · B. Wan
China Electric Power Research Institute, Wuhan 430070, China

© Beijing Paike Culture Commu. Co., Ltd. 2024

X. Dong and L. Cai (eds.), *The Proceedings of 2023 4th International Symposium on Insulation and Discharge Computation for Power Equipment (IDCOMPU2023)*, Lecture Notes in Electrical Engineering 1102, https://doi.org/10.1007/978-981-99-7405-4_29

negative effects of corona discharge [1]. Audible noise may cause irritability, which limits the threshold of AN in transmission line design and restricts the economy of line design. In high altitude areas, low density of air makes the average free path of charged particles longer, which often leads to more serious corona discharge [2, 3].

Since the 1970s, studies on the generation of audible noise caused by corona discharge have been progressively conducted. In 1976, The measurement of the electromagnetic environment of ± 600 kV DC transmission lines, including corona loss, radio interference, television interference, and audible noise, was conducted jointly by BPA and EPRI [4]. In 1981, BPA deduced the general calculation formula of A-weighted audible noise of AC lines on rainy days and DC lines on sunny days based on previous experimental data [5]. In 1989, Japan's Central Electric Power Research Institute (CRIEP) studied and obtained the assumption that the magnitude of AN and corona current is determined by the maximum conductor surface gradient in the presence of space charge and is independent of the arrangement of surrounding electrodes [6]. Based on the above assumptions, CRIEP adopts the corona cage test to predict the actual audible noise of the line.

In recent years, with the development of corona discharge and living room noise measurement technology and simulation research, the research on the generation mechanism of corona discharge audible noise has been gradually improved [7, 8]. Zhao et al. [9] proposed a digital twin model of audible noise of UHV DC transmission lines, which provides a new research method of audible noise and guides the design of transmission lines. Li et al. [10] analyzed two typical overhead line structures, calculated the potential gradient and AN level of the conductor surface, and the relationship between the two is discussed in depth.

In this paper, a climate tank test platform with artificially adjustable air pressure is built. The corona discharge characteristics and audible noise measurement experiments of needle-plate electrodes under negative DC voltage are carried out. The corona discharge current pulse characteristics and audible noise characteristics under different air pressures are analyzed. The main conclusions of this paper can provide some reference value for the study of audible noise mechanism of DC corona discharge in complex environment.

2 Testing Platform and Testing Method

2.1 Artificial Climate Tank for Corona Discharge

The physical diagram of the experimental device used in the experiment is shown in Fig. 1.There is a cube gas chamber of 0.7 m × 0.7 m × 2 m inside the tank, and the outer wall is made of organic glass. When the external environment is atmospheric pressure, the internal pressure can be reduced to 45 kPa. The needle-plate electrode is placed in the air chamber. The plate electrode is a circular metal plate with a diameter

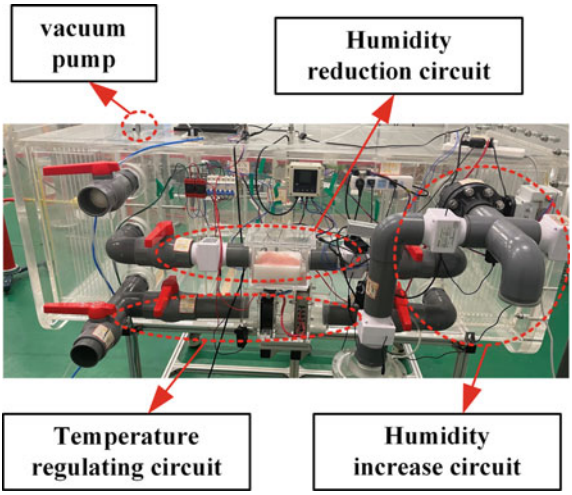

Fig. 1 The physical map of the artificial climate tank used in the experiment

of 100 mm. The gap between the needle plate electrode is 20 mm. The needle-electrode is connected to the high voltage side, and the plate electrode is grounded. The device is connected with the vacuum pump to adjust the internal pressure value of the equipment. In addition, the device has two circuits of dehumidification and temperature regulation, which are used to maintain the constant temperature and humidity of the experiment and eliminate the interference of other environmental factors.

The pressure levels selected in this experiment are 101.3 kPa, 89.4 kPa and 78.9 kPa, respectively. The average pressure at altitudes of 0 m, 1000 m and 2000 m is simulated respectively.

2.2 Acquisition of High Frequency Current Pulse Signal

The acquisition logic of the high frequency current acquisition system is shown in Fig. 2. The high-frequency current signal is obtained by collecting the voltage signals at both ends of the non-inductive resistor and calculating by the Ohm theorem. The high-frequency current signal generated during the corona discharge process is collected as an electrical signal by the acquisition card, and then output as a digital signal through the photoelectric conversion module to facilitate post-processing on the PC side.

The non-inductive resistor used in the experiment is composed of multiple resistors in parallel, which makes the magnetic field generated by the current passing through each resistor cancel each other at the axis, thereby increasing the upper limit bandwidth of the current sensor.

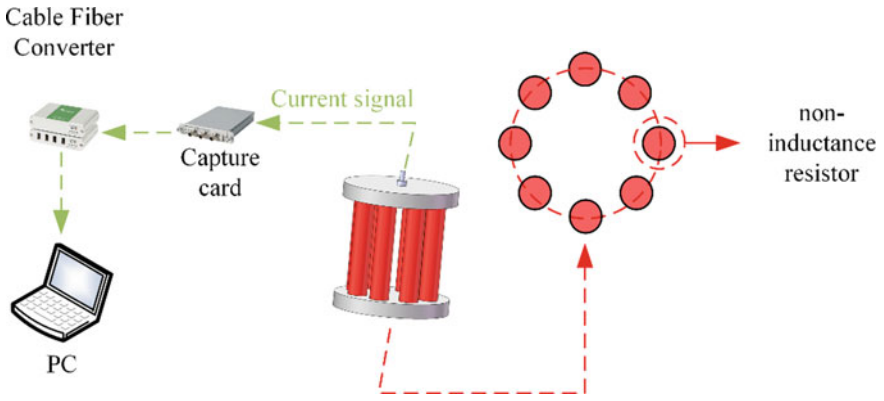

Fig. 2 High frequency current acquisition system logic diagram

2.3 Acquisition of Audible Noise Signal

The audible noise acquisition system is shown in Fig. 3. In order to isolate the possible influence of external environmental noise on the noise data measured in the test, the test was carried out in an anechoic chamber.

The acoustic signal generated by corona discharge is converted into electrical signal by the sound pressure sensor sealed inside the experimental device, and then the electrical signal is input into the PC for further statistical processing in the data acquisition unit.

The noise measurement system includes sound pressure sensor and B&K data acquisition unit. The sound pressure sensor is responsible for converting the collected sound signal into an electrical signal, and the data acquisition unit is responsible for

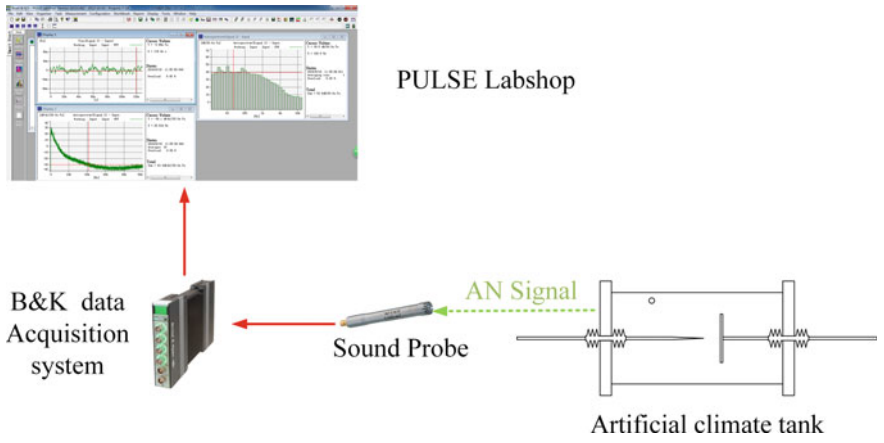

Fig. 3 Audible noise acquisition system

inputting the sound pressure signal collected by the sensor into the PC. Among them, the acoustic pressure sensor (4189, Brüel&Kjær, Denmark) used has a sensitivity of 50 mV/Pa and an effective frequency range of 1–40 kHz. The data acquisition unit (3050, Brüel & Kjær, Denmark) provides 4–6 input channels with a frequency range of DC signal ~51.2 kHz.

3 Results and Discussions

3.1 Corona Discharge Characteristics and Statistical Analysis

Because the negative DC corona does not form a relatively stable Trichel pulse when the voltage is low, the statistical data of the pulse is highly accidental, and when the voltage is high, the low pressure test group may not be able to measure the corresponding value due to breakdown. Considering comprehensively, 23 kV is selected as the test voltage.

In order to control the variables, the test environment conditions were maintained at relative humidity of 60% and temperature of 20. The negative corona discharge pulses within 2 ms at 101.3, 89.4 and 78.9 kPa are shown in Fig. 4. It can be seen intuitively from the pulse contrast diagram that the repetition frequency of the negative corona pulse increases, while the change of the pulse amplitude is not obvious.

In order to obtain the current pulse discharge characteristics under different pressures, it is necessary to statistically analyze the pulse eigenvalues of multiple sets of data under the above conditions. The statistical results of the average value of the corona current pulse amplitude and the average number of pulses under different negative pressures within 2 ms are shown in Fig. 5.

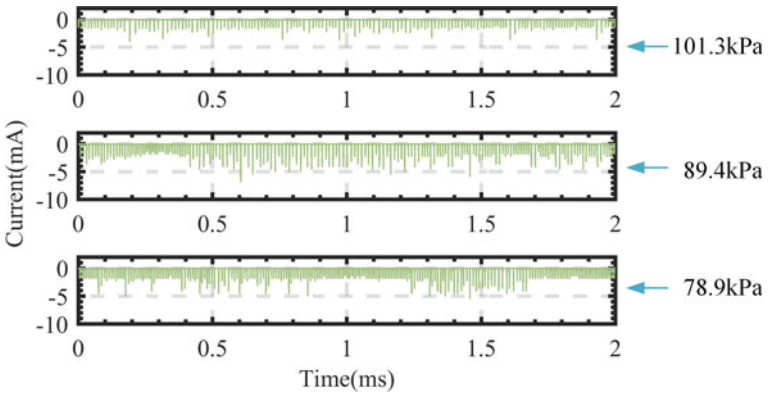

Fig. 4 Negative discharge pulses at different pressures

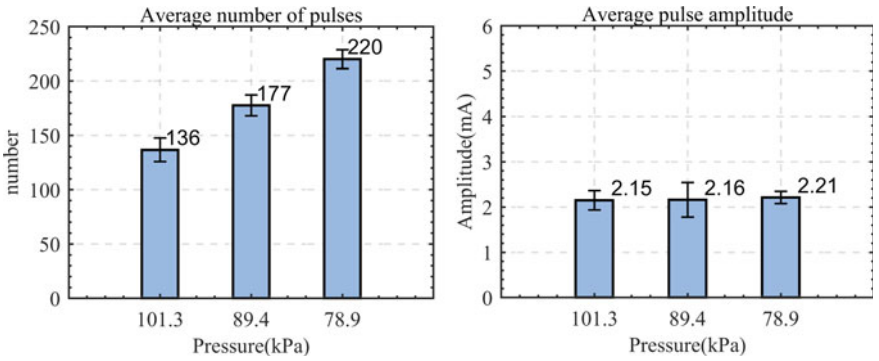

Fig. 5 The average value of negative discharge characteristic parameters at different pressures

As the pressure decreases, the average number of pulses increases, while the pulse amplitude does not change much. This phenomenon is mainly due to the increase of the mobility of negative ions with the decrease of air pressure, resulting in more severe corona discharge under the same voltage conditions.

3.2 The Influence of Air Pressure on Noise Characteristics

The A-weighted spectral characteristic curves at different pressures are shown in Fig. 6. Because the experiment is carried out in the anechoic chamber and the acoustic sensor is placed inside the test chamber, the sound pressure level of the background noise is very low, which is negligible compared with the audible noise generated by corona discharge.

By analyzing the spectrum feature map, it can be concluded that the noise generated by the negative polar needle plate discharge is only 80 Hz component in the middle and low frequency band(<1.6 kHz), which is significantly different from the background, and increases with the decrease of air pressure.

For the high frequency band(>1.6 kHz), as the air pressure decreases, the high frequency component increases first, and unlike the middle and low frequency bands, the components under low pressure show higher sound pressure level values, not just a frequency point.

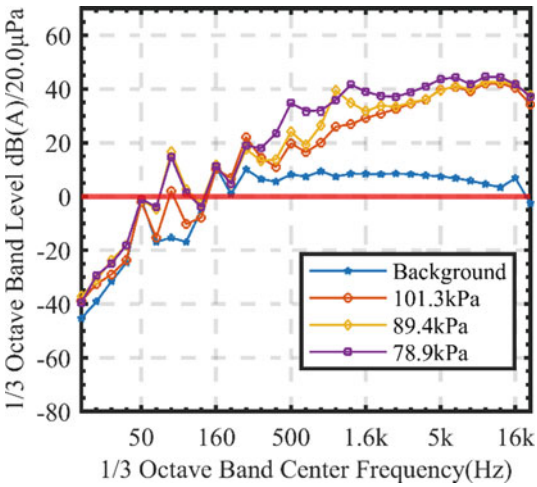

Fig. 6 Noise spectrum characteristics of needle-plate discharge under different pressure conditions

3.3 The Relationship Between Corona Discharge and Noise Parameters

Since the mean value of the negative pulse amplitude changes little with the pressure, in this section, only the relationship between the mean number of pulses and the A-weighted sound level under the same experimental conditions is discussed.

Table 1 displays the correlation between the mean number of corona pulses and the A-weighted sound pressure level (SPL). Based on the data presented in the table, it can be concluded that there is a positive relationship between the number of corona pulses and the resulting noise effect, where an increase in the former leads to a rise in the latter. In high altitude areas, low pressure environment will lead to more serious audible noise effect.

Table 1 A-weighted sound level statistics and mean number of pulses at different pressures

Air pressure (kPa)	Sound pressure level (dB(A))	Average number of pulses
101.3	49.4	136.7
89.4	50.6	177.5
78.9	53.1	220.2

4 Conclusion

In this paper, the corona discharge characteristics of negative DC needle plate corona discharge at different pressures and the acoustic characteristics of audible noise are studied in an anechoic chamber by using an artificial climate experimental device with adjustable air pressure. The conclusions of the paper are as follows.

An increase in the applied voltage results in a rise in the number of negative discharge pulses, while the pulse amplitude remains relatively constant. The comprehensive characteristic discussion shows that when the applied voltage is the same as other environmental conditions, low pressure will lead to more severe corona discharge.

With the decrease of air pressure, the noise effect of negative DC corona discharge is intensified, and the analysis data shows that the noise effect is positively correlated with the pulse frequency of corona discharge.

Acknowledgements This study was supported by the Science and Technology Project of State Grid Corporation of China (Contract No.: 5200-202155587A-0-5-GC).

References

1. Maruvada PS (2000) Corona performance of high-voltage transmission lines. Research Studies Press, Baldock, UK
2. He W, Lei L, Wan B, Zhang J, Wei L (2017) Radio interference performance of hvac conductor bundles at high-altitude location: measured data analysis and altitude correction. IEEE Trans Electromagnet Compatibility 99:1–8
3. Bian X, Wang L, Liu Y, Yang Y (2013) High altitude effect on corona inception voltages of dc power transmission conductors based on the mobile corona cage. IEEE Trans Power Delivery 3:28
4. Hill HL, Capon AS, Ratz O, Renner PE, Schmidt WD (1976) Transmission line reference book HVDC to ±600kV. United States
5. Chartier VL, Stearns RD (2007) Formulas for predicting audible noise from overhead high voltage ac and dc lines. IEEE Trans Power Apparatus Syst PAS-100(1):121–130
6. Nakano Y, Sunaga Y (1989) Availability of corona cage for predicting audible noise generated from HVDC transmission line. Power Delivery IEEE Trans 5(3):1436–1442
7. Zhang X, Cotton I, Li Q, Rowland SM, Emersic C, Chengxing L, Li W (2022) Experimental verification of the potential of superhydrophobic surfaces in reducing audible noise on HVAC overhead line conductors. High Voltage 4
8. Lv J, Zhao P, Yuan H, Xinyu L (2022) Research on the detection technology of audible noise sources of UHVDC transmission lines. J Phys: Conf Ser 1
9. Zhao P, Fu L, Yuan H, Liu Y, Zhao L (2022) Research on audible noise of ultra-high voltage direct current (UHV DC) transmission lines with a digital twin. Digital Twin
10. Li Q, Li Y, Rowland S, Hu J, Cotton I, Jiang X (2022) Audible noise evaluation for six-phase overhead lines transformed from existing three-phase double circuit infrastructures with uprated voltages. High Voltage 5

First-Principle Calculation of Bi_2Te_3-Based Thermoelectric Materials

Ge Tian, Chunping Niu, Hailong He, Tao Xiong, Yuqian Zhang, Yi Wu, Mingzhe Rong, and Haoyang Tian

Abstract Thermoelectric materials have received a lot of attention due to their unique ability to convert waste heat into electricity directly, and the thermoelectric figure of merit zT is the main criterion for characterizing the performance of thermoelectric materials. In this paper, Bi_2Te_3-based materials are investigated using the first-principle calculation software VASP, and the energy band structures of Bi_2Te_3, $BiSbTe_3$, and Sb_2Te_3 have been calculated and analyzed under the consideration of SOC. The results show that the Bi_2Te_3-based materials are heavily affected by SOC, which provides further understanding of the high thermoelectric figure of merit of Bi_2Te_3-based materials. The defect formation energy of the p-type Sb_2Te_3 has been also calculated and the result is analyzed with Yb element doped to form a point defect, and the result of the study shows the possible occupancy of the dopant atom, which provides guidance for experiments.

Keywords Bi_2Te_3 · Thermoelectric materials · First-principles calculation · Semiconductor doping

1 Introduction

With the development of economy and society, energy crisis has become an important issue. Thermoelectric materials are known as a possible candidate of the alternative new energy sources because of their unique thermoelectric effect and their ability to convert thermal energy into electricity. Thermoelectric materials are promising in the area of power generation and refrigeration. Electronic refrigeration appliances made with thermoelectric materials have the advantages of small size, stability and

G. Tian · C. Niu · H. He (✉) · T. Xiong · Y. Zhang · Y. Wu · M. Rong
School of Electrical Engineering, Xi'an Jiaotong University, Xi'an 710000, PR China
e-mail: hhlong@xjtu.edu.cn

H. Tian
State Grid Shanghai Electric Power Research Institute, Shanghai 200000, PR China

© Beijing Paike Culture Commu. Co., Ltd. 2024

X. Dong and L. Cai (eds.), *The Proceedings of 2023 4th International Symposium on Insulation and Discharge Computation for Power Equipment (IDCOMPU2023)*, Lecture Notes in Electrical Engineering 1102, https://doi.org/10.1007/978-981-99-7405-4_30

reliability, which is a feasible solution to solve thermal management problems of next-generation communication technologies [1].

The performance of thermoelectric materials depends on a figure of merit zT, whose magnitude is determined by the combination of the Seebeck coefficient (S), thermal conductivity (κ) and electrical conductivity (σ) of the material, $zT = S^2\sigma T/\kappa$ [2]. In order to obtain figure of merit, the Seebeck coefficient and thermal conductivity of the material are required to be as large as possible, while the thermal conductivity need to be as small as possible in order to maintain the temperature difference of the material, however, these parameters are not independent of each other, but are coupled and affect each other [3]. Among all of them, the thermal conductivity is affected by both lattice thermal conductivity and electron thermal conductivity, and in order to pursue a high figure of merit, the lattice thermal conductivity can be reduced by doping to form defects.

Industrially, Bi_2Te_3-based alloys have become a focused research direction due to the high Seebeck coefficient of Bi_2Te_3-based materials, whose zT can reach about 1 at room temperature, as well as the mature fabrication process of these materials. Both Bi_2Te_3 and Sb_2Te_3 are rhombohedra crystal structures with five atoms. Bi_2Te_3-based materials are topological insulators with narrow band gap [4], the atoms them are mainly connected by covalent bonds, while there are also layer-to-layer Van der Waals forces internally. In recent years, a lot of research have been done both at home and abroad on improving zT of Bi_2Te_3 materials, and the literature [5] calculated the electronic structure and thermoelectric properties of Bi_2Te_3 using the first principle theory and found a high degree of anisotropy of the effective mass near the energy band valley of Bi_2Te_3. The literature [6] investigated the pressure-induced power factor change of the materials and provided guidance for the fabrication of high-performance thermoelectric materials using pressurized processing strategies. The literature [7] summarized the strong bipolar conduction properties due to the narrow band gap of Bi_2Te_3 and compared the performance improvement of p-type and n-type materials subjected to point defects, results showing that p-type can achieve more desirable results by controlling point defects. The literature [8] introduced Ge to improve zT of p-type $(Bi, Sb)_2Te_3$ and demonstrated by defect energy calculations that Ge tend to occupy Sb and form defects. In the literature [9], the bipolar effect of Bi_2Te_3-based materials at high temperatures was suppressed by Ca-doped alloys to improve the thermoelectric properties of the materials, and finally the zT of $Bi_{0.48}Ca_{0.02}Sb_{1.5}Te_3$ at 400 K could reach 1.3.

In this paper, the basic properties of Bi_2Te_3-based materials are investigated based on density functional theory (DFT), as well as the first principle calculation software Vienna ab initio simulation package (VASP) to calculate the properties of the materials. The band structure of Bi_2Te_3-based materials were calculated, the reasons for the good properties presented by the materials were explained, the calculated results of Bi_2Te_3-based materials under different conditions were compared to determine the experimental schemes. The defect formation energy of Bi_2Te_3-based materials when introducing impurities was calculated on the basis of the method in the literature [9], which Verified and provided guidance for the selection of impurity substitution sites in the experiments.

2 Methods

Bi_2Te_3 is Semiconductor Materials with Trigonal crystal structure, which is composed of two main group elements, V and VI, and the space group is D5 3d (R_3m, No.166). The unit cell of Bi_2Te_3 is shown in Fig. 1, there are five atoms along the c-axis in the order Te1-Bi-Te2-Bi-Te1 [10]. The structure of Bi_2Te_3 can be visualized as rhombohedra structure hexagonal cell, where the layers in the cell are bound to each other by van der Waals forces.

First-principles calculations are based on the DFT and are used in the framework of quantum mechanics to obtain information on the properties of materials by taking an approximation to the actual material system and solving Schrödinger's equation directly, which has been widely used in the calculation of electronic structures and physical properties of materials [11]. In this paper, a rhombohedra unit cell of Bi_2Te_3 is chosen for structural optimization and band structure calculation, and the first principle calculation software we used is VASP 5.4.1. The initial cell parameters are chosen as a = b = 4.42 Å and c = 29.84 Å. The calculation is performed using the projector augmented wave (PAW) pseudopotential, and PBE-GGA method is used to estimate the exchange–correlation interaction, and orbital electrons are considered as valence electrons in the pseudopotential. The plane wave cut-off energy is taken as 450 eV in the calculation, the standard MP-grid with 8 × 8 × 8 grid is selected for the K-points of the structure optimization, the energy convergence criterion is 1×10^{-5}, and the convergence criterion of the force is 0.02 eV/nm^{-1}.

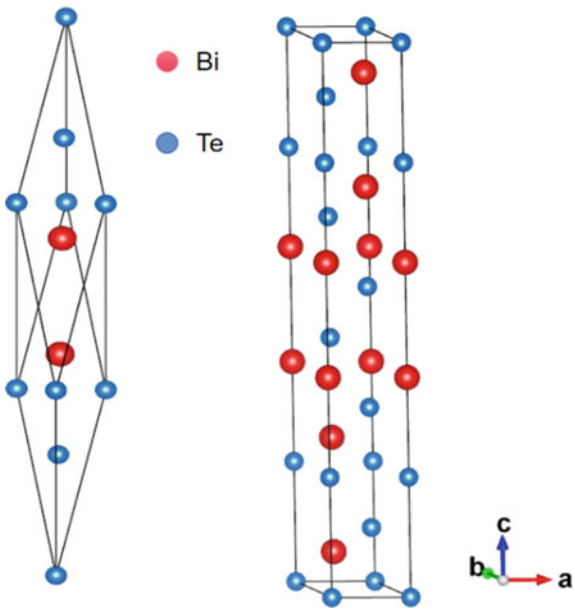

Fig. 1 Crystal structure of Bi_2Te_3

Table 1 Lattice parameters from calculation and experimental measurement

Materials	Calculations (Å)	Volume ($Å^3$)	Experiments (Å)
Bi_2Te_3	a = 4.45Å, c = 31.42	179.79	a = 4.53Å, c = 30.6
$BiSbTe_3$	a = 4.40Å, c = 31.18	173.94	a = 4.32Å, c = 30.49
Sb_2Te_3	a = 4.33Å, c = 31.26	169.43	a = 4.26Å, c = 30.45

3 Results and Analysis

3.1 Lattice Parameters of Bi_2Te_3-Based Materials

Bi and Sb elements are both V main group elements with similar structure and properties, and the doping of Sb atoms can improve the thermoelectric properties of the materials to different degrees. The formation of Bi_2Te_3-based materials Sb_2Te_3 and $BiSbTe_3$ after doping with Sb atoms was studied and analyzed based on the calculation results under different conditions. The crystals formed by replacing Bi atoms by Sb atoms have the same crystal structure, but there will be some differences in the lattice parameters, and this difference may have a significant effect on their band structures. The structures of Bi_2Te_3, Sb_2Te_3 and $BiSbTe_3$ were optimized separately, and the results were obtained with the optimized lattice parameters as shown in Table 1.

The lattice parameters after theoretical optimization calculations are in general agreement with the experimental results [12, 13], and the volumes of the crystal unit cell tend to decrease after Sb replacement of Bi sites due to the smaller radius of Sb atoms than Bi atoms. Therefore, the lattice constants tend to decrease slightly with the increase of Sb concentration in $Bi_{2-x}Sb_xTe_3$ [14].

3.2 Band Structure

The band structure calculation is performed using the optimized Bi_2Te_3 primitive cells, and the high symmetry point paths are selected using SeeK-path [15], and the diagrams are drawn in order G–Z–F–G–L. Results show that Bi_2Te_3 is strongly affected by spin–orbit coupling (SOC), and the band structures of Bi_2Te_3 without and with SOC involved are shown in Fig. 2.

According to the calculated results, the first band gap obtained from the calculations when SOC is not considered is 0.38 eV, and this result is much larger than the experimental value, and both the valence band maximum (VBM) and the conduction band minimum (CBM) are located on the high symmetry point GAMMA. After considering SOC, the calculated band structure has changed considerably [16]. The positions of the VBM and CBM are moved from the GAMMA point to the position of the non-high symmetry point, and the band structure changes from a direct band

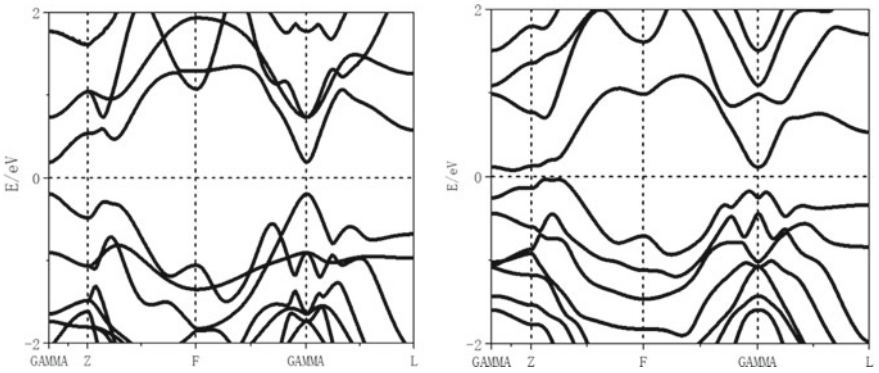

(a) Band structure without SOC (b) Band structure with SOC

Fig. 2 Band structure of Bi_2Te_3 without and with SOC involved

gap to an indirect band gap type. The calculated band gap reduces 0.11 eV, a result that is more in line with the experimentally derived result $\Delta E_{e,g} = 0.15$ eV compared to the case where SOC is not considered [17].

The calculated results here are lower than experimental results, it is mainly because conventional PBE functional tends to underestimate the band gap, so the theoretically calculated band gap will be narrower. In addition, the experimentally calculated energy band gap is influenced by SOC, but also by the initial crystal structure, the pseudopotential, and the accuracy of the theoretical calculation, which may be more obvious for a narrow band gap material such as Bi_2Te_3. Table 2 summarizes the results of the band gap under different calculation conditions and lattice parameters.

The effects of SOC, crystal structure and pseudopotential on the optimized structure as well as the band gap are considered in the table, respectively. Different initial crystal structures is sat for experiments 2, 3 and 4, and the results are obtained under the conditions of considering SOC and using PBE-GGA for calculations. It can be found that the initial structure has a large effect on the energy band structure, and a poor initial structure will cause the calculated band gap and the energy band structure to deviate far from the experimental values. Experiment 4 is optimized with fixed lattice parameters, and the lattice parameters are chosen exactly from the experimental values, and the calculated band gap results are consistent with

Table 2 Band gap energies under different calculating conditions and lattice parameters

Number	Condition	Lattice parameters ($Å^3$)	Band gap(eV)
1	PBE	a = 4.45Å, c = 31.42	0.3838
2	PBE + SOC	a = 4.45Å, c = 31.42	0.1079
3	PBE + SOC	a = 4.42Å, c = 32.26	0.0197
4	PBE + SOC	a = 4.38Å, c = 30.36	0.1468
5	LDA + SOC	a = 4.36Å, c = 29.92	0.0975

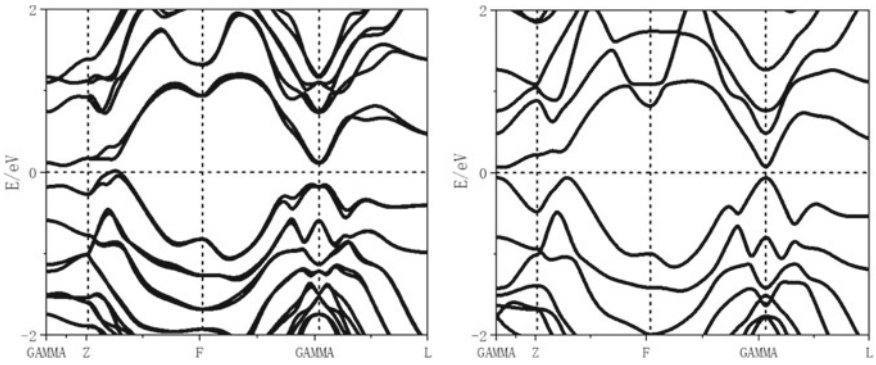

(a) Band structure of $BiSbTe_3$ (b) Band structure of Sb_2Te_3

Fig. 3 Band structure of $BiSbTe_3$ and Sb_2Te_3

the experimental ones. Experiment 5 is calculated using LDA generalized function, and the optimized lattice parameters are smaller than the experimental values, and the optimized structure is closer to the ideal structure, but the calculated band gap structure is not accurate enough. Compared with LDA, PBE further considers the non-local and non-uniform effects, and the calculation results will be more accurate. In order to ensure certain accuracy, the optimal structure is selected by PBE + SOC for calculation in all this calculation.

Sb doping has some effect on the energy bands of Bi_2Te_3-based materials, as shown in Fig. 3, for $BiSbTe_3$ and Sb_2Te_3, respectively. The band structure of $BiSbTe_3$ has some changes, with band splitting at points other than the high symmetry points, which is due to the doping of Sb atoms that breaks the original symmetry of the structure, thus showing the Weyl semimetallic state [18]. The band structure of Sb_2Te_3 shows an indirect band gap with the VBM in the Z-F direction and the CBM in the GAMMA-Z K-point direction, which is consistent with Bi_2Te_3, with a band gap of 0.128 eV, which is basically consistent with the experimental results [19].

3.3 Calculation of Doping Defect Energy

In this paper, the introduction of dopants in Bi_2Te_3-based materials reduces the bipolar effect and thus significantly improving the thermoelectric performance figure of merit of materials. Impurities have different substitution sites, and in order to investigate whether impurity atoms in the $Bi_{2-x}Sb_xTe_3$ system form defects at the Sb site, the defect formation energy of the material is calculated in this paper to determine whether the defects in Sb site can be formed spontaneously. The formula for calculating X's defect formation energy under a charge q is defined as [20].

$$E_f = E_x - E_{bulk} - \sum_i n_i \mu_i + q E_F + E_{corr} \tag{1}$$

where E_x denotes the energy of the doped supercell structure, E_{bulk} denotes the energy of the original supercell structure, n_i and μ_i terms are the gain or loss of particles and their potential energy during the defect formation process, respectively, and the energy of the doped atoms is positive and the energy of the replaced atoms is negative, E_F and E_{corr} is related to the Fermi energy level and the correction value.

Doping of Sb_2Te_3 with Yb element and considering the case of a Yb atom replacing an Sb site to form a point defect, whether the defect is formed spontaneously or not, without considering the charged case. A $4 \times 3 \times 2$ supercell structure containing 120 atoms is used in the calculations of this paper [9], Then the defect formation energy can be expressed as:

$$E_f = E(Sb_{47}Te_{72}Yb_1) - E(Sb_{47}Te_{72}) - E(Yb_1) \tag{2}$$

The defect formation energy depends on the chemical potential of the atoms, and the energy of an individual atom can be determined from the energy of the compound it forms, subject to the following constraints:

$$\begin{cases} 2 \cdot \mu_{Sb} + 3 \cdot \mu_{Te} = E(Sb_2Te_3) \\ \mu_{Sb} \leq E(Sb)/n_{Sb} \\ \mu_{Te} \leq E(Te)/n_{Te} \\ \mu_{Yb} \leq E(Yb)/n_{Yb} \end{cases} \tag{3}$$

The cut-off energy in the calculation is sat to be 450 eV, $2 \times 2 \times 2$ MP grid is chosen for the K-points. the energy convergence criterion is 1×10^{-4}, and the convergence criterion of the force is less than 0.05 eV/nm^{-1}. DFT is only applicable to the calculation of the weakly correlated materials, as a result, it is difficult to handle the system with Yb element involved using normal pseudopotential, which is strongly correlated. Therefore, some electrons in f-orbit are treated as core electrons in the calculations approximately. The calculated defect formation energy with the substitution of Yb is $E_f = -4.0098$ eV and the defect formation energy is negative, indicating that the defects of Yb in the Sb site can form spontaneously, in the $Bi_{2-x}Sb_xTe_3$ system Yb atoms are known to form defects in the Sb site.

4 Conclusion

In this paper, the properties of Bi_2Te_3-based materials are calculated based on first-principle methods, and structural optimization and band structure studies are carried out for $Bi_{2-x}SbxTe_3$. The results show that the energy band structure of Bi_2Te_3-based materials is significantly affected by the SOC effect, and the effects of lattice constant,

pseudopotential and SOC on the band structure calculation results have been studied. The supercell structure of Sb_2Te_3 has been constructed, and the defect formation energy of the material has been calculated in the case of a single Yb atom doped to form a point defect, which can be judged to be spontaneously formed according to the final negative value of the defect formation energy obtained, providing a guide for the experiments.

Acknowledgements This work was supported by the State Grid Corporation of China through the Science and Technology Project under Grant (52094020006Z).

References

1. Pei J, Cai B, Zhuang H et al (2020) Bi_2Te_3-based applied thermoelectric materials: research advances and new challenges. National Sci Rev 7(12):1856–1858
2. Ma J, Xin XY, Liu HQ et al (2023) Origin of improved average power factor and mechanical properties of SnTe with high-dose Bi_2Te_3 alloying. Ceramics Int 49(13):21916–21922
3. Qi Z, Teng F, Feng L et al (2020) Tuning optimum temperature range of Bi_2Te_3-based thermoelectric materials by defect engineering. Chem An Asian J 15(18):2775–2792
4. Cichoň S, Drchal V, Horáková K, et al. (2022) Topological insulator Bi2Te3: the effect of doping with elements from the VIII B column of the periodic table. The J Phys Chem C 126(34):14529–14536
5. Mishra KS, Satpathy S, Jepsen O (1997) Electronic structure and thermoelectric properties of bismuth telluride and bismuth selenide. J Phys: Condensed Matter 9(2):461
6. Andrew G, Qing P, J D S, et al. (2017) Pressure-induced insulator-to-metal transitions for enhancing thermoelectric power factor in bismuth telluride- based alloys. Phys Chem Chem Phys: PCCP 19(20):12784–12793
7. Hong M, Chen Z, Zou J (2018) Fundamental and progress of Bi2Te3-based thermoelectric materials. Chinese Phys B 27(4):048403
8. Qiang Z, Minhui Y, Kaikai P et al (2023) High-performance industrial-grade p-Type (Bi, Sb)$_2Te_3$ thermoelectric enabled by a stepwise optimization strategy. Adv Mater 35(21):2300338
9. Muzaffar M, Zhu B, Yang Q, et al. (2019) Suppressing bipolar effect to broadening the optimum range of thermoelectric performance for p-type bismuth telluride–based alloys via calcium doping. Mater Today Phys 9(C):100130
10. Shen Y, Yu H, Xu T et al (2022) Tailoring Bi_2Te_3 edge with semiconductor and metal properties under electron beam irradiation. Nano Res 15(5):4710–4716
11. Sholl DS, Steckel JA (2022) Density functional theory: a practical introduction. Wiley & Sons
12. Yan X, Zheng W, Liu F, et al. (2017) Electronic structure and transport coefficients of the thermoelectric materials Bi_2Te_3 from first-principles calculations. J Wuhan Univer Technol Mater Sci Ed 32(1):11–15
13. Kasalak TF, Babani A, Çakmak S et al. (2016) Structural and electronic properties of Bi_2-xSbxTe_3 ternary and Bi_2-xSbxTe_3-ySey quaternary compounds. Optoelectron Adv Mater 10(5–6):391–396
14. Zou Y, Zhang X (2019) First-principle study of electronic structure of Se doped Bi_2Te_3. J Pingxiang Univer 36(3):34–37 (in Chinese)
15. Hinuma Y, Pizzi G, Kumagai Y et al (2017) Band structure diagram paths based on crystallography. Comput Mater Sci 128:140–184
16. Park K, Heremans JJ, Scarola VW et al. (2010) Robustness of topologically protected surface states in layering of Bi_2Te_3 thin films. Phys Rev Lett 105(18):186801

17. Lan Y, Minnich JA, Chen G et al (2010) Enhancement of thermoelectric figure-of-merit by a bulk nanostructuring approach. Adv Funct Mater 20(3):357–376
18. Singh S, Garcia-Castro CA, Valencia-Jaime I et al (2016) Prediction and control of spin polarization in a Weyl semimetallic phase of BiSb. Phys Rev B 94(16):161116
19. Larson P (2006) Effects of uniaxial and hydrostatic pressure on the valence band maximum in Sb_2Te_3: an electronic structure study. Phys Rev B 74(20):205113
20. Freysoldt C, Grabowski B, Hickel T et al (2014) First-principles calculations for point defects in solids. Rev Modern Phys 86(1):253

Simulation of Arc Erosion on the Main Contact of On-Load Tap Changer

Yuanxiang Zhou, Yasong Dai, Jianning Chen, Yuhang Li, Xuzhao Hou, and Zhen Zhang

Abstract Long-term operation and switching of transformer on-load tap-changers can cause degradation and deterioration of the main contact material, even leading to contact arcing damage in severe cases. However, the arcing mechanism of the main contact during the switching has not been clarified yet. A magneto-hydrodynamic simulation method of main contact arcing has been proposed. The geometry of the main contact in transformer oil is simplified, and the simulation model of the arc temperature field of the main contact in transformer oil coupled with electric, magnetic, thermal and fluid fields is proposed. The dynamic evolution of the arc temperature has been investigated at peak currents of 2100 A, 1500 A, 600 A and 300 A, respectively. The results show that with the increase of the spacing between contacts, the temperature at arc core rises rapidly and then decreases slowly, and the temperature can reach 50177 K at 2100A. Due to the electron bombardment at the anode surface, the temperature at anode surface is higher than that at cathode surface under different chopped currents. The highest temperatures at anode and cathode surface can reach 4142.5 K and 4081.7 K respectively.

Y. Zhou (✉) · Y. Dai · J. Chen · Y. Li · X. Hou
State Key Laboratory of Control and Simulation of Power Systems and Generation Equipment, Department of Electrical Engineering, Tsinghua University, Beijing 100084, China
e-mail: zhou-yx@tsinghua.edu.cn

Y. Dai
e-mail: dys18056961003@163.com

J. Chen
e-mail: chen-jn18@mails.tsinghua.edu.cn

Y. Li
e-mail: yh-li20@mails.tsinghua.edu.cn

X. Hou
e-mail: hxz22@mails.tsinghua.edu.cn

Z. Zhang
The Wind Solar Storage Division of State Key Laboratory of Power System and Generation Equipment, School of Electrical Engineering, Xinjiang University, Urumqi 830047, China
e-mail: zhzhen24@163.com

© Beijing Paike Culture Commu. Co., Ltd. 2024

X. Dong and L. Cai (eds.), *The Proceedings of 2023 4th International Symposium on Insulation and Discharge Computation for Power Equipment (IDCOMPU2023)*, Lecture Notes in Electrical Engineering 1102, https://doi.org/10.1007/978-981-99-7405-4_31

Keywords Tap-changer · Contact · Arc · Chopped current · Temperature

1 Introduction

On-load tap-changer is a key component of the converter transformer, which adjusts the valve-side voltage and valve-side trigger angle in high-voltage DC transmission systems [1–4]. Long-term switching of the on-load tap-changer causes deterioration of the material and component properties of the current-carrying system, fatigue fracture of the connections, damage to the main contacts, and arcing erosion of the vacuum tube contacts. The result is a contact that is difficult to open reliably [5–8].

Wu [9] used magneto-hydrodynamic (MHD) to establish a numerical model simulation of steady-state heat transfer in a DC fault arc. The results show that the arc conduction to both sides of the electrode will occur a sudden drop in temperature, and the electrode spacing on the arc conduction temperature effect is not significant. Zhong [10] introduced copper vapor for the simulation and testing of small-current DC arcs, and it was found that the simulation of arcs containing copper vapor medium was closer to the experimental data than that of pure air medium. Cressault [11] established the arc erosion model of air and metal vapor by adopting the two-temperature model. Jolly [12] simulated the current value of anode contact point at melting. Wang [13] established an arc melt pool model to obtain electrode erosion The current studies on arc fault characteristics and simulation modeling are mainly on isolating switches, relays, circuit breakers, vacuum tubes, but less on the main contact arc of on-load tap-changers. Unlike gas discharges, the main contact is immersed in transformer oil for switching, and the mechanism of arc erosion in the oil of the on-load tap-changer main contact is not yet clear. So the study of its physical mechanism has important scientific significance and engineering value.

In order to analyze the erosion of the on-load tap-changer main contacts in transformer oil, a finite element simulation model of arc erosion of the on-load tap-changer main contacts based on magneto-hydrodynamics was established. The dynamic evolution of the temperature at the main contact with varied chopped currents was studied and analyzed.

2 Numerical Simulation

This paper has carried out a simulation study on the arc characteristics during the contacts disconnection process, and analyzed the dynamic evolution of the arc temperature at different moments of the contact and the temperature rise law of the arc area under the conditions of the peak chopped currents of 2100 A, 1500 A, 600 A and 300 A, respectively.

2.1 Geometric Modeling

The on-load tap-changer main contacts are mostly made of copper and are immersed in transformer oil. In order to save computation, the simulation model simplifies the material shape and uses the two-dimensional model shown in Fig. 1 as the geometric model for the arcing process of the on-load tap-changer main contacts. The overall calculation area is 45 mm long and 30 mm wide. The copper electrode is 5 mm long and 5 mm wide with a radius of 1 mm at the chamfer. The other area is the transformer oil and the initial spacing between the two electrodes is 0.2 mm. A triangular mesh is used for unstructured meshing of the simulation area. The number of triangular cells is 24,099, the number of nodes is 84,524, and the mesh is partially shown in Fig. 2. The arc region occurs in the spacing part between the two electrodes and involves multi-physical fields coupling, where the parameters of each physical property of the material in the simulation model are shown in Table 1.

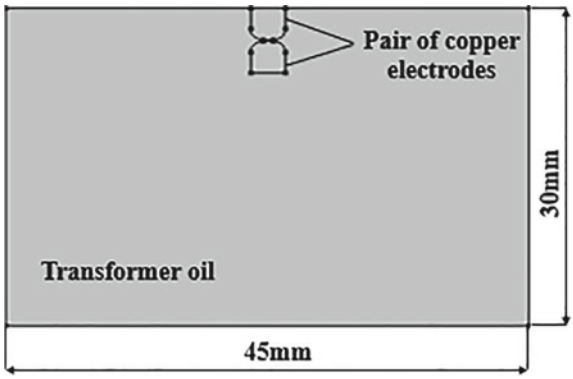

Fig. 1 Simulation of geometric models

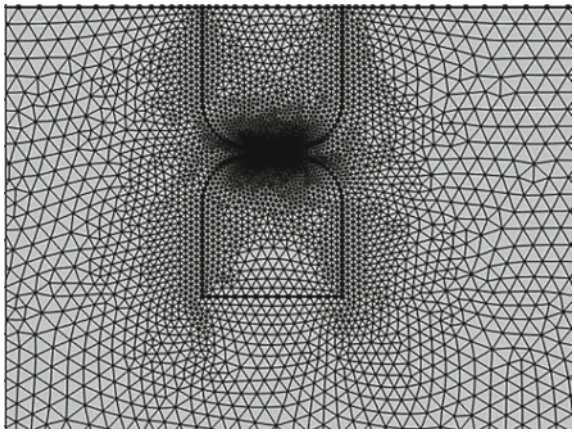

Fig. 2 Partial grid subdivision

Table 1 Parameters of physical properties of materials in numerical model

Parameter	Value
Copper density /(kg/m^3)	8960
Copper thermal conductivity /[W/(m· K)]	400
Copper specific constant pressure heat capacity /[J/(kg· K)]	385
Copper conductivity /(S/m)	5.998×10^7
Relative dielectric constant of transformer oil	2.125
Conductivity of transformer oil (S/m)	0.0714

2.2 Magneto-Hydrodynamic Control Model

This paper simulates contact arc erosion based magneto-hydrodynamic equations, which includes hydrodynamic equations and Maxwell's equations [5, 6].The simulation of arc plasma is a multi-physical field coupled electric–magnetic-thermal-fluid interaction process. The arc equations include the mass conservation equations, momentum conservation equations, energy conservation equations in fluid dynamics, and also Maxwell's equations in electromagnetism. The control equations are as follows:

Conservation of mass equations:

$$\rho \nabla \cdot \mathbf{u} = 0 \tag{1}$$

Conservation of momentum equations:

$$\rho \frac{\partial \boldsymbol{u}}{\partial t} + \rho(\boldsymbol{u} \cdot \nabla)\boldsymbol{u} = \nabla \cdot \left[-p\mathbf{I} + \mu\left(\nabla \boldsymbol{u} + (\nabla \boldsymbol{u})^{\mathrm{T}}\right)\right] + \boldsymbol{F} \tag{2}$$

$$\boldsymbol{F} = \boldsymbol{J} \times \boldsymbol{B} \tag{3}$$

Conservation of energy equations:

$$\rho C_\rho \left(\frac{\partial T}{\partial t} + \boldsymbol{u} \cdot \nabla T\right) - \nabla \cdot (k \nabla T) = Q \tag{4}$$

$$Q = \frac{\partial}{\partial t}\left(\frac{5k_{\mathrm{B}}T}{2\mathrm{e}}\right)(\nabla T \cdot \boldsymbol{J}) + \boldsymbol{E} \cdot \boldsymbol{J} - Q_{\mathrm{vd}} \tag{5}$$

where: ρ is the fluid density; $\boldsymbol{u}$ is the fluid velocity vector; p is the pressure; $\boldsymbol{I}$ is the unit matrix; μ is the kinetic viscosity; and $\boldsymbol{F}$ is the force source term (Lorentz force); $\boldsymbol{J}$ is the current density vector; $\boldsymbol{B}$ is the magnetic induction intensity vector; C_ρ is the constant pressure heat capacity; T is the temperature; k is the thermal conductivity; Q is the heat source term, mainly including enthalpy transfer, Joule heat and viscous dissipation, corresponding to the three terms in Eq. (5); k_{B} is the Boltzmann constant;

e is the unit charge; Q_{vd} is the viscous dissipation loss, which is an inherent physical parameter of transformer oil.

Electric field equations:

$$\nabla \cdot \boldsymbol{J} = 0 \tag{6}$$

$$\boldsymbol{J} = \sigma \boldsymbol{E} \tag{7}$$

$$\boldsymbol{E} = -\nabla \varphi \tag{8}$$

Magnetic field equations:

$$\nabla \times \boldsymbol{H} = \boldsymbol{J} \tag{9}$$

$$\boldsymbol{B} = \mu_r \mu_0 \boldsymbol{H} \tag{10}$$

$$\boldsymbol{B} = \nabla \times \boldsymbol{A} \tag{11}$$

where: $\boldsymbol{J}$ is the current density; $\boldsymbol{E}$ is the electric field strength vector; φ is the potential; $\boldsymbol{H}$ is the magnetic field strength; $\boldsymbol{B}$ is the magnetic induction strength; μ_r is the relative magnetic permeability, which takes the value of 1 here; μ_0 is the magnetic permeability of the vacuum; and σ is the electrical conductivity.

2.3 Boundary Conditions

In the geometric model shown in Fig. 1, the copper contact electrode pairs are divided into dynamic contact and static contact, where the top contact is fixed as static contact and the bottom contact is dynamic contact whose movement speed is 0.2 m/s. In the current field setting, the current of the dynamic contact is set to the starting amplitude of 2100 A, 1500 A, 600 A, 300 A oscillating decay chopped current, and the waveform is shown in Fig. 3. The initial value of temperature in the calculation domain is set to 293.15 K, the initial value of transformer oil domain pressure is 101 kPa, and the wall condition is set to no slip.

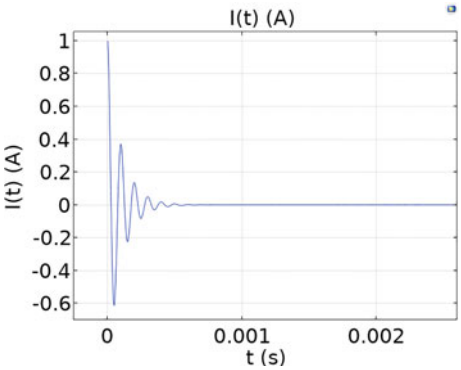

Fig. 3 Chopped current unit initial waveform

3 Research Results

Based on the established model, this paper explores the dynamic evolution characteristics of the arc and copper contact electrode surface temperature in transformer oil with the opening process, and investigates the influence of different peak chopped currents on the temperature distribution characteristics of the arc region.

3.1 Dynamic Process Arc Temperature Distribution Characteristics of Contacts Under 1500A Chopped Current

The contact erosion process was simulated for a peak interruption current of 1500 A and the temperature distribution in the arc region at different moments was obtained, as shown in Fig. 4.

As can be seen from Fig. 4, with the simulation time progressing, the contact spacing gradually increases and the arc temperature first increases sharply, up to 2.59×10^4 K. Then until the final moment of simulation 0.012 s, the arc temperature slowly decreases to 1.02×10^4 K. During the opening process, the shape of the arc gradually evolves from the initial arc column to arc wire shape, and the highest temperature is mainly concentrated in the arc center near the electrode area of the two contacts.

The changes of upper and lower electrode surface temperatures over time are shown in Fig. 5. As can be seen from Fig. 5, the arc generated in the breaking process has different influences on the surface temperature of the lower electrode on the contact. The surface temperature of the upper electrode is higher than that of the lower electrode, which is mainly caused by electron bombardment on the anode surface.

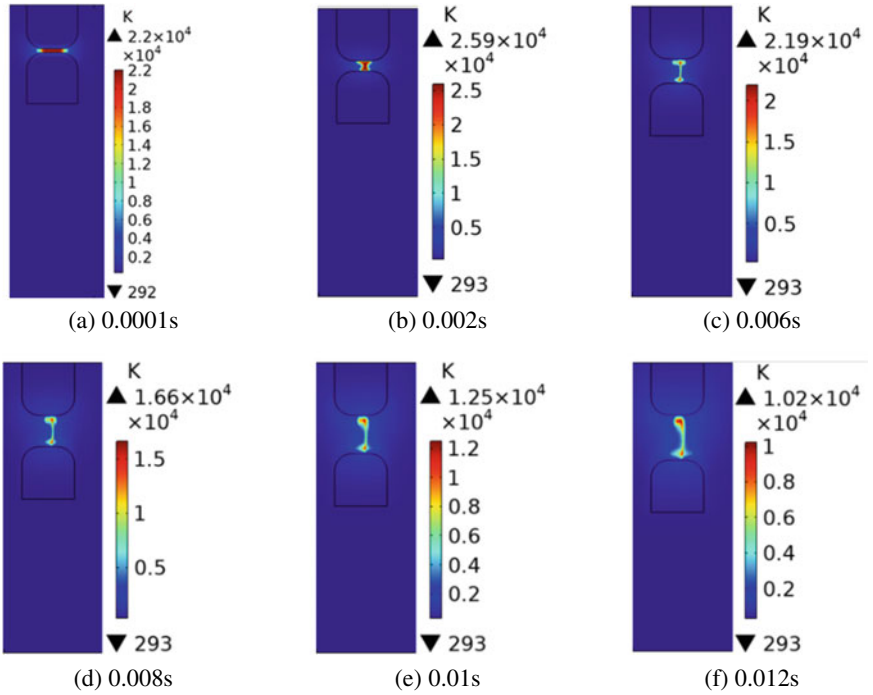

Fig. 4 Arc temperature distribution in transformer oil at different time of 1500 A chopped current amplitude

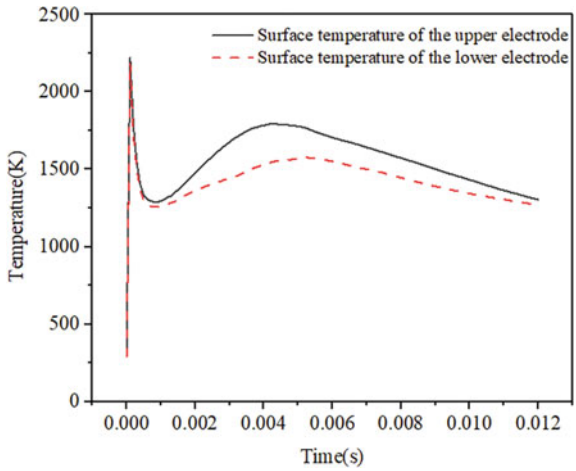

Fig. 5 Temperature distribution of upper and lower electrodes with a chopped current amplitude of 1500 A

3.2 *Characteristics of Peak Chopped Current on Arc Temperature Distribution in Oil*

To investigate the effect of peak chopped current on the temperature distribution characteristics of the arc in oil, the temperature plots with the currents of 2100, 1500, 600 and 300A were selected for analysis at 0.012 s, as shown in Fig. 6.

When the chopped current reaches the maximum of 2100A at 0.012 s, the maximum temperature of the arc at the end of simulation can reach 4.37 × 104 K. With the decrease of the peak current, the arc temperature gradually attenuates to 2.19×10^4 K, 3.44×10^3 K and 1.05×10^3 K, respectively. The variation curve of the maximum temperature in the arc region over time under different current is shown in Fig. 7.

In the whole process of discharge, under different peak chopped currents, the arc temperature increases sharply first and then rises slowly. Gradually, it shows a decreasing trend after reaching the peak value. With the increase in peak chopped

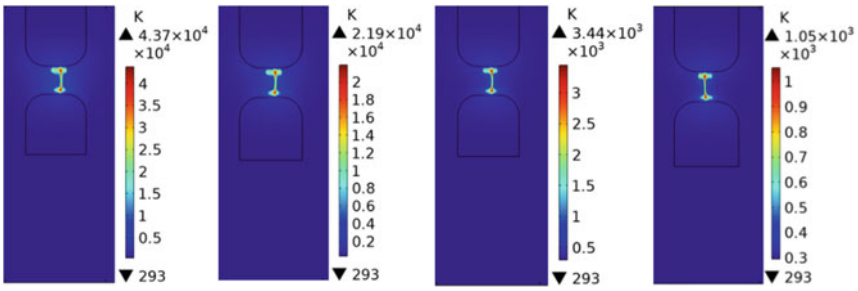

(a) 2100A (b)1500A (c) 600A (d) 300A

Fig. 6 Arc temperature distribution in oil with different chopped current amplitudes at 0.012 s

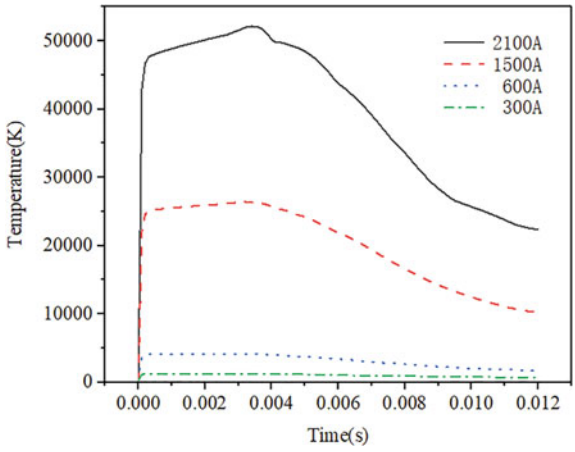

Fig. 7 Curve of maximum arc temperature with time under different chopped current amplitudes

current, the peak arc temperature also increases. When the peak current is 2100 A, the arc temperature reaches a maximum of 52116 K.

3.3 *Effect of Arc on Temperature Field Distribution of Contact Electrode Surface*

Figures 8 and 9 respectively show the temperature distribution laws of the arc on the upper and lower electrode surfaces for different chopped current amplitudes

Similar to the law in Fig. 5, the surface temperature of the upper electrode is higher than that of the lower electrode due to the effect of the electron bombardment on the

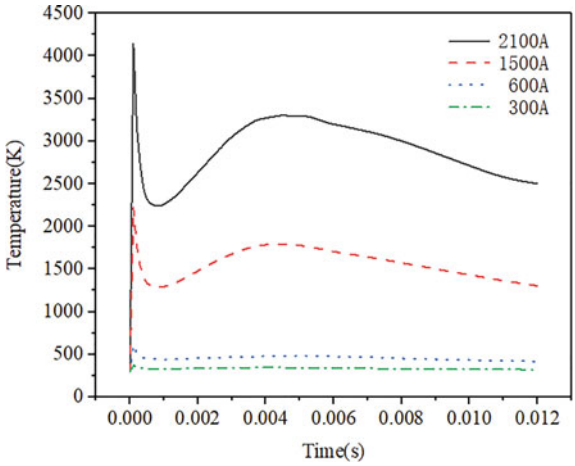

Fig. 8 Temperature distribution curves of upper electrode surface with different chopped currents

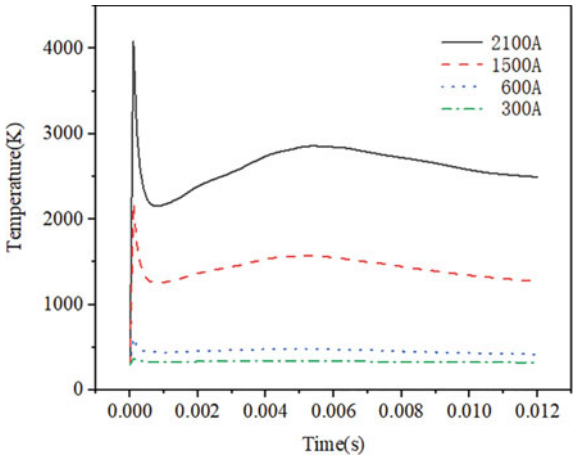

Fig. 9 Temperature distribution curves of lower electrode surface with different chopped currents

anode surface. The electrode surface temperature is closely related to the peak size of chopped current. When the maximum chopped current is 1500 A, the maximum electrode surface temperature is 747.02 K. When the minimum chopped current is 250 A, the maximum surface temperature of the upper electrode is just 306.6 K.

4 Conclusion

In this paper, a coupled multi-physical field simulation model of arc erosion on the main contact of an on-load tap-changer is established and the influence of arc erosion on the temperature change of the main contact is calculated for different chopped currents.

(1) During the current breaking process, the temperature of arc core rises rapidly first and then decreases slowly with the increase of breaking distance. The main reason is that the arc plasma channel is formed under the action of the initial moment of chopped current. After the arc is formed, the temperature rises rapidly. Later, with the increase of the opening distance, transformer oil convection occurs, which takes away part of the arc heat, making the arc temperature show a slow decline trend.
(2) At different chopped currents, the anode surface temperature is higher than the cathode surface temperature due to the electron bombardment of the anode surface. During the formation of an electric arc, there is a continuous thermal movement of electrons and ions. However, the electrons are moving much faster than the ions. The number of electrons impinging on the anode is much greater than that of the cations impinging on the cathode. As a result, the temperature of the anode is higher than the surface of the cathode in the arc process.

Acknowledgements This work is supported by Science and Technology Project of State Grid Co., Ltd. (Research on the Improvement of Explosion Proof Design Technology for Oil Tanks and Components of UHV Transformer Equipment, 5500-202056464A-0-0-00).

References

1. Dhanunjayudu N, Yuvaraju A, Vishnuvardhan RK (2015) Implementation of LCC HVDC converter transformer tap changer controller, H-I-L validation using real time digital simulator. In: 2015 Annual IEEE India conference,New Delhi,India
2. Wenxia S, Liuhui, et al. (2022) Analysis method of electrical stresses during switching process of vacuum on-load tap-changer in converter transformers. Proceedings of the CSEE 42(18):6908–6918 (in Chinese)
3. Yinghao Z,Dazhong S (2012) Electric mechanism of on-load tap changer. Beijing, China Electric Power Press, pp 43–57 (in Chinese)
4. Shaowu W, Peng L, Jinzhong L et al (2022) The overview of transformer vacuum-type on-load tap changers. Proc CSEE 42(18):6893–6908 (in Chinese)

5. Zhicheng P, Jun D, Xiang P, et al. (2022) Research on arc test in oil chamber of vacuum on-load tap-changer for converter transformer. vol 35(12). Guangdong Electric Power, pp 76–83 (in Chinese)
6. Xiaosong Z (2019) Typical fault simulation and optimum design method of on-load tap-changer based on virtual prototype. Chongqing University, Chongqing (in Chinese)
7. Wei L, Ting J, Haoyang T et al (2019) Analysis on spring fracture failure of quick switching structure of transformer on-load tap changer. Power and Energy 40(6):707–711 (in Chinese)
8. Fangrong WEI (2007) Stress relaxation dynamic properties and service life evaluation of helical compress spring. Tianjin University, Tianjin (in Chinese)
9. Qirong W, Rencheng Z, Ran T (2021) Simulation study on steady-state heat transfer characteristics of DC arc fault. Trans China Electrotech Soc 36(13):2697–2709 (in Chinese)
10. Yuming Z, Lan X, Zikang Y (2020) Numerical simulation and experiment of small current DC arc considering copper vapor medium. Trans China Electrotech Soc 35(13):2913–2921 (in Chinese)
11. Cressault Y (2008) Influence of metallic vapours on the properties of air thermal plasmas. Plasma Sources Sci Technol 17(3):35016–35016
12. Jolly DC (1982) Anode surface temperature and spot formation model for the vacuum arc. J Appl Phys 53(9):6121
13. Wang LJ, Zhou X, Wang HJ et al (2012) Anode activity in a high-current vacuum arc: three-dimensional modeling and simulation. IEEE Trans Plasma Sci 40(9):2237–2246

Evaluation on Health Status of Microgrid Equipment in Tropical Islands Based on D-S Evidence Theory

Jifang Chen, Lihong Ma, Dan Qin, Kaijian Feng, Chengyi Wen, Meiyin Wang, and Yu Zheng

Abstract In order to improve the reliability of electrical equipment for isolated microgrids in tropical islands, it is necessary to accurately assess the health status of key equipment to carry out differentiated operation and maintenance. We propose a health status assessment model that comprehensively considers multi-dimensional information such as equipment operating parameters, meteorological environment, operation and maintenance history, and equipment resume. Based on D-S evidence theory, multi-source data is fused and analyzed, and the effectiveness of the assessment model is verified using a diesel generator as an example. The results show that the defects of diesel generators are mainly concentrated in five major functional systems, including fuel, startup, heat dissipation, electrical, and motive power systems. Among them, the number of defects involving power and electrical systems is relatively large and the severity of defects is higher. About 40% of the defects involving environmental impacts. According to the defect type and experience, the health status under different defects is given, and then the trust allocation function is preset. The credibility of the integrated assessment results of diesel generator's health status is significantly improved compared to using single assessment information. Our study can provide a reference for the differentiated operation and maintenance of microgrid equipment in tropical islands.

Keywords Isolated microgrid · Tropical island · Health status assessment · Reliability of equipment · Differentiated operation and maintenance

J. Chen · L. Ma · D. Qin · K. Feng · C. Wen · M. Wang
Hainan Power Grid Co., Ltd, Haikou 570100, China

Y. Zheng (✉)
School of Electrical Engineering and Automation, Wuhan University, Wuhan 430072, China
e-mail: zywhuee@whu.edu.cn

© Beijing Paike Culture Commu. Co., Ltd. 2024

X. Dong and L. Cai (eds.), *The Proceedings of 2023 4th International Symposium on Insulation and Discharge Computation for Power Equipment (IDCOMPU2023)*, Lecture Notes in Electrical Engineering 1102, https://doi.org/10.1007/978-981-99-7405-4_32

1 Introduction

With the proposal and promotion of China's marine power strategy, the development and utilization of tropical island resources are gradually being valued. Since tropical islands are usually far away from the mainland, small in area and permanent population, considering the technical and economic efficiency, it is difficult to use submarine cables to provide power energy through the mainland. Therefore, these islands mainly use diesel generator, photovoltaic panels, wind turbines and other power sources to build isolated microgrids (hereinafter referred to as isolated grids) for power supply. In order to improve the reliability of isolated network systems, it is necessary to study the health status assessment of electrical equipment under the special geographical and climatic environment of tropical islands. Accurate evaluation and prediction on the health status of equipment is the basis for differentiated operation and maintenance strategies.

At present, researches on island isolated networks mostly focus on the stability and control of isolated network systems [1], energy optimization configuration and planning [2], and new energy generation prediction [3]. There are few researches on the operation and maintenance strategies of isolated network equipment. Tropical islands have special meteorological environments such as high temperature, high humidity, high salinity, strong sunlight, heavy rainfall, and strong typhoons, which can lead to serious corrosion of equipment on islands, thereby reducing equipment reliability. On the other hand, due to the island's distance from the mainland, the supply of spare parts required for maintenance is relatively lagging. This brings new challenges to the operation and maintenance of isolated network equipment on tropical islands. It is necessary to consider the impact of multiple factors such as the environment on the health status of equipment and establish an evaluation model in line with the actual operation of power equipment on tropical islands.

Researchers have focused on the status assessment of power equipment in tropical island environment [4]. By analyzing the types and causes of equipment defects in tropical islands, an environmental status assessment index for vacuum circuit breakers has been constructed. The combination of sequential relationship analysis and independence weight method is used to achieve comprehensive evaluation of the operating status of vacuum circuit breakers. In addition, a monitoring scheme for electrical equipment in tropical island environment is proposed to monitor the atmospheric environment, service microenvironment and typical equipment operation status, and provide effective data for equipment test correlated with environment. At the same time, the environmental adaptability and related standards of distribution automation terminals in tropical islands were analyzed, and it was pointed out that environmental effects such as corrosion and aging have reduced the reliability of equipment operation. There is still room for improvement in anti-corrosion treatment, moisture-proof structure, and environmental control technology. Due to the significant difference between the comprehensive environment of tropical islands and the conventional continental environment, it is particularly important to establish a new operational reliability assessment system [5]. In addition, the monitoring

and protective measures for the "three high" environmental conditions of the island microgrid were studied, and it was found that the island's high humidity and high salt environment has extremely strong corrosiveness to equipment metal materials and components, reaching G3 level. Experiments have found that selecting appropriate materials and coatings can effectively reduce or avoid corrosion [6]. The above research provides important references for the health status assessment of power equipment on tropical islands, but it is still in the preliminary exploration stage, involving only a few types of equipment, and the influencing factors considered are not comprehensive enough. Therefore, it is necessary to establish a multi-dimensional information fusion method for evaluating device health status.

D-S evidence theory is mainly used for information fusion decision making, which can realize multi-source information synthesis and has been widely used in equipment diagnosis [7]. In this paper, we consider the special climatic environment of tropical islands, equipment operation data and O&M (operation and maintenance) data, equipment history and other factors to establish a multidimensional health status assessment model of isolated network equipment in tropical islands based on D-S evidence theory, and combine the actual data of typical equipment diesel generators to verify the validity of the model.

2 Health Status Assessment Model

The D-S evidence theory can simulate human thought processes for equipment health status assessment, the evaluation process is shown in Fig. 1, Firstly, the identification framework of health degree needs to be determined, which is finally used to evaluate the specific health status of the output. Information is then observed and collected, i.e. the evidence for the evaluation, which can come from different dimensions of evidence information. Then a trust allocation function is given for each piece of evaluative evidence, i.e. the trust value for each category of health status evaluated on the basis of that evidence. Finally, the multi-dimensional information is synthesized to make D-S fusion judgment, that is, evidence synthesis, so as to obtain the final evaluation result of the health status of the device. The key steps are determining the health status range (identification framework), the probability corresponding to the evidence set assignment (trust allocation function), and the synthesis of evidence probability data (D-S synthesis rules).

The modelling and solution method for equipment health state assessment using D-S evidence theory is as follows: let Θ be the identification frame and the trust allocation function m on the identification frame Θ satisfies the conditions shown in Eq. (1).

$$\begin{cases} m(\emptyset) = 0 \\ \sum\limits_{A \subseteq \Theta} m(A) = 1 \end{cases} \tag{1}$$

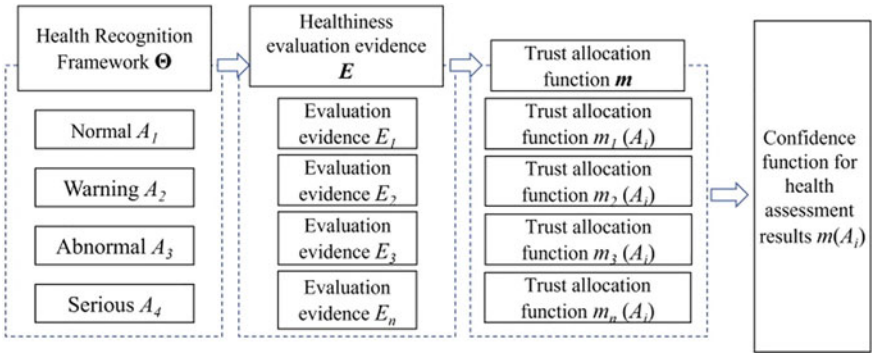

Fig. 1 Process of equipment health assessment using D-S evidence theory

$m(A)$ reflects the support of the evidence for health state A. Its value is the assigned value of trust for health state A. The null set has a trust value of zero and all other subsets have a trust value equal to 1. Assuming that there are n sets of evidence $E1$, $E2$ … En and $m1$, $m2$ … mn are the corresponding trust allocation functions under the same identification framework Θ, the D-S synthesis rule can be expressed in Eq. (2). K is called the conflict coefficient and can be calculated by Eq. (3), which reflects the degree of conflict between different evidences, with a larger K indicating a greater conflict between evidences.

$$m(A) = \begin{cases} \dfrac{1}{1-K} \displaystyle\sum_{\cap Ai=A} \prod_{0\le i\le n} m_i(A_i) \\ 0, \end{cases} \tag{2}$$

$$K = \sum_{\cap Ai=\emptyset} \prod_{0\le i\le n} m_i(A_i) \tag{3}$$

The evaluation evidence can be any quantity related to the health status of the equipment, such as the micro-environment of the equipment that may have a significant impact on the health status, the service life of the equipment, and the amount of operation and maintenance status. Each piece of evidence can be given an initial trust assignment function in conjunction with the equipment's operation and maintenance experience. As the operation and maintenance data accumulates, a trust assignment function will be derived that brings the evaluation results closer and closer to the true state of health.

3 Typical Equipment Health Condition Assessment

As shown in Fig. 2, the defects of diesel generators found in the operation and maintenance of isolated microgrids on a tropical island are classified, which are obtained from the actual operation and maintenance data of seven diesel engines over the past 2 years. It can be seen that the defects are mainly concentrated in five major systems, including fuel, startup, heat dissipation, electrical and motive power systems. The defects are classified into three categories: major, emergency and general according to the severity of their impact, while environment-related defects are considered according to the unique environment of tropical islands, mainly corrosion-related contact point rust, oxidation and leakage of sealed containers such as fuel tanks and water tanks. Those marked with a number in the chart are the number of times the defect has been repeated, for example, a water tank leakage defect due to corrosion is 3 times. All other defects not marked with a number have a number of 1 occurrence.

It can be seen that, in terms of defect types, the number of defects involving electrical and motive power systems is the highest, and the severity is higher. This is because the electrical and motive power systems operate in a more complex environment and are subjected to strong electromagnetic, high temperature and high pressure for a long period of time, which accelerates the ageing of materials. At the same time, the electrical and motive power systems are the core of the diesel engine and defects involving these two systems usually develop directly into downtime failures, hence the higher severity of the defects. In addition, environment-related

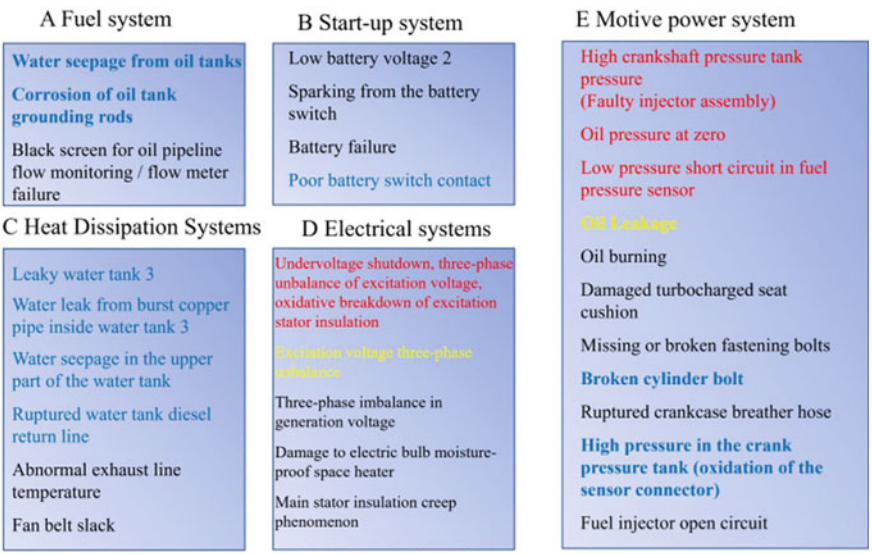

Fig. 2 Defect types of different functional systems of diesel generators (Red represents major defects, yellow represents abnormal defects, black represents attention defects and blue represents environmental related defects)

defects reached 13 times, accounting for about 40% of the total number of defects, but such defects usually take longer to develop into failures and can generally be detected and eliminated in time.

The possible subset categories in the health status identification framework for diesel generators derived from the above analysis are shown in Table 1. For equipment corrosion caused by the environment, it is often difficult to determine its health status as normal or warning, and there are fuzzy intervals between these two states. There are also fuzzy intervals for inspection items where multiple states are difficult to identify.

Using a typical case illustration of a water tank leakage defect found during an inspection, the results of a fusion assessment using D-S evidence theory are shown in Table 2. The figures in the table indicate the probability of assessment using different information, or the confidence level of the corresponding state. The defect occurs in the heat sink and is a corrosion-related problem at the ambient weather information level, and since it has not been long since the tank was last shut down for cleaning, the assessment from the ambient weather information is more likely to be that the equipment is currently in a 'normal' state, but there are other states that are possible with a lower degree of confidence. From an operations and maintenance inspection perspective, the inspection found water leaking from the tank is more inclined to consider the equipment to be in the 'warning' state, but due to the low rate of leakage, there is a certain probability that it is in the 'normal' or 'normal and warning' status. From the perspective of the equipment ledger, because the equipment has just been put into operation, its reliability should be in the stable section at the bottom of the 'bathtub curve', so the probability of a 'warning' or 'abnormal' state is not high, and it is even considered unlikely that a 'serious' condition will occur at this time. After fusing the information from the three different dimensions using D-S evidence theory, it was found that the reliability of the 'normal' state was still the highest, followed by the 'warning' state, and the 'between normal and warning' state. The reliability of the "between normal and warning" dimension is significantly lower

Table 1 Possible subsets in the health status identification framework of diesel generator

Serial number	Status	Remarks
1	Normal	/
2	Warning	/
3	Abnormal	/
4	Serious	/
5	Normal, Warning	Judgement between normal and warning
6	Warning, Abnormal	Judgement between warning and abnormal
7	Abnormal, Serious	Judgement between abnormal and serious
8	Warning, Abnormal, Serious	Judgement between warning, abnormal and serious

than that of the single information evaluation. Based on the fusion results, the device status can be evaluated as healthy.

The above case study shows that when using D-S evidence theory for multidimensional information fusion assessment, the consistency between different evidence has a greater impact on the fusion results. For example, in Table 2 the results evaluated using environmental meteorological information and equipment ledger information have a good consistency, which leads to both overwhelming the operations and maintenance inspection information. The assessment of environmental meteorological information in practical testing varies with increasing equipment operating time, as determined by the corrosion rate of the equipment. Table 3 shows the effect on the D-S fusion results of changes in the assessment of the ambient weather information. For the purpose of this analysis, the sum of the confidence levels for the normal and warning states is kept constant, while only the confidence level for normal or warning is changed. The results show that when the confidence level of 'normal' is reduced to 0.3, the D-S fusion result will be assessed as 'warning', which also illustrates the advantages of using the D-S evidence fusion approach for assessing the health status of electrical equipment on tropical islands, i.e. it allows for more accurate assessment results by fully considering the multidimensional information that affects complexity. Theoretically, the more evidence is obtained and the more consistent the different evidence is, the more accurate the assessment result will be.

Table 2 Multidimensional fusion result for health status evaluation of diesel generator

Serial number	Environmental Weather	Operations and maintenance	Equipment ledger	D-S Fusion
1	0.5	0.2	0.6	0.7040
2	0.2	0.6	0.2	0.2816
3	0.1	0.04	0.05	0.0023
4	0.025	0.01	0	0
5	0.1	0.1	0.1	0.0117
6	0.025	0.02	0.05	0
7	0.025	0.02	0	0
8	0.025	0.01	0	0

Table 3 Impact of changes in environmental information on fusion evaluation results

Normal in environmental weather	Warning in environmental weather	Normal in D-S fusion	Warning in D-S fusion
0.5	0.2	0.7040	0.2816
0.4	0.3	0.5632	0.4224
0.3	0.4	0.4224	0.5632
0.2	0.5	0.2816	0.7040
0.1	0.6	0.1408	0.8448

On the other hand, it is also evident that where there is a single piece of evidence that conflicts with other evidence, fusion assessment using D-S evidence theory often results in a minority of evidence being submerged in the majority. However, these few pieces of evidence are likely to be key pieces of evidence as well, and therefore the weighting of the different pieces of evidence needs to be considered when fusing, which is a direction that needs further research when using D-S evidence theory for equipment health status assessment.

4 Conclusions

(1) A multidimensional assessment model of the health status of isolated microgrid equipment on tropical islands considering environmental impacts, operation and maintenance inspection data, and ledger data is proposed, and the D-S evidence theory is used to fuse and assess the multidimensional information. The model is illustrated with diesel generators as a typical case to achieve an intelligent assessment of the health status of equipment that simulates human thought processes.
(2) The characteristics of diesel-fired defects in isolated microgrids in tropical islands were analysed. It was found that the number and severity of defects in electrical and motive power systems are high, and the number of defects brought about by corrosion due to environmental meteorology accounts for more than 40%, but the defects develop slowly and can usually be eliminated in time, so the severity of defects is not high. The defect characteristics analysis can provide an important reference for equipment health status assessment.

Acknowledgements Thanks for the support from the technology project of China Southern Power Grid Corporation under Grant 070000KK52200023.

References

1. Lopes J, Moreira CL, Madureira AG (2006) Defining control strategies for microgrids islanded operation. IEEE Trans Power Syst 21(2):916–924
2. Craparo E, Karatas M, Singham DI (2017) A robust optimization approach to hybrid microgrid operation using ensemble weather forecasts. Appl Energy 201:135–147
3. James H, Negnevitsky M, Wang X et al (2019) High penetration renewable generation within Australian isolated and remote power systems. Energy 168:684–692
4. Zhao HL, Pang SL, Huo MY et al (2021) State evaluation of vacuum circuit breakers in tropical island environment based on G1-independence weight method. Equipm Environ Eng 18(11):58–65 (in Chinese)
5. Pang SL, Zhao HL, Zhi L, et al. (2021) An empirical test scheme for power equipment in a tropical island environment. Environ Technol 39(6):91–95. (in Chinese)

6. Zhang C, Zeng J, Lv WY, et al. (2019) Monitoring and protection of environmental conditions of high temperature, humidity and salt in island microgrid. 3:89–94. (in Chinese)
7. Cheng JT, Ai L, Duan ZM et al (2014) Fault diagnosis based on improved D-S evidential theory for hydroelectric generator units. J Hydroelelectric Eng 33(5):216–220 (in Chinese)

Trichel Pulse Characteristics of SF_6/N_2 Gas Mixture Under Power Frequency Voltage

Zilin Tao and Yu Zheng

Abstract In order to explore the partial discharge Trichel pulse of SF_6/N_2 mixed gas, and study the development process and change characteristics of the Trichel pulse, this paper carried out partial discharge tests under power frequency voltage based on the pulse current method, and obtained test data such as the initial voltage of partial discharge, discharge amount and discharge times. It is found that the discharge amount of the Trichel pulse is positively proportional to the voltage at both ends, and positively proportional to the equivalent capacitance of the external port. Through the classic Trichel pulse discharge model, this article analyzes the development process of the Trichel pulse on the negative half cycle. It is believed that the main reason for the formation of the Trichel pulse is the electric field distortion caused by the slow migration of negative ion clouds, which causes the discharge process to occur intermittently and regularly. This study can provide a certain reference for the study of the discharge mechanism of the Trichel pulse.

Keywords SF_6/N_2 gas mixture · Partial discharge · Trichel pulse · Discharge quantity

1 Introduction

Partial discharge (PD) is an electrical discharge that guides the insulation between bodies to be only partially bridged. In the non-uniform electric field of gas medium, its partial discharge is usually a self-sustaining pulse discharge phenomenon [1]. Among them, the Trichel Pulse is a special partial discharge phenomenon. According to the research of scholars at home and abroad, Trichel pulse generally appears in the negative corona of electronegativity gas, and its main characteristics are summarized as follows: (1) the rising edge is very narrow, a few microseconds, and the falling

Z. Tao · Y. Zheng (✉)
National Key Laboratory of Power Grid Environmental Protection, Wuhan University, Wuhan, China
e-mail: zywhuee@whu.edu.cn

© Beijing Paike Culture Commu. Co., Ltd. 2024

X. Dong and L. Cai (eds.), *The Proceedings of 2023 4th International Symposium on Insulation and Discharge Computation for Power Equipment (IDCOMPU2023)*, Lecture Notes in Electrical Engineering 1102, https://doi.org/10.1007/978-981-99-7405-4_33

edge is long, tens of microseconds; (2) The time interval between pulses is almost equal, greater than 100 μs. The pulse frequency is independent of conditions such as electrode curvature; (3) The pulse amplitude is roughly equal and is not affected by experimental conditions such as air pressure and electrode curvature. However, there is currently no clear definition and theoretical explanation of the Trichel pulse [2, 3]. Further research is needed on the generation conditions, electrical characteristics, and development process of the Trichel pulse to provide a theoretical basis for the withstand voltage of electrical equipment. Therefore, SF_6/N_2 mixed gas, as a common insulation medium in high-voltage electrical equipment such as GIS and GIL, is of great significance to study its Trichel pulse under power frequency voltage.

In recent years, scholars at home and abroad have conducted extensive research on the Trichel pulse, exploring its physical process, occurrence mechanism, and change characteristics through experiments [4]. Pang et al. [5] studied the influence of gas pressure and electric field non-uniformity on partial discharge initial voltage (PDIV) by building a negative DC high voltage partial discharge test platform, and divided the gas partial discharge process into three stages: discharge initiation, streamer development, and intermittent breakdown. Wang et al. [6] focused on studying the effect of electrode structure on the Trichel pulse phenomenon through a combination of theory and experiment, and found that electrode curvature has no significant effect on pulse frequency. Anna et al. [7] conducted experiments using carbon coated electrodes with low photoionization factors and believed that discharge similar to a positive streamer mechanism rather than cathode secondary electron emission was the main mechanism of pulse generation. In addition, Akishev et al. [8] found that Trichel pulse can also be found in non electronegativity gas. At present, there is no consensus on the generation conditions and formation mechanism of the Trichel pulse. At the same time, the impact of changes in gas mixing ratio on the Trichel pulse discharge under AC voltage is not yet clear. Therefore, studying the Trichel pulse generation process of SF_6/N_2 gas mixtures is of great significance.

This article is based on the pulse current method to conduct partial discharge tests on SF_6/N_2 gas mixtures under power frequency voltage, and to study the Trichel pulse during the test process. This article analyzes the main stages of the Trichel pulse.

2 Construction of Power Frequency Partial Discharge Test Platform

The experiment adopts the pulse current method. Build an SF_6/N_2 mixed gas test platform, with the main circuit structure shown in Fig. 1. The protective resistance Z value is 50 kΩ, protecting the transformer from damage such as flashover and breakdown. The working frequency of coupling capacitor C is 50 Hz, the capacitance value is 350 pF, and the partial discharge is $\leq$ 5 pC. The measured impedance Z_m is

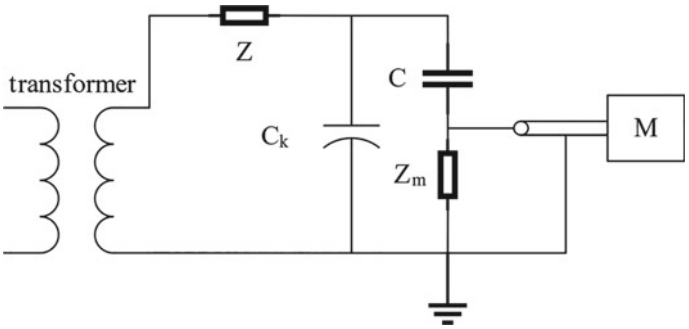

Fig. 1 Schematic diagram of the local discharge test circuit

a partial discharge input unit with a central tap, and its tuning range is 100–1500 pF. The experimental electrode is a needle-plate electrode.

Before the formal test, the partial discharge instrument was calibrated. A partial discharge test was conducted in a cavity filled with 0.4 MPa SF_6 gas and without needle plate electrodes. It was found that under the power frequency voltage of 20–35 kV, the partial discharge instrument detected zero discharge times in the cavity, and the discharge level remained around 2 pC, almost unchanged. Therefore, it can be considered as background noise generated by external circuits such as the partial discharge instrument and coupling capacitor. This article marks the beginning of partial discharge with a discharge frequency greater than 1 and a discharge capacity greater than 10 pC within 30 s, and regards the voltage at this time as the starting voltage of partial discharge.

3 Partial Discharge Test of SF_6/N_2 Gas Mixture

In this paper, partial discharge test groups of SF_6/N_2 with different mixing ratios are set up, and the initial partial discharge voltage, positive and negative half cycle discharge amount and discharge times of each gas are recorded. The test data are as follows.

3.1 PDIV

Under the experimental conditions of this article, pure N_2 hardly experiences partial discharge [9], and only when it is about to break down will there be scattered, discontinuous, and irregular pulse signals near the peak of the negative half cycle of the voltage. The breakdown voltage at different gas pressures is shown in the Fig. 2.

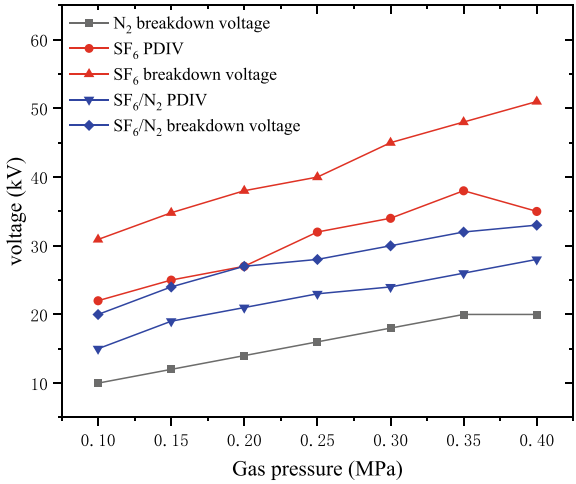

Fig. 2 Relationship between PDIV, breakdown voltage and air pressure for different gases

The partial discharge of SF_6 is relatively obvious, starting around 10 kV before the breakdown voltage.

The PDIV and breakdown voltage of SF_6/N_2 gas mixture under different air pressures are shown in the following figure, and the mixing ratio of the test gas is 30%. It was found that PDIV and breakdown voltage increased with increasing air pressure.

The PDIV and breakdown voltage of SF_6/N_2 gas mixtures under different mixing ratios are shown in the Fig. 3, and the pressure of the test gas is both 0.2 MPa. It was found that PDIV and breakdown voltage slightly increased with the increase of SF_6 ratio.

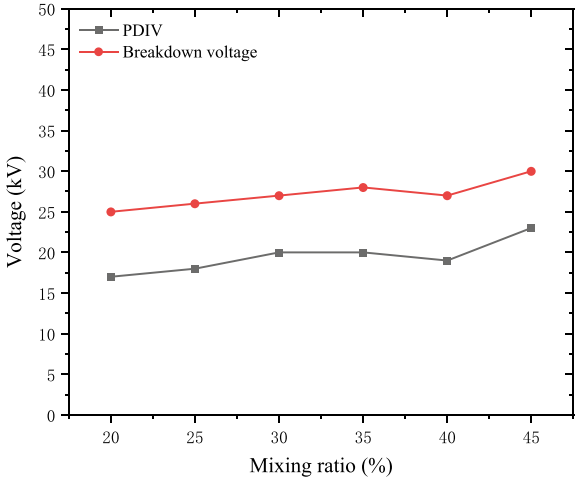

Fig. 3 PDIV and breakdown voltage of SF_6/N_2 gas mixtures at different mixing ratios

3.2 *Discharge Quantity and Discharge Frequency*

Due to the different characteristics of gas partial discharge in the positive and negative half cycles within a cycle. Therefore, this paper sorts out the maximum values of the discharge amount and the number of discharges in different half cycles, as well as the changes in voltage and air pressure.

The discharge amount and number of discharges of 30% SF_6/N_2 gas mixture vary with voltage as shown in the Figs. 4 and 5. It can be observed that the variation characteristics of discharge quantity and discharge frequency with increasing voltage are roughly the same in the positive and negative half cycles. As the voltage increases, the single discharge quantity gradually decreases but the discharge frequency significantly increases. However, there is a slight difference between the positive and negative half cycles. Firstly, the number of discharges in the positive half cycle at the beginning of partial discharge is significantly smaller than that in the negative half cycle. Secondly, the discharge amount in the positive half cycle is significantly smaller than that in the negative half cycle near the breakdown voltage.

4 Analysis and Discussion

According to the experimental phenomena and the waveform of the Trichel pulse, the Trichel pulse in the process of mixed gas partial discharge is divided into three stages: initial stage, ion cloud migration and electric field distortion.

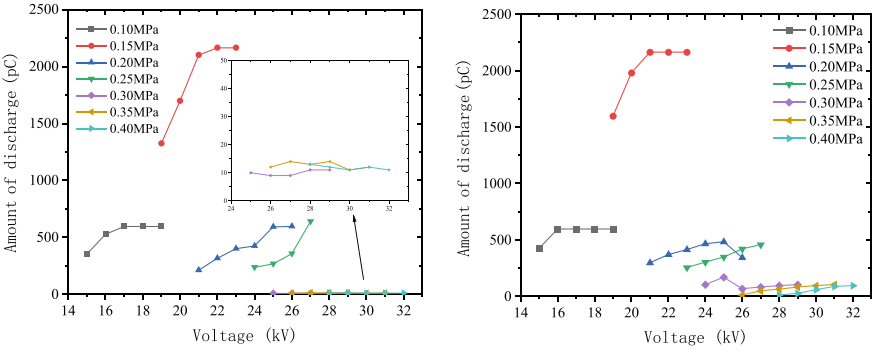

(a) Positive half cycle (b) negative half cycle

Fig. 4 Discharge of gas mixtures at different air pressures as a function of voltage

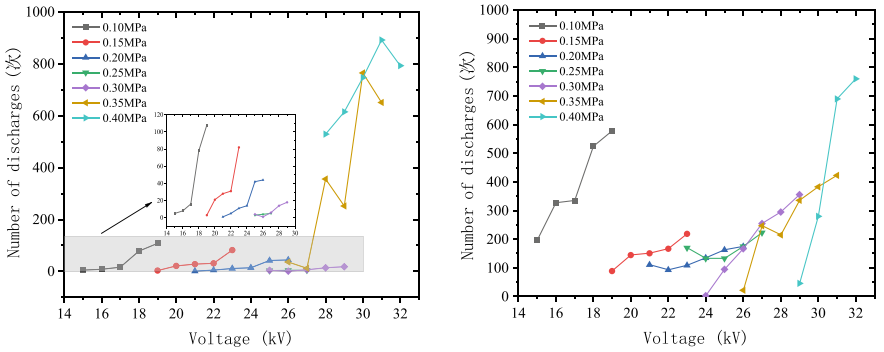

(a) Positive half cycle (b) negative half cycle

Fig. 5 Number of discharges versus voltage for gas mixtures at different air pressures

4.1 Initial Stage

The tip produces a large number of electrons and positive ions due to the Thomson avalanche, and the positive ions migrate to the cathode to rapidly produce the neutralization of the charge, a process that leads to a rapid rising edge of the Trichel pulse.

4.2 Ion Cloud Migration

The process of electrons generated by avalanches moving towards the anode undergoes collision and adsorption reactions, resulting in a slow migration of negative ion clouds and a slowly decaying gap current. The discharge process is shown in Fig. 6.

In summary, the amount of charge released in the circuit is related to the voltage and parameters in the discharge circuit. Under the condition that the circuit parameters do not change, the discharge parameter is positively correlated with the voltage. And when the air pressure rises, or the gas with stronger electronegativity is used, or the proportion of strong electronegativity gas is increased, the discharge frequency of the whole pulse will decrease.

4.3 Electric Field Distortion

According to Ref. [10], under the condition of power frequency partial discharge, the movement characteristics of ions are different. Positive ions are the dominant particles in positive half cycle discharge, while negative ions are the dominant particles in negative half cycle discharge. At the beginning of the positive half cycle,

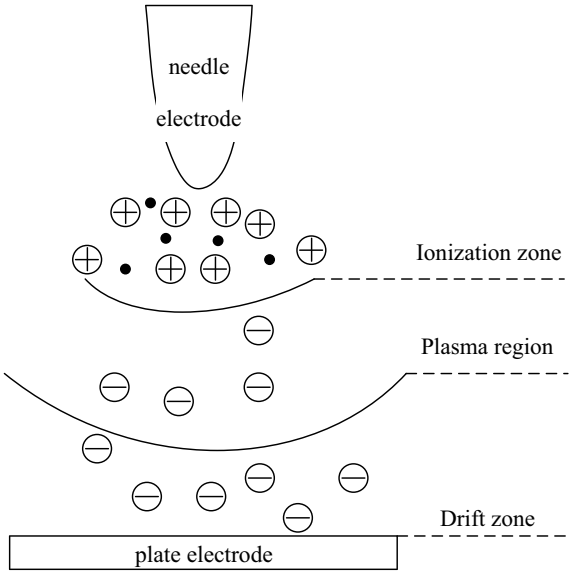

Fig. 6 Schematic diagram of the equivalent capacitance of the electrode breakdown air gap

positive ions often form a banded area near the electrode and move towards the plate electrode, while at the beginning of the negative half cycle, negative ions move faster and quickly disperse in the needle plate electrode gap. Only one negative ion cloud can be found in the negative half cycle until entering the cycle of the second half cycle.

The negative ion cloud reduces the electric field near the needle tip below the critical value, preventing the formation of new electron avalanches and causing shock during the discharge process. Until the negative ion cloud migrates to the anode, the field strength near the cathode returns to the initial stage of discharge, and a new Trichel pulse begins. In the positive half cycle, the positive ions move in a band towards the plate electrode, and their distortion effect is not significant. Therefore, the distribution of the positive half cycle pulse waveform is relatively chaotic, not as good as the negative half cycle rule.

5 Conclusion

In this paper, through the power frequency partial discharge test of SF_6/N_2 gas mixture, SF_6, N_2, and the study of the three stages of partial discharge of mixed gas, the variation of the characteristics of Trichel pulse of mixed gas with the parameters of voltage, air pressure, mixing ratio, etc. is obtained:

(1) Due to the different behavior of the dominant particles on the positive and negative half cycle, the partial discharge pulse appearing on the positive half cycle is a chaotic and scattered pulse, while the pulse is generated intermittently

on the negative half cycle due to the distortion of the negative ion cloud, so the obvious Trichel pulse can be found.

(2) The discharge amount of the Trichel pulse is positively proportional to the voltage at both ends, and positively proportional to the equivalent capacitance of the external port.

Acknowledgements This work was supported by National Natural Science Foundation of China Youth Project (No. 52107161) and Postdoctoral Innovation Talents Support Program (BX20200252).

References

1. Li J, Han X, Liu Z (2015) Review on partial discharge measurement technology of electrical equipment. High Volt Eng 41(08):2583–2601. https://doi.org/10.13336/j.1003-6520.hve.2015.08.011
2. Zhang X, Guo Y, Sun A (2020) The pulsed mode of negative DC corona in nitrogen at atmosphere pressure: Comparison with Trichel pulses in air. Phys Plasmas 27(3):033501–033511. https://doi.org/10.1063/1.5136042
3. Niemeyer L (1995) A generalized approach to partial discharge modeling. IEEE Trans Dielectr Electr Insul 2(4):510–528. https://doi.org/10.1109/94.407017
4. Sun A, Zhang X, Guo Y (2021) Review on ionization and quenching mechanisms of Trichel pulse. Chin Phys B 30(05):420–427. https://doi.org/10.1088/1674-1056/abd75d
5. Pang P, Sun Z, Zhang Q (2019) Partial discharge initial characteristics of SF_6/N_2 mixture in extremely inhomogeneous elecyric field under DC high voltage. J Xi'an Jiaot Univ 53(4):44–50. https://doi.org/10.7652/xjtuxb201904007
6. Wang C, Chen X, Liang X (2020) Effect of electrode structure on Trichel pulse and its electromagnetic radiation field of negative corona discharge. Acta Armamentrii 41(S2):291–298
7. Zahoranová A, Šimor M, Černák (2002) Negative corona current pulses in oxygen. In: Proceedings of the 20th symposium plasma physics and technology. Institute of Plasma Physics, Czech Republic, pp 886–895
8. Akishev YS, Kochetov IV, Loboiko AI (2002) Numerical simulations of Trichel pulses in a negative corona in air. Plasma Phys Rep 28(12):1049–1059
9. Guo C, Zhang Q, You H (2017) Influence of electric field non-uniformity on discharge characteristics and phenomenon of critical radius in SF_6/N_2 gas mixtures under power frequency voltage. High Volt Eng 43(03):780–787. https://doi.org/10.13336/j.1003-6520.hve.20170303012
10. Gao Q, Wang X, Yang A (2021) Discharge current and charged species temporal-spatial distribution of AC corona discharge in SF_6. High Volt Eng 47(9):3355–3366. https://doi.org/10.13336/j.1003-6520.hve.20201060

Accuracy Analysis of Substation 3D Model Based on Oblique Photography

Cong Hu, Fuhua Xie, Xian Zhou, Li Cai, Xin Yang, Jianguo Wang, and Yadong Fan

Abstract Substation safety is extremely important to the electric power system. In order to improve the efficiency of substation inspection, a three-dimensional model of the substation can be used to set the inspection route and improve the work efficiency. In this paper, parameter experiments of oblique photography 3D modeling of substation drones are conducted. Four different UAVs were used for oblique photography 3D modeling. The UAV models, flight heights and modeling software were set up to control the experiments. The best accuracy of the 3D model was obtained when the DJI Mavic 2 Enterprise was used for oblique photography of the substation at a flight altitude of 40 m, and then the 3D modeling was performed with ContextCapture software. Under this condition, the image data of the substation was obtained by oblique photography by selecting the appropriate overlap rate of the side phase and the overlap rate of the heading. Then, after aerial triangulation, multi-view image dense matching, irregular triangulation network construction and texture mapping steps to obtain the substation 3D model for inspection route setting.

Keywords Oblique photography · 3D modeling · Substation inspection

1 Introduction

As an important part of the power system, the safety of the substation directly affects the stable operation of the power system. In order to ensure the normal operation of various electrical equipment in substations, regular maintenance and inspection

C. Hu · X. Yang
Foshan Power Supply Bureau, Guangdong Power Grid Co., LTD, Foshan, China

F. Xie · X. Zhou · L. Cai (✉) · J. Wang · Y. Fan
Engineering Research Center of Ministry of Education for Lightning Protection and Grounding Technology, School of Electrical Engineering and Automation, Wuhan University, Wuhan, China
e-mail: 2580968099@qq.com

School of Electrical Engineering and Automation, Wuhan University, Wuhan, China

© Beijing Paike Culture Commu. Co., Ltd. 2024

X. Dong and L. Cai (eds.), *The Proceedings of 2023 4th International Symposium on Insulation and Discharge Computation for Power Equipment (IDCOMPU2023)*, Lecture Notes in Electrical Engineering 1102, https://doi.org/10.1007/978-981-99-7405-4_34

are required [1]. Many substations in China are carrying out to achieve online monitoring of electrical equipment, mainly through the installation of fixed cameras and various types of sensing probes [2], however, these fixed points have a single angle of image data and a relatively limited shooting angle. With the advantages of small size and freedom of flight, UAV can move back and forth in substations, shoot equipment in multiple directions and perspectives, and shoot the top of equipment more clearly, which undoubtedly brings a more comprehensive basis for equipment status assessment. Manually operated UAV for inspection on the operator UAV flight technology requirements are high, so you can use the UAV oblique photography to get a three-dimensional model of the substation before the inspection line settings.

There are three main types of methods for real-world 3D modeling: manual modeling [3], LiDAR 3D modeling [4], and oblique photography 3D modeling [5]. Yalcin et al. [6] applied oblique photography technology to 3D city modeling in Turkey, which is the initial attempt of oblique photography in urban modeling. Lingua et al. [7], in order to protect historical buildings, reconstructed them in 3D to lay the foundation for subsequent conservation work, and the reconstruction method was chosen. The results showed that this method is efficient and low cost, which is more suitable for cultural heritage investigation. Yu et al. [8] used UAV oblique photography for 3D reconstruction of road slopes in order to prevent road slope disasters, and used 3D point cloud data to identify road slope landslides, collapses, rock falls and other disaster scenarios in order to prepare corresponding preventive measures.

Oblique photogrammetry modeling can be used not only for the construction of 3D models of urban buildings, but also for power scene models. Wu et al. [9] introduced in detail the key techniques for data processing and production of 3D real-world models using InambiCapture software based on a substation site oblique photography data, focusing on the quality evaluation of 3D calculation results, and briefly introduced the application of 3D real-world model in power engineering planning and design. Wen et al. [10] proposed a method to remove the redundant data of transmission line oblique photography, which effectively shortened the modeling time and optimized the modeling efficiency while ensuring the modeling effect. Yang et al. [11] considered the work of three-dimensional modeling of substation oblique photography from the aspects of safety technology and operation mode to accumulate experience for subsequent related exploration.

In this paper, the 3D modeling technology of substation UAV oblique photography is studied, and the experiment of 3D modeling of substation under different conditions is carried out for 220 kV substation site. The results show that the 3D model reconstructed by ContextCapture software has the highest accuracy of 0.34 m when DJI Mavic 2 Enterprise performs oblique photography at 40 m height, and the model accuracy is optimal when the overlap rate of side direction and heading overlap rate is kept at 80% under the same height and the same model, which can be used for inspection route setting.

Table 1 The parameters of the four UAV models

Parameters	4 Pro V2	4 RTK	2 Pro	2 Enterprise
Wheelbase (mm)	350	350	354	354
Weight (g)	1375	1391	905	909
Maximum flight time (min)	30	30	31	31
Maximum flight altitude (m)	6000	6000	6000	6000

2 Comparative Test Setup

2.1 UAV Selection

The UAV models used in this paper for substation oblique photography are DJI Phantom 4 Pro V2, DJI Phantom 4 RTK, DJI Mavic 2 Pro, and DJI Mavic 2 Enterprise. Among them, DJI Phantom 4 RTK and DJI Mavic 2 Enterprise carry RTK modules, which are based on RTK (Real-time kinematic) carrier phase differential technology and mainly serve for satellite positioning measurements. Table 1 shows the parameters of the four UAV models, two of which with RTK modules are a bit more accurate because of the RTK technology.

Figure 1 shows the four types of UAV, the cameras they carry and the matching remote controls, of which the DJI Phantom 4 Pro V2 and DJI Phantom 4 RTK need to be connected to a mobile device through a data cable, and the mobile device will download the corresponding APP to control the UAV, and the DJI Mavic 2 Pro and DJI Mavic 2 Enterprise The DJI Phantom 4 Pro V2 and DJI Phantom 4 RTK are equipped with camera aerial pictures with a resolution of 4864 $\times$ 3648, the DJI Mavic 2 Pro camera aerial pictures with a resolution of 5472 $\times$ 3078, and the DJI Mavic 2 Enterprise camera aerial pictures with a resolution of 8000 $\times$ 6000.

2.2 Route Parameters

All four UAVs require flight control software for oblique photography aerial photography tasks, and the DJI Polit, which is compatible with all four UAV models, was chosen as the flight control software. First of all, create the tilt photography task in the software, and then frame out the area of the substation in the map, and the software automatically generates five routes. One route is the main route, responsible for vertical photography, and four routes are oblique routes, responsible for oblique photography, as shown in Fig. 2. The angle of the main route is 80°, that is, the angle between the main route and the regional boundary is 80°, the margin of the oblique photography area is 8 m, that is, the distance between the flight route and the border of the oblique photography area is 8 m, all routes oblique photography when the head pitch angle is set to 60°, the photo mode are equidistant interval photo, the speed of

Fig. 1 The used four types of UAV

take-off from the ground are 10 m/s, the flight speed of the five routes are 5 m/s The flight speed of all five routes was 10 m/s, the angle of all main routes was set to 80°, and the UAV returned automatically after completing the task.

In this paper, we first set both the heading overlap rate and the side overlap rate to 80% and only adjust the height, setting up three sets of experiments with heights of 60 m, 50 m and 40 m. The difference in height will lead to changes in the range of UAV image acquisition during oblique photography, which will result in changes in the route. The higher the height, the wider the area covered by the aerial photography. Three sets of experiments were conducted with four types of UAVs to compare the advantages and disadvantages of the final 3D models and to select the most suitable UAV model and altitude, and then only the most suitable UAV model was used to conduct experiments on heading overlap rate and side overlap rate at the most suitable altitude. The heading overlap rate and the side overlap rate each have three sets of values, 80, 70 and 60%, respectively, and the side overlap rate will make the route change. The two overlap rates are combined with each other to form a total of nine control groups to compare the final model advantages and disadvantages and to filter out the most suitable aerial photography parameters for the 220 kV substation site in this paper.

Fig. 2 Schematic diagram of the five routes of oblique photography

3 Experimental Results and Analysis

3.1 Substation 3D Modeling

In order to study how to efficiently construct a 3D model of the substation, a practical operation was modeled at the 220 kV substation of Wuhan University, which includes multiple types of high-voltage electrical equipment such as oil-immersed transformers, current transformers, voltage transformers, Y-type circuit breakers, and disconnect switches in the substation site, and the scene is shown in Fig. 3. Aerial triangulation is performed based on the original images obtained from oblique photography and the UAV geographic location information (POS) at the time of shooting. The aerial triangulation includes the main operations such as image area leveling, image dense matching, and automatic texture mapping. The main purpose

of aerial triangulation is to obtain the specific position and attitude information of the image in the air at the time of shooting.

According to the information obtained after the air triangle calculation, a 3D model can be established. The initially established 3D model is a white model, with only the outline and no surface texture information, and the most suitable image corresponding to the specific location of the 3D model needs to be selected to fit the texture to the surface of the white film, so as to obtain the substation 3D model as shown in Fig. 4.

Fig. 3 The overview of the substation

Fig. 4 The substation 3D model

3.2 3D Model Accuracy Analysis

The geometric accuracy of the 3D model is compared and analyzed, and the coordinates of the model can be measured on both software. 10 significant feature points are selected in the modeling area, which can be clearly found in the site and the model, and the actual coordinates of these points are measured and taken as the real value, and the model coordinates of the corresponding locations are collected through the model observation platform, and the difference between them is calculated and counted. The reference system chosen for both the site and the model is WGS-84 coordinate system, and the coordinates of the points are latitude and longitude, which are calculated according to the error formula, and the geometric accuracy of the model is evaluated based on the error formula as follows:

$$m_w = \sqrt{\frac{1}{n}\sum_{i=1}^{n}(dw_i)^2} \tag{1}$$

$$m_j = \sqrt{\frac{1}{n}\sum_{i=1}^{n}(dj_i)^2} \tag{2}$$

$$\sigma = \sqrt{m_w^2 + m_j^2} \tag{3}$$

Table 2 shows the geometric accuracy errors for four UAV models and three altitudes modeled using ContextCapture. Table 3 shows the geometric accuracy errors for four UAV models and three altitudes modeled using DJI terra. From the table, we can see that the modeling accuracy of DJI terra, except for DJI Phantom 4 Pro V2, which is closer to that of ContextCapture modeling, all other groups are greater than the accuracy of ContextCapture modeling, indicating that the accuracy of using ContextCapture software to build 3D models is better. Except for the first two heights of DJI Mavic 2 Pro, which may lead to excessive error due to GPS signal instability during aerial photography, the higher the height, the greater the error, so for this paper the substation site modeling was selected at 40 m height for oblique photography. Comparing the errors of three heights of four models of UAVs, the average error of DJI Mavic 2 Enterprise is the smallest, and the error of 40 m is the smallest, so DJI Mavic 2 Enterprise is chosen as the UAV model for oblique photography.

After determining the UAV model, flight altitude and modeling software, you need to choose the appropriate heading and bypass overlap rate for 3D modeling. When the overlap rate of bypass and heading is too low, the shooting time and modeling time is less, but the accuracy of the established 3D model will also be worse. When the overlap ratio of bypass and heading is too high, the accuracy of the 3D model is higher, but it will consume a lot of shooting time and modeling time.

Table 2 The geometric accuracy errors of model used ContextCapture

UAV	Error		
	40 m	50 m	60 m
4 Pro V2 (m)	3.44	3.40	3.66
4 RTK (m)	0.91	1.61	2.61
2 Pro (m)	10.96	10.93	4.16
2 Enterprise (m)	0.34	0.92	1.53

Table 3 The geometric accuracy errors of model used DJI terra

UAV	Error		
	40 m	50 m	60 m
4 Pro V2 (m)	3.38	3.32	3.75
4 RTK (m)	1.51	2.25	3.85
2 Pro (m)	13.69	11.78	4.12
2 Enterprise (m)	0.84	1.19	3.42

4 Conclusion

In this chapter, the UAV oblique photography 3D modeling is studied, and the oblique photography 3D modeling experiments under different conditions are carried out for the 220 kV substation site in this paper, and the experimental optimal parameters are selected according to the final model accuracy. The final result is the highest accuracy of 0.34 m for the 3D model after reconstruction of the image obtained by DJI Mavic 2 Enterprise oblique photography at 40 m height.

Acknowledgements This study was supported by the technology project of China Southern Power Grid (Project No. 030600KK52220016).

References

1. Wang C, Yin L, Zhao Q et al (2020) An intelligent robot for indoor substation inspection. Ind Rob Int J Robot Res Appl 47(5):705–712
2. Xin L, Jin H, Tu Y et al (2020) Defect detection and characterization of RTV silicone rubber coating on insulator based on visible spectrum image. IEEE Trans Power Deliv 35(6):2734–2736
3. Lelièvre PG, Carter-McAuslan AE, Dunham MW et al (2018) FacetModeller: software for manual creation, manipulation and analysis of 3D surface-based models. SoftwareX 7:41–46
4. Wen C, Tan J, Li F et al (2021) Cooperative indoor 3D mapping and modeling using LiDAR data. Inf Sci 574:192–209
5. Qiu Y, Jiao Y, Luo J et al (2023) A rapid water region reconstruction scheme in 3D watershed scene generated by UAV oblique photography. Rem Sens 15(5):1211
6. Lingua A, Noardo F, Spanò A et al (2017) 3D model generation using oblique images acquired by UAV. Int Arch Photogram Rem Sens Spat Inform Sci 42

7. Yalcin G, Selcuk O (2015) 3D city modelling with Oblique photogrammetry method. Procedia Technol 19:424–431
8. Yu J, Xue X, Chen C, Chen R, He K, Li F (2022) Three-dimensional reconstruction and disaster identification of highway slopes based on UAV oblique photography. Natl J Highways 35(04):77–86 (in Chinese)
9. Wu H, Wang Y, Xing L et al (2021) Application analysis of three-dimensional real scene modeling of substation site based on UAV tilt photography. In: 2021 2nd international conference on intelligent design (ICID). IEEE, pp 220–225
10. Wen H, Xiao Q, Li X et al (2022) A method for refining oblique photography data of power transmission lines. In: 2022 prognostics and health management conference (PHM-2022 London). IEEE, pp 293–297
11. Yang ZH (2022) A 3D realistic modeling method for substations based on oblique photography. Electron Test 36(9):126–128 (in Chinese)

Study on Lightning Overvoltage in Long Span Section After AC to DC Operation of Transmission Lines

Houkun Cui, Fengju Zhu, Qing Wu, Zhihao Lin, Xueqin Zhang, and Yujun Guo

Abstract Transmission lines to DC operation, due to the polarity effect of the wire and the space electric field is different, the lightning pilot development process has changed, and large span section of the line gear distance is long, tower height is more vulnerable to lightning strikes. Therefore, it is necessary to compare and analyze the similarities and differences of lightning overvoltage under different operation modes of AC and DC. In this paper, through the establishment of large span section transmission line electromagnetic transient simulation model, calculate the transmission line in the original AC insulation configuration, AC and DC operation mode of the difference between the large span section lightning overvoltage. The results show that the same insulation configuration of DC operation when the line is subject to lightning overvoltage value is greater than the overall AC mode of operation. When the lightning current is above 100 KA, the lightning current bypasses the transmission line, the DC line overvoltage is about 18.3% larger than the AC line overvoltage, bringing a hidden danger to the insulation configuration of the original AC line.

Keywords Change from AC to DC · Long-span · Lightning overvoltage · Shielding failure and back flashover

H. Cui · F. Zhu
State Grid Jiangsu Electric Power Design Consulting Co., Ltd., Nanjing 210008, China
e-mail: 13951876341@163.com

F. Zhu
e-mail: zhufengju_thu@163.com

Q. Wu (✉) · Z. Lin · X. Zhang · Y. Guo
Southwest Jiaotong University, Chengdu 610031, China
e-mail: wuqing578@163.com

Z. Lin
e-mail: linzhihao@my.swjtu.edu.cn

X. Zhang
e-mail: xq_zhang@swjtu.edu.cn

Y. Guo
e-mail: yjguo@swjtu.edu.cn

© Beijing Paike Culture Commu. Co., Ltd. 2024

X. Dong and L. Cai (eds.), *The Proceedings of 2023 4th International Symposium on Insulation and Discharge Computation for Power Equipment (IDCOMPU2023)*, Lecture Notes in Electrical Engineering 1102, https://doi.org/10.1007/978-981-99-7405-4_35

1 Introduction

With the rapid development of China's economy and the diversification of electricity demand, some areas, especially economically developed areas, have the problem of insufficient power supply capacity [1]. DC distribution networks can ensure higher power quality as well as better operation, in addition to reducing power losses [2] and effectively increasing transmission capacity [3, 4]. However, additional DC transmission networks require expensive costs and precious land resources, and line siting is more difficult across large spans. Therefore, converting existing AC lines to DC transmission is a better option to solve the above problems.

After the AC to DC operation, the structure and operation of the large span section of the line also changed, the positive polarity of the DC transmission line conductor is more susceptible to lightning strikes, showing an obvious polarity effect, when passing through the large span section, the transmission line due to high tower height, long line stall distance, large lightning area, the probability of suffering a lightning strike at this time is much greater than the ordinary section of the transmission line [5]. And DC voltage has an electrostatic adsorption effect, insulators operating under DC voltage, transmission conductor surface dirt accumulation is more serious, more prone to flashover phenomenon; existing standards for DC overhead lines of lower voltage levels lack effective lightning protection configuration of the study. To address the above problems, building ATP/EMTP model can effectively simulate the lightning strike process in large span sections [6], and better study the lightning overvoltage propagation law and insulation coordination scheme of DC transmission lines.

In this paper, we study the lightning overvoltage characteristics of transmission lines when lightning strikes towers at different locations under the original AC configuration of the large span section, as well as the overvoltage characteristics of lines at different locations when lightning current strikes back at transmission lines, combined with grounding resistance, insulators and other related configurations to analyze the lightning protection design of the large span section after changing to DC operation, and propose practical line lightning protection design solutions.

2 Calculation Parameters of Long-Span Section

Due to the project cost and transmission corridor saturation and other factors, China's current stage of high-voltage AC to DC transmission line crossing section mostly along the original channel, its foundation and the main structure of the tower is still utilized. In this study, the large span program is a tension tower—stress tower—stress tower—tension tower program, using a combination of span tower and anchor tower to transform the AC transmission line into a DC transmission line, mainly replacing the number or type of insulators and recalibrating the tower grounding resistance. Cross-sectional schematic diagram at the crossing point is shown in Fig. 1.

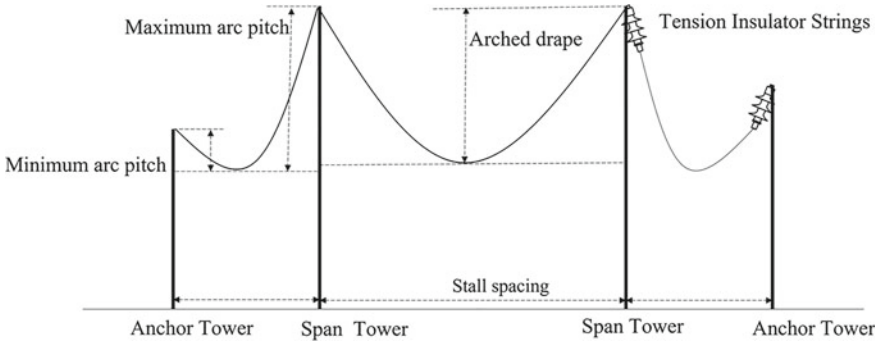

Fig. 1 Section diagram at the crossing point

Not changing the main structure of the spanning tower can reduce the construction difficulty, and choosing reasonable conductors can improve the transmission density of the transmission channel [7] and tap the transmission potential of the existing grid equipment. At present, the main conductors used in China's long-span lines are high-strength steel-core aluminum alloy strand and high-strength steel-core heat-resistant aluminum alloy strand. Compared with the general section of the transmission line, the increase in the cross-section and splitting number of large span wires has a greater impact on the load size and investment. long-span section as an important channel of high-voltage AC to DC lines, high transmission capacity and susceptible to lightning strikes, in order to meet the requirements of the transmission capacity, taking into account the strength of the wire, engineering costs, maintenance costs and other factors. The transmission line conductor type in this study is 4 × JLHA1/G4A-400/150 with 600 mm split spacing and OPGW-210 for ground wire.

3 EMTP Simulation Model of Long-Span Section

3.1 Power Transmission Tower Simulation Model

Multi-wave impedance tower model. The height of the tower and the structure of the transmission line lightning overvoltage amplitude has a great impact [8], scientific and reasonable in the electromagnetic transient simulation software to build the tower model closer to the accuracy of the simulation results. Large span section tower has a very high height (more than 100 m) characteristics, lightning current wave process is more obvious, a single wave impedance method does not take into account the structure of the tower itself, it is difficult to reflect the impact of the tower on the level of line lightning resistance. The multi-wavelength impedance model of the tower reflects the wave process when the wave passes through the tower, and also considers the wave attenuation and distortion [9–11], which reduces the simulation error. In

this study, the height of the spanning tower is 106 m and the full height is 141 m. The spanning tower is located in the ditch and crosses the river in a "straight-straight" way.

Line model of long-span section. In the simulation software distribution parameter model, JMarti model can be fitted to the line dependent characteristics of the ground line, responding to the amplitude and phase distortion of the traveling wave, more reflective of the actual line in the lightning bypass when the transmission characteristics of the traveling wave. This study selected the basic physical parameters of the large span section of the guide line as shown in Table 1.

The selected span of the main span is 1100 m, and the DC resistance of the conductor running at normal atmospheric temperature (20°) is 0.06418 Ω/km.

Lightning current model. China's lightning current mostly uses 2.6/50 us standard lightning current, and the model uses the double exponential waveform closest to the actual lightning current waveform, with the waveform function.

$$U_t = A\left(e^{-at} - e^{-bt}\right) \tag{1}$$

where A is the lightning current amplitude, a, b is the time constant related to the wave head and wave tail, by the relationship between the thunderstorm day and the peak of the lightning current, take the peak of the lightning current is 100 KA. The size of the main discharge channel wave impedance and the size of the lightning current, in general, the larger the lightning current wave impedance, scientific observation calculations when the lightning current amplitude between 30 and 100 KA, wave impedance of 700–300 Ω, negative polarity lightning amplitude and regional altitude, soil resistivity and the shape of the object struck by lightning, the lightning current size and probability distribution results from the formula (2) to determine.

$$p = \frac{1}{\left[1 + \left(\frac{I}{31}\right)^{2.6}\right]} \tag{2}$$

where p is the relative lightning current probability size and I is the lightning current size. In order to explore the margin of the insulation configuration of AC and DC transmission lines under the maximum lightning current in the large span section,

Table 1 Basic parameters of transmission line ground conductors

Type	Model	Splitting number	Intrabundle spacing (mm)	The lowest point (m)	Sub line radius (cm)
Transmission lines	JLHA1/ G4A-400/150	4	600	51.6	1.527
Lightning conductor	OPGW-210	0	0	48	0.955

this study takes the lightning current of 100 KA with a lightning strike probability of 15%, while taking the wave impedance of 300 Ω.

4 Current Characteristics of the Line When Struck by Lightning

In this section, the electromagnetic transient simulation model of the large span section is established based on the calculation parameters selected above, and the transient currents at each of the AC and DC towers and on the transmission lines are observed by simulating lightning strikes on transmission lines, lightning arrester lines, and lightning strikes on towers at different locations to compare and analyze the current distribution between AC and DC in the same lightning strike conditions.

4.1 Lightning Arrester and Transmission Lines in AC and DC Cases

Combined with the local area lightning current size probability of lightning strike large span at the lightning line and the connection of the tower, Fig. 2 DC transmission line power supply for 200 kV, using the same tower three circuits with the same voltage operation mode, the tower three different height cross-arms corresponding to Three independent DC transmission lines.

Figure 3 for the lightning current amplitude of 100 KA around the AC transmission line A phase and the same location of the DC transmission line of the positive polarity wire, the corresponding line on the lightning current waveform, Fig. 3a AC transmission line A phase lightning overvoltage peak value of 3.27 kV, DC transmission line positive polarity wire overvoltage peak value of 4.18 MV, selected far from

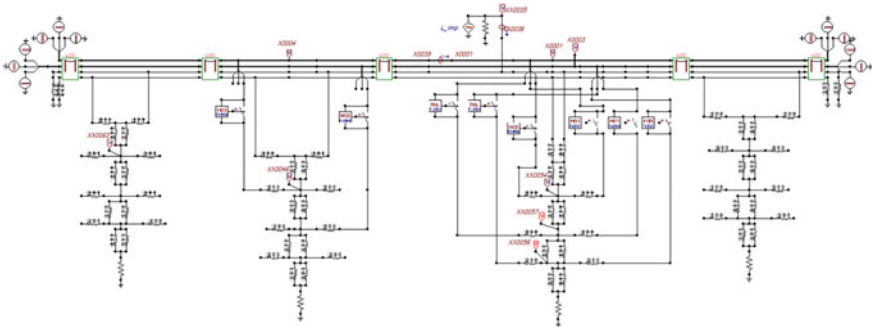

Fig. 2 Simulation diagram of lightning strike lightning line in DC operation mode

the lightning strike point at the lower cross-arms transmission line Fig. 3b shows that the AC operation of the C-phase transmission line overvoltage amplitude of 2.64 kV, and DC operation under the cross-arms at the positive conductor overvoltage amplitude of 3.25 kV. Figure 6 for the lightning current 100 kV when lightning arrester line under the AC and DC transmission lines under the same configuration of different locations of the overvoltage value, from Fig. 4a can be seen, across the tower on the cross-arms connected transmission line AC operation under the peak overvoltage of 2.61 MV, DC mode operation under the peak overvoltage of 3.41 MV; from Fig. 4b can be seen, across the tower under the cross-arms connected transmission line The peak overvoltage under AC operation is 2.51 MV, while the peak overvoltage under DC mode operation is 3.18 MV.

From the above Figs. 3 and 4 multiple experimental analysis can be obtained, large span section of transmission lines under the action of 100 KA lightning current, DC operating mode produced by the backlash, bypass over-voltage is greater, it can be seen that the same insulation configuration of AC and DC lines on the response to lightning over-voltage there is a difference in over-voltage above. Combined with the local area lightning current size distribution probability, calculate the different lightning current size lightning back strike lightning line, bypass transmission line to get the AC and DC transmission line overvoltage size, its lightning current size and transmission line overvoltage between the fitting curve shown in Figs. 5 and 6.

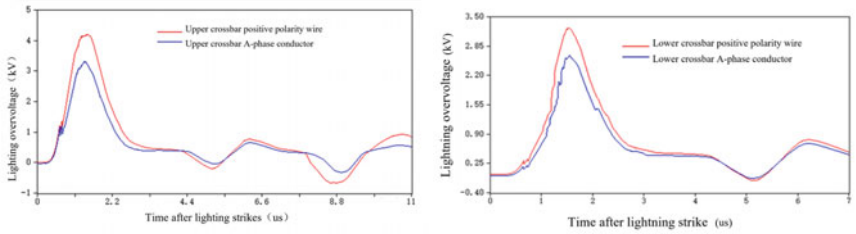

(a) Overvoltage at upper cross-arms (b) Overvoltage at lower cross-arms

Fig. 3 Lightning currents wind around transmission lines

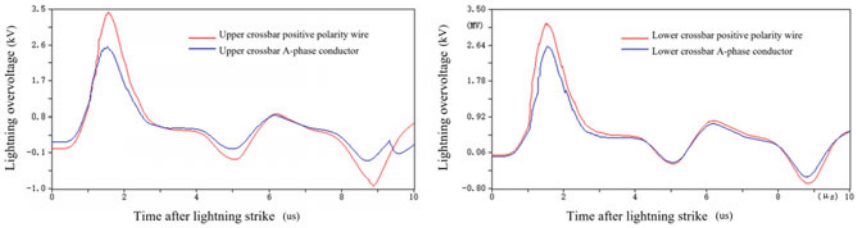

(a) Overvoltage at upper cross-arms (b) Overvoltage at lower cross-arms

Fig. 4 Lightning current counterattacks the lightning protection wire

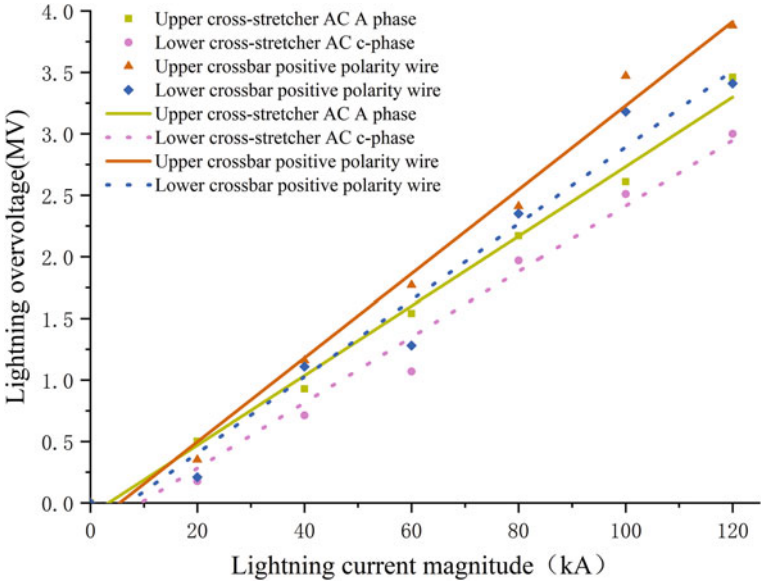

Fig. 5 Different lightning current magnitudes counter lightning protection wires

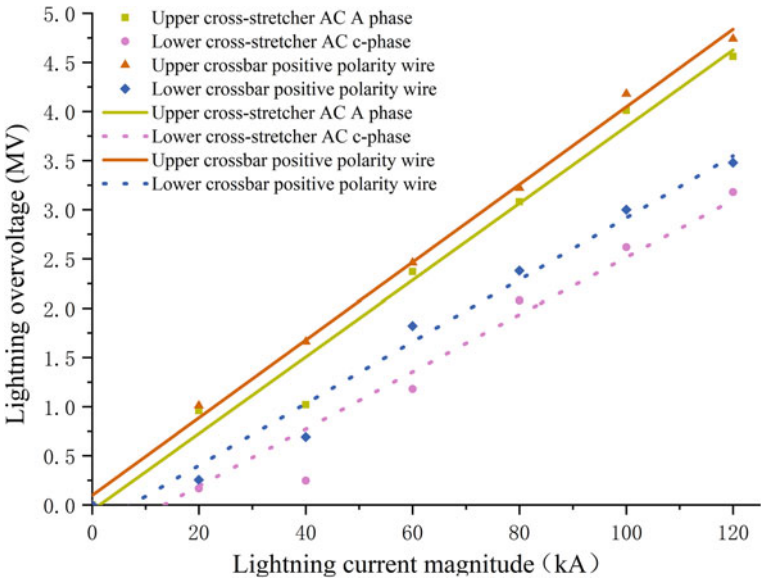

Fig. 6 Different lightning currents hit the upper transverse transmission line

From the data in Fig. 5 and the fitted curve, it can be seen that the large span section of the transmission line suffers from lightning backlash lightning line, its tower at the upper cross-arms and the lower cross-arms connected to the transmission line, DC operation mode overvoltage size are greater than the AC operation mode, and with the increase in lightning flow, the difference in overvoltage size between the two modes of operation in gradually increasing, it is clear that the larger the lightning flow on the different modes of operation of the line impact more obvious. As can be seen from Fig. 6, when lightning bypasses the transmission line at the transmission line, the line overvoltage trend is similar to the lightning line, but the figure shows that with the increase in lightning flow, AC and DC operation mode overvoltage size gap basically remains constant, it can be seen when lightning bypasses the transmission line, the size of the lightning flow is not the main factor affecting the difference between the lightning flow in the two modes of operation.

5 Conclusion

This paper analyzes the change of transmission line lightning overvoltage in the original AC operation insulation configuration to DC operation, and the influence of different factors on DC operation under lightning overvoltage by establishing a simulation model of electromagnetic transients in AC to DC transmission lines in large span sections. The main conclusions drawn are as follows: different operation modes have a significant impact on the transmission line lightning overvoltage value, the same insulation configuration under the line suffers lightning bypass and backlash, DC transmission line overvoltage value is significantly greater than the AC transmission line. And the larger the lightning current, the greater the difference between AC and DC lines suffer overvoltage value. When the lightning current is above 100 KA, the lightning current bypasses the transmission line, the DC line overvoltage is about 18.3% larger than the AC line overvoltage, bringing a hidden danger to the insulation configuration of the original AC line.

Acknowledgements I would like to thank the State Grid Jiangsu Electric Power Co., Ltd. for the financial support of this research funded by the science and technology project (SGTYHT/21-JS-223).

References

1. Chen Q, Wang J, Xiong S, Wang Q, Long Y (2020) Emergency overload operation strategy for wind power delivery channel considering dynamic overload capacity of equipment. Power Syst Autom 44(15):163–171 (in Chinese)
2. Chen HX, Li T, Li A (2021) Research on the coordinated control strategy of AC-DC system to enhance grid operation. Power Syst Protect Control 49(10):123–134 (in Chinese)

3. Wood TB, Macpherson DE, Banham-Hall D et al (2014) Ripple current propagation in Bipole HVDC cables and applications to DC grids. IEEE Trans Power Deliv 29(2):926–933
4. Elserougia A, Massoud AM, Abdelsalam I et al (2018) Self-balanced non-isolated hybrid modular DC-DC converter for medium-voltage DC grids. IET Gener Transm Distrib 12(15):3626–3636
5. Tian H, Wang N, Chen T et al (2015) Simulation study of line arrester to improve the lightning resistance level of UHV large span overhead line bypassing strike. High Volt Technol 41(01):63–68 (in Chinese)
6. Hu J, Zhang D, Zhou L et al (2022) Study on the installation strategy of lightning arrester for extra-high voltage DC lines considering the distribution characteristics of lightning overvoltage. Electr Porcelain Lightning Arrester 4:177–184 (in Chinese)
7. Jaber DS, Fardin E (2023) Operation recommendations for tension joints and clamps on a 63 kV overhead transmission line conductor based on experimental tests. Electr Power Compon Syst 51(7)
8. Si, Ma WX, Xie B, Yang Q et al (2010) Classification and identification method of lightning overvoltage in UHV transmission line. High Volt Eng 36(2):306–312 (in Chinese)
9. Zhou LJ, Huang L, Wang LJ, Zhang D, Liu B, Xu H, Chen SX (2020) Multi-wave impedance modeling and transient response analysis of 110 kV transmission towers with lightning strikes. Power Autom Equip 40(10):158–164 (in Chinese)
10. Singh RS, Ćuk V, Cobben S (2020) Measurement-based distribution grid harmonic impedance models and their uncertainties. Energies 13(16)
11. Du L, Mi X, Xiao Z et al (2012) Study on transmission line tower cross-load and inclined material equivalent model. High Vol Eng 38(11):3025–3032

Temperature Rise Calculation and Optimization of Ceramic Sealed DC Contactor

Cong Qin, Xian Cheng, Guowei Ge, Qinglin Bai, and Shuai Du

Abstract Aiming at the geometric model of 300 A DC contactor for electric vehicle and its charging pile, three-dimensional finite element electromagnetic field and steady-state thermal analysis simulation are carried out based on COMSOL. In the equivalent treatment of the heat source, the influence of the contact resistance in the contact system and the coil resistance in the electromagnetic system on the temperature rise is emphatically considered. In the simulation, the heat conduction inside the contactor and between the contactor and the connecting copper bar, the convective heat dissipation and radiation heat dissipation between the contactor and the external environment are considered, and the convective heat dissipation coefficient of each outer surface is calculated according to the thermal similarity theory. Using this model, the effects of the cross-sectional area of the connecting copper bar, the contact pressure between the contacts, the shell material, and the coil wire diameter on the temperature field distribution are studied, and the optimal design suggestions for improving the temperature rise characteristics are proposed, which can provide a reference for the miniaturization and large capacity design of the contactor.

Keywords Ceramic seal · DC contactor · Thermal analysis · Contact resistance · The optimization design

1 Introduction

Ceramic sealed DC contactors are widely used in new energy electric vehicles, charging piles, battery power sup-ply, converter capacitor pre-charging, DC power control, circuit protection and other electric vehicles [1]. The contactor is the main component of the functional failure of the switching module. It is urgent to improve

C. Qin · X. Cheng · G. Ge (✉) · Q. Bai · S. Du
School of Electrical Engineering, Zhengzhou University, Zhengzhou 450001, China
e-mail: ggw@zzu.edu.cn

He'nan Engineering Research Center of Power Transmission and Distribution Equipment and Electrical Insulation, Zhengzhou 450001, China

© Beijing Paike Culture Commu. Co., Ltd. 2024

X. Dong and L. Cai (eds.), *The Proceedings of 2023 4th International Symposium on Insulation and Discharge Computation for Power Equipment (IDCOMPU2023)*, Lecture Notes in Electrical Engineering 1102, https://doi.org/10.1007/978-981-99-7405-4_36

the performance and large capacity development of the required HVDC contactor [2]. The dynamic and static contacts of the ceramic contactor are sealed by special ceramics and filled with high-pressure arc extinguishing gas. Excessive temperature rise will lead to a decrease in mechanical strength and increase the contact resistance of the connecting part, further affecting the contact resistance and electrical performance of the contact. The contactor is developing towards miniaturization and large capacity, that is, it can withstand higher voltage and larger current loads without increasing the volume or even reducing the volume of the contactor [3]. This will lead to an increase in the load volume ratio of the contactor. Therefore, in order to ensure the long-term safe and reliable operation of the contactor, it is necessary to carry out thermal analysis.

Thermal analysis of power equipment is a complex problem involving the coupling of current field, gas field and temperature field [4]. A lot of research work has been done on electrical equipment. Polchow simulated the thermal field of the power connector, and considered the influence of the increase of contact resistance caused by wear on the temperature rise of the contact [5]. Barcikowski found that the influence of the internal convection and radiation heat transfer process on the steady-state temperature rise of the overall conductive circuit can be neglected [6]. Bo built a test platform for measuring the temperature rise characteristics of vacuum contactors. The temperature rise characteristics of the conductive circuit of the vacuum contactor contact system were simulated and compared with the test results [7]. Niu established the model to study the heat dissipation characteristics of the contactor and proposed a thermoelectric coupling calculation method to improve the calculation efficiency [8]. Luo conducted electro-magnetic thermal coupling simulation and experimental analysis on the temperature field of aviation variable frequency AC vacuum contactor [9]. Hu studied the influence of contact pressure, heat dissipation area, shell thickness and material, connecting rod material on the temperature field by changing different factors [10]. There are few literatures on the temperature rise characteristics of high-power DC contactors at home and abroad. The existing research is mainly focused on empirical formulas and electromagnetic mechanisms.

In this paper, the electromagnetic field simulation of the contactor is carried out based on the electromagnetic field theory, and the heating power of different components in the contactor is obtained. Based on the law of conservation of energy, the heat transfer differential equation is established to obtain the temperature distribution at different positions inside the contactor. By analyzing the in-fluence of different factors on the temperature distribution, the structural design, material selection and parameter optimization of the product are guided to meet the requirements of miniaturization and large capacity.

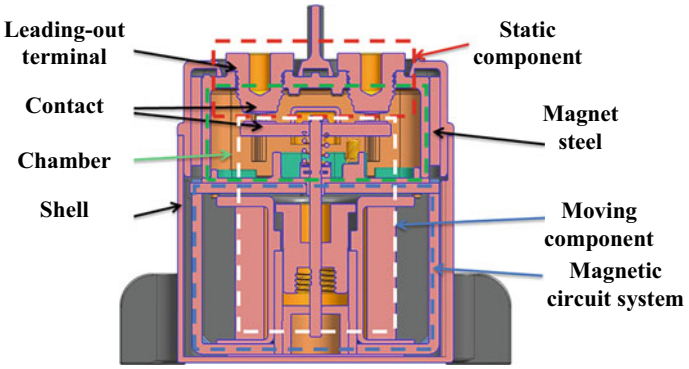

Fig. 1 Structure of the ceramic sealed DC contactor

2 Thermal Field Modeling and Parameter Calculation of Contactor

2.1 Research Object

The structure diagram of the research object is shown in Fig. 1, which is composed of magnetic circuit system, arc extinguishing chamber, contact and extraction end. The model is assumed as follows: The geometric features such as small fillets and screw holes in the model are ignored; the heating and heat transfer characteristics of small components such as spring system are ignored.

2.2 Heat Source Analysis and Parameter Calculation

In the simulation, the coil is equivalent to a hollow cylinder, as shown in Fig. 2.

The calculation formula of the equivalent heating rate of the coil resistance is:

$$q_{\mathrm{v}} = \frac{P}{V} = \frac{U^2/R}{\pi\left(r_1^2 - r_2^2\right)h} \tag{1}$$

where q_{v} is equivalent heating rate, P is coil heat loss, V is coil volume, U is coil voltage, R is coil resistance, r_1 is coil outer diameter, r_2 is coil inner diameter, h is coil height.

The conductive bridge method is used to simulate the contact current shrinkage phenomenon in the electromagnetic analysis. In the thermal field analysis, the thin layer method is used to replace the contact resistance. The conductive bridge model and the thin layer model are shown in Fig. 3a, b.

The equivalent conductive radius of the conductive bridge is

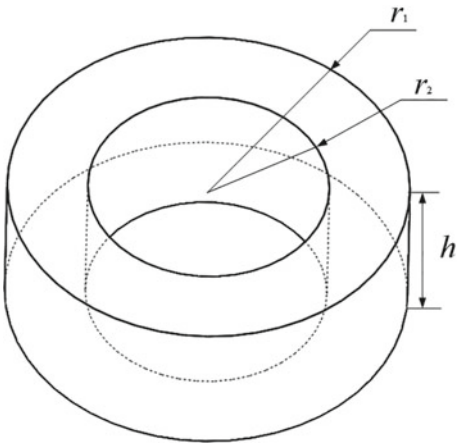

Fig. 2 Coil equivalent resistance model

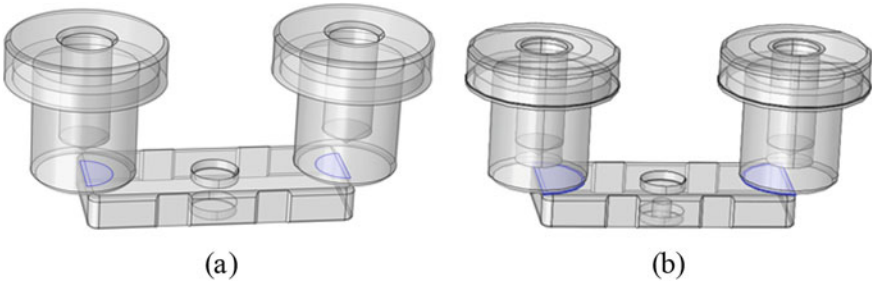

Fig. 3 Conductive bridge model and contact thin layer model

$$r = \sqrt{\frac{F}{\pi \xi H}} \tag{2}$$

where F is the pre-pressure; ξ is a correction coefficient related to the contact condition of the contact surface, which ranges from 0.3 to 1. H is the Brinell hardness.

2.3 Heat Dissipation Characteristics Analysis and Parameter Calculation

The heat conduction satisfies the Fourier law:

$$q = -\lambda \frac{\partial T}{\partial n} \tag{3}$$

where q is the heat flux, λ is the thermal conductivity, and n is the length along the normal direction.

The thermal conductivity of the contact thin layer is obtained by Wiedemann–Franz formula:

$$\lambda = \frac{LT}{\rho} \tag{4}$$

where λ is the thermal conductivity of the contact thin layer, L is the Lorentz number, T is the absolute temperature, ρ is the resistivity of the contact thin layer.

The thermal convection inside and outside the contactor is natural convection. The basic formula of heat flow is Newton cooling formula:

$$q = h(T_{\mathrm{W}} - T_{\mathrm{f}}) \tag{5}$$

where h is the convective heat transfer coefficient, T_{W} is the wall temperature, and T_{f} is the fluid temperature.

For the contactor shell, the calculation formula is as follows:

$$\begin{cases} Gr = \dfrac{g\beta(t_w - t_f)l^3}{v^2} \\ Nu = f(Gr, \mathrm{Pr}) = C(Gr\,\mathrm{Pr})^n \\ h = Nu\dfrac{\lambda}{l} \end{cases} \tag{6}$$

where Gr is the Grashev number; g is the acceleration of gravity; β is the bulk expansion coefficient; v is gas kinematic viscosity; l is the characteristic length; Nu is the Nusselt number; Pr is the Prandtl number; c and n are empirical constants.

Table 1 gives the selection basis of each parameter. On this basis, the convective heat dissipation coefficient of the surface of the contactor is calculated, as shown in Table 2.

The analysis of thermal convection inside the contactor belongs to the problem of natural convection heat dissipation in a limited space. For the vertical interlayer gas, when $Gr \leq 2860$, the heat transfer is completely dependent on heat conduction.

Table 1 Selection of parameters for the calculation of convective heat dissipation coefficients

Surface shape	Gr	C	n	L
Cast or plate	10^4–10^9	0.59	1/4	Height
	10^9–10^{11}	0.10	1/3	
Plate, up	2×10^4–5×10^6	0.54	1/4	Rectangle: length; circle: diameter
	5×10^6–10^{11}	0.15	1/3	
Plate, down	3×10^5–3×10^{10}	0.27	1/4	

Table 2 Anisotropic convective heat dissipation coefficient of contactor outer surface

Contactor surface in all directions	Heat convection coefficient (W m^{-2} K^{-1})
Flank	5.00
Top surface	5.90
Bottom surface	2.95

$$G_{r_\delta} = \frac{g\beta\Delta T\delta^3}{v^2} \tag{7}$$

The maximum thickness of the internal gas in this model is 13 mm. When the outer wall temperature is 57.1 °C, the $G_{r\delta}$ is 2340, so only heat conduction can be considered.

The radiation energy can be obtained by Stefan-Boltzmann law:

$$E = \varepsilon\sigma\left(T^4 - T_0^4\right) \tag{8}$$

where E is the radiation energy, ε is the emissivity, σ is the blackbody radiation constant, T^4 is the surface temperature and $T^4{}_0$ is the ambient temperature.

The radiation emissivity of the shell is set to 0.90, and the copper part is set to 0.22.

3 Thermal Analysis Results

Firstly, the current density distribution is calculated by the AC / DC module, and then the corresponding heating power of each conductor is calculated. The temperature distribution of the contactor section is shown in Fig. 4.

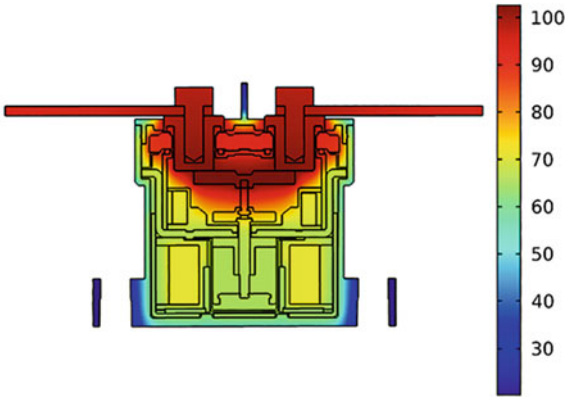

Fig. 4 Temperature distribution at the center interface of the DC contactor

The highest temperature of the contactor with connecting line appears near the main contact, which is 78.15 °C, and the temperature of the terminal is 75.8 °C, which meets the requirements of the national standard. In the temperature rise test, the temperature rise at the terminal is 50.1 °C, while the simulated temperature rise is 48.8 °C, and the error is only 2.6%. The model can be used for the analysis of the influencing factors of temperature field. Analysis of influencing factors of temperature field.

3.1 External Factors

The terminal is fixed by a screw to connect the copper plate to the power supply. The copper plate will take away a certain amount of heat through heat conduction and heat convection. The influence of copper plate must be considered. The cross-sectional area in the initial model is 35 mm^2, and the contact temperature rise is 49.2 °C. When the cross-sectional area increases by 47%, the temperature rise decreases by 8.0 °C. When the cross-sectional area increases, not only the heat conduction effect of the main circuit will be enhanced, but also the overall heat dissipation area will increase, which enhances thermal convection and thermal radiation (Fig. 5).

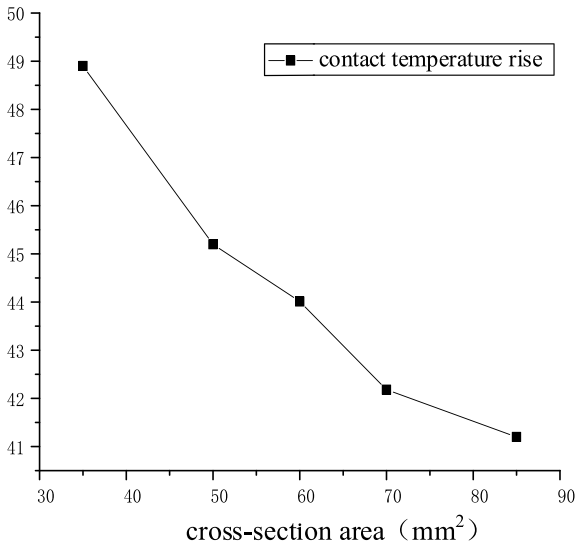

Fig. 5 Relationship between contact temperature and cross-sectional area of copper plate

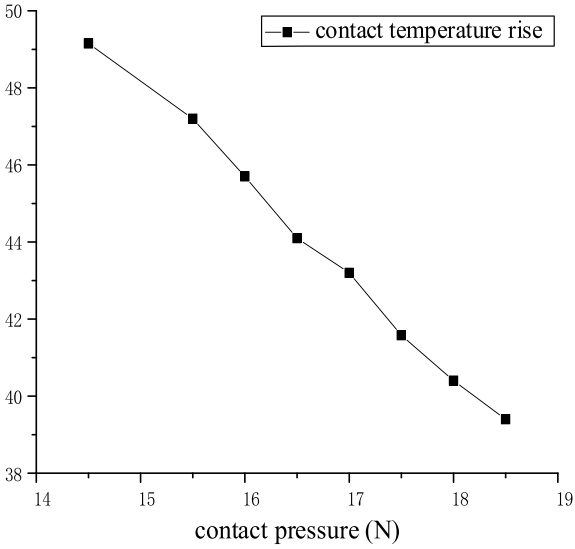

Fig. 6 Relation between contact temperature rise and contact pressure

3.2 Internal Factors

The contact pressure in-creases by 4 N, and the temperature rise of the contact decreases by 16.6 °C. This is because the contact pressure between the contacts is an important factor affecting the contact resistance, and the greater the contact pressure, the smaller the contact resistance (Fig. 6).

The property of the shell is one of the important factors. The conductivity of the original contactor is 0.24 W m^{-1} K^{-1}. After changing the BMC with a thermal conductivity of 3.0 W m^{-1} K^{-1}, the temperature rise of each key point is shown in Fig. 7. The shell material with better thermal conductivity can significantly reduce the temperature of the contacts and coils, but the temperature of the shell will increase.

The empirical formula of the thermal conductivity of the coil is:

$$\lambda = \sqrt{a\lambda_1\lambda_0(d_1/d_2 - 1)} - b\lambda_0 \tag{9}$$

where a and b are 1.45 and 1.6, λ_1 is the conductivity of the insulation, λ_0 is the conductivity of the air, d_1 is the diameter of the wire, and d_2 is the insulation thickness (Table 3).

The larger the coil diameter, the lower the coil temperature rise. Increasing the wire diameter reduces the thermal conductivity of the coil and enhances the heat transfer effect; without changing the number of ampere turns, the larger the wire diameter of the coil, the smaller the resistance value, the smaller the heat loss, and the smaller the temperature rise.

The following is the temperature rise of each key component before and after optimization (Fig. 8).

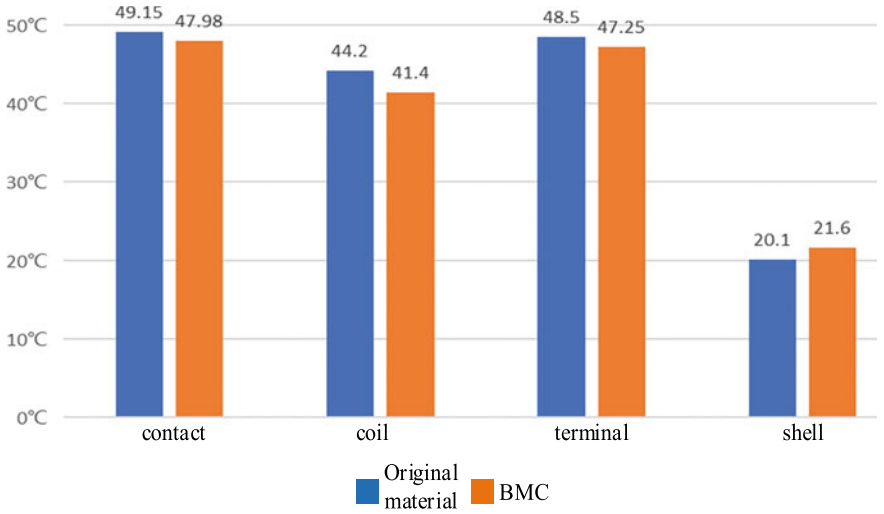

Fig. 7 Temperature rise of key parts after changing shell material

Table 3 Simulation values of thermal conductivity and coil internal temperature rise

Diameter of wire d_1 (mm)	Insulation thickness d_2 (mm)	Thermal conductivity λ (W/(m K))	Maximum scale temperature-rise (°C)
0.5	0.025	0.312	44.2
0.55	0.025	0.331	40.6
0.6	0.025	0.348	31.6

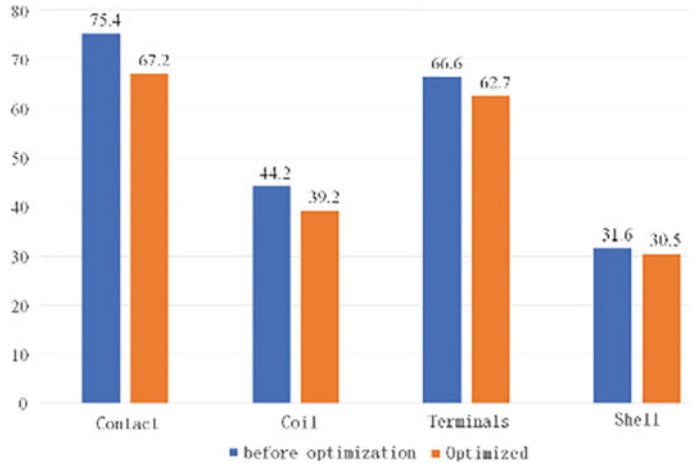

Fig. 8 Temperature rise of key components before and after optimization

The temperature rise of each key component decreases after optimization, and the temperature rise of the contact decreases the most, which is 8.2 °C. The effectiveness of the above optimization measures is proved. From the perspective of the temperature rise of long-term stable operation, without changing the structure and without increasing its volume, these optimization measures can be taken to improve the current level and make it withstand a larger capacity load.

4 Conclusions

(1) The influence of the cross-sectional area of the connecting copper plate on the temperature field is analyzed. With the increase of the cross-sectional area of the connecting copper plate, the temperature rise of the contact will decrease.
(2) The influence of the temperature field distribution of the contact pressure contactor is analyzed. When the contact pressure increases by 4 N, the temperature rise of the contact decreases by 16.6 °C. That increasing the contact pressure of the contact can reduce the contact resistance, thereby reducing the temperature rise of the contact.
(3) The influence of shell material on the temperature field distribution of contactor is analyzed. The shell material with stronger thermal conductivity can reduce the temperature rise of each key part.
(4) The influence of the coil diameter is analyzed without changing the number of coil ampere turns. The increase of coil diameter is beneficial to the decrease of temperature rise from both heating and heat dissipation characteristics.

References

1. Subramaniam K (2020) Intelligent three tie contactor switch unit-based fault detection and isolation in DC microgrids. IEEE Trans Ind Appl 56(1):95–105
2. Gonzalez D (2020) Switching behavior of a gas-filled model DC-contactor under different conditions. IEEE Trans Plasma Sci 48(7):2515–2522
3. Ghassemi M (2015) A coupled computational fluid dynamics and heat transfer model for accurate estimation of temperature increase of an ice-covered FRP live-line tool. IEEE Trans Dielectr Electr Insul 21(6):2628–2633
4. Mohsin L (2014) Finite element analysis of stress intensity factor of pre-cracked coated substrate under contact sliding. In: Electronics 2014 IEEE 36th international conference on manufacturing technology, pp 1–4
5. Polchow JR (2010) A multi-physics finite element analysis of round pin high power connectors. In: Proceedings of the 56th IEEE holm conference on electrical contacts and the 25th international conference on electrical contacts, pp 30–38
6. B.F. (2000) Simulations of the heat balance in low-voltage switchgear. In: Proceedings of 20th international conference on electrical contacts, pp 322–329
7. Luo X (2021) Study on thermal characteristics of aviation frequency AC vacuum contactor based on electromagnetic-thermal coupling. Vacuum Electron 353(04):57–63 (in Chinese)

8. Niu C (2021) Thermal dissipation characteristics analysis and coupling iterative thermal analysis method of aviation contactor. High Volt Eng 47(02):487–494 (in Chinese)
9. Bo K (2019) Experiments and simulation analysis of the temperature-rise characteristics of high current vacuum contactor. Trans China Electrotech Soc 34(24):5135–5143 (in Chinese)
10. Zhang X (2019) Discussion on the lectotype design of high voltage distribution box for electric vehicles. Popul Sci Technol 21(12):42–43+41 (in Chinese)

Research on the Water and Temperature Dependency of Oil-Immersed Pressboard Surface Conductivity

Zhaoyang Ran, Zhiyong Lv, Chenghao Liang, and Yuan Li

Abstract The valve side of converter transformer needs to bear DC electric field component, which makes it important to investigate the characteristics and the influencing factors of the conductivity of oil-pressboard insulation. Therein the surface conductivity of oil-immersed pressboard under the influence of water content, temperature and electric field strength were studied. Results showed that the surface conductivity of oil-immersed pressboard increases exponentially with the increase of water content and temperature. When the water content of the pressboard increases from 0.7 to 4.2%, the surface conductivity increases by about 5 times. When the temperature rises from 25 to 70 °C, the surface conductivity of the pressboard increases by 67 times. As for the electric field strength from 1 to 5 kV/mm, the surface conductivity changes insignificantly. The above results may provide theoretical references for the optimal design of valve side insulation of converter transformer.

Keywords Converter transformer · Oil-pressboard insulation · Oil-immersed pressboard · Surface conductivity

1 Introduction

In recent years, failures of several converter transformers have happened in China due to improper manufacturing, processing or installing. These failures have led to explosion, fire and resulted in great power loss and a big risk to the system [1, 2]. The main insulating materials in converter transformer are transformer oil and oil-immersed pressboard [3]. In the compound insulation, the distribution of electric field and therefore the discharging process are greatly influenced not only by the permittivity, but also by the conductivity of the insulating materials, for oil-pressboard in converter transformers needs to bear DC voltage component as well [4]. Therefore, it is of

Z. Ran · Z. Lv · C. Liang · Y. Li (✉)
Sichuan University, Chengdu, Sichuan, China
e-mail: hvliyuan@scu.edu.cn

© Beijing Paike Culture Commu. Co., Ltd. 2024

X. Dong and L. Cai (eds.), *The Proceedings of 2023 4th International Symposium on Insulation and Discharge Computation for Power Equipment (IDCOMPU2023)*, Lecture Notes in Electrical Engineering 1102, https://doi.org/10.1007/978-981-99-7405-4_37

great significance to understand of the conducting phenomenon of oil-pressboard insulation.

Previous researches on the conductivity and its dependencies were mainly focused on transformer oil. For example, Zhu analyzed the source of water impurities in transformer oil, and determined the influence of water with different states on the conducting characteristics of transformer oil [5]. Badicu proposed a method to assess the condition of oil based on its DC conductivity [6]. Professor Liao compared the wet transformer oil with the dried one, and found that the resistivity, partial discharge inception voltage and breakdown field strength of oil decreased significantly after the absorption of water [7]. However, it is noteworthy that although the above studies have clarified the influence of water content and temperature on the conductivity of transformer oil, the internal insulation of the real transformer includes paper/pressboard and transformer oil simultaneously. Therefore, it is important to study the conductivity characteristic and its dependencies of oil-immersed pressboard as well.

The existing research on the conductivity characteristics of oil-immersed pressboard mainly focuses on the bulk conducting process. For example, Li noticed that when temperature and/or electric field strength increase, the conductivity increasing rate with oil aging decreased simultaneously, yet the result was contrary for the oil-immersed pressboard [8]. In 2016, Fabian Schober thoroughly studied the transient and steady-state DC behavior of oil-impregnated pressboard, mainly focusing on volume conductivity of low and high density pressboard, immersed in low conductive and high conductive oil [9]. In a real converter transformer, the DC electric field strength at the surface of the pressboard is greatly affected by the surface conductivity of the dielectric, therefore, it is of great importance to investigate the characteristics and the influencing factors of the surface conductivity of oil-immersed pressboard.

This paper studied the surface conductivity of oil-immersed pressboard considering the effect of water content, temperature, and electric field strength, and characterized the influence of water content and temperature quantitatively. The internal mechanism of the above parameters affecting the surface conductivity of the pressboard were also analyzed. The results may provide theoretical references for the optimal design of valve side insulation of converter transformer.

2 Experimental

2.1 Sample Preparation

The oil we used was KI25X, which was produced by China National Petroleum Corporation (CNPC). The relative permittivity, bulk conductivity and water content after drying were 4.3, 10^{-12} S/m and 7.4 ppm, respectively. Before the experiment, the oil was put into a vacuum drying oven, and dried at 80°C for over 24 h. The IEC B3.1 pressboard we used in the experiment was produced by Jinsong Corporation,

with a relative permittivity 4.3, volume conductivity 10^{-14} S/m and density 1.15 g/cm^3. The water content of the pressboard was measured by Karl Fischer titration method.

To conduct the experiment, the pressboard was first dried in the vacuum drying tank to ensure its water content less than 1%. Then take out the pressboard and quickly put it into a thermostat with a temperature of 30 °C and an ambient humidity of 50%, to initiate water absorption. By controlling the absorption time, pressboard samples with different water content can be prepared.

Afterwards, put the pressboard samples into the vacuumed experimental chamber, and inject the fully dried and purified transformer oil, until the pressboard was completely covered by the oil. To adjust the experimental temperature, a vacuum heating chamber was adopted. A remote-controlled heating plate was set at a constant power, so the temperature of the experimental atmosphere was fixed at a certain value. During the measurement, the temperature was set to 25, 40, 50, 60 and 70 °C, respectively.

2.2 Experimental Platform

Figure 1 shows the platform we adopted. DC voltage was generated via the doubling circuit, and measured by a resistance divider. Pressboard sample was connected to the divider, in series with the Keithley 6517B pico-ammeters to measure the current along the surface of the pressboard. The oscilloscope was to read the DC voltage amplitude.

The design of measuring electrodes is based on the method recommended by IEC, which is shown in Fig. 2. The length/width of the electrode were 60 mm/10 mm, respectively. To ensure the close contact of electrodes and pressboard samples, adhesive and bolts were used.

To start the measurement of the surface conductivity, direct current voltage generated via the doubling circuit was applied to the high voltage electrode. However, the current on the pico-ammeter should only be recorded as the conducting current when it became stable, for the polarization process does not finish simultaneously with the

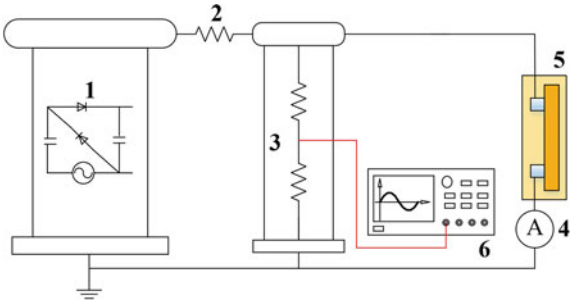

Fig. 1 Schematic of the measuring system (1-DC source; 2-Protective resistance; 3-Resistance divider; 4-Keithley 6517 B; 5-Measuring electrodes and pressboard sample; 6-oscilloscope)

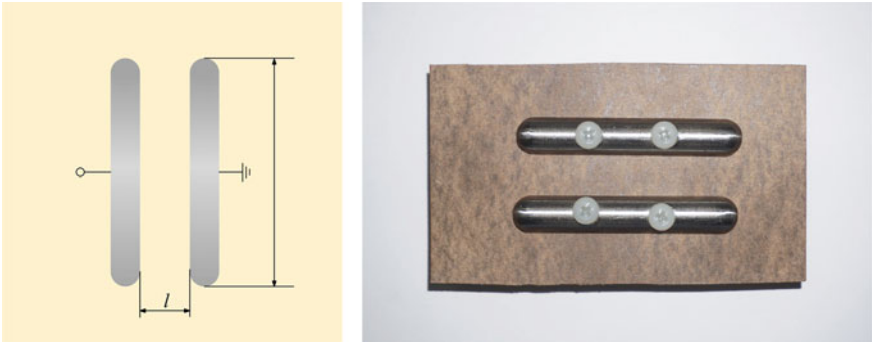

Fig. 2 Schematic and the real image of the experimental sample

appliance of voltage U_o. Once the final conductive current was measured as I_x, the surface conductivity of the pressboard can be obtained by formula (1).

$$\gamma_p = \frac{lI_x}{bU_0} \tag{1}$$

where, $l =$ Distance between measuring electrodes; $b =$ Length of the electrodes.

3 Results and Discussion

3.1 Influence of Water Content on Pressboard Surface Conductivity

The term of conductivity is not a constant property of material and it depends on different parameters. One of the important dependencies of oil-immersed pressboard conductivity is their water content. To investigated this dependency of conductivity, long-term surface conductivity was investigated with increasing water content of pressboard samples which are prepared based on described procedure in Sect. 2.1. Hereby, the surface conductivity is measured after a polarization time of 10,000 s. In Fig. 3, the increasing rate of surface conductivity with water content is obvious.

The investigation shows that the water content can influence the surface conductivity of oil-immersed pressboards dramatically. It is also worthwhile to mention that a logarithmic increase of the surface conductivity with water is observed.

Mathematical formula as cited in [10] tells that pressboard's water content can be calculated using

$$\frac{1}{w} = l - k\ln(\gamma_p) \tag{2}$$

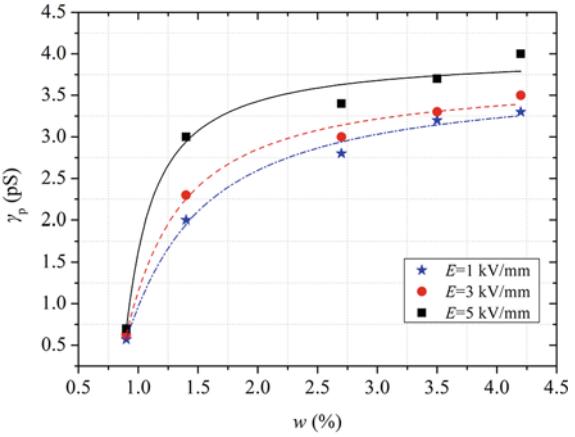

Fig. 3 Surface conductivity of oil-immersed pressboard varied with water content

In formula (2), w stands for the water content in pressboard; γ_p is the surface conductivity of the sample; k and l are constants. Adopt the data from Fig. 4 to formula (2), the exact value of k and l can be easily derived. The final form of formula (2) is,

$$\frac{1}{w} = 1.8233 - 0.2057\ln(\gamma_p) \tag{3}$$

Now that formula (3) is derived, γ_p can therefore be expressed as

$$\gamma_p = \exp^{4.8614(1.8233-\frac{1}{w})} \tag{4}$$

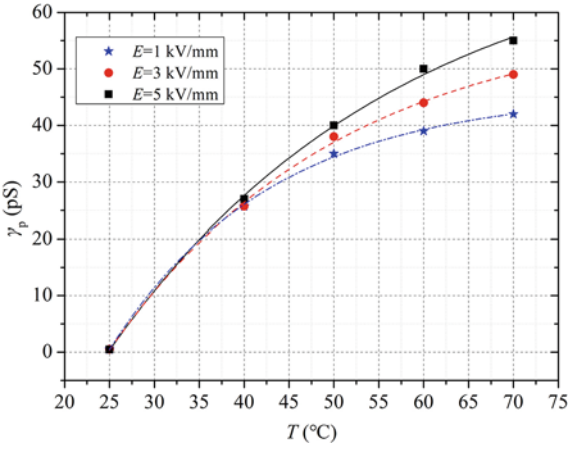

Fig. 4 Surface conductivity of oil-immersed pressboard varied with temperature

3.2 *Influence of Temperature on Pressboard Surface Conductivity*

Further investigation was performed to compare variation of long-term surface conductivity with temperature and electric field strength of specimens. An example of surface conductivity changes dependent on temperature is presented in Fig. 4.

In Fig. 5, a logarithmic-similar curve is draw. The energy of molecular thermal vibration obeys Boltzmann distribution. The number of effective thermal vibrations that dissociate in each second can be calculated as formula (5)

$$\nu = \nu_0 \exp^{-\frac{u_0}{kT}} \tag{5}$$

where v_0 is the thermal vibration frequency of atomic group; u_0 is the molecular dissociation energy; k is Boltzmann constant ($k = 8.61733 \times 10^{-5}$ eV/K) and T is the absolute temperature.

Under dynamic equilibrium condition, the ion concentration n_0 can be derived with formula (6)

$$n_0 = \sqrt{\frac{N_0 \nu_0}{\xi}} \exp^{-\frac{u_0}{2kT}} \tag{6}$$

In formula (6), N_0 is molecular concentration; ζ is the ion recombination coefficient. On the other hand, the migration rate of ions in the direction of the electric field μ is

$$\mu = \frac{q\delta^2 \nu_0}{6kT} \exp^{-\frac{U}{kT}} \tag{7}$$

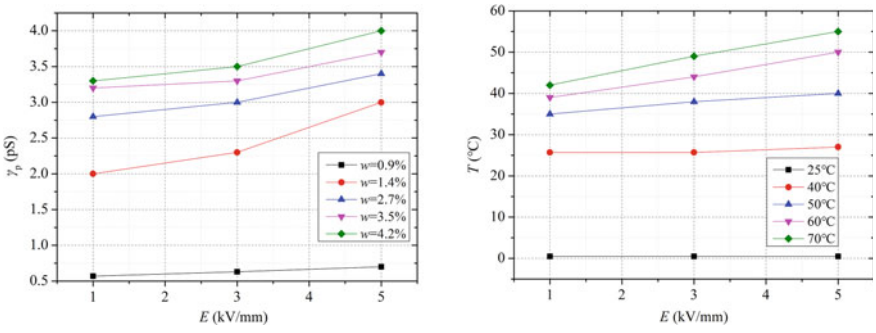

(a) with different water content (b) with different temperature

Fig. 5 Surface conductivity of oil-immersed pressboard varied with electric fields

Combine the above-mentioned formulas, the ionic conductivity of oil-paper insulation can be calculated as (8)

$$\gamma = n_0 q \mu = \frac{n_0 q^2 \delta^2}{6kT} \nu_0 \exp^{-\frac{U}{kT}} \tag{8}$$

In this formula, γ is the ionic conductivity; q is the ion charge; δ is the mean free path of ions; U is the average energy barrier that the ion transition needs to overcome.

Typically, the temperature related constant of the first order is much smaller than that of the exponential term, therefore formula (8) can be rewrite as

$$\gamma = A \exp^{-\frac{B}{T}} \tag{9}$$

Basically, A is irrelevant with temperature, whereas $B = U/k$. Change the temperature into Kelvin temperature and fit the results with formula (9), an empirical formula can be derived,

$$\gamma_p = 1.421 \times 10^5 \exp^{(-0.673/T)} \tag{10}$$

3.3 *Influence of Electric Field Strength on Pressboard Conductivity*

Another factor that alters the surface conductivity of pressboard samples is the electric field strength. Usually the measurement of surface conductivity is performed only under low electric field ($\leq$ 1 kV/mm), under which the electron emission from electrodes and the dissociation effects are weak to increase the transmission of ions. However, for oil-immersed pressboards used in real apparatus, the operation field strength can reach up to 10 kV/mm or higher [11]. Therefore, further study should be conducted under higher electric field strength. Figure 5 presents the experimental results of pressboard samples' surface conductivity altered with the electric field strength, under different temperature and water content.

Samples with same water contents exhibit different surface conductivities under electric field strength of each level. When the electric field is 1 kV/mm, surface conductivity at 4.2% water content is 3.24 pS, whereas for 5 kV/mm, the conductivity is 4.02 pS. Changes with electric field strength do exist, but the relative value has no big differences. Therefore, compared with electric field strength, water content is a much more critical. Although water content is carefully restricted from the oil-pressboard insulation system, water from the atmosphere can still penetrate into the transformer. Besides, the migration of water from oil to pressboard will also increase the water content in pressboards. Therefore, even the least water will cause

devastating damage to oil-pressboard insulation, especially under high electric field strength.

3.4 General Remarks

The mechanism of solid material's conduction can be categorized into three types according to the type of carriers in the dielectric: 1. Ionic conduction (or electrolytic conduction); 2. Ionized molecules conduction (or electrophoresis conduction); 3. Electronic conduction. From the micro perspective, solid dielectrics can be regarded as a kind of semi-conductor with wide-band gap, on which free electron and holes of dielectric itself have little effect. However, carriers generated due to impurities and defects caused by impurities (especially the ionized impurity molecules) contributes to the conduction phenomenon of solid materials. Besides, electrons emitted from electrodes under high electric field also contributes to the conduction.

As the main impurity in pressboard, water molecule will easily disassociate into free ions. These free-moving particles will become neatly organized once an electrical stress is imposed on the dielectric. The more water in pressboard, the more these free ions are. All these conductive materials contribute to the change of pressboards' surface conductivity. On the other hand, once the temperature increases, whether the ionization rate or the movement rate of impurity particles increase. At high temperature, oil in capillary cracks of pressboards may vaporize, which leaves a lot of gas-filled micro-defects both at the surface and within the pressboard. Before the generation of micro-defects, free ions are easily blocked by the high-density structure of the material. However, once the micro-defects emerge, ions can move within the cracks. Therefore, the surface conductivity of the sample increases. The influence of electric field strength on pressboards' surface conductivity is also due to many different reasons. First of all, the enhanced electric field can accelerate the movement rate of free ions, which increase the surface conductivity of the material. Second, under high electric field strength, electrons will begin to emit from the electrode, which also act as carriers to increase the samples' surface conductivity. However, in this paper, the pressboard samples were applied with DC voltage. Considering that the bulk conductivity of the sample is much lower than the surface conductivity, the DC electric field concentrates within the volume, not at the surface of the pressboard. Changes of electric field strength had little influence on the generation and the migration of the ion, leading to an unobvious change of the surface conductivity of the pressboard samples.

4 Conclusion

In this paper, water content, temperature and electric field strength dependencies of pressboard surface conductivity are studied. First of all, role of water and its influence on immersed pressboard's surface conductivity is analyzed. For higher water content in pressboard, a logarithmic function can describe the surface conductivity behavior. In addition, temperature dependency of immersed pressboard conductivity is studied. The surface conductivity of pressboard at 70 °C was 67 times more than that at 25 °C, while an increase of water content from 0.7 to 4.2% leads to 5 times higher surface conductivity values. In last section of this investigation, the influence of applying the stress on electrical conductivity is verified and in an electric field strength from 1 to 5 kV/mm, a non-significant increase is noticed by surface conductivity measurements.

Acknowledgements This work is supported by the College Student Innovation and Entrepreneurship Training Program of Sichuan University (C2023124999), and the Project of Natural Science Foundation of Sichuan Province (2022NSFSC1872).

References

1. Zhang YX, Han Y, Cheng YC et al (2022) Fault analysis for valve side winding of converter transformer. Power Syst Technol 46(7):2794–2803
2. Zhang GJ, Tian F, Du ZB et al (2022) Deep analysis of breakdown fault in UFV converter transformer regulating winding. Transformer 59(7):61–65
3. Saha TK, Purkait P, Muller F (2005) Deriving an equivalent circuit of transformers insulation for understanding the dielectric response measurements. IEEE Trans Power Deliv 20(1):149–157
4. Li Y, Zhang QG, Wang TL et al (2016) Study on micro bridge impurities in oil-paper insulation at DC voltage: their generation, growth and interaction with partial discharge. IEEE Trans Dielectr Electri Eng 23(4):2213–2222
5. Zhu YW, Cui HZ, Li SJ et al (2018) Polarization characteristics of aged oil impregnated paper insulation by thermally stimulated current tests. Proc CSEE 38(8):2513–2520
6. Badicu LV, Gorgan B, Dumitran LM, Notingher PV (2012) Assessment of transformer mineral oil condition based on dc and ac conductivity. IEEE Trans Dielectr Electric Eng 19(5):1544–1551
7. Liao RJ, Shao SF, Cheng L et al (2018) Breakdown characteristics of oil-paper insulation in UHVDC converter transformer under ac/dc voltage and its selection of oil and paper. Power Syst Technol 42(2):387–392
8. Li HQ, Zhong LS, Yu QX, Mori S, Yamada S (2014) The resistivity of oil and oil-impregnated pressboard varies with temperature and electric field strength. IEEE Trans Dielectr Electric Eng 21(4):1851–1856
9. Takahashi E, Shirasaka Y, Okuyama K (1994) Analysis of anisotropic nonlinear electric field with a discussion of dielectric tests for converter transformers and smoothing reactors. IEEE Trans Power Deliv 9:1480–1486
10. Bartnikas R (2009) Some general remarks on the dielectric loss mechanisms in mineral oils. IEEE Trans Dielectr Electric Eng 16(6):2113–2121
11. Li Y, Zhou K, Zhu GY et al (2019) Study on the influence of temperature, moisture and electric field on the electrical conductivity of oil-immersed pressboard. Energies 12(16):3136

Influence Analysis of Damp Defect of Composite Insulated Zinc Oxide Arrester Based on Finite Element Calculation

Wenyan Li, Jiangming Liu, Lintao Sun, Changbiao Liu, Yunfei Ai, Zhi Wang, Jie Zhou, and Ke Ye

Abstract Composite insulated zinc oxide arrester is important electrical equipment in power systems, and is prone to insulation failure during operation. For a case of abnormal leakage current and heat generation of zinc oxide arrester, the cause of the abnormality was identified as internal dampness through testing and disintegration analysis. The finite element analysis method was used to study the effects of zinc oxide valve plate moisture, insulating sheath moisture and insulating sheath cracking on the voltage distribution of arrester. The results show that when the resistivity of the arrester varistors and sheaths drops to a certain extent, it will lead to a significant change in the voltage distribution on the varistors, and the overall change trend is that the voltage of the varistors around the object is reduced, and the voltage of the other varistors is raised. It plays a certain a certain reference role in the analysis and disposal of the insulation moisture abnormality of the composite insulated zinc oxide arrester.

Keywords Arrester · Dampness · Defect · Finite element calculation

1 Introduction

Zinc oxide arrester is an overvoltage limiting device with excellent nonlinear voltammetric characteristics, and its operating performance plays a major role in the safe operation of power equipment [1]. Statistical analysis data show that internal moisture, impact damage, pollution damage, improper use are the main reasons for the failure of the arrester. Among them, the proportion of internal moisture caused by seal failure and external force failure can reach 85.6% of the statistics of the number of arrester failure causes [2].

W. Li (✉) · J. Liu · L. Sun · C. Liu · Y. Ai · Z. Wang · J. Zhou · K. Ye
State Grid Zhejiang Electric Power Co., Ltd., Ultra-High Voltage Branch Company, Hangzhou 310000, China
e-mail: 526152295@qq.com

© Beijing Paike Culture Commu. Co., Ltd. 2024

X. Dong and L. Cai (eds.), *The Proceedings of 2023 4th International Symposium on Insulation and Discharge Computation for Power Equipment (IDCOMPU2023)*, Lecture Notes in Electrical Engineering 1102, https://doi.org/10.1007/978-981-99-7405-4_38

Aiming at the moisture phenomenon of porcelain sleeve structure arrester, it is pointed out that the resistance value of the resistance valve plate decreases when the arrester is wet, the leakage current flowing through the arrester increases, the dielectric loss increases, and there is local overheating in the damp part [3]. A simulation test was carried out on the internal and external temperature distribution characteristics and electrical parameters of a single section of the arrester under the condition of moisture with 1000 kV zinc oxide arrester as the research object, and it was pointed out that the optical fiber temperature measurement method and infrared temperature measurement method could effectively determine the internal moisture defects of the zinc oxide arrester, while the electrical parameters were not sensitive enough for the moisture reaction of the single section of the UHV zinc oxide arrester [4]. Scholars at home and abroad use simulation tests, live detection and finite element simulation analysis to characterize the internal temperature, voltage and electric field distribution of the arrester under abnormal conditions such as internal moisture and external surface pollution [5–14]. The optical fiber-current method is used to verify the correctness of the finite element analysis calculation method and results in the calculation of arrester voltage and electric field distribution [15]. However, there is less research on the insulation failure of single-section composite insulated zinc oxide arrester partial valve plate and sheath.

Aiming at the influence of local moisture in composite insulated zinc oxide arrester, the author uses the finite element method to study and analyze the influence of moisture exposure and sheath cracking on the overall voltage distribution of the arrester valve by a case of abnormal leakage current of 220 kV composite insulated zinc oxide arrester.

2 Device Abnormality

The live detection of a 500 kV substation found that the leakage current of phase B and C of a 220 kV line zinc oxide arrester increased significantly, and the heating was abnormal. The arrester model is YH10W-216/562, which is made of two stages in series, and the main components include flange, zinc oxide valve plate, zinc oxide valve fixture, insulating cylinder, silicone rubber umbrella skirt. Each section of the arrester contains 30 resistive valve plates, each 15 resistive valve plates are fixed with a insulating sheath, and the zinc oxide valve plate and the sheath are filled with micro-positive pressure nitrogen. In order to adjust the height of the zinc oxide valve plate so that it fits with the outer insulation, metal gaskets are placed between the partial zinc oxide valve plates. The structure of the device is shown in Fig. 1.

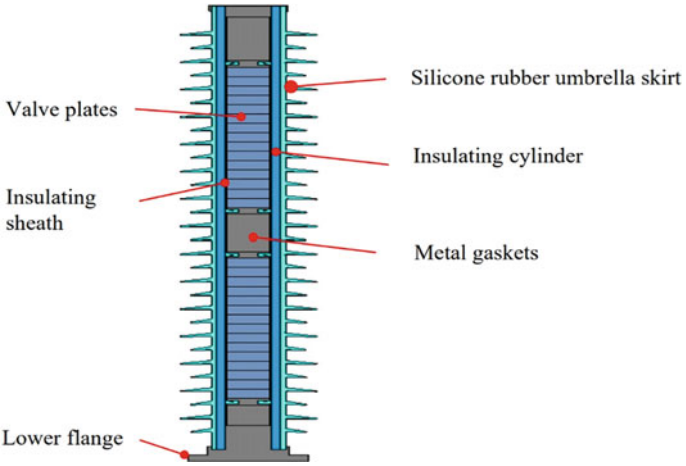

Fig. 1 Structural diagram of polymeric insulated zinc oxide arrester

2.1 Leakage Current Detection at Continuous Operating Voltage

The leakage current detection of the zinc oxide arrester shows that the full current and resistive current components of the B-phase and C-phase arresters are significantly increased, and the leakage current live detection data are shown in Table 1.

As can be seen from Table 1:

(1) Compared with the detection data in 2019 and 2020, the impedance angle of the three-phase arrester detection data in 2021 is reduced by 2–5 degrees, and the full current of the B-phase and C-phase arresters and the resistive current of the three-phase arrester increased significantly, of which the full current of the B-phase arrester increases by 0.03 mA and the resistive current increased by 0.032 mA compared with 2020, with growth rates of 8.0 and 94.1% respectively;

Table 1 Leakage current of polymeric insulated zinc oxide arrester

Phase	φ/°	I_X/mA	Ir/mA	Irp/mA	Ir1p/mA	Ir3p/mA	Year of detection
A	**86.88**	**0.442**	**0.025**	0.035	0.034	0.007	2019
	87.11	**0.441**	**0.024**	0.032	0.031	0.007	2020
	84.42	**0.447**	**0.045**	0.069	0.061	0.007	2021
B	**84.10**	**0.377**	**0.039**	0.059	0.055	0.007	2019
	84.91	**0.375**	**0.034**	0.049	0.047	0.005	2020
	80.72	**0.405**	**0.066**	0.097	0.092	0.007	2021
C	**86.81**	**0.398**	**0.023**	0.033	0.031	0.007	2019
	86.97	**0.399**	**0.023**	0.033	0.029	0.005	2020

The full current of C-phase arresters increased by 0.17 mA and resistive current increased by 0.028 mA compared with 2020, with growth rates of 4.3 and 47.8%, respectively.

(2) In the A-phase and C-phase angle test, automatic edge replenishment technology is used to counteract the interference effect of stray capacitance between phases on the linear arrester resistance current sensing data. That is, the B-phase detection data in the automatic edge complement mode is the real value, while the A-phase and C-phase resistive current detection data are related to the compensation angle, if one phase equipment is abnormal, the other phase equipment data will be affected. According to the full current detected in 2021 and the compensation angle under normal conditions in 2019, the resistance current data of the A-phase and C-phase arresters are calculated to be 0.023 and 0.059 mA, respectively. That is, the detection data of A-phase arrester in 2021 had no significant change compared with previous years, and the C-phase arrester resistive current increased by 0.036 mA, with a growth rate of 156.5%.

2.2 Infrared Imaging Temperature Measurement

The infrared imaging spectrum of the arrester is shown in Fig. 2. Comparing the temperature of the upper section of the three-phase arrester, it can be found that the maximum surface temperature of the B-phase and C-phase arresters is 22.4 and 20.2 °C, respectively, which are greater than 3.8 and 1.6 K of the A-phase arrester, which exceeds the requirements of DL/T664-2008 “Infrared Diagnostic Application Specification for Live Equipment” for the temperature difference of the arrester is not more than 1 K, which is a serious defect.

3 Disintegration Examination

The B-phase arrester was disassembled, and it was found that the upper section valve plate group had high resistance during the disassembly process, and the insulation sheath cracked and deformed many times. The upper section of the A phase with normal test data was disassembled, and it was found that the valve plate group was taken out smoothly, and the outer insulation sheath of the valve plate group was intact and there was no abnormality. The appearance of the upper insulating sheath of the A-phase and B-phase arresters is shown in Fig. 3.

The two valve groups taken out of the upper section of the B-phase arrester have different degrees of insulation sheath cracking, in which 7 zinc oxide valve plates are exposed at the top crack of the insulation sheath of the upper valve plate group, and some of the exposed surfaces of the valve discs together with the surface of the top metal electrode have obvious ablation marks, as shown in Fig. 4.

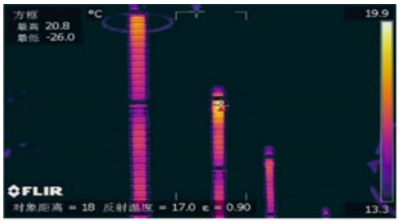

(a) Three-phase arrester as a whole

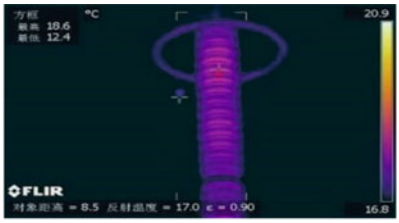

(b) A-phase arrester section above

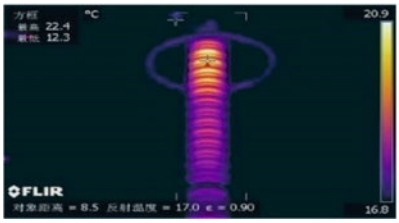

(c) B-phase arrester section above

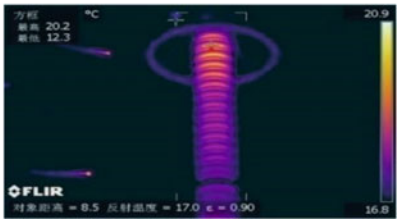

(d) C-phase arrester section above

Fig. 2 Infrared imaging temperature measurement picture

(a) A-phase arrester section above

(b) B-phase arrester section above

Fig. 3 The appearance of insulated sheath

The insulation resistance test was carried out on 4 zinc oxide valve plates with obvious ablation marks on the exposed surface of the valve plate, and the insulation resistance data was obtained as shown in Table 2.

As can be seen from Table 2, the insulation resistance test results carried out immediately after the disintegration of the four resistance valve plates show that the insulation resistance of the valve plate is 2–4 MΩ. After wiping the surface of the

(a) (b)

Fig. 4 The cracked sheath and discharged trace

Table 2 Insulation resistance of zinc oxide varistor

Valve plate serial number	After disintegration/MΩ	After the surface is cleaned/MΩ	After drying treatment/MΩ
1	2.6	560	1640
2	2.91	680	1440
3	2.65	1860	2210
4	3.24	2160	2240

valve plate with alcohol, the insulation resistance increased significantly, and after further drying in the oven, the insulation resistance of the four valve plates reached more than 1500 MΩ. The above indicates that the resistive valve has significant insulating moisture.

Based on the resistive current test, infrared imaging temperature measurement and disintegration of the arrester, it is judged that the abnormal development process of the arrester is that the internal insulation of the valve plate and sheath is moisture, and the insulation resistance decreases. The heating effect caused by the increase of resistive current causes the sheath to crack, the internal electric field is distorted, and the side of the sheath and valve plate is partially discharged.

4 Arrester Voltage and Electric Field Analysis Based on Finite Element Method

In order to study the influence of moisture inside the arrester, the finite element method is used to study the voltage distribution of the arrester under the condition of arrester valve plate, sheath moisture and sheath cracking.

4.1 Finite Element Analysis Method and Simulation Model

The surrounding area of the arrester can be approximated as a fixed-frequency time harmonic field with the high-voltage end as the source. The power frequency voltage of China's power system is 50 Hz, and the wavelength is about 6000 km, which is far greater than the structural height of the arrester, so the coupling between the electric field and the magnetic field is very weak and can be regarded as a quasi-static field. Maxwell's equation under quasi-static conditions is used to establish the computational model of electromagnetic phenomena, and the medium containing poor conductors satisfies the following Poisson equation and boundary conditions.

$$\begin{cases} -(\sigma + \mathrm{j}\omega\varepsilon)\nabla^2\varphi = 0, \quad \text{Within the boundary } \Omega \\ \varphi = \mathrm{u}, \quad \text{Within the boundary } \Gamma_1 \\ \dfrac{\partial\varphi}{\partial n} = \Psi \quad \text{Within the boundary } \Gamma_2 \\ \oint_{\Gamma 0}(\sigma + \mathrm{j}\omega\varepsilon)\dfrac{\partial\varphi}{\partial n}d\Gamma = Q_C, \varphi = \varphi_c, \quad \text{Within the boundary } \Gamma_2 \end{cases}$$

Wherein, Ω is the solution field of potential, which is enclosed by the first class boundary Γ_1 and the second class boundary Γ_2, and contains a suspended conductor Γ_0 in the field; u is the potential function given on Γ_1, is the function given on Γ_2, is the net charge on the potential suspension conductor Γ_0, δ, ε, ω are the conductivity, relative permittivity and power frequency of the material, respectively, and the conductivity and relative permittivity of the material can be regarded as constants at power frequency. φ_C is the potential values to be sought.

Ignoring the upper leads, equalizing rings and other structures, the YH10W-216/562 composite insulated zinc oxide arrester was used as the simulation model, and a three-dimensional axisymmetric model was established in ANSYS electromagnetic field analysis software. Set the two-dimensional element type to plane 230, the three-dimensional element type to solid 231, and the permittivity and resistivity parameters of the conductor and dielectric under good insulation are shown in Table 3. Load a power frequency voltage with the amplitude of the peak phase voltage of the 220 kV line operation at the top electrode of the arrester; A 0 potential is loaded at the bottom electrode and the outer air boundary and solved using the ICCG solver. Extract the

Table 3 Material parameters

Material properties	Gas	Silicone rubber	Insulating cylinder	Insulating sheath	Valve plate	Metal electrode
Dielectric constant	1	4.75	3	3.5	750	60,000
Resistivity/ $\Omega\ m^{-1}$	1e8	1e12	5e11	1e12	1e12	–

potential at the upper and lower points of each valve plate, and calculate the voltage borne by the valve plate (Table 3).

4.2 The Valve Plate is Affected by the Degree of Moisture on the Voltage Distribution of the Arrester

When the resistivity of the 1–15 valve plates of the upper section arrester from top to bottom is set Separately to 1e12, 1e6, 1e5 and 1e4 $\Omega\ m^{-1}$, the voltage distribution of the arrester is shown in Fig. 5.

It can be seen from Fig. 5 that due to the comprehensive factors of its own capacitance and stray capacitance, the potential distribution of the arrester resistance valve plate is uneven. In the absence of pressure equalization measures, the potential distribution is characterized by high voltage sharing of the upper valve plate and low voltage sharing of the lower valve plate, which makes the charge rate of some valve plates high. When the resistivity of the 1–15th valve plate changes in the range of 1e6–1e12 $\Omega\ m^{-1}$, the overall voltage distribution of the arrester does not change significantly, but when the resistivity of the 1–15th valve plate drops to 1e4 $\Omega\ m^{-1}$,

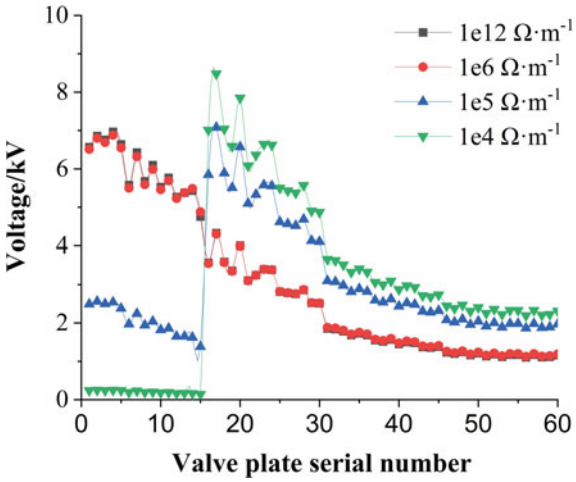

Fig. 5 The voltage distribution under different electrical resistivity of zinc oxide varistor

the bearing voltage of the single valve plate with the decrease in resistivity decreases significantly, from a few thousand volts to hundreds of volts, while the voltage of other valve plates rises significantly, resulting in uneven voltage distribution.

4.3 Effect of Sheath Cracking Angle on Arrester Voltage Distribution.

Under the condition that the cracking angles of the outer sheath of the 1–15 valve disc from top to bottom are 15°, 30° and 45°, the voltage distribution of the arrester valve plate is shown in Fig. 6.

It can be seen from Fig. 6 that in the absence of moisture in the insulation layer, the cracking of the sheath has a great effect on the voltage of the lightning arrester valve near it, and the voltage change of the lightning arrester valve piece far from the cracking position of the sheath is not obvious. Compared with the case that the sheath is not cracked, after the sheath is cracked, the bearing voltage of the top resistive valve plate dominated by the 1–6 pieces decreases, and the withstand voltage of the middle and lower resistive valve plates increases slightly, that is, the voltage distribution of the upper arrester valve plate tends to be uniform.

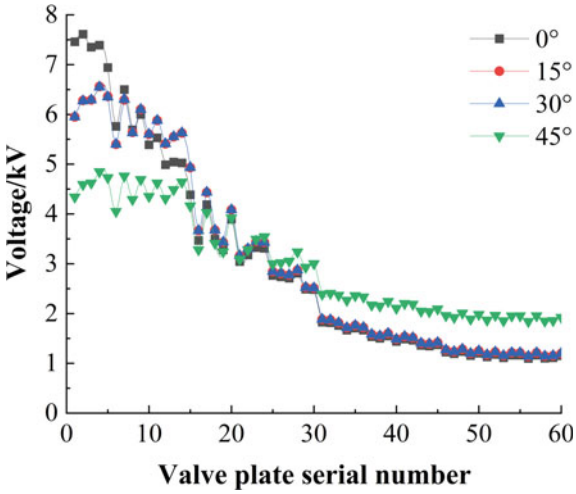

Fig. 6 The voltage distribution under different cracked angles of insulated sheath

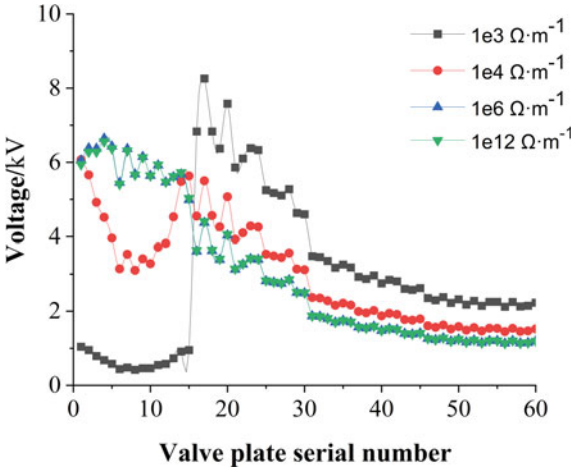

Fig. 7 The voltage distribution under different electrical resistivity of insulated sheath

4.4 The Influence of Moisture Degree of the Sheath on the Voltage and Electric Field Distribution of the Arrester

The sheath cracking angle is set to 45°, and the sheath resistivity changes in the range of 1e3–1e12 Ω m^{-1}, and the voltage distribution on the arrester valve plate under the condition of simulating the sheath under moisture is shown in Fig. 7.

It can be seen from Fig. 7 that when the sheath resistivity is in the range of 1e3–1e12 Ω m^{-1}, the arrester voltage distribution curve is highly coincident, that is, the decrease in sheath insulation resistance in this range has little effect on the voltage distribution of the valve piece. When the sheath resistivity drops to 1e4 Ω m^{-1}, the valve plate voltage distribution changes significantly. This change is mainly manifested as the voltage bearing of the valve plate adjacent to the position of the moisture-bearing sheath drops, the voltage of other valve plates rises, and the bearing voltage of individual valve plates becomes about 2 times that of normal.

4.5 Analysis of the Influence of Insulation Moisture on Composite Insulation Arrester

The full current of metal zinc oxide arrester mainly includes the current through the valve plate, the current through the fixed valve plate insulation material and the current through the umbrella skirt. Under normal operating conditions, the full current is mainly capacitive current, and the resistive current only accounts for 10–20%.

From the calculation results of finite element analysis, it can be seen that the resistivity of any material in the arrester valve plate and sheath caused by insulation

moisture will lead to a significant change in the voltage distribution on the valve plate, and the overall change trend is that the voltage of the valve plate around the object with low resistivity decreases, while the voltage of other valves increases, mainly because the insulation moisture causes the impedance change of the valve plate, sheath and other insulation materials, so that the voltage distribution changes.

5 Concluding Remarks

Combining the abnormal characterization of arresters, equipment disintegration and ANSYS finite element analysis, the following conclusions are drawn:

(1) The internal insulation of the arrester will increase the resistive current under the operating voltage, and the heating effect is obvious. Therefore, resistive current testing, infrared imaging temperature measurement and other tests can be carried out in strict accordance with the equipment detection cycle, which can effectively find the internal moisture defects of the arrester.
(2) When the resistivity of the arrester valve plate and sheath drops to a certain extent, it will cause the voltage distribution on the valve plate to change significantly. The overall change trend is that the voltage around the resistivity falling object bears the voltage; The voltage of other valve plates rises, and the charge rate increases.

References

1. Qiao X, Zhang Z, Sundararajan R et al (2021) The failure arc paths of the novel device combining an arrester and an insulator under different pollution levels. Int J Electr Power Energy Syst 125:106549
2. Lyu H (2021) Key technologies and applications of power transmission and transformation equipment lightning arrester. China Electric Power Press, Beijing (in Chinese)
3. Liu W, Xiao J, Jin S et al (2022) Analysison damp defect of 500 kV zinc oxide arrester based on field-circuit coupling. Insul Surge Arresters 1:118–125 (in Chinese)
4. Shi Z, Duan T, Li Z et al (2020) Experimental analysis on dampness defect of UHV zinc oxide arrester. Insul Surge Arrest 6:117–121 (in Chinese)
5. 3D potential distribution calculation and design of grading rings for post-type ZnO surge arrester for 1000 kV substation. In: Proceedings of the Chinese Society for electric engineering (2007), vol 27 (in Chinese)
6. Wang X (2015) MOA failure diagnosis and practical case analysis based on live detection technology. Insul Surge Arresters 3:69–73 (in Chinese)
7. Yan Y, Huang W, Jiang J et al (2011) Principle and instrument comparison of arrester live line test and analysis on the flaw in field. Insul Surge Arresters 2011(2):57–62 (in Chinese)
8. Zhang J (2015) Application of infrared temperature measurement technology to live detection of zinc oxide arrester. High Volt Appar 51(6):200–204 (in Chinese)
9. Zeng G, Li G, Zhang C et al (2020) Simulation analysis of temperature rise distribution characteristics of damp arrester. Hubei Electric Power 44(5):34–41 (in Chinese)

10. Zhang B,Li G, Zhang C et al (2011) Internal temperature rise of MOA under pollution condition. High Volt Eng 37(08):2065–2072 (in Chinese)
11. Liu J (2021) Simulation of radial electric field and voltage distribution of 500 kV MOA under different pollution conditions. Insul Surge Arrest 1 (in Chinese)
12. Wang Q, Gu C, Shi Fet al (2014) Analysis of surge arresters cavity humid caused flashover accident. Appl Mechan Mater 543–547:717–7221
13. Chrzan KL (2010) Failures and destructions of surge arresters. Energetyka 5:281–284
14. Singh RP, Singh TVP (2002) Influence of pollution on the performance of metal oxide surge arresters. In: IEEE Canadian conference on electrical and computer engineering (CCECE 2002), vol 1, pp 224–229
15. Sun H, Li X (2010) Finite element calculation and experiment of potential distribution for a 500 kV Porcelain zinc oxide arrester. High Volt Apparat 3 (in Chinese)

Study on the Fan Layout Method of SF_6 Leakage in Confined Space

Fuhua Sun, Yue Zhao, Fengxiang Ma, Feng Zhu, Wangchao Dong, Xin Liu, Bo Li, and Ming Sun

Abstract When SF_6 gas insulation equipment is in operation, if there is a sudden leakage fault, especially SF_6 gas leakage in a closed space such as a transmission pipe gallery, underground substation, and indoor substation, The leaked SF_6 will endanger the life and health of operation and maintenance personnel and pollute the environment, and it will mix with the air in the environment, which increases the difficulty of recovery. In order to solve the problem of leaking gas in space, different arrangements of exhaust pipes and fans are tested. The results show that the SF_6 gas concentration in the confined space can be effectively reduced by using the arrangement of a small flow fan to supply air into the pipeline and large flow fan output in the front stage; At the same time, appropriate tee form and SF_6 concentration sensor layout are selected to optimize the test model further.

Keywords SF_6 gas · Gas leakage · Confined space · Fan layout

1 Introduction

Sulfur hexafluoride (SF_6) gas is widely used in the insulation of electrical equipment in the power industry due to its excellent insulation and arc extinguishing properties. However, as SF_6-insulated equipment is used for longer periods, aging and damage are inevitable, leading to the occurrence of leakage failures [1]. SF_6 gas has a density much higher than air under the same conditions. When it leaks into the environment, it accumulates in low-level spaces, causing local oxygen deficiency. Additionally, under the action of corona discharge, spark discharge, and high-temperature arcs, SF_6 gas reacts with impurities in the equipment to produce corrosive, irritating, and

F. Sun (✉) · B. Li · M. Sun
Henan Relations Co., Ltd., Zhengzhou 450001, China
e-mail: sunfuhua@relations.com.cn

Y. Zhao · F. Ma · F. Zhu · W. Dong · X. Liu
Electric Power Research Institute of State Grid Anhui Electric Power Co. Ltd., Hefei 230000, China

© Beijing Paike Culture Commu. Co., Ltd. 2024

X. Dong and L. Cai (eds.), *The Proceedings of 2023 4th International Symposium on Insulation and Discharge Computation for Power Equipment (IDCOMPU2023)*, Lecture Notes in Electrical Engineering 1102, https://doi.org/10.1007/978-981-99-7405-4_39

toxic decomposition products, such as SO_2, SOF_2, and SO_2F_2, which pose a health risk to maintenance personnel and increase potential hazards. On the other hand, the Kyoto Protocol has listed six gases, including SF_6, as greenhouse gases. SF_6 gas has a GWP of approximately 23,500 times that of CO_2 and an atmospheric lifetime of 3200 years. Once it leaks, it will cause serious atmospheric pollution [2–4].

Enclosed spaces such as GIL, underground substations, and indoor substations have the characteristics of large space and a large number of equipment. When SF_6 gas leaks from the electrical equipment running in these spaces, the leaked SF_6 gas will mix with the ambient air, and the SF_6 concentration in the space will rapidly decrease while the volume rapidly increases, making the recovery of SF_6 gas difficult. If the leaked gas is not immediately discharged through the ventilation system, it will pose a risk to maintenance personnel and cause environmental pollution [5].

Therefore, when SF_6 leaks, the optimized design of exhaust pipes, fans, and ventilation systems is particularly important [6]. Xiao et al. [7] established 1D Flowmaster and 3D Fluent numerical analysis models to simulate SF_6 leakage in ultra-high voltage shield tunnels and optimized the ventilation system, finding that using a GIL tunnel with an upper and lower chamber structure can achieve rapid absorption and discharge of SF_6. Guo et al. [8] found that when the supply and exhaust ports are arranged in the center of the wall, it is more conducive to the uniform flow of ventilation. A symmetrical arrangement of exhaust ports is better than a single exhaust port for ensuring convection and exhaust diffusion of ventilation, and symmetrical supply and exhaust arrangements are conducive to forming controllable flow with the outside under micro-positive pressure conditions. Sui et al. [9] conducted a simulation study on SF_6 gas leakage in a comprehensive GIL tunnel and determined the most unfavorable leakage position and working condition based on GIL cabin exhaust ventilation data and SF_6 gas diffusion characteristics. They suggested placing SF_6 sensors in critical tunnel locations, such as sumps and low-lying areas, to ensure the safety of maintenance personnel. However, current studies have not provided specific recommendations for the layout of exhaust pipes and fans in the gas recovery system in enclosed spaces when SF_6 leaks.

In this paper, three experimental models with different pipeline and fan layouts were established, and the influence of different experimental models on the discharge rate of SF_6 gas in enclosed spaces was determined through experiments. Based on the optimal experimental model, experimental verification was conducted, and reasonable optimization suggestions were proposed to provide reference for the installation optimization of fans in enclosed spaces.

2 Experimental Plan

According to the spatial diffusion model of SF_6 gas under ideal conditions, when SF_6 gas leaks, due to its density being greater than that of air, SF_6 gas will not only diffuse in the air, but also be affected by its own gravity, falling uniformly and steadily, and

depositing near the ground [10–14]. Therefore, in this experiment, the exhaust duct will be arranged in different forms on the ground of the experimental chamber.

2.1 Experimental Methods

1. Before starting the experiment, multiple SF_6 concentration sensors are dispersedly arranged in the experimental chamber (with a volume of about 250 m^3) to detect the SF_6 gas concentration in different areas of the chamber.
2. According to the three different layout designs of the experiment, ventilation pipes and fans are set along the ground surrounding the experimental chamber, and the exhaust of the ventilation pipes is connected to the SF_6 recovery device.
3. The experimental chamber is sealed at all locations, filled with a certain volume of air, and the change in air pressure is observed to check the overall airtightness of the chamber.
4. A certain volume of SF_6 gas is introduced into the experimental chamber, and the SF6 concentration is monitored using SF_6 concentration sensors until the required concentration is achieved. Then, the fan and the recovery device are started to observe and record the changes in SF_6 gas concentration data in the experimental chamber.
5. The layout design is changed, and the above experimental procedures are repeated for the next group of experiments.

2.2 Different Pipeline and Fan Layout Effects

Recycling pipeline and fan layout method 1. As shown in Fig. 1, numbers 1, 2, and 3 represent three fans arranged in a "mouth" shape by being connected in series with the pipeline. The black arrows indicate the direction of gas flow in the pipeline, and the intake and exhaust ports are connected to the pipeline in this direction, with the outlet of fan 1 connected to the recycling device.

To increase the intake volume of the pipeline, it is proposed to drill holes at the position shown by the green arrow in Fig. 1, to increase the intake port of the recycling pipeline, and to use the pressure difference between the inlet and outlet of each fan to suck in as much leaked gas as possible.

Experimental results show that the layout of recycling pipelines and fans according to method 1 results in a slow decrease in SF_6 gas concentration in the experimental chamber. This is because the air flow sent out from the outlet of fan 3 will flow out of the air holes between fans 2 and 3 when flowing in the pipeline, and the intake air volume at the back end of the pipeline is small, leading to low recycling efficiency and slow decrease in SF_6 gas concentration. Therefore, layout method 1 is not feasible.

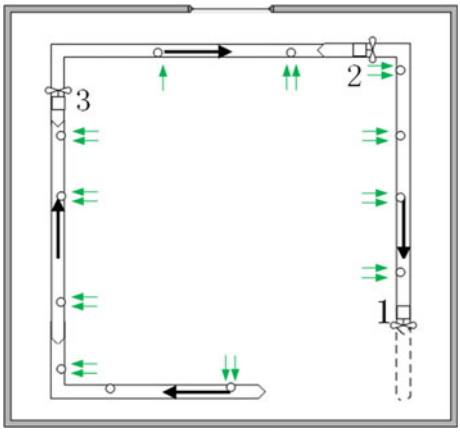

Fig. 1 Recycling pipeline and fan layout method 1

Recycling pipeline and fan layout method 2. As shown in Fig. 2, three fans are connected in series to the outlet, increasing the wind pressure, but the wind volume remains the same.

Experimental results show that the layout of recycling pipelines and fans according to method 2 also results in a slow decrease in SF_6 gas concentration in the experimental chamber. This is because of the wind pressure loss in the pipeline, and there is basically no gas entering the intake port at the back end, resulting in a significant decrease in the recycling speed when the SF_6 gas concentration in the experimental chamber drops to a certain value. Therefore, layout method 2 is not feasible.

Recycling pipeline and fan layout method 3. As shown in Fig. 3, small flow fans 1 and 2 are used to deliver gas to the pipeline, and large flow fan 3 is used to output gas.

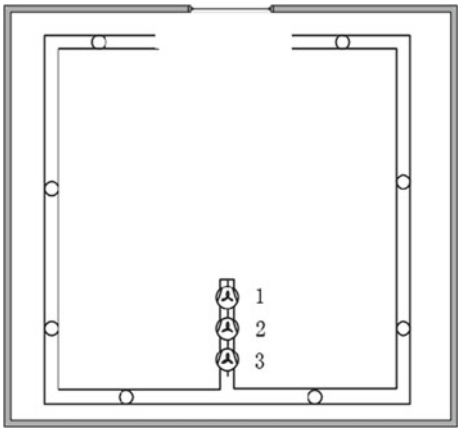

Fig. 2 Recycling pipeline and fan layout method 2

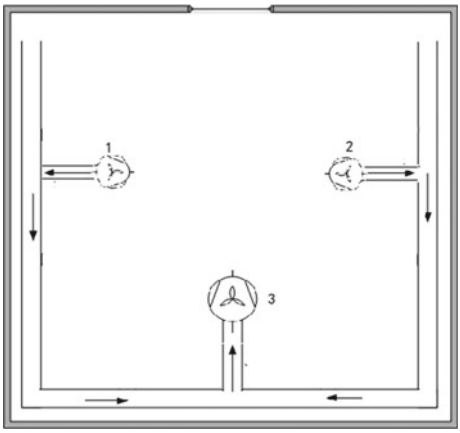

Fig. 3 Recycling pipeline and fan layout method 3

Experimental results show that the SF_6 gas concentration in the experimental chamber decreases significantly in the same period of time using layout method 3 compared to the first two methods. This is because no intake port is set up on the pipeline, and the gas is directly sucked into the pipeline through the fan's intake port, reducing the wind pressure loss in the pipeline and increasing the SF_6 recycling rate. Therefore, recycling pipeline and fan layout method 3 is adopted as the optimal experimental model.

3 Solution Optimization and Result Analysis

Based on the optimal recycling pipeline and fan layout method three, further optimization was carried out for this layout.

3.1 Solution Optimization

Pipeline Optimization. When using pipeline to transport gas, the flow resistance of gas in the duct is not only due to the viscosity of the air itself and the friction between the air and the duct wall, but also due to the local eddy currents caused by the change in flow velocity and direction when the air flows through fittings such as tees and elbows in the pipeline, which results in local resistance. In the case of constant frictional resistance, local resistance should be minimized as much as possible.

The size of the local resistance of the tee is related to the central angle of the branch pipe, the section shape of the tee, the area ratio of the branch pipe to the main pipe, and the flow rate. In order to reduce the local resistance of the tee, the central angle α of the branch pipe should be as small as possible. Compared with the

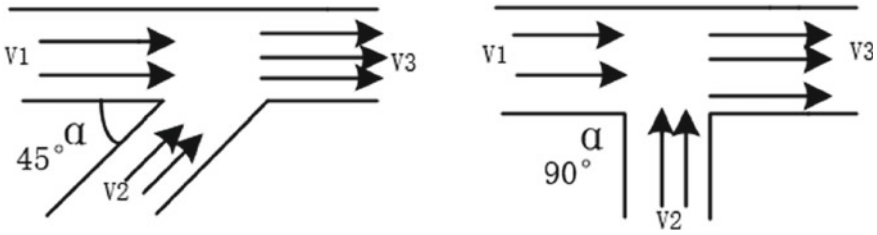

Fig. 4 Two common forms of tees

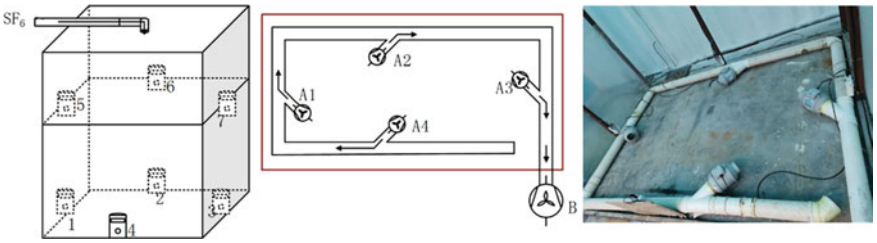

Fig. 5 Experimental Platform and Sensor Distribution

two common tee forms shown in Fig. 4, a 45° oblique tee is used at the connection between the duct and the fan, and an elbow is used at the bend of the duct.

Sensor Layout Optimization. In the layout of the SF_6 concentration detection sensors, optimization is carried out for layered placement, which is more conducive to detecting the difference in SF_6 gas concentration between the upper and lower spaces.

After optimization, the sensors are arranged in two layers. The SF_6 gas is filled from the top. The layout of the SF_6 concentration detection sensors and the pipeline fan layout inside the experimental platform are shown in Fig. 5:

The length of the experimental compartment is 3 m, the width is 2.1 m, and the height is 2.5 m, with a volume of about 15.8 m^3. Sensors 1–4 for SF_6 concentration detection are installed near the ground, and sensors 5–7 are installed at a position about 1.5 m above the ground. The flow rate of pipeline fans A1–A4 is 100 m^3/h, and the flow rate of pipeline fan B is 500 m^3/h. The outlet of pipeline fan B is connected to the SF_6 recovery device.

3.2 Result Analysis

After injecting a certain concentration of SF_6 gas and starting the fan, the changes in SF_6 gas concentration of each sensor are shown in Fig. 6. The data curve shows:

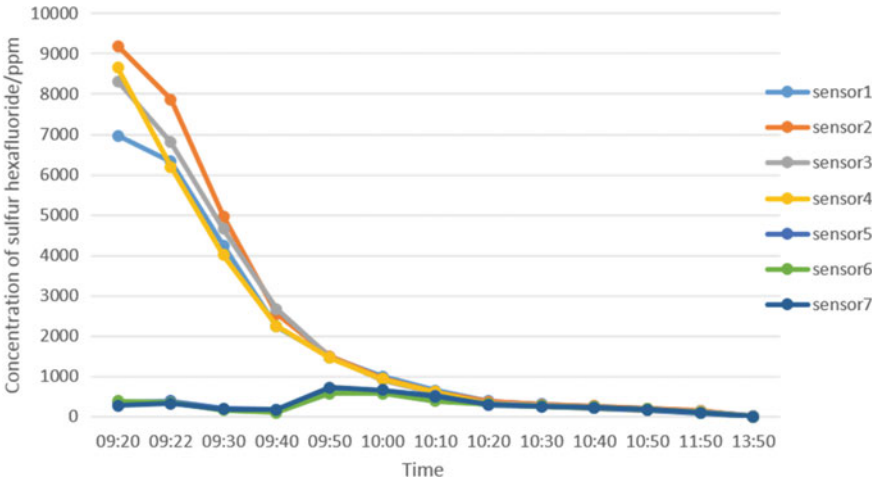

Fig. 6 SF_6 concentration change curve

1. After injecting SF_6 gas, the initial concentration of sensors 1, 2, 3, and 4 near the ground is much higher than that of sensors 5, 6 and 7 in the upper layer, indicating that SF6 gas is mainly concentrated near the ground.
2. At the end of the experiment, the SF_6 gas concentration of all sensors is close to 0, indicating that the method of using the fan and exhaust duct to discharge the leaked gas from the space can effectively reduce the SF_6 content in the space.
3. When the fan runs for about 40 min, the SF_6 content in the space can be reduced to 1000 ppm; with the increase of the running time of the fan, the SF_6 content in the space can be reduced to 0 ppm, which takes about 270 min.

4 Conclusion

This paper conducted experiments on the discharge of SF_6 leaks in enclosed spaces based on different layouts of exhaust ducts and fans, and optimized the layout. The following conclusions were drawn:

1. The layout of SF_6 recovery ducts and fans using method three, which involves small flow rate fans sending air into the ducts and large flow rate fans outputting, can effectively reduce the concentration of SF_6 gas leaked into enclosed spaces and has practical application significance.
2. By using a reasonable tee form and optimizing the layout of SF6 concentration sensors, the discharge and recovery efficiency of the model can be further improved, and the remaining SF_6 gas content can be measured more accurately.

Acknowledgements This research was supported by the Science and Technology Project of State Grid Corporation of China (5200202120090A-0-0-00)

References

1. Ma Y (2021) Analysis of common faults in gas insulated substation. J Phys Conf Ser 1865(2)
2. GB/T 28534-2012 (2012) The release of sulfur hexafluoride (SF_6) gas in high voltage switchgear and controlgear equipment and its impact on the environment and health (in Chinese)
3. Wu B, Shu L, Sima W (2000) SF_6 gas insulation and global greenhouse effect. High Volt Appar 36(6):23–269 (in Chinese)
4. Tatemi M, Inami H, Rokunohe T, Hirose M (2020) Study on field demonstration of high-sensitivity SF_6 leakage detection method for gas insulated switchgear. Electr Eng Japan 214(1)
5. Liu C, Gu W, Shi L, Wang F (2020) A method to construct early-warning and emergency response system for sulfur hexafluoride leakage in substations. IEEE Access 8
6. Han O, Zhang Y, Li A, Li J, Li Y, Liu H (2020) Experimental and numerical study on heavy gas contaminant dispersion and ventilation design for industrial buildings. Sustain Cities Soc 55(C)
7. Xiao G, He N (2021) Simulation of SF_6 leakage and optimization of ventilation system in ultra-high voltage shield tunnel. Guangdong Electric Power 34(03):122–129 (in Chinese)
8. Guo S, Huang W, Xue L et al (2013) Ventilation mode of indoor substation based on comprehensive environmental control. J Beijing Jiaotong Univ 37(3):19–26 (in Chinese)
9. Sui X, Zhang Z, Min X, Downie S, Padhani S, Zhao L (2020) Experimental study on SF_6 gas leakage simulation in ultra-long GIL comprehensive corridor. Modern Tunnell Technol 57(03):91–98+107 (in Chinese)
10. Zhang Y (2018) Design of SF_6 gas environmental monitoring system based on gas sensor. Machin Electron 2018(30):105–106 (in Chinese)
11. Gao Q (2012) Application research of inspection robot in Changzhi Jiuan substation. North China Electric Power University, Beijing, pp 2–45 (in Chinese)
12. Wang T, Yu B, Liu R et al (2021) Application of intelligent robot in SF_6 leakage detection of substation. Ind Instrum Autom 3:109–114 (in Chinese)
13. Li Y (2018) Experimental and numerical simulation study on heavy gas diffusion of SF_6 leakage. Xi'an University of Architecture and Technology, Xi'an (in Chinese)
14. Chen B, Li F, Zhao W (2022) Research on SF_6 gas leakage and diffusion in GIL corridor and optimization of fan installation. Water Resour Power 38(6):177–180 (in Chinese)

Effect of Fiber Waviness on the Elastic Properties of Pultruded Glass Fiber Reinforced Composites

Zhangxing Chen, Jiapeng He, Guowei Zhou, Linjun Zhang, and Chao Liu

Abstract Pultruded glass fiber reinforced composites are widely used in high-voltage transmission engineering due to their excellent electrical and mechanical properties. However, the formation process of glass fiber reinforced composites inevitably results in fiber waviness, leading to fluctuations in macroscopic properties. In this study, we investigate the effect of fiber waviness on the tensile modulus of the composite material. Using XCT scanning technology, we obtain the geometric properties of the fibers, and we establish a voxel mesh based representative volume element model to compare the results of the finite element model with the analytical calculation of the elastic modulus. The results show that the fiber waviness caused by the pultrusion process has a significant effect on the fiber direction modulus, causing fluctuations of approximately 6 GPa in modulus at similar fiber volume fractions. In contrast, analytical calculations can only reflect the effect of fiber content. For transverse tensile modulus, there is a large discrepancy between simulation results and analytical calculations, and the adoption of voxel mesh fiber elements is the reason for the higher simulation results.

Keywords Glass fiber reinforced composites · Fiber waviness · Tensile modulus · Representative volume element

Z. Chen (✉) · L. Zhang · C. Liu
Key Laboratory of Composite Materials on Electrical Insulation, National Energy Administration, Jiangsu Shemar Electric Co., Ltd., Nantong 226017, China
e-mail: chenzx_tsinghua@mail.tsinghua.edu.cn

Z. Chen
School of Aerospace Engineering, Tsinghua University, Beijing 100084, China

J. He
School of Mechanical Engineering, Shanghai Jiao Tong University, Shanghai 200240, China

G. Zhou
School of Naval Architecture, Ocean and Civil Engineering, Shanghai Jiao Tong University, Shanghai 200240, China

© Beijing Paike Culture Commu. Co., Ltd. 2024

X. Dong and L. Cai (eds.), *The Proceedings of 2023 4th International Symposium on Insulation and Discharge Computation for Power Equipment (IDCOMPU2023)*, Lecture Notes in Electrical Engineering 1102, https://doi.org/10.1007/978-981-99-7405-4_40

1 Introduction

The safe and stable operation of overhead transmission lines is a critical for national energy security. In overhead transmission lines, glass fiber reinforced composite (GFRP) insulators are widely used due to their excellent electrical and mechanical properties. However, in actual operation, poor-quality composite insulators often cause brittle fractures due to insufficient mechanical performance. Therefore, establishing the relationship between the microstructure and macroscopic mechanical properties of GFRP insulators is of great importance for proper insulator mechanical design.

GFRP insulators are produced by the pultrusion process. During production, the resin continuously solidifies while the fibers are compressed against each other within the mold, causing local bending deformation and deviation from their ideal paths, resulting in a complex three-dimensional fiber waviness. The complex fiber waviness leads to significant fluctuations in the macroscopic mechanical properties of the material [1], posing considerable challenges for the mechanical performance design and serviceability analysis of GFRP insulators. However, such microscopic geometric defects cannot be completely eliminated. Assessing their impact on the elastic properties is essential for practical applications.

XCT has been widely applied in the detection of microscopic fiber morphology. Umahat et al. [2] utilized XCT technology to observe the fiber waviness characteristics in several crucial states during the compression failure process of carbon fiber materials. Wang et al. [3] investigated the failure process of unidirectional fiber layups under compression using XCT and identified several typical damage modes, such as fiber breakage, matrix microcracking, and fiber bundle splitting.

Finite element simulation methods based on representative volume elements (RVE) are one of the most important methods in composite materials research [4], providing effective tools for studying composite material properties. Shen [5] established an RVE model containing waviness defects based on a two-step homogenization technique and mixed boundary conditions. The results indicated that as the corrugation ratio increased, the axial displacement gradient in the wrinkled region gradually increased. Li et al. [6] proposed a novel Latin hypercube random sequence expansion method, developed a finite element model considering the initial fiber waviness, and investigated its impact on compressive performance. Mi et al. [7] established finite element models of two ideal fiber waviness arrangements and analyzed the effects of different initial defect sizes on axial compressive performance. The axial compressive strength improved with the decrease in the amplitude of the initial fiber corrugation and the increase in wavelength. Sun et al. [8] utilized a cosine curve model to analyze the damage evolution process and predicted the strength under various loading conditions when considering fiber corrugation defects. The aforementioned studies demonstrated the significant influence of fiber waviness on the macroscopic properties of composite materials and revealed basic impact patterns. However, existing research mainly focuses on unidirectional laminated composites,

for pultruded GFRP composites, the waviness impact on the mechanical properties and the behind failure mechanism remains unclear.

To address the aforementioned issues, this paper directly constructs a RVE model based on XCT scanning results and conducts a study on the impact of fiber waviness on the tensile modulus of pultruded GFRP composites.

2 Experimental Methods and Procedures

The material studied in this paper is unidirectional composite solid rods made of E-glass fiber and epoxy resin produced by continuous pultrusion (Jiangsu Shenma Electric Power Co., Ltd., Jiangsu, China), with a fiber volume content of approximately 75%. Samples were prepared along the fiber direction using machining methods. The experiment employed a Zeiss Xradia Versa 620 XCT scanner, scanning the samples at a pixel resolution of 1.5 μm, as shown in Fig. 1.

Long-term observation shows that actual transmission line galloping has some common characteristics. The actual observation results show that the vibration amplitude of the conductor in the vertical direction increases over time and finally stabilizes near a fixed value, while the amplitude in the horizontal direction is small, and the trajectory is usually elliptical. Therefore, according to the excitation mechanism of Den Hartog's theory, pulse mechanical excitation can be carried out on the conductor in the vertical plane, and the positive mechanical energy will increase in the transmission line system to simulate the vertical instability in actual and the energy accumulation process of the system absorbed from the wind.

The scanning results were reconstructed using the commercial software AVIZO, and the actual material region obtained from the scan was a solid cylinder. The original grayscale images were threshold-segmented, dividing them into resin matrix and

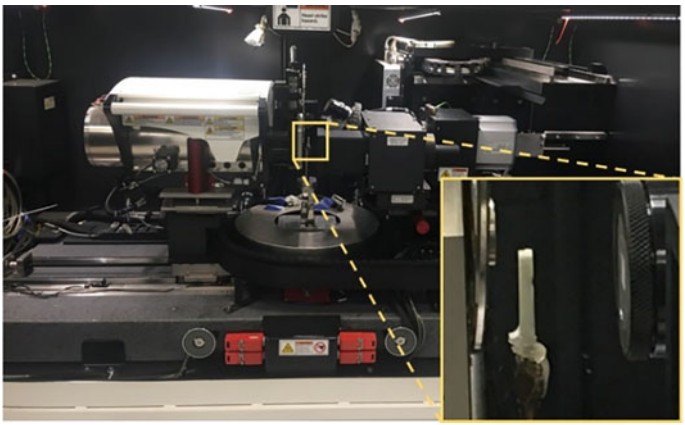

Fig. 1 Set up for XCT scanning

fibers. After segmentation, unconnected fiber regions were removed, and Gaussian filtering was applied to smooth the segmentation results. Three cubic sub-regions with side lengths of 0.3 mm were randomly extracted from the scanning results and used for further analysis. The data processing workflow is shown in Fig. 2. The specific fiber morphologies at various locations are shown in Fig. 3, where the white arrows indicate the ideal fiber morphology. It can be observed that in pultruded composites, the microscopic geometry of fibers deviates from the ideal direction, and different fibers exhibit distinct geometric shapes. By converting the image voxels into eight-node hexahedral elements, a finite element RVE model can be further established, containing a total of $200 \times 200 \times 200$ C3D8R elements. Both the resin matrix and glass fibers were considered as elastic and isotropic. The specific material parameters are shown in Table 1. The fluctuations of the longitudinal tensile modulus (Z direction) and transverse tensile modulus (X direction) were investigated in this paper. The RVE model is shown in Fig. 4, where a displacement load of 1% strain was applied, and fixed constraints were imposed on the opposite side of the loading surface. All loads acted on the nodes.

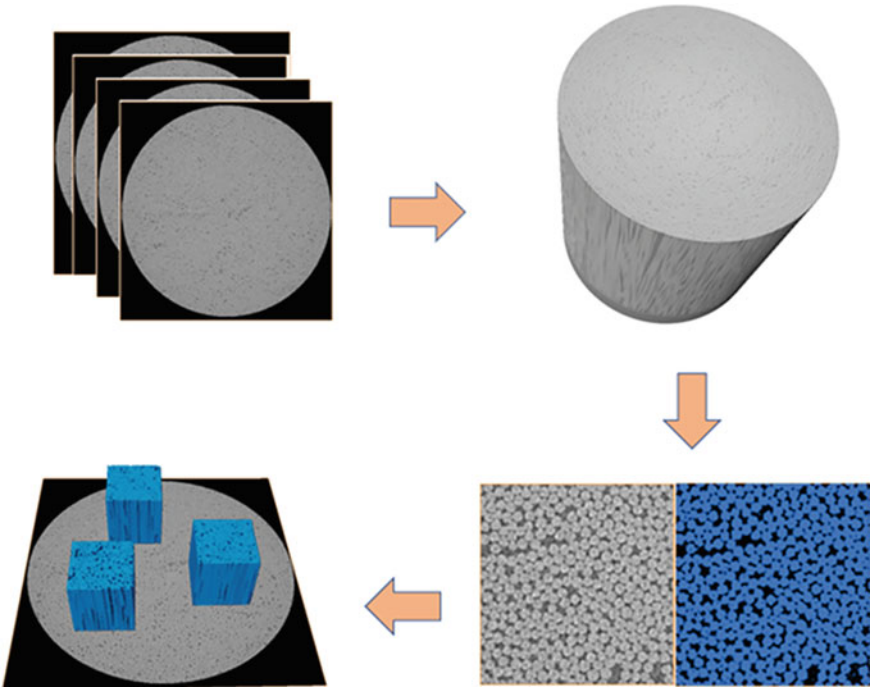

Fig. 2 Procedure for data processing

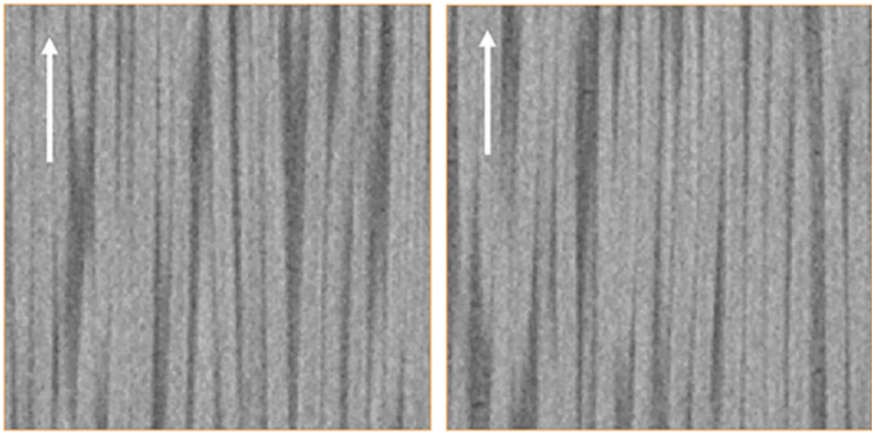

Fig. 3 Fiber geometry in different slices of XCT scanning

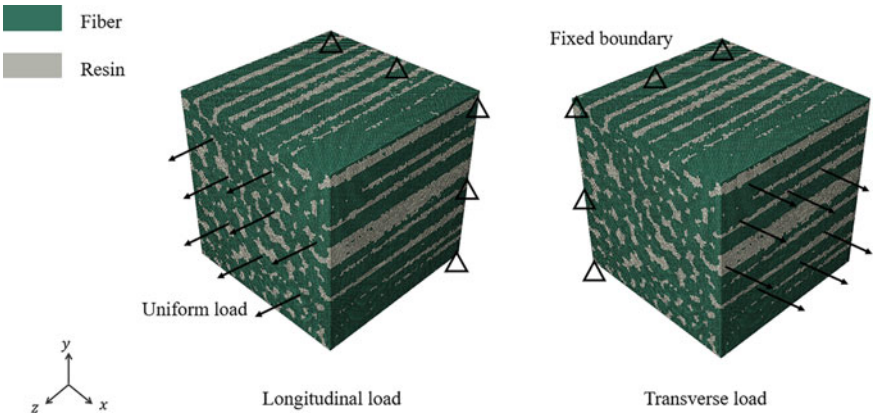

Fig. 4 RVE model and boundary condition

Table 1 The mechanical parameters for materials

Resin modulus E_m	Resin Possion's ratio ν_m	Fiber modulus E_f	Fiber Possion's ratio ν_f
3.80 GPa	0.3	72 GPa	0.2

3 Results and Discussion

The uniaxial tensile stress–strain curves of the fiberglass composite are shown in Fig. 5, where it can be seen that the stress and strain during the loading process exhibit a relatively good linear relationship. The corresponding elastic modulus was obtained through linear fitting, as shown in Table 2. For unidirectional fiber composites, when

given the fiber and resin elastic modulus and fiber volume content, the elastic modulus in the fiber direction and transverse direction can be estimated through analytical calculations, as detailed in Ref. [9]. For unidirectional composites, the analytical formula for the longitudinal elastic modulus is:

$$E_z^0 = V_f E_f + \left(1 - V_f\right) E_m$$

for the transverse modulus is:

$$\frac{1}{E_x^0} = \frac{V_f}{E_f} + \frac{1 - V_f}{E_m}$$

E_f, E_m is the modulus for fiber and matrix, respectively. V_f is the fiber volume fraction. E_z^0 and E_x^0 is the longitudinal and transverse modulus for GFRP composites, respectively.

Table 2 compares the finite element prediction results considering fiber geometry with the analytical calculation results. Firstly, it can be seen that in this experiment, the fiber volume fractions of the three different samples show good consistency with minimal fluctuations. Secondly, the finite element predicted modulus in the fiber direction is consistent with the analytical calculation results. The difference in the elastic modulus obtained from the analytical calculation is relatively small, but there is a significant fluctuation between the finite element prediction results considering fiber geometry, with differences between samples reaching up to 6 GPa. The theoretical value of the longitudinal modulus E_z^0 caused by the volume fraction fluctuations is significantly lower than the fluctuations in E_z^0 obtained from the RVE model calculations. This indicates that the fiber waviness has an important impact on the longitudinal elastic modulus.

On the other hand, for the transverse modulus, the RVE model predicted E_x^0 to be much higher than the theoretical value. By analyzing the finite element model, it can be found that due to the high fiber volume content in the composite material studied in this paper, there are inevitably many fiber element connections when using voxel elements to discretize geometry, which may form a continuous whole. In reality, interfaces formed between fibers and the resin matrix exist, and fibers cannot be considered as a single entity even if they are in contact. The modulus of the interface and resin is much lower than that of the fibers, but the current voxel element discretization modeling method cannot effectively consider this impact, leading to an overestimated transverse prediction modulus. To investigate the influence of fiber waviness on transverse properties, more refined geometric modeling is needed.

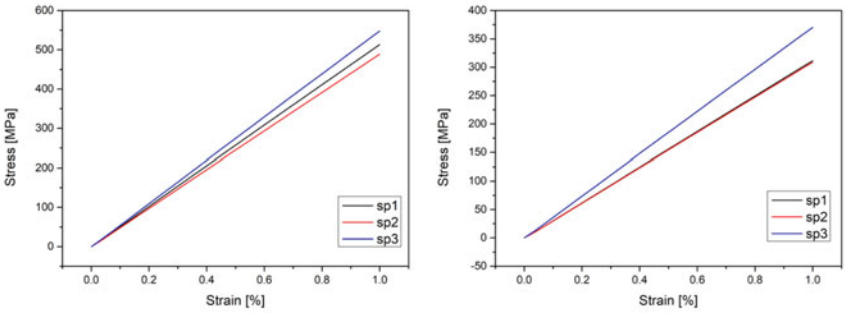

(a) Longitudinal. (b) Transverse.

Fig. 5 Axial tensile stress–strain curves

Table 2 Elastic modulus of GFRP

Specimen id	1	2	3
Fiber volume content V_f	0.744	0.725	0.744
Longitudinal modulus E_z	51.437	48.984	54.889
Theoretical value E_z^0	54.541	53.245	54.541
Transverse modulus E_x	31.257	30.996	37.133
Theoretical value E_x^0	12.870	12.130	12.870

4 Conclusions

In this paper, the influence of the fiber waviness on the pultruded unidirectional GFRP composite was investigated. Firstly, accurate fiber geometry was obtained through XCT scanning, and discrete reconstruction was performed based on the XCT results. Then, a finite element RVE model was established based on voxel elements. A comparison between finite element model results and analytical calculation of elastic modulus was conducted. The research results show that the fiber geometry caused by the pultrusion process has a significant impact on the longitudinal tensile modulus. Under similar fiber volume fractions, it can cause about 6 GPa of modulus fluctuations, while the analytical calculation results can only reflect the influence of fiber content. As for the transverse tensile modulus, there is a significant difference between the simulation results and the analytical calculation values. Upon analysis, it was found that when using voxel element discretization modeling with high fiber content, fiber elements exhibit significant connectivity, leading to overestimated simulation results for the transverse elastic modulus. To accurately study the impact of fiber waviness on transverse properties, more refined geometric modeling is needed.

Acknowledgements This work was funded by 'JiangSu Superior Postdoc Plan' (No.2022ZB893).

References

1. Potter K, Khan B, Wisnom M et al (2008) Variability, fibre waviness and misalignment in the determination of the properties of composite materials and structures. Compos A Appl Sci Manuf 39(9):1343–1354
2. Jumahat A, Soutis C, Jones FR et al (2010) Fracture mechanisms and failure analysis of carbon fibre/toughened epoxy composites subjected to compressive loading. Compos Struct 92(2):295–305
3. Wang Y, Burnett TL, Chai Y et al (2017) X-ray computed tomography study of kink bands in unidirectional composites. Compos Struct 160:917–992
4. El Said B, Hallett SR (2018) Multiscale surrogate modelling of the elastic response of thick composite structures with embedded defects and features. Compos Struct 200:781–798
5. Shen C (2021) Research on response characteristics of defects in fiber reinforced composite plates and its application in optics-mechanics detection. Zhejiang University
6. Zhang L, Xu D et al (2018) Effect of random fiber distribution on longitudinal compressive behavior of composite materials. J Mechan Strength 40(04):875–881
7. Zhang M, Guan Z et al (2017) Longitudinal compressive properties of composites considering fiber initial misalignment. Acta Materiae Compositae Sinica 34(08):1754–1763
8. Sun Q, Guo H, Zhou G et al (2018) Experimental and computational analysis of failure mechanisms in unidirectional carbon fiber reinforced polymer laminates under longitudinal compression loading. Compos Struct 203:335–343
9. Hyer MW, White SR (2009) Stress analysis of fiber-reinforced composite materials. DEStech Publications, Inc

Numerical Calculation of Temperature Field of Energy Storage Battery Based on Finite Element Method and Analysis of Influencing Factors

Wei Xiao, Xiaowen Wu, Jingling Sun, Li He, and Zhuangxi Tan

Abstract The heat dissipation performance of energy storage batteries is of great importance to the efficiency, life and safety of the batteries. An energy storage battery module with 60 series large cylindrical battery cells and a rated capacity of 11.52 KWh is designed. A numerical calculation model of the fluid-temperature field coupling of the battery module is established based on the finite element method, and the heat generation power of the battery cells at different charge/discharge multipliers is estimated by the measured data, which is used as the homogeneous heat source for the numerical calculation model, and the air flow rate of the air duct inside the battery module is analyzed. The air flow rate of the air duct inside the battery module and the distribution law of the temperature field of the battery pack are analyzed, and the validity of the numerical calculation results is verified by using the charging and discharging temperature rise and wind speed tests of the prototype energy storage battery module.

Keywords Energy storage battery · Finite element method (FEM) · Temperature field · Analysis of influencing factors

1 Introduction

With the increasing popularity of clean energy, energy storage technology has received wide attention worldwide as an important part of it [1–3]. Lithium-ion batteries are gradually becoming one of the mainstream technologies in the field of energy storage due to their high energy density, long life, light weight and environmental protection advantages [3–6]. At the same time, energy storage batteries can

W. Xiao · X. Wu (✉) · J. Sun · L. He · Z. Tan
School of Information and Electrical Engineering, Hunan University of Science and Technology, Xiangtan 411201, China
e-mail: xwu@hnust.edu.cn

W. Xiao
e-mail: xiaowei@mail.hnust.edu.cn

© Beijing Paike Culture Commu. Co., Ltd. 2024

X. Dong and L. Cai (eds.), *The Proceedings of 2023 4th International Symposium on Insulation and Discharge Computation for Power Equipment (IDCOMPU2023)*, Lecture Notes in Electrical Engineering 1102, https://doi.org/10.1007/978-981-99-7405-4_41

be used as an effective way to cut peaks and fill valleys, and play a role in the grid to balance the difference between peak and trough of grid load in order to improve the quality and efficiency of grid energy supply. However, the problem of thermal failure of Li-ion batteries has been one of the challenges in their application, such as overcharge, overdischarge, external short circuit and other conditions may lead to an increase in the internal temperature of the battery and even cause safety accidents such as fire [7]. Therefore, the thermal performance of Li-ion batteries has become one of the important factors affecting their safe and stable operation.

At present, scholars' research on energy storage batteries mainly focuses on analyzing the thermal performance of energy storage batteries and optimizing the design of the battery thermal system. Document [8] established a finite element simulation model and proposed a method to improve the internal air duct of the battery pack by changing the number of air outlet holes and the shape of the fan baffle. Document [9] proposed an optimization method to improve the heat dissipation capacity of the battery compartment by adding flow baffles to the battery compartment. Document [10] established a simulation model and proposed to improve the thermal performance of the battery module by optimizing the spacing of the battery cells.

In this paper, starting from the modeling process of energy storage battery module, an energy storage battery module with 60 series large cylindrical battery cells as the basic unit and rated power of 11.52 kWh is designed, and the cells are combined into a battery pack with the arrangement of 6P12S. The numerical calculation model of the energy storage battery module is established based on the finite element method, and the thermal experimental platform of the energy storage battery module is established to analyze the thermal performance of this energy storage battery module. The accuracy of the simulation model in the paper is verified by comparing the simulation and experimental results. The boundary conditions such as charge/discharge multiplier, ambient temperature and wind speed are introduced to calculate the temperature and flow field distribution of the energy storage battery under different boundary conditions and analyze the influence of different working conditions on the working state of the energy storage battery.

2 Energy Storage Battery Module Model

2.1 Simplified 3D Model of Energy Storage Battery Module

Using 60 series large cylindrical battery cells as the basic unit, an energy storage battery module with a rated power of 11.52 kWh is designed, and the 3D simulation model of this energy storage battery module is constructed in the same scale by using solidworks 3D modeling software. Due to the complexity of the storage battery model, in order to reduce the number of meshes and save computational resources, the model needs to be simplified when the finite element simulation is carried out.

The simplification process is to omit the protrusions, side seams and box links that have little effect on the flow field of the battery module, and equate the battery cells to cylinders of equal volume. For the fan model, the fan details can be omitted and a cylinder of equal cross-sectional area can be used for equivalence, and the rotational air supply effect of the fan can be simulated by setting the velocity inlet boundary conditions in ANSYS Fluent. It should be noted that the accuracy of the flow field simulation should be ensured in the model simplification process. The simplified model of the energy storage battery module is shown in Fig. 1. The selected cooling fan has a rated power of 3.12 W, air volume of 1.510 m^3/min, sound pressure level noise of 46.2 dB, and its size and structure style are shown in Fig. 2.

As mentioned above, the cooling fan model is simplified to a cylinder of equal cross-section, and the fan rotation is simulated by setting the velocity inlet boundary condition, and the relationship between inlet velocity and air volume and cross-sectional area can be expressed as:

$$Q = v \times A \tag{1}$$

$$A = \pi(r_1^2 - r_2^2) \tag{2}$$

where, Q represents the Fan air volume, v represents the air velocity, A represents the Cross-sectional area, r_1 represents the Fan radius, r_2 represents the Radius of fan base.

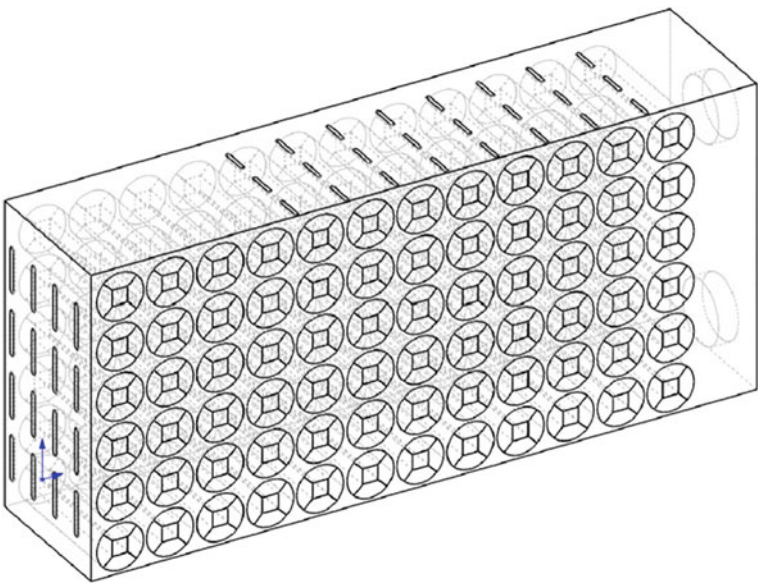

Fig. 1 Simplified model of energy storage battery module

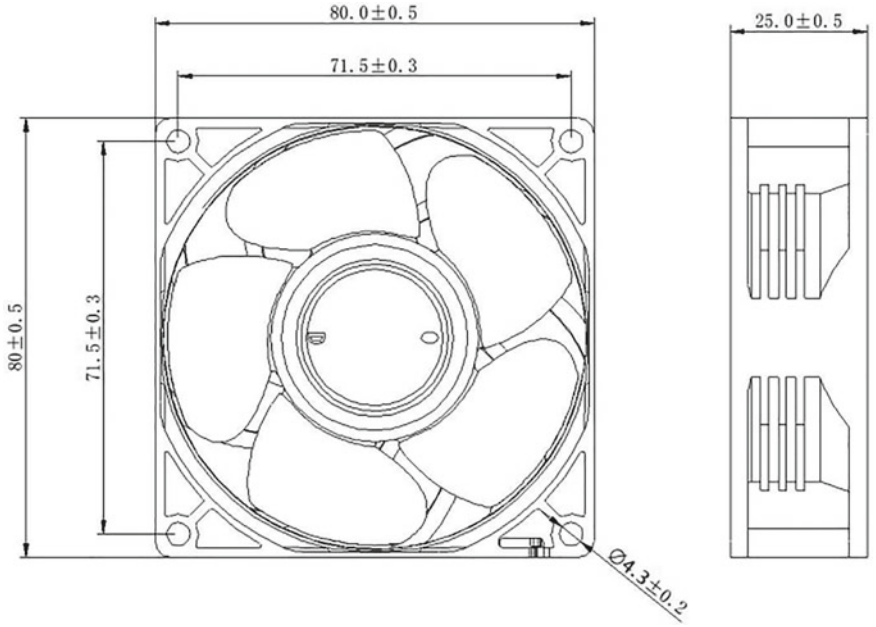

Fig. 2 Cooling fan model

2.2 Finite Element Analysis Model for Energy Storage Battery

The parameters of the energy storage cell model used for the coupled fluid-temperature field simulation analysis are shown in Table 1.

In finite element analysis, good mesh dissection is often the key to numerical computation. In order to improve the computational accuracy and enhance the computational convergence, the electric core is divided into a copper coin-like body sweeping mesh profile, the fluid domain is divided into a tetrahedral mesh profile, and the mesh is encrypted at the air inlet and air outlet. The mesh profile is shown in Fig. 3, which is divided into 1,407,919 grid cells and 357,628 nodes.

Table 1 Physical property parameters of the cell

Parameters	Nominal value
Materials	$LiFePO_4$
Size/mm	60 * 184
Rated capacity/Ah	50
Rated voltage/v	3.2
Battery internal resistance/mΩ	0.4 ± 0.1
Weight/kg	60 * 184

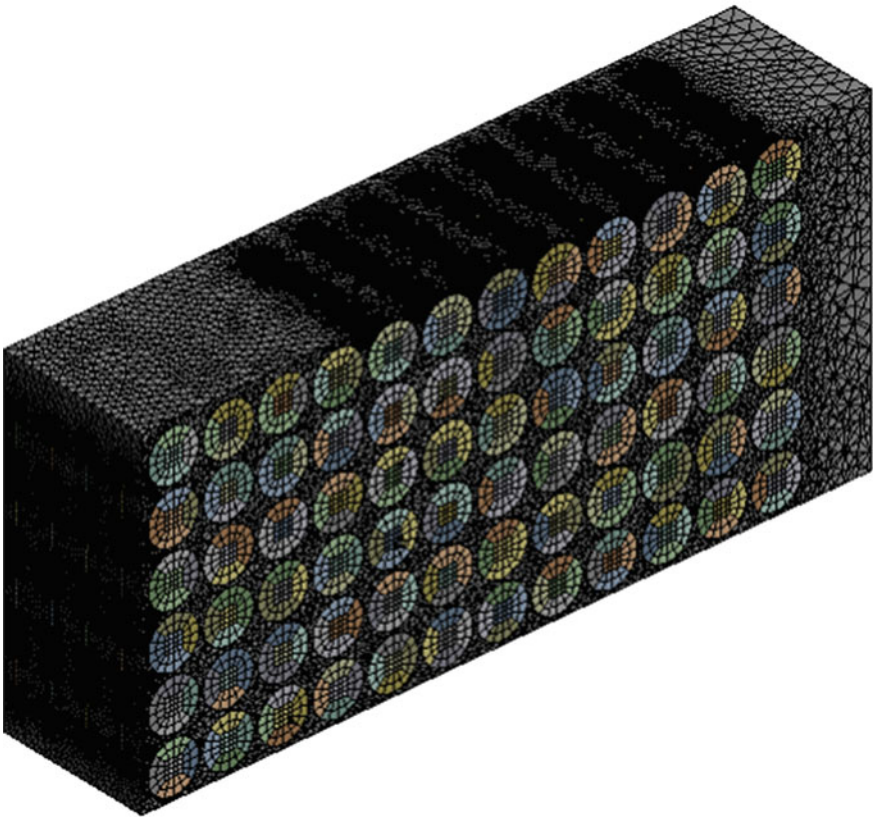

Fig. 3 Finite element mesh schematic

2.3 Thermal Modeling of Energy Storage Batteries

The heat production model of the energy storage battery can be described by the Bernardi equation:

$$q_{avg} = \frac{I}{V}[(E_{oc} - U)] - T\frac{dE_{\mathrm{oc}}}{dT} \tag{3}$$

where, q_{avg} represents the heat production rate of the battery, I represents the operating current, V represents the battery volume, E_{oc} represents the open circuit voltage, U represents the operating voltage, T represents the ambient temperature.

According to the principle of heat transfer, Fourier's law (Eq. 1) and Newton's cooling equation (Eq. 2) can be used to describe the heat conduction and thermal convection heat exchange processes of the energy storage cell respectively [11]:

$$\rho_{avg} c_p \frac{\partial T}{\partial t} = \nabla \cdot (\lambda \nabla T) + q_{avg} \tag{4}$$

$$q = h(T_s - T_b) \tag{5}$$

where, ρ_{avg} represents the average battery density, Cp represents the Cell constant pressure specific heat capacity, T represents the battery temperature, λ represents the battery thermal conductivity, q represents the heat flow density, h represents the Convection heat transfer coefficient, T represents the battery temperature, T_s represents the battery thermal conductivity, T_b represents the Ambient temperature.

3 Analysis of Simulation Results and Experimental Verification

3.1 Fluid-Temperature Field Coupling Results and Analysis

Through experiments, the energy loss of cells under different charge and discharge rates is shown in Table 2:

The charging and discharging average heat generation power estimation formula is as follows:

$$P_{avg} = Q/t \tag{6}$$

where, P_{avg} represents the charge and discharge average heat power, Q represents the Energy loss, t represents the Work step time.

Figure 4 gives the temperature field distribution of the energy storage battery module at a charge/discharge multiplier of 0.5 C and an ambient temperature of 26.85 °C; Fig. 5 gives the flow rate field distribution of the energy storage battery module at a charge/discharge multiplier of 0.5 C and an ambient temperature of 26.85 °C.

Analysis of the temperature field and flow velocity field of the energy storage battery module shows that the maximum flow velocity at the air inlet reaches 10.78 m/s, and the air flow velocity inside the box is obviously lower than that at the air inlet, so the heat dissipation effect at the air inlet is better than that inside the box. With the

Table 2 Battery cell energy loss at different multipliers

Charge/discharge multiplier	Energy loss (Wh)
0.5 C charge/discharge	1.786
1 C charge/discharge	6.007
2 C charge/discharge	15.270
3 C charge/discharge	28.310

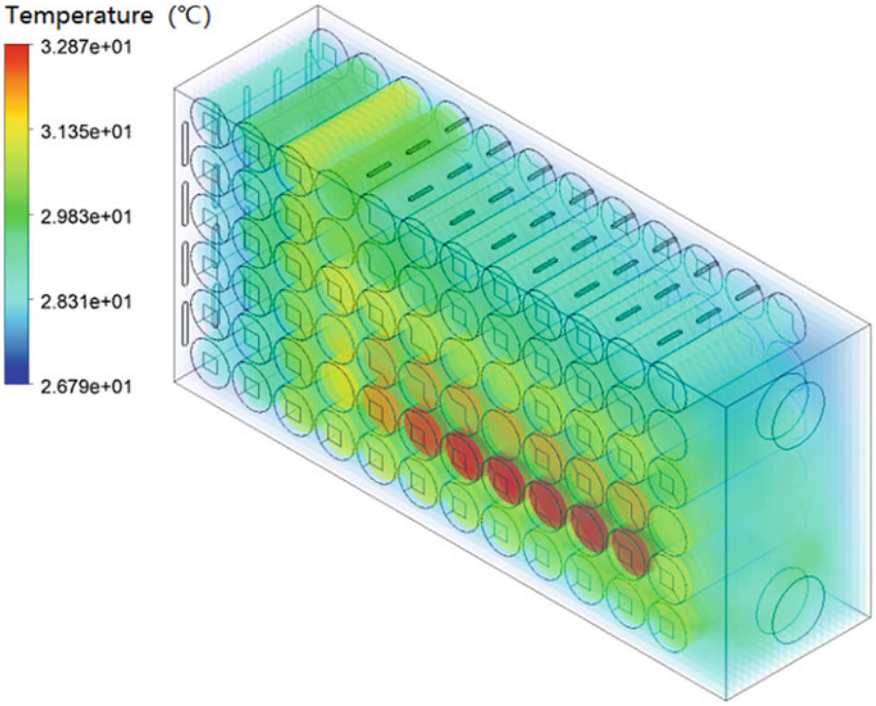

Fig. 4 Simulation results of temperature field

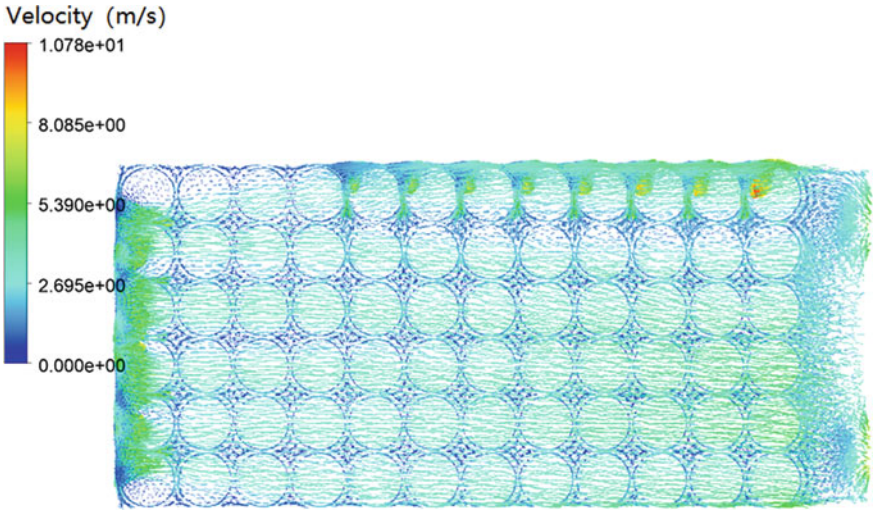

Fig. 5 Simulation results of flow velocity field

air flow inside the storage battery box, the heat is also concentrated on the cooling fan side, and due to the asymmetric structure design of the air inlet of the original model, the second row of battery modules at the bottom near the fan side of the cores heat up seriously, and the number of the most hot cores is 6, and the maximum temperature rise reaches 6 °C.

3.2 Experimental Verification

In order to verify the accuracy of the fluid-temperature field coupling numerical model, the charging and discharging temperature rise and wind speed tests were conducted on the prototype of the energy storage battery module, and the sensors were arranged to measure the cell temperature and air flow rate at the designated parts to verify the accuracy of the simulation model by comparing the simulation results with the experimental data.

Through the charging and discharging experiments, the temperature and flow rate data of the measurement points were obtained and compared with the temperature and flow rate magnitudes of the corresponding positions obtained from the finite element simulation, and the simulation temperature results were compared with the experimental data as shown in Fig. 6.

It is easy to see from Fig. 7 that the simulation value of the temperature of each measurement point of the energy storage battery matches with the experimental value, and the highest temperature rise and its location are also consistent with the experimental data, and the error between simulation and experiment is less than 3%; meanwhile. The simulation accuracy is high, which proves the accuracy of the simulation model in this paper.

4 The Effect of Different Working Conditions on the Temperature Field

The battery charging and discharging rate, the ambient temperature of the battery and the air supply speed of the fan are changed respectively to study the temperature distribution of the energy storage battery under different working conditions and analyze the influence of the above three factors on the temperature of the energy storage battery.

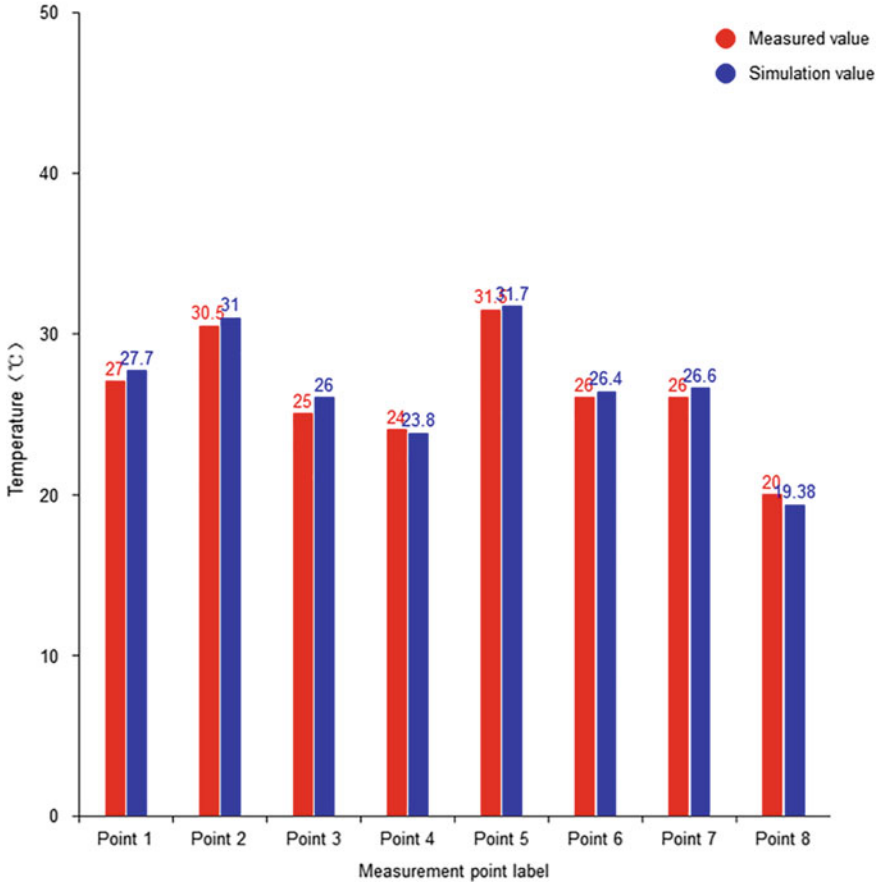

Fig. 6 Comparison of temperature simulation value and actual measurement value

4.1 Effect of Charge/discharge Multiplier

Keeping the boundary conditions such as ambient temperature and cooling fan air supply speed constant, different cell heat production rates are set in ANSYS Fluent simulation software to simulate different charge/discharge multipliers of the battery. After calculation, the heat production rates of 0.5, 1, 2 and 3 C cells are 3432.98 W/m^3, 11,546.42 W/m^3, 29,351.4 W/m^3 and 54,416.38 W/m^3 respectively, and the numerical simulation of the energy storage battery module is carried out at the ambient temperature of 26.85 °C and the fan air speed of 8.2162 m/s. The temperature field distribution of the battery at 0.5, 1, 2 and 3 C charge/discharge rate was calculated. Three measurement points in the battery module were selected to compare the temperature differences at different charging and discharging rates, and the results are shown in Fig. 7.

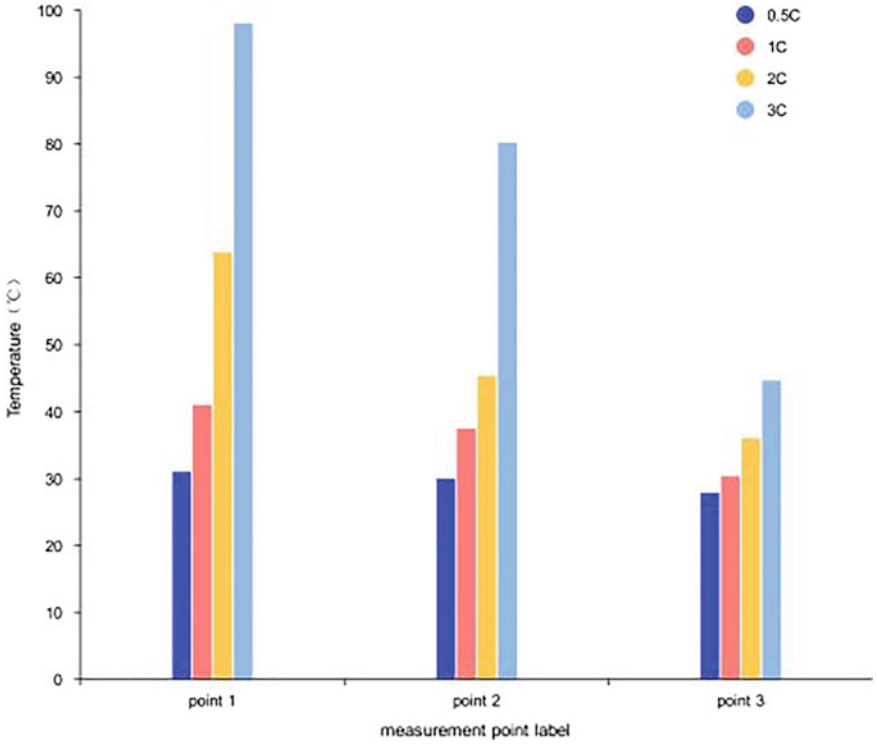

Fig. 7 Effect of charge/discharge multiplier on battery temperature

It can be seen that with the increase of the charge/discharge rate, the temperature of the core at each measurement point increases. It can be seen that when the charge/discharge rate increases from 0.5 C to 1 C, the maximum temperature of the cell reaches 40.96 °C, which is still within the reasonable working temperature range of the battery, but in order to make the battery work better, additional heat dissipation paths such as air conditioning can be considered for the energy storage battery at the charge/discharge rate of 1 C. When the battery charge/discharge rate exceeds 2 C, the maximum temperature of the battery cell is 63.7 °C and 97.5 °C respectively, which is far beyond the allowed working range of the battery. If working at this temperature for a long time, the battery is very prone to failure, which will have a great impact on the life of the battery and the safety of the staff. If the battery is to work at a charge/discharge rate exceeding 2 C, the thermal system of the energy storage battery should be redesigned to improve the thermal performance by increasing the power of the cooling fan, etc.

4.2 Effect of Ambient Temperature

Under the wind speed of 8.216 m/s, the working ambient temperature of the energy storage battery and the charge/discharge multiplier are changed respectively, and the effect of ambient temperature on the maximum temperature of the energy storage battery under different charge/discharge multipliers is calculated, and the calculation results are shown in Fig. 8.

As can be seen from Fig. 11, the trend of the maximum cell temperature increasing with the ambient temperature is basically the same at 0.5 and 1 C charge/discharge multipliers, i.e., the maximum cell temperature is basically proportional to the ambient temperature, and the maximum cell temperature increases by approximately 2 °C for every 2 °C increase in ambient temperature at both charge/discharge multipliers. Based on the above characteristics, the maximum cell temperature of an energy storage battery can be estimated by measuring the maximum cell temperature when the battery is operating at a fixed ambient temperature and the maximum cell temperature of the battery after the ambient temperature changes. This method can avoid the waste of resources caused by the need to re-measure the cell temperature due to the change of ambient temperature, and has some guidance significance for the research on the thermal failure of energy storage batteries.

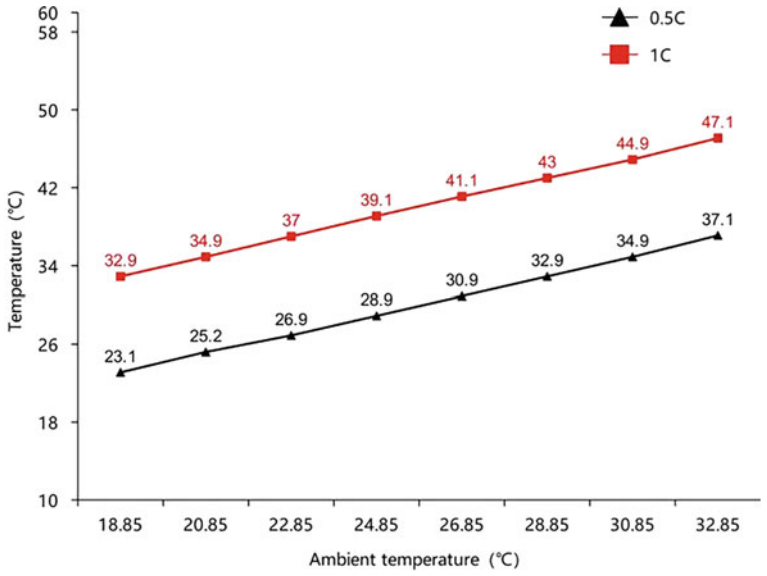

Fig. 8 Effect of ambient temperature on battery temperature

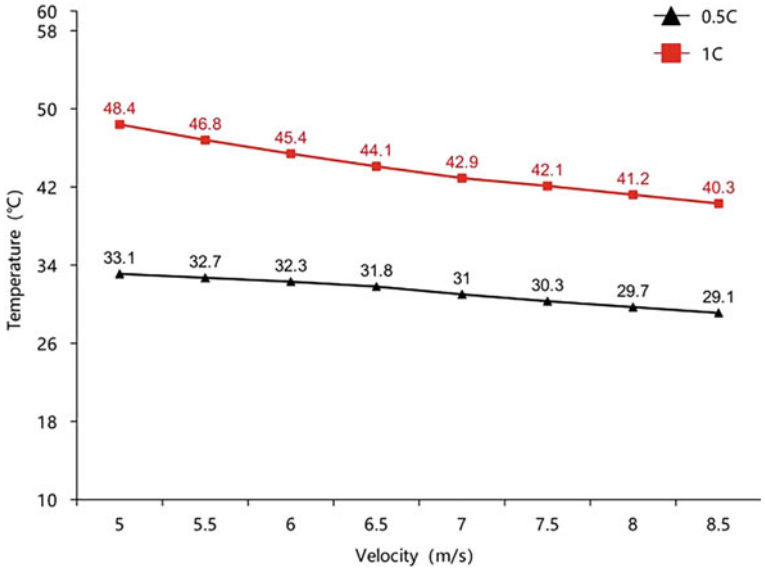

Fig. 9 Effect of fan speed on battery temperature

4.3 Effect of Fan Air Speed

At the ambient temperature of 26.8 °C, the air speed of the cooling fan of the energy storage battery and the charge/discharge rate were changed to calculate the effect of the wind speed on the maximum temperature of the energy storage battery under different charge/discharge rates, and the calculation results are shown in Fig. 9.

As can be seen from Fig. 12, the air speed of the cooling fan is basically inversely proportional to the maximum cell temperature at 0.5 and 1 C charging and discharging rates. Therefore, the maximum temperature of the core can be adjusted by adjusting the fan speed of the cooling fan. For example, when the ambient temperature rises, the fan speed can be increased to offset the effect of rising ambient temperature and cool down the core; conversely, when the ambient temperature decreases, the fan speed can be reduced to save power by reducing the fan power consumption.

5 Conclusion

In this paper, based on the finite element method, a coupled fluid-temperature field model of a 6P12S energy storage battery is established using ANSYS Fluent simulation platform, and the distribution of the battery temperature field and flow rate field is obtained, and the results can provide some reference for the thermal fault study of the energy storage battery. The correctness of the finite element model is

verified by comparing the experimental data. Based on the established finite element simulation model, the analysis of the influence factors related to the temperature of the energy storage battery module is carried out. The temperature distribution of the battery module is simulated for different charge/discharge rates, different ambient temperatures and different fan speeds, and the maximum temperature of the battery cell is extracted for comparison under various conditions. The results show that the maximum cell temperature increases with the increase of ambient temperature and the change of both is similar, and decreases with the increase of fan wind speed, and the change is related to the charge/discharge rate.

References

1. Zhang SC, Shen ZY, Lu YY et al (2021) Research progress of thermal runaway and safety for lithium metal batteries. Acta Physico Chimica Sinica 37(1):61–78
2. Zhang S, Chen WY (2021) Assessing the energy transition in china towards carbon neutrality with a probabilistic framework. Nat Commun 13(1):87
3. Hales A, Marzook MW, Diaz LB et al (2019) The cell cooling coefficient: a standard to define heat rejection from lithium. J Electrochem Soc 166(12):2383–2395
4. Wei JW (2019) Research on states estimation and thermal fault diagnostics of lithium-ion battery based energy storage system. University of Science and Technology of China, Hefei
5. Yang Y, Xu XM, Zhang YJ et al (2020) Synergy analysis on the heat dissipation performance of a battery pack under air cooling. Ionics 26(1):1–10
6. Xu XT (2015) A three-dimensional thermal model of lithium-ion batteries and its application. Tsinghua University, Beijing
7. Zhang L, Li X, Yang M et al (2021) High-safety separators forlithium-ion batteries and sodium-ion batteries: advances and perspective. Energy Storage Mater 41(1):522–545
8. Lü C, Zhang S, Zhu SH et al (2021) Thermal simulation analysis and optimization of forced air cooling system for energy storage lithium-ion battery pack. Power Syst Protect Cont 49(12):48–55
9. Du SX, Jin Y (2022) Numerical simulation and optimization of air cooling heat dissipation of lithium-ion battery storage cabin. Electric Power Eng Technol 46(6):48–55
10. Zhu DC, Wang XC (2022) Research on optimal design of air cooling and heat dissipation of energy storage battery module. Chinese J Power Sources 46(5):523–527
11. Zhao ZN (2008) Heat transfer theory. Higher Education Press, Beijing pp 177–179

Mechanism of Hygrothermal Aging of Sealing Materials for Electric Power Equipment

Guangmao Li, Lu Chen, Hongling Zhou, Gang Du, and Jie Yang

Abstract Aiming at the problem of hygrothermal aging of sealing materials used for power equipment, fluororubber and Ethylene propylene diene monomer (EPDM) were subjected to hygrothermal aging at 90%RH and 85 °C. The aging mechanism and performance changes of the two sealing materials were compared. The chemical components and molecular structure of fluororubber are stable in the process of hygrothermal aging, and the resistance to hygrothermal aging is strong, but it is easy to be affected by external stress and defects. EPDM has good resistance to hygrothermal aging and stable physical and chemical properties, but the phenomenon of internal stearic acid precipitation occurs in the process of hygrothermal aging.

Keywords Sealing material · Hygrothermal aging · Fluororubber · EPDM

1 Introduction

During operation, rubber sealing materials are often affected by various environmental factors. Their mechanical properties and chemical structure gradually deteriorate with the increase of operation time, leading to aging of rubber sealing materials, embrittlement, hardening, pulverization, cracking, elasticity decline [1]. The seriously aged sealing elements can not even meet the normal sealing requirements, leading to seal failure, which may further lead to accidents. For example, the leakage of transformer oil in the transformer may lead to fire or even explosion accidents [2]. Studying the aging mechanism of rubber sealing materials is of great significance for selecting appropriate sealing materials according to the working environment of sealing elements, which is also beneficial to improve the anti-aging performance of sealing materials and evaluate the service life of sealing materials.

G. Li · L. Chen · H. Zhou · G. Du (✉) · J. Yang
Guangzhou Power Supply Bureau Electric Power Test and Research Institute, Guangdong Power Grid Co Ltd., Guangzhou 510410, China
e-mail: dudu-2566@163.com

© Beijing Paike Culture Commu. Co., Ltd. 2024

X. Dong and L. Cai (eds.), *The Proceedings of 2023 4th International Symposium on Insulation and Discharge Computation for Power Equipment (IDCOMPU2023)*, Lecture Notes in Electrical Engineering 1102, https://doi.org/10.1007/978-981-99-7405-4_42

During operation, the key to forming a good seal is that the sealing element with good elasticity generates enough pressure on the sealing surface [3]. However, the mechanical properties of the seals may gradually lose during long-term operation, leading to a decline in sealing performance [1, 4]. Seals often operate in high temperature environment in power equipment, for example, the operating temperature in oil immersed type can reach 60–70 °C [5]. The sealing element is under high temperature for a long time and exposed to the external environment, which is prone to aging and lead to performance degradation [6–8].

At present, there are abundant researches on the aging of sealing materials at high temperatures [8]. The crosslink density of nitrile rubber and styrene butadiene rubber after high temperature aging was compared. The crosslink density of the two rubbers increased after high temperature aging, but the change of crosslink density of nitrile rubber was lower and the change of activation energy was higher [9]. The thermal stability and activation energy of NBR decreased after thermal oxidative aging [10]. Thermal oxygen aging was carried out for nitrile rubber, and swelling method and nuclear magnetic method were used in the detection of its crosslinking density. It was found that when nuclear magnetic method was used, the crosslinking density of nitrile rubber increased with the increase of aging time, while when swelling method was used, the crosslinking density would decrease at the early stage of aging [11]. After aging at high temperature, it was found that hydroxyl was formed during aging of nitrile rubber, cross-linking was the main reaction during aging, and hydroxyl was the main product of oxidation reaction of nitrile rubber during thermal oxidative aging [12]. While EPDM was subjected to thermal oxidative aging, and the results showed that EPDM was oxidized to carbonyl group during thermal oxidative aging [13]. The study of NBR reinforced by carbon black after high temperature aging showed that the tensile strength of NBR increased significantly and the failure strain decreased significantly, mainly due to the increase of rubber surface crosslinking density [14].

Sealing materials show different aging characteristics in hygrothermal environment, for example, calcium ions in humid air will react with additives in rubber to produce whitening layer [15]. The hygrothermal aging of fluororubber was carried out, and the main role of temperature in the aging of fluororubber was clarified. At the same time, it was found that more hydrolysis reactions occurred in the hygrothermal aging of fluororubber [16–18]. The nitrile rubber was aged in the tropical marine atmospheric environment. Ten years later, it was found that the nitrile rubber was mainly cross-linked by oxygen absorption. At the same time, the migration and enrichment of two plasticizers to the surface led to the reduction of elasticity [19]. By studying the influence of hygrothermal factors on the aging of fluororubber, it was found that the temperature, humidity and the interaction of temperature and humidity were different in different aging periods, and the interaction of temperature and humidity was significant in the early aging period [20].

In coastal areas of China, high temperature is often accompanied by high humidity. In the hygrothermal environment, sealing materials show different failure mechanisms and performance changes from those in the high-temperature environment [21]. At present, the aging research of various rubber sealing materials under

high temperature environment has been relatively rich, but there is still a lack of aging research of sealing materials under hygrothermal environment. Therefore, it is necessary to study the hygrothermal mechanism and characteristics of sealing materials.

In order to study the hygrothermal aging characteristics and mechanism of sealing materials, a hygrothermal environment was set up in this paper. Fluororubber and EPDM were subjected to hygrothermal aging at 85 °C and 90% relative humidity for 20 days. In order to simulate the compression stress of the seals in use, a compression device was used to compress the cylindrical samples, and the changes of their compression set were obtained. Through macro and micro analysis and detection methods, the aging characteristics and aging mechanism were studied. According to the analysis results of different sealing materials, the hygrothermal aging resistance of sealing materials was compared.

2 Sample Preparation and Aging Method

In this paper, fluororubber and EPDM produced by Shenma Company are selected to make Type 1A standard dumbbell samples according to ISO 37:2005. During aging, the dumbbell sample was sampled and analyzed by mass, ATR, SEM and thermal analysis.

Type A cylindrical sample is made according to ISO 815-1:2008. The compression performance of the sample is tested during aging, and a compression rate of 25% is set during aging.

The samples of fluororubber and EPDM shall be subject to hygrothermal aging. The humidity is 90% RH, and the temperature is set at 85 °C. Samples are taken for analysis and testing during the test.

During sampling and analysis, the compression set rate is tested for cylindrical samples, and the mass, tensile strength and strain at break are tested for dumbbell samples.

3 Analysis of Test Results

3.1 Mass Test

In hydrothermal aging, the mass change of fluororubber and EPDM with aging time is shown in Fig. 1.

As Fig. 1 shows that the mass of fluororubber and EPDM gradually increases during the hydrothermal aging, which is mainly due to the moisture absorption of rubber during the hydrothermal aging. The results show that the moisture absorption capacity of fluororubber is stronger than that of EPDM. After 20 days of hydrothermal

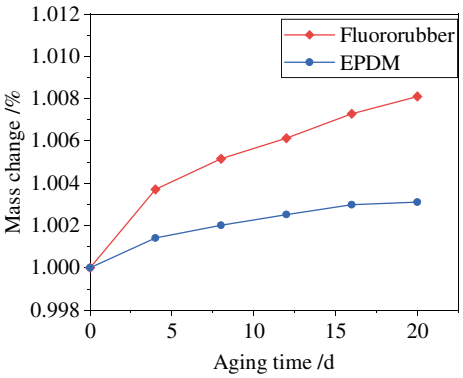

Fig. 1 Mass change of fluororubber and EPDM with hygrothermal aging time

aging, the mass of fluororubber and EPDM increased by 0.8% and 0.3% respectively, but the mass increase was not obvious.

3.2 Compression Set

The change of compression set of fluororubber and EPDM samples during hygrothermal aging is shown in Fig. 2. Fluororubber showed a high compression set, reaching 28.5% at the highest point, while EPDM finally reached 10.6%.

EPDM only experienced major compression set at the early stage of aging, and then the change was relatively slow, while fluororubber continued to produce permanent set during the whole hygrothermal aging process. It can be seen from Fig. 2 that its compression set still maintained a high growth rate after 10 days of hygrothermal aging. Fluororubber is prone to permanent deformation caused by external stress,

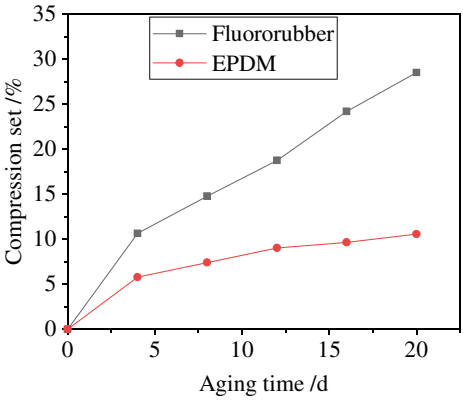

Fig. 2 Change of compression set of fluororubber and EPDM with hygrothermal aging time

and its compression resistance is poor, while the mechanical properties of EPDM samples are more stable during aging.

3.3 Tensile Test

The change of strain at break and tensile strength of fluororubber and EPDM samples during hydrothermal aging is shown in Fig. 3.

It can be seen from Fig. 3 that before and after hydrothermal aging, the strain at break of fluororubber is higher than that of EPDM, while the tensile strength is lower than that of EPDM, which is determined by the material properties. The main chain strength of the fluorine rubber sample is different from that of the EPDM rubber sample. The higher the main chain strength of the fluorine rubber, the higher the elongation at break will be, while the higher the crosslinking density of EPDM rubber, the tensile strength will be significantly improved.

Different filler reinforcement systems of samples also cause differences in tensile properties. More fillers are added to EPDM samples, which hinders molecular chain slip and elongation, making them more prone to defects in the tensile process, so the strain at break is lower.

In hygrothermal aging, the tensile properties of EPDM did not change significantly, which shows that the molecular structure of EPDM was relatively stable in hygrothermal environment.

The strain at break of fluororubber gradually decreased during the hydrothermal aging process, which was caused by the chemical degradation of fluororubber and the change of matrix structure during the hydrothermal aging. In addition, the tensile strength of fluororubber was improved at the initial stage of the hydrothermal aging, because the crosslinking density of fluororubber was moderately increased in the hydrothermal environment, which improved the tensile strength of the material [22,

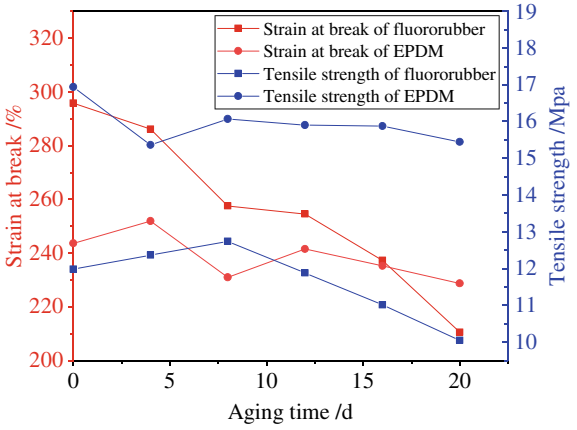

Fig. 3 Change of tensile properties of fluororubber and EPDM with hydrothermal aging time

23]. However, with the further development of hygrothermal aging, the change of molecular structure of fluororubber leads to the obvious deterioration of tensile properties of materials.

3.4 FTIR-ATR Analysis

With FTIR analysis, changes of functional group in fluororubber and EPDM samples can be depicted as shown in Figs. 4 and 5 respectively.

In Fig. 4, the peak at 3336 cm^{-1} is the O–H vibration, and the peak at 2913 and 2850 cm^{-1} is the C−H vibration in $-CH_3$ or $-CH_2-$. After hydrothermal aging, the strength of the −OH peak in fluororubber increases to a certain extent, and the C−H peak weakens, because hydroxyl groups are produced by hydrolysis during hydrothermal aging. The peak intensities of $C-F_2$ at 1394, 1155, and 11080 cm^{-1} were also reduced, which means that the fluororubber was mainly hydrolyzed during hydrothermal aging, producing a certain amount of hydroxyl group, but there was no unsaturated bond. Figure 4 shows that the peak strength and position of each wave band of fluororubber have not changed significantly after hydrothermal aging, indicating that the molecular structure of fluororubber is stable.

In Fig. 5, the peak strength of EPDM at 3330 cm^{-1} increased, indicating that hydroxyl was generated during hydrothermal aging. The peaks of 2850 and 2920 cm^{-1} are C−H vibration in $-CH_3$ or $-CH_2-$, and the strength increases after hydrothermal aging. The peak of 1590 cm^{-1} represents the calcium stearate accumulated on the surface of EPDM. This is because EPDM products have a sulfur curing system. Stearic acid may migrate to the surface during aging, and calcium cations existing in hydrothermal environments are combined with it.

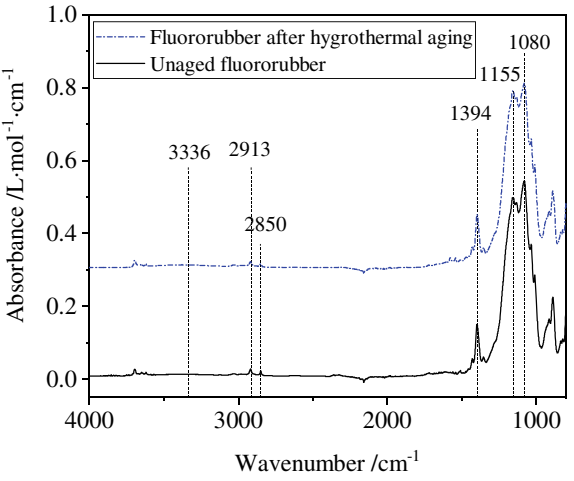

Fig. 4 FTIR-ATR spectra of fluororubber before and after hygrothermal aging

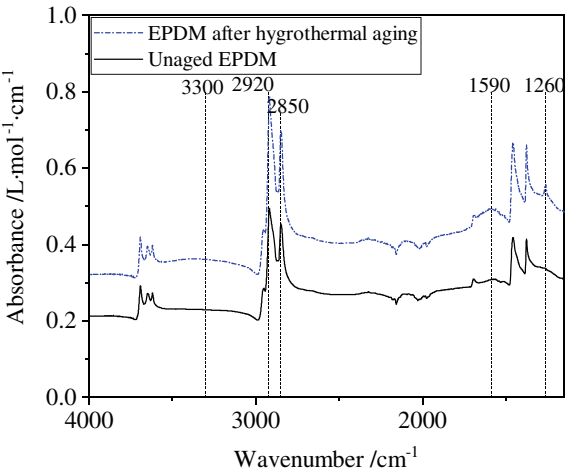

Fig. 5 FTIR-ATR spectra of EPDM before and after hydrothermal aging

The new peak at 1260 cm^{-1} is the vibration of C–O–C. In hydrothermal aging, such groups may be generated if hydrolysis and cross-linking occur. It indicates that EPDM is hydrolyzed and cross-linked, and the internal filler in EPDM will migrate to the surface during hydrothermal aging.

To sum up, although both materials are hydrolyzed during hydrothermal aging, and are accompanied by cross-linking. The structure of fluororubber is relatively stable after hydrothermal aging. EPDM in the hydrothermal environment, although the degree of aging is small, but also showed a certain change, mainly because some fillers and additives inside the EPDM concentrate on the surface, and combine with the substances in the environment to generate impurities on the surface.

3.5 TG/DTG Analysis

TG/DTG analysis was conducted on fluororubber and EPDM samples, as shown in Figs. 6 and 7.

The TG/DTG of the two samples have almost no change before and after hydrothermal aging, but the residual weight of the two samples increases after hydrothermal aging, because the internal crosslinking density of the samples is higher, the molecular structure is more compact, and the internal small molecular monomer has volatilized during the aging process, which leads to the improvement of their residual weight. TG/DTG analysis showed that the effect of hydrothermal aging on the components of fluororubber and EPDM is not significant.

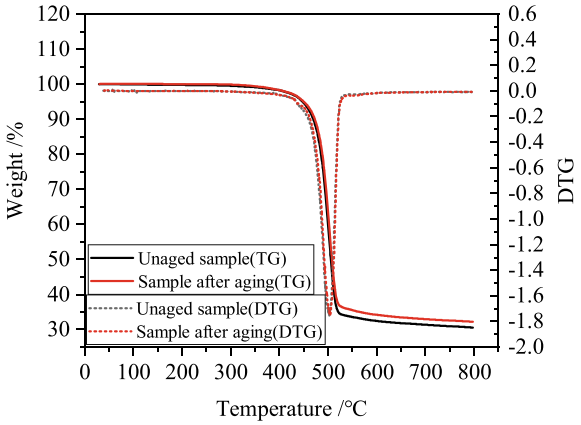

Fig. 6 TG/DTG of fluororubber before and after hydrothermal aging

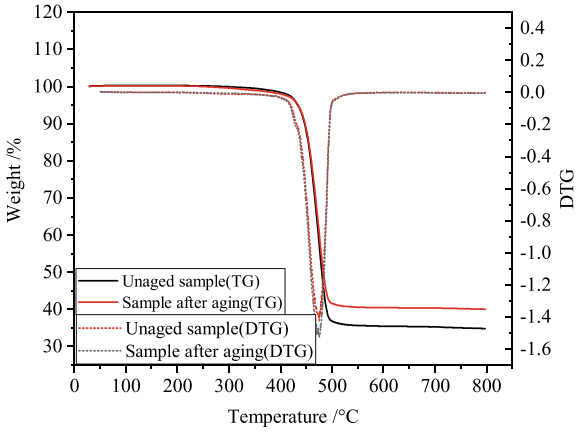

Fig. 7 TG/DTG of EPDM before and after hydrothermal aging

3.6 SEM Analysis

SEM of samples of fluororubber and EPDM before and after hydrothermal aging is shown in Figs. 8 and 9.

Figure 8 shows the magnified surface morphology of the fluororubber sample. The surface of the sample before hydrothermal aging is relatively flat, but after aging, the surface becomes rough, holes and surface peeling appear on the surface, and a large number of impurities appear.

Figure 9 shows the magnified surface morphology of EPDM sample. Before and after aging, the samples showed a relatively flat surface morphology, and there were fewer various defects on the surface, which reflected the good stability of EPDM in hydrothermal aging.

Fluororubber has more surface defects, which is conducive to the moisture absorption reaction of fluororubber. In the mass test of fluororubber in this section, it is

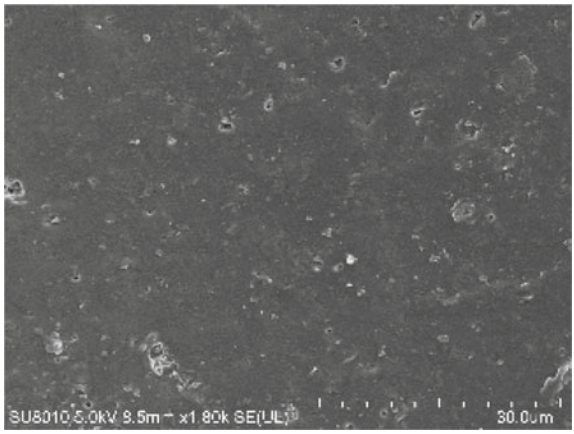

(a) Unaged fluororubber

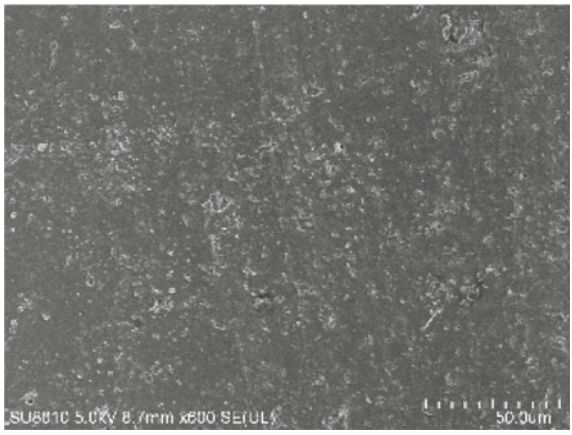

(b) Fluororubber after hygrothermal aging

Fig. 8 SEM of fluororubber samples

also found that the moisture absorption of fluororubber is more obvious. Various kinds of deterioration appear in the SEM of fluororubber, which corresponds to the phenomenon that the moisture absorption rate of fluororubber is higher in the mass change.

At the same time, in the tensile test, the strain at break of fluororubber after aging is lower than that of EPDM, and various defects on the surface of fluororubber also cause it to break more easily. The change of tensile properties of fluororubber is corresponding to the change in SEM.

Fig. 9 SEM of EPDM sample

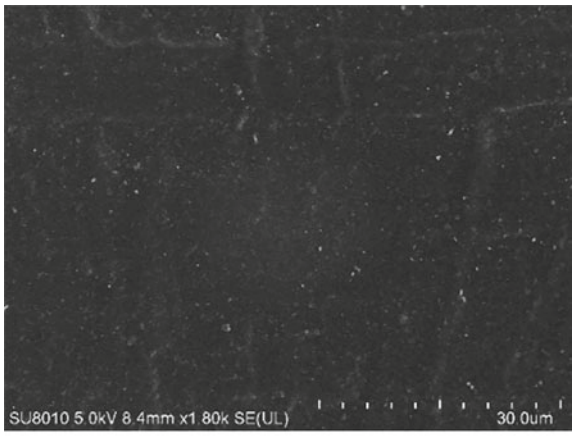

(a) unaged EPDM

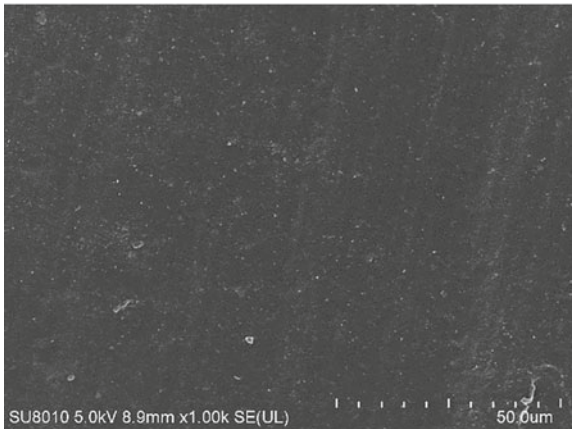

(b) EPDM after hygrothermal aging

4 Conclusion

In this paper, through the hygrothermal aging test of fluororubber and EPDM, the samples before and after aging are analyzed and tested macroscopically and microscopically, and conclusions are drawn on the hygrothermal aging resistance of different sealing materials:

1. The mechanical properties of different sealing materials change differently during hydrothermal aging. The hygrothermal aging led to the deterioration of the tensile properties of fluororubber, while the mechanical properties of EPDM were stable, and its tensile properties did not deteriorate significantly due to the hygrothermal

aging. Sealing materials will have a higher compression set rate growth at the early stage of aging. fluororubber are vulnerable to external stress, have poor compression resistance, and have a higher compression set rate, and still maintain a higher growth rate at the late stage of aging.

2. The precipitation of stearic acid can be observed in EPDM during hydrothermal aging. The internal components of fluororubber are relatively stable.
3. Different sealing materials are affected by hydrothermal aging to different degrees. Hydrolysis and cross-linking can be observed during hydrothermal aging of fluororubber. After hydrothermal aging, defects appear in the surface micromorphology, but its microstructure is relatively stable, and its resistance to hydrothermal aging is good. EPDM has the best hygrothermal aging resistance, its performance is less affected by aging, and its chemical structure and composition are stable.

Acknowledgements This work was funded by Key research project of China Southern Power Grid, China (No. GZHKJXM20190110).

References

1. Zhang W, Lou W, Liu X et al (2019) The effect of accelerated aging on the properties of nitrile butadiene rubber (NBR) O-rings. J Test Eval 47(2):1533–1550
2. Christina AJ, Salam MA, Rahman QM et al (2018) Investigation of failure of high voltage bushing at power transformer. J Electrostat 96(1):49–56
3. Peng XD, Wang YM, Huang X et al (2009) Current situation and development trend of sealing technology. Hydraulics Pneumatics Seals 29(4):4–11 (in Chinese)
4. Qiao L, Keller C, Zencker U et al (2019) Three-dimensional finite element analysis of O-ring metal seals considering varying material properties and different seal diameters. Int J Pressure Vessels Piping 176(1):103953
5. Deng YQ, Ruan JJ, Gong YJ et al (2021) Three dimensional simulation calculation of temperature fluid field of 10kV transformer based on parametric thermal equivalence. Electric Power Automation Equipment 41(4):212–218 (in Chinese)
6. Lou W, Zhang W, Jin T et al (2018) Synergistic effects of multiple environmental factors on degradation of hydrogenated nitrile rubber seals. Polymers 10(8):897
7. Zheng X, Li B (2021) Study on sealing performance of packer rubber based on stress relaxation experiment. Eng Fail Anal 129:105692
8. Mahankar PS, Dhoble AS (2021) Review of hydraulic seal failures due to effect of medium to high temperature. Eng Fail Anal 127:105552
9. Choi SS, Kim JC (2012) Lifetime prediction and thermal aging behaviors of SBR and NBR composites using crosslink density changes. J Ind Eng Chem 18(3):1166–1170
10. Ammineni SP, Nagaraju C, Lingaraju D (2022) Thermal degradation of naturally aged NBR with time and temperature. Mater Res Express 9(06):065305
11. Liu R, Wang S, Yin WH et al (2019) Effect of hot air aging on crosslinking density of nitrile rubber. New Chem Mater 47(7):201–203 (in Chinese)
12. Liu XR, Zhang WF, Lou WT et al (2017) Investigation on thermal oxidative aging of nitrile rubber (NBR) O-rings under compression stress. IOP Conf Ser Mater Sci Eng 265(1):012003
13. Bouguedad D, Mekhaldi A, Jbara O et al (2015) Physico-chemical study of thermally aged EPDM used in power cables insulation. IEEE Trans Dielectr Electr Insul 22(6):3207–3215

14. Alcock B, Jorgensen JK (2015) The mechanical properties of a model hydrogenated nitrile butadiene rubber (HNBR) following simulated sweet oil exposure at elevated temperature and pressure. Polym Testing 46:50–58
15. Choi SS, Chung HS, Joo YT et al (2012) Analysis of whitening phenomenon of EPDM article by humid aging. J Appl Polym Sci 123(4):2451–2457
16. Chang XL, Liu WL, Cheng JL et al (2012) Study on hygrothermal aging performance of solid rocket motor seals. J Projec, Rockets, Missiles and Guid 32(04):222–224 (in Chinese)
17. Chang XL, Jiang F (2012) Study on the failure of fluororubber sealing ring under high temperature and hygrothermal environment. Equipment Environm Eng 9(01):23–25+38 (in Chinese)
18. Zhang XJ, Chang XL, Zhang SY et al (2013) Hydrothermal aging mechanism of fluororubber sealing materials. Lubricate Engineering, 38(05): 38–40+45(2013). (in Chinese)
19. Wei X, Wu H, Zhang L et al (2018) Failure analysis of nitrile rubber O-rings static sealing for packaging barrel. J Fail Anal Prev 18(3):628–634
20. Fan SF, Zhang XJ, Xing PT (2021) Two factor variance analysis of F108 fluororubber hygrothermal aging effect. Equipm Environ Eng 18(2):115–119. (in Chinese)
21. You HJ (2016) Study on property evolution and life prediction of nitrile rubber under simulated marine environment. Qingdao University of Science and Technology, Qingdao (in Chinese)
22. Zheng X, Li B, Fei G (2022) Evaluation of sealing performance of a compression packer at high temperature. Sci Prog 105(1):1–24
23. Wang QL, Pei JK, Li G et al (2020) Accelerated aging behaviors and mechanism of fluoroelastomer in lubricating oil medium. Chin J Polym Sci 38(8):853–866

Evaluation of Insulation Performance and Life of Epoxy Resin Based on Accelerated Thermal Aging

Yan Wang, Chuan Chen, Sen Qian, Qiang Zhang, and Ximin Zhang

Abstract Epoxy resin (EP) is widely used as insulation materials for high frequency and ultra-high frequency sensors because of its excellent mechanical and electrical properties. Long-term thermal stress can lead to breakage of epoxy resin molecular chains and reduce the insulation performance of materials. In order to study the effect of thermal aging on the insulation performance of epoxy resin and achieve its aging evaluation, samples with different aging states are prepared according to the accelerated thermal aging criterion and the frequency domain dielectric spectrum (FDS) characteristics of different samples are investigated. The results indicate that aging has a significant effect on the middle frequency band (0.01–100 Hz) of epoxy resin tanδ-f curve, while it has little effect on other low and high frequency bands. With the increase of aging time, the middle frequency band of tanδ-f curve rises gradually and the dielectric loss increases. Then, the changes of molecular chemical bond and functional groups during aging are studied by Fourier transform infrared spectroscopy (FTIR). Finally, based on the changes in the dielectric response characteristic parameters of materials during aging, a method for evaluating insulation aging of epoxy resin is proposed, and the life distribution and reliability curve of epoxy resin under thermal aging are obtained.

Keywords Epoxy resin · FDS · Aging assessment · Reliability

Y. Wang · C. Chen (✉) · S. Qian · Q. Zhang · X. Zhang
State Grid Smart Grid Research Institute Co., Ltd., Beijing 102209, China
e-mail: 11347575@qq.com

S. Qian
e-mail: qiansen@geiri.sgcc.com.cn

Q. Zhang
e-mail: zhangqiang2@geiri.sgcc.com.cn

© Beijing Paike Culture Commu. Co., Ltd. 2024

X. Dong and L. Cai (eds.), *The Proceedings of 2023 4th International Symposium on Insulation and Discharge Computation for Power Equipment (IDCOMPU2023)*, Lecture Notes in Electrical Engineering 1102, https://doi.org/10.1007/978-981-99-7405-4_43

1 Introduction

Under the background of smart grid construction and the development of new power system, high-frequency and ultra-high-frequency sensors, as an important part of the sensor network of power system, become more important. Epoxy Resin (EP) is widely used as the main insulation material for typical sensors at high and ultra-high frequencies due to its excellent dielectric and mechanical properties [1, 2].

However, the working environment in substations is harsh. The thermal stress endured by high frequency and ultra-high frequency sensors during long-term operation is the main reason for the deterioration of device insulation [3, 4]. This long-term thermal effect can cause the epoxy molecular chains in the epoxy resin to oxidize and re-crosslink, leading to the cracking of the epoxy resin material and reducing its insulation performance [5, 6]. In addition, a certain number of hot electrons will be generated during the thermal aging process of epoxy resin, which will be easier to inject into the material and intensify the occurrence of partial discharge (PD) [7]. Therefore, conducting research on the insulation performance and life assessment of epoxy resin based on accelerated thermal aging is of great significance for the long-term reliable operation of typical sensors in substations.

The main detection method for insulation defects in insulation materials is the electrical parameter characterization method, which measures the dielectric loss tangent, capacitance, absorption ratio, dielectric constant, etc. of the material [8]. However, traditional measurement methods have a single testing frequency and low sensitivity, resulting in low detection accuracy. In recent years, frequency domain spectroscopy (FDS) based on dielectric response has been widely applied. This method extends the dielectric loss and capacitance under power frequency to a wider frequency range (0.1–5 kHz). Compared to conventional power frequency and capacitance testing, it has the advantages of low measurement voltage, rich insulation information obtained, and strong anti-interference ability [9, 10].

Domestic and foreign scholars have conducted relevant research on the impact of long-term thermal aging on the dielectric response of insulation materials. Fofana [11] prepared oil-paper insulation samples with different degrees of thermal aging, and tested that as the aging time increased, the dielectric loss values at each frequency point in the tanδ-f curve showed different amplitudes of increase. Linhjell [12] performed accelerated thermal aging of insulating paper and tested its FDS curves, finding that small molecule acids are generated during the thermal aging process. In the study of evaluating the aging degree of insulation materials based on dielectric response, Liao [13] studied the relationship between capacitance values at characteristic frequencies and the degree of polymerization of insulation paper aging, and used the "curve translation method" to eliminate the influence of temperature on the test curve, which provides theoretical guidance for the evaluation of on-site equipment insulation status. Wang [14] established a fitting function relationship between the integration value and the degree of aggregation by integrating within a specific

frequency band. However, the above research is mostly limited to oil-paper insulation, and there is little research on epoxy resin materials, lacking reliability evaluation research on insulation materials under long-term aging conditions.

In this paper, based on the idea of accelerating thermal aging, epoxy resins with different aging degrees are prepared. The FDS curves of several aging samples are obtained, and the influence of thermal aging on the insulation properties of samples is analyzed. The breakage of chemical bonds was measured by Fourier Infrared Absorption Spectrometer (FTIR), and the reasons for the changes of dielectric response curves in aging samples are further explored. Finally, a method for evaluating the aging status and lifespan of epoxy resins is proposed.

2 Basic Theory and Testing Principles of Dielectric Response

2.1 Basic Theory of Dielectric Response

When the external excitation electric field $E(t)$ is applied to the dielectric, the potential shift vector under polarization can be expressed as:

$$D(t) = \varepsilon_0 E(t) + P(t) \tag{1}$$

The current density $j(t)$ inside the dielectric is the sum of conduction current and displacement current:

$$\begin{aligned} j(t) &= \sigma_0 E(t) + \frac{dD(t)}{dt} \\ &= \sigma_0 E(t) + \varepsilon_0 \frac{dE(t)}{dt} + \varepsilon_0 \frac{d}{dt} \int_0^t f(t-\tau) E(\tau) d\tau \end{aligned} \tag{2}$$

where ε_0 is called the vacuum dielectric constant, σ_0 is called the DC conductivity, and the function $f(t)$ is used to characterize the polarization characteristics of the dielectric. Transform Eq. (2) to the frequency domain to obtain:

$$\begin{aligned} j(\omega) &= \sigma_0 E(\omega) + i\omega D(\omega) \\ &= \left\{\sigma_0 + i\omega\varepsilon_0\left[1 + \chi'(\omega) - i\chi''(\omega)\right]\right\} E(\omega) \\ &= \left\{\sigma_0 + \omega\varepsilon_0\chi'' + i\omega\varepsilon_0\left[1 + \chi'(\omega)\right]\right\} E(\omega) \end{aligned} \tag{3}$$

where ω is the frequency, $\chi(\omega)$ is the polarizability of the dielectric, $\chi'(\omega)$ is the real part of the complex polarizability, and $\chi''(\omega)$ is the imaginary part of the complex polarizability.

The electric displacement vector $D(\omega)$ is expressed as:

$$\begin{aligned} D(\omega) &= \varepsilon_0 \varepsilon_r(\omega) E(\omega) \\ &= \varepsilon_0 [1 + \chi'(\omega) - i\chi''(\omega)] E(\omega) \end{aligned} \tag{4}$$

The complex relative permittivity is:

$$\begin{aligned} \varepsilon_r(\omega) &= \varepsilon_r'(\omega) - i\varepsilon_r''(\omega) \\ &= 1 + \chi'(\omega) - i\chi''(\omega) \end{aligned} \tag{5}$$

Then the dielectric dissipation factor tanδ can be calculated by the following formula:

$$\tan\delta(\omega) = \frac{\varepsilon_r''(\omega)}{\varepsilon_r'(\omega)} = \frac{\chi''(\omega)}{1 + \chi'(\omega)} \tag{6}$$

The calculation of the dielectric dissipation factor in formula (6) only takes into account the polarization loss, but the conductivity loss should also be included in the actual measurement of the sample or device, where the complex relative permittivity is:

$$\begin{aligned} \underset{r}{\widetilde{\varepsilon}}(\omega) &= \varepsilon_r'(\omega) - i\varepsilon_r''(\omega) \\ &= 1 + \chi'(\omega) - i[\chi''(\omega) + \frac{\sigma_0}{\varepsilon_0 \omega}] \end{aligned} \tag{7}$$

Then the actual measured dielectric dissipation factor value is:

$$\begin{aligned} \tan\delta(\omega) &= \frac{\varepsilon_r''(\omega)}{\varepsilon_r'(\omega)} = \frac{C''(\omega)}{C'(\omega)} \\ &= \frac{\varepsilon''(\omega) + \sigma_0 \big/ (\varepsilon_0 \omega)}{\varepsilon_r'(\omega)} \end{aligned} \tag{8}$$

where $C''(\omega)$ is the imaginary part of the complex capacitance and $C'(\omega)$ is the real part of the complex capacitance.

2.2 Principles of Dielectric Response Testing

Frequency Domain Spectroscopy (FDS) is a testing method that extends the dielectric loss and capacitance at power frequency to a wider frequency range (0.1–5 kHz). The testing principle is shown in Fig. 1. The industrial control computer excites a voltage signal with different frequencies by controlling the voltage source and applies it to the test object. The device has a built-in voltage and current signal acquisition device. The

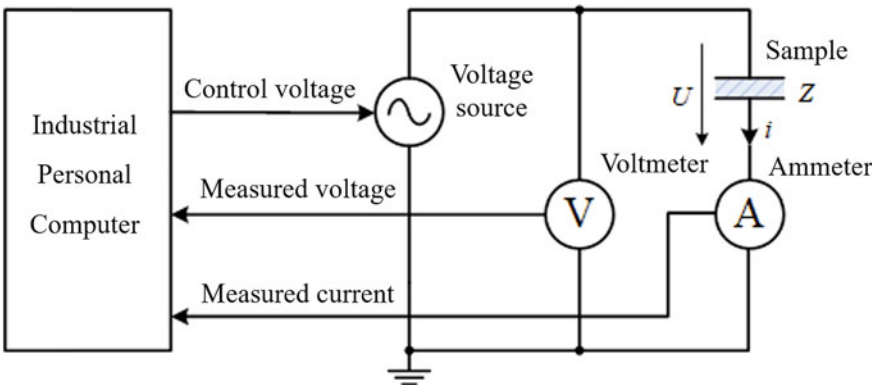

Fig. 1 Principle of FDS measurement

measured voltage and current data are processed internally by the dielectric response diagnostic instrument, and the dielectric loss, capacitance, dielectric constant and other parameter values at different frequency point are displayed on the industrial computer.

As shown in Fig. 2b, there is a phase angle $\Delta\varphi$ between the applied voltage and the excitation current. The tangent value of its remaining angle can characterize the dielectric loss:

$$\tan\delta = \tan(90^\circ - \Delta\varphi) \tag{9}$$

When using a dielectric response diagnostic instrument to test the frequency domain spectroscopy, the complex impedance Z of the dielectric can be calculated from the known excitation voltage and the measured response current. Meanwhile, the complex impedance Z is related to the complex capacitance as follows:

$$Z = \frac{1}{j\omega(C' - jC'')} \tag{10}$$

(a) Dielectric diagram at applied voltage (b) Current Vector

Fig. 2 Relationship between tan δ and I_R, I_C

Combined with the derivation in Sect. 2.1, the $\tilde{\varepsilon}_r(\omega) - f$ and $\tan\delta - f$ curves over a wide frequency range can be obtained.

3 Design of the Experiment

3.1 FDS Testing Platform

The frequency domain dielectric spectroscopy testing platform is shown in Fig. 3. The entire testing system consists of a computer, a dielectric response diagnostic instrument (Dirana), a vacuum pump, a vacuum drying oven, and a three-electrode structure.

The dielectric response diagnostic instrument (Dirana) is the main acquisition and processing module for voltage and current signals. The device can not only realize the band range, output voltage and other parameters and test mode settings, but also display measured data in real-time, achieving dynamic visualization of dielectric spectrum curve display.

To ensure the stability of the surrounding environment of the sample during the testing process and prevent interference from external factors such as moisture, temperature, and impurities, a vacuum drying oven is selected as the test sealed chamber for the experiment. The experimental chamber has been modified to introduce measurement terminals from the back end, which are respectively connected to the three-electrode structure and the dielectric responder. The external temperature control panel can adjust the temperature inside the cavity in real-time. Combined with the vacuum pump, it can realize the frequency domain dielectric spectrum test of epoxy resin under different temperature and pressure.

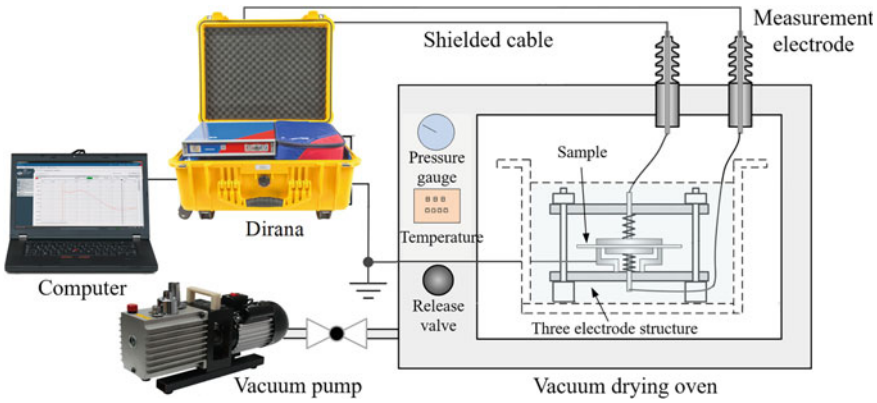

Fig. 3 FDS experimental platform

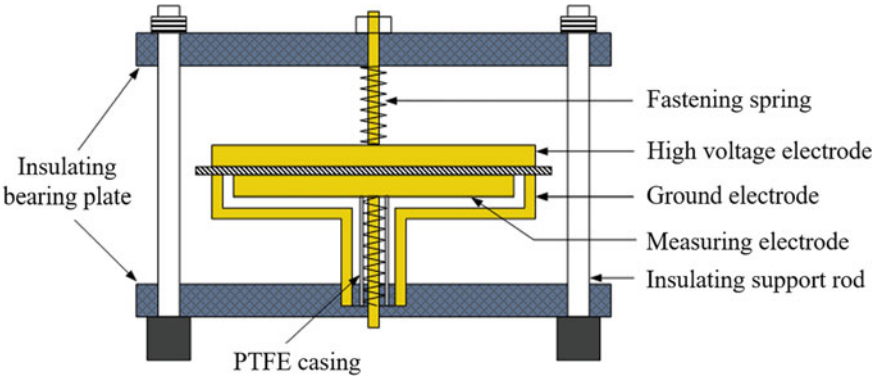

Fig. 4 Three-electrode structure

In order to improve the testing accuracy, the three-electrode structure is designed and used in this experiment according to GB/T 1410-2006, as shown in Fig. 4. The three-electrode are mainly composed of the cylindrical high-voltage electrode, the measuring electrode, and the protective electrode. The high-voltage electrode can measure the bulk current passing through the interior of the sample when voltage excitation is applied. The protective electrode is responsible for introducing the leakage current on the surface of the sample to the ground, avoiding its superposition with the bulk current, which affects the calculation of the dielectric loss value and capacitance.

3.2 Preparation of Experimental Samples

The structure of the high-frequency sensor is shown in Fig. 5, and its main insulation is epoxy resin. The research object of this article is epoxy resin samples under different aging insulation states.

The raw materials for epoxy resin production include epoxy resin matrix, curing agent, toughening agent, and accelerator. The specific materials are shown in Table 1. After pre-treatment of the materials, the three samples are mixed with the accelerator imidazole in a ratio of 100:95:10:1. They are then mixed and stirred through a magnetic stirrer, removed bubbles through an ultrasonic oscillator, poured into a mold, heated and cured in a vacuum drying oven, and demolded to obtain the required epoxy resin samples.

In order to explore the insulation aging characteristics of epoxy resin within a limited time, accelerated thermal aging experiments are conducted on the tested samples with reference to the standard GB/T 20,112–2015 [15]. Based on the "10 °C aging criterion", for every 10 °C increase in temperature, the aging rate of the sample doubles, i.e. the insulation service life decays to half of the original. The corresponding relationship between the aging time of the sample and the actual

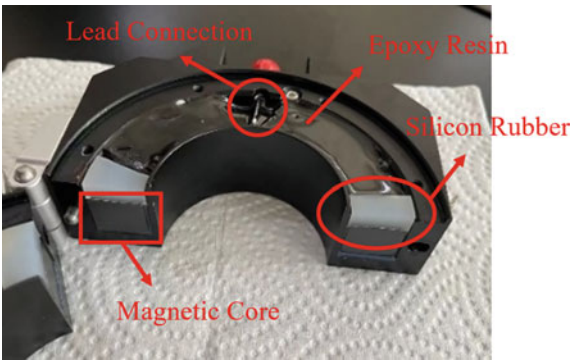

Fig. 5 HFCT structure

Table 1 Selection of epoxy resin material

Part	Material
Raw material	Diglycidyl ether of bisphenol A (E51)
Hardener	Methyl tetrahydrophthalic anhydride (MTHPA)
Flexibilizer	Dibutyl phthalate (DBP)
Catalyst	Imidazole

Table 2 Comparison of sample aging time with equivalent running time

No.	Aging time (day)	Equivalent running time (year)
1	0	0
2	5	0.88
3	15	2.63
4	25	4.38
5	45	7.89

working time is shown in Table 2. Figure 6 shows epoxy resin samples at different aging stages. From left to right are epoxy resin samples aged for 0, 5, 15, 25, and 45 days.

4 Results and Discussion

4.1 FDS Test Results

The testing temperature of the dielectric response testing platform is set to 50 °C, and the output voltage is set to 200 V. Dielectric response tests are conducted on epoxy resins under different aging states.

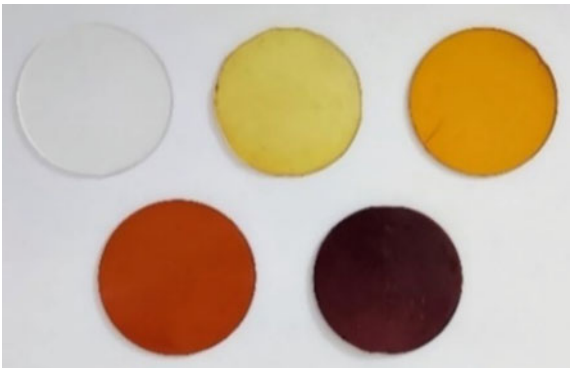

Fig. 6 Epoxy resin samples with different thermal aging degrees

The tanδ-f curves of the epoxy resin at different aging times are shown in Fig. 7. As the frequency increases, tanδ shows a trend of decreasing and then increasing. And the tanδ-f curves of epoxy resins change to varying degrees as aging time increases. According to the dielectric properties of different frequency bands, the tanδ-f curves are divided into S_1(0.001 Hz < f < 0.01 Hz), S_2(0.01 Hz < f < 100 Hz) and S_3(100 Hz < f < 5000 Hz) regions. When the aging is deeper, the changes in S_1 and S_3 areas are not obvious; however, it is obvious to find that the longer the aging time is, the larger the tanδ in S_2 region.

Samples are kept in a high temperature environment during aging. Under the action of thermal stress, the epoxy resin main chain and branch chain begin to crack and oxidize, and the material is filled with a large number of free radicals and dipoles. What's more, due to the gradual decomposition of curing agent into free acid at high temperature, the polarization of materials is significantly increased due to the generation of polar groups. The dielectric loss value of the epoxy resin gradually increases under the action of AC voltage.

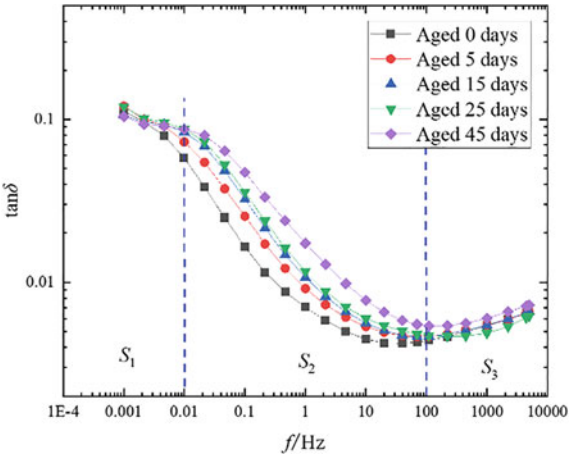

Fig. 7 tanδ-f curves of epoxy resins under different aging times

Figure 8 shows the ε'-f curves of the epoxy resin at different aging times, and the real part of the dielectric constant shows a gradual increase at different aging times as the frequency decreases. In the range of 1–5000 Hz, the increase of ε' is not obvious for each aging sample; while at frequencies between 0.001 and 1 Hz, ε' increase in an approximately exponential form with decreasing frequency, and the slope of the curve increases gradually. The real part of dielectric constant has the same physical meaning as the real part of capacitance, which can be used to characterize the ability of dielectric to store charge. At lower frequencies, the amplitude of the ε'-f curve is larger, indicating that the epoxy resin has a stronger charge storage capacity and greater polarity at lower frequencies. The longer the aging time, the larger the real part of dielectric constant of epoxy resins in the low frequency band (0.001–1 Hz), indicating that polar molecules occur during aging, and the molecular chains of epoxy resins may break under the action of high temperature, generating more polar substances. The insignificant amplitude variation in the real part of the high and medium frequency bands (1–5000 Hz) is due to the relaxation polarization characteristic frequency of the generated polar material closer to the low frequency band.

Figure 9 shows the ε''-f curves of the epoxy resin at different aging times. It can be seen that the change trend of ε'' amplitude with frequency and aging time is similar to that of tanδ, which is due to the physical meaning of both is the internal energy loss caused by external excitation signals applied to dielectrics. Therefore, the reason for ε''-f curve change is similar to that of tanδ-f curve.

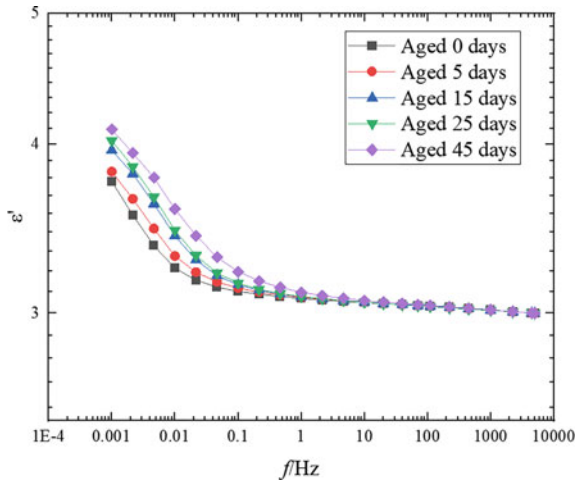

Fig. 8 ε'-f curves of epoxy resins under different aging times

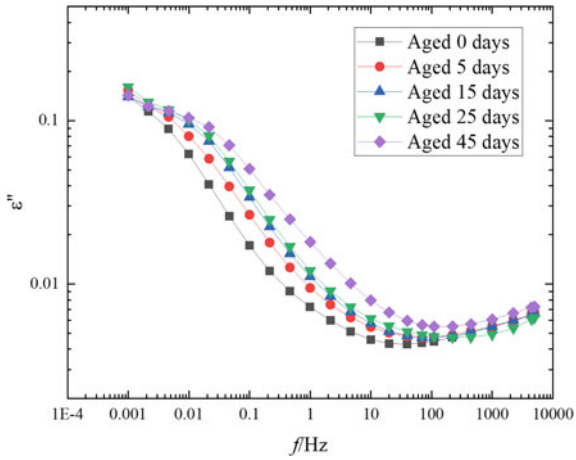

Fig. 9 ε''-f curves of epoxy resins under different aging times

4.2 FTIR Analysis

The FTIR spectra of epoxy resin at different aging times are shown in Fig. 10, where the horizontal coordinate represents the wavelength of the spectrum and the vertical coordinate represents the infrared light absorption of the epoxy resin for the response wavelength. There are several obvious absorption peaks in the graph. Among them, the 3400–3600 cm^{-1} wavelength band represents the stretching vibration of hydroxyl O–H, the 2700–3000 cm^{-1} peak represents the stretching vibration of C-H bond on the aryl group, the absorption peak near 1740 cm^{-1} represents the stretching vibration of C=O, the 1600 cm^{-1} represents the vibration of C=C bond on the aryl group, and the 1000–1200 cm^{-1} mainly results from the vibration of C–O bond [16, 17].

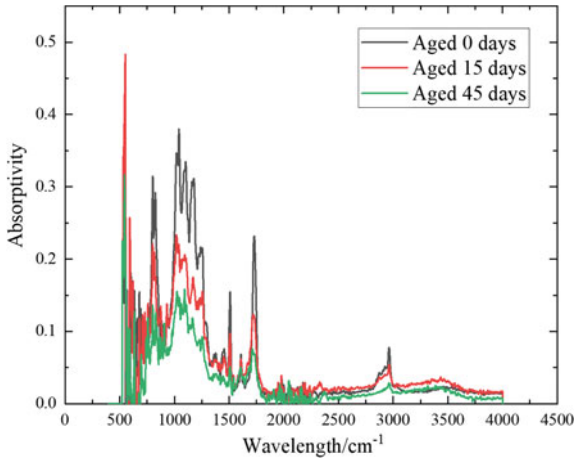

Fig. 10 FTIR spectrum of epoxy resins under different aging times

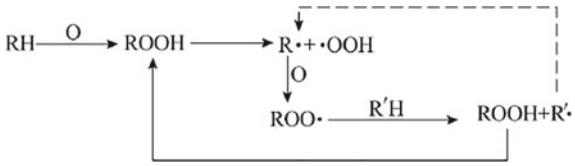

Fig. 11 Effect of oxygen on epoxy molecules

The shape of the spectral absorption curves is similar at different aging times, and there are corresponding absorption peaks at the wavelength bands corresponding to the main chemical bonds. The longer the aging time, the lower the corresponding peak value. This indicates that the thermal stress caused the breakage of epoxy resin molecular chain and the different degree of breakage of each chemical bond under high temperature environment.

In particular, with the participation of oxygen, C–H chemical bonds can react as shown in Fig. 11. The C–H chemical bond is continuously consumed to form carbonyl C=O, while oxidation of hydroxyl and ester groups occurs simultaneously, resulting in the formation of a large number of small molecule acids, aldehydes and other substances. These small molecule substances are easy to volatilize under high temperature, thus resulting in the reduction of chemical bonds such as C–H, C=O, etc. In addition, phenol produced by the reaction with C–C bond, C=C bond and ether bond in epoxy resin is also volatile. Therefore, the absorption peak strength of each chemical bond decreases under the effect of aging.

4.3 Evaluation Method for Insulation Aging of Epoxy Resins

From Fig. 7, it can be seen that the tanδ-f curve of epoxy resin does not change significantly at region S_1 and S_3, but the dielectric loss value increases gradually with aging time at region S_2, which has a more obvious rule. To obtain an evaluation method for the aging degree of epoxy resins, the tanδ value at the S2 region is integrated with the frequency f. The tanδ integral values are calculated for different aging times, and the results are shown in Table 3.

$$S_{S_2} = \int_{0.01}^{100} \tan\delta(f)df \tag{11}$$

The integral values of the dielectric loss at different aging times are shown in Fig. 12. It can be seen that the integral value increases as the aging time increases in the form of an approximate logarithmic function. Fitting the relevant data, an empirical formula for evaluating the aging degree of epoxy resins based on dielectric properties can be obtained as shown in Eq. (12).

$$y = -0.051 + 0.034\ln(5.6818x + 13.948) \tag{12}$$

Table 3 Integral value of tanδ in S_2 area under different aging time

No.	Equivalent running time (year)	Integral value
1	0	0.0373
2	0.88	0.0524
3	2.63	0.0641
4	4.38	0.0698
5	7.89	0.0896

According to the measurement results of samples with different aging degrees, the epoxy resin is considered to have failed when its integrated value of dielectric loss exceeds 0.1. Combined with the failure threshold and Fig. 12, the lifetime of the sample is 12.503 years. Increase the number of samples to 50 to obtain life data for each group of samples and estimate their life distribution based on these data. The lifetime of the material is directly related to its working time, and the daily working time of the device follows a normal distribution, so it is assumed that the sample lifetime also follows a normal distribution. The normal distribution probability density function is as follows:

$$y = f(x|\mu, \sigma) = \frac{1}{\sigma\sqrt{2\pi}} e^{-\frac{(x-\mu)^2}{2\sigma^2}} \tag{13}$$

where μ is the mean of the data and σ is the standard deviation of the data.

By parameter estimation, it is obtained that the sample life approximately obeys the normal distribution with the mean value of 12.484 and the standard deviation of 0.0984. It's normal distribution probability density function is shown in Fig. 13. Based on the lifetime distribution curve, the relationship between sample reliability

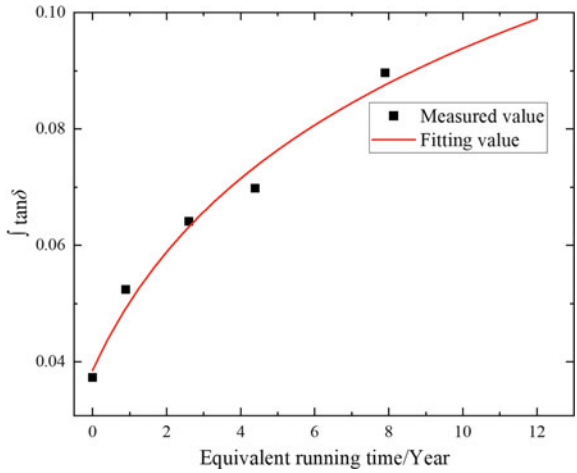

Fig. 12 Integral value of tanδ under different aging time

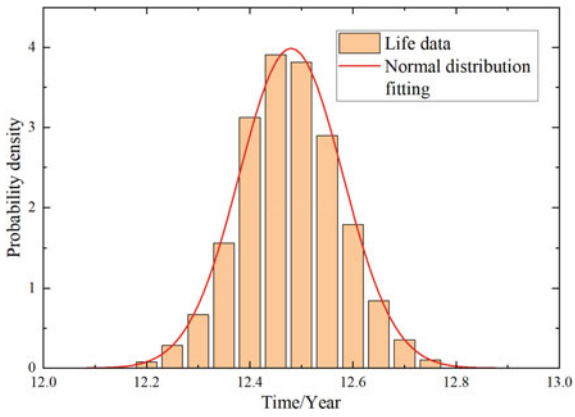

Fig. 13 Normal distribution probability density function plot

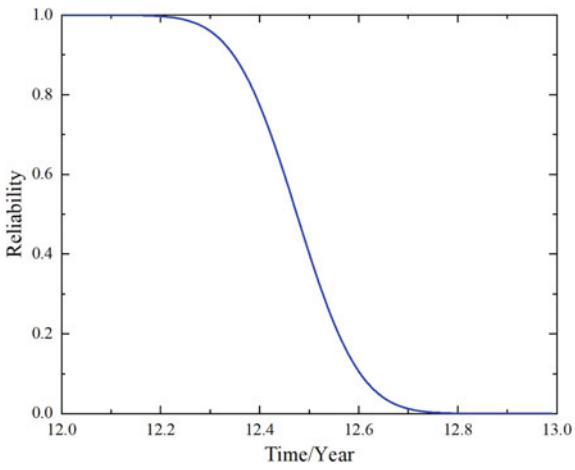

Fig. 14 Sample reliability curves

and time is obtained as shown in Fig. 14. The reliability of epoxy resin samples remains constant at 1 for 12 years and gradually decreases thereafter.

5 Conclusion

In this paper, epoxy resin samples with different aging states are prepared, their FDS curves are tested, and a method for evaluating insulation aging of epoxy resin is proposed. The results are as follows:

1. Aging has a significant effect on the middle frequency band (0.01–100 Hz) of epoxy resin tanδ-f curve, while it has little effect on other low and high frequency bands. With the increase of aging time, the middle frequency band of tanδ-f curve

rises gradually and the dielectric loss increases. Aging also results in an increase in the real dielectric constant at low frequencies (0.001–1 Hz), while the effect on the imaginary dielectric constant is similar to that of dielectric loss.
2. FTIR experiments show that thermal stress leads to changes in chemical bonds and functional groups, i.e. the formation of new substances.
3. A reliability evaluation method based on integral factor is established. The relationship between integral value and aging time is obtained, and a reliability analysis model based on normal distribution is established.

Acknowledgements This work has been supported by State Grid Corporation of China science and technology project "Research and application of reliability improvement technology of substation sensors and sensor network considering the influence of multi-physics coupling" (5700-202232441A-2-0-ZN).

References

1. Wang Y, Wang S, Lu G, Huang Y, Yi L (2017) Influence of nano-AlN modification on the insulation properties of epoxy resin of dry-type transformers. Trans of China Electrotech Soc 32(7):174–180 (in Chinese)
2. Ge L, Cui Q, Li M, Liu Z, Xia M (2023) Overview of new power system situation awareness technologies for low carbon economic operation. Integrated Smart Energy 45(01):1–13 (in Chinese)
3. Zhang S, Liu L, Wu H, Peng Z (2015) Insulating characteristics of UHV resin impregnated paper bushing condenser's materials. In: Properties and applications of dielectric materials. IEEE (2015)
4. Liang Q, Li X, Liu X, Zhao X, Wang L, Wu M, Gao J (2023) Summary of research on insulation aging and condition detection analysis of solid state switchgear. High Vol Elect Apparatus 03(29):1–14 (in Chinese)
5. Gong J, Li Z, Liu X (2016) Space charge and AC field aging in high hygrothermal environment of alumina/Epoxy Resin composites. Trans China Electrotech Soc 31(18):191–198
6. Yang Y, Xian G, Li H, Sui L (2015) Thermal aging of an anhydride-cured epoxy resin. Polym Degrad Stab 118:111–119
7. Wang Y, Feng C, Fei R, Luo Y (2020) Thermal-ageing characteristics of dry-type transformer epoxy composite insulation. High Perform Polym 32(7):741–752
8. DL/T 596-2015 Preventive test procedures for electric power equipment. National Energy Administration (2015). (in Chinese)
9. Hu Y, Dong M, Xie J, Xu G, Ren M, Wang K, Zhang S (2019) Spectrum analyzing and modeling of wide-band frequency dielectric response of oil-paper insulation. Proc CSEE 39(23):7065–7073 (in Chinese)
10. Ding N, Mu H, Ding Q, Yao B, Zhang D, Zhang G (2022) Evaluation and influencing factors of epoxy resin moisture based on frequency domain dielectric spectroscopy. High Vol Tech 48(02):706–715 (in Chinese)
11. Bétié A, Meghnefi F, Fofana I, Yéo Z (2012) On the impacts of ageing and moisture on dielectric response of oil impregnated paper insulation systems. In: 2012 IEEE Annual conference on electrical insulation and dielectric phenomena (CEIDP)
12. Linhjell D, Lundgaard L, Gafvert U (2007) Dielectric response of mineral oil impregnated cellulose and the impact of aging. IEEE Trans Dielectr Electr Insul 14(1):156–169

13. Liao R, Liu J, Yang L, Ma Z, Gao F, Zhang Y (2015) Study on frequency domain dielectric characteristic parameters for oil paper insulation condition evaluation of power transformers. Trans China Electrotech Soc 30(06):247–254 (in Chinese)
14. Wang Y, Gao J, Liu J, Zhang Y, Hao J, Ma Z (2015) Evaluation of aging and moisture content of oil-paper insulation in transformers Frequency domain dielectric characteristics. Trans China Electrotech Soc 30(22):215–221 (in Chinese)
15. Montsinger VM (2013) Abridgment of loading transformers by temperature. J AIEE 49(4):293–297
16. Ning X, Feng H, Zhang H, Liu Peng, Xiang Z, Peng Z (2015) Dielectric properties of multi-layer epoxy resin impregnated crepe paper composites. IEEE Trans Dielect Electrical Insul 22(1):161–168
17. Xie W, Yang Z, Cheng X, Chen S (2020) Study on thermal oxygen aging characteristics of epoxy resin materials. Trans China Electrotech Soc 35(20):4397–4404 (in Chinese)

Breakdown Characteristics of Eco-friendly Gas for Live Tank Multi-break Vacuum Circuit Breakers

Shuai Du, Xian Cheng, Guowei Ge, Sai Liu, and Longyv Guo

Abstract Insulation properties of environment-friendly gas have been widely concerned in recent years. However, breakdown characteristics of environment-friendly gas for live tank multi-break vacuum circuit breakers have not been fully understood at present. In this paper, the structure of environment-friendly live tank multi-break vacuum circuit breakers is proposed, and the electric field simulation is operated to gain the electric field distribution and dielectric weakness. Then, the breakdown tests of dry air under various electrode structures and gas pressures are conducted through gas insulation characteristics experimental platform. The effects of gas pressure and electrodes distance on the breakdown voltage are analyzed under various electrodes structures. The result shows that the breakdown voltage increases with the increasing gas pressures and electrodes distance in general, although there is saturation effect. Under the same condition except electrodes structures in AC breakdown voltage, the dielectric strength comparison is plate-plate > ball-plate > coaxial > needle-plate. In DC breakdown voltage, there is more stable various trend and less fluctuation in positive DC breakdown data. The positive and negative DC breakdown voltage of needle-plate electrodes shows the opposite trend before and after 15 mm distance. The positive DC breakdown voltage is higher than negative DC breakdown voltage in other electrodes. The results can provide a reference for insulation design for environment-friendly gas insulation equipment.

Keywords Breakdown characteristics · Environmental-friendly · Live tank vacuum circuit breakers · Insulating gas · SF_6 alterative gas

S. Du · X. Cheng · G. Ge (✉) · S. Liu · L. Guo
School of Electrical Engineering, Zhengzhou University, Zhengzhou 450001, China
e-mail: ggw@zzu.edu.cn

X. Cheng
e-mail: chengxian@zzu.edu.cn

© Beijing Paike Culture Commu. Co., Ltd. 2024

X. Dong and L. Cai (eds.), *The Proceedings of 2023 4th International Symposium on Insulation and Discharge Computation for Power Equipment (IDCOMPU2023)*, Lecture Notes in Electrical Engineering 1102, https://doi.org/10.1007/978-981-99-7405-4_44

1 Introduction

SF6 has been widely used in gas insulated equipment due to its excellent insulation and arc extinguishing properties. However, SF_6 will be restricted in future because of its global warming potential (GWP = 23,500). Therefore, increasing efforts have been devoted to finding a new environment-friendly insulating gas medium, one that can replace SF_6, will become the critical point for the development and application of environmental-friendly gas-insulated equipment. Live tank multi-break vacuum circuit breakers have great potential to substitute the usage of SF_6 CBs, which meet the worldwide requirements for carbon neutrality, and it gradually becomes the main trend of high voltage environmental-friendly circuit breakers.

In recent decades, the research for an alternative gas to SF_6 mainly focused on three technical routes. One is SF_6 mixed gases, such as SF_6/N_2, SF_6/CF_4 and SF_6/CO_2, which can reduce the content of SF_6. Mixtures of diluted SF_6 into conventional gases are a hot pot of investigation and have been applied in several engineering areas and products [1–5]. These mixtures show an acceptable insulation performance with a lower environmental impact, but they are transitional methods which cannot solve he greenhouse effect absolutely. Another is conventional gases, such as N_2, CO_2 and dry air. These gases are stable and can be used as insulation medium, but the acceptable dielectric strength level could be guaranteed through high filling pressures [6–8]. There also are the new environmental-friendly gases, such as CF_3I, $C_5F_{10}O$ and C_4F_7N, they are usually used with buffer gases as mixtures to avoid liquefaction under elevated pressures. In 2014, ALSTOM proposed the C_4F_7N/CO_2 mixtures named g3 at a CIGRE conference. Some scholars investigated the surface flashover of a cylindrical insulator in a C_4F_7N/CO_2 mixture under switching voltage. Others explored the AC, DC and lightning impulse breakdown characteristics of $C_5F_{10}O$ mixture and C_4F_7N mixture under various electric fields [9–11]. Although $C_5F_{10}O$ mixture and C_4F_7N mixture possess excellent insulation properties, the problem of arc extinguishing and high price limited their widespread promotion.

In this paper, the model of 126 kV environment-friendly live tank multi-break vacuum circuit breakers is proposed, which integrates the advantages of multi-break vacuum interrupters extinguishing arc, dry air as environment-friendly gas insulating and live tank type according with GIS/HGIS development. The electric field simulation is operated to gain the electric field distribution and dielectric weakness. Secondly, the AC and DC breakdown characteristics of dry air are obtained under various electrode structures and gas pressures through experimental circuit. Finally, the test results show the feasibility and reliability for adopting dry air as as insulating gas in 126 kV environment-friendly live tank multi-break vacuum circuit breakers.

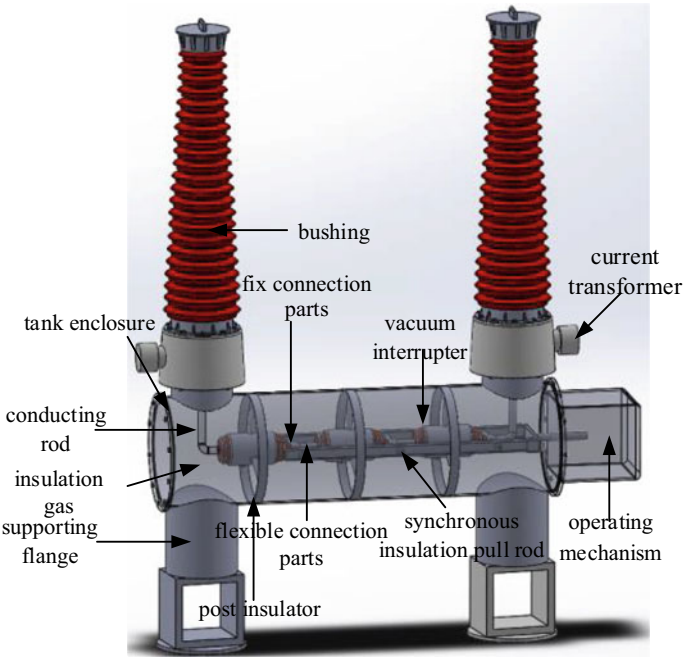

Fig. 1 126 kV environment-friendly live tank multi-break vacuum circuit breakers

2 Geometry and Simulation

2.1 Geometry Model

The three-dimension model of 126 kV environment-friendly live tank multi-break vacuum circuit breakers is shown in Fig. 1, which is composed of the bushing, tank enclosure, conducting rods, insulation gas, synchronous insulation pull rods, operating mechanism, vacuum interrupters, post insulators, fix connection parts, flexible connection parts, supporting flange et al. Moreover, the supporting flange and tank enclosure are located on the ground to provide stable grounding. The synchronous insulation pull rod and operating mechanism could separate the movable contacts from the static contacts of vacuum interrupters synchronously. The post insulator is the insulation support of vacuum interrupters.

2.2 Electric Field Simulation

Figure 2 shows the electric field distribution of live tank multi-break vacuum circuit breakers. The whole electric field distributions are relatively uniform, which also

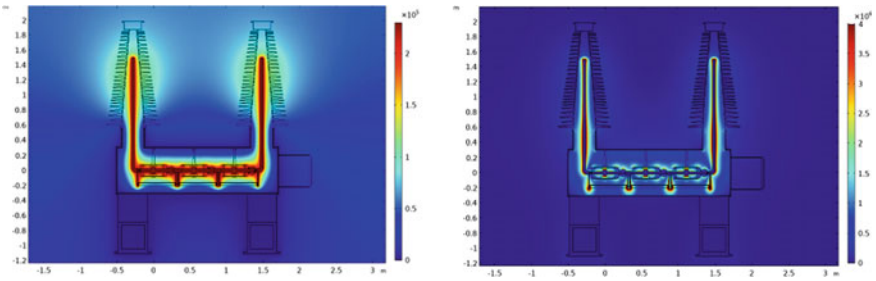

Fig. 2 Electric field distribution

possess dielectric weakness. The maximum electric field strength is located at the linkage between grading capacitors and interrupters, which is 18.5 kV/mm. Other larger electric field strength location are conducting rods corners, interrupters surface, linkage between insulation pull rods and interrupters, respectively.

With the simulation results from Fig. 2, the electric field strength of critical positions are extracted and equivalent to different electrode structures according to the field non-uniformity factors. The linkage between grading capacitors and interrupters is substituted by needle-plate electrodes. Meanwhile, the conducting rods corners and interrupters surface are substituted by ball-plate and coaxial electrodes respectively.

3 Experimental Platform and Results

3.1 Experimental Platform

The breakdown test of dry air filling in test chamber is carried out using a 126 kV gas-insulated switchgear, as illustrated in Fig. 3. The experimental platform includes a 100-kV AC Source, a protection resistor, a resistance–capacitance divider, a multiplier rectifier circuit consist of diodes and capacitors. The AC breakdown test is conducted by connecting AC source to the test chanmber directly, whether the DC breakdown test requires multiplier rectifier circuit to generating DC voltage.

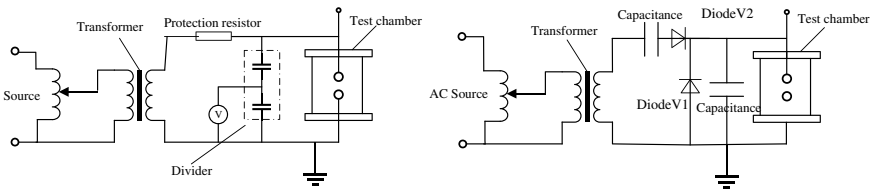

Fig. 3 Schematic of the experimental platform

3.2 AC Breakdown Characteristics

Four electrodes structures, plate-plate electrodes, ball-plate electrodes, coaxial electrodes, needle-plate electrodes are settled in test chamber. The gas pressure is in the range of 0.5 to 1.0 MPa. During the experiments, the voltage was applied by the continuous ramp-up method. To ensure the accuracy of experimental results, five times were carried out in each group.

1. Plate-plate electrodes

Figure 4 shows the AC breakdown characteristics under various electrodes structures. Under the plate-plate electrodes, the AC breakdown voltage increases linearly with the increasing gap distance. When gas pressure exceeds 0.9 MPa, there is a slight reduction in AC breakdown voltage. The AC breakdown voltage of plate-plate electrodes shows a linear increase with electrode distance under 0.9 and 1.0 MPa air pressure, which also has the similar trend. With 5 mm gap distance, 1.0 and 0.9 MPa dry air both reach 75 kV without breakdown.

2. Needle-plate electrodes

Under the needle-plate electrodes, which is extremely uneven electric field, the AC breakdown voltage presents saturation phenomenon in the range of 5–25 mm gap

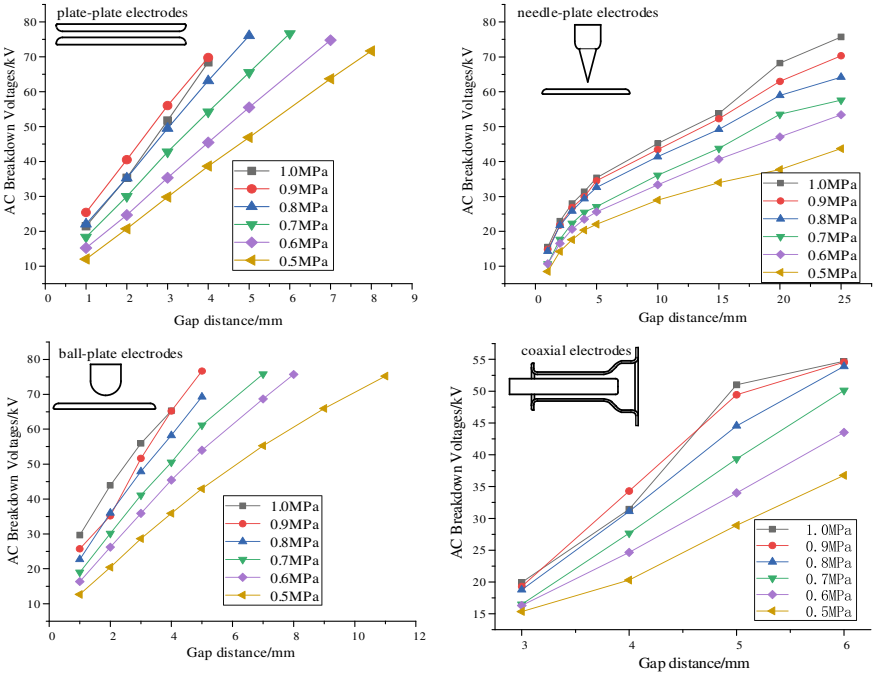

Fig. 4 AC breakdown characteristics under various electrodes structures

distance. With the influence of extremely uneven electric field, there are more distortion points in the trend of the AC breakdown voltage, and the effect of increasing the air pressure is less than increasing the gap distance. The AC breakdown voltage increased from 68.2 to 75.7 kV when the gap distance increased from 20 to 25 mm at 1.0 MPa, while the AC breakdown voltage from 70.3 to 75.7 kV.

3. Ball-plate electrodes

Under the ball-plate electrodes, which is slightly uneven electric field, the AC breakdown voltage presents linear growth with the increasing gap distance in general, However, due to the influence of slightly uneven electric field, there are many distortion points under low gap distance. It is observed that the AC breakdown voltage presents slight saturation phenomenon when gap distance exceeds 3 mm. With 5 mm gap distance, 1.0 and 0.9 MPa dry air both reach 75 kV without breakdown.

4. Coxial electrodes

Under the coxial electrodes, the AC breakdown voltage shows poor regularity. When the gap distance is 3 mm, the AC breakdown voltage increases little with the air pressure, and the saturation phenomenon is obvious. At the 4 mm and 6 mm gap distance, the AC breakdown voltage of 0.9 MPa is larger than that of 1.0 MPa, which also happens in plate-plate electrodes. At 0.9 MPa dry air and 6 mm gap distance, the AC breakdown voltage reaches 53 kV, which is bigger than the needle-plate electrodes, and smaller than the ball-plate electrodes.

3.3 DC Breakdown Characteristics

1. Needle-plate electrodes

Figure 5 shows the DC breakdown characteristics under various electrodes structures. The positive DC breakdown voltage tends to increase significantly and fluctuate slightly with increasing air pressure below 4 mm gap distance. At 5, 10 and 15 mm gap distance, the growth trend begins to rise slowly. The positive DC breakdown voltage at 1.0 MPa gas pressure fluctuates upwards and has little difference with 0.9 MPa gas. At 25 mm gap distance and 1.0 MPa gas pressure, the positive DC breakdown voltage is + 93.5 kV.

The negative DC breakdown voltage of the needle-plate electrode increases with the increasing gap distance, and the trend is more obvious. Overall, the positive DC breakdown voltage is larger than the negative DC breakdown voltage in the range of 1–15 mm gap distance, while the opposite phenomenon occurs that the negative DC breakdown voltage exceeds the positive DC breakdown voltage beyongd 15 mm gap distance. At 25 mm gap distance, the negative DC breakdown voltage of 1.0 MPa dry air reaches − 150.2 kV.

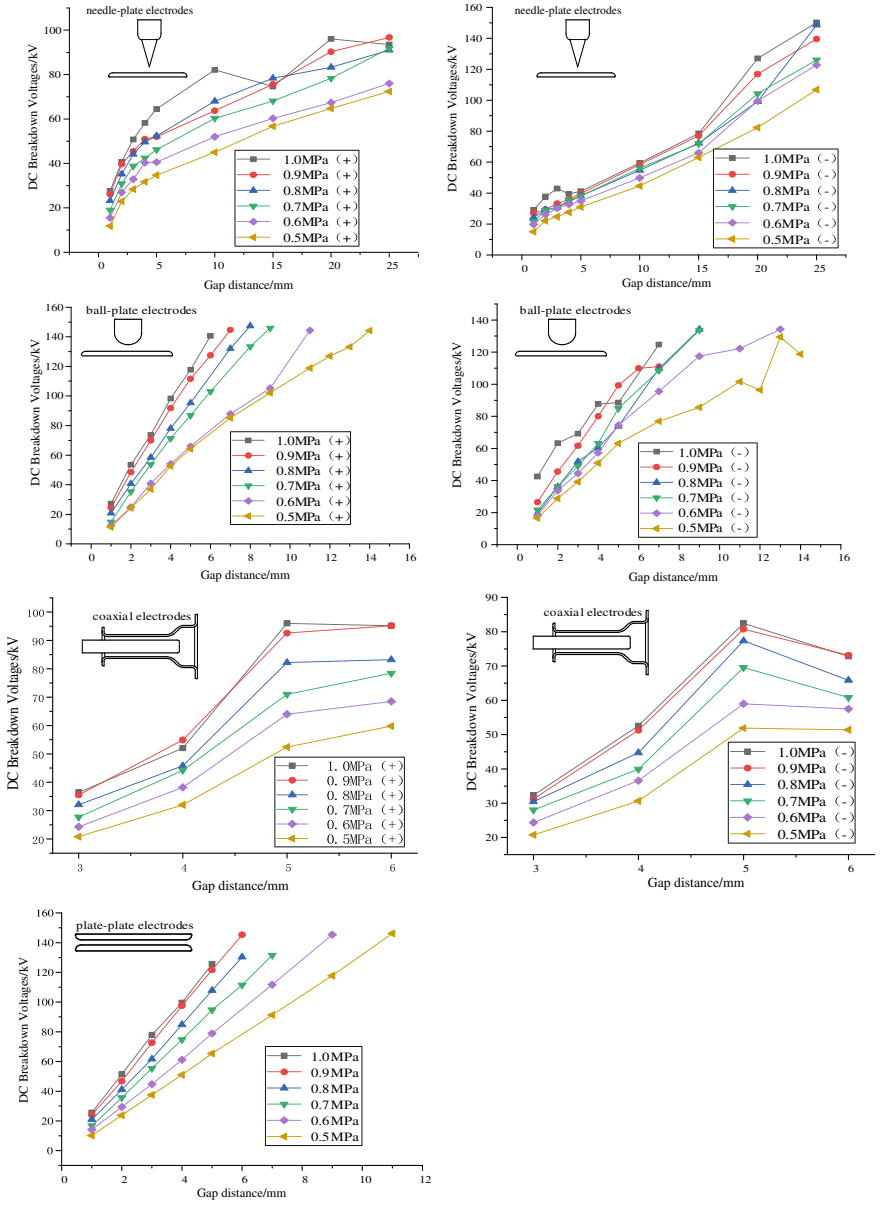

Fig. 5 DC breakdown characteristics under various electrodes structures

2. Ball-plate electrodes

Considering the ball-plate electrode, the positive DC breakdown voltage increased slowly when it is in the range of 0.5–0.6 MPa gas pressure. In the range of 0.6–0.9 MPa gas pressure, the positive DC breakdown voltage increases with the increasing gas pressure, and then it enters into the saturation region at 1.0 MPa gas pressure. At 6 mm gap distance, the positive DC breakdown voltage of 1.0 MPa dry air reaches + 140.6 kV.

When the applied DC voltage is negative, the growth trend of the breakdown voltage and gas pressure increases linearly, and the volatility and dispersion of data shows the poor regularity. The insulation capacity of 0.8 MPa dry air is reduced comparing to 0.7 MPa dry air. At 7 mm gap distance, the negative DC breakdown voltage of 1.0 MPa dry air reaches − 124.7 kV.

3. Coxial electrodes

The positive DC breakdown voltage of the coaxial electrode at different air pressures tends to increase with the increasing electrode distance. When the gap distance increases from 5 to 6 mm, the positive DC breakdown voltage increases unobviously, which exists a saturation trend. At 5 mm gap distance, the positive DC breakdown voltage of 1.0 MPa dry air reaches + 96.0 kV.

When the applied DC voltage is negative, the breakdown voltage of the coaxial electrode increases with the gap distance in the range of 3–5 mm, but decreases slightly when the gap distance increases from 5 to 6 mm. The positive and negative DC breakdown voltage could reach to 90 kV at the 5 mm gap distance. There is also a possibility that the insulation capacity even decreases beyond 5 mm gap distance.

4. Plate-plate electrodes

The DC breakdown voltage of plate-plate electrodes increases with the increasing air pressure linearly. Below 4 mm gap distance, the difference in DC breakdown voltage at each air pressure is not significant, and the trends and values of 1.0 and 0.9 MPa are similar. At 6 mm gap distance, the 1.0 MPa dry air are applied 150 kV and the breakdown does not occur. At 0.9 MPa, the DC breakdown voltage of dry air reaches 145.3 kV.

4 Conclusion

This paper investigated the possibility that the dry air is adopted as the alternative of SF6 to guarantee the insulation capacity in the gas insulation equipment. The breakdown tests of dry air under various electrode structures and gas pressures through gas insulation characteristics experimental platform. The experimental results shows that the AC and DC breakdown voltage of 5 mm ball-plate at 0.9 MPa are

75, + 111.7 and − 99.3 kV, which are 49.4, + 92.6 and − 80.7 kV of coxial electrodes. The results can provide a reference for insulation design for environment-friendly gas insulation equipment.

References

1. Zeng Y, Zhou W, Li H, Ma C (2020) Experimental and calculation study on insulation strength of C4F7N/CO_2 at low temperature. IEEE Trans Dielectr Electr Insul 27(4):1102–1109
2. Sun J, Song S, Zheng J, Li Z et al (2022) A review on surface flashover phenomena at DC voltage in vacuum and compressed gas. IEEE Trans Dielectr Electr Insul 29(1):1–14
3. Zeng F, Xie B, Chen X, Zou J, Yao Q, Tang J (2022) AC breakdown characteristics of C5F10O/CO_2 gas under different electrode surface roughness. IEEE Trans Dielectr Electr Insul 29(4):1425–1432
4. Han XT, Zhang XR, Wang HT, Sun Y, Zhou Y, Li JH (2023) Partial discharge characteristics of SF6 and SF6/N-2 in nonuniform electric field under negative DC voltage. IEEE Trans Dielectr Electr Insul 30(1):131–138
5. He YL, Ding W, Sun AB, Zhang GJ (2021) Effect of gas-mixture ratio on the characteristics of positive DC corona discharge in SF6/N2 gas mixtures. IEEE Trans Dielectr Electr Insul 28(3):829–837
6. Kumar S, Huiskamp T, Pemen AJM et al (2021) Electrical breakdown study in CO_2 and CO_2-O_2 Mixtures in AC, DC and pulsed electric fields at 0.1–1 MPa pressure. IEEE Trans Dielectr Electr Insul 28(1):158–166
7. Zhang BY, Uzelac N, Cao Y (2018) Fluoronitrile/CO_2 Mixture as an eco-friendly alternative to SF6 for medium voltage switchgears. IEEE Trans Dielectr Electr Insul 25(4):1340–1350
8. Jee SW, Lim DY (2021) Surface discharge mechanism with a change of gas pressure in N_2/O_2 mixed gas for insulation design of SF6-free high-voltage power equipment. IEEE Trans Dielectr Electr Insul 28(3):771–779
9. Ye FC, Zhang XX, Li Y, Li YL et al (2021) AC breakdown strength and its by-products of eco-friendly perfluoroisobutyronitrile/O_2/N_2 gas mixture at high pressure for HV equipment. IEEE Trans Dielectr Electr Insul 28(3):1020–1027
10. Loizou L, Chen L, Liu Q, Waldron M (2020) Lightning impulse breakdown characteristics of SF6 and 20% C3F7CN/80% CO_2 mixture under weakly non-uniform electric fields. IEEE Trans Dielectr Electr Insul 27(3):848–856
11. Wang C, Cheng Y, Tu YP et al (2018) Characteristics of C3F7CN/CO_2 as an alternative to SF6 in HVDC-GIL systems. IEEE Trans Dielectr Electr Insul 25(4):1351–1356

First-Principles Study on the Cu–Cr Interfaces in Vacuum Circuit Breaker Contacts

Xianxian Gui, Chuanqi Wu, Zhao Yuan, Cao Wang, Liming Liu, and Lixue Chen

Abstract Based on the experimental phenomenon that the breakdown position of the CuCr contact head in a vacuum circuit breaker may be the Cu–Cr phase boundary, the Cu–Cr interfacial binding models have been developed. The work function, work of interfacial separation, interfacial energy, charge transfer, and charge density distribution of Cu, Cr and W, Fe, Ni and Mo doped Cu/Cr interfaces are calculated from the first principles. The CuCr interface junction was found to have a smaller work function than pure copper and pure chromium. The reduced work function is prone to field emission, thus increasing the possibility of electrical breakdown. Three interfacial binding models Cu(110)/Cr(110), Cu(111)/Cr(111) and Cu(110)/Cr(100) are established in this paper. By comparing the separation work and interfacial energy, it is found that Cu(111)/Cr(111) is relatively stable. The charge transfer is ordered as W > Mo > Ni > Fe from large to small. This order is roughly the same as the atomic numbers of the four metals. The doping of W, Fe, Ni and Mo to make their work function reach the expected value is ranked as W > Ni > Fe > Mo. In this paper, we provide a theoretical basis for increasing the voltage strength of vacuum circuit breakers.

Keywords Vacuum circuit breaker · Contact · Cu/Cr interfaces · DFT · Work function

X. Gui · Z. Yuan (✉) · C. Wang · L. Liu · L. Chen
State Key Laboratory of Advanced Electromagnetic Engineering and Technology, School of Electrical and Electronic Engineering, Huazhong University of Science and Technology, Wuhan 430074, Hubei, China
e-mail: hustyuanzhao@qq.com

C. Wu
State Grid Hubei Electric Power Research Institute, Wuhan 430077, Hubei, China
e-mail: wuchuanqi1986@foxmail.com

© Beijing Paike Culture Commu. Co., Ltd. 2024

X. Dong and L. Cai (eds.), *The Proceedings of 2023 4th International Symposium on Insulation and Discharge Computation for Power Equipment (IDCOMPU2023)*, Lecture Notes in Electrical Engineering 1102, https://doi.org/10.1007/978-981-99-7405-4_45

1 Introduction

The contacts are enclosed in a vacuum chamber, an essential structure of a vacuum circuit breaker. Contact material is one of the most critical factors in determining the performance of vacuum circuit breakers. The ideal contact material for vacuum circuit breakers should have a large circuit outage capacity, endurance and resistance to high voltages, reliable resistance to welding, high electrical and thermal conductivity, low arc burn loss rate, and low chopping current. The properties of the contact material, such as melting point, work function, electron emission properties, ionization potential, and electrical and thermal conductivity, have complex interactions with the performance requirements of typical vacuum circuit breakers [1]. However, no contact material can satisfy these conditions simultaneously. Preliminary experimental studies of high-current vacuum arcs have been performed on pure copper electrodes [2]. The first successful high-current contact material for vacuum circuit breakers was a copper-based material added with other metals, namely a copper-based alloy. Through the continuous exploration of researchers, Cu–W, Ag–W, and Cu–Bi alloy contact materials have emerged one after another. Currently, Cu–Cr alloys with different compositions (25–75% Cu) are widely used as contact materials in the field of high voltage vacuum switching [3].

The compressive strength of a contact material is the ability to withstand a voltage between a given pair of contacts without being broken down. Zhao et al. [4] made contact breakdown with CuCr25 and found that the breakdown prime was the Cr phase, and a few breakdown points were at the Cu–Cr phase boundary. Zhang et al. [5] found that the first breakdown of CuCr25W1 contacts occurred at the Cu–Cr phase boundary. Yang et al. [6] conducted electrical breakdown experiments with coarse and nanocrystalline CuCr5 contacts, and found that in rough crystals, spots were limited to the Cr phase due to the large size of the Cr phase. Still, in the nanocrystalline, spots were continuously distributed on the contacts. This phenomenon may be due to the existence of more phase interfaces between the Cr particles and the Cu matrix. Cao et al. [7, 8] adopted the same contact breakdown method to doping Fe and Mo in CuCr alloy. With the increase of doping amount, the breakdown position gradually changed from the Cr phase to the Cu–Cr phase boundary, and finally transferred to the Cu phase. This doping strengthening effect increased the work function of the Cr phase, and then the breakdown position changed, and the breakdown voltage increased.

From the above discussion, the CASTEP used in this paper is based on a first-principles computational approach. This module studies the band energy, density of states, work function, charge transfer, the work of interfacial separation, interfacial energy, electrostatic potential and charge density, providing theoretical data reference for further development of Cu–Cr alloys. It also provides a theoretical basis for the material properties of the contacts of vacuum circuit breakers.

2 Computational Details

In the CASTEP module, the General Gradient Approximate (GGA) method is used instead of the Local Density Approximation (LDA) method [9]. PBE functional deals with exchange cross-linking between electrons [10]. The pseudopotential is the Norm conserving, and the truncation energy is 550 eV. The Energy convergence accuracy (Energy) is set to 1.0×10^{-5} eV/atom, the Energy gradient (Max. force) is set to 0.03 Ha/Å, and the atomic displacement (Max displacement) is set to 0.001 Å [11, 12]. Stress was set to 0.05 GPa. Max iterations was set to 100, the convergence precision of SCF tolerance was set to 1.0×10^{-6} eV/atom, and the maximum self-consistent field iteration cycle was set to 500. Brillouin k-point grid (k-point) was set as $5 \times 5 \times 3$ [13, 14]. The vacuum layer of all structural models was selected as 20 Å [15].

Work function is an important parameter in studying field emission, defined as the minimum energy required for free electrons in the metal to escape from the surface and enter the vacuum at absolute zero [16]. Equation 1 is the calculating expression of the work function [17].

$$\varphi = E_{vac} - E_F \tag{1}$$

where φ is the work function, E_{vac} is the surface barrier, and E_F is the Fermi level of the metal at 0 K.

The work of interfacial separation (W_{sep}) could be defined as the reversible work per unit area required to separate the two-phase interface into two free surfaces. As a result, W_{sep} can be used to assess the interfacial binding strength. [18–20]:

$$W_{sep} = \frac{E_{Cu} + E_{Cr} - E_{Cu-Cr}}{S} \tag{2}$$

where, E_{Cu} is the energy of the Cu surface in the Cu–Cr interfacial model, E_{Cr} is the energy of the Cr surface in the Cu–Cr interfacial model, E_{Cu-Cr} is the total energy of the Cu–Cr interfacial model, and S is the interfacial area [21].

The system formed in the interface between the interface structure and the change of the atomic bonds strain causes excess energy per unit area called the interfacial energy (γ_{int}) [22–24]. The interfacial energy is often used to assess interfacial stability [25]:

$$\gamma_{\text{int}} = \sigma_{cu} + \sigma_{cr} - W_{sep} \tag{3}$$

In the type, σ_{cu} and σ_{cr} represent the free surface energy of Cu and Cr, respectively. W_{sep} is the work of interfacial separation resulting from the combination of free surfaces.

When the Cu–Cr interface is combined to form a phase boundary, the system charges are transferred between the Cu–Cr crystal planes. The expression for the

calculated charge transfer in the interfacial binding process is as follows [26]:

$$Q = Q_{Cu1} - Q_{Cu2} \tag{4}$$

Q_{Cu1} and Q_{Cu2} represent the interfacial combination of the Cu crystal before and after the charge carrying, respectively. Q can be used to measure the charge transfer across the Cu–Cr crystal surface during the bonding process at the Cu–Cr interface.

3 Results and Discussion

3.1 Cu/Cr Interface Bonding and Electronic Properties

As shown in Fig. 1, Fig. 1a–e show the top view and side view of the different crystal surfaces of Cu and Cr. Figure 1f–h show the Cu(110)/Cr(110), Cu(111)/Cr(111) and Cu(110)/Cr(100) interfaces.

Table 1 lists the results of the calculations for the system energies, charges, work functions (φ), work of interfacial separation (W_{sep}), interfacial energies (γ_{int}), and

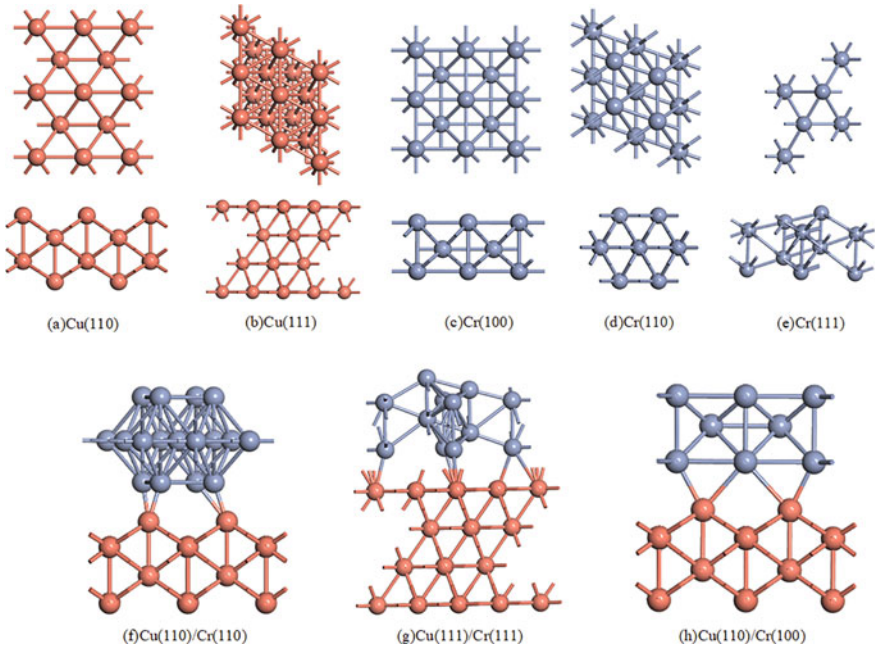

Fig. 1 Top and side views of **a** Cu(110) surface, **b** Cu(111) surface, **c** Cr(100) surface, **d** Cr(110) surface, **e** Cr(111) surface and **f** Cu(110)/Cr(110) interface, **g** Cu (111)/Cr(111) interface and **h** Cu(110)/Cr(100) interface

interfacial distances (d). The value of the work function is around 4 eV for all crystal surfaces. If the work function is calculated for all Cu and Cr crystal surfaces, the average work function is 4.53 eV and 4.11 eV, which are relatively high. From the point of view of the difficulty of electron emission, the field strength required for field emission in the presence of an external electric field can be as high as 108 V/m, irrespective of other factors such as surface protrusion. The work functions of the three boundary-binding models are 2.727 eV, 3.839 eV and 3.401 eV, respectively, which are decreased to a certain extent compared with the pure surface work functions, and the reduction of the work function of the Cu(110)/Cr(110) system is the most significant. So, it is easier to emit electrons at the phase-to-phase junction than in the pure plane. From this, it is inferred that the first breakdown occurs at the intersection of the phase and the phase on the contact of the vacuum breaker.

The system charge at each crystal surface is 0, and the electro-neutral state is maintained. The charge of the Cr phase is calculated after the phase and phase combination. The calculations show that all three phase boundary bonding modes acquire electrons in the Cr phase, that is, the charge is transferred from the Cu phase to the Cr phase. The amount of charge transfer corresponds to the amount of work function reduction. Cu(110)/Cr(110) with the largest amount of work function reduction has the largest corresponding charge transfer, and Cu(111)/Cr(111) with the least amount of work function reduction has the smallest corresponding charge transfer. At the same time, the interfacial spacing also presents the same rule. Cu(110)/Cr(110) with the largest reduction of work function has the largest corresponding charge transfer and the smallest interfacial spacing. Cu(111)/Cr(111) with the least work function reduction has the smallest charge transfer and the largest interfacial spacing.

In the Table 1, the work of interfacial separation of Cu(110)/Cr(110), Cu(111)/Cr(111) and Cu(110)/Cr(100) is 35.13, 68.80 eV/Å^2 and 112.47 eV/Å^2, respectively, all of which are positive values. This indicates that the three interfaces can be combined to form a stable interface. The value of work of interfacial separation of

Table 1 The calculations for the system energies, charges, work functions, work of interfacial separation, interfacial energies and interfacial distances

Interface	Energy/eV	Q/e	Work function/ eV	Wsep/ eV/Å^2	γ_{int}	S/ Å^2	d/ Å
Cu(110)	−18,689.38	0	3.746	/	/	/	/
Cu(111)	−18,694.20	0	4.533	/	/	/	/
Cr(100)	−1552.5	0	3.775	/	/	/	/
Cr(110)	−3111.5	0	4.579	/	/	/	/
Cr(111)	−1554.4	0	4.204	/	/	/	/
Cu(110)-Cr(110)	−23,098.4	Cr1.66	2.727	35.13	−35.46	36.93	2.451
Cu(111)-Cr(111)	−21,808.3	Cr1.51	3.839	68.80	−69.60	22.67	2.580
Cu(110)-Cr(100)	−24,395.4	Cr1.65	3.401	112.47	−112.80	36.93	2.426

Cu(111) /Cr (111) is the largest, suggesting that the bonding force between Cu(111) and Cr(111) is the strongest, and the interface bonding strength is the highest. The higher the bonding force between Cu(111) and Cr(111) is, the smaller the electron emission ability is, and the larger the corresponding work function is. The interfacial energies of Cu(110)/Cr(110), Cu(111)/Cr(111) and Cu(110)/Cr(100) are all negative values, and the absolute value of interfacial energies of Cu(110)/Cr(110) system is the smallest and the most stable. The absolute value of the interfacial energy of the Cu(110)/Cr(100) system is the largest, and the difference between the two systems is large, showing instability.

In Fig. 2, the left column shows the total charge density distribution and the right two columns show the differential charge distribution. From the charge density of the Cu(110)/Cr(110), Cu(111)/Cr(111) and Cu(110)/Cr(100) systems, it can be seen that the charge density around the Cu atom is yellow and that around the Cr atom is green. As can be seen from the legend, the charge density around the Cu atom is higher compared to the Cr atom. In the plot of the differential charge distribution in the middle column, blue represents the electrons gained and yellow represents the electrons lost. The Cu atoms are surrounded by yellow regions and the Cr atoms are cross-distributed with blue and yellow regions. And the electrons lost by Cu and some Cr atoms are transferred to the remaining Cr atoms, in agreement with the electron data obtained for the entire Cr atom discussed above. It can also be seen from the figure that in the differential charge density diagram of Cu(110)/Cr(110), the Cr atom at the top is more yellow than red. And the number of electrons obtained is more than that of the other two groups, which is consistent with the maximum number of electrons obtained by Cu(110)/Cr(110) discussed above.

3.2 W, Fe, Ni and Mo Doped Cu/Cr Interface and Electronic Structure

The current work on increasing the insulating capacity of copper-chromium alloys has been extended to the doping of a third component. Li et al. [27] obtained CuCrMo by magnetron sputtering and studied the microstructure evolution, nanomechanical properties and arc ablation resistance of CuCrMo alloy films before and after annealing. The CuCrMo film exhibits a strong resistance to vacuum arc ablation at a 40 kA vacuum arc for 9 ms. Li et al. [28] successfully prepared CuCr/CNTs composites through powder vacuum hot pressing sintering. By analyzing the microstructure and properties, it was found that the presence of an appropriate Cr3C2 nanophase at the interface improves the interfacial wettability, enhances interfacial bonding, and facilitates current transfer. In a large number of studies of doped Cu–Cr alloys, it has been shown that the doped third component is soluble in the chromium phase, such as the transition metal elements W, Ni and Fe. The breakdown strength of these doped compounds is higher than that of copper-chromium alloys. We are trying to get to the root cause of their increased breakdown strength.

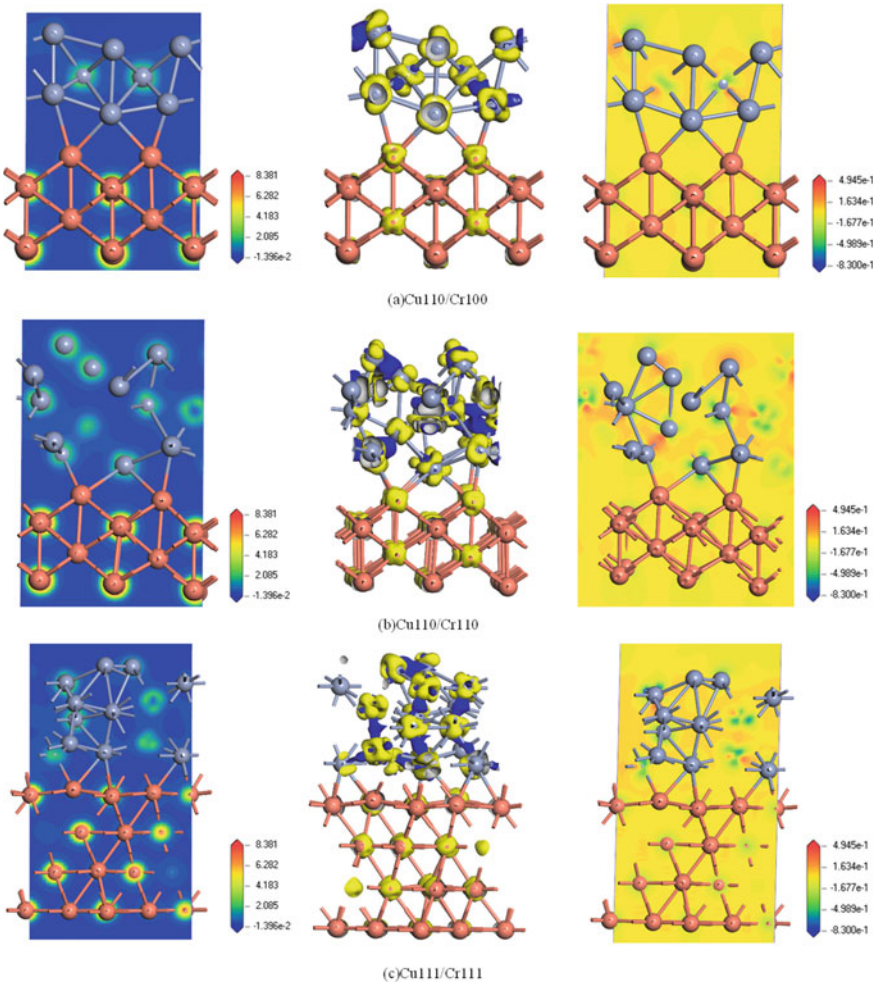

Fig. 2 The total charge density distribution on the left column and the differential charge distribution on the right two columns of **a** Cu(110)/Cr(100), **b** Cu(110)/Cr(110) and **c** Cu(111)/Cr(111)

Figure 3 shows the structure of the Cu–Cr phase boundary model for the third component doping Cr phase. Two different doping sites, site 1 and site 2, are considered, with the green atom representing the third doped component. A single dopant replaces only one Cr atom. Table 2 records the calculated results after W, Fe, Ni and Mo doping Cu(110)/Cr(110), Cu(111)/Cr(111) and Cu(110)/Cr(100), including work function, charge transfer and interfacial distance. By observing and comparing the change trend in Table 2, it is found that the work function of Cu(110)/Cr(110), Cu(111)/Cr(111) and Cu(110)/Cr(100) is improved by most doping. However, the work function of Cu(110)/Cr(100) in W, Fe, Ni and Mo doping fluctuates around

3.401 eV with a range of 0.2 eV. It can be approximated that the doping of W, Fe, Ni and Mo keeps the work function of Cu(110)/Cr(100) unchanged. For the Cu(110)/Cr(110) phase boundary with strong defects, the work function of Cu(110)/Cr(110) increases after doping of W, Fe, Ni and Mo. The minimum increase of Cu(110)/Cr(110) is 0.3 eV with doping of Mo, and the maximum increase of 0.5 eV with doping of W. It can be seen from these data that the doping of W, Fe, Ni, and Mo can reduce the ability of electron emission at the strong defect phase boundary. The mean and maximum values of the two sites are taken into account. Although the increase of work function at the Ni-doped site 2 is the largest, the increase of work function at the site 1 is the smallest. As a result, the work function is unstable to changes due to Ni doping. According to the expected contact performance of the vacuum arc extinguishing chamber, that is, to reduce the electron emission capacity of the contact surface, the doping of W, Fe, Ni and Mo to make their work function reach the expected value is ranked as W > Ni > Fe > Mo.

The amount of charge transfer in Table 2 is the amount of charge variation on the Cu surface. As can be seen from Table 2, the doping of W, Fe, Ni and Mo all causes the loss of electrons on the surface of Cu, and the charge transfer is ordered as W > Mo > Ni > Fe from large to small. This order is roughly the same as the atomic numbers of the four metals. Only in the system of Cu(110)/Cr(100) doped with W, Fe, Ni and Mo, the charge transfer is increased compared with that before doping. The charge transfer of Cu(110)/Cr(110) and Cu(111)/Cr(111) is reduced. On

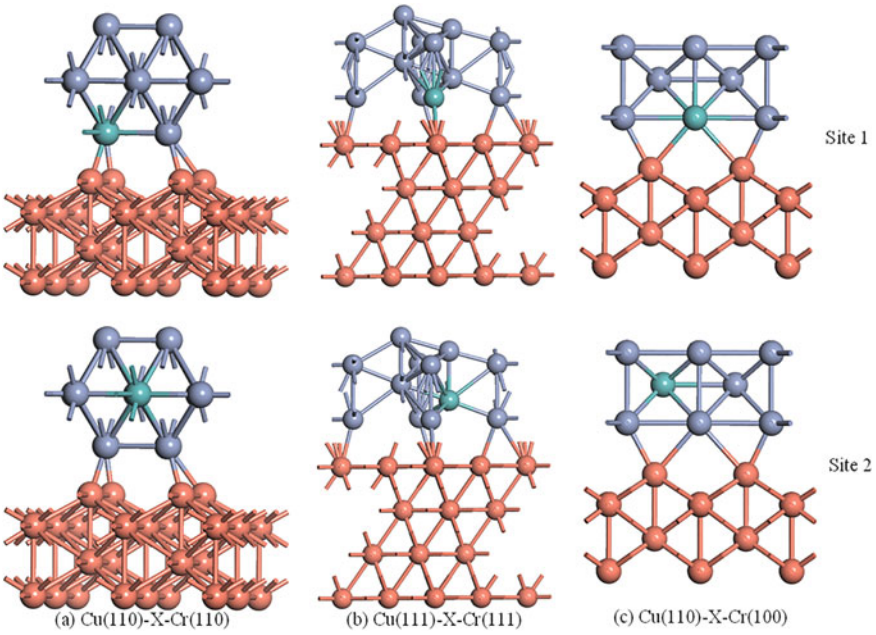

Fig. 3 Structure models of **a** Cu(110)/Cr(110), **b** Cu(111)/Cr(111) and **c** Cu(110)/Cr(100) doping sites

Table 2 The calculations for the charges, work functions, and interfacial distances of Cu(110)/Cr(100), Cu(111)/Cr(111) and Cu(110)/Cr(110) after doping W, Fe, Ni and Mo

Interface	Q/e	Work function/eV	d/ Å
Cu(110)-W1-Cr(100)	−2.38	3.508	2.383
Cu(110)-W2-Cr(100)	−2.86	3.346	2.439
Cu(110)-Fe1-Cr(100)	−1.50	3.353	2.402
Cu(110)-Fe2-Cr(100)	−1.84	3.321	2.485
Cu(110)-Ni1-Cr(100)	−1.93	3.199	2.431
Cu(110)-Ni2-Cr(100)	−1.74	3.591	2.447
Cu(110)-Mo1-Cr(100)	−2.11	3.266	2.437
Cu(110)-Mo2-Cr(100)	−2.97	3.303	2.442
Cu(111)-W1-Cr(111)	−1.26	4.021	2.560
Cu(111)-W2-Cr(111)	−1.44	4.203	2.636
Cu(111)-Fe1-Cr(111)	−1.32	3.79	2.509
Cu(111)-Fe2-Cr(111)	−1.04	3.968	2.553
Cu(111)-Ni1-Cr(111)	−1.49	4.184	2.499
Cu(111)-Ni2-Cr(111)	−1.20	4.211	2.505
Cu(111)-Mo1-Cr(111)	−1.48	3.949	2.538
Cu(111)-Mo2-Cr(111)	−1.59	3.908	2.552
Cu(110)-W1-Cr(110)	−1.85	3.184	2.558
Cu(110)-W2-Cr(110)	−1.60	3.262	2.457
Cu(110)-Fe1-Cr(110)	−1.55	3.146	2.522
Cu(110)-Fe2-Cr(110)	−1.50	3.273	2.524
Cu(110)-Ni1-Cr(110)	−1.12	3.034	2.466
Cu(110)-Ni2-Cr(110)	−1.52	3.364	2.516
Cu(110)-Mo1-Cr(110)	−1.50	3.009	2.469
Cu(110)-Mo2-Cr(110)	−1.65	3.182	2.460

the other hand, the reduction in charge transfer prevents the electrons from moving and hence, to some extent, from escaping from the surface. This is useful if one wants to suppress the emission of electrons. Figure 4 shows the differential charge density distribution, with the gain of electrons in blue and the loss of electrons in yellow. A more intuitive observation on the amount of charge transfer is made. The interfacial distance basically did not change significantly with that before doping, but the doping of W, Fe, Ni and Mo made the atom distribution of Cr phase more disorderly, while the atoms of Cu phase still maintained regular distribution, which was consistent with the fact that doped metal and Cr phase formed solid solution.

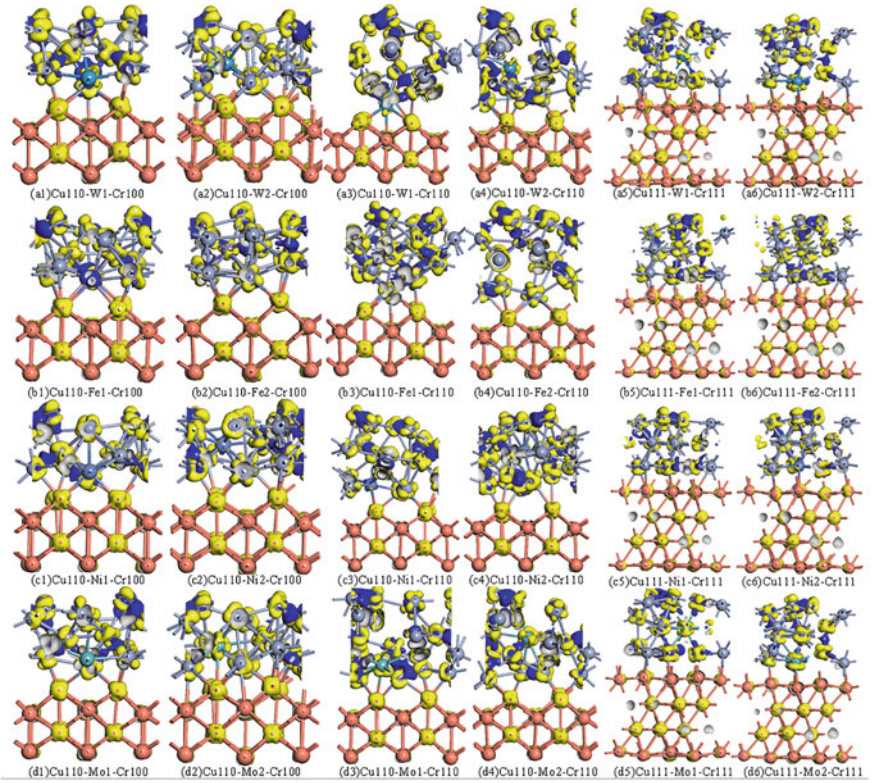

Fig. 4 The differential charge distribution of Cu(110)/Cr(100), Cu(110)/Cr(110), and Cu(111)/Cr(111) after doping **a** W, **b** Fe, **c** Ni and **d** Mo

4 Conclusions

Based on the experimental phenomenon that the breakdown position of the CuCr contact head in a vacuum circuit breaker may be the Cu–Cr phase boundary, a Cu–Cr interfacial binding model has been developed. The work function, density of states, work of interfacial separation, interfacial energy, charge transfer, band energy, and charge density distribution of Cu, Cr, Cu/Cr interfaces and W, Fe, Ni and Mo doped Cu/Cr interfaces are calculated from the first principles. The internal properties of CuCr contact breakdown have been analyzed from the microscopic atomistic point of view. In this paper, we provide a theoretical basis for increasing the voltage withstand ability of vacuum circuit breakers. This paper draws the following conclusions:

1. The CuCr interface junction was found to have a more minor work function than pure copper and pure chromium. The reduced work function is prone to field emission, thus increasing the possibility of electrical breakdown.

2. Three interfacial binding models Cu(110)/Cr(110), Cu(111)/Cr(111) and Cu(110)/Cr(100) are established in this paper. By comparing the separation work and interfacial energy, it is found that Cu(111)/Cr(111) is relatively stable.
3. The charge transfer is ordered as W > Mo > Ni > Fe from large to small. This order is roughly the same as the atomic numbers of the four metals. The doping of W, Fe, Ni and Mo to make their work function reach the expected value is ranked as W > Ni > Fe > Mo.

Acknowledgements This work was supported by the Science and Technology Project of State Grid Corporation of China (5500-202099518A-0-0-00).

References

1. Slade PG (1994) Advances in material development for high power, vacuum interrupter contacts. IEEE T Comp Pack Man 17(1):96–106
2. Lopes OF, Varela H (2018) Effect of annealing treatment on electrocatalytic properties of copper electrodes toward enhanced CO_2 reduction. ChemistrySelect 3(31):9046–9055
3. Chen XH, Zhou HL, Zhang T, Bi LM, Tian W, Fu SL, Li W, Liu XK, Ma FC, Zhang K, Sun H, Liu P (2019) Mechanism of interaction between the Cu/Cr interface and its chemical mixing on tensile strength and electrical conductivity of a Cu–Cr–Zr alloy. Mater Des 180:107976
4. Zhao F, Xu H, Yang ZM, Ding BJ (2000) Preparation of CuCr25 alloys through vacuum arc smelting and their properties. Trans Nonferrous Met Soc China 10(1):73–75
5. Zhang CY, Yang ZM, Wang YP, Ding BJ, Guo Y (2006) Preparation of CuCr25 contact materials by vacuum induction melting. J Mater Process Tech 178:283–286
6. Yang ZM, Zhang QL, Wang QF, Zhang CY, Ding BJ (2006) Vacuum arc characteristics on nanocrystalline CuCr alloys. Vacuum 81(4):545–549
7. Cao WC, Liang SH, Zhang X, Wang XH, Yang XH (2011) Effect of Fe on microstructures and vacuum arc characteristics of CuCr alloys. Int J Refract Met H 29:237–243
8. Cao WC, Liang SH, Zhang X, Wang XH, Yang XH (2011) Effect of Mo addition on microstructure and vacuum arc characteristics of CuCr50 alloy. Vacuum 85:943–948
9. Perdew JP, Burke K, Ernzerhof M (1996) Generalized gradient approximation made simple. Phys Rev Lett 78(7):1396–1396
10. Dobrota AS, Pašti IA, Mentus SV, Johansson B, Skorodumova NV (2020) Altering the reactivity of pristine, N- and P-doped graphene by strain engineering: a DFT view on energy related aspects. Appl Surf Sci 514:145937
11. Wang JX, Zhou Q, Lu ZR, Wei ZJ, Zeng W (2019) Gas sensing performances and mechanism at atomic level of Au-MoS2 microspheres. Appl Surf Sci 490:124–136
12. Li K, Li N, Yan NN, Wang TY, Zhang YT, Song Q, Li HJ (2020) Adsorption of small hydrocarbons on pristine, N-doped and vacancy graphene by DFT study. Appl Surf Sci 515:146028
13. Grimme S, Antony J, Ehrlich S (2010) A consistent and accurate ab initio parametrization of density functional dispersion correction (DFT-D) for the 94 elements H-Pu. J Chem Phys 132(15):154104
14. Clementi E, Raimondi DL (1963) Atomic screening constants from SCF functions. J Chem Phys 38(11):2686–2689
15. Gui XX, Zhou Q, Peng SD, Xu LN, Zeng W (2020) Dissolved gas analysis in transformer oil using Sb-doped graphene: a DFT study. Appl Surf Sci 533:147509

16. Jin Y, Liu M, Zhang CH, Leygraf C, Wen L, Pan JS (2017) First-principle calculation of volta potential of intermetallic particles in aluminum alloys and practical implications. J Electrochem Soc 164(9):465–473
17. Peng X, Hu L, Qin F, Zhou YH, Chu PK (2018) Low work function surface modifiers for solution-processed electronics: a review. Adv Mater Inter 5:1701404
18. Xu YX, Chen L, Pei F, Chang KK, Du Y (2017) Effect of the modulation ratio on the interface structure of TiAlN/TiN and TiAlN/ZrN multilayers: first-principles and experimental investigations. Acta Mater 130:281–288
19. Sun WM, Zhang L, Huang XY, Liu J, Wang H, Bu YX (2017) Works of separation for (0001)ZnOl(111)ZrO2 interfaces: a first-principle study. Comp. Mater. Sci. 136:157–162
20. Hashibon A, Elsässer C, Rühle M (2005) Structure at abrupt copper-alumina interfaces: An Ab initio study. Acta Mater 53:5323–5332
21. Dudiy SV, Lundqvist BI (2004) Wetting of TiC and TiN by metals. Phys Rev B 69:125421
22. Sun DQ, Wang YX, Lu YL, Chen Z, Rao QL (2016) Influence of atom termination and stacking sequence on the θ′/Al interfaces from first-principles calculations. Superlattice. Microst. 94:215–222
23. Wang L, Shang JX, Wang FH, Zhang Y (2013) First principles study of α2-Ti3Al(0001) surface and γ-TiAl(111)/ α2-Ti3Al(0001) interfaces. Appl Sur Sci 276:198–202
24. Shi ZJ, Liu S, Zhou YF, Yang QX (2018) First-principles calculation on the relationships of h-WC/γ-Fe interface. J Phys Chem Solids 123:11–18
25. Xian YJ, Qiu RZ, Wang X, Zhang PC (2016) Interfacial properties and electron structure of Al/B4C interface: a first-principles study. J Nucl Mater 478:227–235
26. Liu DK, Gui YG, Ji C, Tang C, Zhou Q, Li J, Zhang XX (2019) Adsorption of SF6decomposition components over Pd (1 1 1): a density functional theory study. Appl Surf Sci 465:172–179
27. Li K, Miao XJ, Qian D, Li YL, Meng Y, Pang YJ, Yang B, Li YH, Hao LC, Fan YY (2021) Arc erosion resistance of CuCrMo films deposited via magnetron sputtering. Mater Res Express 8(6):066402
28. Li J, Zuo TT, Xue JL, Ru YD, Zhao XK, Gao ZS, Han L, Xiao LY (2021) Optimization of microstructure and properties of CuCr /CNTs composites by hot-pressed sintering and rolling. Mater Rev 35(1B):02078–02085

Simulation on the Contact Temperature of Sliding Friction Pair Under Rain Condition

Congxin Han, Tunan Wang, Min Wang, Jing Xu, and Fengyi Guo

Abstract The pantograph slide contact temperature and wear of contact surface are greatly affected the electric locomotive working condition under the rain. In this paper, a sliding electrical contact roughness surface model with high speed and different current under the rain is established, which effectiveness is verified by the high performance sliding electrical contact experiment system. Then, the correlation between contact temperature, average roughness slope and average roughness height under the rain is researched via the simulation model. The results show that the impact of rainfall on contact temperature is more pronounced than that of contact current. As the average roughness height increases in various rainfall scenarios, the contact temperature initially undergoes a decrease, followed by an increase, and ultimately returns to a decrease. The average roughness slope is negatively correlated with the contact temperature of slide under different rainfall. The above conclusion has great significance for effectively reducing t the temperature experienced by the pantograph slide at the contact interface within the sliding friction pair.

Keywords Contact temperature · Average roughness slope · Average roughness height · Rainfall

C. Han
The Faulty of Electrical and Control Engineering, Liaoning Technical University, Huludao 125105, China
e-mail: 471820204@stu.lntu.edu.cn

T. Wang · M. Wang · J. Xu · F. Guo (✉)
The College of Electrical and Electronic Engineering, Wenzhou University, Wenzhou 325035, China
e-mail: 20195207@wzu.edu.cn

T. Wang
e-mail: 20451840019@wzu.edu.cn

M. Wang
e-mail: 21451841025@wzu.edu.cn

J. Xu
e-mail: 21451842014@wzu.edu.cn

© Beijing Paike Culture Commu. Co., Ltd. 2024

X. Dong and L. Cai (eds.), *The Proceedings of 2023 4th International Symposium on Insulation and Discharge Computation for Power Equipment (IDCOMPU2023)*, Lecture Notes in Electrical Engineering 1102, https://doi.org/10.1007/978-981-99-7405-4_46

1 Introduction

Pantograph-Catenary (PC) system is one of the important components of electrified railway. The electric energy required by the train is collected through the contact point of the pantograph, so the real contact area directly affects the security and effectiveness of the train. Due to the sliding friction and contact current, the contact area temperature between the slide and the contact wire increases quickly during the operation of pantograph. This situation will change the contact state of the slide surface. Furthermore, the actual contact area will also change, the surface of the friction pair is worn [1]. There are many reasons for the temperature rise in the contact area, such as the pantograph vibration pressure, sliding friction, contact current, contact wire exposed to the rain, frost conditions, etc. In recent years, the train accident caused by extreme environment has emerged in endlessly. To maintain electrical performance, PC system need to operate within a range of temperatures. Therefore, it is significance to research the surface temperature rise characteristics of the sliding friction pair in PC system under special environment.

In recent years, the researches on contact surface of PC system mainly focus on dynamic pressure characteristics, arc erosion, current collection quality, friction and wear, etc. [2–4]. The specific research factors include mechanical friction, contact pressure, contact current and contact resistance. Xie [5] established an arc ablation model to study the directional movement behavior of the arc under the magnetic field force, which can reduce catenary ablation. Yang [6] established an arcing model based on MHD, the influence of cross wind and input current on arc motion behavior and arc voltage was studied. Through the establishment of a simulation model for the temperature field, Wang [7] performed simulations to investigate the thermal time constants and steady-state temperature rise of the contact area. Guo [8] constructed a simulation model of the temperature field in sliding electrical contacts, taking into account the presence of rough surfaces. There are few researches on the influence of micro surface temperature of slide and environmental factors. In particular, the temperature rise of contact surface will be affected when pantograph is exposed to rain, which will further affect the stability and security of train operating.

This paper presents the development of a contact model for rough surfaces based on a microscopic analysis of surface topography. And the relationship between the contact surface attributes and the contact area temperature rise of the slide is studied under rain condition.

2 Construction of Rough Surface Contact Model of Sliding Friction Pair

2.1 Three-Dimensional Roughness Surface Topography Simulation

The contact between rough surfaces exists in the form of contact spots, so the actual contact surface is rough and discontinuous. In this paper, the contact problem in PC system is simplified as the contact between rough surface and smooth surface, where the sliding surface is rough surface, and the contact line is smooth surface [9]. The contact model for rough surfaces in sliding electrical contacts is established using the W-M function [10], as depicted in (1). At first, the surface roughness data of slide in experimental equipment are collected. The structure function method is utilized to calculate the G and D of the system. [10]. Finally, the three-dimensional simulation diagram of rough surface can be established.

$$Z(x, y) = L\left(\frac{G}{L}\right)^{(D-2)}\left(\frac{\ln\gamma}{M}\right)^{\frac{1}{2}}\sum_{m=1}^{M}\sum_{n=0}^{n_{\max}}\gamma^{(D-3)n}* \left[\cos\varphi_{mn} - \cos\left(\frac{2\pi\gamma^{n}\sqrt{x^2+y^2}}{L}\right)\cos\left[\left(\tan^{-1}\left(\frac{y}{x}\right) - \frac{\pi m}{M}\right)\right] + \varphi_{mn}\right] \tag{1}$$

$$n_{\max} = \text{int}\left[\frac{\log\left(\frac{L}{L_S}\right)}{\log\gamma}\right] \tag{2}$$

where, L is sample length, which means the contact surface side length. G represents the fractal roughness. D represents the geometric characteristics of two-dimensional surfaces, with values typically ranging from 2 to 3 for surface profiles. γ is the scale parameter and $\gamma > 1$, which is set to be 1.5. M determines the superimposed ridges number random topography in different directions, and $M > 10$. φ_{mn} represents a random phase that follows the uniform distribution from 0 to 2π. $n_{\max}$ is the highest frequency order. int $[X]$ means the integer part of X. L_S is the cut-off frequency.

2.2 Physical Models and Boundary Conditions of Temperature Field

The physical model in this paper is established according to the experimental equipment by COMSOL Multiphysics, so the geometric and related material parameters

of the physical model are all obtained by actual measurement, and their values are presented in Tables 1 and 2, respectively.

The whole rough surface contact physical model of sliding electrical contact establishment process can be described in Fig. 1. In the established physical model, the temperature field involves friction heat and current heat, thus, the boundary conditions of current and heat transfer are necessary. In order to illustrate the boundary conditions clearly involved in the temperature field calculation, the simplified geometry schematic of established PC system physical model is shown in Fig. 2. The part highlighted in red represents the name of the model. Blue are used to distinguish material properties. And the black words provide the boundary conditions of the model, where the initial contact current through the slide is set in current field, and the brush is grounded.

The motion boundary conditions are indicated by arrows, which is achieved by adding the structural mechanical field. Based on the direction of the arrow, the copper contact wire undergoes circular motion within the x–y plane, while the slide undergoes reciprocating motion along the x-axis. Thus, it is possible to simulate the "z-shaped" motion between the pantograph and the contact wire. The initial simulation temperature is set as 20 °C in heat transfer filed. The heat dissipation mode of the upper slide surface is set as forced convection heat dissipation. Finally, the simulation model is meshed and the temperature field can be calculated.

Table 1 Geometric parameters of model

Material	Parameters	Size
Contact wire	Main radius (mm)	491
	Radius (mm)	8
	Abrasion value (mm)	1
Slide	Length (mm)	250
	Height (mm)	35
	Width (mm)	25

Table 2 Material parameters of contact wire and carbon slide

Parameters	Slide	Contact wire
Young's modulus (Pa)	1.26×10^{10}	110×10^{9}
Poisson's ratio	0.425	0.35
Electrical conductivity (S/m)	7.8×10^{3}	5.56×10^{7}
Thermal conductivity (W/m k)	260	380
Density (kg/m^3)	2400	8700
Resistivity (Ω·m)	8×10^{-6}	1.72×10^{-8}
Heat capacity at constant pressure (J/(kg K)	700	380
Friction coefficient	0.2	0.2

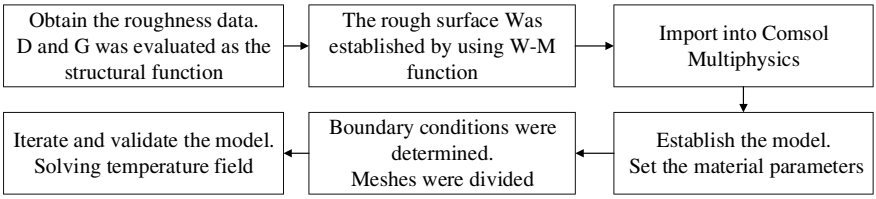

Fig. 1 Flow chart of physical model establishment

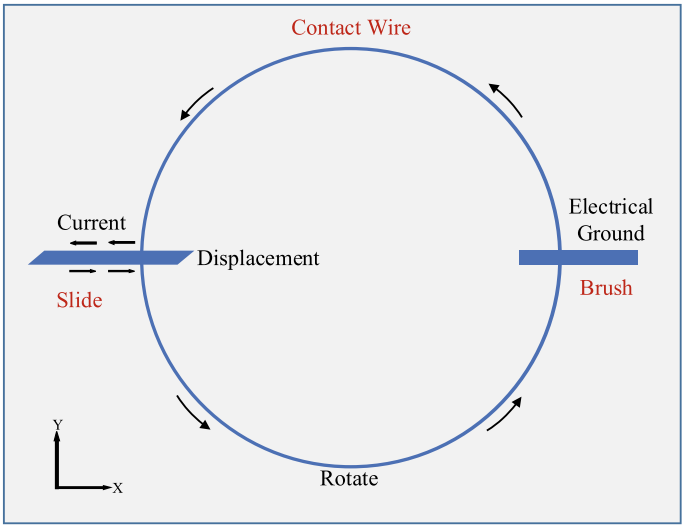

Fig. 2 Simplified geometry schematic of PC system finite element simulation model

2.3 Instructions of Important Surface Roughness Parameters

The important surface roughness parameters are the root-mean-square (RMS) roughness which are defined as

$$\text{RMS roughness} = \sqrt{\frac{1}{L}\int_0^L y^2(x)dx} \tag{3}$$

where $y(x)$ is the distance of points in the surface from the mean plane and L is the length of the trace.

The average roughness slope is defined as

$$m = \frac{1}{L}\int_0^L |\frac{dy(x)}{dx}|dx \tag{4}$$

The two parameters of surface roughness are given by (5).

$$\sigma = \sqrt{\sigma_1^2 + \sigma_2^2} \text{ and } m = \sqrt{m_1^2 + m_2^2} \tag{5}$$

where σ_1 and σ_2 are the effective RMS surface roughness and m_1 and m_2 are the mean absolute asperity slope of the contacting surfaces, respectively.

3 Experimental Verification

3.1 Experimental Equipment

A high speed and high current sliding electrical contact experimental system is used to verify the simulation model built in this paper. The experimental system includes two parts, whose schematic diagram is shown in Fig. 3. One is the sliding electrical contact experimental equipment, which includes the contact wire embedded on a turntable and the pantograph slide. The other is the control and measurement equipment, which can adjust and record the contact current, sliding speed, contact pressure and so on. The real-time data can be stored in the data acquisition (DAQ) card and displayed on the upper computer.

3.2 Experimental Verification

To validate the accuracy of the proposed model, a series of sliding electrical contact experiments and simulations are conducted under identical conditions. To ensure that the roughness of the slide surface meets the testing requirements, it is polished using sandpaper and a file. The roughness parameters are then measured by an SJ-210 roughness tester. The transient temperature of contact area can be detected by FLIR T530 infrared thermal imager.

After several experiments and simulation tests, it can be seen that the slide surface temperature can always reach the steady state before 100 s. Therefore, the experimental and simulation duration is set as 100 s, and the maximum temperature of the slide surface is measured at the 100th seconds. The first group of verification experiments is conducted under the following conditions: a contact current of 60 A, a contact pressure of 50 N, a sliding speed of 40 km/h, and a slide surface roughness of 2 μm.

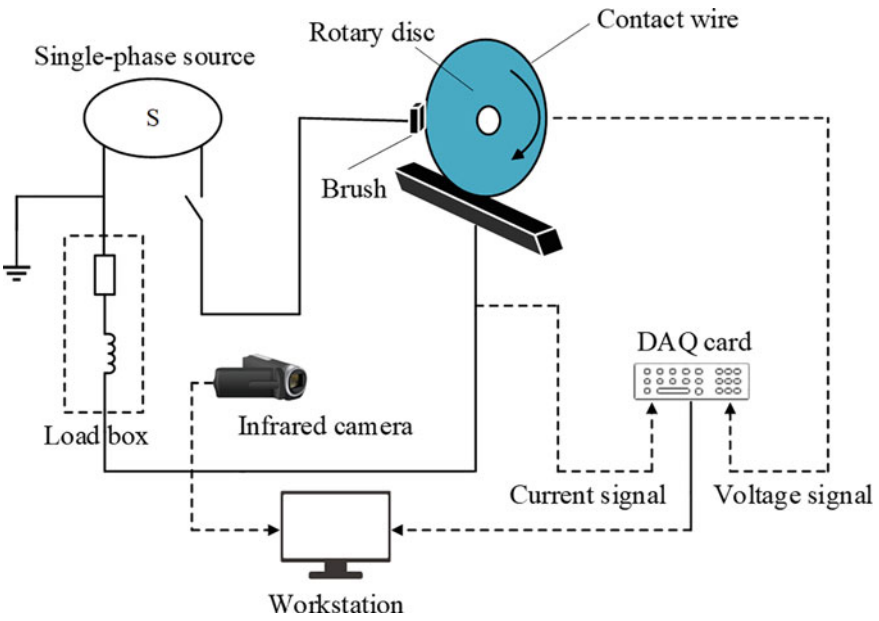

Fig. 3 Schematic diagram of the sliding electrical contact experimental system

In Fig. 4, the maximum temperatures of the slide surface obtained by simulation and experiment were 40.2 and 38.6 °C, respectively. Via comparing the experimental and simulation results, the simulated error of the maximum temperature is only 1.6 °C, which means the rough surface contact model of sliding friction pair established in this paper is feasible.

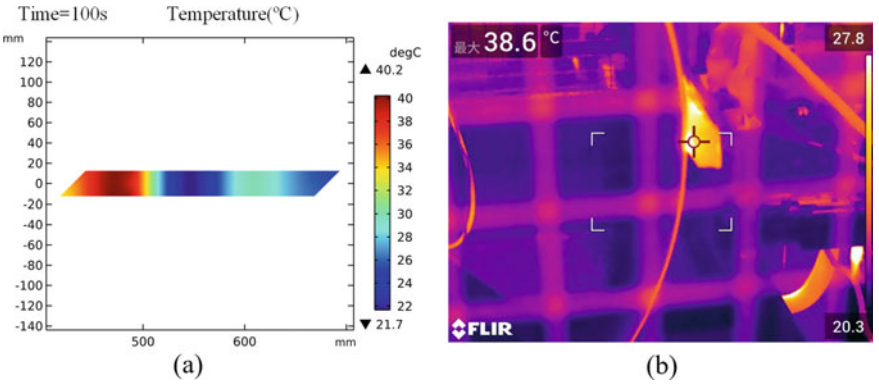

Fig. 4 The slide surface temperature distribution cloud diagram. **a** Simulation result. **b** Experiment result

4 Results and Analysis

To research the relationships between contact surface properties and contact area temperature rise under rain condition. A thin layer of water molecules is set on the contact surface to simulate the rainfall, the thin layer material is set as the physical property of water, and the different thickness of thin layer can simulate the different rainfall [11]. Under light rain condition, the thin layer is set as 0.01, and 0.09 mm is set under heavy rain condition.

4.1 Surface Temperature Distribution of Slide Under Rain Condition

The simulation is conducted with the following set of conditions: a contact current of 100A, a contact pressure of 60 N, a sliding speed of 380 km/h, and a simulation time of 100 s. The simulation results are shown in Fig. 5, which are the surface temperature distribution cloud diagrams of slide and contact wire under no-rain and light rain conditions respectively. In Fig. 5, under no-rain and light rain condition, the maximum temperature of slide surface is 61.2, 56.8 °C, respectively. Figure 5 shows the surface temperature distribution of slide is more likely to form high-temperature trailing under no-rain condition, while the surface temperature distribution of slide is more uniform in light rain.

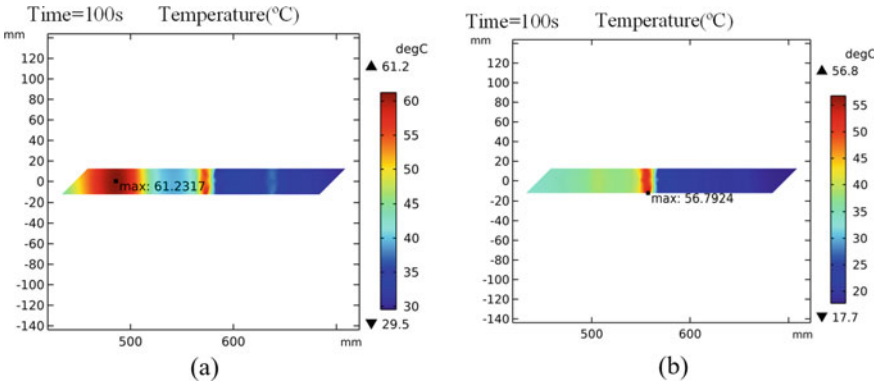

Fig. 5 Slide surface temperature deformation diagram. **a** No-rain condition. **b** Light rain condition

4.2 *Effect of Average Roughness Height on Contact Temperature*

The established simulation model is used to research the distribution relationships between average roughness height and contact temperature rise under different rainfall conditions. The simulation conditions are set as follows: an average roughness slope of 0.4, a contact currents of 100 A, a sliding speed of 380 km/h, and a simulation time of 100 s, respectively. The average roughness height ranges from 1.0 to 4.0 μm. As shown in Fig. 6, with the average roughness height increasing, the contact temperature shows a fluctuating trend of first decreasing, then increasing and then decreasing.

The rainy condition can enhance the heat dissipation ability of slide. The temperature rise in light rain is higher than that in heavy rain. According to Fig. 6, the initial stage of temperature rise curve gradually decreases. Due to the increase of contact spots, with the average roughness height increasing from 1 to 2 μm, the slide roughness decreases, thus the friction heat reduces and the contact temperature decreases. And in the rising stage of the temperature rise curve, when the average roughness height increases, the asperities spikes of slide become higher, contact spots become fewer, contact resistance becomes larger and heat production increases. Thus, the contact area temperature at this time shows an increasing trend. When the average roughness height increases from 3 to 4 μm, the friction pair deforms gradually with the contact area temperature increasing. Stress and strain cause rough surface to be more uneven, which increases the friction heat. However, the contact spots of slide increased again, so the contact resistance becomes less and heat production decreases, so the contact area temperature decrease again. It can be found that the influence of friction heat on contact temperature rise gradually decreases and

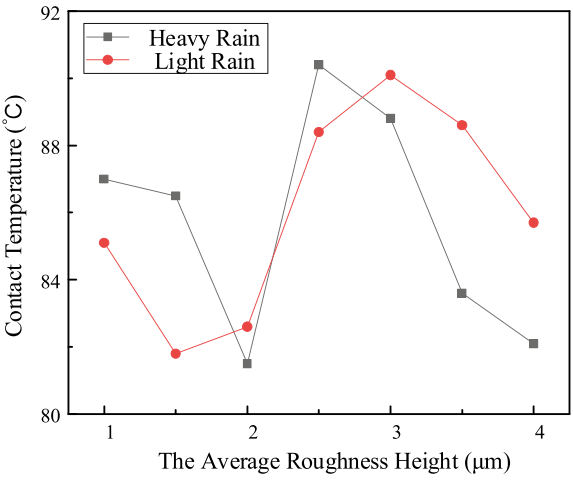

Fig. 6 Correlation analysis of average roughness height and contact temperature under the different rainfall conditions

the influence of joule heat on contact temperature rise gradually increases with the average roughness height increasing.

4.3 *Effect of Average Roughness Slope on Contact Temperature*

The relationships between average roughness slope and temperature rise of contact area is researched under different rainfall conditions. The average roughness height is set to 1.0 μm, while the remaining simulation parameters remain consistent with the aforementioned conditions. The average roughness slope ranges from 0.1 to 0.8. As shown in Fig. 7, only when the average roughness slope is less than 0.3, the temperature rises curves cross with different rainfall. In other cases, the contact temperature rise in heavy rain is lower than that in light rain. In addition, with an increase in the average roughness slope, there is a gradual reduction in the slide contact temperature.

The number of slide contact spot gradually decreases when the average roughness slope increases from 0.1 to 0.4. And the temperature rise curves crosses over in Fig. 7. The current density increases at each contact spot and the contact temperature increases. According to the section above, the heat dissipation capacity of slide in light rain is worse than that in heavy rain, therefore, the temperature decreases slowly or increases slightly under light rain condition. The asperities become larger when average roughness slope gradually increases from 0.4 to 0.8, and the adjacent contact spots fusing makes slide surface smoother. Further, the contact resistance decreases, resulting in less joule heat and contact temperature rise decreasing gradually.

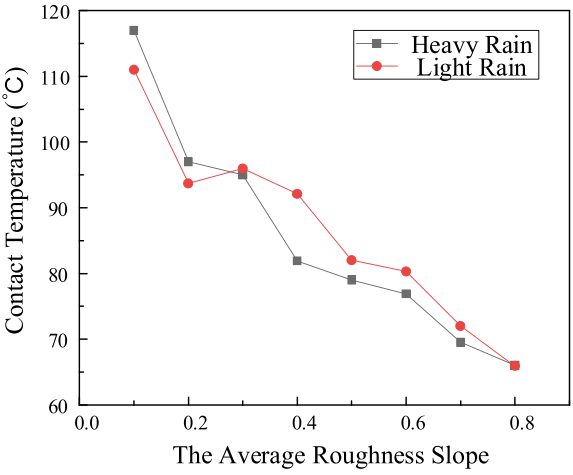

Fig. 7 The correlations between the average roughness slope and the contact temperature under the different rainfall

5 Conclusion

In this paper, A contact model for the rough surface of a sliding friction pair in a pantograph-catenary system was developed. The study further investigated the effects of two roughness parameters on the temperature rise in the contact area. The main conclusions are as follows.

1. With the average roughness height increasing from 1.0 to 4.0 μm, the influences of friction heat on contact temperature rise gradually decreases and the influence of joule heat on contact temperature rise gradually increases.
2. As the average roughness slope increases, there is a gradual decrease in the contact area temperature of the slide, indicating a consistent exponential decline trend. However, when the average roughness slope is small enough, such as 0.2, heavy rain is more favorable to the heat dissipation of slide compared with light rain condition.

References

1. He Z, Ni Z, Wang H, Yang Z, Fu W (2021) Effect of magnetic field on the current-carrying friction and wear performance of C/Cu contact pairs. In: 2021 international conference on electrical materials and power equipment (ICEMPE), pp 1–4 (2021)
2. Xu Z, Song Y, Liu Z (2022) Stress analysis and fatigue life prediction of contact wire located at steady arms in high-speed railway catenary system. In: IEEE transactions on instrumentation and measurement 71:1–12
3. Tian W, Yan P et al (2022) Effects of launch mass on sliding electrical contact. IEEE Trans Plasma Sci 50(7):2263–2269
4. Zhang C, Ren W, Wang T (2019) Modeling and experimental verification of contact sliding behavior for flexible spring components within electromechanical relays. IEEE Trans Compon Packag Manuf Technol 9(10):2046–2054
5. Xie W, Wu G, Wei W, Yang Z, Gao G (2020) Research on characteristics of the pantograph arc under the action of magnetic field. In: 2020 IEEE international conference on high voltage engineering and application, pp 1–4
6. Yang Z, Xu P, Wei W et al (2020) Influence of the crosswind on the pantograph arcing dynamics. IEEE Trans Plasma Sci 48(8):2822–2830
7. Wang Z, Guo F, Li S, Baatar B, Wang Y, Liang H (2017) Temperature characteristics of sliding friction pair under high-speed and strong-current conditions. 2017 IEEE Holm Conference on Electrical Contacts, pp 187–193
8. Guo F, Gu X, Li L, Wang Z, Wang T, Jia S (2022) Effect of surface microparameters on contact temperature of sliding electrical contact. IEEE Trans Ind Inf 18(9):5972–5981
9. Feng Y, Yang P, Zhang Y, Shi L, Hang Z, Feng Y (2022) Fractal model of thermal elastic-plastic contact of rough surfaces. Chinese J Const Mach 29(5):1500–1509(2022) (in Chinese)
10. Wei J, Wu C, Tian J, Chen Z, Liu C, Yu G, Wang J, Li L (2022) Study on adaptability of structure function method for calculating the fractal dimension of surface profile curve of coating. Electro Finis 36(17):911–914 (2022) (in Chinese)
11. Li L, Wang Z, Yang L, Hao Y, Zhang F (2017) Shed parameter optimization of large-diameter composite post insulators under wet condition based on electric field simulation. High Voltage Eng 43(6):1930–1936 (in Chinese)

Calculation of Pressure Distribution at the Interface of Polypropylene Insulated Cables and Joints

Ouyang Benhong, Wang Ge, Wang Yuli, Zhang Hongjun, Zhao Peng, and Huang Kaiwen

Abstract Thermoplastic polypropylene insulation material has excellent performance, high temperature resistance grade, recyclability, and significant economic and environmental advantages. Therefore, it has broad prospects in replacing traditional cross-linked polyethylene (XLPE) insulated cables. However, the long-term operational reliability of polypropylene insulated power cables is still being evaluated, especially the matching performance with traditional cold shrink joints needs to be effectively verified. By establishing a theoretical calculation model for the cold shrink intermediate joint structure of distribution network cables, this paper combines mechanical properties testing of silicone rubber material and Yeoh parameter model fitting to analyze the pressure distribution at the interface of polypropylene insulated cables. The study suggests that the pressure at the interface of cable joints gradually decreases radially from the inner layer to the outer layer, and the interface pressure is relatively high at the root of the stress cone and the high-voltage shielding pipe. The interference amount and conductor temperature will have an impact on the interface pressure, and a threshold analysis method for the failure of the interface pressure of the joint has been proposed, which can provide technical guidance for the matching of polypropylene insulated cable systems.

Keywords Polypropylene cable · Cold shrink joint · Interface pressure

1 Introduction

Polypropylene is a thermoplastic insulation material with excellent insulation performance, high temperature resistance, and plasticity for recycling [1]. Compared to traditional thermosetting XLPE insulated cables, the new type of thermoplastic polypropylene insulated cables have recyclable insulation materials after retirement,

O. Benhong · W. Ge (✉) · W. Yuli · Z. Hongjun · Z. Peng · H. Kaiwen
State Key Laboratory of Power Grid Environmental Protection China Electric Power Research Institute, Wuhan 430074, China
e-mail: 1144279028@qq.com

© Beijing Paike Culture Commu. Co., Ltd. 2024

X. Dong and L. Cai (eds.), *The Proceedings of 2023 4th International Symposium on Insulation and Discharge Computation for Power Equipment (IDCOMPU2023)*, Lecture Notes in Electrical Engineering 1102, https://doi.org/10.1007/978-981-99-7405-4_47

which not only solves the environmental protection problem of XLPE cable material recycling, but also eliminates cross-linking and degassing processes in the polypropylene cable manufacturing process. The manufacturing process is simple and efficient, and the energy consumption in the production process is significantly reduced [2]. The global warming potential (GWP) of polypropylene insulated cables can be reduced by about 40% throughout their entire life cycle [3, 4].

At present, through the copolymerization modification method, medium voltage polypropylene insulated power cable has been successfully developed. At the same time, the compatibility between cable accessories and new polypropylene insulated cables has not been verified. In particular, there is a lack of systematic technical means to analyze the thermal mechanical stress matching performance [5, 6]. The cold shrink intermediate joint cold shrink pipe support pipe shrinks inward after being pulled apart, and finally sticks to the insulation layer of the cable body and produces interference fit, forming interface pressure, thus ensuring the insulation strength and sealing performance of the cable line [7]. However, due to the presence of composite interfaces and concentration of electric field stress inside cable accessories, they have become weak links in cable insulation and typical parts of operational faults. Interface pressure control can affect the structural size and interface electrical resistance performance of polypropylene insulated power cables [8]. At this point, the electrical strength of the interface will approach the breakdown field strength of the material body [9]. Liu Song et al. studied the AC breakdown voltage characteristics of the XLPE insulation surface of cables that were sanded with different mesh numbers to form a interlayer medium with silicone rubber insulation. The results showed that when the interface was sanded with 400 mesh or more sandpaper, its breakdown voltage was higher than that of the ungrounded sample. The temperature of the cable increases during operation, which can cause deterioration of the insulation performance of the cable [10–12].

Based on the above situation, in order to analyze the interface pressure between medium voltage polypropylene insulated power cables and traditional cold shrink accessories, this paper establishes a theoretical calculation model for the cold shrink intermediate joint structure of distribution network cables, derives the calculation formula for the interface pressure between silicone rubber and polypropylene insulation in the intermediate joint, and combines the mechanical properties testing of silicone rubber materials to form Yeoh parameter fitting results [13]. Finally, by establishing a joint simulation model, Simulate the pressure distribution at the interface and analyze the influencing factors.

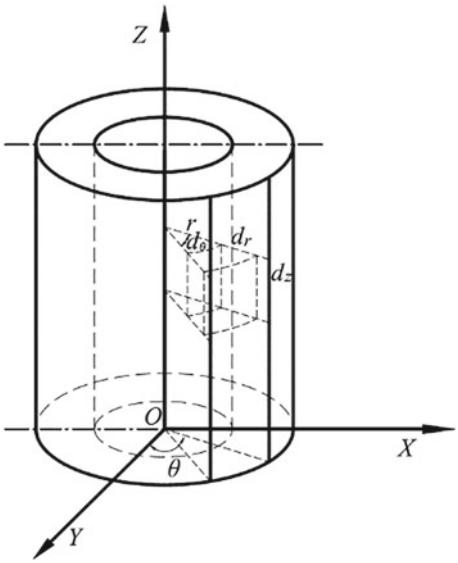

Fig. 1 Analysis model of thick walled cylinder

2 Computation Model

2.1 Interface Pressure Calculation Model

After installation, the inner surface of the cable accessory will be compressed by the cable body, resulting in a certain amount of swelling and deformation of the cable accessory. According to elastic–plastic mechanics, before installation, when the ratio of the outer radius b to the inner radius a of the cylinder is greater than 1.2, it is called a thick walled cylinder. The thick walled cylinder model is shown in Fig. 1. The thick walled cylinder model can be used to analyze the interface pressure of cable accessories.

2.2 Joint Simulation Model

A two-dimensional axisymmetric 10 kV joint model was established. The simulation model structure is shown in Fig. 2.The cable cold shrink accessories are assembled with the main insulation polypropylene of the cable to form a composite interface with different media. The silicone rubber of the accessories compresses and deforms at the composite interface with a certain amount of interference, generating pressure.

The boundary conditions at both ends of the model are set as roller support constraints. In the mesh generation of two-dimensional models, the deformation and

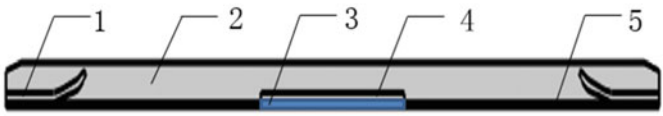

1- Stress cone 2- Accessory insulation 3- Pressure connecting pipe 4- High voltage shielding pipe 5- Polypropylene

Fig. 2 Simulation Model of 10 kV cable intermediate joint

stress of silicone rubber on the interference surface are studied, so the division of silicone rubber is relatively fine, while the mesh in polypropylene and conductor models is less. The silicone rubber material of the cable intermediate connector accessories has a small volume change during the compression deformation process, which is generally regarded as an approximately incompressible and isotropic hyperelastic material. The change process is complex and highly nonlinear. Therefore, based on the rubber hyperelastic Yeoh constitutive model, the project uses the three material parameters C_{10}, C_{20} and C_{30} related to the material strain energy bias to calculate the interface pressure.

3 Simulation Result

3.1 Interface Pressure Distribution

In order to analyze the axial distribution of interface pressure at the composite interface, the axial interface pressure data on the joint at the composite interface was collected, and the interface pressure distribution was obtained as shown in Fig. 3. It can be seen that the middle joint of the cable is an axisymmetric structure, and the trend of interface pressure change from both ends to the center point is the same.

The contact surface between semi conductive silicone rubber and polypropylene with a stress cone at 0–30 mm and 380–410 mm, with an interface pressure of about 0.255 MPa. On the contact surface between insulating silicone rubber and polypropylene, the interface pressure is 0.213 Mpa. On the contact surface between the semi conductive silicone rubber of the high-voltage shielding tube and the pressure connecting pipe, the maximum interface pressure is 0.263 MPa. It can be seen that the interface pressure at the semi conductive silicone rubber is higher, which is because the elastic modulus of semi conductive silicone rubber is greater than that of insulating silicone rubber.

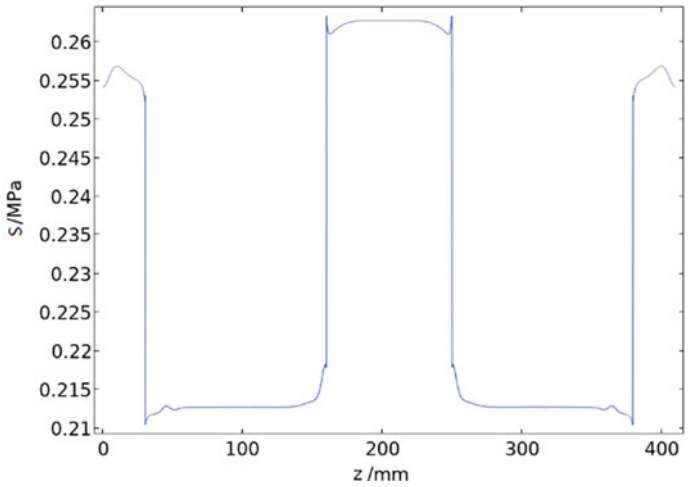

Fig. 3 Axial distribution of interface pressure

3.2 Analysis of the Impact of Interference

By changing the interference of the model, simulate and analyze the impact of interference on interface pressure. The axial distribution of pressure at the interface under different interference amounts is shown in Fig. 4. The curve of pressure change at different positions of the interface with interference amounts is shown in Fig. 5. The maximum and minimum stresses corresponding to different interference amounts are shown in Table 1.

According to Table 1, for every 1 mm increase in interference, the maximum interface pressure increases by approximately 0.06 MPa.

In order to simulate the gradual failure of the joint during the expansion process of silicone rubber, the interference amount increased from 1 mm in steps of 1–12 mm. The simulation analyzed the effect of the interference amount on the composite interface strain, and the results are shown in Fig. 5. From the figure, it can be seen that during the process of increasing the interference from 1 to 9 mm, the strain change pattern at the interface is the same. When the interference amount is 10 mm, the strain curve at the interface has severely deformed, while when it exceeds 10 mm, the simulation results do not converge. It can be considered that when the interference amount exceeds 9 mm, the silicone rubber material of the joint has torn and failed.

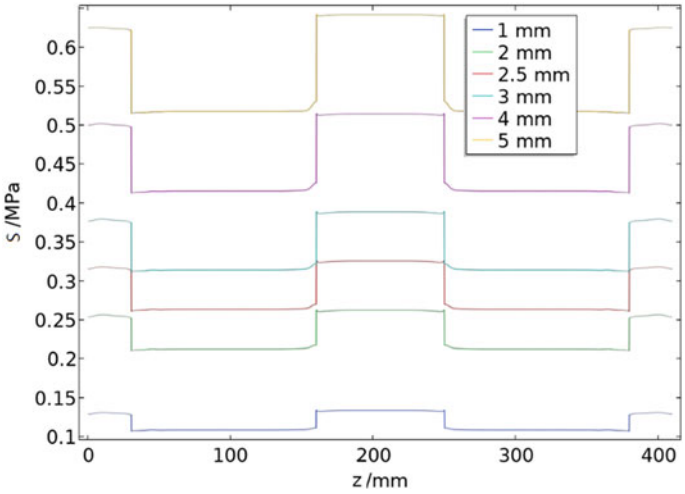

Fig. 4 Effect of different interference values on interface pressure distribution

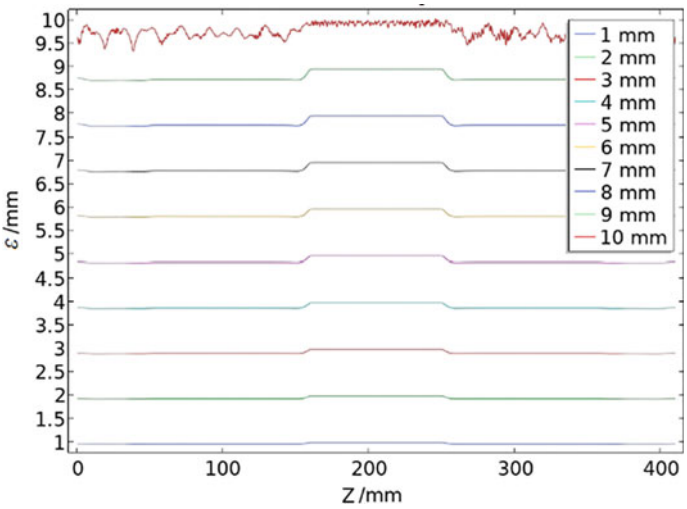

Fig. 5 The effect of different interference values on interface strain

Table 1 Maximum and minimum stress with different interference values

Interference amount	1 mm	2 mm	2.5 mm	3 mm	4 mm	5 mm
Maximum stress (MPa)	0.14	0.27	0.33	0.39	0.52	0.65
Minimum stress (MPa)	0.11	0.21	0.26	0.31	0.41	0.51

3.3 Temperature Impact Analysis

The parameters of the non aging silicone rubber constitutive model were brought into the simulation model, and the interface pressure distribution of the joint at different temperatures was calculated when the interference was 2 mm, as shown in Fig. 6.

According to the calculation results of interface pressure in Fig. 6, take one point at the root of the stress cone, one point at the insulation silicone rubber, and one point at the high-voltage shielding tube. The variation of interface pressure with temperature is shown in Tables 2, 3 and 4.

From the above results analysis, it can be concluded that as the temperature increases, the pressure at the composite interface shows a trend of first increasing and then decreasing. At 75 °C, the interface pressure at the three positions will reach its maximum value. The interface pressure values at the root of the stress cone and the high-pressure shielding tube have a relatively high change rate with the increase

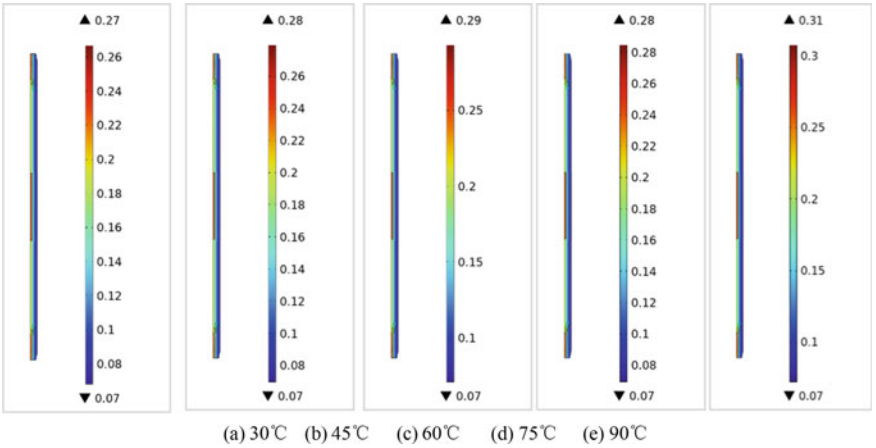

Fig. 6 Simulation distribution of interface pressure at intermediate joints under different temperatures

Table 2 Interface pressure and its change rate at the root of the stress cone at different temperatures

Temperature/°C	30	45	60	75	90
Interface pressure/MPa	0.257	0.269	0.281	0.295	0.273
Change ratio/%	/	4.67	4.46	4.98	−7.46

Table 3 Changes in interface pressure of insulated silicone rubber with temperature

Temperature/°C	30	45	60	75	90
Interface pressure/MPa	0.213	0.218	0.222	0.225	0.217
Change ratio/%	/	2.35	1.83	1.35	−3.56

Table 4 Changes in interface pressure of high voltage shielding tube with temperature

Temperature/°C	30	45	60	75	90
Interface pressure/MPa	0.262	0.275	0.288	0.302	0.280
Change ratio/%	/	4.96	4.73	4.86	−7.28

of temperature, and the change rate is basically the same: within the range of 0–75 °C, for every 15 °C increase in temperature, the interface pressure increases about 0.012 MPa. The interface pressure value at the insulation silicone rubber has a relatively low change rate with the increase of temperature. When the temperature is higher than 75 °C, the interface pressure decreases, mainly due to changes in the material properties of silicone rubber. When the temperature is higher than 75 °C, the effective crosslinking density of silicone rubber materials decreases, intermolecular and intermolecular chain segment interactions weaken, and stress decreases. When the temperature reaches 90 °C, although the interface pressure value decreases, it still meets the requirements for interface pressure for normal operation of the attachment, indicating that within the temperature range of normal operation of the cable intermediate joint, the temperature effect will not cause interface pressure failure of the joint.

4 Conclusion

1. Through simulation, it is shown that the interface pressure of the cable joint gradually increases radially from the outer surface to the inner contact surface, and is symmetrically distributed along the axial direction about the high-voltage shielding tube.
2. As the interference increases, the interface pressure at different axial positions of the joint increases linearly. When the interference exceeds 9 mm, the silicone rubber material of the joint tears and fails.
3. As the temperature increases, the interface pressure increases to its maximum value at 75 °C. For the interface pressure, for every 15 °C increase in temperature within the range of 0–75 °C, it increases by approximately 0.012 MPa.
4. Combined with the interference of cold shrink joints and the thermal deformation performance of polypropylene insulation materials, the structural stability and reliability of polypropylene insulated power cables during long-term operation can be analyzed, and accelerated aging tests are carried out on the new polypropylene cable system to support the reliability evaluation and verification of polypropylene cables in the distribution network.

Acknowledgements Supposed by Long term research project of China Electric Power Research Institute (GY80-22-005)

References

1. Xingyi H, Jun Z, Pingkai J (2018) Thermoplastic power cable insulation materials: history and development. High Voltage Tech 44(5) (in chinese)
2. Jiankang Z, Peng Z, Zhengzheng C et al (2017) Review of research progress on insulation materials for high voltage DC cables. High Voltage Tech 43(11) (in chinese)
3. Kurahashi K, Matsuda Y, Ueda A et al (2002) The application of novel polypropylene to the insulation of electric power cable. In: IEEE/PES transmission and distribution conference and exhibition, Yokohama, Japan
4. Albertini M, Bareggi A, Caimi L et al (2014) Development and qualification of 150 kV cable produced with highly innovative P-Laser technology. CIGRE 2014; PARIS: B1–304
5. Enel reduces the environmental impact of its supply chain through P-Laser. Italy, Prysmain Group 2012
6. Xia W, Dong Y, Shengjie D etc (2018) Discussion on several key issues in the design of high voltage cable accessories. High Voltage Tech 44(8):7
7. Jing Z, Shengnan H, Liang H etc (2022) The effect of long-term cold and hot cycles on the interface pressure of cable accessories. Insulat Mater 55(2):5. (in chinese)
8. Zhidong J, Yujin Z, Weinan F et al (2017) Calculation and analysis of interface pressure at the cold shrinkage intermediate joint of 10kV XLPE Cable. High Voltage Tech 43(2):5 (in chinese)
9. Guangxu D, Chunhua F, Rong X et al (2022) The effect of temperature and thermal aging on the interface pressure of cable silicone rubber accessories. Insulat Mater 55 (11):100–108. (in chinese)
10. Song L, Jiakang P, Xia W etc (2013) Analysis of factors influencing the interface pressure of high voltage cable accessories. Insul Mater 46(6):4. (in chinese)
11. Jing Z, Shengnan H, Liang H etc (2022) The effect of long-term cold and hot cycles on the interface pressure of cable accessories. Insul Mater 55(2):5
12. Guangxu D, Chunhua F, Rong X et al (2022) The effect of temperature and thermal aging on the interface pressure of cable silicone rubber accessories. Insulmaterial, 55(11):100–108
13. Bragatto T, Cresta M, Gatta FM et al (2019) A 3-D nonlinear thermal circuit model of underground MV power cables and their joints. Electric Power Syst Res 173(AUG):112–121

Transition of the Long-Term Stability of Stable ZnO Varistors Due to the Elevated Aging Temperature

Wuzhou Zhu, Yanqun Liao, Danbing Liu, Di Li, Qiang Wang, Huihong Li, Yadi Wang, and Ao Gao

Abstract ZnO varistor ceramics are important for overvoltage protections in power system owing to their outstanding nonlinear current density–electric field characteristics. Stable ZnO varistor ceramics with steadily decreasing power loss are gradually applied despite common understandings about their aging behaviors. In this study, they are employed for accelerated dc aging at an elevated aging temperature. They are found to exhibit a power loss transition during the aging. The typical "crossover" in J–E curves disappears after the transition. They continuously move to high-current regions afterwards. The further recovery experiments suggest that irreversible electrical degradation has been caused by the elevated temperature. The frequency-domain spectroscopy results show that the real part of the dielectric constant also cannot be recovered. The above results suggest the interface states of stable samples can only remain stable at a certain range of temperature. Otherwise, they would combine with mobile ions in depletion layers, causing the ZnO varistor ceramics to lose their long-term stability. The findings of the study provide a reference for establishing the condition assessment method for stable ZnO varistor ceramics.

Keywords Stable ZnO varistor ceramics · Dc aging · Long-term stability · Double Scottky barrier

W. Zhu · Y. Liao · D. Liu · D. Li · Q. Wang · H. Li · Y. Wang
Zhuhai Power Supply Bureau of Guangdong Power Grid Company Limited, Zhuhai 519000, China
e-mail: wukning@xjtu.edu.cn

D. Li
e-mail: lijy@xjtu.edu.cn

A. Gao (✉)
State Key Laboratory of Electrical Insulation and Power Equipment, Xi'an Jiaotong University, Xi'an 710049, China
e-mail: gao1020@stu.xjtu.edu.cn

© Beijing Paike Culture Commu. Co., Ltd. 2024

X. Dong and L. Cai (eds.), *The Proceedings of 2023 4th International Symposium on Insulation and Discharge Computation for Power Equipment (IDCOMPU2023)*, Lecture Notes in Electrical Engineering 1102, https://doi.org/10.1007/978-981-99-7405-4_48

1 Introduction

ZnO varistor ceramics are the key elements of metal oxide arresters (MOAs), which are widely used for overvoltage protections and surge absorptions due to their outstanding nonlinear current density–electric field (J–E) characteristics [1]. In most cases, they are connected in parallel with electrical equipment, thereby clipping off overvoltage shocks [2]. The electrical performance of MOAs plays an important role in determining the insulation level of power equipment and the reliability of power system. However, the long-term operation leads to the aging of ZnO varistor ceramics, which further causes degradation or failure of MOAs. Therefore, the aging of ZnO varistor ceramics is a long-standing concern for the varistor community [3, 4].

The aging of ZnO varistor ceramics generally manifests as increasing power loss accompanied by the deterioration of electrical properties, e.g., a reduction in the nonlinear coefficient, and a rise in the leakage current [5]. Their power loss also increases with the elevated aging temperatures. The classic ion migration model proposed by Gupta explains those aging phenomena as the degradation of the double Schottky barrier (DSB) at grain boundaries (GBs) [6]. The model indeed applies to these traditional instable samples, and becomes the theoretical foundation of the current IEC standard for condition assessments [7]. However, stable ZnO varistor ceramics with steadily decreasing power loss have been produced. At higher temperatures within a certain range, they show an even faster decreasing trend. However, their microstructures and crystal structures are almost identical with those traditional instable samples, despite their completely different power loss trends. Their aging pattern is beyond the existing understandings. The investigation into their aging nature has been proposed as a major future challenge by CIGRE in 2013 and 2017 [3, 4].

Recently, several studies have been done on the aging of stable ZnO varistor ceramics. Cheng et al. studied the accelerated dc aging of a commercial stable ZnO varistor ceramic at 120 °C [8]. Reversibility in aging and a "crossover" in the forward J–E curves were discovered, and the singly charge zinc interstitial ($Zn_i^{\cdot}$) was identified as the major mobile ion during the aging. Wu et al. found that stable samples show an increasing power loss at low voltages, and a decreasing power loss at high voltages [9]. The above results suggest the aging of stable samples is not only controlled by ion migration. So far, only the donor ion redistribution (DIR) model proposed by Wu and Li et al. can explain the decreasing or increasing power loss in ZnO varistor ceramics [10]. They noted that the ion migration and ion diffusion in the depletion layers of the DSB could lead to "U-shape" depletion layers, which cause a decreasing power loss. The consumption of the interface states would result in an increasing power loss. The decreasing power loss is described to arises from the stable interface states with dynamics of mobile ions.

The aging of ZnO varistor ceramics is the result of the competition between donor redistribution and consumption of the interface states according to the DIR model [10]. However, little is known about the stability of the interface states. Thermal treatment, in particular, is acknowledged to be beneficial in revising the electrical

performance of the DSB. Stucki et al. reported that annealing ZnO varistor ceramics in air or vacuum changed their *J–E* characteristics by affecting the interface charge [11]. It is reasonably to deduce that the stability of interface states could also be influenced by elevated temperatures. Therefore, studying the aging of stable samples at different temperatures could be rewarding for understanding their aging nature.

In this paper, an accelerated dc aging experiment is carried out on stable ZnO varistor ceramics at an elevated aging temperature. Power loss transition and destruction of long-term stability of the sample aged at a higher temperature are found. The observations in this study provide a reference for the condition assessment of stable samples, and propose a method for the investigation of the stability of the interface states.

2 Experiments

The same batch of commercial stable ZnO varistor ceramics (40 mm in diameter D and 9.8 mm in thickness *h*) were employed in this study. They were employed for an accelerated dc aging experiment at 120 and 150 °C. The applied dc voltage is 0.8 times of the breakdown voltage (U_b) of the sample. U_b is the voltage at the current density of 1 mA/cm^2. It was obtained by their nonlinear *J–E* characteristics, which were measured by an automatic test system. The system is made up of a dc voltage source (TD2200, SLAMAN, China), a multimeter (DMM 7510, Keithley, USA), and a voltmeter (8145C, Victor, China).

The power loss of the samples was continuously recorded during the aging. The evolution of *J–E* characteristics was also measured in situ. The aged samples were then recovered at the aging temperature at zero bias after the dc aging, during which *J–E* characteristics were measured. Moreover, frequency-domain spectroscopy (FDS) was performed on the sample during the aging and recovery. The FDS results were measured from 10^{-1} to 10^5 Hz at − 100 °C by an impedance analyzer (Concept 80, Novocontrol, Germany) at an ac signal of 1 V_{rms}.

3 Results and Discussion

3.1 Transition of the Electrical Properties

Figure 1 presents the normalized power loss of the stable ZnO varistor ceramics aged at 120 and 150 °C. An obvious power loss transition is observed at about 30 h for the sample aged at 150 °C. This is an indicator of the transition of long-term stability of stable samples. The sample aged at 120 °C shows typical decreasing power loss, as previously reported. The power loss is approximately linear with the aging time in the first hundred hours. The power loss decreases faster for the sample aged at 150 °C

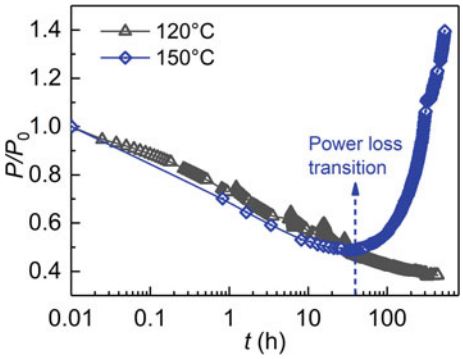

Fig. 1 Dependences of normalized power loss on aging time of stable ZnO varistor ceramics at different temperatures

in the first 30 h. However, it then increases from $0.5P_0$ to $1.4P_0$ at about 500 h. It is in accordance with the aging pattern of the instable samples [5]. The increase in power loss relates to the reduction in the barrier height ϕ_b of the DSB according to the thermionic emission theory [12]:

$$J = A^* T^2 e^{-\frac{q\phi_b + \xi_b}{kT}} \left(1 - e^{-\frac{qU}{kT}}\right) \quad (1)$$

where J is the leakage current, A^* is the effective Richard constant, T is the absolute temperature, q is the elementary charge, ξ_b is the bulk Fermi level relative to the conduction band, and k is the Boltzmann constant. The degradation of the DSB indicates the consumption of the interface states gradually overlaps the effect of the redistribution of donor ions at a higher temperature.

The evolution of the nonlinear *J–E* characteristics also shows an obvious discrepancy before and after the power loss transition. Figures 2a, b show the nonlinear *J–E* characteristics before the transition in the forward and reverse directions, respectively. Here, the forward direction is the same direction as the applied dc voltage, and the reverse direction is opposite to the voltage. A "crossover" in the forward direction is obviously recognized. It is a special aging phenomenon in stable ZnO varistor ceramics, i.e., the current density increases at low voltages, and decreases at high voltages. The "crossover" results from the formation of the "U-shape" depletion layers, which leads to a dynamic response of ϕ_b at different voltages [8, 9]. As a result, donor ion redistribution dominates the aging at the first 30 h.

However, the interface states could not remain stable for a long time at the high temperature. Figures 3a, b presents the evolution of the *J–E* characteristics after the power loss transition. Both the forward and reverse *J–E* curves move towards the high-current region. The "crossover" could no longer be observed in the forward direction. Moreover, the deterioration in the reverse direction is more severe than on the forward side. This aging pattern is common in instable ZnO varistor ceramics. It potentially suggests the transition of the long-term stability.

The electrical properties of the sample aged at 150 °C are calculated from the nonlinear *J–E* curves to further find the changes before and after the power loss

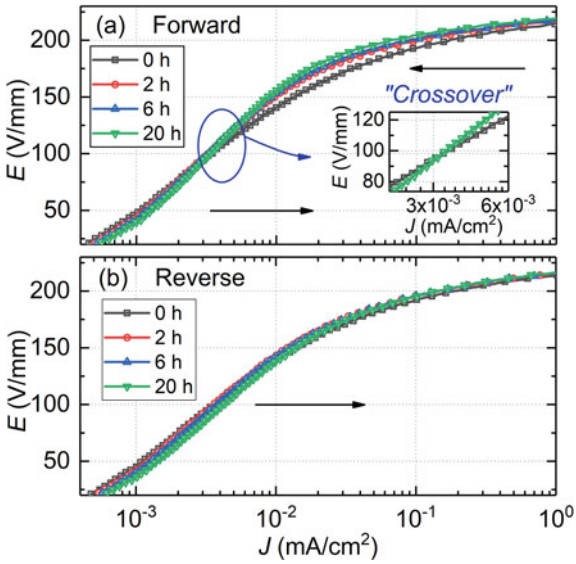

Fig. 2 The evolution of the nonlinear J–E characteristics before the power loss transition at 150 °C, **a** the forward direction, **b** the reverse direction

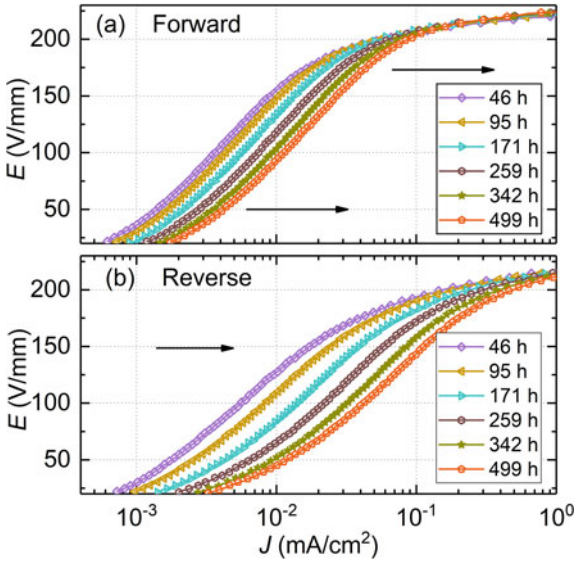

Fig. 3 The evolutions of the nonlinear J–E characteristics after the power loss transition at 150 °C, **a** the forward direction, **b** the reverse direction

transition. The nonlinear coefficient α is calculated from the voltages $U_{0.1\text{mA}}$ and $U_{1\text{mA}}$ measured at 0.1 and 1 mA/cm^2, respectively:

$$\alpha = 1/\lg(U_{1mA}/U_{0.1mA}) \tag{2}$$

The breakdown electric field strength E_b is calculated by:

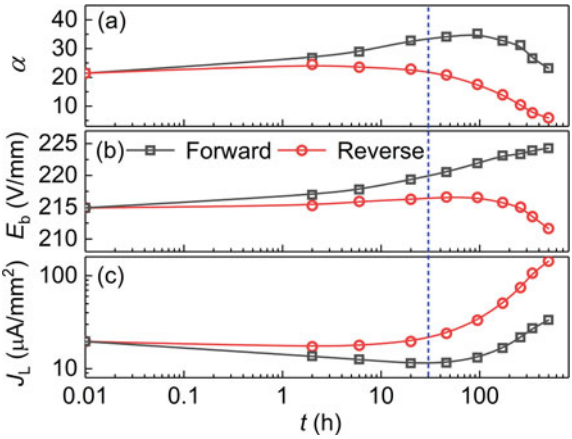

Fig. 4 Dependences of the nonlinear coefficient α, the breakdown electric field strength E_b, and the leakage current J_L on time during the aging at 150 °C, the blue line indicates the time of power loss transition

$$E_b = U_{1mA}/h \tag{3}$$

The leakage current J_L is the current density at $0.75U_{1mA}$. Variations of these electrical parameters are shown in Fig. 4. The blue dashed line indicates the transition time point. Most of the electrical parameters are enhanced before the transition, e.g., α increases from 21.4 to 32.8, and E_b increases from 214.9 to 219.4 V/mm in the forward direction. The sample shows excellent long-term stability at this time. However, dramatic electrical degradation happens after the transition. Especially, α drops from 22.9 to 5.9, and J_L rises from 19.7 to 143.7 μA/cm^2 in the reverse direction. The degradation follows the aging pattern of instable samples, which is caused by the consumption of the interface states according to the classical ion migration model [6].

3.2 Recovery Characteristics

The dc voltage is removed after the aging to recover the sample at the same temperature. Figure 5 show the evolution of the nonlinear *J–E* characteristics of the sample aged at 150 °C. See the totally recovered electrical properties of the sample aged in 120 °C in [8]. With increasing recovery time, the forward- and reverse-direction *J–E* curves gradually move towards the unaged curve. They gradually become symmetric as donor ions gradually recover to their initial shape at zero bias. However, the *J–E* curves cannot recover even after 493 h due to the consumption of the interface states.

Variations of the electrical parameters during the recovery are derived and shown in Fig. 6. The gray dashed lines indicate their unaged values. It is obvious that α, E_b, and J_L all cannot be recovered, although the forward- and reverse-direction values regain symmetry. After 300 h, the leakage current J_L becomes almost unchanged.

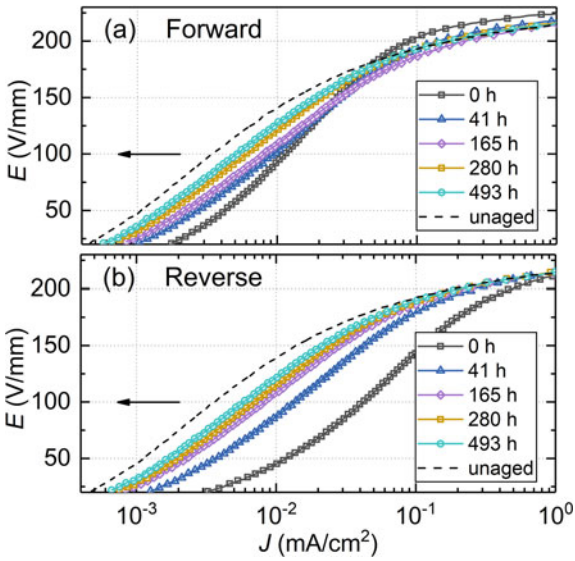

Fig. 5 The evolution of the nonlinear *J–E* characteristics during the recovery, **a** the forward direction, **b** the reverse direction

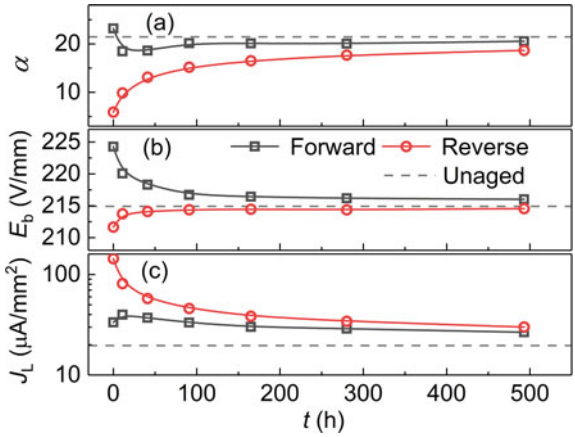

Fig. 6 Dependences of the nonlinear coefficient α, the breakdown electric field strength E_b, and the leakage current J_L on time during the recovery

It reaches 26.6 μA/cm^2 at 493 h, which still has a big difference from the unaged value of 19.7 μA/cm^2.

3.3 FDS Characteristics

As a powerful technique, FDS measurement is often used to characterize the dynamics of the charge trapping in dielectrics [13]. Here, the FDS of the sample aged at 150 °C is measured during the aging and the recovery to uncover the dynamics

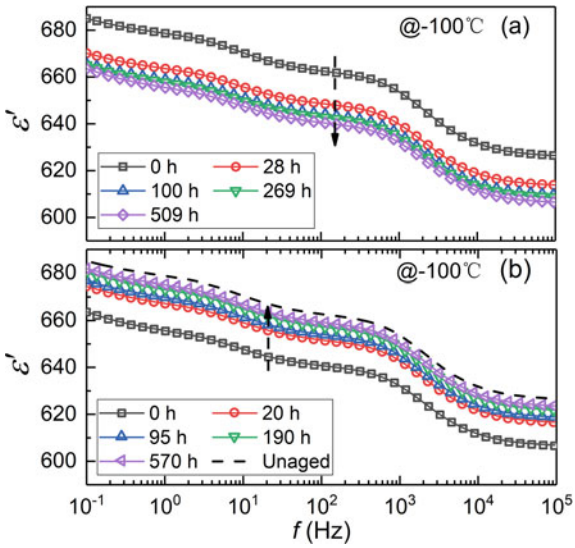

Fig. 7 Measured FDS results of the ZnO varistor ceramics aged at 150 °C, during **a** the aging and **b** the recovery

of depletion charges. The ε' spectra during the aging are shown in Fig. 7a. The real part of the dielectric constant decreases overall without distortion of its shape. It decreases rapidly in the first 28 h. This is the result of Zn_i redistribution in depletion layers [10]. During the recovery, the depletion charges are trying to recover to its unaged distribution, leading to the increase in ε'. However, ε' cannot recover to the unaged black dashed line even after 570 h. However, they could recover completely at 120 °C [8]. The irreversibility of ε' mainly caused by the combination of the positive $Zn_i^{\cdot}$ and the negative interface states after the power loss transition according to the classic ion migration model. It further confirms the transition of the long-term stability of the stable sample at a higher temperature.

4 Conclusions

In summary, this study investigates the aging of modern stable ZnO varistor ceramics at a relatively high temperature. The main conclusions are summarized as follows:

(1) The power loss firstly decreases, and then continuously increases after 30 h during aging at 150 °C, which is different from the steadily decreasing power loss at 120 °C. The transition of power loss is accompanied by a severe deterioration in nonlinear *J–E* characteristics. The *J–E* curves move towards the high-current region as a hole after the transition, and the "crossover" can no longer be observed.

(2) The high temperature causes irreversible aging of the stable sample. Both the nonlinear *J–E* characteristics and electrical properties cannot recover to their unaged values. Stable ZnO varistor ceramics can only remain stable within a certain temperature range.
(3) FDS results indicates that at high temperatures, singly charged zinc interstitial would possibly combine with the negative interfaces states. Thereby the ε' spectra cannot be recover even after enough recovery. The deterioration of the interface states subsequently leads to the transition of long-term stability.

Acknowledgements This work was supported by the Science and Technology Project of China Southern Power Grid Co., Ltd. No. 030400KK52220032(GDKJXM20220829).

References

1. Greuter F (2021) ZnO varistors: from grain boundaries to power applications. In: Ray AK (ed) Oxide electronics. Wiley, London, pp 157–234
2. Guo M, Zhao X, Shi W, Zhang B, Wu K, Li J (2022) Simultaneously improving the electrical properties and long-term stability of ZnO varistor ceramics by reversely manipulating intrinsic point defects. J Eur Ceram Soc 42(1):162–168
3. CIGRE Working Group A3.17 (2013) MO surge arresters—stresses and test procedures. In: International council on large electric systems, Paris, France
4. CIGRE Working Group A3.25 (2017) MO surge arresters—metal oxide resistors and surge arresters for emerging system conditions. In: International council on large electric systems, Paris, France
5. Leite ER, Varela JA, Longo E (1992) A new interpretation for the degradation phenomenon of ZnO varistors. J Mater Sci 27(19):5325–5329
6. Gupta TK, Carlson WG (1985) A grain-boundary defect model for instability/stability of a ZnO varistor. J Mater Sci 20(10):3487–3500
7. International Electrotechnical Commission (2014) Surge arresters Part 4: metal-oxide surge arresters without gaps for a.c. systems. IEC, Geneva, Switzerland
8. Cheng Z, Hou Z, Wang Y, Guo M, Wu K, Li J, Lin Y (2022) Steadily decreasing power loss of a double Schottky barrier originating from the dynamics of mobile ions with stable interface states. Phys Rev Appl 17(3):034042
9. Wu K, Hou Z, Cheng Z, Wang Y, Li R, Lin Y, Li J, Li S (2022) Revisiting the feasibility of distinguishing the long-term stability of MOVs by power loss. IEEE Trans Dielectr Electr Insul 29(5):1983–1990
10. Li J, Cheng Z, Li S, Wu K (2022) Anomalous decreasing power loss of ZnO varistor ceramics during the dc aging: phenomena, insights and perspectives. In: 9th international conference on condition monitoring and diagnosis (CMD). IEEE, Kitakyushu, pp 11–17
11. Stucki F, Greuter F (1990) Key role of oxygen at zinc oxide varistor grain boundaries. Appl Phys Lett 57(5):446–448
12. Blatter G, Greuter F (1986) Carrier transport through grain boundaries in semiconductors. Phys Rev B 33(6):3952
13. Wu K, Huang Y, Li J, Li S (2017) Space charge polarization modulated instability of low frequency permittivity in $CaCu_3Ti_4O_{12}$ ceramics. Appl Phys Lett 111(4):042902

Simulation and Experimental Research on Temperature Field of Tightly Coupled Split Reactor Based on Fluid-Thermodynamic Temperature Field Analysis

Yong Wang, Lu Zhu, Jie Yang, Lu Chen, Guangmao Li, Junxiang Liu, Hongling Zhou, and Haibo Su

Abstract At present, the research on tightly coupled split reactor is generally limited to its functions such as automatic current sharing/current limiting in parallel circuit breaker circuits, while the temperature rise of this type of reactor under continuous current is rarely studied. In order to evaluate the temperature rise under continuous current, this paper adopts the method of combining fluid-thermodynamic temperature field simulation analysis and experimental verification. The test results show that: 1. The test value and the simulation value of the tightly coupled split reactor's temperature rise are basically in agreement when the double-arm coil or the single-arm coil is operated under the calculated current. 2. When the double-arm coil is running, the temperature rise of each package is evenly distributed, but the packages in the middle are slightly higher than the packages on the inner and outer sides. When a single arm is running, the temperature rise of the coil gradually decreases from the inside to the outside; 3. The tightly coupled split reactor has the characteristic of small reactance on the single-arm coil, and low magnetic leakage on the double-arm coil. According to the comparison of simulation calculation and test results, the maximum continuous current of the tightly coupled split reactor in the article can reach about 7000 A with double-arm and 3500 A with single-arm, which can meet the requirements of the maximum current of the reactor in the project. The research results can provide a theoretical and reference basis for the temperature rise calculation and temperature rise monitoring of the tightly coupled split reactor.

Keywords Tightly coupled split reactor · Temperature rise · Test · Temperature field simulation

Y. Wang · L. Zhu (✉) · J. Yang · L. Chen · G. Li · J. Liu · H. Zhou · H. Su
Guangzhou Power Supply Bureau of Guangdong Power Grid Co., Ltd., Guangzhou, Guangdong, China
e-mail: zhulu_gd@163.com

© Beijing Paike Culture Commu. Co., Ltd. 2024

X. Dong and L. Cai (eds.), *The Proceedings of 2023 4th International Symposium on Insulation and Discharge Computation for Power Equipment (IDCOMPU2023)*, Lecture Notes in Electrical Engineering 1102, https://doi.org/10.1007/978-981-99-7405-4_49

1 Introduction

In recent years, with the rapid development of power transmission and transformation projects, the continuous growth of power demand, and the continuous increase of the installed capacity of power generation in the power grid, the short-circuit current level of the system has shown an increasing trend year by year, and even exceeded the breaking current capacity of circuit breakers in some regions [1–8]. In recent years, many projects have started to use two single arms of tightly coupled split reactors connected in series with one circuit breaker, in order to achieve automatic current sharing and limiting, thereby improving the breaking capacity of parallel circuit breakers, and ultimately effectively achieving the goal of breaking the short circuit current of the system [9–11]. In previous projects, tightly coupled reactors were mostly used under short-term operating conditions, so temperature rise was not an important assessment indicator for tightly coupled reactors and often did not require temperature rise tests. Given that there is little research on the temperature rise of tightly coupled reactors under continuous operating current, the article analyzes the temperature rise of tightly coupled split reactors under continuous operating current.

The modeling of high coupling split reactors and the simulation of the temperature field of dry type hollow reactors were studied in references [12, 13], but the accuracy of the temperature rise results of dry type hollow reactors cannot be determined due to the lack of verification through actual experimental results. Reference [14–16] introduces the temperature rise test process of reactors, as well as the determination method of hot spot temperature rise and average temperature rise. However, the average temperature rise cannot reflect the temperature rise distribution at different positions of the reactor, and the temperature rise determination method introduced in this reference cannot verify the temperature rise situation of tightly coupled split reactors with special structures.

Based on the above analysis, this article uses JFKK-15-2 $\times$ 80000-0.223 type tightly coupled split reactor prototype was used as the research object. The ANSYS FLUENT finite element analysis method was used to explore the temperature rise distribution of the tightly coupled split reactor under several conditions, such as single arm flow and double arm flow, and the accuracy of the finite element analysis was verified through temperature rise tests.

2 Structure of a Tightly Coupled Split Reactor

As a device for automatic current sharing and limiting in the power system, tightly coupled split reactors differ from conventional reactors in both principle and structure.

The encapsulation insulation structure of the tightly coupled split reactor coil body includes two or more coil encapsulation layers, and all coil encapsulation layers are in a concentric circular structure. In general, in order to ensure the coupling coefficient

of tightly coupled split reactors, the windings of single arm 1 and single arm 2 coils are generally wound in a staggered manner, that is, a layer of single arm 1 winding is first wound, and then a layer of single arm 2 winding is wound. The reactor prototype studied in this article adopts a structure of one layer of clockwise winding and one layer of counterclockwise winding to form a sealing layer. Both clockwise and counterclockwise windings use wire wrapping and interlayer insulation materials are added between the two winding wires to achieve interlayer and turn to turn insulation [17]. As shown in Fig. 1, the clockwise winding refers to the first small layer of each encapsulation that together forms a single arm coil, while the counterclockwise winding refers to the second small layer of each encapsulation that together forms another single arm coil. Two single arm coils are connected to the corresponding parallel circuit breaker through two insulated outgoing arms.

In order to ensure the coupling coefficient of two single arm coils, the design of a tightly coupled split reactor studied in this paper adopts a design method where two single arm coils are wrapped in a single envelope, that is, the first envelope layer includes the first layer of winding of single arm 1 and the first layer of winding of single arm 2, and then a ventilation strip is laid to ensure the ventilation of the air

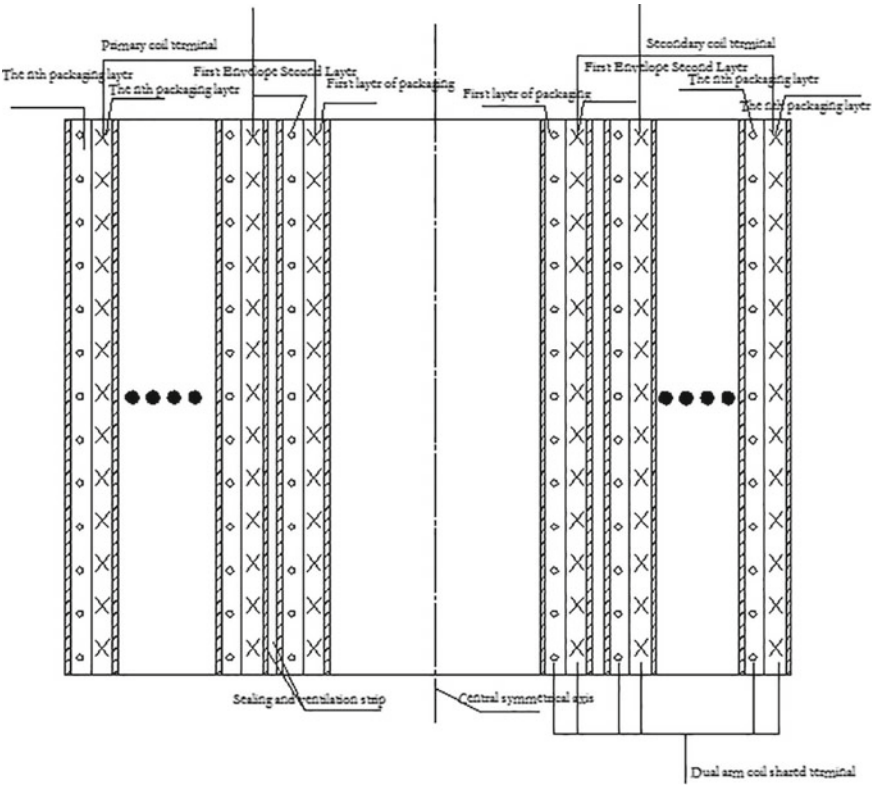

Fig. 1 Schematic diagram of tightly coupled split reactor design

Fig. 2 Prototype of tightly coupled split reactor

duct between the envelope layers. The second envelope layer includes the second layer of winding of single arm 1 and the second layer of winding of single arm 2, and so on. The two single arm coils are insulated between the wire layers using epoxy glass yarn. As shown in Fig. 2, the prototype of a tightly coupled split reactor studied in this paper is presented.

3 Temperature Rise Calculation

At present, the dry air core reactor is mainly cooled by air Free cooling, and the heat dissipation of the reactor is mainly generated by the combined action of three modes of heat conduction, heat convection and heat radiation [18]. When the reactor flows through, the winding conductor serves as the heat source for the reactor and conducts heat transfer with other non-conductive solid structures such as the encapsulation layer. The essence of heat transfer is the transfer of internal energy from a large number of molecules, which is a heat transfer process that occurs when internal energy is transferred from a high-temperature object to a low-temperature object. This heat transfer process follows the Fourier heat conduction equation:

$$Q = -\lambda A \frac{\partial T}{\partial x} \tag{1}$$

In the formula, Q is the heat flow rate, W; λ is the thermal conductivity, W/(m °C); A is the cross-sectional area perpendicular to the direction of heat flow, m^2; $\frac{\partial T}{\partial x}$ is the rate of temperature change in the direction; "−" indicates that the heat transfer direction is opposite to the temperature gradient direction.

Thermal convection is the heat generated by the coil that propagates from the surface of the coil to the surrounding air. During the flow process, when the hot

fluid comes into contact with the solid surface, heat is transferred from one location to another, forming convective heat transfer. The convective heat transfer can be calculated using the Newton cooling formula:

$$Q = \alpha A(t_w - t_a) \tag{2}$$

In the formula, A is the heat flow rate, W is the convective heat transfer coefficient, W/(m °C); is the convective heat transfer area, m^2 is the surface temperature of the encapsulation, °C is the temperature of the surrounding air, °C.

Thermal radiation refers to the heat transfer caused by electromagnetic wave radiation between the winding and the outside world due to different temperatures. The radiative heat transfer can be expressed using the Stephens Boltzmann law:

$$Q = \varepsilon A \delta T^4 \tag{3}$$

In the formula, Q is the heat flow rate per unit time of a given area, W; ε is the emissivity of the object surface; A is the surface area of radiation, m^2; T is the thermodynamic temperature of black body, K is the Boltzmann constant, whose value is 5.67×10^{-8} W/(m^2 K^4).

When the reactor is flowing, the coil winding heats up due to eddy current and DC losses inside the reactor. The loss calculation formula for the reactor is as follows:

$$P_e = \sum_{i=1}^{m} \frac{\pi^2 \gamma \omega^2 D_i d_i^4}{64} (B_{zi}^2 + B_{ri}^2) \tag{4}$$

$$P_{\mathrm{d}} = \sum_{i=1}^{m} I_i^2 R_i \tag{5}$$

In the formula, P_e is eddy current loss, W; P_d is the DC loss, W; m The number of wire layers for the reactor; γ is the conductivity, S/m; ω is the angular frequency, rad/s; D_i is the diameter of the layer of encapsulation, m; d_i is the diameter of the wire inside the layer of encapsulation, m; B_{zi} is the axial magnetic induction intensity at the position of the second layer winding, T; $B_{\mathrm{r}i}$ is the radial magnetic induction intensity at the location of the second layer winding, T; I_i is the current of the second layer winding, A; R_i is the DC resistance of the second layer winding, Ω.

In ANSYS FLUENT finite element analysis, the heat source is given based on the unit volume heat density of the winding, and the unit volume heat density is calculated as follows:

$$q_i = \frac{P_e + P_d}{V_i} \tag{6}$$

In the formula, V_i is the volume of the third layer of winding, m^3, and the calculation formula is as follows:

$$V_i = (\pi r_{oi}^2 - \pi r_{ii}^2)H \tag{7}$$

In the formula, r_{oi} is the outer diameter of the wire in the second layer of winding, m; r_{ii} is the inner diameter of the wire in the layer of winding, m; H is the height of the winding wire section, m.

4 Simulation Results of Temperature Rise of Tightly Coupled Split Reactors

4.1 Parameters of Tightly Coupled Split Reactor

The main design parameters of the tightly coupled split reactor prototype studied in this article are shown in Table 1.

Based on temperature rise design principles and experimental data statistical analysis of reactors in previous projects, the temperature rise design of the tightly coupled split reactor is carried out. When the dual arm current is 7000 A and the single arm current is 3500 A, the temperature rise of the coil hot spot does not exceed 90 K, meeting the requirements of Class B insulation and heat resistance level. Therefore, this study will take 7000 A for the double arm current of the tightly coupled split reactor, and 3500 A for both single arm 1 and single arm 2 currents. Simulation

Table 1 Design parameter table of tightly coupled split reactor

Projec	Parameters
Model	JFKK-15-2 × 80000-0.223
Coil type	Dry hollow
Cooling method	Air-cooling
Wire type	Copper stranded wire
Insulation level	B
Outer diameter/mm	1630
Inner diameter/mm	830
Coil height/mm	880
Ventilation strip width/mm	19
Number of packages	9
Coil weight/kg/kg	5435
Single arm 1/2 inductance/mH	0.223
Single arm DC resistance (20 °C)/mΩ	< 0.5
Coupling coefficient	> 99%
Unbalance	< 1%

calculations and experimental verification will be conducted for these three cases, respectively.

4.2 Temperature Rise Simulation Model and Results of Tightly Coupled Split Reactor

This article conducts temperature rise simulations on a tightly coupled split reactor prototype under two conditions: single arm flow and double arm flow.

By simulating and settling the heat density assigned to each wire layer under the conditions of dual arm flow of 7000 A, single arm 1 and single arm 2 flow of 3500 A respectively, the calculation results are shown in Figs. 3, 4 and 5.

From the cloud diagram of FLUENT fluid thermodynamic temperature field analysis, it can be seen that the simulation environment temperature is 26.85 °C, and the temperature rise of single arm and double arm hot spots under different currents is shown in Table 2.

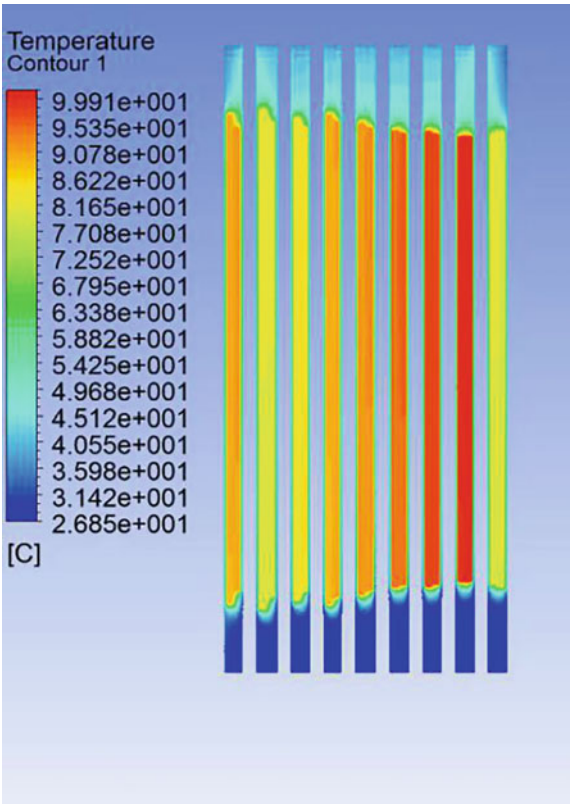

Fig. 3 Simulation results of temperature rise when 7000 A through two arms

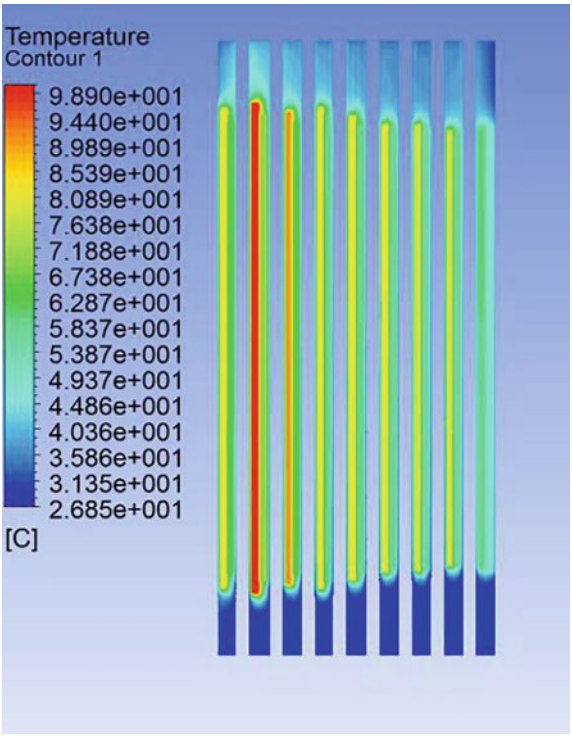

Fig. 4 Simulation results of temperature rise when 3500 A through single arm 1

According to the simulation results, it can be seen that when the dual arm current is 7000 A and the single arm 1 and single arm 2 current are 3500 A respectively, the hot spot temperature rise of the reactor is far from reaching the heat resistance capacity of the reactor.

5 Temperature Rise Test Results of Tightly Coupled Split Reactor

The tightly coupled split reactor prototype undergoes temperature rise test in the testing hall, which is basically a closed environment that meets the requirements of temperature rise test conditions [19, 20].

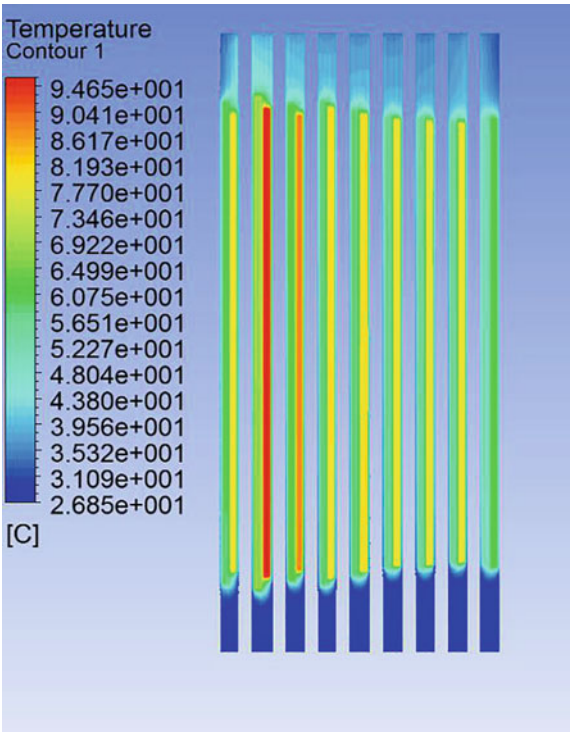

Fig. 5 Simulation results of temperature rise when 3500 A through single arm 2

Table 2 Simulation results of tightly coupled split reactor temperature rise

Project	Current/A	Hot spot temperature rise/K
Double arm	7000	73.1
Single arm	3500	72.1
Single arm	3500	67.8

5.1 Temperature Rise Test Under Dual Arm Flow Conditions

This experiment first conducted a temperature rise test on the tightly coupled split reactor coil under long-term dual arm current flow. According to the prototype scheme, the coil has a total of 9 packages, with the first layer of each package being a single arm 1 inductance winding and the second layer being a single arm 2 inductance winding. When passing through two arms, the coils of single arm 1 and single arm 2 are connected in parallel, connecting the outgoing terminals of the two single arms, and passing through the upper and lower terminals as a whole. Due to the current sharing effect of the tightly coupled reactor, it can be considered that both single arm coils flow through half of the current at this time.

Before the test, the coil shall be Free cooling to room temperature, and the double arm through current 7000 A test shall be conducted. Record the temperature rise

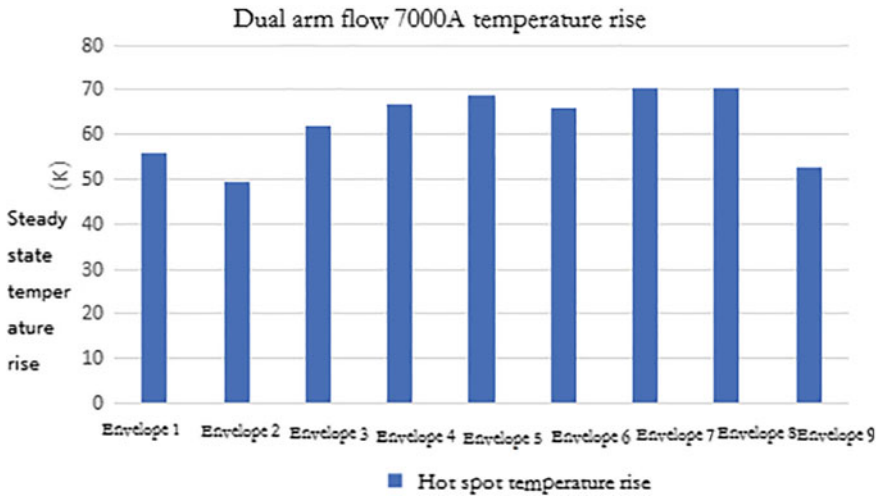

Fig. 6 Column diagram of temperature rise at the hottest package when 7000 A through two arms

of each packaging hot spot every half an hour, and finally obtain the steady-state temperature rise of each packaging for two tests, as shown in Fig. 6.

From Fig. 6, it can be seen that under the dual arm flow, when the temperature rise of the reactor reaches steady state, the overall temperature rise is relatively uniform. The temperature rise of the intermediate packaging layer is slightly higher than that of the inner and outer packaging layers. When the dual arm flow is 7000 A, the hottest point temperature rise is 70.2 K, which is 2.9 K different from the simulated hot point temperature rise.

The insulation level of this prototype is Class B, and it can withstand a hot spot temperature rise of 90 K. For this reactor, it can withstand long-term current flow and still has a large margin.

5.2 Temperature Rise Test Under Single Arm Flow Conditions

(1) Temperature rise of single arm 1

After the tightly coupled split reactor is Free cooling to room temperature, the temperature rise test is carried out on the single arm 1 of the tightly coupled split reactor. The current is 3500 A, and the temperature rise of each packaging hot spot is recorded every half an hour. Finally, the temperature rise of each packaging hot spot is obtained as shown in Fig. 7.

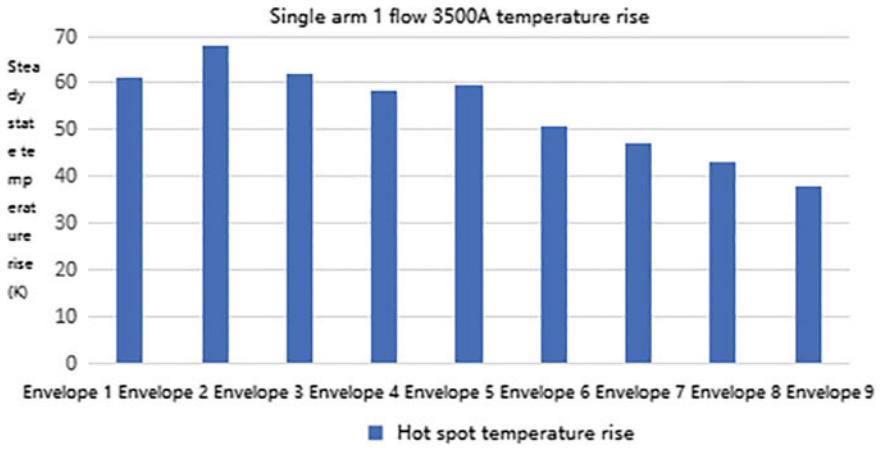

Fig. 7 Column diagram of temperature rise at the hottest package when 3500 A through single arm 1

(2) Temperature rise of single arm 2

After the tightly coupled split reactor is Free cooling to room temperature, the temperature rise test is carried out on the single arm 2 of the tightly coupled split reactor. The current is 3500 A, and the temperature rise of each packaging hot spot is recorded every half an hour. Finally, the temperature rise of each packaging hot spot is obtained as shown in Fig. 8.

From Figs. 7 and 8, it can be seen that when the temperature rise of the reactor reaches a steady state under single arm flow, the hot spot temperature rise gradually

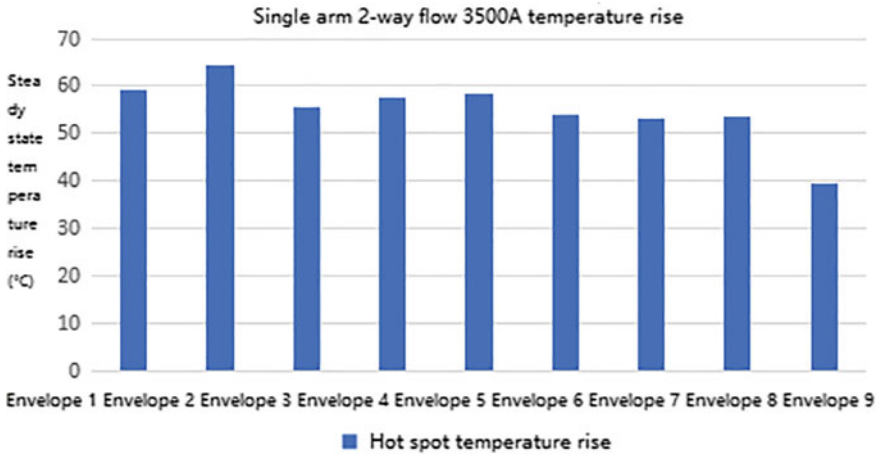

Fig. 8 Column diagram of temperature rise at the hottest package when 3500 A through single arm 2

decreases from the inner sealing to the outer sealing. The temperature rise of the first few sealing layers is the highest, with the hottest temperature rise of 68.1 K under single arm 1 flow and 64.6 K under single arm 2 flow, which is within 7 K of the simulated hot spot temperature rise under single arm flow.

The analysis of the reasons why the temperature rise distribution during single arm operation is different from that during double arm operation suggests that due to the presence of both single arm 1 winding and single arm 2 winding within a single envelope, the distance between single arm 1 winding and single arm 2 winding is very small. When only one winding has flow, the other winding can effectively transfer and dissipate heat, while the area of the wrapped layer wire near the outer side of the reactor is larger than that of the wrapped layer wire on the inner side, effectively increasing the heat dissipation area, Therefore, the external temperature cooling capacity has also significantly increased.

For this reactor, there is still a large margin for it to withstand long-term current flow.

6 Comparison and Analysis of Temperature Rise Simulation and Test Results for Tightly Coupled Split Reactors

Based on the temperature rise simulation and experimental results of the tightly coupled split reactor mentioned above, the comparison results of the hot spot temperature rise data at 7000 A for dual arm flow and 3500 A for single arm 1 and single arm 2 flow are as follows:

According to thermodynamic principles, when the coil is flowing, under the driving force of buoyancy, the temperature rise of each layer of winding generally presents a situation of high at the upper end and low at the lower end. The top of the winding is basically an encapsulated structure and has a large contact area with air. Therefore, we compared the temperature rise simulation results at the highest point of the coil wire with the experimental results in the above three situations, and the comparison results are shown in Figs. 9, 10 and 11.

According to the comparison between the temperature rise simulation results and the experimental results in Figs. 9, 10 and 11, the overall trend of the simulation results and the experimental results is basically matched in both double arm flow and single arm flow. The simulation results are basically accurate in calculation, and the consistency of the simulation calculation trend is also relatively high. The deviation between the simulation calculation value and the experimental value is within 7 K.

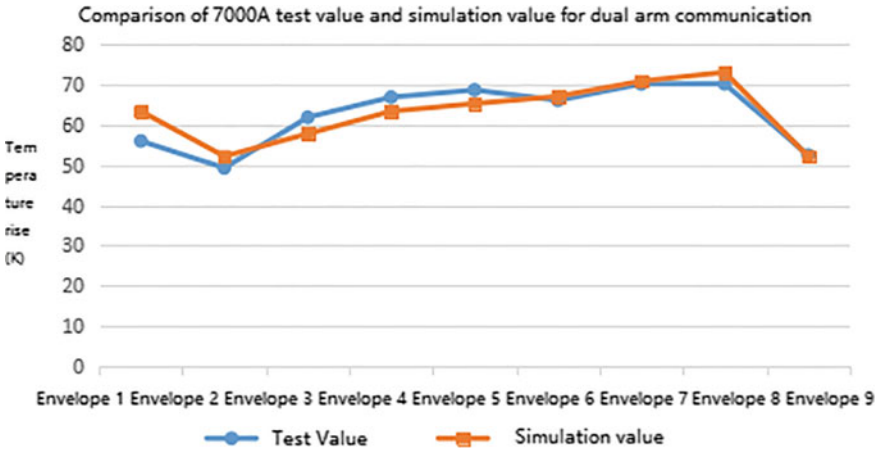

Fig. 9 Comparison of simulation and test results of temperature rise of each package when 7000 A through two arms

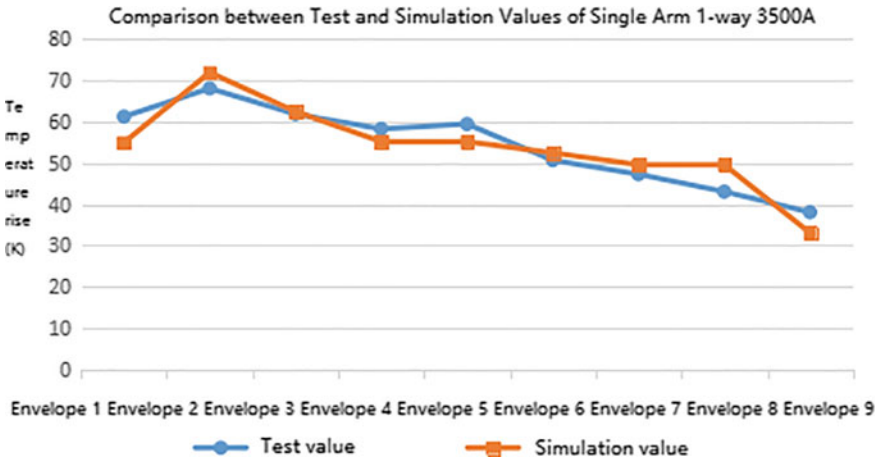

Fig. 10 Comparison of simulation and test results of temperature rise of each package when 3500 A through single arm 1

7 Conclusion

In this paper, the temperature rise of tightly coupled split reactor is studied based on the simulation calculation and test verification method of fluid thermodynamic temperature field, and the following conclusions are obtained:

(1) The temperature rise simulation values and experimental measurements of the tightly coupled split reactor in the case of dual arm flow and single arm flow are basically consistent, and the temperature rise distribution of hot spots in each

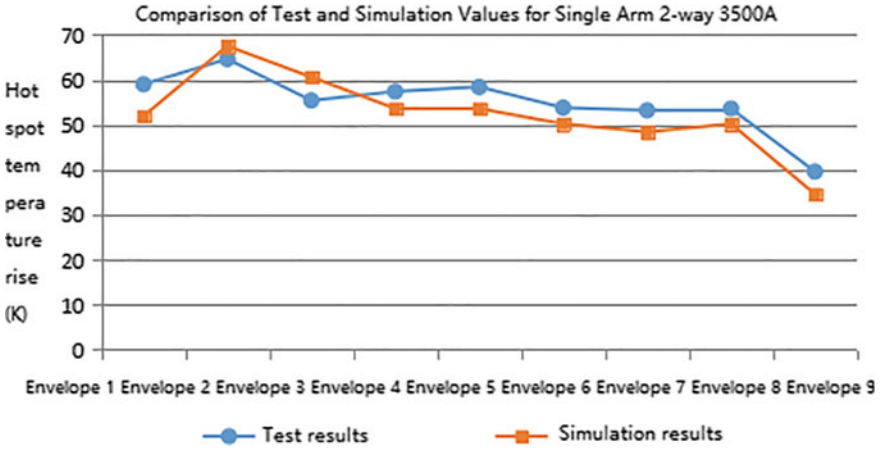

Fig. 11 Comparison of simulation and test results of temperature rise of each package when 3500 A through single arm 2

sealing layer is basically consistent, verifying the accuracy of the simulation calculation.

(2) Summarized the temperature rise distribution law of tightly coupled split reactors. When running with both arms, the temperature rise distribution is relatively uniform, and the temperature rise shows a trend of slightly higher in the middle package than in the two side packages; When operating with one arm, the temperature rise shows a trend of higher internal encapsulation than external encapsulation of the coil.

(3) The tightly coupled split reactor has a small reactance on one arm and only presents leakage magnetic characteristics on both arms. Through simulation calculation and experimental verification, it can withstand a large current and meet the maximum current requirements of reactors in the current power system.

The above research results can provide a theoretical basis and reference for temperature rise calculation and monitoring of tightly coupled split reactors.

Acknowledgements This work was funded by Southern Power Grid Corporation Technology Project: Design and Research of High Impedance and High Coupling Reactors, China (No. 080037KK52190032).

References

1. Fu X, Wang X, LI F et al (2020) Limiting short-circuit current of southern Qinghai power grid. Distrib Energy 5(1):65–70 (in Chinese)
2. Fang B, Cheng H, Xu Q et al (2018) 220 kV network expansion planning considering short-circuit current constraint. Electr Meas Instrum 55(21):25–30 (in Chinese)

3. Cai H, Qi W, Wang W et al (2018) Study on current-limit technology of series reactor in Jiangsu power grid. Power Capacitor React Power Compensation 39(1):102–106 (in Chinese)
4. Chen W, Liu Y, Liu X (2018) Transmission expansion planning considering adaptability of grid to short-circuit current. Sichuan Electr Power Technol 41(1):74–77, 82
5. Fan X, Zhang Y, Su L et al (2018) Research on short circuit current control in multi-infeed DC receiving power grid. Smart Power 46(3):61–67 (in Chinese)
6. Wen L, Shan Y, CHANG L et al (2021) Research on comprehensive diagnosis and online monitoring of distribution network under short- circuit fault. Electric Drive 51(14):73–80 (in Chinese)
7. Chen W, Fan Y, Zhang F et al (2022) Short-circuit current over-standard comprehensive treatment plan of power supply-intensive large-scale differential grid. Electr Meas Instrum 59(1):134–140
8. He L, Gao S, Ye H (2020) Characteristic analysis on short-circuit current for asymmetric bipolar modular multilevel converter based multi-terminal direct current grid. Autom Electr Power Syst 44(12):101–107 (in Chinese)
9. Liu J, Ye J, Yuan Z et al (2021) A topology of 500 kV fault current limiter based on a high coupling split reactor. High Volt Eng 47(8):2828–2837 (in Chinese)
10. Xiang C, Xiang Z, Xu W (2020) TRV characteristics of post-breaker circuit breaker based on high coupling split reactor current limiter. High Volt Appar 56(1):18–23 (in Chinese)
11. Liu B, Chen X, Lan ZB et al (2019) Analysis and experiment study on dynamic stability of setup for impulse generator protection circuit breaker based on tight coupling split reactor. High Volt Appar 55(12):23–31
12. Zhou Y, Huo Q-G (2021) Design and simulation of high coupling split reactor. Electric Power Syst Equip 11:29–30
13. Wu S, Ma H, Jiang N et al (2019) Simulation and analysis of temperature field of high voltage reactor based on multi physical field coupling. Power Syst Protect Control 47(4):17–24
14. Wang S, Zhang Y, Li C et al (2018) Temperature field simulation and analysis in field test of laminate dry-type air-core reactor. Electr Meas Instrum 55(18):9–13, 20
15. Yang J, Xu Z, Nie J et al (2019) Study on temperature rise simulation technology of dry-type air core reactor. Power Capacitor React Power Compens 40(6):68–72
16. Deng Q, Li Z, Yin X et al (2013) Steady thermal field simulation of forced air-cooled column-type air-core reactor. High Volt Eng 39(4):839–844
17. Beijing Power Equipment Group Co., Ltd. (2019) The structure of tightly coupled split reactor: CN201821091519.5
18. Yang S, Tao W (2006) Heat transfer, 4th edn. Higher Education Press, Beijing
19. International Electrotechnical Commission (2007) IEC 60076-6 International Standard Power Transformers—Part 6: reactors
20. International Electrotechnical Commission (1993) IEC 60076-2 International Standard Power Transformers—Part 2: temperature rise

Surface Electric Field Calculation and Structure Parameters Configuration of Converter Valve Fittings on Offshore Converter Platform

Weiming Yan and Lei Qi

Abstract In order to optimize the insulation design and layout of the valve hall of the offshore converter platform. Taking a flexible converter valve tower of ± 500 kV/3000 MW offshore wind power as an example, the mixed AC and DC electric fields of the converter valve tower were calculated by finite element method. The electric field distribution on the surface of the valve tower was given, and the weak insulation positions were located. The effect of distance between the valve tower and wall, distance between valve towers and size parameters of the fixture on surface field strength were studied with the design goal of no corona generated on the surface of the fittings and the limit of corona inception field strength. The results showed that the edge of the shield cover of the converter valve tower and the pressure equalizing ring of the insulator are in weak insulation positions. The distance between the valve tower and the wall, the distance between the valve towers and the size parameters of the fittings could significantly affect the distribution of the electric field on the valve tower surface. On this basis, the valve tower fittings parameters selection and valve tower position configuration scheme were proposed.

Keywords Converter valve · Surface electrical field · Hardware fittings · Corona discharge · Insulating property

1 Introduction

With the rapid development of long-distance offshore wind power, offshore flexible DC transmission technology has become the main power transmission medium [1]. Contrary to what happens onshore, the valve hall of the offshore converter platform

W. Yan · L. Qi (✉)
State Key Laboratory of New Energy Power System, North China Electric Power University, Beijing 102206, China
e-mail: qilei@ncepu.edu.cn

W. Yan
e-mail: Yanweiming21@foxmail.com

© Beijing Paike Culture Commu. Co., Ltd. 2024

X. Dong and L. Cai (eds.), *The Proceedings of 2023 4th International Symposium on Insulation and Discharge Computation for Power Equipment (IDCOMPU2023)*, Lecture Notes in Electrical Engineering 1102, https://doi.org/10.1007/978-981-99-7405-4_50

has to meet the requirement of compact and lightweight configuration [2]. Therefore, it is of great significance to study the electric field distribution and size configuration of offshore flexible direct converter valve fittings to reduce the size of the valve hall on the premise of ensuring insulation safety.

The Finite Element Method (FEM) has been widely used in the multi-physical field calibration of electrical equipment in the valve hall for the advantages of high accuracy and mature commercial software. Bin et al. calculated and analyzed the electrical field distribution of the 800 kV inverter valve system shield housing from FEM [3]. Dong et al. analyzed the electric field distribution of ± 800 kV converter valve under the insulation type test and optimized the shield plate at the top of the valve tower by using PTC Creo and ANSYS [4].

This paper could be organized by the following parts: Firstly, the physical structure and potential boundary condition of the ± 500 kV offshore flexible DC transmission converter valve tower were introduced. Secondly, the surface electrical field of the converter valve tower was calculated and analyzed in the stationary state. The weak insulation positions were located on this basis. Finally, the method of setting the position paraments of the valve towers and the measurement paraments of the fittings under transient condition was studied. A design scheme considering insulation performance and light weight design was proposed.

2 Physical Structure and Electric Field Modeling of Converter Valve

2.1 Physical Structure and Voltage Boundary Conditions of ± 500 kV Converter Valves

Figure 1a showed the three-dimensional model of the converter valve tower, which included the shield cover, voltage balancing rings, interlayer insulators, cable-stayed insulators and post insulators. The overall size of the model was about 9 m × 8 m × 13 m. In order to reduce the complexity of model solving, the connection structure between the internal sub-module housing and the support of the valve tower were ignored in the model, and the insulator umbrella skirts were simplified into cylinders.

The converter valve tower contained a certain number of sub-modules in series whose fittings were connected to the closest sub-modules at the same potential. For the towers on the same bridge, the connection mode between the valve towers was indicated in Fig. 1b. The amplitude of AC voltage at the AC side of No. 1 valve tower was 500 kV, and the amplitude of AC voltage at the DC side of No. 3 valve tower was 0 kV. Similarly, the DC voltage amplitude at the AC side of No. 1 valve tower was 0 kV, and the DC voltage amplitude at the DC side of No. 3 valve tower was 500 kV. The AC and DC voltage components were evenly shared by all submodules of the bridge arm valve towers.

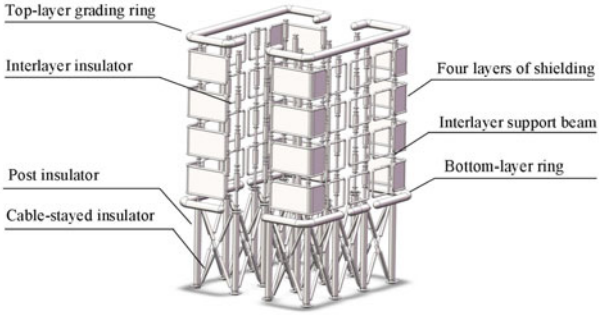

(a) Physical structure diagram of converter valve tower

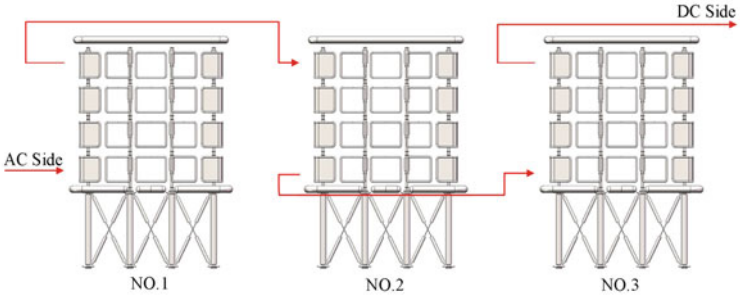

(b) Electrical connection between valve towers

Fig. 1 Valve tower structure and voltage loading

2.2 *Electric Field Calculation Settings Under Transient and Steady Conditions*

Under the power frequency voltage, the influence of induced electric field could be ignored, and it was considered that the electric field of the converter valve tower was quasi-static electric field. In the closed air field domain, the current met the current continuity equation, thus:

$$\begin{cases} \nabla \times \dot{\boldsymbol{E}} \approx 0 \\ \dot{\boldsymbol{E}} = -\nabla \dot{\varphi} \\ \nabla \cdot \dot{\boldsymbol{J}} = 0 \\ \dot{\boldsymbol{J}} = \gamma \dot{\boldsymbol{E}} + j\omega\varepsilon_0\varepsilon_r \dot{\boldsymbol{E}} \end{cases} \tag{1}$$

where: ω is the angular frequency; ε_0 is the dielectric constant of vacuum; ε_r is the relative dielectric constant; γ is the conductivity; φ is the potential; $\dot{\boldsymbol{E}}$ is the electrical field; according to Formula (1):

$$(j\omega\varepsilon_0\varepsilon_r + \gamma)\nabla^2\dot{\varphi} = 0 \tag{2}$$

Ratio of conduction current density $\boldsymbol{J}_c$ to displacement current density $\boldsymbol{J}_d$

$$\frac{|\boldsymbol{J}_c|}{|\boldsymbol{J}_d|} = \frac{|\gamma \dot{\boldsymbol{E}}|}{|j\omega\dot{\boldsymbol{E}}|} = \frac{\gamma}{j\omega\varepsilon_0\varepsilon_r} \tag{3}$$

Depending on the ratio between the displacement current density to conduction current density in various media, the principle of the electrostatic field or the constant electric field was chosen to solve the problem. For the coupling of solution principles, the potential distribution on the surface of the insulator was firstly solved according to the principle of constant electric field, which was taken as the first type of boundary condition and coupled to the calculation of the remaining electrostatic field [5, 6].

In the transitory state, the influence of nonlinear dielectric constant of the material was ignored in the model to simplify the computation. The electrostatic field distribution on the valve tower surface at the peak impact voltage was used to replace the transient electric field distribution of the valve tower at the impact voltage [7]. For an offshore converter platform, the impact of operating overvoltage on insulation performance was much greater than lightning overvoltage. Therefore, voltage was set as the peak value of operating impact overvoltage in Sect. 4.

3 Electric Field Calculation and Analysis Under Steady State Condition

3.1 Computational Domain and Boundary Conditions

The computational domain should be designed far enough to avoid the influence of wall on the calculation result in the electric field calculation of valve tower fittings under steady state condition. The computational domain settings in the study were shown in Fig. 2a considering computer resources required. The potential boundary setting on the valve tower surface was shown in Fig. 2b base on the introduction of Sect. 2.

3.2 Limit Value of Surface Electric Field of Fittings

To ensure the safe and stable operation of the valve tower, it was necessary to strictly monitor the electrical field intensity of the valve tower fittings to prevent coronation. The gap form and potential distribution of valve tower fittings were so complicated that there was no unified standard for selecting the surface electric field limit value of valve tower fittings. Liu Peng obtained the relationship between corona inception

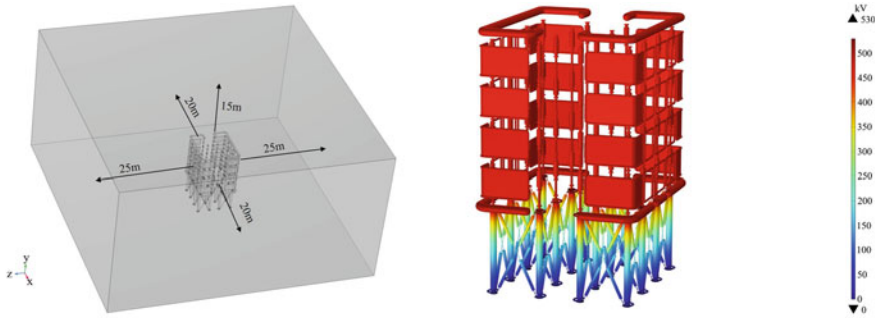

(a) Computational domain (b) Valve tower potential distribution

Fig. 2 The model calculation field and boundary condition

field strength and equivalent curvature radius of the instrument per corona test [8]. Wei et al. drew similar findings from the simulation calculation. Figure 3 showed the variation law of the limit value of the fittings field strength along with the equivalent radius of the electrode and its fitting curve [9] whose goodness of fit R^2 was 95.7%. This paper has selected the limit value of the field strength of different electrodes in relation to this curve.

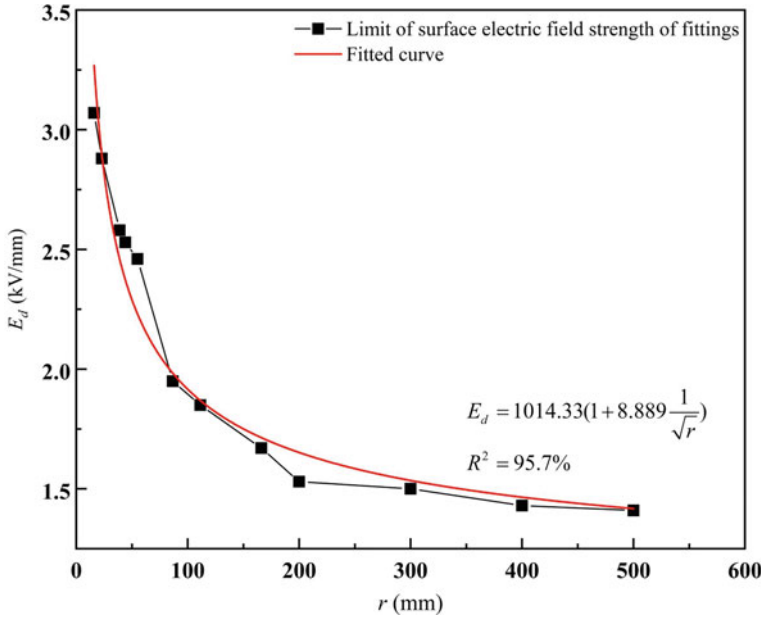

Fig. 3 Limit curve of surface electric field strength of fittings

3.3 *Electric Field Distribution of Key Parts of Converter Valve*

Figure 4 showed the electrical field distribution of converter valve tower shield cover, insulator fittings, interlayer support beams, internal support insulators and cable-stayed insulator fittings under equilibrium conditions. From the calculation results, it could be seen that:

The positions of the uneven electrical field of the shield were located at the corner of each shield and the end of the pressure equalizing rings with the maximum field strength of 0.722 kV/mm. The pillar insulators and the inter-layer insulators exhibited similar uneven positions with a maximum field strength of 0.771 and 0.255 kV/mm. The maximum point field strength of interlayer insulator and cable-stayed insulator were located at the change of medium. The maximum value field strength of cable-stayed insulator was 1.98 kV/mm, which exceeded the surface electric field strength limit of 1.61 kV/mm.

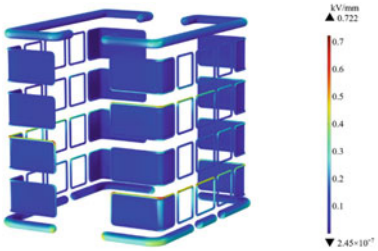

(a) Electric field distribution of shield surface

(b) Electric field distribution of insulator fittings

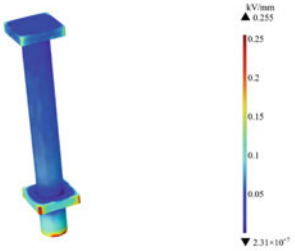

(c) Electric field distribution of layer bracing beam

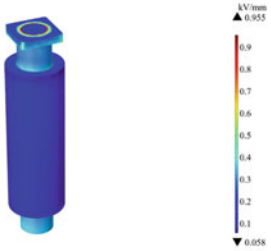

(d) Electric field distribution of layer insulators

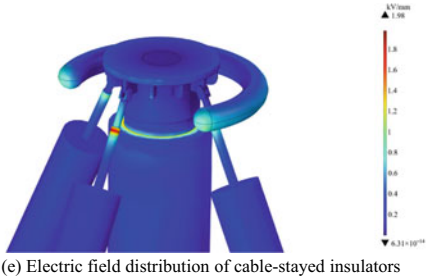

(e) Electric field distribution of cable-stayed insulators

Fig. 4 Electric field distribution on the surface of fittings

4 Configuration of Structure Parameters of Converter Valve Tower Under Transient Condition

4.1 The Position Design of Valve Tower in Valve Hall

The influence of the distance D between the converter valve tower and the wall, the distance L_1 between the bridge arm valve towers and the distance L_2 between the adjacent bridge arm valve towers on the surface field of valve tower shield case were considered in this section.

Figure 5a showed the relation between the maximum electrical field strength of the valve tower shield surface and D along the x, y, and z directions. It could be easily seen from the figure that the field strength of the shield surface gradually decreases with the increase of D. The limit of surface field strength is 1.7532 kV/mm, and corona will not be generated on the shield surface when $D > 5$ m.

Figure 5b, c demonstrated the influence of L_1, L_2 on the shielding electrical field of the valve towers. When $L_1 = 6$ and 8 m, the inflection points of electric field intensity appeared whose maximum value electric field intensity of the two valve towers was

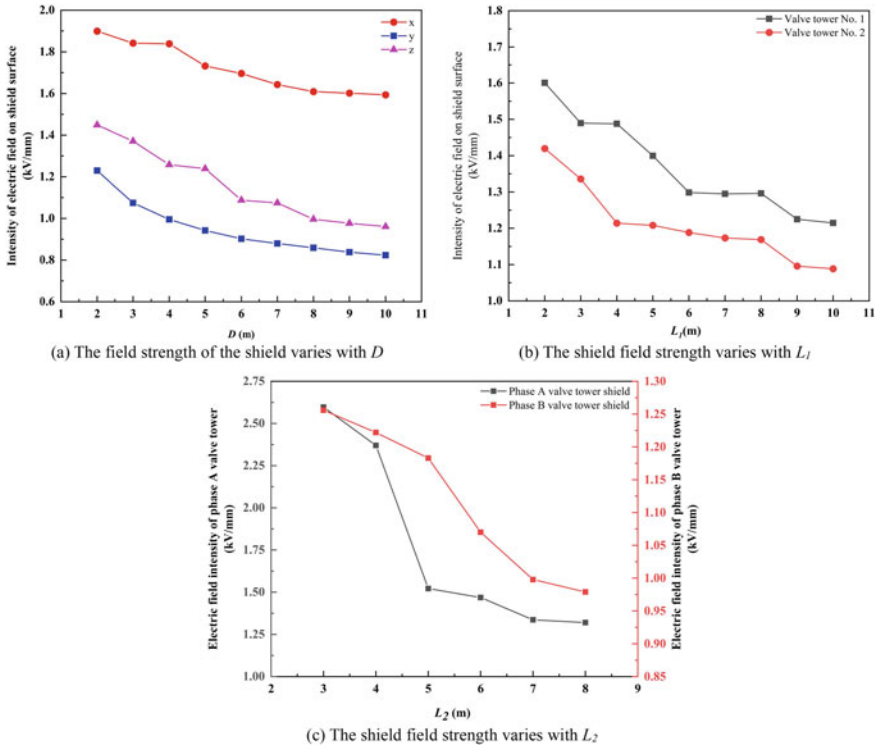

(a) The field strength of the shield varies with D

(b) The shield field strength varies with L_1

(c) The shield field strength varies with L_2

Fig. 5 The electric field strength of valve tower shield varies with valve tower positions

1.298 and 1.188 kV/mm respectively. Considering that the absolute value of the decrease of electric field intensity was only 0.1 kV/mm after $L_1 > 6$ m, $L_1 = 6$ m was a more appropriate choice. The curve trend in Fig. 5c was similar to that in Fig. 5b. When $L_2 < 7$ m, the electric field intensity of the shield rapidly decreases. When $L_2 = 7$ m, the electric field intensity of the two valve towers was 1.336 and 0.998 kV/mm, respectively. It was reasonable to select this point as the distance between valve towers of adjacent bridge arms because of a gradual slowing of the curve when $L_2 > 7$ m.

4.2 *Parameter Design of Voltage Balancing Ring for Cable-Stayed Insulators*

In order to avoid corona, voltage equalizing rings should be set for the cable-stayed insulators fittings, as shown in Fig. 6a. The influence of the diameter d and radius R of the voltage equalizing rings of the voltage equalizing effect were studied.

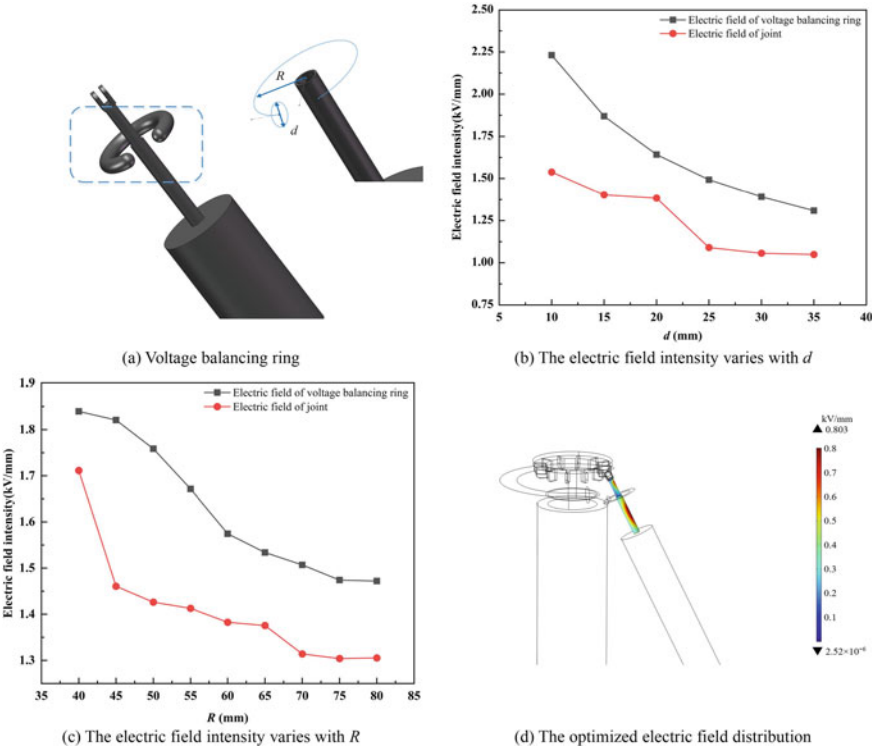

Fig. 6 The electric field strength of valve tower shield varies with valve tower position

According to the analysis of the results in Fig. 6b, c, the electric field intensity at the contact position between the cable-stayed insulators and their fixtures decreased obviously after the installation of voltage equalizing rings. At the same time, with the increase of pipe diameter d and radius R, the electric field intensity at the contact position decreased to 1.305 and 1.049 kV/mm, respectively. And the decreases reach 34.1 and 47.03% with the surface limiting field strength of 2.2463 and 1.6154 kV/mm respectively.

When the diameter d and radius R of the voltage equalizing ring were 25 and 70 mm respectively, the electric field intensity decreased significantly compared with the previous data points. The electric field intensity did not change obviously when d and R continued to increase. Therefore, the parameters of the voltage balancing ring selection in this paper were $d = 25$ mm and $R = 70$ mm. The electrical field balancing effect was shown in Fig. 6d with the field strength value of 0.803 kV/mm.

4.3 Shield Case Size Parameters Design

In this section, the pipe diameter ρ of the edge of the shield and the layer height h of the shield were selected as the research objects, as shown in Fig. 7a. With the increase of ρ, the surface field strength decreased significantly, as shown in Fig. 7b. The electric field intensity decreased obviously when $\rho = 45$ mm compared with the previous data point, and the maximum electric field intensity of the shield edge surface was 0.7506 kV/mm under the limit value of 1.3885 kV/mm. The electric field intensity decreased only by 0.1665 kV/mm with the subsequent increase of ρ with 35 mm. Therefore, tube diameter $\rho = 45$ mm was the choice of both insulation performance and economy.

Figure 7c reflected the influence of shield h on the field intensity of shield surface. With the increase of h, the electric field intensity decreased and the downward trend gradually slowed down. Since the value of h not only depended on the insulation performance [10, 11], the research results could provide a reference for designers to minimize the valve tower volume when other requirements were met.

5 Conclusion

(1) A 3D model of ± 500 kV converter valve tower based on practical engineering was established, and the insulation performance of the outer shield of valve tower was analyzed emphatically. According to the transient and steady-state conditions, the calculation model was set differently.

(2) The electric field distribution of the valve tower under steady state condition was calculated and analyzed. The calculation results showed that the maximum value of the field strength of the valve tower was concentrated on the edge of the shield, the end of the field equalized rings, the contact between the insulator

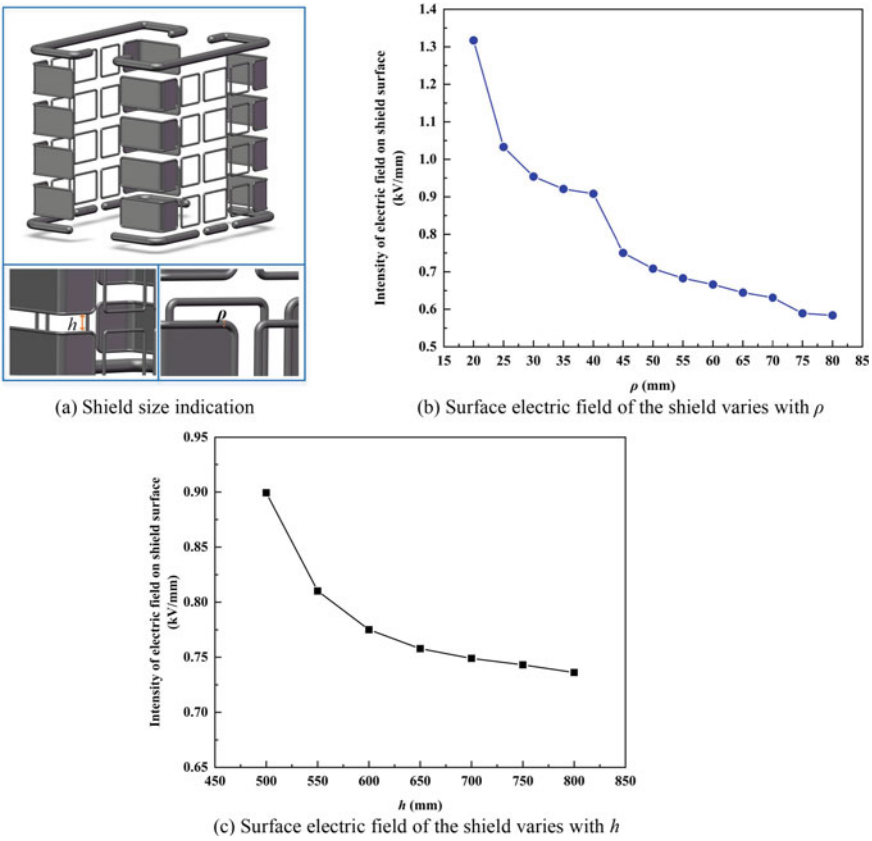

(a) Shield size indication

(b) Surface electric field of the shield varies with ρ

(c) Surface electric field of the shield varies with h

Fig. 7 The electric field intensity varies with the parameters of the shielding case

and the support beams, and the contact interface between the stayed insulator and the connecting fixture.

(3) The spacing D between valve tower and wall, the spacing L of valve towers, the radius R of cable-stayed insulators, the diameter d of tube, the diameter ρ of the tube at the edge of the shield, and the configuration methods of the parameters h of floor height were determined which provided the basis for lightweight design and electrical equipment layout of valve hall.

References

1. Chen P, Zhou GL, Ma L et al (2021) Valve Hall layout and dimension calculation method of offshore flexible DC converter station. Southern Power Syst Technol 15(11):62–66 (in Chinese)
2. Gontijo GF, Bakhshizadeh MK, Kocewiak LH et al (2022) State space modeling of an offshore wind power plant with an MMC-HVDC connection for an eigenvalue-based stability analysis. IEEE Access 10:82844–82869
3. Xie B, Mei N, Zhang ZX et al (2021) Electric field simulation and insulation optimization of metal parts and insulator in ±1100 kV DC converter valve module. High Volt Appar 57(02):105–115 (in Chinese)
4. Zhang D, Ouyang YP, Shang HY et al (2017) Electric field simulation of voltage source converter valve under insulation type test. Electric Power 36(02):76–81 (in Chinese)
5. Qiu Z, Ruan J, Lu W, Wang X, Jin Q (2018) Feature extraction of electric field distribution and its application in discharge voltage prediction of large sphere-plane air gaps. IEEE Trans Dielectr Electr Insul 25(3):1030–1038
6. Zhang X, Sun J, Zhang ZJ et al (2019) Structure improvement of ±1100 kV converter valve shield and U_{50} test. High Volt Eng 45(11):3693–3699 (in Chinese)
7. Yang X, Wang QY, Liao JT et al (2017) Calculation of transient electric field of 750 kV composite cross arm under standard lightning overvoltage. High Volt Eng 43(02):645–653 (in Chinese)
8. Zhang W, Yang GH, Li YJ et al (2022) Typical electrode corona characteristics and shielding electrode design of UHV converter station in high altitude area. High Volt Appar 58(04):124–130 (in Chinese)
9. Liu P, Wu ZH, Cheng JW et al (2021) Simulation analysis and differentiation Optimization method of electric field distribution of DC shielding equipment in UHV multiterminal soft direct converter station. Power Syst Technol 45(06):2405–2412 (in Chinese)
10. Liu C, Hu S, Han K, Hu Q, Gao S, Yao W (2019) Electric-field distribution and insulation status of ±800 kV UHVDC converter valve after implanting full-view micro-sensor detector. IEEE Access 7:86534–86544
11. Bouhaouche M, Mekhaldi A, Teguar M (2017) Improvement of electric field distribution by integrating composite insulators in a 400 kV AC double circuit line in Algeria. IEEE Trans Dielectr Electr Insul 24(6):3549–3558

Quantitative Analysis of the Impact of Harmonics on Ampacity of ACSR Using Finite Element Simulation

Lei Zhang, Rui Li, Liang-yuan Chen, Shao-ming Pan, and Xia-jin Rao

Abstract This paper proposes a novel approach to evaluate the impact on ampacity of the aluminum conductor steel reinforced (ACSR) induced by the harmonics. This approach is conceived from the following ideas. First, the Bessel function is used to solve the Maxwell equations of the ACSR, so as to derive the expression of distribution of current density for the ACSR. Based on it, considering the harmonic heating, the analytical expression of the ampacity of the transmission line is modeled by using the heat balance equation. Finally, a two-position finite element model of the ACSR is established in COMSOL to verify the effectiveness and accuracy of the proposed approach by injecting different harmonic distortion. The results demonstrate that harmonics can definitely reduce the maximum ampacity of ACSR, especially in the case of poor heat dissipation conditions, i.e. (1) low wind speed and (2) high temperature.

Keywords Aluminum conductor steel reinforced (ACSR) · Harmonic · Bessel function · Transmission line

L. Zhang (✉) · R. Li · L. Chen · S. Pan · X. Rao
Guangxi Key Laboratory of Intelligent Control and Maintenance of Power Equipment, Electric Power Research Institute of Guangxi Power Grid Co., Ltd., Nanning, Guangxi 530023, China
e-mail: 464873459@qq.com

R. Li
e-mail: 1193736858@163.com

L. Chen
e-mail: chen_ly.sy@gx.csg.cn

S. Pan
e-mail: peterpansm@foxmail.com

X. Rao
e-mail: rao_xj.sy@gx.csg.cn

© Beijing Paike Culture Commu. Co., Ltd. 2024

X. Dong and L. Cai (eds.), *The Proceedings of 2023 4th International Symposium on Insulation and Discharge Computation for Power Equipment (IDCOMPU2023)*, Lecture Notes in Electrical Engineering 1102, https://doi.org/10.1007/978-981-99-7405-4_51

1 Introduction

With the increasing applications of renewable energy, many countries improve the capacity of transportation of clean energy by establishing more transmission lines [1, 2]. However, the maximum ampacity of the existing transmission line will change in real time with the impact of the temperature, sunshine, wire sag and other factors [3, 4], Thus, many scholars have conducted the dynamic capacity-increase technology to improve the maximum capacity of the transmission line under different operation conditions [5–7].

Essentially speaking, the dynamic capacity-increase technology of the power transmission line is based on the accurate dynamic calculation and prediction for the ampacity of the transmission line, and the dynamic thermal rating technology (DTR), as an effective calculation and prediction approach, has been widely adopted to real-time calculation of the ampacity. DTR can calculate the maximum ampacity based on immediate environmental and conductor conditions, which has the advantage of being fast and low cost. Studies have verified that the use of DTR technology can effectively increase the capacity of the transmission line by 10–30% [8–10]. Reference [11] proposed a modified DTR for predicting the change of wind speed in different areas of the line through a scenario prediction model. The model data comes from the weather conditions in twelve hours and 2–3 km range of the Italian weather forecast agency combined with a large number of real-time monitoring data. Based on it, Ref. [12] further developed a method to exploit the potential of existing transmission facilities by using OTS and DTR technology, thus ensuring the reliability of the power system. Where OTS is one type of the optimal transmission switching technology, which can optimize and reduce the operating cost by disconnecting part of the transmission lines [13].

In recent years, the existing studies have revealed that the ampacity of the transmission line is affected by factors i.e. wind speed, sunshine, current size and other factors involved in the heat balance. Reference [14] proves that wind speed and line capacity have a strong correlation. Authors in [15–18] have adopted the stochastic optimization and robust optimization to improve the transmission capacity of the power transmission system under different wind speeds. However, with the increase of new energy power, the harmonic in the transmission line is gradually increasing, and the harmonic heat generation will also become an important factor affecting the heat balance of the transmission line, thereby affecting its ampacity. Therefore, this paper studies the influence of harmonics on the ampacity of transmission lines, which has practical application significance for the improvement of transmission capacity of transmission lines.

Inspired by the above studies, this paper establishes the mathematical relationship between the harmonic AC resistance and the ampacity of the transmission line by solving the Maxwell equations and heat balance equations of the target conductor, so as to evaluate the impact on the ampacity of the transmission line induced by harmonics. Finally, a two-dimensional finite element model for the ACSR is established to verify the accuracy of the proposed approach. The results demonstrate

that harmonics can definitely reduce the maximum ampacity of ACSR due to the harmonic heating.

2 Calculation of AC Resistance of ACSR

Taking the cylindrical conductor as an example, its internal electric field strength E is evenly distributed within the surface of the conductor section from the center of the cross-section circle r, and when the internal current of the wire is sinusoidal current, the internal electric field vector of the wire is shown as Eq. (1).

$$\vec{E} = \mathrm{Im}\left(\dot{E}_{\max} \exp(j\omega t)\right) \tag{1}$$

To find the distribution of the current density inside the conductor, Maxwell's system of equations is established as shown in Eq. (2).

$$\begin{cases} \nabla \cdot \vec{D} = \rho \\ \nabla \times \vec{E} = -\dfrac{\partial \vec{B}}{\partial t} \\ \nabla \cdot \vec{B} = 0 \\ \nabla \times \vec{H} = \vec{j}_c + \dfrac{\partial \vec{D}}{\partial t} \\ \nabla \times \vec{F} = \vec{e}_r\left(\dfrac{1}{r}\dfrac{\partial F_z}{\partial \alpha} - \dfrac{\partial F_\alpha}{\partial z}\right) + \vec{e}_\alpha\left(\dfrac{\partial F_r}{\partial z} - \dfrac{\partial F_z}{\partial r}\right) + \vec{e}_z\left(\dfrac{1}{r}\dfrac{\partial (rF_\alpha)}{\partial r} - \dfrac{1}{r}\dfrac{\partial F_r}{\partial \alpha}\right) \\ \vec{j}_c = \sigma \vec{E} \\ \vec{B} = \mu \vec{H} \end{cases} \tag{2}$$

where $\vec{D}$ is the electrical displacement vector, ρ is the amount of charge, $\vec{E}$ is the Electric field intensity vector, $\vec{B}$ is the magnetic induction intensity vector, H is the magnetic field strength vector, $\overrightarrow{j_c}$ is the current density, $\vec{F}$ is a vector, r, α, z respectively represent the three coordinate variables under the cylindrical reference frame, $\overrightarrow{e_r}$, $\overrightarrow{e_\alpha}$, $\overrightarrow{e_z}$ are the three unit vectors perpendicular to each other under the cylindrical coordinate system, respectively. And σ is the electrical conductivity, μ is the permeability.

Joint Eqs. (1) and (2), Differential equation about the strength of the electric field and the radius of the conductor can be obtained as shown in Eq. (3).

$$r^2 \frac{d^2 \dot{E}_{\max}}{dr^2} + r\frac{d\dot{E}_{\max}}{dr} - j\omega\mu\sigma r^2 \dot{E}_{\max} = 0 \tag{3}$$

Solving Maxwell's equations using Bessel's equations yields Eq. (4).

$$\dot{E}_{\max} = \frac{\dot{I}_{\mathrm{m}}\sqrt{\mathrm{j}\omega\mu}}{2\pi R\sqrt{\sigma}\sum_{i=0}^{\infty}\frac{(-1)^i}{i!\Gamma(1+i+1)}\left(\frac{R\sqrt{\mathrm{j}\omega\mu\sigma}}{2}\right)^{2i+1}}\sum_{i=0}^{\infty}\frac{(-1)^i}{i!\Gamma(0+i+1)}\left(\frac{r\sqrt{\mathrm{j}\omega\mu\sigma}}{2}\right)^{2i+0} \tag{4}$$

Substituting Eqs. (1) and (4) into Eq. (2) solves for the current density inside the conductor as shown in Eq. (5). From Eq. (5), it can be seen that the factors that affect the distribution of wire current density are wire conductivity, permeability, radius and internal current frequency.

$$\vec{j}_c = \mathrm{Im}\left(\frac{\dot{I}_{\mathrm{m}}\sqrt{\mathrm{j}\omega\mu\sigma}}{2\pi R\sum_{i=0}^{\infty}\frac{(-1)^i}{i!\Gamma(1+i+1)}\left(\frac{R\sqrt{\mathrm{j}\omega\mu\sigma}}{2}\right)^{2i+1}}\sum_{i=0}^{\infty}\frac{(-1)^i}{i!\Gamma(0+i+1)}\left(\frac{r\sqrt{\mathrm{j}\omega\mu\sigma}}{2}\right)^{2i+0}\exp(j\omega t)\right)\vec{e}_z \tag{5}$$

Assuming that the conductivity of each part of the wire is unchanged, in the case of a certain current size of the wire and the internal current distribution of the wire, the size of the wire resistance is proportional to the reciprocal of the conductivity of the wire. It can be deduced that in the case of the product of wire conductivity, wire permeability, and wire frequency, the size of the wire AC resistance changes linearly with the reciprocal of the conductivity.Then the calculation equation for the AC resistance of the set wire is shown in Eq. (6) (Fig. 1).

$$R_{ac} = \frac{K}{\sigma}f\left(\sqrt{\omega\sigma\mu}\right) \tag{6}$$

The AC resistance of the wire can be calculated as shown in Eq. (7).

$$R_{ac} = \left(\int_0^R j_c^2 \times 2\pi r \times \frac{1}{\sigma}dr\right) \div \mathrm{I}_0^2 \tag{7}$$

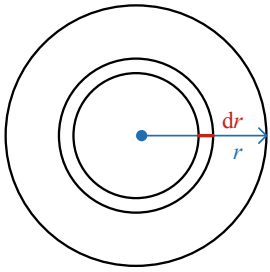

Fig. 1 Conductor cross-sectional view

Substituting Eq. (5) into Eq. (7) can calculate the AC resistance of the conductor as shown in Eq. (8).

$$R_{ac} = \frac{\omega\mu}{4\pi} f\left(\sqrt{\omega\mu\sigma}R\right) \tag{8}$$

Due to the demand for mechanical strength, conductivity and economy of power transmission lines in power engineering, as well as the advantages of ACSRs that are easy to erect, simple in structure, good in economic benefits, and strong adaptability, ACSRs are widely used in overhead lines in transmission and distribution networks. Aluminum in the ACSR mainly bears the conductive role, while the steel core mainly improves the mechanical strength of the wire in order to erect the wire.

The AC resistance of the wire is determined by the radius, conductivity, permeability and internal current frequency of the wire, and the conductivity of the wire changes abruptly with the change of material. Suppose that the radius of the ACSR steel core is R_1, and the radius of the ACSR as a whole is R_2, the equation can be obtained (9).

$$\begin{aligned} R_{\mathrm{ac}} = & \int_0^{R_1} \left(\mathrm{j_c}\pi\left((r+dr)^2-(r)^2\right)\right)^2 \frac{1}{\sigma}\frac{1}{\pi\left((r+dr)^2-(r)^2\right)} \\ & + \int_{R_1}^{R_2} \left(\mathrm{j_c}\pi\left((r+dr)^2-(r)^2\right)\right)^2 \frac{1}{\sigma}\frac{1}{\pi\left((r+dr)^2-(r)^2\right)} \end{aligned} \tag{9}$$

It can be seen from Eq. (9) that the AC resistance of the steel-cored aluminum stranded wire is jointly determined by seven variables: the permeability, conductivity, and radius of the steel core, the permeability and conductivity of the aluminum stranded wire, the thickness of the aluminum core, and the current frequency. In practical applications, a temperature gradient will form inside the ACSR, resulting in different parameters at each location, and k is no longer a function of linear variation with r. Obviously, the equation derived in this paper does not consider this actual situation, and certain errors will occur in engineering applications.

3 Effect of Harmonics on the Ampacity of Aluminum Stranded Wires in Steel Cores

On the one hand, in order to improve the efficiency of power transmission, make full use of the power transmission capacity of power lines. On the other hand, in order to prevent the line from being overloaded, causing the line temperature to be too high, causing safety accidents and causing line loss, it is often necessary to calculate the maximum ampacity of the transmission line under different environments and

working conditions. The ampacity of a transmission line is often determined by the maximum allowable temperature of the line, and heat source and heat dissipation are the two main factors that affect the line temperature. The heat source includes Joule heat generated by current, corona heaand solar radiation heat. While heat dissipation includes radiation heat dissipation of wires, convection heat dissipation, evaporative heat dissipation, etc.

In this paper, only Joule heat, solar radiation heat, radiation heat dissipation, and convection heat dissipation are considered as factors affecting the line temperature, and the heat balance equation can be obtained as shown in Eq. (10).

$$Q_r + Q_f = Q_s + I^2 R_{ac} \tag{10}$$

where Q_r is thermal radiation power of steel-cored aluminum stranded wire, Q_f is the Air convection cooling power, Q_s is the heat absorption power of the light generated by solar radiation to the wire on the wire, $I^2 R_{ac}$ is the current Joule Thermal Power.

Then the calculation equation for the carrying capacity of the ACSR can be obtained as shown in Eq. (11).

$$I = \sqrt{\frac{0.57\lambda_f \mathrm{Re}^{0.485} + \pi D E_1 S_1 \left[(T_c + 273)^4 - (T_a + 273)^4\right] - \alpha_s J_s D}{R_{\mathrm{ac}}}} \tag{11}$$

where $E_1 = 0.9,\ S_1 = 5.67 \times 10^{-8}\ \mathrm{W/m^2},\ \alpha_s = 0.9,\ J_s = 1000\ \mathrm{W/m^2}$.

According to Eq. (11), the stronger the intensity of insolation, the smaller the ampacity. The greater the maximum allowable temperature, the greater the ampacity. The higher the current frequency, the more pronounced the skin effect and the smaller the ampacity. In addition, it should be noted that the calculation equation for the AC resistance of the wire in the second part is derived under the premise of only the amount of fundamental wave. However, in the actual power grid operation, there are harmonics of different orders in the line, which will produce corresponding AC resistance and is equivalent to adding an additional heat source on the basis of the fundamental wave.

In the power system, only the fundamental wave is used, so the line ampacity is only for the fundamental wave. When considering the presence of harmonics, assuming that the harmonic size of each order is I_i and the corresponding AC resistance is R_{aci}, the calculation equation of the line ampacity can be obtained as shown in Eqs. (12) and (13).

$$I = \sqrt{\frac{Q_r + Q_f - Q_s - \sum_i {I_i}^2 R_{aci}}{R_{\mathrm{ac}}}} (i \geq 2) \tag{12}$$

$$R_{aci} = \frac{1}{2} f_0 i \mu \left(a x^b + c\right) (i \geq 1)$$

$$x = \sqrt{2\pi f_0 i \mu \sigma} D \tag{13}$$

where $f_0 = 50\,\text{Hz}$, a, b, c are determined by the parameters of the reinforced aluminum strand.

According to Eqs. (12) and (13), the presence of harmonics will reduce the maximum ampacity of the transmission line. On the one hand, the AC resistance generated by it will increase the line resistance; On the other hand, it generates more heat, resulting in a reduction in the extreme value of heat generated by the fundamental wave at the same line temperature, resulting in a lower maximum ampacity.

4 Simulation

In order to verify the negative impact of harmonics on the current capacity of transmission lines and the accuracy of the above analysis. In this paper, a two-dimensional finite element model of the ACSR with the model LGJ-150/25 is established in the comsol for simulation experiments, as shown in Fig. 2, and the strand parameters are shown in Table 1.

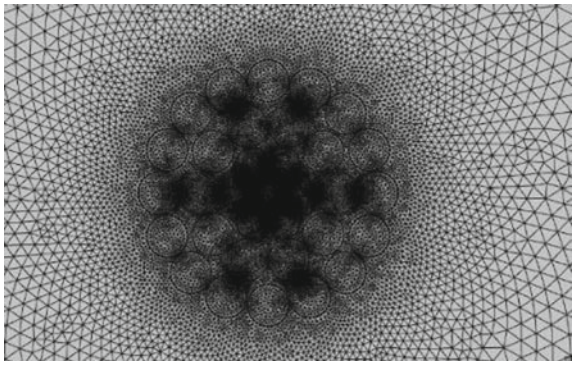

Fig. 2 The two-dimensional finite element model of a ACSR

Table 1 ACSR (LGJ-150/25) data sheet

Parameters	Numeric value	Parameters	Numeric value
ACSRed model	LGJ-150/25	DC Resistance $\leq$ /(Ω/km)	0.1939
Number of steel core strands	7	Total cross-sectional area/ mm^2	173.11
Diameter per strand of steel core/mm	2.10	Cross-sectional area of the steel core/mm^2	148.86
Number of aluminum core strands	26	Aluminum core cross-sectional area/mm^2	24.25
Diameter per strand of aluminum core/mm	2.70	Number of aluminum core layers	2

In the test, the maximum allowable temperature of the line is set to 70 °C, and the endothermic and exothermic heat that affect the line temperature at this time are calculated as follows.

$$Q_r = 8.87\,\text{W},\ Q_f = 35.20\,\text{W},\ Q_s = 7.70\,\text{W}$$

In the finite element model of ACSR, a fundamental current of 450 A and harmonics as shown in Table 2 are injected. Among them, the harmonics of each group are doubled in turn.

When the wind speed is 0.5 m/s and the ambient temperature is 20 °C, the change of the ampacity in the wire is measured as shown in Fig. 3. According to Fig. 3, under the reference environment factor, the larger the amount of harmonics, the smaller the ampacity. The existence of harmonics does have a negative impact on the ampacity, but the impact is small.

Table 2 Harmonic injection amount

Test order	The magnitude of harmonic current (A)									THD (%)
	2	3	4	5	6	7	8	9	10	
1	0.85	0.8	0.75	0.7	0.65	0.6	0.55	0.5	0.45	0.436
3	2.55	2.4	2.25	2.1	1.95	1.8	1.65	1.5	1.35	1.310
5	4.25	4	3.75	3.5	3.25	3	2.75	2.5	2.25	2.183
7	5.95	5.6	5.25	4.9	4.55	4.2	3.85	3.5	3.15	3.057
9	7.65	7.2	6.75	6.3	5.85	5.4	4.95	4.5	4.05	3.931
11	9.35	8.8	8.25	7.7	7.15	6.6	6.05	5.5	4.95	4.807
13	11.05	10.4	9.75	9.1	8.45	7.8	7.15	6.5	5.85	5.683
15	12.75	12	11.25	10.5	9.75	9	8.25	7.5	6.75	6.561
17	14.45	13.6	12.75	11.9	11.05	10.2	9.35	8.5	7.65	7.441

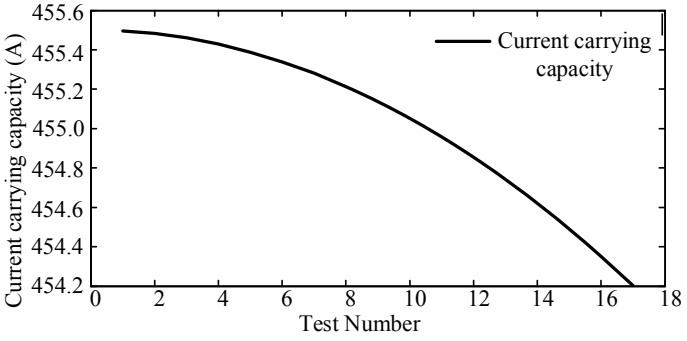

Fig. 3 Ampacity increases with harmonic content

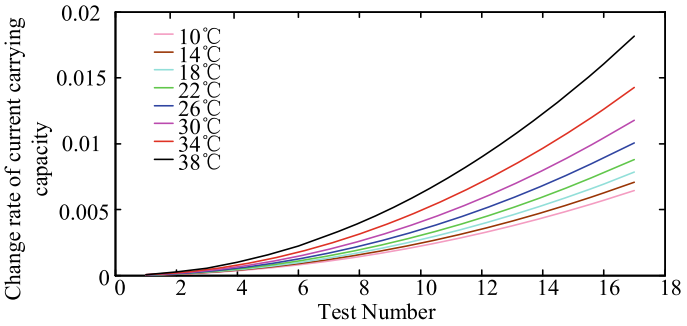

Fig. 4 Variation of ampacity with temperature and harmonic content

Changing the ambient temperature, the change of the ampacity of the wire is obtained as shown in Fig. 4. According to Fig. 4, when the wind speed is 0.5 m/s, with the increase of the ambient temperature, the change of the ampacity of the wire increases, and the sensitivity to the harmonic quantity increases.

Change the wind speed to obtain the change of the ampacity of the wire as shown in Fig. 5. According to Fig. 5, when the ambient temperature is 40 °C, as the wind speed increases, the change in the carrier capacity of the wire decreases, and the sensitivity to harmonics decreases.

According to the above content, in the case of poor heat dissipation conditions such as higher ambient temperature and lower wind speed, the negative impact of harmonics on the wire is greater.

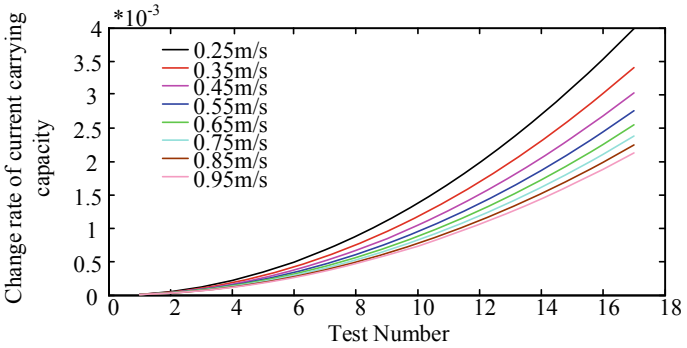

Fig. 5 Variation of conductor ampacity with wind speed and harmonic content

5 Conclusion

This paper has proposed and demonstrated a novel approach to evaluate the impact on ampacity of the transmission line induced by harmonics, the distinguished feature and contribution of this paper are summarized as follows. (1) maxwell equations are solved by using Bessel equations to obtain the current density distribution inside a uniform cylindrical conductor, and the analysis results have revealed that its AC resistance is affected by the conductor conductivity, permeability, radius size and internal current frequency. (2) Due to the impact of the skin effect, harmonics with higher frequencies will increase the AC resistance of the conductor, thereby reducing its ampacity. (3) Harmonic heating will reduce the maximum ampacity of the transmission line, this result is obtained by deriving and evaluating the analytical expression of the ampacity of the transmission line, which is also verified by the finite element simulation.

Acknowledgements This paper is supported by Science and Technology Project of Guangxi Power Grid CO under project number **GXKJXM20220072**.

References

1. Rahman M, Atchison F, Cecchi V (2020) Grid integration of renewable energy sources: utilization of line thermal behavior. In: SoutheastCon 2019, pp 1–7. IEEE, USA
2. Rácz L, Szabó D, Göcsei G, Németh B (2018) Grid management technology for the integration of renewable energy sources into the transmission system. In: 7th international conference on renewable energy research and applications (ICRERA) 2018, pp 612–617, IEEE, USA
3. Zhu J, Zhou L, Wang S, Zhou X, Kang L, Zhao W (2021) Meteorological boundary analysis of overhead transmission lines carrying capacity in Zhejiang Province. In: 2021 6th international conference on power and renewable energy (ICPRE), pp 164–167. IEEE China
4. Sun L, Zhang R, Tian M, Zhang H, Tian W, Xu J (2021) Power flow calculation and conductor temperature change process analysis of single-line direct supply traction network. IEEE Access 9:57632–57644
5. Huan Z, Sha Y, Zhou M, Sun Y, Wu Y, Yuan X (2020) Evaluating transmission network flexibility considering uncertainties. In: IEEE 4th conference on energy internet and energy system integration (EI2). IEEE, USA, pp 1822–1827
6. Zhan J, Liu W, Chung CY (2019) Stochastic transmission expansion planning considering uncertain dynamic thermal rating of overhead lines. IEEE Trans Power Syst 34(1):432–443
7. Zhang H, Zhang S, Cheng H, Wang Z, Zhang J (2019) Probabilistic transmission network expansion planning considering integration of wind power. In: IEEE innovative smart grid technologies—Asia (ISGT Asia) 2019. IEEE, China, pp 3194–3198
8. Douglass D et al (2016) Real-time overhead transmission-line monitoring for dynamic rating. IEEE Trans Power Deliv 31(3):921–927
9. Douglass DA, Edris AA, Pritchard GA (1997) Field application of a dynamic thermal circuit rating method. IEEE Trans Power Deliv 12(2):823–831
10. Seppa TO, Clements M, Payne R, Damsgaard-Mikkelsen S, Coad N (2000) Application of real time thermal ratings for optimizing transmissionline investment and operating decisions. In: Proceedings of CIGRE, pp 22–301

11. Alessandro B, Alberto B, Dinh-Duong L, Fabio B, Giorgio G (2019) Improving DTR assessment by means of PCA applied to wind data. Electric Power Syst Res 172:193–200
12. EL-Azab M, Omran WA, Mekhamer SF, Talaat HEA (2021) Congestion management of power systems by optimizing grid topology and using dynamic thermal rating. Electric Power Syst Res 199–205
13. Fisher EB, O'Neill RP, Ferris C (2008) Optimal transmission switching. IEEE Trans Power Syst Publ Power Eng Soc 23(3):197–208
14. The J, Cotton I (2016) Reliability impact of dynamic thermal rating system in wind power integrated network. IEEE Trans Reliab 65(2):1081–1089
15. Zhan J, Chung CY, Zare A (2017) A fast solution method for stochastic transmission expansion planning. IEEE Trans Power Syst 32(6):4684–469
16. Park H, Baldick R, Morton DP (2015) A stochastic transmission planning model with dependent load and wind forecasts. IEEE Trans Power Syst 30(6):3003–3011
17. Ruiz C, Conejo AJ (2015) Robust transmission expansion planning. Eur J Oper Res 242:390–401
18. Yu H, Chung CY, Wong KP, Zhang JH (2009) A chance constrained transmission network expansion planning method with consideration of load and wind farm uncertainties. IEEE Trans Power Syst 24(3):1568–1576

Simulation and Experimental Study on Vibration and Noise of Power Transformer Under Load

Jun Xiong, Yi Luo, Shubo Ren, Shiyu Lu, Xuekai Pei, Xiaoming Zha, and Wenjun Zhou

Abstract In this study, we conducted an analysis of transformer electromagnetic vibration noise. We studied the vibration and noise characteristics using a multi-field coupling approach through the use of finite element simulation software. Additionally, we conducted an experiment on a laboratory transformer to measure its acoustic and vibration characteristics using an acoustic array and vibration sensor. Our research focused on a 10 kV distribution transformer. The results of our finite element simulation showed that transformer noise mainly comes from the vibration of the core due to magnetostriction, particularly when the load rate was 66%. We analyzed the time-dependent vibration acceleration of a typical position on the surface of the oil tank using a spectrum, which showed that the acceleration concentration was at 100 Hz. We also found a small amount of vibration component at 200–600 Hz. In terms of noise distribution, it was stronger at the top but weaker around certain times. To improve the accuracy of our noise test, we used the acoustic array method during our laboratory experiment to measure vibration displacement, acceleration, and noise characteristics. The experimental results were consistent with our simulation results, providing guidance and reference for the later on-site analysis of vibration and noise on transformers. Overall, our study provides valuable insights into the vibration and noise characteristics of transformers, which can inform future efforts to reduce noise pollution and improve the efficiency of these critical components in the energy infrastructure.

Keywords Transformer · Vibration · Noise · Frequency

J. Xiong · Y. Luo · S. Ren · S. Lu · X. Pei (✉) · X. Zha · W. Zhou
School of Electrical and Automation, Wuhan University, Wuhan 430072, China
e-mail: peixuekai@whu.edu.cn

X. Zha
e-mail: xmzha@whu.edu.cn

J. Xiong
Guangzhou Power Supply Company, Guangdong Power Grid Co., Ltd., Guangzhou 510620, China

© Beijing Paike Culture Commu. Co., Ltd. 2024

X. Dong and L. Cai (eds.), *The Proceedings of 2023 4th International Symposium on Insulation and Discharge Computation for Power Equipment (IDCOMPU2023)*, Lecture Notes in Electrical Engineering 1102, https://doi.org/10.1007/978-981-99-7405-4_52

1 Introduction

Power transformers play a vital role in power systems by transforming voltage and distributing electrical energy. However, when transformers are in operation, they generate noise due to the influence of the electromagnetic environment. This noise is caused by the magnetostrictive effect, which results in vibration as the core changes size and the winding is stressed in the magnetic field. The vibration signal is transmitted to the air, creating acoustic signals that contribute to transformer noise. Understanding the relationship between vibration and acoustic signals is crucial in developing effective noise reduction strategies. By reducing transformer noise, we can improve the efficiency and reliability of power systems while minimizing their impact on the environment and surrounding communities [1–3]. In term of noise, not only can it cause pollution to people's living environment and endanger human health, but also it can affects the service life of equipment, so it is significant to get a better understanding of the vibration and noise from transformer.

At present, the existing studies on transformer vibration and noise are still not mature and lack of combination theory with experiments in lab or under actual operation, focusing on just only theoretical analysis of vibration of the core and winding or just experiments. As to magnetostriction of the core, relevant scholars [4, 5] have conducted some numerical analysis and measured the strain of the core based on different methods. In basis of this, the magnetostrictive force in the core was calculated, which provided a theoretical basis for further study of the magnetostrictive characteristics of the core. He et al. [6] and Foster et al. [7] analyzed the magnetic flux density and vibration displacement distribution of the core for single-phase transformer under the power frequency condition through simulation. In addition, Shao et al. [8] analyzed the time-domain vibration of converter transformer windings by using 3D simulation model, but did not use corresponding tests for verification. Wu et al. [9] used harmonic response analysis method to simulate and calculate the vibration characteristics of transformer surface. Besides, Weiser et al. [10] studied the factors of transformer noise only through experiments, and concluded that the main cause of transformer no-load noise was core magnetostriction. But in case of vibration signals, they ultimately reflected the level of the acoustic, so it is necessary to perform evaluation on the acoustic noise. In terms of noise analysis, Cui et al. [11] used a single capacitive microphone to test the acoustic noise from transformer. Due to difference in distribution of the acoustic field, the test with a single microphone would likely lead to inaccuracy of detection results, thus affecting the formulation of relevant strategies for noise prevention and control.

Based on the analysis above, on one hand, this study used finite element simulation software to conduct theoretical simulation analysis of noise on the basis of vibration generation mechanism according to the characteristics of multi-physical field of vibration and noise. On the other hand, the optimized acoustic detection array was used to carry out relatively accurate evaluation of mechanical vibration and noise of transformer, which can better provide reference and basis for the accurate evaluation of transformer vibration and noise.

2 Theory of Analysis Model of Magnetostrictive Vibration

Assuming that the voltage supplied is

$$U_1 = U_S \sin \omega t \tag{1}$$

According to electromagnetic induction principle, the magnetic induction intensity in core is

$$\mathrm{B} = \frac{\varphi}{S} = \frac{U_s}{\omega N S}\cos\omega t = B_0 \cos\omega t \tag{2}$$

where φ is core magnetic flux, S is the core cross-sectional area and B_0 is the magnitude of magnetic induction intensity.

Because of the relationship between magnetic flux density and magnetic field under unsaturated state, the magnetic field strength is

$$\mathrm{H} = B/\mu = B H_c / B_s = B_0 H_c \cos\omega t / B_s \tag{3}$$

where B_s is saturation magnetic induction and H_c is the coercive force.

As to magnetostriction effects, the magnetostriction ratio is

$$\varepsilon = \Delta \mathrm{L}/L \tag{4}$$

where ε is the magnetostriction ratio, ΔL is the maximum expansion and L is the original dimension.

When under magnetic field, deformation of core resulted from magnetostriction satisfies the relationship:

$$\frac{\Delta L}{L}\frac{1}{dH} = |H|\frac{2\varepsilon_s}{H_c^2} \tag{5}$$

where ε_s is the saturation magnetostriction of core.

By further deduction, we can know that

$$\Delta \mathrm{L} = \mathrm{L}\int_0^H |H|\frac{2\varepsilon_s}{H_c^2}dH = L\frac{\varepsilon_s H^2}{H_c^2} = \frac{L\varepsilon_s U_s^2}{(\omega N_c S B_s)}\cos^2\omega t \tag{6}$$

Taking the derivative of ΔL, the acceleration of vibration is

$$\mathrm{a} = \frac{d^2(\Delta L)}{dt^2} = \frac{2\varepsilon_s U_s^2 L}{(N_c S B_s)^2}\cos 2\omega t \tag{7}$$

From Eq. (7), if operating under 50 Hz, it can be deduced that the basic frequency spectrum of vibration acceleration will be 100 Hz. However, due to the nonlinearity of the core, the magnetic flux density waveform may be not a standard sinusoidal wave. So apart from the fundamental frequency component, vibration signal of the core may contain a number of high harmonic components.

3 Simulation and Results

3.1 Simulation Parameters

Finite element simulation software was used to simulate the vibration and noise of the transformer under specific working conditions. A three-phase oil-immersed transformer (S13-M-30/10 kV) was modeled as a reference, and the transformer core, winding, oil tank and other structures was simplified. In this study, casing and heat sink on the surface of the tank have been ignored, and the laminated structure of the core is not considered (Fig. 1).

Materials and corresponding parameters were set for each structure. Materials type of air, winding, iron core and oil tank were respectively set as air, copper, soft iron (without loss) and structural steel. Parameters like permeability, electrical conductivity and density were shown in Table 1.

During the process of simulation, load rate of 66% was selected as the research condition. Sinusoidal current with phase difference of 120° was applied to the section of three-phase winding that located at the side of high and low voltage, and the influence of excitation current on the assignment was considered. Meanwhile, the number of turns of high and low voltage winding was calculated respectively. Besides, the interface of magnetic field, solid mechanical field and acoustic field was also set. When calculating the coupling field, the transient solution was performed, setting size of the solver to 0.001 s and the total solution time to 0.2 s.

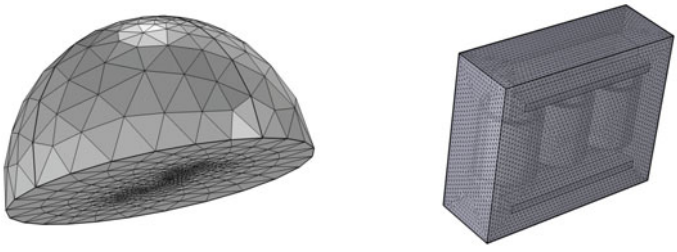

a) Left: Acoustic domain b) Right: Transformer

Fig. 1 Grid division and meshing of simulation model

Table 1 Material parameters of transformer

Material	Relative permeability	Relative permittivity	Conductivity/ (S/m)	Density/ (kg/m^3)	Acoustic velocity (m/s)	Young's modulus (Pa)	Poisson's ratio
Air	1.0	1.0	2.0	1.29	340	–	–
Oil tank	1.0	1.0	$4.032 * 10^6$	7850	12	$2.0 * 10^{11}$	0.3
Core	0.1	1.0	0.1	7268	12	$1.0 * 10^{11}$	0.29
Winding	1.0	1.0	$6.0 * 10^7$	6960	8	$1.1 * 10^{11}$	0.35
Insulating oil	1.0	1.0	1.0	895	1450	–	–

3.2 *Distribution of Magnetic Flux Density on Winding and Core*

Leakage magnetic of transformer between windings will not only lead to local overheating, but also cause electromagnetic force and accompanying vibration as well as noise in the winding. Therefore, when analyzing the vibration and noise of transformer, it is necessary to consider the magnetic leakage on the surface of primary windings and secondary windings (Fig. 2).

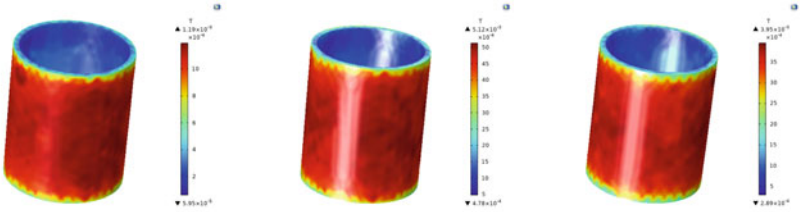

a) Left: Primary winding (phase A) b) Middle: Primary winding (phase B)
c) Right: Primary winding (phase C)

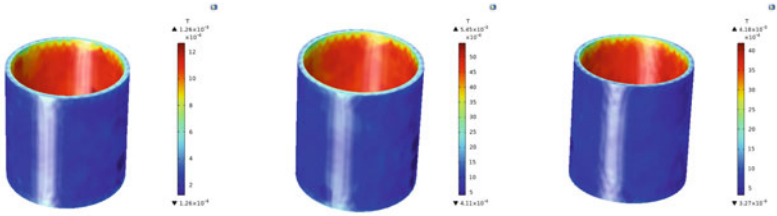

d) Left: Secondary winding (phase A) e) Middle: Secondary winding (phase B)
f) Right: Secondary winding (phase C)

Fig. 2 Distribution of magnetic flux density of primary and secondary windings

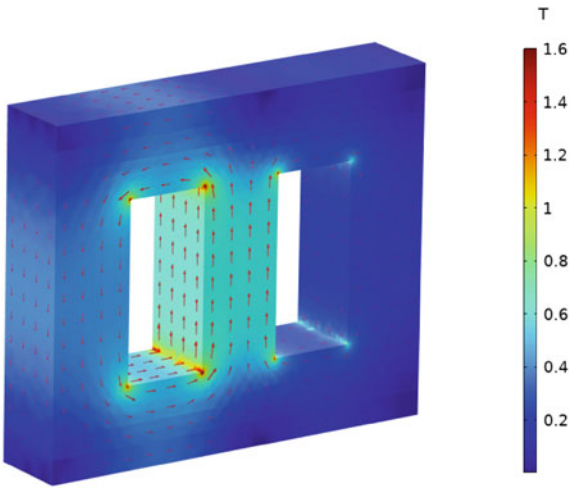

Fig. 3 Flux density distribution of the core (0.134 s)

0.134 s was selected as the research time. At this moment, maximum magnetic flux density of the surface of primary side winding of phase B was 5.45 * 10^{-3} T, which was larger than that of windings in other phase. However, compared with the main magnetic flux density of the transformer under normal operation, the value was much smaller, indicating that the leakage magnetic between the windings could be ignored. Because of that, the vibration of oil tank caused by vibration of the core would be focused on. At 0.134 s, the main magnetic flux density in the core was much higher than that in windings, and the magnetic flux density on the core column corresponding to phase B was larger than other positions (Fig. 3).

3.3 Analysis of Vibration and Noise Characteristics of Transformer

As to distribution transformer, the main cause of vibration comes from the core, and analyzing the characteristics of vibration and accompanying noise will help further clarify the vibration characteristics of the transformer under load.

In this study, vibration of the core and the oil tank was analyzed. Under the condition of fixed constraints on the upper and lower surfaces of the core, the magnetostrictive effect resulted in obvious deformation of the core column in the phase B and the middle part of the upper and lower iron choked at corresponding positions. When it came to position where obvious deformation occurred, it was mainly concentrated in the upper yoke ends of core and core column which may relate to the reason that the upper and lower ends of the core were constrained, which led to larger vibration of the core column area when the core vibrated. Then, deformation of the core caused by magnetostriction was transferred to surface of oil tank through structural

parts. At 0.134 s, the maximum displacement of the core is about 0.47 μm, while the maximum displacement of the tank surface is 0.91 μm. To further analyze, such vibration would led to core loosening and other failures after a long time (Figs. 4 and 5).

Since the actual experimental object of vibration characteristic was the surface of oil tank, thus point D on surface of oil tank was selected as the research object to carry out vibration acceleration and corresponding spectrum analysis.

As could be seen from Fig. 6, due to periodic deformation of the structure in the alternating magnetic field, the vibration acceleration at point D on the tank surface also presented periodic changes on the whole. Fourier transform process was performed on the vibration acceleration data at point D to obtain the results in the frequency domain within the range of 0–1000 Hz. Figure 6 showed the frequency domain distribution of vibration acceleration at point D, indicating that the vibration

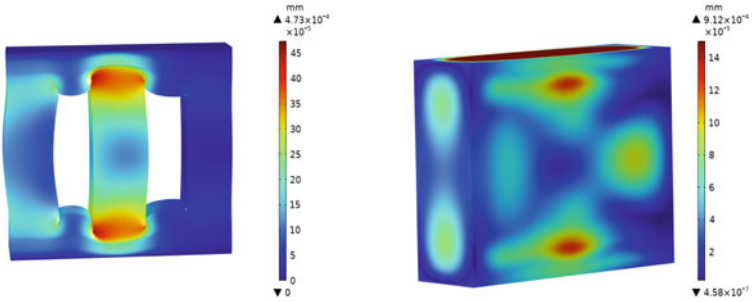

a) Left: Surface of core b) Right: Surface of oil tank

Fig. 4 Vibration displacement of core and oil tank surface

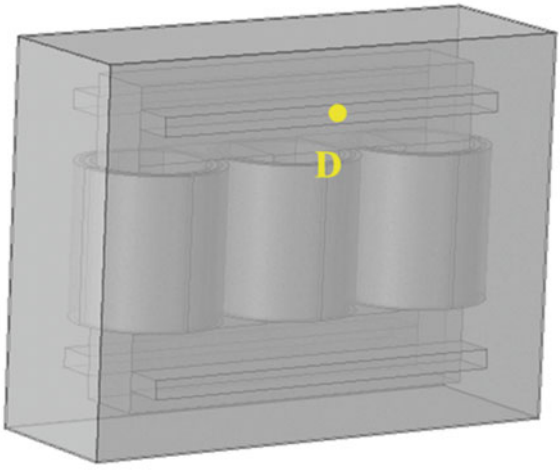

Fig. 5 Selection of research point for vibration characteristics of oil tank surface

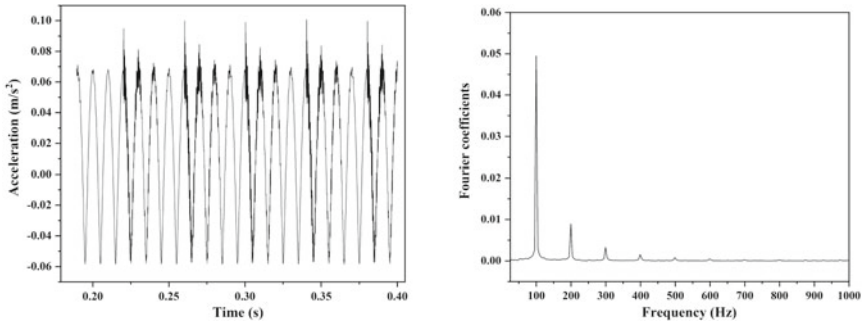

a) Left: Acceleration of research point b) Right: Spectrum corresponding to acceleration

Fig. 6 Acceleration and corresponding spectrum of the research point on the surface of oil tank

acceleration signal took 100Hz as the fundamental frequency and a small number of vibration components were distributed ranging from of 200 to 600 Hz, while at the frequency of 700 Hz and above, vibration component of the core basically attenuated to zero. According to principle of electromagnetic induction and the relationship between magnetic flux density and magnetic field intensity, the deformation expansion of silicon steel sheet under magnetostrictive effect has a synchronous relationship with the 50 Hz power frequency and the vibration acceleration has a two-fold relationship with the 50 Hz power frequency, which could well verify the simulation results.

The acoustic domain of the transformer with a radius of approximately 1.3 m was analyzed. Results showed that acoustic field at the top was intense at 0.134 s and the maximum value was 60.7 dB. In order to make an overall evaluation for the noise on the side of oil tank, 8 points on the side of the hemispherical acoustic domain were selected to analyze the acoustic pressure level. After calculating, results showed that the average value was 50.3 dB (Fig. 7).

4 Experiment and Results

4.1 Parameters of Transformer and Related Device

The experimental object in lab was a three-phase oil-immersed transformer (S13-M-30/10 kV) with connection group of Dyn11. The experimental acoustic array was Bionic-M with 112 microphones, equipped with sampling rate of 48 kHz, the microphone frequency range of 10 Hz–24 kHz, and the imaging frequency range of 1–12 kHz, meanwhile, the acoustic field operating range was 33–1200 dB. The model of vibration acceleration sensor was SMARTSTONE CA3014-100 with a sensitivity of 100 mV/g and a sampling frequency of 0.5 Hz–10 kHz. Since the vibration could

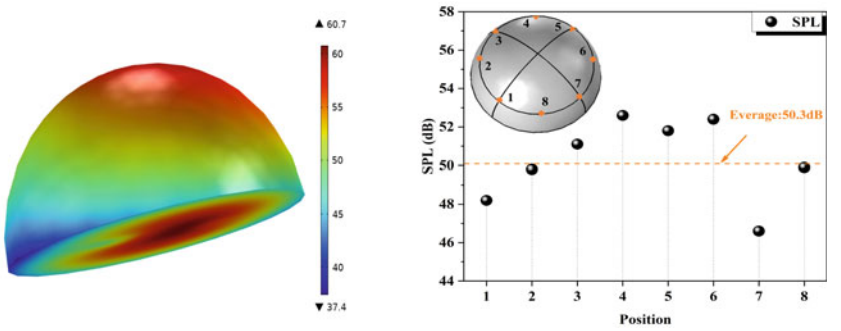

a) Left: Acoustic field distribution around the transformer

b) Right:A coustic field value distribution acoustic of each selected point around the transformer

Fig. 7 Distribution of acoustic field around transformer

be transmitted directly to the surface of the transformer through the connectors, the sensor was arranged on the front of the oil tank. As shown in Fig. 8, vibration displacement and acceleration were collected by vibration acceleration sensor, accordingly, noise caused by vibration was measured and analyzed by acoustic array (Table 2).

a) Left: acoustic array

b) Right: vibration sensor

Fig. 8 Vibration and noise experiment in laboratory

Table 2 Parameters of transformer

Parameter	Value	Parameter	Value
Capacity/kVA	30	Rated voltage/kV	10/0.4
Operating frequency/Hz	50	Rated current/A	1.73/43.3

4.2 *Analysis of Vibration and Noise of Transformer in Laboratory*

The vibration acceleration sensor was installed on the front of surface of oil tank (non-heat sink), and the acoustic array test device was placed on the side of oil tank to carry out vibration and noise test under 66% load. Figure 9 showed that the vibration acceleration of research point on the front of the transformer and the corresponding spectral analysis results. As can be seen from Fig. 9, the vibration acceleration also presented certain periodicity. After transforming vibration acceleration to corresponding frequency domain results, it could be seen that the vibration acceleration signal also took 100 Hz as the fundamental frequency, and at the frequency of 200–600 Hz, there still existed the vibration component, which was similar to the simulation results. However, it was worth noting that according to the spectrum analysis of measured noise, there were relatively intense signals with power frequency like the base frequency and odd harmonic signals (50, 150, 250 Hz, etc.), which may contain some environmental noise factors (Fig. 10).

To ensure that the distance of acoustic field simulation was similar to that of laboratory experiment, the noise generated by the transformer was detected from the

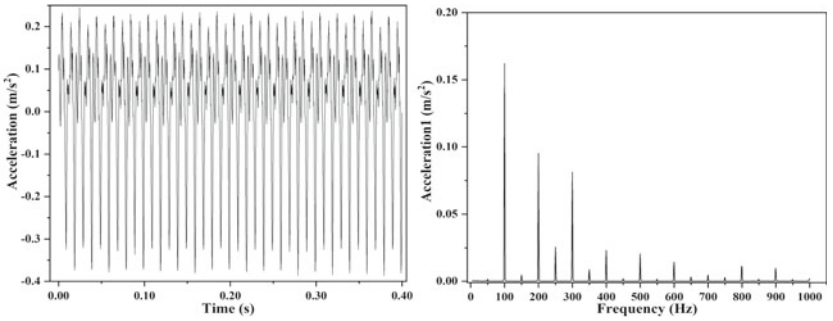

a) Left: Time-domain diagram of vibration acceleration of acceleration b) Right: Frequency-domain diagram

Fig. 9 Vibration characteristics of tested points on transformer oil tank in laboratory

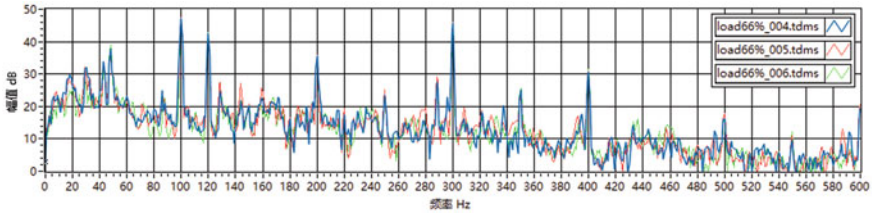

Fig. 10 Frequency-domain diagram of noise

Table 3 Results of vibration characteristics

Indicator	Value	Indicator	Value
Acceleration RMS/m/s^2	0.15	Base frequency/Hz	100
Velocity RMS/mm/s	0.198	Fundamental frequency ratio/%	60.5
Displacement RMS/μm	0.403	Frequency complexity	1.566

side, and the maximum value was 47.2 dB. Comparing the simulated with experimental results, there was a slight difference of 3.1 dB between them. Furthermore, by comparing acceleration, displacement and fundamental frequency parameters, it could be inferred that the simulated results were consistent with the test results to a certain extent. Both of these two parts of results may provide appropriate guidance for the on-site transformer vibration and noise analysis (Table 3).

5 Conclusion

This study focuses on oil-immersed distribution transformers and aims to analyze their vibration and noise characteristics using multi-field coupling theory. The research includes simulation calculations and experimental research using acoustic array and vibration sensors. The following conclusions were drawn:

(1) The finite element simulation results showed that at a 66% load rate, the transformer's vibration noise was mainly caused by the magnetostrictive effect of the core due to weak magnetic leakage between the windings.
(2) Vibration displacement and acceleration were simulated and analyzed for the core and surface of the oil tank, with vibration displacement at 0.134 s being in the order of microns. Vibration acceleration signals showed a fundamental frequency of 100 Hz with additional vibration components at 200–600 Hz. Noise distribution caused by vibration was found to be stronger at the top and weaker around the trans-former.
(3) The experimental research on a 10 kV distribution transformer with a load rate of 66% showed consistent results with the simulation. However, odd harmonic signals at 50, 150, 250 Hz, etc. were also observed in the spectrum, which may be related to ambient noise. The similarity between test and simulated results could provide guidance for on-site vibration and noise analysis. These findings could be useful for developing effective noise reduction strategies to enhance power system efficiency, reliability, and reduce environmental impact.

References

1. Thompson JE (1963) Magnetostriction and transformer noise. J Inst Electr Eng 9(98):72–74
2. García B, Burgos J et al (2006) Transformer tank vibration modeling as a method of detecting winding deformations—Part I: theoretical foundation. IEEE Trans Power Deliv
3. He Q, Nie J, Zhang S et al (2021) Study of transformer core vibration and noise generation mechanism induced by magnetostriction of grain-oriented silicon steel sheet. Hindawi
4. Kitagawa W, Ishihara Y (2010) Analysis of structural deformation and vibration of a transformer core by using magnetic property of magnetostriction. Electr Eng Jpn 172(1):19–26
5. Hilgert T, Vandevelde L et al (2008) Comparison of magnetostriction models for use in calculations of vibration in magnetic cores. IEEE Trans Magn 44(6):874–877
6. He Q, Fan C, Yang G et al (2022) Numerical calculation of vibration characteristics of transformer core under inter-harmonics. IOP Publishing Ltd., pp 1–5
7. Foster SL, Reiplinger E (1981) Characteristics and control of transformer acoustic. IEEE Trans Power Syst PAS-100(3):1072–1077
8. Shao P, Luo L, Yong L et al (2011) Electromagnetic vibration analysis of the winding of a new HVDC converter transformer. IEEE Trans Power Deliv 27(1):123–130
9. Wu X, Zhang Z, Ling Y, Zhang F, Cao H, Mei S (2022) Simulation research on influence of load factors on vibration characteristics of 10 kV three phase oil immersed distribution transformer. High Volt Electr Appar 58(10):106–115 (in Chinese)
10. Weiser B, Pfutzner H (2000) Relevance of magnetostriction and forces for the generation of audible noise of transformer cores. IEEE Trans Magn 36(5):3759–3777
11. Cui J, Ma H, Li N et al (2022) Simulation and analysis of vibration and noise of oil immersed transformer core based on COMSOL. J Electr Meas Instrum 36(04):48–55 (in Chinese)

Propagation Characteristics Analysis of Partial Discharge Between Windings of Converter Transformer

Chen Mao, Qiang Liu, Yu Shang, Ziwei Wang, Junfang Zeng, and Tianyan Jiang

Abstract During the factory test of the converter transformer, the partial discharge withstand voltage test is usually used to judge whether the internal insulation structure is intact. In this study, a simulation model of the converter transformer based on distributed parameters is established. The basis for the establishment of the model is that the windings of the converter transformer have distributed parameter characteristics, and different partial discharge locations are considered. And by changing the position of the partial discharge signal applied to different positions of the winding, the signal waveforms at different points at the monitoring impedance are obtained. Through the analysis of the partial discharge signal transmission relationship in the partial discharge test of the valve side winding of the converter transformer, combined with the distribution parameter based partial discharge signal transmission model of the converter transformer winding, finally through the time domain waveform and frequency spectral density analysis and demonstration of the converter Propagation characteristics of partial discharges between transformer windings. At the end of this paper, a summary and outlook are also made, which provides a theoretical basis for the follow-up research.

Keywords Converter transformer · Partial discharge · Propagation characteristics

C. Mao · Q. Liu · Y. Shang · Z. Wang
State Grid Shaanxi Electric Power Research Institute, Xi'an, Shaanxi 710100, China

J. Zeng (✉) · T. Jiang
School of Electrical and Electronic Engineering, Chongqing University of Technology, Chongqing 400054, China
e-mail: zengjunfang@stu.cqut.edu.cn

© Beijing Paike Culture Commu. Co., Ltd. 2024

X. Dong and L. Cai (eds.), *The Proceedings of 2023 4th International Symposium on Insulation and Discharge Computation for Power Equipment (IDCOMPU2023)*, Lecture Notes in Electrical Engineering 1102, https://doi.org/10.1007/978-981-99-7405-4_53

1 Introduction

The converter transformer is a special transformer, which is the key equipment for connecting DC and AC in the converter station, and realizes long-distance effective power transmission. The converter transformer has a grid-side winding and a valve-side winding [1], which are respectively connected to the AC transmission system and the DC converter valve. During operation, it not only needs to be connected to the AC-DC power transmission system [2], but also needs to change the voltage level of the system so that the voltage on both sides meets the rated voltage and remains within a controllable voltage offset range [3].

The valve side winding of the converter transformer is a key component that is directly connected to the valve and thyristor devices and works under high voltage and high current [4], and is also one of its most important partial discharge areas [5]. When the electric field strength of the valve side winding exceeds the dielectric breakdown. When the intensity is high [6], partial discharge phenomena such as gas discharge and solid discharge will occur [7]. Although the partial discharge phenomenon will not cause large-scale damage [8], long-term discharge will damage the quality of the insulating medium and affect the service life. Security risks. Therefore, it is necessary to regularly inspect and maintain the winding on the valve side to ensure its good insulation status [9].

Therefore, the local discharge experiment of valve side winding of converter transformer can not only check its insulation performance [10], but also timely check the defects, in order to formulate relevant solutions. ATPDraw is a power system simulation tool like drawing software. It provides a wide range of power component models that users can build by simply dragging and splicing the components, and analyze and debug the system using its built-in simulation tools. In this paper, based on ATPDraw, the distributed parameter model of valve side winding of converter transformer is established, and partial discharge simulation experiment is carried out on this basis. Through the analysis of simulation results, the propagation characteristics of partial discharge between converter transformer windings are studied.

2 Distributed Parameter Model of Converter Transformer Winding

The distribution parameter model of converter transformer winding is based on its distributed parameter characteristic. Its winding is generally composed of multiple winding units, including capacitance and inductance. By abstracting the windings into a distributed parameter chain network, calculating the parameters of each part and combining them into a more complex equivalent circuit model, the distributed parameter model of converter transformer windings can be obtained. Typically, in this model, the resistance and capacitance values of each branch are determined

based on the physical size of the converter transformer, material characteristics, and the layout of the windings.

The established winding model can be used to study the propagation characteristics of the winding under impulse voltage. Partial discharge signal is also a kind of high frequency signal, which has similar transmission model theoretically, so the transmission rule of partial discharge signal can be analyzed by similar method.

2.1 Equivalent Capacitance Parameters

The valve-side winding of a converter transformer can be modeled as an LC series circuit with equivalent capacitance, where the equivalent capacitance represents the inter-winding capacitance. Although the actual valve-side winding is not an ideal capacitance, the equivalent capacitance can be used to represent the capacitance between the windings in order to calculate the high-frequency current that can pass through the windings. The value of the equivalent capacitance can be calculated by the following formula:

$$C = 0.0778 * (N1 * N2)^{\frac{1}{3}} * \left(\frac{u}{10^3}\right)^{\frac{2}{3}} * \frac{H}{D} \tag{1}$$

where C is the value of the equivalent capacitance (μF). N1 and N2 are the turns of the valve side winding and the whole transformer, respectively. u represents the dielectric constant of the insulating material (μF/cm). H is the height of the winding and D is the diameter of the winding (cm). It should be noted that the equivalent capacitance value per unit length (1 cm) is calculated in the above formula, but the actual equivalent capacitance value can be obtained by multiplying the capacitance value by the length of the entire valve side winding in practical application. It needs to be corrected under actual circumstances.

2.2 Equivalent Inductance Parameter

The equivalent inductance of the valve-side winding of the converter transformer can be modeled as an inductance group with multiple coils connected in parallel and in series, where the equivalent inductance value represents the inductance between the winding interfaces. The valve side winding of a converter transformer usually consists of multiple individual coils, so the total magnetic flux across each coil needs to be calculated and weighted according to the corresponding resistance and magnetic coupling coefficient of each coil. The equivalent inductance value can be calculated by the following formula:

$$L = \frac{[N * \phi]^2}{R} * \left(\frac{1}{1+k}\right) \tag{2}$$

In the above formula, L is the equivalent inductance value (H), N is the number of turns of the valve side winding, Φ is the magnetic flux of a single coil, R is the resistance of each coil, and k is the magnetic coupling coefficient between the coils.

The equivalent inductance parameter of valve side winding of converter transformer is also affected by coil geometry, coil position and many other factors. Therefore, it is necessary to adjust according to the characteristics of the actual transformer.

3 Simulation Calculation of Partial Discharge in Converter Transformer Winding

3.1 Power Model of Partial Discharge

The signal generated by partial discharge of converter transformer windings is essentially a narrow-band pulse signal with a high frequency component, usually in the 100 kHz to MHz class. PD signals change rapidly, with very steep rising edge and relatively gentle falling edge. The duration of PD signals is generally short, usually in the nanosecond to microsecond level.

The Heidler function model is used for partial discharge simulation. This is because the pulse voltage signal generated by PD has similar characteristics to the pulse waveform of Heidler power supply. The specific Heidler function model functions are as follows:

$$i(0,t) = \left(\frac{I_0}{\eta}\right)\left[\frac{k_s^n}{1+k_s^n}\right]e^{\left(\frac{-t}{\tau_2}\right)} \tag{3}$$

where $k_s = t/\tau_1$; η is the peak current correction coefficient ($\eta = \exp(-\tau_1/\tau_2) \times (n\tau_2/\tau_1)\text{^}(1/n)$), when $n \gg 1$, $\tau_1/\tau_2 \gg 1$, take $\eta \approx 1$); n is the index, usually take $n = 10$. The factor of τ_1 and τ_2 are the frontier time and the delay time constant respectively.

The current output of the above formula can be directly converted into voltage output in ATPDraw. In the software, the specific waveform of the signal can be modified directly by modifying some parameters, as shown in the following Table 1.

The resulting voltage waveform of the PD source is shown in Fig. 1. Tc refers to the time from t = 0 to the Peak of its waveform, and peak here refers to the peak of its voltage. Tau refers to the time between t = 0 and the point at which the function's amplitude drops to 37% of its peak. Parameter n is the factor that affects the rise rate of the function. Tstart and Tstop are the start time and end time, respectively. Among these parameters, the time is in seconds and the voltage is in volts.

Table 1 Parameters of the power supply of Heidler

Data	Unit	Value
Peak	Volt	1
T_c	s	4E−7
T_{au}	s	4E−6
n		2
T_{start}	s	0
T_{stop}	s	1000

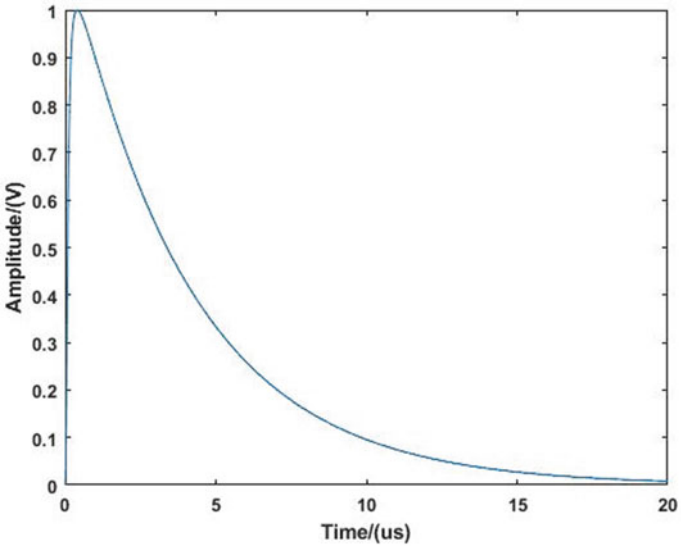

Fig. 1 Voltage waveform diagram of partial discharge power supply

3.2 Simulation of Winding Partial Discharge

Simulation model and parameter setting. The simulation of partial discharge in valve side winding of converter transformer is shown in Fig. 2. The partial discharge outside the winding is simulated by increasing the capacitance to ground.

In the simulation process, 3 voltage monitoring points are set on the whole model, which can fully detect the propagation of partial discharge pulse signals in each part of the winding. The equilibrium method is a common method in PD detection, which can eliminate the capacitive coupling interference and improve the stability of the system. Generally, the impedance used for PD measurement can be divided into RC type and RLC type. When the number of PD pulses per unit time is calculated and the correlation analysis of pulse waveform is required, the RC type non-oscillatory impedance detection is usually selected. In this simulation, the RC type non-oscillatory impedance detection is also adopted.

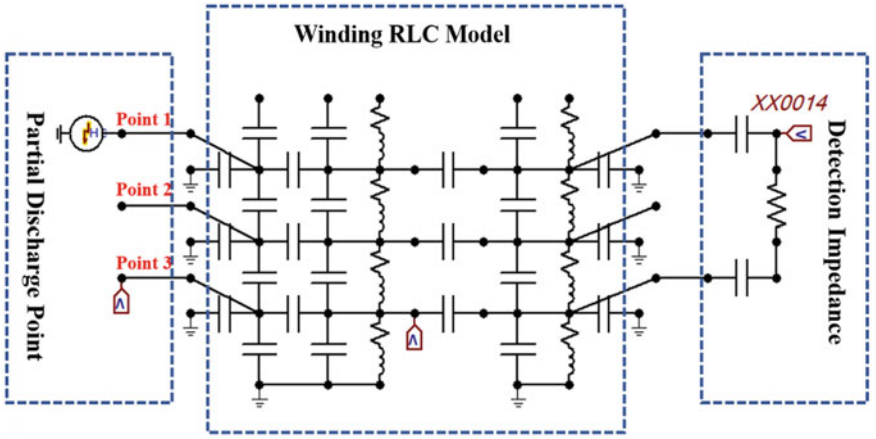

Fig. 2 Simulation diagram of valve side winding partial discharge

Table 2 Simulation parameters

Parameter name	Unit	Value
Delta T	s	1E−8
T_{max}	s	1E−4
F_{req}	Hz	1E+5

The parameters of the simulation are shown in Table 2. Delta T is the step size of this simulation, T_{max} is the end time of this simulation, and F_{req} is the frequency of this simulation.

The equivalent RCL model of valve side winding of converter transformer is shown in Fig. 2, including winding resistance, winding self-inductance, winding capacitance to ground, etc. Considering that the actual partial discharge signal is a high frequency signal, the capacitor plays a major role in the actual potential distribution.

In this simulation, three partial discharge point positions are set on the left side of the RCL model of the winding. From top to bottom, they are point 1 to point 3 respectively. From top to bottom, the position of partial discharge point is changed successively. The propagation characteristics of partial discharge between transformer windings are analyzed.

Simulation Results and Analysis. First use ATPDraw to simulate, obtain the voltage time-domain waveform data at the monitoring impedance after different partial discharge point simulations, and then import these data into MATLAB, and use the FFT function to make the corresponding normalized frequency spectrum. The voltage waveform monitored at the detection impedance monitoring point XX0014 is shown in Fig. 3. Figure 3a–c are the voltages obtained by detecting the impedance

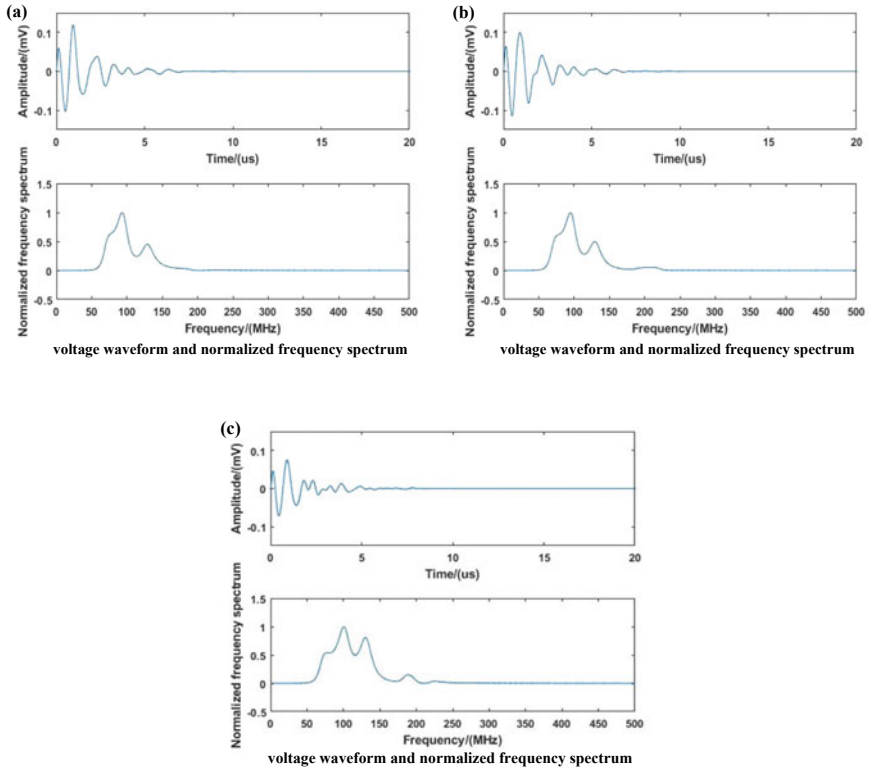

Fig. 3 The measured waveforms and the corresponding normalized frequency spectra at the detection points of different partial discharge positions, **a** point 1, **b** point 2, **c** point 3

when the partial discharge power source is at point 1 to point 3 respectively. Time domain waveform and corresponding normalized frequency spectrum.

Typically, the frequency range of the partial discharge signal is between a few kilohertz and several hundred megahertz. After the high-frequency signal is input, the normalized frequency spectrum of the PD signal is obtained by performing FFT analysis on the signal output by the sensor. By normalizing the frequency spectrum, we can observe the main frequency components and harmonic frequency content in the PD signal, and compare the detected PD signal with the preset threshold to determine whether there is a PD phenomenon.

It can be seen from Fig. 3 that the voltage waveform at the detection point shows a trend of oscillation and attenuation in the time domain, because in the process of actual partial discharge signal pass through winding, the signal will go through the conductor and interface between the winding and the winding, etc. Differences in impedance at these interfaces can cause reflections and interference of the signal. The signal will be affected by factors such as electromagnetic wave radiation, resistive loss, scattering and absorption during the propagation process, causing it to gradually

attenuate during the propagation process. The degree of attenuation depends on factors such as signal frequency, energy, and propagation medium. The resistors, inductors, and capacitors in the simulation model just realized these characteristics.

From their corresponding normalized frequency spectrum, it can be found that there are high-frequency components in the figure, mostly in the range of 50–200MHz. As the partial discharge point moves down in the winding RCL model, the normalized frequency spectrum measured at the detection point has more high-frequency components, and the frequency is getting higher and higher. It also confirms that the normalized frequency spectrum can help detect and diagnose partial discharge phenomenon in electrical equipment, improve the reliability and operation effect of electrical equipment.

4 Conclusion and Outlook

In this study, a simulation model of the converter transformer based on distributed parameters is established. And by changing the position of the partial discharge signal applied to different positions of the winding, the signal waveforms at different points at the monitoring impedance are obtained. Through time domain analysis and frequency spectral density analysis, the propagation characteristics of partial discharge between windings of converter transformer are demonstrated.

The partial discharge signal spreads inside the winding along the surface of the conductor or near the surface, and its propagation speed is affected by many factors, usually between tens of meters per second and hundreds of meters per second. It can be seen the waveform change at the detection point has a certain lag compared with the original signal.

The propagation path of the partial discharge signal is not only affected by the geometry and size of the conductor, but also by environmental factors and the type of partial discharge, which usually spreads to a larger area over time, but this time The simulation does not consider the influence of the environment, and only uses the Heidler partial discharge model for simulation, which has certain limitations.

The partial discharge signal will be affected by various factors during the propagation process, so that the waveform obtained at the detection impedance shows a trend of oscillation and attenuation. In this simulation experiment, the RCL model of the converter transformer is very good restored this feature.

Through the application and analysis of these conclusions, we need to better diagnose and prevent partial discharge faults, thereby improving the reliability and safety of converter transformers.

Acknowledgements This research is supported by the Science and Technology Project of State Grid Shaanxi Electric Power Company, Project No. 5226KY23000Z, Research on rheological partial discharge balancing method and anti-interference technology based on wireless synchronous zero correction.

References

1. Li Y, Luo L, Rehtanz C et al (2009) Study on characteristic parameters of a new converter transformer for HVDC systems. IEEE Trans Power Deliv 24(4):2125–2131
2. Gao Y, Liu G, Liu X et al (2011) Calculation and analysis of electrical field in valve side winding of converter transformer. Adv Mater Res 383–390:4865–4870
3. Fu T, Wang J, Zhong J et al (2009) DC transmission ± Insulation structure analysis of 800 kV converter transformer. Transformer 46(03):1–5 (in Chinese)
4. Jangjoo MA, Allahbakhshi M, Mirzaei HR (2023) UHF sensors positioning on the power transformer tank to enhance the partial discharge localization accuracy. Electr Power Syst Res 218:109174
5. Antoni J (2016) The infogram: entropic evidence of the signature of repetitive transients. Mech Syst Signal Process 74:73–94
6. Zhang J, Ye Z, Wang Q et al (2022) Insulator condition monitoring based on F-P optical fiber leakage current sensor. High Volt Eng 48(8):2915–2923 (in Chinese)
7. Sheng B, Zhou C, Hepburn DM et al (2014) Partial discharge pulse propagation in power cable and partial discharge monitoring system. IEEE Trans Dielectr Electr Insul 21(3):948–956
8. Qing Z, Li Z, Yan S (2012) Spectrum analysis of thunder wave based on Heidler function model. In: The 10th forum on lightning prevention and mitigation—lightning hazard and risk assessment, pp 226–229 (in Chinese)
9. Yu X, Jia P, Wu C et al (2021) Research of PD transfer ratio analysis of converter transformer IPVD test based on distributed parameters. J Phys Conf Ser 2005(1):012032
10. Wu Z, Zhou L, Zhou T et al (2020) A new testing method for the diagnosis of winding faults in transformer. IEEE Trans Instrum Meas 69(11):9203–9214

Optimization Design of Anti-offset of PCB Koch Snowflake Coil in Wireless Power Transfer System

Yiping Liu, Zongrong Long, Jie Fang, Xi Chen, Maoqiang Bi, and Tianyan Jiang

Abstract At present, in order to reduce the positioning accuracy requirements of wireless power transmission (WPT) system, improving the anti-migration of magnetic coupling mechanism has become a research focus. In this paper, Koch Snowflake coil is proposed as the transceiver coil. Firstly, Koch Snowflake coil is optimized, and then the anti-bias performance of Koch Snowflake coil and circular coil is compared by finite element simulation. Through simulation analysis, it can be concluded that under the condition of the same coupling coefficient retention rate, the larger the area of the coil, that is, the stronger the anti-bias ability of the coil. Finally, the simulation results are verified by experiments. The results show that Koch coil has better coupling coefficient and anti-bias performance than circular coil in the range of offset distance. And with the increase of the offset distance, the reverse offset tends to be the same. The above results confirm the validity of the simulation results.

Keywords Wireless power transfer · Koch snowflake coil · Anti-offset

1 Introduction

The past several years witnessed growing interests in the wireless energy transmission technology. Simultaneous transmission theory is constantly being refined. Soljacic et al. proposed a wireless energy transfer technique based on magnetically coupled resonance theory in 2007 [1]. Their results indicate that the transmission efficiency is up to 90% within 1 m and still 40% even if the distance increases to 2 m. Sun et al. used thin copper coils to wind resonant coils, a new form of magnetically coupled resonance, for low-power transmission of implanted devices [2]. In February 2017, Md. Rubel Basar, applied the Helmholtz coil model to the development of

Y. Liu · Z. Long · J. Fang · X. Chen · M. Bi · T. Jiang (✉)
School of Electrical and Electronic Engineering, Chongqing University of Technology, Chongqing 400054, China
e-mail: jiangtianyan@cqut.edu.cn

© Beijing Paike Culture Commu. Co., Ltd. 2024

X. Dong and L. Cai (eds.), *The Proceedings of 2023 4th International Symposium on Insulation and Discharge Computation for Power Equipment (IDCOMPU2023)*, Lecture Notes in Electrical Engineering 1102, https://doi.org/10.1007/978-981-99-7405-4_54

wireless energy transmission technology. And incorporated the technology into the development of robotic capsules [3].

Because the energy transmission technology has high requirements on the relative position of the transceiver coil. When the transceiver coil is misaligned, the output efficiency will be greatly reduced. Therefore, in order to reduce the requirement of device alignment accuracy in wireless charging process, it is very important to study the anti-offset of coupling mechanism [4].

Two ways are currently available for improving the anti-offset ability of the system, i.e., the compensation network of anti-offset ability and, the magnetic coupling structure of anti-offset ability. Huh et al. proposed an 'I' type narrow guide rail-wide pickup electromagnetic coupling mechanism [5]. The mechanism adopts self-decoupling double coil structure to enhance lateral locomotivity. Elliott et al. proposed DDQ (Double-D-Quadrature) and DD coils based on multi-winding structure [6]. Multiple windings with different directions on DDQ winding. This coil doubles the relative moving range of a single circular coil.

The term fractal was introduced into the field of natural science by Mandelbrot in the 1970s [7]. The purpose is to represent complex graphics and complex process. Fractal geometry is a kind of geometry which takes irregular geometry as its research object. Fractal geometry is a general term for graphs and structures with certain self-similarity and self-replication. It can solve complex fractal graph by iterative algorithm according to simple geometric graph [8]. For example, Hilbert curve, Peano curve, Koch curve, etc. Since the 1990s, these advantages of fractal geometry have extended its application to the design of antenna elements. In this way, the multi-band characteristics of the antenna can be realized and its size can be reduced. Based on the above advantages, the Koch snowflake coil was found to have a high coupling coefficient. Therefore, the Koch curve is analyzed in this paper.

This paper takes the power transformer as the research object, and finally realizes the wireless transmission for charging the power transformer terminal. The coupling mechanism and migration characteristics of magnetically coupled resonant radio energy transmission systems are studied in this paper. At the same time theoretical analysis, simulation analysis and experimental analysis. The coupling mechanism with good anti-bias ability can improve the stability of the device picking power, so it is of great significance to study this topic.

2 Coil Simulation Analysis

2.1 Coil Optimization

The coupling coefficient of coil with different angle difference is obtained by simulation. When the top coil coincides with the bottom coil, the coupling coefficient is 0.629. When the angle difference between top coil and bottom coil is 30°, the coupling coefficient is 0.726. The large change of coupling coefficient is due to the

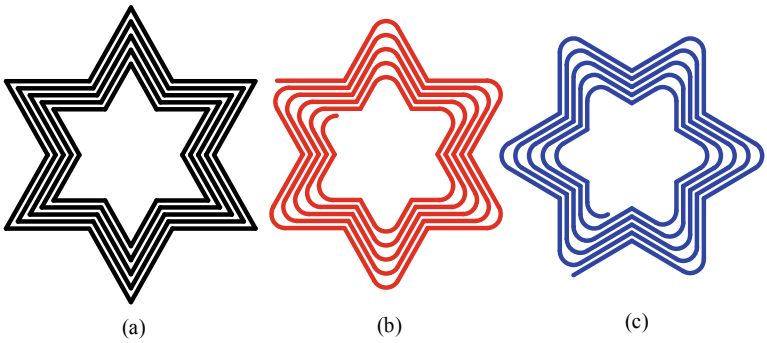

Fig. 1 Koch coil

double-layer coil and the increase of coil turns. Therefore, we choose the model with the angle difference of 30° between the top and bottom [9].

The coupling coefficient reaches its maximum when the arc length at the chamfer is 5 mm. At this time, the effect of chamfering on coupling coefficient is greater than that of coil size. The final Koch coil is shown in Fig. 1a. Figure 1b is the top layer of the Koch coil. Figure 1c is the bottom layer of the Koch coil.

2.2 Anti-offset Analysis

In order to better demonstrate the Anti-offset of the Koch coil, a circular coil will be used for comparison. Two coils use the same parameters in simulation. Coupling coefficient retention rate is defined to compare the anti-offset performance of two coils. Coupling coefficient retention rate k_h [4]:

$$K_h = \frac{K_{after}}{K_{before}} \times 100\% \tag{1}$$

Two coil models are established in the simulation software, as shown in Fig. 2. Through simulation, the coupling coefficient of the Koch coil is 0.751, the coupling coefficient of circular coil is 0.701. Therefore, when the transmitting and receiving coils are aligned, the coupling coefficient of the Koch coil is greater than that of the circular coil.

In order to compare the anti-offset performance of the two coils on the X axis, the retention rate of the coupling coefficient of the two coils is compared. As shown in Fig. 3a. Coupling coefficient retention rate represents the ratio of coupling coefficient after offset to that without offset. Therefore, the greater the retention rate of coupling coefficient, the stronger the anti-offset of the coupling mechanism [10]. As can be seen from the figure, the retention rate of coupling coefficient is 1 when the transmitting coil and receiving coil are aligned. Coupling coefficient retention rate

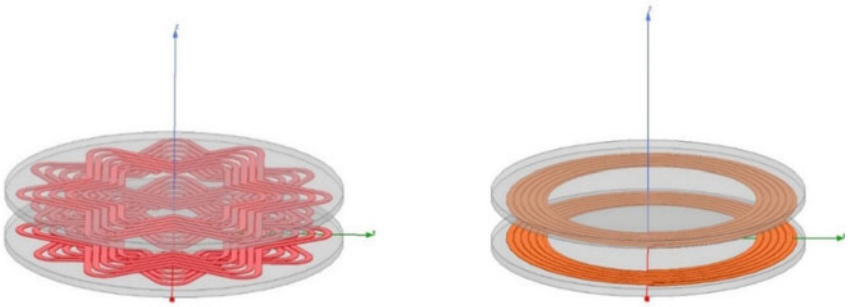

(a) Koch coil simulation model (b) Circular coil simulation model

Fig. 2 Coil simulation mode

of Koch coil is greater than that of circular coil when offset occurs. So, the anti-offset performance of Koch coil is better than that of circular coil. And the advantage is the most obvious in the range of ± 4 mm to ± 10 mm, with the maximum of 5%. Then the anti-offset ability of the two coils tends to be consistent at ± 12 mm.

Since both types of coils are symmetric, the Y-axis offset of the coils will not be repeated. Theoretically, the offset on the Y axis is almost identical to that on the X axis. The coupling coefficient retention rate of the coil on the Y-axis is shown in Fig. 3b. In the range of Y axis − 12 mm to + 12 mm, the anti-offset performance of Koch coil is still better than that of circular coil. The advantage of Koch coil is the most obvious in the range of ± 2 mm to ± 8 mm, and the maximum is 4%.

The color bar on the right in Fig. 4 represents the retention rate of coupling coefficient. The dotted in the figure represents the same retention rate of coupling coefficient. Obviously, when the retention rate of coupling coefficient is the same, the larger the area of the coil, the stronger the anti-offset ability of the coil. After calculation, it is concluded that the area of Koch coil whose coupling coefficient retention rate is higher than 0.95 is 1.38 times that of circular coil. The area of Koch

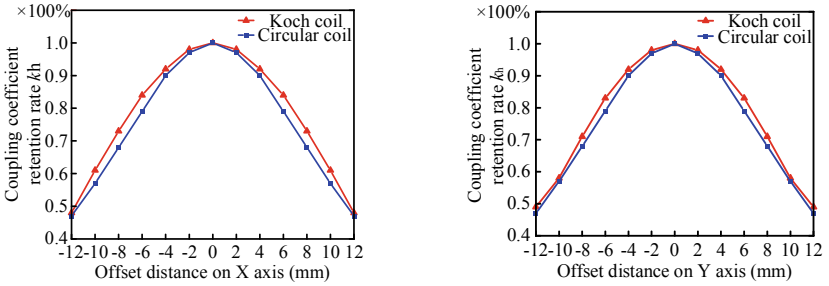

(a) Contrast diagram of X-axis anti-offset (b) Contrast diagram of Y-axis anti-offset

Fig. 3 Contrast diagram of anti-offset

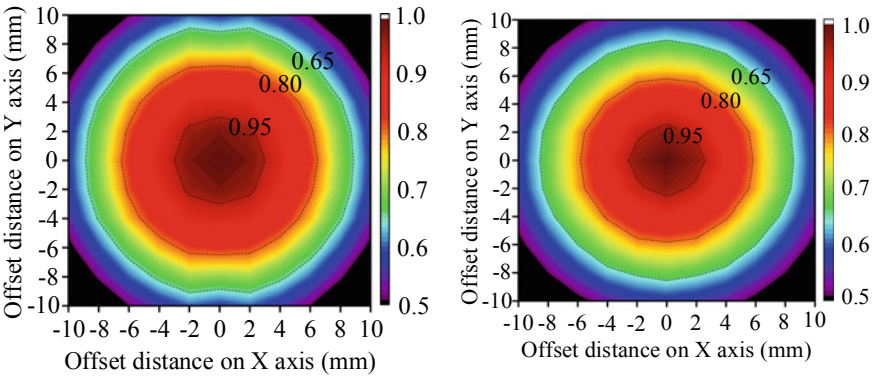

Fig. 4 The retention rate of coupling coefficient when the coil moves in XOY plane

coil whose coupling coefficient retention is higher than 0.80 is 1.25 times that of circular coil. The area of Koch coil whose coupling coefficient retention is higher than 0.65 is 1.11 times that of circular coil. This shows that Koch coil has better anti-offset performance than circular coil in this region.

Offset on the Z axis is simply an increase in the transmission distance between the transmitting coil and the receiving coil. Set the initial transmission distance to 5 mm in the simulation. The offset distance ranges from 2 to 12 mm. The magnetic induction intensity distribution and coupling coefficient variation of Koch coil are obtained, as shown in Figs. 5 and 6.

3 Experimental Verification

To validate the simulation results, a test platform is built as shown in Fig. 7.

Test the self-inductance and mutual-inductance of objects through test platform. Then the coupling coefficient and coupling coefficient retention rate of the coil are calculated by formula. Then offset the coil in turn and record the test data. The retention rates of the coupling coefficients of the two coils offset on the X and Y axes are shown in Fig. 8.

Test results for offset on Z axis are shown in Fig. 9. It shows that the anti-offset of Koch coil is better than that of circular coil in the range of offset distance. With the increase of offset distance, the anti-offset of the two tends to be consistent. The above shows that the simulation results are effective.

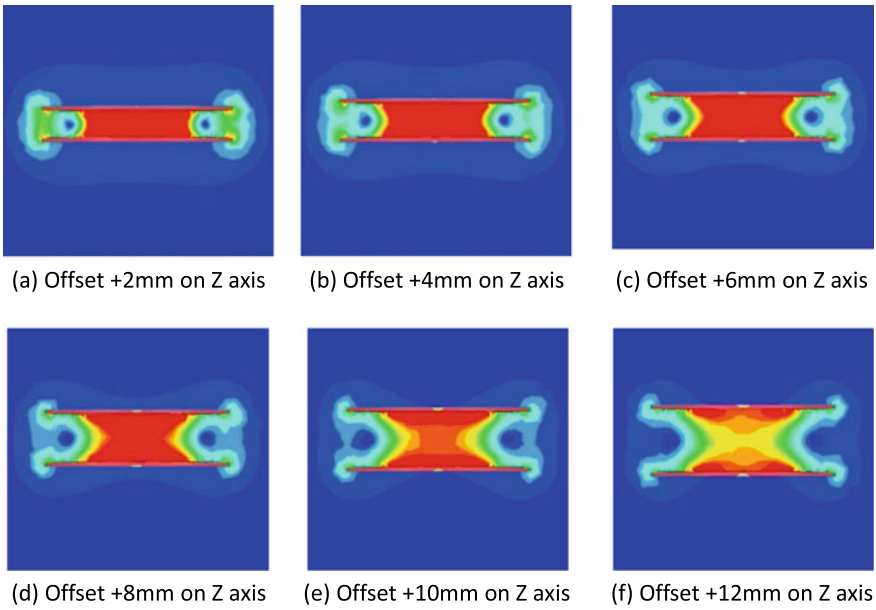

Fig. 5 The change of magnetic induction intensity when offset on z axis

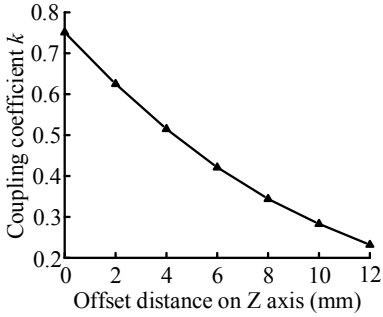

Fig. 6 Graph of coupling coefficient of Koch coil with Z—axis offset

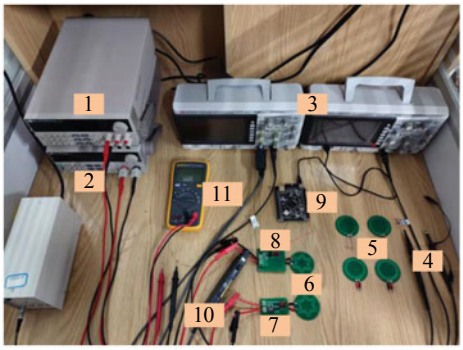

1: DC power supply, 2: Electronic load, 3: Digital oscilloscope, 4: Voltage probe, 5: Circular coil, 6: Koch coil, 7: Receiving-end, 8: Transmitter, 9: STM32 microcontroller, 10: Current probe, 11: Multimeter

Fig. 7 Test platform

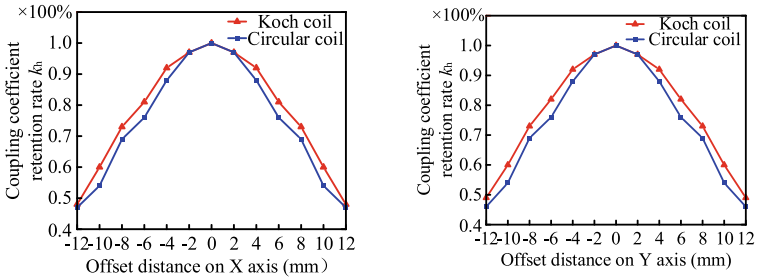

(a) X-axis anti-offset test diagram (b) Y-axis anti-offset test diagram

Fig. 8 Anti-offset test diagram

Fig. 9 Z-axis anti-offset test diagram

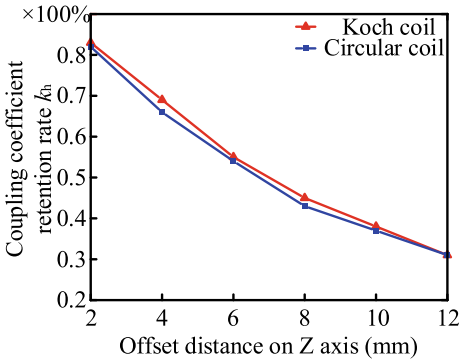

4 Conclusion

In this study, fractal coils are applied to the magnetically coupled resonant wireless power transmission system. The influence of various parameters on Koch snowflake coil is analyzed, and the Koch coil is optimized. Theoretical analysis and experimental results show that Koch coil has better coupling coefficient and anti-offset than circular coil within a certain range. The maximum advantage is 7%. The performance of the two coils tends to be consistent with the increase of offset distance. This study provides a reference for reducing device alignment accuracy during wireless power transfer.

The research of this paper focuses on the application of low power devices. But with the development of intelligence, the power of many daily products is increasing. Further optimization is needed to adapt to the application of high-power system.

Acknowledgements This work was supported by the National Natural Science Foundation of China (Grant No. 52177129).

References

1. Joannopoulos JD, Karalis A, Soljacic M (2017) Wireless non-radiative energy transfer: US, US9831722
2. Zhang F, Liu X, Hackworth S-A et al (2009) In vitro and in vivo studies on wireless powering of medical sensors and implantable devices. IEEE/NIH Life Sci Syst and Appl Works 2009:84–87
3. Basar M-R, Ahmad M-Y, Cho J et al (2018) An improved wearable resonant wireless power transfer system for biomedical capsule endoscope. IEEE Trans Industr Electron 65(10):7772–7781
4. Chen H, Liu X, Zou X et al (2022) Study of the moving offset characteristics of multi-loop moving coil linear compressor. Int J Refrig 133:289–301
5. Suh I-S, Lee K, Lee M (2013) Dynamic model and control algorithm of HVAC system for dynamic wireless charging EV application. In: Electric machines and drives conference. 2013 International electric machines and drives conference, pp. 241–246
6. Nagendra G-R, Covic G, Boys J-T (2014) Determining the physical size of inductive couplers for IPT EV systems. IEEE J Emerg Select Top Power Electron 2(3):57I – 583
7. Baptista A (1987) Encycloped Phys Sci Tech 5:579–593
8. Kim J-H, Cho J-H, Seong K-W (2021) A new type of wireless transmission based on digital direct modulation for use in partially implantable hearing aids. Sensors 21(8):2809–2809
9. Li M, Zhang Y, Li K et al (2022) Self-powered wireless sensor system for water monitoring based on low-frequency electromagnetic-pendulum energy harvester. Energy 251:123883
10. Zou T, Guo Y, Dai P et al (2020) Axial and radial offset characteristics of high temperature superconducting wireless power transfer system. Phys C: Superconductivity Appl 576:0921–4534

Analysis for Typical Fault of 12.5 kV Cabinet Bushing Based on Electro-Thermal Coupling Simulation

Xuanhe Cao, Shan Li, Jianqing Yang, Yanyan Lu, Zhiwen Zhou, Jinlong Guo, Xing Li, and Chuyan Zhang

Abstract The cases of transformer outlet short circuit caused by the failure of cabinet bushing in the GIS are relatively common in the operation of the power grid. This article establishes an electro-thermal coupling finite element analysis model for the 12.5 kV cabinet bushing fault event of the No.1 main transformer in a 220 kV substation. The electric field distribution and temperature characteristics of the bushing about the fault are obtained by simulating the air gap defect inside the bushing, and the combination of the FEM and Townsend discharge Theory. And it was found that the partial discharge in the internal air gap of the bushing gradually caused the insulation degradation. The temperature rise effect of the bushing under the influence of short-circuit current further accelerates the occurrence of the faults.

Keywords Cabinet bushing · Insulation degradation · Breakdown · Electro-thermal coupling simulation

1 Introduction

The cabinet bushing is a key equipment in the Gas Insulated Switchgear (GIS) which bears the insulation of the busbar to the cabinet body, and its operational reliability affects the lifetime of the 10 kV systems [1, 2]. At present, dry bushing made of epoxy resin is widely used in substations, which has a compact structure and is maintenance free [3–6]. However, the high potential shielding suspension can cause air insulation breakdown between the busbar and the bushing. And the air gap defects

X. Cao · X. Li · C. Zhang (✉)
School of Information Engineering, China University of Geosciences, Beijing 100083, China
e-mail: zcy@cugb.edu.cn

S. Li
State Grid Xinjiang Electric Power Research Institute, Xinjiang, Urumqi 830011, China

J. Yang · Y. Lu · Z. Zhou · J. Guo
State Grid Xinjiang Integrated Energy Service Company Limited, Xinjiang, Urumqi 830011, China

© Beijing Paike Culture Commu. Co., Ltd. 2024

X. Dong and L. Cai (eds.), *The Proceedings of 2023 4th International Symposium on Insulation and Discharge Computation for Power Equipment (IDCOMPU2023)*, Lecture Notes in Electrical Engineering 1102, https://doi.org/10.1007/978-981-99-7405-4_55

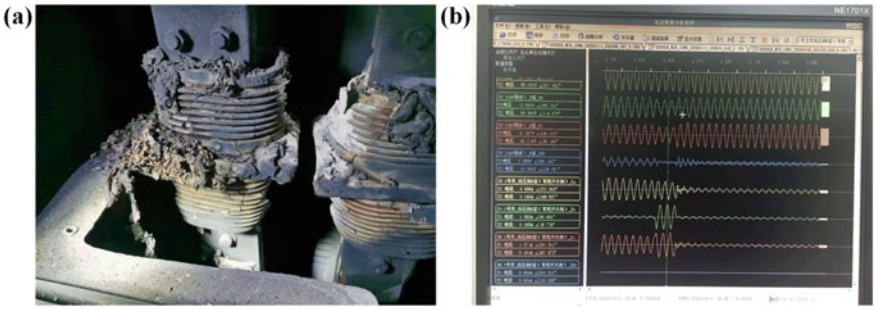

Fig. 1 **a** The accident site. **b** The fault waveform

present during the manufacturing process can also induce partial discharge, gradually leading to the aging of the insulation materials [7–10].

At present, there are many scholars researching on the calculation of the electric field and temperature field for the cabinet bushing under different voltage levels, which has a great reference value. However, there is a lack of physical field analysis of bushing under defect conditions in existing literature. And the connection of FEM simulation with the on-site operational accidents is weak.

This article conducts an electro-thermal coupling simulation and partial discharge analysis on a short circuit explosion accident of a 220 kV substation in Xinjiang, China, which occurred in January 2020. The analysis of the on-site accident data indicates that this event was caused by a three-phase short circuit fault on the low-voltage side of the No.1 main transformer. During the fault, the steady-state short-circuit current was 19.6 kA, with a duration of 1.69 s. The accident site and fault waveform are shown in Fig. 1.

2 The Finite Element Model

Based on the design drawings and material parameters of the bushing, an equal scale 3D simulation model of the 12.5 kV cabinet bushing was established in COMSOL Multiphysics. The model includes the bushing, busbar, installation flange, cabinet shell, and air domain. The bushing is mainly made of epoxy resin as the insulation material, and the model's geometry is shown in Fig. 2a. To simulate the degradation of the insulation of the bushing, randomly distributed internal air gaps were added for comparison, as shown in Fig. 2b.

The electric field distribution and the temperature distribution under the electrothermal coupling of the bushing are calculated respectively by using the three interfaces of COMSOL: Static electricity, Magnetic field and Solid and fluid heat transfer. The electric field control equation based on Poisson's equation is:

$$E = -\nabla V \tag{1}$$

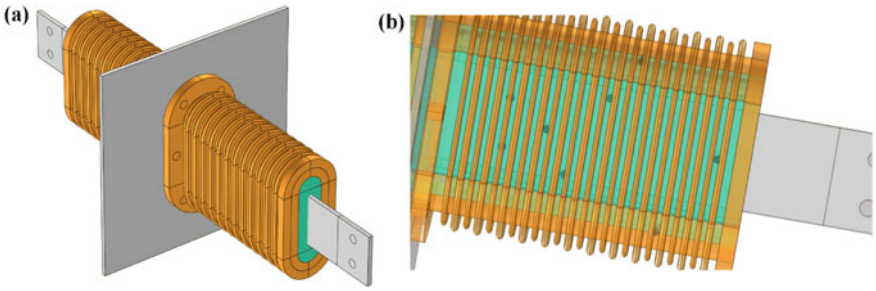

Fig. 2 **a** Simulation model of the cabinet bushing. **b** Internal air gaps of bushing

$$\nabla \cdot (\varepsilon_0 \varepsilon_r E) = \rho_v \tag{2}$$

where E is the electric field strength, V is the electric potential, ε_0 is the dielectric constant of vacuum, ε_r is the relative dielectric constant of the material, ρ_v is Volume charge density.

A partial differential equation system is built for electromagnetic thermal coupling to define and solve the heat transfer problem inside the bushing, where the magnetic field control equation is:

$$E = -j\omega A \tag{3}$$

$$\nabla \times H = J \tag{4}$$

$$\mu_0 \mu_r H = B = \nabla \times A \tag{5}$$

$$J = \sigma E + j\omega(\varepsilon_0 \varepsilon_r E) \tag{6}$$

The control equation that describing the heat transfer problem between solid and fluid inside the bushing is:

$$\rho C_p \frac{\partial T}{\partial t} - \nabla \cdot (k \nabla T) = Q_e = J \cdot E \tag{7}$$

$$-n \cdot q = h(T_{amb} - T) + \varepsilon\sigma(T_{amb}^4 - T^4) \tag{8}$$

where ρ is the density of the material; C_p is the heat capacity at constant pressure; T is the temperature; k is the thermal conductivity of the material; h is the Heat transfer coefficient of air convection. In Eq. (8), ε is the surface radiation coefficient; σ is the Stefan Boltzmann constant; T_{amb} is the external ambient temperature. In Eq. (7), the Fourier heat transfer term is used to describe the internal heat transfer of the bushing.

Table 1 The material parameters of the cabinet bushing

Material	Conductivity (S m)	Thermal conductivity (W/(m K))	Density (kg/m^3)	Heat capacity (J/(kg K))
Epoxy resin	1e−15	0.92 − 0.21e−2 T	1037.90 − 0.27 T	1650
Aluminum	1/(6.62e−17T^3 − 8.19e−14T^2 + 1.45e−10 T − 1.04e−8)	464.14 − 2.84 T + 1.25e−2T^2 − 2.34e−5T^3 + 1.57e−8T^4	2751.78 − 0.18 T + 4.66e−5T^2 − 1.52e−7T^3 + 6.83e−11T^4	595.66 + 1.51 T − 0.21e−2T^2 + 1.30e−6T^3

The loss obtained from solving the electromagnetic field is added as a heat source to the solid heat transfer equation to achieve the coupling of the electromagnetic and thermal. In Eq. (8), Newton's law of cooling and Stefan Boltzmann's law are used to describe the convection and radiation heat transfer between the bushing surface and the air.

The calculation considers the relationship between the electromagnetic properties of the material and temperature to achieve bidirectional coupling of the heat and electromagnetic field. The parameters used of the material of the bushing in the calculation are shown in Table 1.

3 Simulation Results and Analysis

3.1 Under Normal Conditions

The internal electric field distribution of the simulated bushing is shown in Fig. 3a and b. It can be seen that there is a high field strength area in the center of the installation flange where the bushing through the cabinet. As the calculation result, the maximum field strength value inside the bushing is 809 kV/m, which appears on the inner surface of the bushing crossing the wall.

Figure 3c and d respectively show the radial field strength curves along the axis parallel to the busbar and perpendicular to the busbar. It can be seen that in the direction of the busbar, the internal electric field gradually decreases from the end of the cabinet to the outer end of the bushing, with a maximum value of 125 kV/m, appearing at the wall penetration of the cabinet. In the direction perpendicular to the busbar, there are double peaks in the field strength on the inner surface of the bushing, which appear at the upper and lower flush ends of the bushing and the conductive busbar. The peak field strength is maintained at 111 kV/m, and the lowest field strength value is 763 V/m, appearing at the center of the upper surface of the bushing.

The steady-state temperature distribution of the bushing under normal condition is shown in Fig. 4. It can be seen that the overall temperature of the bushing decreases from the middle section to both sides. The highest temperature value in the air domain

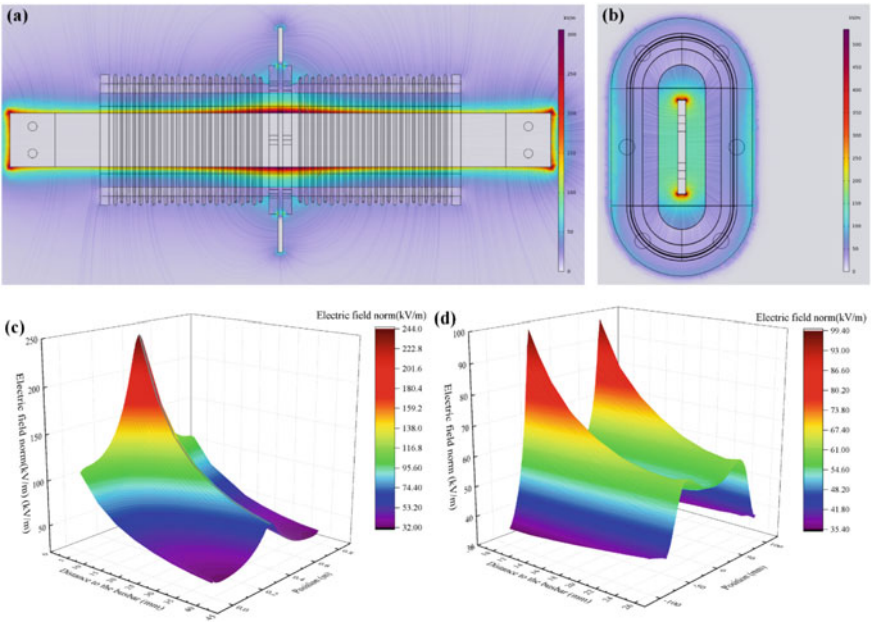

Fig. 3 **a** Electric field distribution on the axial section of the bushing. **b** Electric field distribution on the radial section of the bushing. **c** Axial electric field distribution. **d** Radial electric field distribution

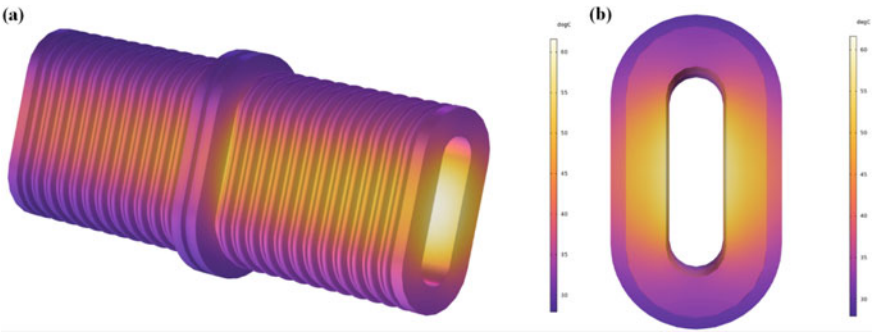

Fig. 4 Temperature distribution of the bushing. **a** Axial section. **b** Radial section

is 54.4 °C, which appears at the center of the bushing near the busbar. The temperature rise of the bushing body is mainly reflected on the inner surfaces on the left and right sides, as well as the parts on the inner side which are flush with the busbar. The maximum temperature value on the surface of the bushing is 56.6 °C, which occurs on the side surface of the middle section where the bushing does not pass through the cabinet. The minimum value is 27.3 °C, located at the outer end of the bushing.

3.2 Under Defect Conditions

To simulate the operation of the bushing during the short-circuit fault, the electromagnetic and thermal field were calculated again on the bushing with added insulation defects under the condition of three-phase short-circuit. In defect conditions, the short-circuit current of the busbar is 19.6 kA, with a duration of 1.69 s. The calculated electric field distribution of the bushing at peak time is shown in Fig. 5.

It can be seen that when there is an air gap inside the bushing, there is distortion of the electric field, and two high field strength regions appear at the air gaps 1 and 2, which are much greater than the surrounding area. The maximum value can reach 427 kV/m, which is far greater than the breakdown field strength of air. At this gap distance, it will lead to breakdown discharge within the air gap, which in turn will lead to the degradation of the epoxy resin. When the internal deterioration of the bushing reaches a certain level, it will cause a wide range of internal breakdown and discharge, ultimately leading to a short circuit explosion accident.

Figure 6 compares the steady-state temperature distribution of the bushing under normal condition with that when the busbar passes the first short-circuit current and triggers the warning. It can be seen that due to the presence of abnormal short-circuit current and air gap discharge, the temperature of the epoxy bushing has significantly increased, with a maximum value of 114.6 °C. The minimum temperature of the entire bushing is 55.6 °C, which still appears at the outer port.

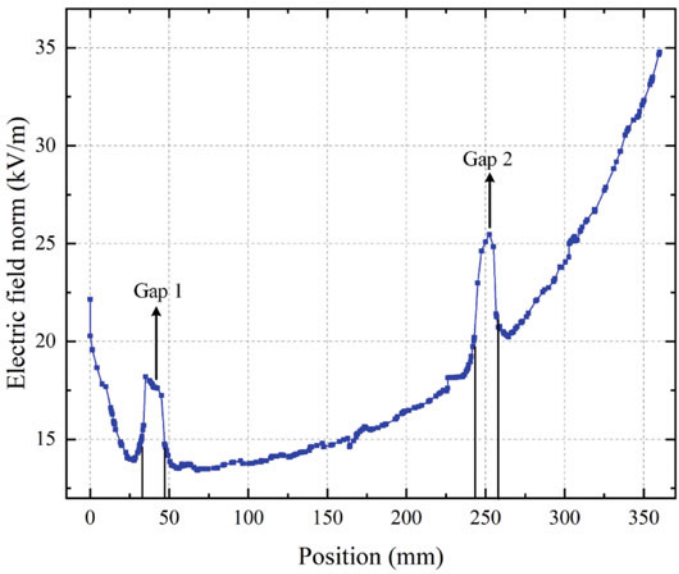

Fig. 5 Electric field distribution inside the bushing

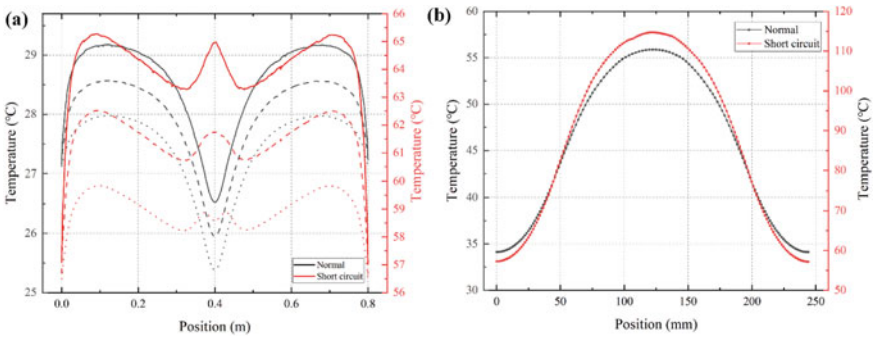

Fig. 6 Temperature distribution of the bushing **a** Axial section. **b** Radial section

3.3 Discharge Analysis

In order to further verify the effect of air gap on the insulation failure of the bushing, the Electrical breakdown detection interface in the COMSOL plasma module is used for the discharge analysis of the defective bushing. It is difficult to establish a fully self-consistent discharge plasma model due to the complex structure of the bushing and the cabinet. Therefore, this paper uses a method by integrating the Townsend growth coefficient along the electric field line to estimates whether the Electrical breakdown will occur in the air gap without solving the complete plasma model [11].

The breakdown condition for self-sustaining discharge in gas is:

$$\gamma_i \left(\exp\left(\int_0^D N\alpha ds \right) - 1 \right) = 1 \tag{9}$$

where γ_i is the secondary emission coefficient, N is the Number density, α is the converted Townsend growth/Attenuation coefficient, S is the arc length along the ion particle trajectory, and D is the distance from the source boundary to any target boundary. By using this formula, we can divide the discharge in the test gas into three situations:

1. No discharge:

$$\int_0^D N\alpha ds < \ln\left(1 + \frac{1}{\gamma_i}\right) \tag{10}$$

2. Continuous discharge:

$$\int_0^D N\alpha ds > \ln\left(1 + \frac{1}{\gamma_i}\right) \tag{11}$$

3. Streamer discharge:

$$\int_0^D N\alpha ds > 17.7 + \ln(d/1[\text{cm}]) \tag{12}$$

In the calculation, information from all three states is embedded in the converted Townsend growth coefficient α, it is a strong function of the reduced electric field:

$$\alpha = \alpha\left(\frac{E}{N}\right) \tag{13}$$

where E is the electric field parallel to the streamline, the integral is calculated by solving the Ordinary differential equation along the test particle trajectory:

$$\frac{d\alpha_D}{ds} = \alpha\left(\frac{N}{N_{stp}}\right) \tag{14}$$

where N_{stp} is the Number density at standard temperature and pressure. The Townsend growth coefficient of dry air in the calculation was interpolated using the growth coefficient relative to the reduced electric field [12].

Figure 7a shows the simulated Electrical breakdown indicator. In the breakdown indicator, 0 represents no breakdown and there's no discharge will occur, 1 represents Townsend discharge (current limiting), and 2 represents the streamer with infinite current flow. Due to the different distribution of air gap positions, their breakdown situations vary. In the four gaps of ABCD, there is no breakdown and discharge in gap D which is far from the side surface. While Townsend discharge will occur in gaps B and C which near the center of the side surface, with a low possibility of producing streamers at the center of the gap. There is already a great possibility of large-scale streamer discharge occurring in gap A which is closest to the cabinet.

Figure 7b shows the calculation results of the integral Townsend growth coefficient, which forms a streamer when its value is higher than 18.3. The integral growth coefficient in gap BCD is basically lower than the streamer's threshold, where the value in D is much smaller than that in BC. This result indicates that there is a greater

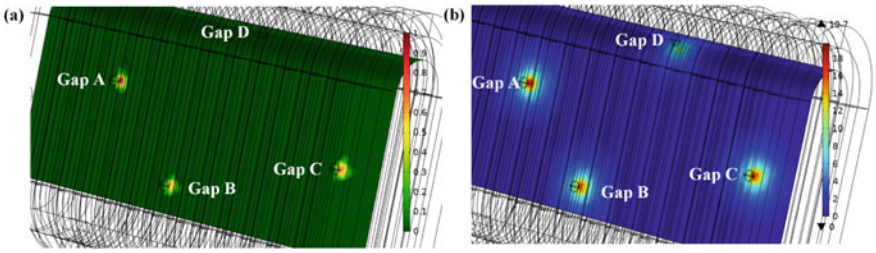

Fig. 7 **a** Breakdown indicator. **b** Integral Townsend growth coefficient

likelihood of more severe discharge when the air gap appears on the side surface of the bushing or near the side of cabinet.

4 Conclusions

1. The insulation structure of the bushing is damaged when there are air gaps inside it, and the internal electric field distortion and abnormal temperature rise can lead to the deterioration and denaturation of the epoxy resin.
2. There is a greater likelihood of more severe discharge occurring when the air gap appears on the side surface of the bushing or near the cabinet side.
3. Partial discharge live detection should be carried out during the operation and maintenance of the cabinet bushing to detect the discharge in the air gaps as early as possible and prevent further faults from occurring.

References

1. Zhixiang DENG, Chen KANG, Huayun WANG et al (2019) Partial discharge detection and structure optimization of bushing for 10 kV switchgear. Insulators Surge Arresters 2:226–230 (in Chinese)
2. Zhifeng LUO, Xian CAO, Boyong WANG et al (2021) Climbing field strength calculation and structure optimization of 10 kV switchgear casing inner wall. J Nanchang Univ (Eng Tech) 43(2):191–196 (in Chinese)
3. Yongyong J, Jinggang Y, Shan G et al (2017) Simulation of internal electric field of high-voltage metal-enclosed switchgear and influencing factors. High Voltage Apparatus 53(6):154–160 (in Chinese)
4. Haiyan W, Zhihao Z, Xiang F et al (2019) Electric field optimization and structure design of wall bushing in 40.5 kV air-insulated switchgear. High Voltage Apparatus, 55(1):59–63 (in Chinese)
5. Xiaolei ZHAO, Jun HU, Zhikang YUAN et al (2021) Design of adaptive bushing based on field grading materials. High Voltage 6(4):625–636
6. Haowei YAO, Kefeng LV, Zhen LOU et al (2023) Simulation study on oil pressure problems caused by internal faults in oil-immersed transformers. Process Saf Environ Prot 175:190–198

7. Shiling Z, Zongren P (2020) Application of finite element method in three-dimensional electric field simulation of UHVDC wall bushing. High Voltage Eng 46(03): 782–789 (in Chinese)
8. Shiling Z, Zongren P, Peng L et al (2015) Design and dielectric characteristics of the ±1100 kV UHVDC wall bushing in China. IEEE Trans Dielectr Electr Insul 22(1):409–419
9. Dexin N, Hailong Z, Zhong C et al (2013) Optimization design of grading ring and electrical field analysis of 800 kV UHVDC wall bushing. IEEE Trans Dielectrics and Electr Insul 20(4) 1361–1368
10. Monga S, Gorur RS, Hansen P, Massey W (2006) Design optimization of high voltage bushing using electric field computations. IEEE Trans Dielectr Electr Insul 13:1217–1224
11. Larry KW, Jorgenson RE, Nicolaysen SD (2003) Ionization coefficient approach to modeling breakdown in nonuniform geometries. Sandia Report
12. Dutton J (1975) A survey of electron swarm data. J Phys Chem Ref Data 4(3):577–856

The Study on Charging Mechanism and Motion Characteristics of Particles for DC GIL/GIS

Peng Liu, Yutong Zhang, Luming Xin, Zehua Wu, and Zongren Peng

Abstract The metal particles in GIL/GIS and their failure-inducing characteristics have been fully confirmed in failure analysis in recent years. After the DC GIL/GIS equipment is put into operation in the future, affected by the DC voltage, the internal metal particles have a high speed, a wide range of activities, and the probability of causing insulation failure. Therefore, more attention should be paid to such problems. In this paper, the source and possible location of metal particles in gas-insulated transmission lines and the influence of particles on the electric field when they exist in different locations are analyzed. The force on metal particles in the GIL/GIS cavity was analyzed and the lifting field strength was calculated. Particle lifting and motion characteristics observation experiments under the flat electrode are designed to verify the above theory, which has great important academic and engineering significance for the study of particle capture methods in DC GIL/GIS.

Keywords Metal particle · Lifting voltage · DC GIL/GIS · Motion characteristics

1 Introduction

In recent years, with the continuous development of social economy, the electricity demand is growing. As a new type of pipeline transmission line, Gas-insulated Metal-enclosed Transmission Line (GIL) overcomes its defects while inheriting the advantages of cables and overhead lines in terms of voltage level and capacity. Because the pipeline structure is isolated from the outside world, it will not be affected by bad weather, environmental pollution, etc. during operation, and has a longer service life and higher reliability [1–4]. However, a prominent issue that requires attention during its operation is the issue of particulate contamination. The transmission

P. Liu · Y. Zhang (✉) · L. Xin · Z. Wu · Z. Peng
The State Key Laboratory of Electrical Insulation and Power Equipment, Xi'an Jiaotong University, Xi'an 710049, China
e-mail: zhangyt2021@stu.xjtu.edu.cn

© Beijing Paike Culture Commu. Co., Ltd. 2024

X. Dong and L. Cai (eds.), *The Proceedings of 2023 4th International Symposium on Insulation and Discharge Computation for Power Equipment (IDCOMPU2023)*, Lecture Notes in Electrical Engineering 1102, https://doi.org/10.1007/978-981-99-7405-4_56

pipeline structure of GIL/GIS is made of metal materials, so particles will be generated due to factors such as friction and vibration during production, transportation, installation and maintenance. Metal particles will be charged when the GIL/GIS equipment is running [5–8]. When the charge is large enough that the electric field force on it is greater than its own gravity, the metal particles will lift up and move in the pipeline. When the metal particles move between the electrodes, it will cause faults such as discharge and breakdown. If the particles are attached to the surface of the insulator, an electric field concentration area will be formed. Under DC voltage, they will also interact with the accumulation of charges, which will easily cause insulator surface failures [9–11]. To sum up, the prevention and control of particulate pollutants is an important link in the process of designing and developing DC GIL/GIS products.

In this paper, aiming at the important issue of metal particles treatment in GIL/GIS under DC voltage, on the basis of existing research at home and abroad, taking ± 320 kV DC GIL as the research object, using a combination of theoretical analysis, simulation calculation and experimental research, mainly complete the following research content: For metal particles of different shapes, types, and sizes, consult relevant information, analyze the charging mechanism and force of metal particles in GIL/GIS, and on this basis, conduct a study on the starting voltage of the particles deduce, analyze the action mechanism of particle trap trapping particles, design and carry out particle actuation test under flat electrode and particle trap capture test to verify it.

2 Charging Mechanism and Force Analysis of Particles

2.1 Source and Type of Particles

The source of metal particles in GIL/GIS is mainly due to the relative friction between the parts in contact with each other due to vibration during its production, transportation, installation, operation, maintenance, etc., and the shape, type and size of the particles produced are relatively different. The types of particles can be mainly divided into two types: metal particles and non-metal particles. Since non-metal particles have less charge and are less likely to damage equipment, current research is mainly focused on metal particles. The shape and size of particles are also quite different. As shown in Fig. 1, dust as small as microns and particles as large as millimeters have been confirmed to exist in GIL/GIS. At present, most scholars believe that large Large-sized metal particles are more harmful to equipment, so the existing research mainly focuses on large-sized metal particles. Metal particles are mostly irregular in shape. In the current research, in order to perform numerical analysis on the particles, the particles are usually approximately equivalent to three shapes: spherical, linear, and thin, which are convenient for charging, lifting, and motion characteristics.

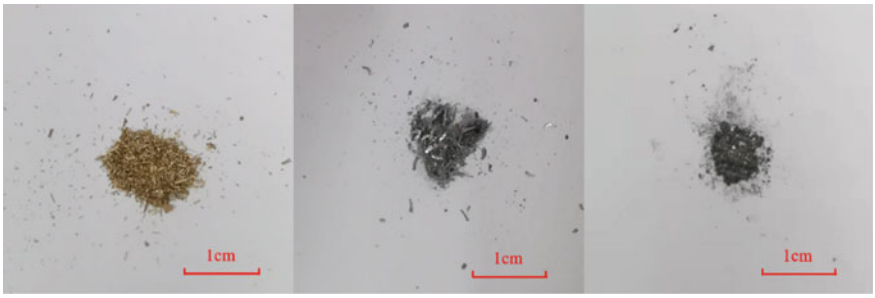

(a) Copper chip (b) Aluminum chip (c) Aluminum powder

Fig. 1 Metal particles produced by vibration friction

2.2 Effect of Metal Particles on the Electric Field

When the metal particle is charged and lifted and moves in the GIL/GIS cavity or falls during operation, and does not contact and collide with the electrode, it is a suspended potential. When it is close to an insulator or an electrode, it will have a certain impact on the surrounding electric field strength. Taking ± 320 kV DC GIL as an example, calculate the electric field distribution when spherical metal particles with a radius of 0.5 mm are close to the surface of the insulator and the electrode.

When metal particles are suspended at 1 mm above the insulator and attached to the surface of the insulator, the cloud map of the electric field distribution change is shown in Fig. 2. When the particle is close to or attached to the surface of the insulator, it will cause the change of the electric field intensity on the surface of the nearby insulator: when the particle is suspended 1 mm above the insulator, the maximum electric field intensity on the path taken increases from 1.72 to 1.82 kV/mm, when the particle attached to the surface of the insulator, the maximum electric field intensity increases to 5.06 kV/mm, exceeding the maximum electric field intensity in the GIL cavity without foreign matter.

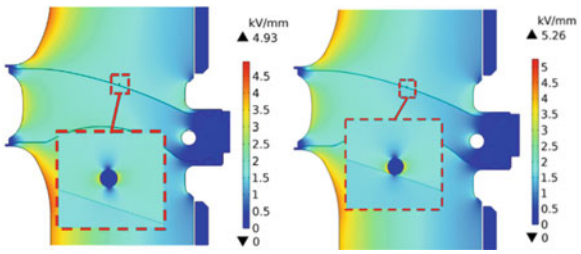

(a) Suspended 1mm above the insulator (b) Attached to the surface of the insulator

Fig. 2 Effect of metal particle on surface electric field of insulator

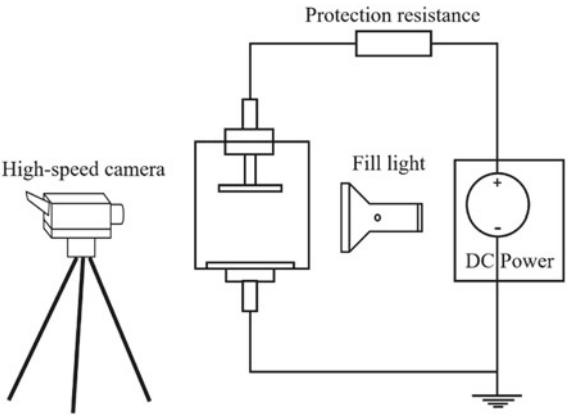

Fig. 3 Plate electrode test device wiring diagram

3 Experimental Research on Particle Actuation and Motion Characteristics

3.1 Flat Electrode Test Platform and Test Conditions

In order to verify the charging mechanism, force analysis and charge change during the movement of the above-mentioned particles, a particle movement test under a flat electrode was designed. The correctness of charge and force analysis of different particles under the action of electric field is verified by the initiation test of particles of different shapes and sizes, and the correctness of the charge change and particle trap capture mechanism after the particles collide with metal parts is verified by the particle capture test. The device is shown in Fig. 3.

The test device includes four parts: test power supply, high-voltage electrode, grounding plate and high-speed camera. Among them, the diameter of the plate of the high-voltage electrode is 150 mm and the thickness is 20 mm. In order to reduce the test voltage, the electrode spacing is set to 30 mm. The power supply is a positive and negative polarity DC voltage source, the maximum voltage can be added to 200 kV, and the test is carried out under atmospheric pressure. A high-speed camera is set up outside the test device to observe the movement of particles.

3.2 Particle Initiation Test

Place spherical aluminum particles with a diameter of 0.5–2 mm under the flat electrode, linear aluminum particles with a length of 5–12 mm and a cross-sectional radius of 0.5–1.2 mm, a disc shape with a thickness of 0.1–0.3 mm and a diameter of 4–12 mm Particles and square particles with a thickness of 0.1–0.3 mm and a side length of 4–12 mm are slowly pressurized until the particles are activated, and

the activation voltage of each particle is recorded and compared with the theoretical value. Each test was repeated 20 times, and a new particle was replaced each time, and the electrode and particle were wiped with alcohol to eliminate the influence of residual charge. After removing the results that were greatly affected by external interference, the average value was taken as the test result. Theoretical calculation results and test results are shown in Fig. 4.

The comparison between theoretical value and experimental value of spherical particles is shown in (a) in the Fig. 4. The theoretical value of the change trend of the starting voltage of spherical particles is basically consistent with the experimental value. When the particle size is small, the error of the experimental results is large. With the increase of the particle size, the starting voltage of spherical particles also gradually increases. The values gradually tend to match. This is because when the particle size is small, the surface is relatively rough due to the manufacturing process, which reduces the contact surface when it is placed on the electrode surface, and the

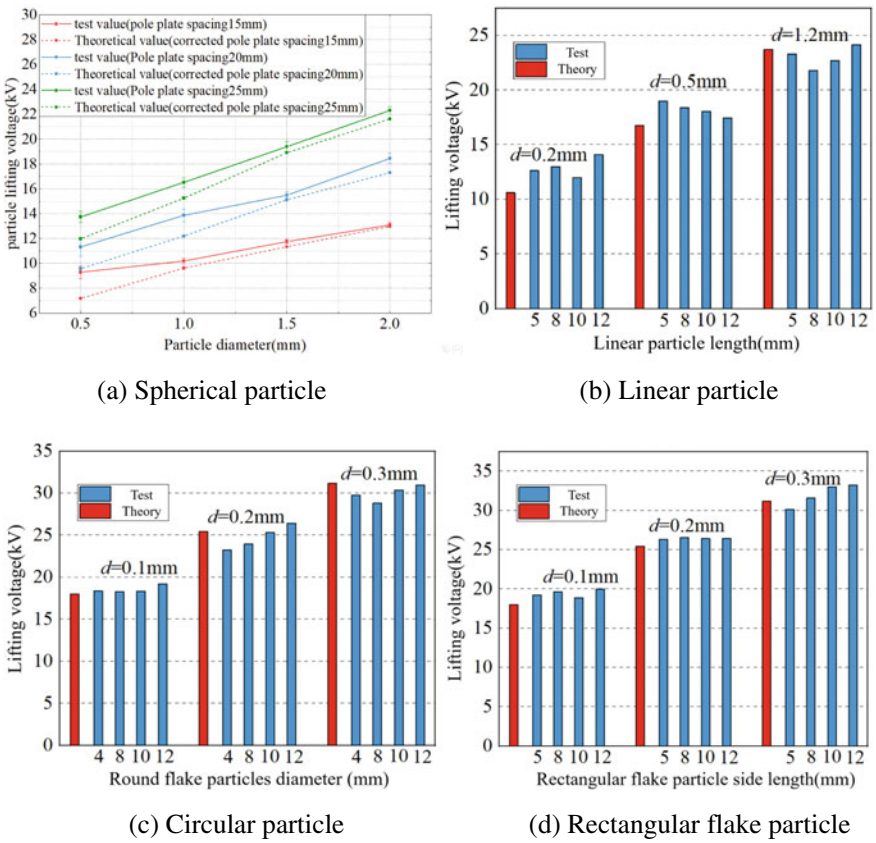

(a) Spherical particle (b) Linear particle

(c) Circular particle (d) Rectangular flake particle

Fig. 4 Comparison between theoretical and experimental results of lifting voltage of particles

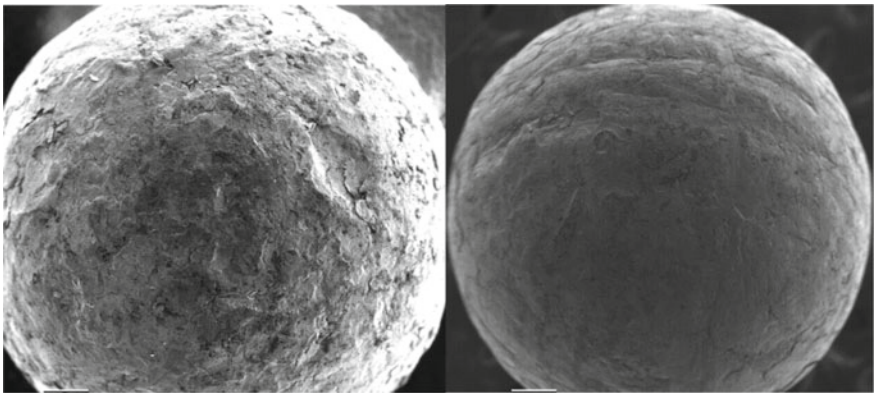

Fig. 5 Surface morphology of spherical particles of different sizes

charge exchange ability is affected. Figure 5 shows the state of the surface after magnification of particles of different sizes.

In the theoretical analysis of linear particles, the initiation voltage has nothing to do with the length, but only with the diameter of the section; in the theoretical analysis of sheet particles, the initiation voltages of circular sheet particles and rectangular sheet particles are only related to their thickness. It has nothing to do with factors such as radius and side length. In the test results, the theoretical value is basically consistent with the experimental value. After the length of the linear particles increases, the diameter and side length of the flake particles increase, the starting voltage does not increase or decrease significantly, and they are all near the theoretical calculation value.

The correctness of the theoretical analysis of the force and charge of spherical, linear and sheet-shaped particles when they are stationary on the electrode surface is verified through experiments on particles of different shapes and sizes.

3.3 Observation and Analysis of Motion Characteristics of Different Particles

Use high-speed photography to record the movement characteristics of spherical, linear, flake particles and metal debris mixture particles of different sizes and shapes produced by contact wear under the flat electrode, as shown in Figs. 6 , 7 and 8.

The movement characteristics of spherical metal particles under the flat electrode are high-speed reciprocating motion between the two plates, as shown in Fig. 6. During the test, there was basically no discharge breakdown when the spherical particles moved.

Fig. 6 Motion characteristics of spherical particles

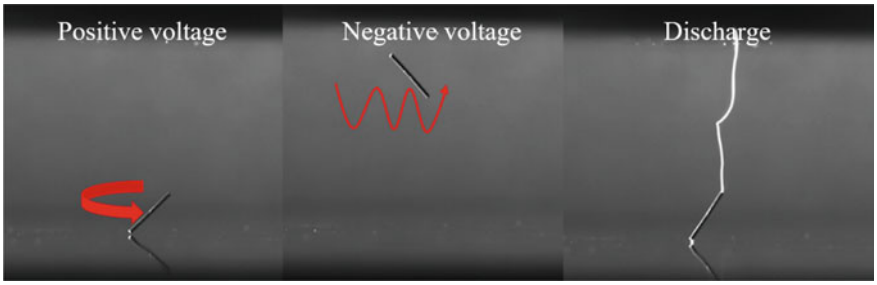

Fig. 7 Motion characteristics of linear particles

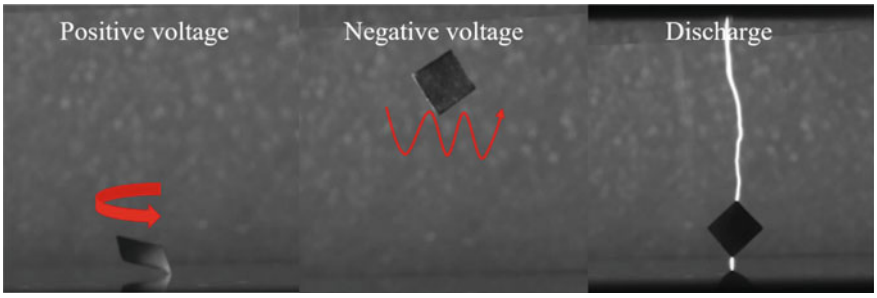

Fig. 8 Motion characteristics of flake particles

Linear metal particles exhibit different motion characteristics under different polarity voltages. If the positive polarity voltage is applied to the high-voltage electrode, its motion state is as a state of touching the ground at one stage, and the other end is lifted and rotated, accompanied by a discharge phenomenon; if the voltage continues to increase, the particles will completely detach from the ground electrode, and then in the pole. Reciprocating motion between plates. Under the negative polarity voltage, the particles appear to be suspended in the air after they are lifted up. After a high voltage is applied, there will be a "flying firefly" state in which they do not touch the ground electrode but collide with the high-voltage electrode many times, or one end is located on the high-voltage conductor, and the other end

standing and rotating phenomenon, as shown in Fig. 7. In the test, the linear particles are prone to discharge breakdown under both positive and negative polarities.

The motion characteristics of flake metal particles are similar to those of linear particles, and they also show the lifting process in which one end is lifted first. After lifting up under positive polarity voltage, the particles first make a "rotation" movement on the ground electrode, and then the voltage will continue to rise. Do reciprocating motion between the electrodes, under negative polarity, the particles will be suspended or fireflies will appear, as shown in Fig. 8. In addition, flake metal particles are also easy to cause discharge breakdown. The larger the thickness of the particle, the larger the diameter (disc particle) or side length (rectangular particle), the greater the frequency of particle discharge and the higher the probability of breakdown.

4 Conclusion

In this paper, theoretical analysis and experimental research are carried out for particles of different shapes and sizes. The possible sources and types of particles are analyzed, and the influence of particles on the electric field intensity in the cavity of GIL transmission line is calculated by simulation. The motion characteristics of particles under different voltage polarities are analyzed. The conclusion is as follows:

1. There are many types of metal particles in gas-insulated transmission lines, and the differences in shape and size are also large. The main cause of the fault caused by particles is the discharge breakdown caused by the movement of the electrode gap or the serious electric field distortion when it is close to the surface of the insulator, which leads to the surface fault.
2. Particles with different shapes and sizes have different charging capacity and influence factors on the initiating voltage, and the initiating voltage of linear and sheet-shaped particles has nothing to do with their length and width. Metal particles of different shapes will exhibit different motion characteristics under different polarity voltages: the movement of spherical particles is relatively simple, mostly as reciprocating motion between electrodes; linear and flake particles will appear to rotate, suspend, reciprocate sports, fireflies and other different sports states.

Acknowledgements This work was supported by the Science and Technology Project of State Grid Corporation SGSNKY00KJJS2100285.

References

1. Li C et al (2022) China's 10-year progress in DC gas-insulated equipment: From basic research to industry perspective. iEnergy 1(4):400–433
2. Li C et al (2022) Insulating materials for realising carbon neutrality: opportunities, remaining issues and challenges. High Volt 7(4):610–632
3. Liang Z et al (2022) Designing HVDC GIS/GIL spacer to suppress charge accumulation. High Volt 7(4):645–651
4. Li C et al (2018) Novel HVDC spacers by adaptively controlling surface charges—part ii: experiment. IEEE Trans Dielectr Electr Insul 25(4):1248–1258
5. Asano K, Anno K, Higashiyama Y (1997) The behavior of charged conducting particles in electric fields. IEEE Trans Ind Appl 33(3):679–686
6. Wu Z et al (2022) Simulation and analysis on motion behavior of metal particles in AC GIL. IEEE Trans Dielectr Electr Insul 29(2):567–574
7. Liang R et al (2022) Research on discharge phenomenon caused by cross-adsorption of linear insulating fibre and metal dust under DC voltage. High Volt 7(2):269–278
8. Ge X et al (2019) Movement behavior and partial discharge of the single metallic particle in GIS at operated voltage. IEEE Trans Plasma Sci 47(9):4319–4328
9. You H et al (2017) Motion and discharge characteristics of metal particles existing in GIS under DC voltage. IEEE Trans Dielectr Electr Insul 24(2):876–885
10. Ma J et al (2018) Breakdown characteristics of particle-contaminated HVDC GIL under superimposed voltage of DC and impulse. IEEE Trans Dielectr Electr Insul 25(4):1439–1447
11. Wang J et al (2021) Metal particle contamination in gas-insulated switchgears/gas-insulated transmission lines. CSEE J Power Energy Syst 7(5):1011–1025

Electric Field Characteristic and Corona Performance of 1000 kV AC for High-Altitude Transmission Lines

Liang Xie, Wei Hu, Duo Lyu, Feng Li, Bin Zou, Changzhi Peng, Yiheng Li, and Xuekai Pei

Abstract Due to the uneven distribution of energy resources across China, transmitting electricity from the west to the east is an important solution. However, some regions in western China have an altitude exceeding 4000–5000 m, making it necessary to conduct research on the corona characteristics of high-altitude transmission lines. This paper employs the finite element method to calculate the electric field distribution characteristics of 750 kV AC high-altitude lines. Furthermore, corona characteristics of high-altitude 750 kV lines are measured using ultraviolet imaging detection technology, which verifies the accuracy of the calculation method. Additionally, this study calculates the electric field distribution of 1000 kV AC high-altitude lines with Gan-type tower and investigates the effect of different conductor sizes. The results of this research can provide guidance for the design of high-altitude transmission lines.

Keywords High altitude · Electrical field · Corona

L. Xie (✉) · W. Hu
State Key Laboratory of Power Grid Environmental Protection, China Electric Power Research Institute Co., Ltd, Wuhan, Hubei, China
e-mail: zeda_sir@sina.com

D. Lyu · F. Li
State Grid Corporation of China, Beijing, China

B. Zou
State Grid Sichuan Economic Research Institute, Chengdu, China

C. Peng · Y. Li · X. Pei
School of Electrical Engineering and Automation, Wuhan University, Wuhan, Hubei, China

© Beijing Paike Culture Commu. Co., Ltd. 2024

X. Dong and L. Cai (eds.), *The Proceedings of 2023 4th International Symposium on Insulation and Discharge Computation for Power Equipment (IDCOMPU2023)*, Lecture Notes in Electrical Engineering 1102, https://doi.org/10.1007/978-981-99-7405-4_57

1 Introduction

State Grid Corporation of China plans to build 1000 kV Ultra High Voltage Alternating Current transmission lines in Sichuan and Chongqing. The line is planned to be built at an altitude of more than 4700 m, and it is expected to be the world's first UHV AC transmission line in that high-altitude environment. There is a lack of operational and experimental data on the corona situation of AC transmission lines in high-altitude areas, especially the high probability of corona discharge risk in high-altitude UHV transmission lines, so research on the corona characteristics of high-altitude UHV AC transmission lines is carried out.

The corona inception voltage of the wire is mainly determined by the surface field strength of the wire, and the surface field strength is affected by many factors, such as wire size, surface roughness and so on. The environmental factors of the transmission line also greatly affect the corona inception voltage of the conductor, such as temperature and humidity, air pressure, dust, etc. [1–4]. Ambient air pressure at high altitudes is lower compared to low altitudes, which means lower particle density and electrons with a greater mean free path. So the air is more easily ionized at high altitudes, which results in lower corona inception voltage and stronger corona discharge, and reducing the electromagnetic interference caused by corona discharge could meet the relevant standards which are made by the environmental protection department [5, 6]. However, if the design margin is too large, the additional costs will be incurred and higher requirements will be placed on the physical strength of fittings and tension insulator strings.

The researches of corona characteristics about high-altitude transmission lines has been carried out earlier in the United States and other countries from mechanism [1, 7, 8]. In 2012, Liu Y P studied the corona characteristics at different altitudes such as 19, 2261, 2829, and 3800 m. The corona inception voltage decreased by about 8.5% per 1000 m as the altitude increased, and the rising numbers of sub-conductors can increase the corona inception voltage [9]. In 2018, Liu Y P carried out the UHV AC corona experiment in the high-altitude environment of Northwest China, and summarized the empirical formula for the calculation of line corona in the sandy environment at an altitude of 2200 m [10]. In 2019, Huang S. L. carried out experiments on the corona loss of different conductors at an altitude of 2200 m. The results show that using conductor size of 8×630 has too large power loss by corona discharge, which is a commonly size used at low altitudes. And the conductor size of 8×720 and 10×720 should be used in high altitude environment, which has a larger split spacing or more split numbers[11]. Then in 2021, Huang S. L. carried out experiments on the characteristics of rainfall on the corona inception voltage of transmission lines at an altitude of 2200 m. The corona characteristics of different numbers of sub-conductors and cross-sectional areas of conductors under saturated rainfall levels are studied, and a prediction method is given based on experimental data [12]. In 2023, Huang S. L. carried out experiments on the correction of electromagnetic noise at different altitudes. The correction coefficients from US Bonneville Power Administration (BPA) standard of 3.33 dB/km has a large error in different weather,

which is commonly used in engineering altitude correction coefficients. According to the research, it should be corrected separately according to the experiment under dry or rainy conditions. 4.5 and 1.5 dB/km [13].

2 Simulation of Electric Field

2.1 Calculation Model

Some sections of the 1000 kV Ultra High Voltage Alternating Current transmission line in this calculation will pass through the ice-covered area, and the V-shaped strings of the conductors are used in the form of single, double, and triple combinations. Since the insulator strings have limited effect on the calculation results of the line, ignoring the insulator strings in this simulation to improve the computational efficiency. In order to meet the corona inception voltage of different altitudes, it is necessary to carry out proportional modeling for different conductor sizes with Gan-type transmission towers, the model is shown in the Fig. 1.

2.2 Calculation Results of Electric Field

The full scale model of 1000 kV AC transmission lines is calculated by the finite element numerical computational method (FEM). The electric field calculation uses the electrostatic charge field, and the physical field equation can be described as Eq. (1):

$$\begin{cases} \nabla^2 \phi = -\frac{\rho}{\varepsilon} \\ E = -\nabla \phi \end{cases} \tag{1}$$

where ϕ is the electrical potential, ρ is the density of the space charge, ε is the dielectric constant of the medium, and E is the strength of the electrical field. Then the boundary conditions of the model are set according to the maximum normal operating conditions. The middle line is assigned the maximum magnitude of the phase voltage, which is calculate by Eq. (2):

$$U_m = 1000\,\text{kV} \times 1.1 \times \sqrt{2} \div \sqrt{3} = 898.15\,\text{kV} \tag{2}$$

The other two phases are assigned $-U_m/2$ by three phases sequence. And the grounding boundary conditions are assigned to the tower, the external air domain boundary and etc. The calculated potential and electric field distribution diagram of the overall model are shown in the Fig. 2.

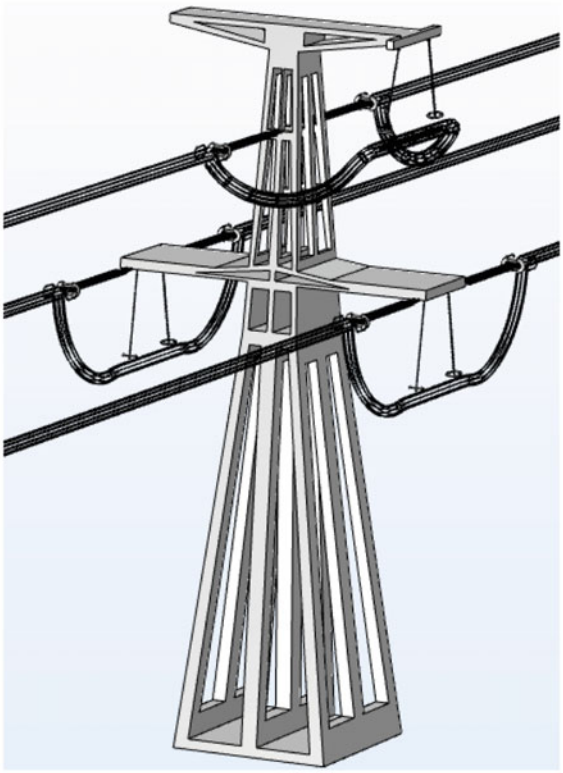

Fig. 1 Full-scale model of Gan-type transmission tower and lines

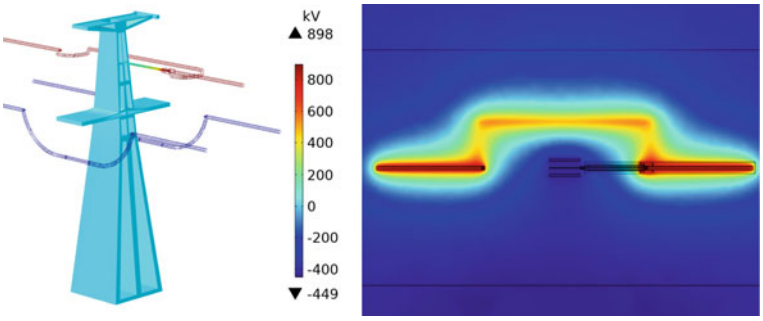

Fig. 2 Potential and electric field distribution

There are 4 sections in the vertical arc part of the middle transmission line, the positions of the sections are shown in the Fig. 3. They are section 1, 2, 3, and 4 along the conductor direction, and the maximum value for each section are 16.52, 17.31, 15.92, 14.85 kV/cm respectively. The maximum value of electric field is 17.31 kV/cm on overall surface of the middle line which is located in the middle vertical arc position, and the electric field along the line show a trend of first increasing and then decreasing. The electric field distribution of different sections are shown in the Fig. 4.

In addition, the electric field distribution between the middle line and the side lines of the Gan-type transmission tower is compared. The conductor size is 10 × 1250, and the peak voltage of middle transmission line is 898 kV. The calculation result shows that the maximum electric field on the surface of the middle conductor is 17.31 kV/cm, and the maximum electric field on side conductor is 16.95 kV/cm. The electric field distribution and the maximum position are shown in the Fig. 5. The maximum value around the surface of the middle phase is slightly higher than that of the sides. Based on the above calculations, this paper obtained the maximum electric field position of each transmission line, and the middle transmission line is focused in the subsequent analysis, which has the maximum value of the electric field.

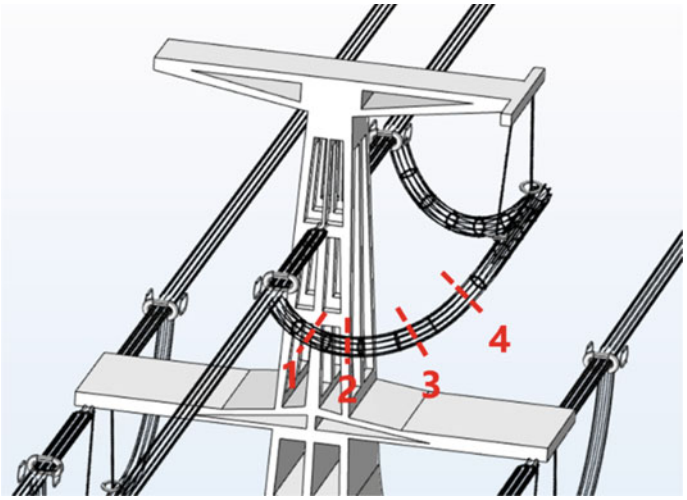

Fig. 3 The position of sections on the middle transmission line

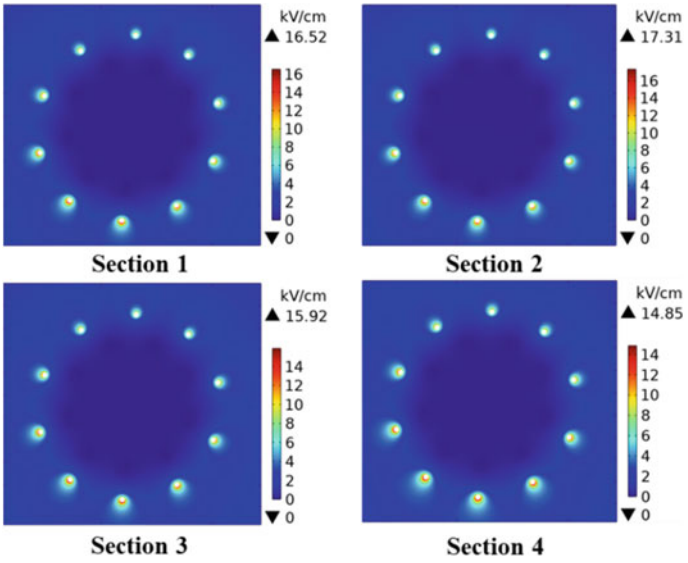

Fig. 4 Electric field distribution of different cross-sections

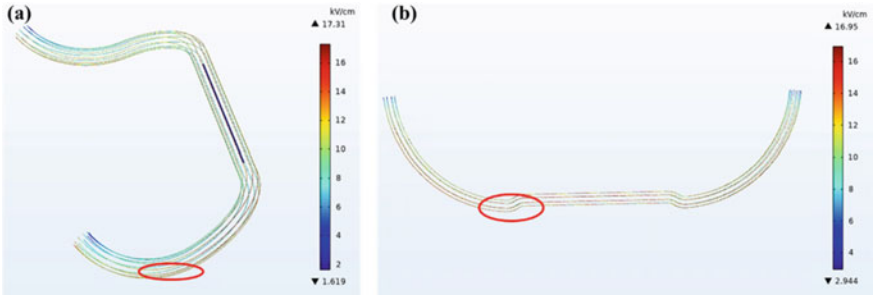

Fig. 5 Calculated corona position of **a** the middle and **b** the side transmission line

3 Calculation and Measurement of 750kV High Altitude AC Transmission Line

3.1 Calculation of 750 kV High Altitude AC Transmission Line

The conductor size of 8 × 630 is used in operating 750 kV AC transmission line at an altitude of 2200 m. The proportional model of 750 kV is established according to the actual size, and assigning the boundary value from Eq. (2) by replacing 1000–750 kV. The electric field distribution of middle transmission line is shown in Fig. 6.

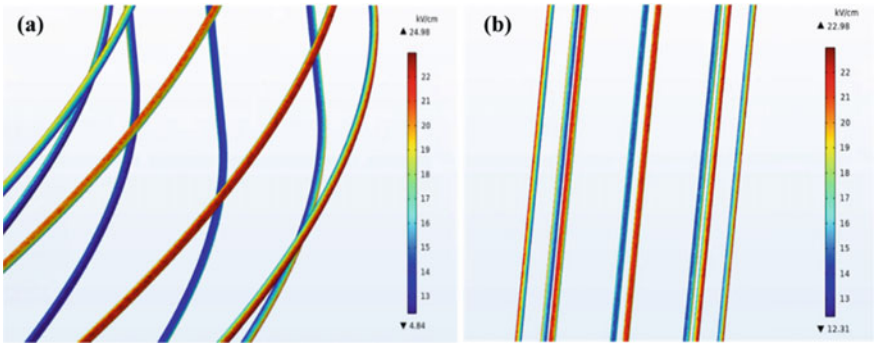

Fig. 6 Electric field distribution of the middle transmission line **a** corner part, **b** straight part

According to the results of Gan-type tower, the maximum field value on the surface of the middle line is 24.98 kV/cm which is located in the corner area, and the value of the rigid straight part is 22.98 kV/cm. The reason for this phenomenon is that the charge density is higher on the corner than on the straight part, which has the smaller radius of curvature of the corner part. And according to the Eq. (1), the higher charge density means a larger electrical potential gradient, so the value of the electric field at the corner area is higher than the straight part.

3.2 Measurement of 750 kV High Altitude AC Transmission Line

The corona characteristics of operating 750 kV AC with Gan-type tower are tested in high altitude, and the measurement results are used to verified the correctness of calculation method which is used in this paper. The Ultraviolet imaging detection technology is used in this measurement of 750 kV corona discharge. The model of UV meter selected for this test is the Superb-XD portable daytime corona camera produced by Ofi Company, and its minimum UV sensitivity is 1.5×10^{-18} W/cm^2.

The measurement results of corona discharge are shown in Figs. 7 and 8. Tower I is at an altitude of 3200 m, and the temperature and humidity are – 4 °C and 50% during measurement; Tower II is at an altitude of 3700 m, and the temperature and humidity are 3 °C and 21% during measurement. It can be clearly seen from the measurement results that the corona intensity is more higher in the middle transmission line, and the corona position is mainly the corner and the vertical arc area of the middle line. There are also some corona discharge situations in the middle line fittings and side lines, although the corona intensity is relatively weak.

The noise pollution of power line is usually caused by corona discharge, and the noise of this tower are also measured. The noise detection results of the two towers are basically the same, and the value of noise are about 33–37 dB and the

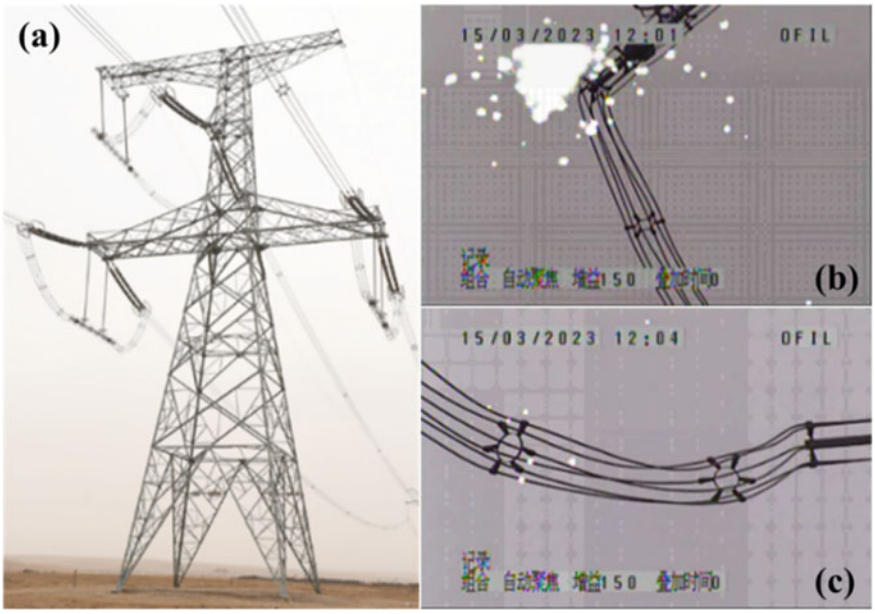

Fig. 7 Corona measurement of Tower I **a** picture of the tower, **b** corner of the middle line, **c** vertical arc of the middle line

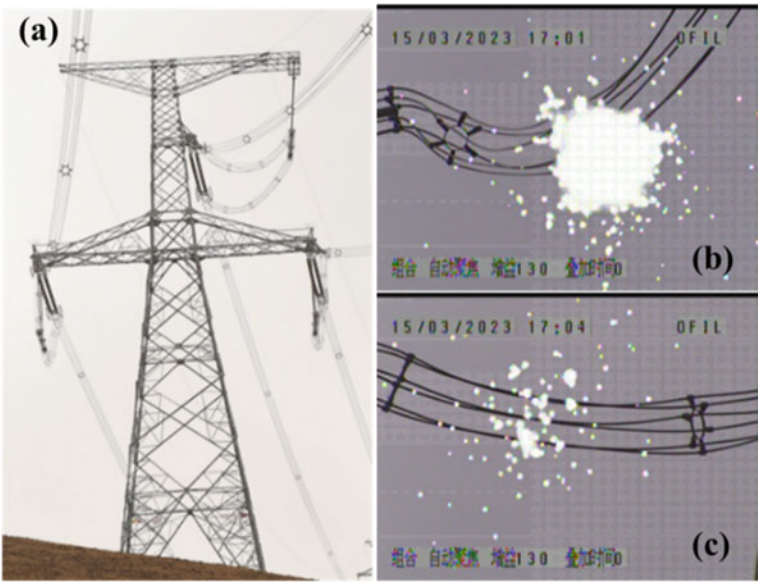

Fig. 8 Corona measurement of Tower II **a** picture of the tower, **b** vertical arc of the middle line, **c** vertical arc of the side line

environmental background are about 24–26 dB. According to the results, although the measured high-altitude 750 kV AC lines has occurred the corona discharge, the noise meets the 45 dB which is required by the relevant standards. However, the corona discharge is relatively obvious which is more than 10 dB higher than the environmental background, which should be controlled in higher voltage or altitude projects. The position of the corona and the difference in the intensity of the discharge are basically same with the calculation results, which verifies the correctness of the calculation method.

4 Electric Field Distribution for Different Conductor Sizes

4.1 Parameters of the Conductor

Three different conductor sizes are calculated to take an appropriate range of the safety margin, and the specific parameters are shown in following table.

4.2 Electric Field Distribution of the Different Conductors

The highest electric field area of the middle line is shown in Figs. 9, 10 and 11, which are calculated from Gan-type tower model with different conductor parameter as Table 1. And the electric field distribution along the transmission line is also shown in Figs. 9, 10 and 11.

The calculation results of the maximum electric field value are shown in Table 2.

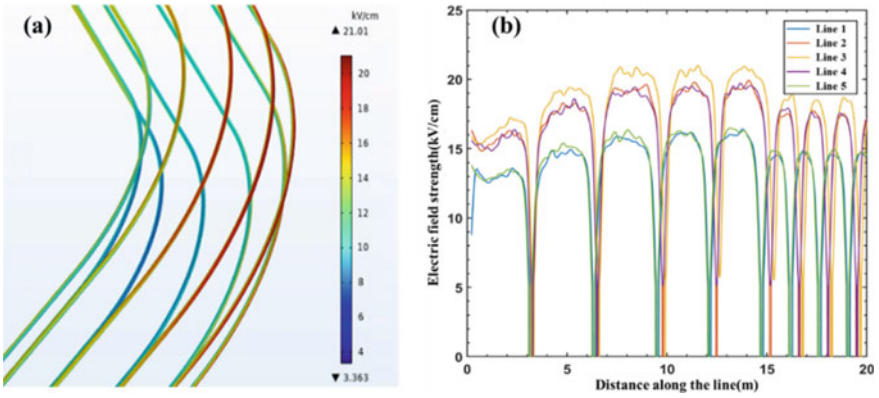

Fig. 9 Electric field distribution of 10 × 900 mm^2 **a** the highest area, **b** field distribution along the line

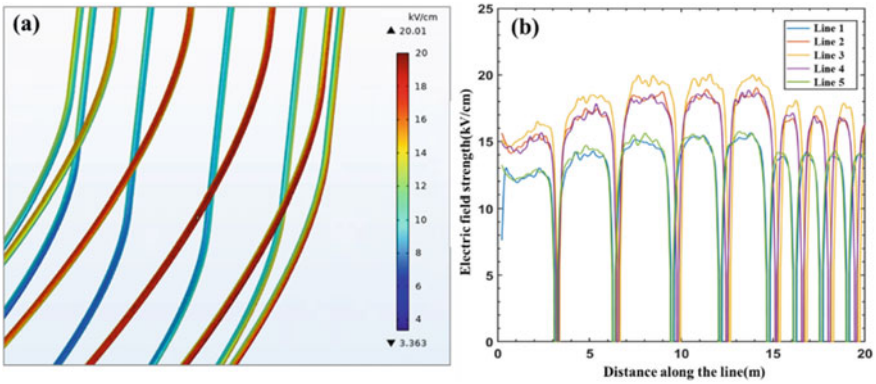

Fig. 10 Electric field distribution of 10 × 1000 mm^2 **a** the highest area, **b** field distribution along the line

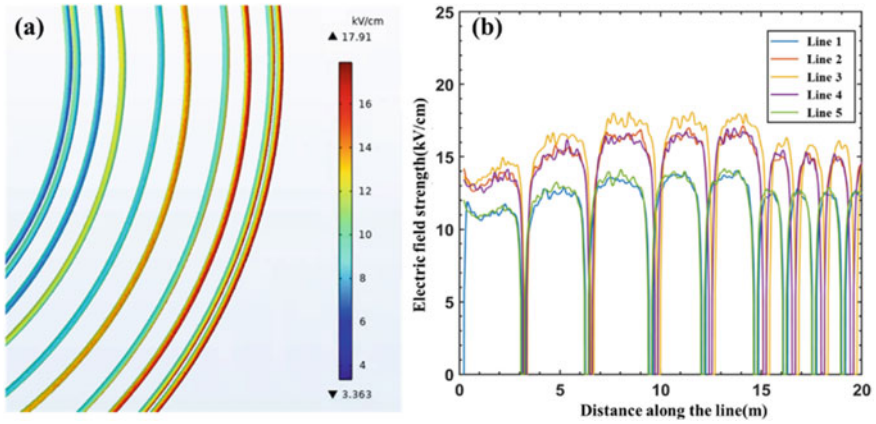

Fig. 11 Electric field distribution of 10 × 1250 mm^2 **a** the highest area, **b** field distribution along the line

Table 1 Conductor type and parameters

Type	Diameter of the conductors/mm	Distance between the conductors/mm
10 × 900 mm^2	40.6	450
10 × 1000 mm^2	42.9	450
10 × 1250 mm^2	47.8	450

Table 2 Conductor type and maximum field values of Gan-type tower

Type	Diameter of the conductors/mm	Distance between the conductors/mm	Maximum field value/ (kV/cm)
10×900 mm^2	40.6	450	21.0
10×1000 mm^2	42.9	450	20.0
10×1250 mm^2	47.8	450	17.9

5 Discussion and Conclusions

Based on the simulation results of the Gan-type tower, the maximum electric field is found at the corner of the middle transmission line. The surface electric field exhibits a trend of increasing and then decreasing with the length of the line. The three-dimensional corner structure of the tower has a smaller radius of curvature, which leads to an increase in the value of the surface field strength in that area. As the length of the line increases along the jumper, the shape of the middle line becomes a rigid straight, and the straight area has almost an infinite radius of curvature, resulting in a smaller and uniform field distribution. Moreover, the horizontal structure of the tower reduces the electric field strength of the line due to the shielding effect. Rising the sectional area of the conductor significantly decreases the electric field strength. When the conductor type of the Gan-type tower is changed from 10×900 to 10×1000, the maximum surface field strength decreases by 1.0 kV/cm, which is approximately 4.8%. The results of using 10×1250 conductor type show that the field strength decreases by 3.1 kV/cm, which is around 14.8%.

Acknowledgements This paper is supported by Science and Technology Project of State Grid Corporation of China "Research on corona and mechanical properties optimization of conductor fittings in high-altitude and overice areas of Sichuan-Chongqing UHV AC project" (No. 5200-202155593A-0-5-GC).

References

1. Riba JR, Larzelere W, Rickmann J (2018) Voltage correction factors for air-insulated transmission lines operating in high-altitude regions to limit corona activity: a review. Energies 11(7):1908
2. Hu Q, Shu LC, Jiang XL et al (2014) Influence of air pressure and humidity on positive direct current corona discharge performances of the conductor in a corona cage. Int Trans Electr Energy Syst 24(5):723–735
3. Li M, Liu L, Li B et al (2016) Prediction method on corona inception field intensity for HVDC fittings in high altitude area. In: 2016 IEEE international conference on high voltage engineering and application (ICHVE) 16558575
4. Zhang W, Yang GH, Li Y et al (2022) Corona inception characteristics and design of grading shielding electrode of typical electrode in UHV converter station in high altitude area. High Voltage Apparatus 58(4):124–130 (in Chinese)

5. He WL, Wan BQ, Liu YP et al (2021) Audible noise spectral characteristics of high-voltage ac bundled conductors at high altitude. IET Gener Transm Distrib 15(8):1304–1313
6. Wan BQ, Feng H, He WL et al (2021) Study on the radio interference of large section conductor bundles at high altitude. Environ Pollut Control 43(8):933–936,979 (in Chinese)
7. Chartier VL, Lee LY, Dickson LD, Martin KE (1987) Effect of high altitude on high voltage ac transmission line corona phenomena. IEEE Trans Power Delivery 2(1):225–237
8. Dallaire RD, Maruvada PS (1981) Analysis of radio interference from short multi-conductor lines. Part 1. Theoretical Analysis. IEEE Trans Power Apparatus Syst 100(4):2100–2108
9. Liu YP, You SH, Lu FC et al (2012) 500-kV EHV bundle conductors' corona onset voltage calculation and analysis in corona cage at different altitudes. IEEE Trans Power Delivery 27(4):2090–2097
10. Liu YP, Huang SL, Liu DR et al (2018) Corona onset gradient of the bundle conductor on AC power lines under sand and dust weather condition at 2200 m altitude. J Electrostat 95:32–41
11. Huang SL, Liu YP, Chen SS et al (2019) Corona loss characteristics of bundle conductors in UHV AC transmission lines at 2200 m altitude. Electric Power Syst Res 166:83–87
12. Huang SL, Ye ZJ, Liu YP et al (2021) Effects of the rainfall rate on corona onset voltage gradient of bundled conductors in alternating current transmission lines in high-altitude areas. Electric Power Syst Res 200:107461
13. Huang SL, Ha L, Liu YP (2023) The altitude correction term of the corona loss on alternating-current transmission lines. Energy Rep 9:2149–2152

Study on Change Law of Pressure and Hydrogen Gas Under Partial Discharge Defects in Transformer Bushing

Xinbin Huang, Chuansheng Luo, Yan Li, Zhou Zhou, Yunliang Zhang, Weiyong Liang, Junjie Qin, and Pengcheng Yang

Abstract For a long time, due to the lack of effective online monitoring technology for insulation status of transformer bushing equipment, some early latent local discharge insulation defects could not be detected early, ultimately leading to serious accidents. Recently, relevant research topics have gradually become the focus of researchers' attention, but most of them have overlooked pressure as a direct influencing factor leading to explosions. Based on this, this paper builds a test platform for detecting pressure and hydrogen parameters of local discharge defects in transformer bushings, simulating common corona discharge defects in transformer bushings, and analyzing the correlation between pressure and hydrogen characteristic quantities and the severity of discharge. The study found that the hydrogen content of corona discharge defects increased at both 500 pC and 1500 pC discharge levels, while the pressure changes increased first and then decreased at 500 pC discharge level, and continued to increase at 1500 pC discharge level. Under short-time discharge conditions, the increase in pressure and hydrogen content almost linearly increases with time. The research results have certain engineering significance for the assessment of the operating state of transformer bushing equipment.

Keywords Transformer bushing · Partial discharge · Internal pressure of bushing · Change law

1 Introduction

Less-oil equipment is a key equipment to ensure the safe and stable operation of the power system. Currently, the internal insulation system of less-oil equipment with a voltage of 110 kV or higher is formed by impregnating the capacitive core with oil

X. Huang (✉) · C. Luo · Y. Li · Z. Zhou · Y. Zhang · W. Liang · J. Qin · P. Yang
Nanning Power Supply Company of Guangxi Power Grid Co., Ltd, Nanning 530022, China
e-mail: Huangxinbin1234@qq.com

© Beijing Paike Culture Commu. Co., Ltd. 2024

X. Dong and L. Cai (eds.), *The Proceedings of 2023 4th International Symposium on Insulation and Discharge Computation for Power Equipment (IDCOMPU2023)*, Lecture Notes in Electrical Engineering 1102, https://doi.org/10.1007/978-981-99-7405-4_58

to form a capacitive oil-paper insulation structure, which has much less insulation oil content than large oil-immersed power equipment such as transformers [1, 2]. The main types of less-oil equipment in the power grid include current transformers (CTs), potential transformers (PTs), and bushings. CTs and PTs are critical equipment for measuring current and voltage within the power system, playing a role in voltage and current transformation and electrical isolation [3–5]. High-voltage bushings are mainly used for the high-voltage input and output terminals of large-scale power equipment, serving as a conduit, insulation, and support. They are all key equipment to ensure the safe and stable operation of the power system. Oil-immersed bushings, CTs, and other less-oil equipment have been widely used in the power system. However, insulation degradation is inevitable during long-term operation, which will become a "time bomb" inside less-oil equipment. When there is latent partial discharge (PD) insulation defect inside the less-oil equipment, the insulation oil will decompose, producing characteristic gases such as hydrogen and acetylene [6–9], which will cause changes in internal equipment pressure and further increase with the deterioration of insulation defects. In severe cases, it will cause explosions, fires, and other safety accidents, affecting the power supply reliability of the power system and causing huge economic losses. In recent years, the power grid has experienced multiple explosions and safety accidents caused by insulation damage of less-oil equipment. For example, from 2015 to 2019, less-oil equipment failures in the Xinjiang power grid accounted for 60% of the total equipment failures in substations, and in 2017 alone, there were two tripping accidents caused by 220 kV current transformers spewing oil due to top bursting and three emergency shutdown events caused by abnormal 750 kV high-voltage bushings on main transformers and high-voltage reactors. In 2013, two CT explosion accidents occurred in the Sichuan power grid, and in 2014, a 110 kV main transformer bushing explosion caused the transformer to burn down at the Jinghu substation. In 2019, a 220 kV main transformer caught fire at a certain substation in the Jiangsu power grid, and after accident analysis, it was confirmed that the insulation was lost due to poor bushing sealing and oil leakage, ultimately leading to the accident. From 2007 to 2008, a high-voltage bushing explosion accident occurred at the inner network side of two converter stations of the South China power grid's DC transmission line due to capacitance screen breakdown, causing the converter transformer to catch fire.

Currently, the commonly used methods for detecting faults in less-oil equipment are difficult to effectively and accurately monitor internal insulation defects in less-oil equipment. In addition, existing detection technologies have overlooked pressure as a direct influencing factor, which makes it difficult for existing fault diagnosis methods to effectively diagnose insulation defects in less-oil equipment. Therefore, it is necessary to carry out research on the diagnosis of insulation defects in less-oil equipment based on hydrogen and pressure.

Fig. 1 Solid-state palladium alloy hydrogen gas sensor

2 Experimental Materials and Methods

2.1 Oil Hydrogen Gas Detection Technology

Insulating oil can degrade into combustible and non-combustible gases under high temperature and discharge faults. The DGA method can accurately determine the components and concentrations of these characteristic gases. The industry standard DL/T 722-2018 "Guidelines for Dissolved Gas Analysis (DGA) of Transformer Oil and Judgment" specifies the gas components corresponding to typical fault types in transformers. Different characteristic gases correspond to different fault types and levels. For example, hydrogen is the main indicator of corona discharge, while acetylene is the main indicator of spark discharge and high-energy arc. However, the industry standard clearly states that hydrogen will be generated whether it is a discharge or overheated insulation defect. Therefore, the hydrogen content in the oil of oil-immersed power equipment has become an important parameter for evaluating the operating status of the equipment.

The article employs a new generation of solid-state palladium alloy hydrogen gas sensors. This type of sensor is not affected by other combustible gases such as carbon monoxide and acetylene, completely eliminating the problem of inaccurate measurement and false alarms in hydrogen measurement of electrochemical single-hydrogen products such as fuel cells. Figure 1 shows the physical diagram of the sensor.

2.2 Internal Pressure Detection Technology

The pressure detection technology is used to measure the oil pressure inside the low-oil equipment, which mainly contains hydrogen and carbon elements. When a discharge or overheat defect occurs, the gas generated in the early stage of the fault is mostly dissolved in the oil. Over time, the internal pressure of the equipment gradually increases due to the continuous accumulation of gas at the top of the equipment. When the pressure exceeds the limit that the rigid body can withstand,

the pressure relief device will burst, and in severe cases, an explosion may occur. The process from the occurrence of the fault inside the low-oil equipment to the explosion can be divided into four stages: defect generation, gas decomposition, pressure increase, and explosion when exceeding the tolerance value of the rigid body.

This article uses a diffusion silicon pressure transmitter to realize online measurement of oil pressure inside the low-oil equipment, which is based on the theory of the Wheatstone bridge in the circuit. The diffusion silicon chip is made into a pressure-sensitive resistor. When a fault occurs inside the low-oil equipment, the characteristic gas causes a change in oil pressure. The pressure is finally applied to the pressure-sensitive resistor of the sensor through the oil medium. At this time, the balance of the bridge is disrupted. The change in resistance value of the pressure-sensitive resistor can be calculated by the corresponding formula, and then combined with the current to calculate the corresponding voltage change signal, which is finally converted into the corresponding pressure value.

This sensor has high sensitivity, and further experimental tests will be conducted on the sensitivity of the two sensors before formal experiments. In addition, the pressure sensor has obvious anti-interference ability, wide power supply voltage, small and compact structure, and convenient installation, and is suitable for pressure measurement of liquids or gases. Figure 2 shows its circuit structure and working principle.

This sensor has a high sensitivity, and further experimental tests will be conducted on the sensitivity of the two sensors before formal experiments. In addition, the pressure sensor has obvious anti-interference ability, a wide supply voltage, a small

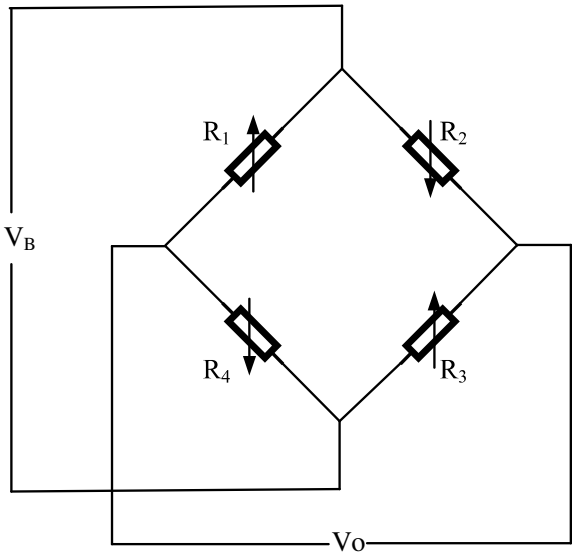

Fig. 2 Sensor working principle diagram

and compact structure, easy installation, and is suitable for pressure measurement of liquids or gases.

The pressure is transmitted through the silicon oil in the membrane box to the sensitive membrane, causing deformation, which in turn results in corresponding changes in the four resistances R_1, R_2, R_3, and R_4 arranged on the membrane. Among them, the resistance R_1 and R_3 arranged in the positive stress area increase in resistance value due to compression, while the resistance R_2 and R_4 arranged in the negative stress area decrease in resistance value due to tension. If the excitation voltage is V_B, then the output voltage V_0 of the bridge is:

$$\frac{[(R_1 + \Delta R_1)(R_3 + \Delta R_3) - (R_2 - \Delta R_2)(R_4 - \Delta R_4)]}{(R_1 + R_2 + \Delta R_1 - \Delta R_2)(R_3 + R_4 + \Delta R_3 - \Delta R_4)} V_B \tag{1}$$

If $R_1 = R_2 = R_3 = R_4$, and $\Delta R_1 = \Delta R_2 = \Delta R_3 = \Delta R_4 = \Delta R$, then the above equation can be simplified as:

$$V_0 = \frac{\Delta R}{R} V_B \tag{2}$$

The output voltage V_0 of the pressure sensor is proportional to the incremental resistance ΔR, and the incremental resistance ΔR is proportional to the external pressure applied to the sensor. Therefore, it can be concluded that the output voltage V_0 is proportional to the external pressure.

2.3 Test Platform

This paper's experimental circuit diagram and some experimental equipment are shown in Fig. 3.

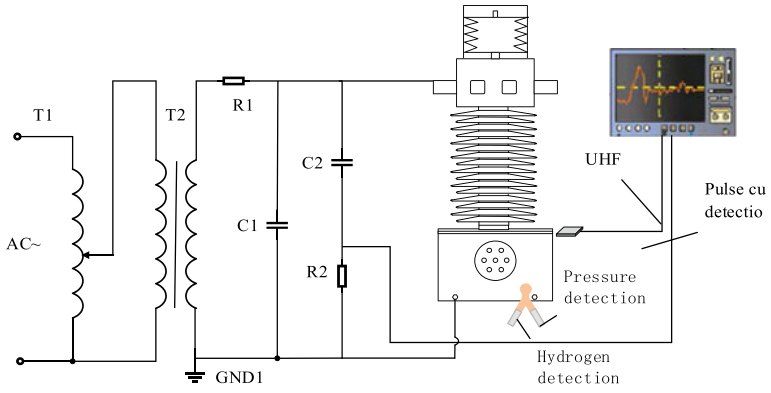

Fig. 3 Test platform

In the manufacturing and long-term operation of low-oil content equipment, insulation defects are inevitably generated. Common defects include: insufficient drying of the main insulation resulting in moisture in the insulation oil, improper vacuum oil injection resulting in bubbles, poor processing resulting in metal protrusions, poor grounding of the end screen, and capacitor screen rupture. After conducting research on accidents that occurred in oil-immersed bushings, maintenance personnel found that the common insulation defects mainly occur at the high-voltage inlet end, bottom flange, and other locations. Therefore, this experiment can set up metal protrusion defects.

Metal protrusion defect is a typical PD defect, which can be caused by rough processing or bumping during transportation, etc. Metal burrs can attach to the winding due to metal particles in the oil, forming metal protrusions. Metal protrusions will change the internal electric field of the equipment, causing slight distortion of the electric field. As the electric field intensity gradually increases, it will eventually reach the partial breakdown field strength of the insulation medium, thus triggering PD. Under normal circumstances, the discharge performance of metal protrusion defects is corona discharge. At non-severe levels, the discharge is relatively stable but can cause decomposition of insulation media such as insulating oil, which may ultimately lead to insulation breakdown accidents.

In order to simulate the metal protrusion defect, a copper metal needle is suspended inside the transformer in advance, and the upper end is connected to the high-voltage inlet end of the test specimen, and the lower end is raised about 1 cm after contacting the ground end, thus forming a metal protrusion defect. The installation position of the metal protrusion defect is shown in Fig. 4.

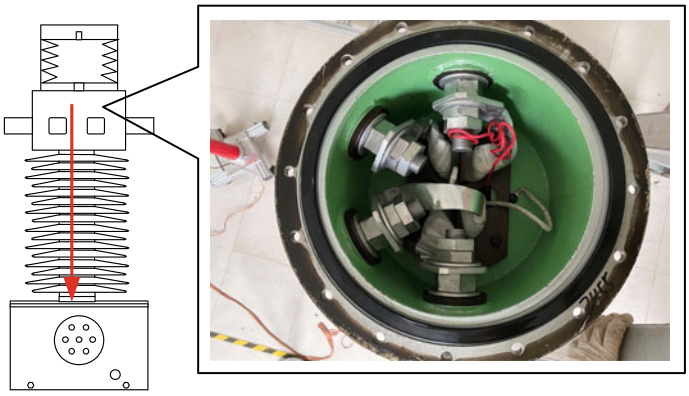

Fig. 4 Metal protrusion defect

3 Experimental Results and Analysis

To obtain PD signals of different severity levels in the experiment, it is often achieved by changing the applied voltage on the test specimen, which is also easier to operate in the experiment. However, when simulating the metal protrusion defect in this study, the test specimen was prone to the phenomenon of breakdown without sustained discharge, making it difficult to carry out long-term sustained pressure experiments. Therefore, considering the feasibility of the experiment, this study adjusted the number of metal protrusions to simulate PD of different severity levels in the presence of metal protrusion defects.

3.1 Results of the Single Metal Protrusion Defect Experiment.

Before the experiment, PD pulse calibrators were used to calibrate the discharge quantity. During the formal experiment, the initial discharge voltage of a single metal protrusion defect was measured at 45 kV, with a constant pressure of 48 kV and a duration of 70 h under continuous pressure. The average discharge quantity was about 500 pC, and the continuous discharge pulse waveform obtained during the experiment is shown in Fig. 5a. It can be seen that both UHF and pulse current detection methods can clearly obtain PD signals.

According to the installation plan proposed in the previous section, pressure and hydrogen content data inside the bushings were continuously collected for 70 h, and the change characteristics over time were plotted as shown in Fig. 5b.

It can be seen that neither pressure nor hydrogen content showed significant changes during the experiment. The indoor temperature was maintained by air conditioning, and the temperature change did not exceed 1 °C. Based on the characteristics

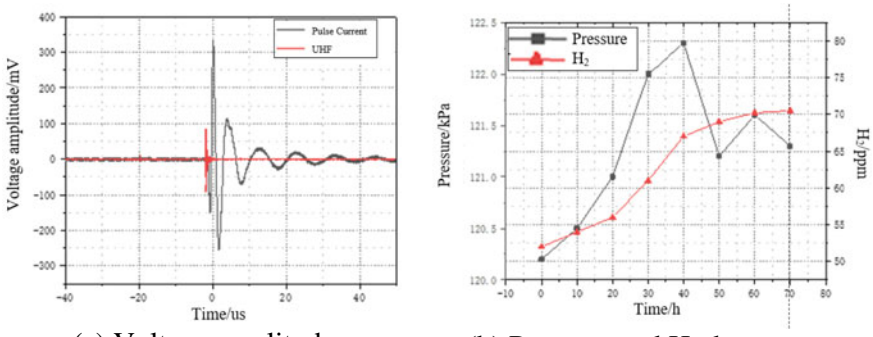

(a) Voltage amplitude (b) Pressure and Hydrogen gas

Fig. 5 Displacement response under excitation at fixed intervals

of the curve changes, it can be roughly divided into the following stages: Within the first 30 h, the defect continued to discharge, and the discharge was relatively frequent. The pressure and hydrogen content increased continuously and rapidly. From 30 to 50 h, the discharge began to weaken. Although the discharge quantity could be stabilized by increasing the voltage at this time, the discharge frequency had already decreased to a considerable extent. The growth rate of pressure and hydrogen content slowed down during this time period. The pressure value even decreased after 40 h, but it was still higher than the initial value. After analysis, it was found that this was because the gas production rate of hydrogen in the oil was smaller than the rate at which the hydrogen accumulated at the top of the equipment was dissolved in the oil due to the weakened discharge intensity. After 50 h, the discharge intensity of the defect further weakened, the growth rate of hydrogen content slowed down significantly, and almost no increase was observed. At this time, the pressure only showed a slight fluctuation with an amplitude of no more than 0.5 kPa. According to related research, this is because some of the characteristic gases generated in the oil-paper insulation under PD dissolve in the oil, while the rest remain free on the oil surface, and the dissolved and free parts eventually reach an equilibrium state.

3.2 Results of the Trible Metal Protrusion Defect Experiment.

Three metal protrusion defects are more prone to and more severe in PD. The experiment measured the starting discharge voltage of 38 kV, constant pressure of 42 kV, and duration of continuous pressure of 70 h with an average discharge amount of 1500 pC. The continuous discharge pulse waveform obtained during the experiment is shown in Fig. 6a, and the pressure and hydrogen content change characteristics are shown in Fig. 6b.

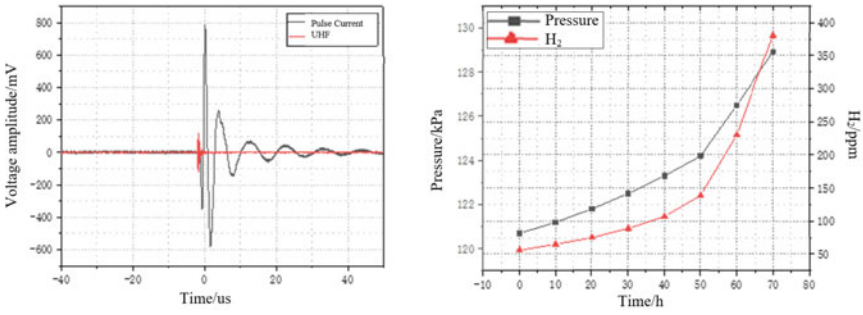

(a) Voltage amplitude (b) Pressure and Hydrogen gas

Fig. 6 Displacement response under excitation at fixed intervals

Due to more intense discharge compared to a single metal protrusion defect, the pressure and hydrogen content continued to increase throughout the entire experiment, and the growth rate gradually accelerated. The pressure increased by 9 kPa, indicating that the rate of insulation oil decomposition and hydrogen gas production under this defect was faster, causing most of the gas to escape and accumulate at the top of the equipment, leading to a significant increase in pressure. After the experiment, when the top sealing valve was opened, a large amount of gas was emitted, proving the fact of the accumulation of characteristic gases at the top.

4 Conclusions

(1) Under the metal protrusion defect, both pressure and hydrogen content increased under two discharge levels, and the overall trend of hydrogen content change was upward, while the pressure change was different.
(2) The hydrogen content of corona discharge defects increased at both 500 pC and 1500 pC discharge levels, while the pressure changes increased first and then decreased at 500 pC discharge lev-el, and continued to increase at 1500 pC discharge level.

Acknowledgements Science and Technology Project Funding by Guangxi Power Grid Company, China (No. GXKJXM20210254).

References

1. Chen L, Su C, Wu X et al (2020) Development of online monitoring device of transformer bushing based on inner pressure response. High Voltage Eng 46(2):569–575 (in Chinese)
2. Qu F, Zhao H, Wang B et al (2017) Application of dissolved gas analysis in oil to fault diagnosis of low-oil equipment. Electric Power Technol 11:107–111 (in Chinese)
3. He XR, Yin J, Zhang GZ et al (2021) Study on pressure variation characteristics of less oil equipment under overheating fault. High Voltage Apparatus 57(8):99–104 (in Chinese)
4. Huang X, Li Q, Wang J et al (2019) Production mechanism of single excessive hydrogen in current transformers: a reactive molecular dynamics simulation study. Mater Des 177:107–118
5. Uddin A, Yaqoob U, Chung GS (2016) Dissolved hydrogen gas analysis in transformer oil using Pd catalyst decorated on ZnO nanorod array. Sens Actuators, B Chem 226(4):90–95
6. Xiang J, Zhou XY, Liu Q et al (2018) Correlation of hydrogen generation with sparking discharges in a mineral insulating oil. IEEE Electr Insul Mag 34(3):7–12
7. Quanmin Dai BQ, Ran Z et al (2017) Discharge process and characteristics of the poor impregnated defect of capacitor core in oil-immigrated paper bushing. Trans China Electrotechnical Soc. 32(7):181–189(2017) (in Chinese)
8. Kiiza RC, Niasar MG, Nikjoo R et al (2014) Change in partial discharge activity as related to degradation level in oil-impregnated paper insulation: effect of high voltage impulses. IEEE Trans Dielectr Electr Insul 21(3):1243–1250
9. Meisel J (1963) Current instrument transformer error calculations. IEEE Trans Power Apparatus Syst 82(69):1082–1085

Establishment of Power Cable Dynamic Three-Dimensional Thermal Model Serving Digital Twin

Boyu Zhang, Chi Ma, and Jiangtao Li

Abstract This paper proposes a cable thermal model that serves digital twin, achieving fast response and high-precision calculations. Firstly, a two-dimensional cable thermal circuit model is established, and the heat transfer mode of air gap layer is analyzed. The equivalent thermal parameters of air gap layer are calculated by using the finite element method, solving the calculation accuracy problem caused by the excessive simplification of IEC standard. Secondly, considering the axial heat transfer of the cable and the corrugated structure of sheath, a method for calculating the equivalent outer diameter of corrugated sheath and a three-dimensional thermal model construction method are proposed. The axial heat transfer ability of each layer is analyzed and the three-dimensional model is optimized. Finally, a framework and construction method for a dynamic calculation model are proposed, realizing dynamic calculation of cable capacity while environmental parameters changes. The superiority of this model is verified through speed and accuracy comparisons with finite element method.

Keywords Power cable · Thermal model · Digital twin · Dynamic calculation

1 Introduction

With the rapid development of the economy and the continuous improvement of the scale and standards of urban construction, the inevitable drawbacks of overhead transmission lines are becoming increasingly prominent and are gradually being replaced by power cables [1]. The thermal state of the cable is an important indicator of the safe operation of the cable, which mainly involves the carrying capacity of

B. Zhang · C. Ma · J. Li (✉)
School of Electrical Engineering, Xi'an Jiaotong University, Xi'an 710000, China
e-mail: jt.lee@foxmail.com

C. Ma
e-mail: Machi@stu.xjtu.edu.cn

© Beijing Paike Culture Commu. Co., Ltd. 2024

X. Dong and L. Cai (eds.), *The Proceedings of 2023 4th International Symposium on Insulation and Discharge Computation for Power Equipment (IDCOMPU2023)*, Lecture Notes in Electrical Engineering 1102, https://doi.org/10.1007/978-981-99-7405-4_59

the cable and the cable temperature distribution and other parameters. Taking cross-linked polyethylene cables as an example, the maximum allowable temperature of the conductor is 90 °C. When the current of the cable exceeds its carrying capacity for a long time, the insulation of the cable will gradually be damaged, and the service life of the cable will be shortened. On the contrary, if the current of the cable is lower than its carrying capacity for a long time, it will waste resources and increase the cost of power transportation. Therefore, accurate calculation of the bearing capacity and temperature distribution of the cable body is of great significance for the safe and economic operation of the cable. There are mainly numerical and analytical methods for analyzing the thermal state of cables. References [2, 3] used numerical methods to analyze the cable current carrying capacity. The analytical method is mainly based on IEC standard, References [4, 5] established two-dimensional thermal circuit model for cables, which has large calculation errors and cannot analyze the changes in current carrying capacity when cables pass through different laying environments. Reference [6] established a three-dimensional thermal circuit model for cables, but the model is complex and slow in calculation speed, and accuracy still needs to be improved. In response to the requirements of digital twins for computational speed and accuracy, this article adopts analytical methods for modeling and optimizes the model to ensure accuracy.

Digital twin is the equivalent mapping of real-world entities in digital space, which digitally describes the entities and completes synchronous evolution with them. It involves technologies such as physical perception, simulation computing, and data analysis. Introducing digital twin into the field of power equipment is of great significance and can achieve full lifecycle management of power equipment. References [7, 8] introduced the application prospects of digital twins in power transmission and transformation equipment, and references [9, 10] studied the perception layer and modeling layer of digital twin for power equipment. This article mainly focuses on the simulation layer of digital twins, and the specific work is as follows:

(1) A two-dimensional full structure thermal circuit model of cables was established, and the heat transfer mode of the cable air gap layer was analyzed. The equivalent values of the thermal parameters of the air gap layer were calculated using the finite element method.
(2) A three-dimensional thermal path model of the cable was established and simplified to ensure accuracy while improving calculation speed.
(3) Designed a framework for dynamic calculation of cables, providing support for other functional layers of digital twins.

2 2D Thermal Circuit Model of Cables

2.1 Establishment of 2D Thermal Circuit Model of Cables

The thermal circuit model is to compare the transfer process of heat energy to the transfer process of electric energy, apply circuit theories such as Ohm's law to the study of the heat transfer process, and compare the temperature field of the cable and the surrounding environment to the circuit in the electric field, heat flow to the current, temperature difference to the voltage difference, and thermal resistance to the resistance.

As the voltage level of the cable increases, the cross-sectional area of the cable becomes larger and the thickness of some structures such as water blocking tape and air gap layers of the cable continues to increase. Moreover, due to poor thermal conductivity, the impact of these structures on the thermal state of the cable cannot be ignored. Therefore, for the thermal circuit modeling of high-voltage cables, it is necessary to consider these structures to establish a thermal circuit model of the entire cable structure, as shown in Fig. 1.

Where P_1, P_2, P_3 refer to cable conductor loss, insulation loss, and sheath loss, T_i represents the temperature of each structure. The thermal resistance in the figure is as follows from left to right: Conductor, Conductor Screen, Insulation, Insulation Screen, Water blocking tape, Air gap, Sheath, Outer serving, Environment. The calculation method of each thermal resistance in the figure can be used for structures with heat conduction as the heat transfer method, using the coaxial cylinder calculation method. The calculation formula is as follows.

$$R_c = \frac{\rho}{2\pi} \ln(1 + \frac{h}{D_c}) \tag{1}$$

where R_c represents thermal resistance, in m^2K/W, ρ Represents the thermal conductivity coefficient, expressed in W/(m · K), h is the thickness of the cylindrical layer, expressed in mm, and D_c is the outer diameter of the inner wall of the cylinder, expressed in mm.

For the corrugated aluminum sheath, its equivalent sine function is shown in Eq. 2. The integral method is used to calculate the equivalent outer diameter, and then the

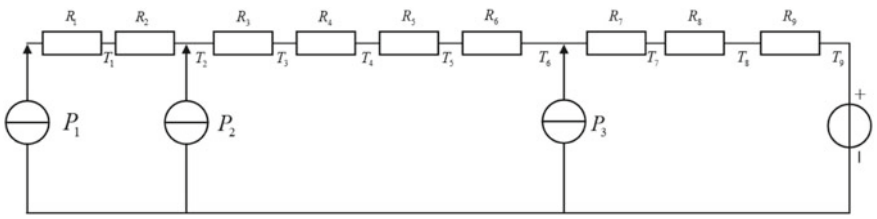

Fig. 1 2D thermal circuit model for the full structure of cables

coaxial cylinder formula is used to calculate the thermal resistance. The calculation method for the outer serving and air gap layer is also used. The calculation method for environmental thermal resistance can refer to the calculation method given in the IEC60287 standard.

$$S(x) = \frac{h}{2}\sin(\frac{2\pi x}{m} - \frac{\pi}{2}) \tag{2}$$

2.2 Analysis of Equivalent Thermal Conductivity of Air Gap

The cable geometry used in this calculation is shown in Table 1. The calculated current carrying capacity is 1650 A, which is much smaller than the actual current carrying capacity of the cable. Therefore, it is necessary to analyze the heat transfer mode of the air gap layer.

For air gaps in narrow spaces, When the air gap is large to a certain extent, convection may form, resulting in a significant decrease in thermal resistance value. This is mainly judged by the product of Prandtl number and Grash of number, the formula is as follows:

$$Gr = \frac{g\alpha\Delta t\delta^3}{v^2} \tag{3}$$

where Gr is a dimensionless number that characterizes the heat transfer effect; g is the constant of universal gravitation, m/s^2, α Is the volume expansion coefficient, 1/°C, Δ t is the temperature difference on both sides of the interlayer, °C, δ Is the interlayer thickness, m, v is the kinematic viscosity, m^2/s. Generally, when the horizontal interlayer $Gr \cdot Pr < 1700$, the fluid in the interlayer conducts heat in the form of pure heat conduction, and Pr is Prandtlnumber.

After calculation, The heat transfer method in air gap is considered heat conduction, indicating that other heat transfer methods are also involved in the air gap. In

Table 1 Geometric parameters of the cable

Structure	Thickness (mm)	Diameter (mm)	Structure	Thickness (mm)	Diameter (mm)
Conductor	–	61.9	Water blocking tape	5	126.4
Conductor screen	2.25	66.4	Sheath	2.8	147
Insulation	24	114.4	Outer serving	5	157
Insulation screen	1	116.4			

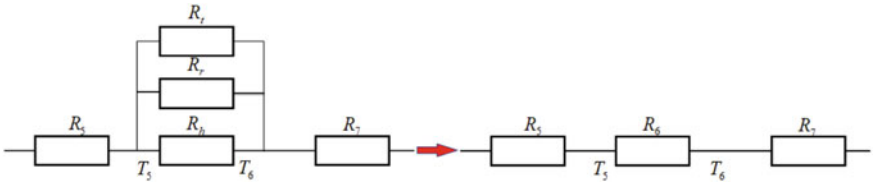

Fig. 2 Equivalent diagram of air gap thermal resistance

fact, due to the close distance between the water blocking tape on both sides of the air gap and the aluminum sheath, their thermal radiation cannot be ignored. In addition, due to the mutual contact between the aluminum sheath and the water barrier, some heat from the water barrier is directly transmitted through the aluminum sheath rather than through the air gap. Therefore, the heat transfer in the air gap is actually achieved through heat conduction, as well as the contact and radiation thermal resistance between the water barrier and the aluminum sheath. The equivalent thermal circuit is shown in Fig. 2. Considering the complexity of calculating contact thermal resistance and radiation thermal resistance, this paper uses finite element method to model the air gap layers of different structures and solve for their equivalent thermal conductivity.

where R_5 is the water blocking tape thermal resistance, R_t is the contact thermal resistance between the water blocking tape and the aluminum sheath, R_r is the radiation thermal resistance, R_h is the air gap heat conduction thermal resistance, R_6 is the equivalent thermal resistance of the air gap.

Firstly, a model of the axial cross-section of the cable corrugated structure and an equivalent cylindrical structure axial cross-section model were established in the finite element software (COMSOL Multiphysics 6.0). The model consists of conductor, insulation, water blocking tape, air gap, aluminum sheath, outer serving, and external air. The corrugated model sets up three physical fields, surface to surface thermal radiation, magnetic field, heat transfer, as well as their coupling. The equivalent model only sets up the magnetic field and heat transfer fields, and the air gap, as well as the water barrier and aluminum protective layer on both sides, are all set as solid heat transfer. Afterwards, continuously adjust the conductor current of the corrugated model until the conductor temperature reaches 90 °C, and then load the equivalent model with the same current to adjust the thermal conductivity of the equivalent air gap until the conductor temperatures of the two models are equal.

Firstly, simulate models with different axial lengths. The equivalent thermal conductivity simulation results are shown in Fig. 3, within a range of 3–150 pitches. The vertical axis represents the thermal conductivity, while the horizontal axis represents the number of pitches. From Fig. 3, it can be seen that the thermal conductivity will vary with the axial length and eventually stabilize. Considering that the assumption in two-dimensional modeling is that the cable axis is long enough to ignore axial heat transfer, this article ultimately selects 100 pitch length values as the thermal conductivity of the air gap layer. Afterwards, the equivalent thermal conductivity of the air gap under the changes of the cable pitch and the thickness of the air gap layer

was analyzed, and the results are shown in Figs. 4 and 5. The fitting formula between the thermal conductivity of the air gap and the pitch and thickness of the air gap layer is shown in Eq. 4, and the coefficients in the equation are shown in Table 2.

For the results in Fig. 4, when the thickness of the cable air gap layer is less than 2.5 mm, the equivalent thickness of the air gap layer is small, and the calculated value of the equivalent thermal resistance is small. In the thermal circuit model, the air gap is approximately short circuited, and the temperature calculation results show a small change with the air gap thermal conductivity, resulting in a significant increase in thermal conductivity.

From Fig. 5, it can be seen that the thermal conductivity of the air gap is inversely proportional to the pitch size and thickness. This also suggests that the air gap of the cable should be as small as possible to reduce the impact on the current carrying capacity, which is consistent with engineering experience. For the cables used in this

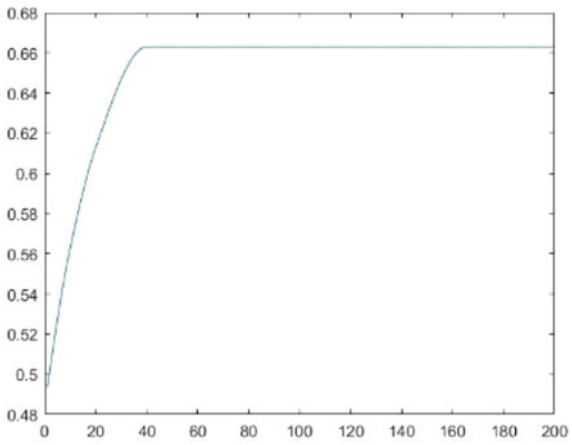

Fig. 3 Thermal conductivity varies with the number of pitches

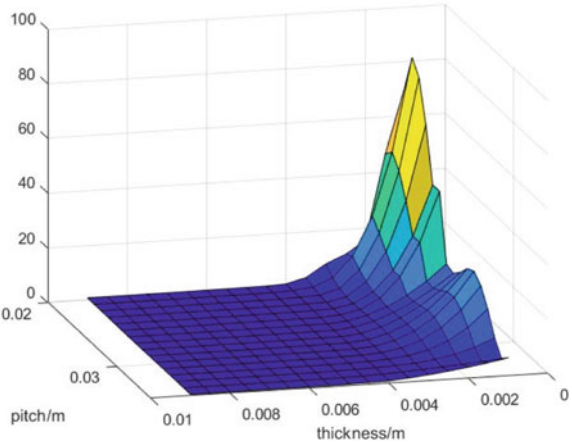

Fig. 4 The variation trend of equivalent thermal conductivity with pitch and thickness

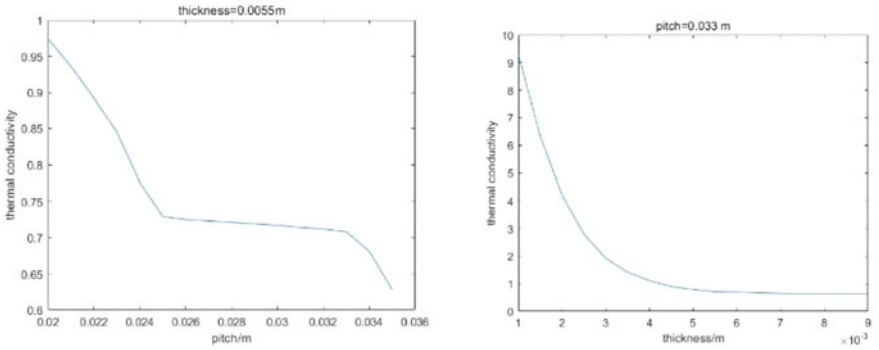

Fig. 5 Trend of thermal conductivity variation under fixed pitch and thickness

Table 2 Fitting formula coefficient value

Coefficient	Value	Coefficient	Value
P_{00}	422.1	P_{02}	9.587e06
P_{10}	− 2.532e^4	P_{30}	− 4.905e06
P_{01}	− 1.007e05	P_{21}	− 2.444e07
P_{20}	5.711e05	P_{12}	− 1.483e08
P_{11}	3.185e06	P_{03}	− 2.985e08

article, the final calculated current carrying capacity is 2238 A, which is greater than the 2115 A calculated according to the IEC standard. The reason for the significant error in the calculation results given in IEC60287 is that the cable air gap is ignored, and the gap in the equivalent structure of the IEC model is filled by the water blocking tape. However, the thermal resistance of the air gap is much lower than that of the water blocking tape. Under the equivalent calculation formula of the corrugated sheath, the thickness of the outer serving increases, and the final calculation result is conservative. The finite element method calculates a current carrying capacity of 2210 A, and the maximum temperature deviation from the equivalent thermal circuit model is 2.3 °C, proving that the accuracy of this thermal circuit model is guaranteed.

$$z = p_{00} + p_{10}x + p_{01}y + p_{20}x^2 + p_{11}xy + p_{02}y^2 + p_{30}x^3 + p_{21}x^2y^2 + p_{12}xy^2 + p_{03}y^3 \quad (4)$$

3 Establishment of 3D Thermal Circuit Model and Dynamic Calculation Model

Due to the fact that the laying environment of the cable line is not the same throughout the entire line, there may be harsh laying environments such as buried cables, and the presence of joints, firewalls can reduce the carrying capacity. However, traditional two-dimensional models cannot analyze the axial heat transfer process, so it is necessary to establish a 3D thermal circuit model to analyze the carrying capacity of the cable in harsh laying environments.

3.1 Establishment of 3D Thermal Circuit Model

The 3D thermal circuit model of the cable is shown in Fig. 6a. Based on the 2D thermal circuit model of the cable, each radial unit is connected by an axial thermal resistance. The calculation of axial thermal resistance adopts flat plate formula. For each node of the model, the KVL equation is listed, and the axial temperature distribution can be obtained by solving the equation. The complete 3D thermal circuit model has a slow calculation speed. Taking a 15 m length calculation as an example, the calculation time is 52 s, so it is necessary to simplify the model. Taking the axial temperature distribution on both sides of the insulation layer as an example, the temperature difference between two nodes in the axial direction is 0.01 °C, the insulation axial thermal resistance is 5.019, and the heat flow can be calculated as 0.002. It can be considered that the axial heat transfer process of the insulation layer is weak and has little impact on the current carrying capacity. This axial branch can be approximated as an open circuit. Similarly, other structures are analyzed and a thermal circuit model is ultimately obtained, as shown in Fig. 6b.

Based on the simplified 3D thermal circuit model, appropriate axial lengths should be selected in the modeling of the 3D thermal model to ensure calculation accuracy and speed. In this paper, 1/3 pitch length is selected as a radial unit. Then a simple model of harsh laying environment is established, tunnel-soil-tunnel model. The tunnel side and soil side are 5.5 m long respectively, and the total length of the line is 16.5 m. The maximum temperature difference between the thermal circuit model and

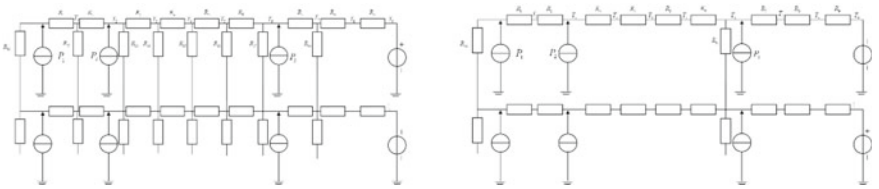

(a) Complete 3D thermal circuit model. (b) Simplified 3D thermal path model.

Fig. 6 3D thermal circuit model diagram

the finite element results is 2.995 °C, the calculation results of the current carrying capacity are 1513 A (thermal circuit) and 1455 A (finite element), and the calculation results of the current carrying capacity of buried cable are 1302 A, with a deviation of 211 A. The axial heat transfer has a great impact on the current carrying capacity. The above work proves the accuracy and significance of 3D thermal circuit model in this paper.

3.2 Dynamic Calculation Model

In order to meet the needs of digital twins, the model also needs to implement dynamic computing functions. The dynamic computing framework designed in this article is shown in Fig. 7. The implementation process is as follows: First, package the simulation program code to generate an executable file. Then the client calls the executable file after startup and generates the local table file. At the same time, the client reads the parameters required for modeling (cable structure, material properties, etc.) from the database and writes them to the local table file. Afterwards, the simulation program reads the local file and completes modeling calculations. The results are output to the local file and are read and uploaded by the client, and the client regularly obtains real-time sensing data from the database and writes it to local files. Finally, the simulation program reads data at the same time interval and performs calculations.

4 Conclusions

(1) Compared with the finite element method, the thermal circuit method has faster calculation speed and lower accuracy. However, through continuous optimization of the model, the calculation accuracy of the thermal circuit model can be improved, and the deviation from the finite element results is small, which can meet engineering requirements.
(2) The water blocking tape and air gap of the cable have a significant impact on the temperature and current carrying capacity calculation results, which cannot be ignored in the model. At the same time, the heat transfer methods of the air gap layer are diverse, and thermal parameters cannot be calculated based on thermal conduction. The current carrying capacity calculation results are nearly 200A higher than the IEC calculation results.
(3) When there is a harsh laying environment in the cable line, axial heat dissipation plays an important role in improving the current carrying capacity. 2D modeling can lead to significant calculation errors, and a 3D thermal circuit model or 3D finite element model should be established for analysis.

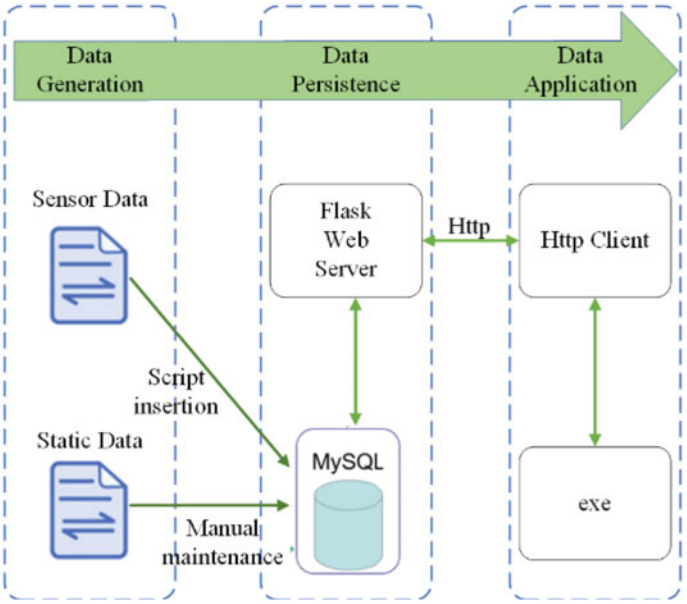

Fig. 7 Dynamic computing framework

References

1. Chen F, Li Z, Bian R et al (2019) The influence of parameter differences in parallel cables on their current distribution. High Voltage Apparatus 55(02):227–233 (in Chinese)
2. Shi DC, Li Q, Yu ZQ et al (2022) Analysis of cable carrying capacity in tunnel laying based on electromagnetic thermal fluid coupling. Insulating Mater 55(12):111–118 (in Chinese)
3. Liu YL, Xiong HW, Xiao HL et al (2022) Research on temperature field distribution of comprehensive pipe gallery cable based on finite element method. J Electric Power Sci Technol 37(06):82–90 (in Chinese)
4. Sedaghat A, Leon FD (2014) Thermal analysis of power cables in free air: evaluation and improvement of the IEC standard ampacity calculations. IEEE Trans Power Delivery 29(5):2306–2314
5. Huang ZY, Pilgrim JA, Lewin PL et al (2015) Thermal-electric rating method for mass-impregnated paper-insulated HVDC cable circuits. IEEE Trans Power Delivery 30(01):437–444
6. Yang F (2019) Research on key technologies for carrying capacity of 110kV cable lines. South China University of Technology, MA thesis (2019) (in Chinese)
7. Liu YP, Liu YJ, Lu FC et al (2022) Application prospects and key technologies of digital twin technology in power transmission and transformation equipment. High Voltage Eng 48(05):1621–1633 (in Chinese)
8. Sheng GH, YQ, Luo LG et al (2021) Key technologies and application prospects for the operation and maintenance of power equipment for new power systems. High Voltage Eng 47(09):3072–3084 (in Chinese)
9. Jing Y, Wang X, Yu Z et al (2022) Diagnostic research for the failure of electrical transformer winding based on digital twin technology. IEEE Trans Electrical Electron Eng 17(11):1629–1636

10. Zheng L, Liu K, Lin M et al (2023) Den Hartog: a zero-sample state evaluation model for valve-side bushing of UHV converter transformer oriented to digital twin under attribute analysis. IET Gener Trans Distrib (Wiley-Blackwell) 17(5):1123–1134

A New Synthetic Test Circuit for High Voltage Circuit Breakers Based on Dual Current Sources and Its Analysis

Wenjie Zhou, Zheyi Qu, Haibo Wang, Guan Hu, Zhanfeng Zheng, and Ling Zhang

Abstract With the breaking short-circuit current of circuit breakers continues to increase, and the requirements for the capacity of test laboratory and corresponding testing equipment are also increased simultaneously. The existing conventional test equipment is difficult to meet the test requirements. This paper proposes a new combined synthetic test circuit of dual current source branches + CTF three-circuit voltage source, and we completed a test which test duty is 550 kV 71kA τ = 120 ms T100a for a single pole breaker, we analyzed the equivalence and problems in the process of the circuit, then we proposed the solutions. On the basis of the existing mature test equipment, it can complete the breaking test of the higher short-circuit current circuit breaker, reduce the test risk, and provide a test basis for the development of new products.

Keywords High power test · Synthetic test circuit · Double current source · CTF voltage source

1 Introduction

In recent years, with the continuous expansion of power grid scale, increasing load level, higher grid density, and growing short-circuit current in power grid, the short-circuit current in some substations has exceeded the interrupting capacity of circuit breakers, which adversely affects the safe and stable operation of power grid. Due to the difficulty in expanding the area of existing substations, there are higher requirements for miniaturization of circuit breakers and their ability to interrupt larger short-circuit current. However, due to the complexity of the circuit breaker breaking process, testing and optimizing the product's breaking performance can only be done through experiments, even for newly developed circuit breakers.

W. Zhou (✉) · Z. Qu · H. Wang · G. Hu · Z. Zheng · L. Zhang
State Grid Electric Power Research Institute Testing and Certification Technology Co.,, Ltd, Changzhou 213126, China
e-mail: zhouwenjie@sgepri.sgcc.com.cn

© Beijing Paike Culture Commu. Co., Ltd. 2024

X. Dong and L. Cai (eds.), *The Proceedings of 2023 4th International Symposium on Insulation and Discharge Computation for Power Equipment (IDCOMPU2023)*, Lecture Notes in Electrical Engineering 1102, https://doi.org/10.1007/978-981-99-7405-4_60

As the traditional Weil loop is used to test circuit breakers that interrupt large short-circuit current in the testing station, the capacity requirement of the voltage source oscillation loop of the testing station is increased accordingly, and an auxiliary circuit breaker with the same capacity of short-circuit interruption is needed for the test. After completing the construction of the testing station, it is difficult to increase the capacity of the voltage source (oscillation loop), and it is impossible to purchase an auxiliary circuit breaker with a corresponding capacity for short-circuit interruption on the market. Therefore, the development of a new testing loop has become an important issue for switch testing.

Based on the synthesis principle of testing and the existing testing loops at home and abroad, this paper proposes a new synthetic loop that is applicable to the testing of circuit breakers with larger capacities to interrupt. The loop reduces the testing capacity and risk while ensuring the equivalence of the breaking process. The voltage source of the loop uses a single-side pressure three-loop (voltage, current jointly introduced into the loop), and the current source uses a short-circuit generator to inject short-circuit current into the test circuit-breaker via a parallel reactor after being combined. Only half of the short-circuit test current flows through the auxiliary circuit breaker in the current source loop, reducing the risk of the product under test.

This paper summarizes the issues that should be noted in practice with the loop, and analyzes the current zero-crossing and TRV. The equivalence and feasibility of the loop were verified in practice, and the loop can be extended to the testing of interrupting larger short-circuit currents.

2 Principle Topology of the New Synthetic Test Circuit

There has been a lot of research on synthetic testing methods for high-voltage circuit breakers in many countries. Different countries and regions have developed their own standards and testing methods, such as IEC62271-100 in Europe, IEEE C37.09 in the United States, and GB 1984–2014 in China. These standards provide guidance on synthetic testing methods for high-voltage circuit breakers, covering various types of breakers and testing requirements.

Based on the foundation of traditional synthetic circuits, W. A. vander Linden proposed a new artificial line for synthetic test [1], G. St-Jean studied wave shape quality of artificial line [2], in 1992, S. Yamashita and others proposed a synthetic testing circuit for a three-phase 3-phase-in-one-tank-type circuit breaker in 1989 [3]. van der Sluis [4] and Aldrovandi [5] made a report at CIGRE conference, and in the report, they conducted a dedicated review and summary of synthetic testing, Y. Kurozawa and others proposed a four-parameter recovery voltage test circuit applicable to extra-high voltage circuit breakers in 1989 [6]. ABB has proposed a new synthetic testing circuit for UHV circuit breaker called EPIC loop [7]. In the 1980s, Wang Renfu's research on four-parameter recovery voltage [8] was one of the representative works in China at that time.

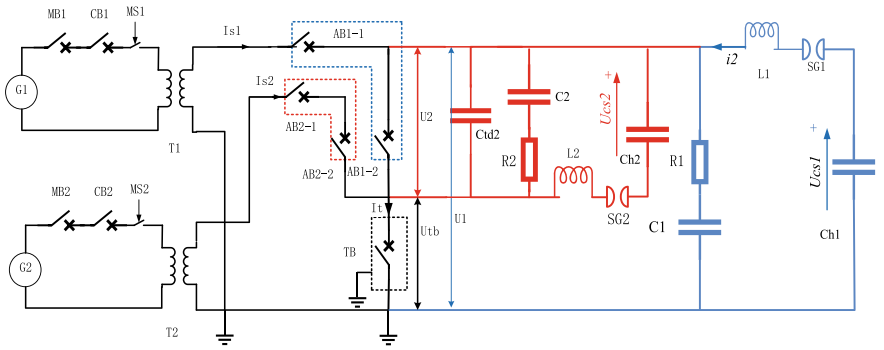

Fig. 1 Principle topology of the circuit

2.1 *Structure of the Circuit*

The structure of the loop is shown in see Fig. 1, which consists of two parts: the current source on the left and the voltage source on the right. The voltage source adopts the CTF (combination of a current and a voltage injection circuit for Terminal Fault), referred to as a "three-loop" circuit in Chinese.

The traditional CTF circuit has been proven to work well for high and extra-high voltage product interruption testing [9–13]. Compared with the traditional current-injection CTF circuit, the innovative loop proposed in this paper is different mainly in the current source. The current source loop consists of two parts and requires two sets of auxiliary circuit breakers. Both sets of auxiliary circuit breakers only pass half of the short-circuit test current. One set of auxiliary circuit breakers is connected to the voltage source (AB1-2 in Fig. 1), and the other set of auxiliary circuit breakers is only connected to the current source loop.

The current limit of conventional circuit breakers for breaking current is 63 kA. If testing needs to be done on products that interrupt short-circuit currents of 80 kA or even larger, related tests cannot be completed. The auxiliary circuit breakers in the loop only pass half of the actual test current, which is a significant advantage for developing new circuit breakers that interrupt larger short-circuit currents.

2.2 *Principle of the Circuit*

Current Source: Two generators G1 and G2 are connected to the circuit breakers MB1 and MB2, and operate the circuit breakers CB1 and CB2. The closing switches MS1 and MS2 are connected to two sets of medium-voltage test transformers. The current source branch 1 of generator No.1 G1 passes through the auxiliary circuit breaker AB1 (including two circuit breakers AB1-1 and AB1-2, or two contacts of an auxiliary circuit breaker), and the current source branch 2 of generator No. 2 G2

passes through the auxiliary circuit breaker AB2, which are connected in parallel to the high-voltage side of the test circuit-breaker. After the excitation voltage of the generator is raised to the required value through the parallel reactor, the two generators are synchronized at the outlet. The short-circuit current I_{s1} of generator No.1 and the short-circuit current I_{s2} of generator No.2 are injected into the test circuit-breaker through the two branches of AB1 and AB2, respectively.

Before 500 μs the test circuit-breaker's current I_t drops to 0 at t_1, the main sphere SG1 is triggered, and the current flowing through TB is the sum of the current source current $I_{s1} + I_{s2}$ and the inject current i_2.

At the short-circuit current zero-point t_2 of the current source, AB2-1, AB2-2, and AB1-1 are breaked, and the inject current i_2 flows through AB1-2 and TB.

At the current zero point of I_t (test circuit-breaker current) t_3, TB and AB1-2 are disconnected, SG1 is still conductive, the first voltage loop Ch1 together with R1 and C1 forms an oscillation loop and applies the first part of TRV to TB;

When the voltage of the first voltage loop oscillates near the peak value, SG2 is triggered, and the second voltage loop Ch2-SG2-L2-C2-R2, Ch2-SG2-L2-Ctd2 form an oscillation, which is superimposed on the TRV generated by the first voltage loop.

By controlling the breakdown time of SG1 and SG2, two sections of TRV are introduced to act on the test circuit-breaker, forming the four-parameter transient recovery voltage required by the standard [10].

3 Analysis of Test Failure Causes and Countermeasures

The laboratory completed the 550 kV 71 kA T100a $\tau = 120$ ms test with two 550 kV double-break circuit breakers as auxiliary circuit breakers for two current source branches, as shown in Fig. 2, AB1-1, AB1-2, AB2-1, and AB2-2 are each using two poles of an auxiliary circuit breaker.

3.1 Analysis of Test Failure Situations

The zero-crossing points of the two current source branches cannot be completely consistent due to the inability to ensure that the variable frequency control speed and excitation boost values of the two generators are completely identical. The energy exchange is small during the synchronous pulling process of the parallel reactor, so the current zero points of the two current source branches cannot be completely consistent.

The voltage source is added to the current source branch of the first generator (AB1-2), so the zero-crossing point of the current source branch of the first voltage loop is used as the synchronization signal reference.

Fig. 2 Actual wire connection

The First Voltage is Injected Too Early. Figure 3 shows the waveform of the failure caused by the first voltage loop being injected too early. The analysis process is as follows:

The zero-crossing point of the current source of generator #1 is before that of generator #2, and the synchronization device determines the current zero-crossing point based on generator #1, so AB1-1 current crosses zero first and break first. At this time, AB1-2 is not disconnected because i2 has been injected. At this time, AB2 has not crossed zero yet, and the test circuit-breaker has not breaked due to $i_2 + I_{s2}$, and most of the i_2 flows into AB1-2 and the test circuit-breaker.

Due to the large difference between the zero-crossing points of the current of generator #1 and generator #2, the test circuit-breaker breaked before AB2 and AB1-2 (relative to the zero point of generator #2, the main gap was injected too early, causing the current of the test circuit-breaker to cross zero earlier than the zero point of the current source of generator #2 after being superimposed with i_2).

After the test circuit-breaker is breaker, i_2 flows into the transformer loop through AB1-2 and AB2, and is disconnected at its natural zero crossing, leading to test failure.

The First Voltage Loop is Injected Too Late

To ensure that the voltage source is successfully injected to generate TRV, the zero-crossing point of the current source of generator #1 should be adjusted to be after the synchronization judgment is incorrect, causing the voltage loop to be injected after the zero-crossing point of the current source of generator #1. Therefore, the test loop

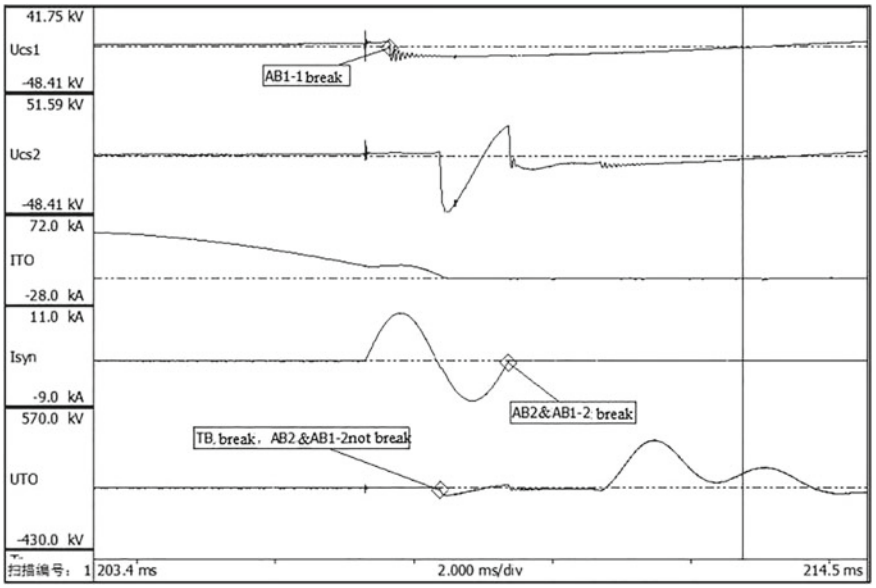

Fig. 3 Failure test waveform of circuit inject too early of the first voltage circuit

actually becomes a voltage injection loop. The current of the AB2 loop has crossed zero before the current of AB1-2, so the short-circuit current I_{tb} actually only comes from generator #1 before the current zero-crossing point of the test circuit-breaker, and the actual di/dt at the zero-crossing point of the test specimen is only half of the required value, and the actual waveform is shown in Fig. 4.

The Zero-crossing Points of the Two Generators Differ Significantly. Figure 5 shows the waveform of the test failure caused by the significant difference between the zero-crossing points of the two generators and the early breaking of the current source loop of generator #1. The analysis process is as follows:

The zero-crossing point of the current source of generator #1 is before that of generator #2, and the synchronization device determines the current zero-crossing point based on generator #1. At this time, the synchronization device issues an ignition command to ignition gap SG1, so AB1-1 and AB1-2 currents have crossed zero and break;

Because the current source of generator #1 has crossed zero, the AB1 loop is disconnected; the current of AB2 has not crossed zero, and the test circuit-breaker flows through the short-circuit current of generator #2. The inject current i_2 forms a loop through Ctd2, so the i_2 current is very small.

When the loop of generator #2 crosses zero, the test circuit-breaker is breaked, and the second voltage loop is about to ignite. TRV is applied to the test circuit-breaker, but the test is invalid.

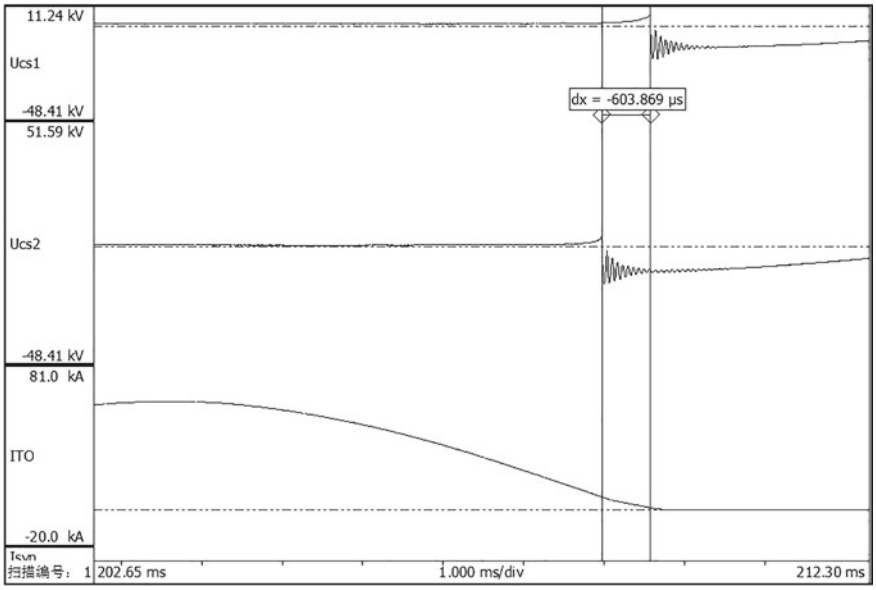

Fig. 4 Test waveform of circuit inject too late of the first voltage circuit

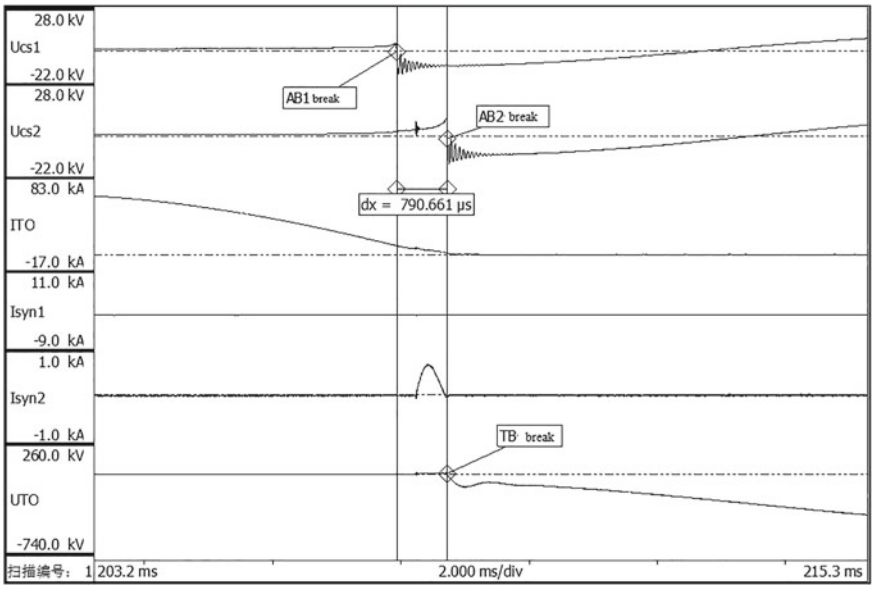

Fig. 5 The significant difference between the current zero points of two generators

3.2 Analysis of Test Success Situations

Since there is a difference in the zero-crossing points of the two generators, the synchronization controller should adjust the lead time based on the last zero-crossing point to ensure that generator #1 crosses zero later to ensure that the synchronization injection time is correct.

Regardless of the order of the zero-crossing points of the current source branches of the two generators, minimize the time difference between them, and synchronize the control i_2 to be injected before the zero-crossing point of the two current source branches, and the half-wave time of i_2 is sufficient to cover the time difference between the zero-crossing points of the two generators. Adjust SG1 ignition time to ensure that the test specimen is alone under the i_2 for the required t_h time and ensure the equivalence of the di/dt at the zero-crossing point of the test circuit-breaker.

The specific method is to adjust the generator terminal voltage and the speed difference between the two generators through short-term control to ensure sufficient energy exchange between the two generators during the synchronous pulling process and make the zero-crossing points of the two generators approach each other.

Figure 6 shows the waveforms of a successful test, and from the figure, it can be seen that the zero-crossing point current of the test specimen is smooth, completely under i_2 current before the zero-crossing point, and alone under the i_2 for the required t_h time. The test is successful.

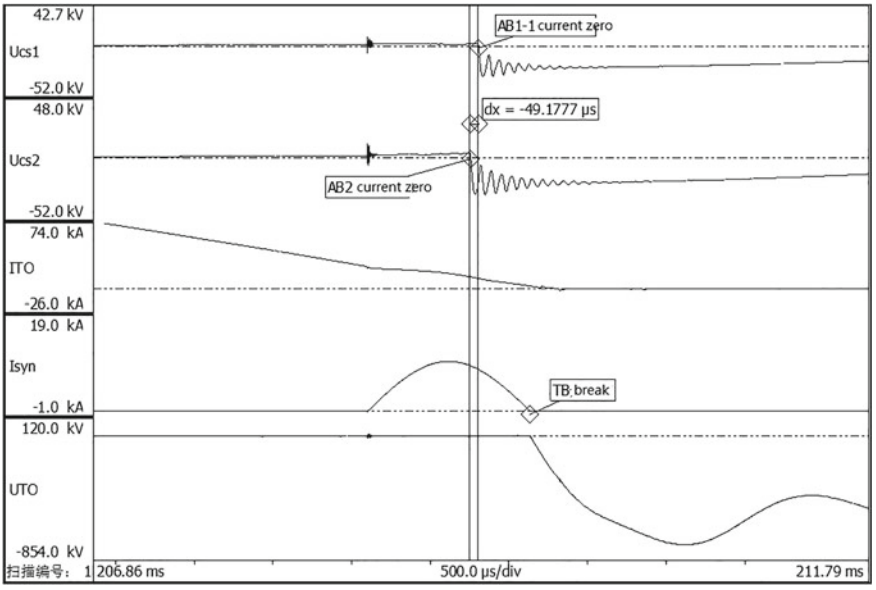

Fig. 6 Test successful

4 Conclusion

Based on the basic principles of synthetic circuits and the current situation of test laboratories at home and abroad, this paper proposes a new synthetic circuit that can be used for high-current and high-voltage circuit breaker testing. The selection and calculation of the circuit voltage source are explained in detail through theoretical analysis, and the reasons for the failure of the circuit during the test are analyzed in detail. The key points for the successful testing of the new circuit are explained, and the new product testing is completed using this circuit.

The circuit uses dual current sources and combines with the dual voltage sources to produce TRV waveforms that meet the standards and actual conditions, which can meet the requirements of larger short-circuit currents and lower the energy requirements of the test laboratory and the technical parameters of related test equipment.

References

1. van der Linden WA, van der Sluis L (1983) A new artificial line for testing high voltage circuit breakers. IEEE Trans Power Apparat Syst 102(4):797–803
2. Jean GS, Landry M (1989) Comparison of wave shape quality of artificial lines used for short-line fault breaking testing on high-voltage circuit breakers. IEEE Trans Power Delivery 4(4):2109–2113
3. Yamashita S, Miyake N, Suzuki K et al (1989) Short-circuit testing method of 3-phase-in-one-tank-type SF6 gas circuit breaker. IEEE Trans Power Delivery 4(1):349–354
4. van der Sluis L, Danastra GC, Kemper HW et al (1992) Synthetic test methods: experience and future developments. Cigre Paper 13-203, Paris, France
5. Aldrovandi G, Bonfanti I, Kuhuhardt G, Pliet H (1992) New application of synthetic circuit development in CESI and IPH. Cigre Paper 13-201, Paris, France
6. Kurozawa Y, Takahashi T, Saito K et al (1997) Four-parameter transient recovery voltage circuits appropriate for test extra high voltage circuit breakers. CIGRE Paper13-32, Sarajevoi Yugoslavia
7. Sheng BL, van der Sluis L (1997) A new synthetic test circuit for ultra-high-voltage circuit breakers. IEEE Trans Power Delivery 12(4):1514–1519
8. Wang RF (1987) Calculation and adjustment limitations of four-parameter TRV in high power testing circuits and their applications. IEEE Trans Power Delivery 2(3):75–764
9. Pei Z, Yao S, He J et al (2017) A new synthetic test circuit for UHV circuit breakers. Proceedings of the CSEE 27(33):65–69 (in Chinese)
10. GB/T 4473-2018 Synthetic testing of high-voltage alternating current circuit-breakers, 2019 (in Chinese)
11. Na H, Xiao C, Xing W et al (2020) Study of duplicate voltage circuit for UHV synthetic test method. Electrotechnics Electric (1):8–20 (in Chinese)
12. Hu X, Luo Y et al (2023) Take synthetic experiment as an example to grasp the equivalence of experiment. Electric Drive Autom 45(20):34–37 (in Chinese)
13. Dechun W, Hui C, Guowei G et al (2022) Parameter design and simulation of 126kV/50kA synthetic test circuit. Guangdong Electric Power 35(6):126–134 (in Chinese)

Simulation of Space Charge Characteristics of Epoxy Materials at High Temperature

Xingqiao Li, Kun Li, Shiyu Jin, Qianchuan Zhao, Ning Huang, Qianchuan Zhao, Honliang Zhang, and Hai Jin

Abstract The main insulating material of converter transformer bushing is epoxy composite material, epoxy composite material has prominent interface effect and obvious space charge accumulation under high temperature, which is easy to cause electric field distortion and aging of insulation material, leading to bushing insulation failure. There is little research on numerical simulation of space charge of epoxy composites at high temperature, and the influence mechanism of space charge effect on casing electric field is not clear. In this paper, the space charge characteristics of epoxy composites are studied from the perspective of space charge. The simulation shows that the charge in the medium has different dynamic characteristics at different temperatures. High temperature conditions promote the injection and mobility of charges, making the extraction rate of holes less than the transport rate, and the migrated holes accumulate due to limited extraction, resulting in the accumulation of heterogeneous charges. The contribution of trapped carriers to space charge is most prominent during the later stage of pressurization. Due to the amass of different polarity charges, the electric field at the two electrodes is seriously distorted.

Keyword Epoxy · Bushing · Space charge · Carriers · Electric field distortion

1 Introduction

The converter bushing bears high voltage and large current carrying capacity during operation, and the temperature of central guide rod and capacitor core exceeds 100 °C [1]. When the insulation is subjected to high temperature, the space charge effect will become more prominent, causing electric field distortion, partial discharge and even breakdown, ultimately accelerating the aging of insulation materials, leading to insulation failure of bushings [2, 3]. Therefore, the properties of space charge in

X. Li · K. Li · S. Jin · Q. Zhao · N. Huang · Q. Zhao · H. Zhang (✉) · H. Jin
School of Electrical Engineering and Information Engineering, Lanzhou University of Technology, Lanzhou 730050, China
e-mail: zhanghl-518@qq.com

© Beijing Paike Culture Commu. Co., Ltd. 2024

X. Dong and L. Cai (eds.), *The Proceedings of 2023 4th International Symposium on Insulation and Discharge Computation for Power Equipment (IDCOMPU2023)*, Lecture Notes in Electrical Engineering 1102, https://doi.org/10.1007/978-981-99-7405-4_61

insulation materials used for bushing at high temperature will provide a theoretical basis for insulation optimization, electric field analysis and many other aspects of the bushing.

In this study, we improve the bipolar carrier transport model and construct the finite element model of single-layer epoxy material in the software is constructed in COMSOL. Based on the course of carrier transport, capture, trapping, injection, and taking into account the limitation of carrier extraction, simulation analysis is carried out under high temperature conditions, and the space charge distribution and electric field distribution characteristics of epoxy materials at 40, 60, 80, 100 °C are obtained.

2 Bipolar Charge Transport Model Based on Limited Carrier Extraction

2.1 Brief Introduction of Physical Model

To make the carrier transport part more obvious, some detailed physical processes are ignored and the following approximation is made:

(1) It is considered that the carrier transport in the medium is continuous and does not distinguish between crystalline and amorphous regions;
(2) Considering only a single trap level, it is considered that the influence of shallow traps is reflected in the change of carrier mobility;
(3) It is considered that the accumulation of heteropolar charges originates from electrode injection, and impurity ionization is not considered.

Based on the above approximation, Fig. 1 shows the physical model of bipolar carrier transport based on extraction restriction.

As shown in Fig. 1, When DC voltage is applied on both sides, holes and electrons are injected from the anode and cathode respectively, and some holes accumulate in the cathode and some electrons accumulate in the anode due to the limitation of carrier withdrawal. $S_{e\mu,ht}$ and $S_{et,h\mu}$ represent the recombination process of trapped charge (trapped electron/hole) and free charge (hole/free electron). Similarly, $S_{e\mu,h\mu}$ and $S_{et,ht}$ represent the recombination process between free charges and trapped charges of different polarity.

2.2 Mathematical Model

The mathematical model of bipolar charge transport is mainly composed of the injection, extraction equation and transport equation of the electrode. For carrier injection, Schottky emission mode is adopted in this paper: when the applied field

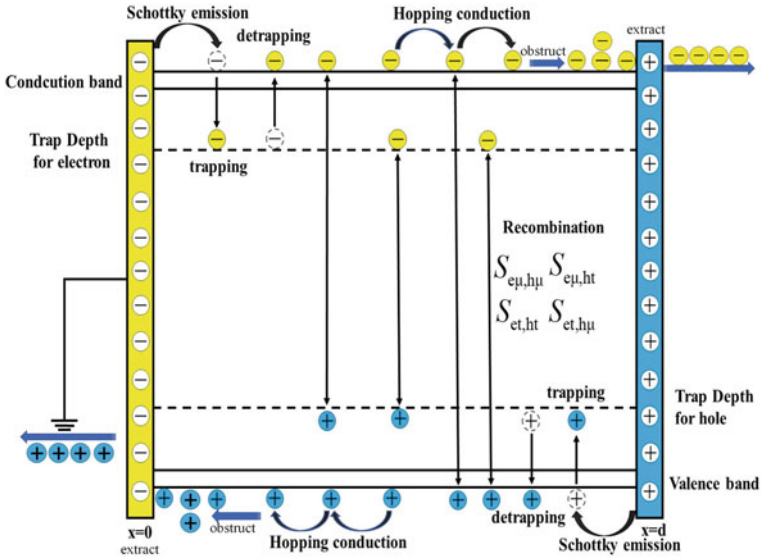

Fig. 1 Physical model of bipolar charge transport based on carrier extraction constraints

strength is lower than 100 kV/mm, for the injection of electrons and holes on the surface of the cathode and anode [4], Schottky's law includes:

$$j_{\text{eihi}}(x,t) = AT(x)^2 \exp\left(\frac{-e\omega_{\text{eihi}}}{kT(x)}\right)\exp\left(\frac{e}{kT(x)}\sqrt{\frac{e|E(x,t)|}{4\pi\varepsilon_0\varepsilon_r}}\right) \tag{1}$$

In the above equation, T(0) and T(d) represent the temperature of the cathode and anode, j_{ei} and j_{hi} represent the injection current density of the cathode and anode, and w represents the injection barrier of holes and electrons at the interface; E(x, t) Is a random time electrode surface electric field; K is Boltzmann constant; Medium A is Richardson constant [5]. In order to prevent the non physical behavior when the electric field is 0 and the injection current is not 0, it can be obtained by modifying formula (1):

$$j_{\text{elhi}}(x,t) = AT(x)^2 \exp\left(\frac{-e\omega_{\text{eihi}}}{kT(x)}\right)\left[\exp\left(\frac{e}{kT(x)}\sqrt{\frac{e|E(x,t)|}{4\pi\varepsilon_0\varepsilon_r}}\right) - 1\right] \tag{2}$$

In this paper, in order to better express the withdrawing influence of electric field and temperature on carriers, the withdrawing process is defined in the same way as carrier injection ω_{eo} and ω_{ho} It represents the withdrawal barrier, and the carrier withdrawal limit is as follows [6]:

$$j_{\mathrm{eo/ho}}(x,t) = AT(x)^2 \exp\left(\frac{-e\omega_{\mathrm{eo/ho}}}{kT(x)}\right)\left[\exp\left(\frac{e}{kT(x)}\sqrt{\frac{e|E(x,t)|}{4\pi\varepsilon_0\varepsilon_{\mathrm{r}}}}\right) - 1\right] \quad (3)$$

The carrier transport in the epoxy composite can be described by the coupled PDE equations composed of current continuity (carrier convection reaction) equation, conduction equation and electrostatic field Poisson equation [7], which are expressed as follows:

$$\begin{cases} \frac{\partial n(x,t)}{\partial t} + \frac{\partial j(x,t)}{\partial x} = S_i(x,t) \\ j(x,t) = \mu(x,t)n(x,t)E(x,t) \\ \frac{\partial E(x,t)}{\partial x} = \frac{\rho(x,t)}{\varepsilon} \end{cases} \quad (4)$$

In the above equation, j is the current density in the medium; μ Is carrier mobility; ρ Is the net charge density, which represents the sum of all carrier charges at time t and position x; Si is the source term, representing the interaction of different carriers; E is the electric field strength; ε Is the relative dielectric constant. The convection term on the left side of the continuity equation represents the change of free charge caused by conduction current [8].

The carrier source term Si in formula (4) is specifically expressed as follows:

$$\begin{cases} S_{\mathrm{e}\mu} = -e \cdot S_{\mathrm{e}\,\mu,\mathrm{ht}} \cdot n_{\mathrm{e}\mu} \cdot n_{\mathrm{ht}} - B_{\mathrm{e}} \cdot n_{\mathrm{e}\mu} \cdot \left(1 - \frac{e \cdot n_{\mathrm{and}}}{N_{\mathrm{eot}}}\right) + D_{\mathrm{e}} \cdot n_{\mathrm{and}} \\ S_{\mathrm{and}} = -e \cdot S_{\mathrm{and,h}\,\mu} \cdot n_{\mathrm{and}} \cdot n_{\mathrm{h}\mu} - e \cdot S_{\mathrm{and,ht}} \cdot n_{\mathrm{and}} \cdot n_{\mathrm{ht}} + B_{\mathrm{e}} \cdot n_{\mathrm{e}\mu} \cdot \left(1 - \frac{e \cdot n_{\mathrm{and}}}{N_{\mathrm{eot}}}\right) \\ \quad -D_{\mathrm{e}} \cdot n_{\mathrm{and}} \\ S_{\mathrm{h}\mu} = -e \cdot S_{\mathrm{and,h}\,\mu} \cdot n_{\mathrm{and}} \cdot n_{\mathrm{h}\mu} - B_{\mathrm{h}} \cdot n_{\mathrm{h}\mu} \cdot \left(1 - \frac{e \cdot n_{\mathrm{ht}}}{N_{\mathrm{hot}}}\right) + D_{\mathrm{h}} \cdot n_{\mathrm{ht}} \\ S_{\mathrm{ht}} = -e \cdot S_{\mathrm{and,h}\,\mu} \cdot n_{\mathrm{and}} \cdot n_{\mathrm{h}\,\mu} - e \cdot S_{\mathrm{and,ht}} \cdot n_{\mathrm{and}} \cdot n_{\mathrm{ht}} - B_{\mathrm{h}} \cdot n_{\mathrm{h}\,\mu} \cdot \left(1 - \frac{e \cdot n_{\mathrm{ht}}}{N_{\mathrm{hot}}}\right) \\ \quad -D_{\mathrm{h}} \cdot n_{\mathrm{ht}} \end{cases} \quad (5)$$

where, $S_{\mathrm{e}\mu,\mathrm{ht}}$,$S_{\mathrm{et,h}\mu}$,$S_{\mathrm{et,ht}}$ Represent the recombination rate of free electron and trapped hole, trapped electron and free hole, trapped electron and trapped hole respectively; B_e and B_h represent the sinking coefficients of electrons and holes respectively; N_{eot} and N_{hot} represent the concentration of trapped electrons and trapped holes respectively; D_e and D_h represent the trapping rates of trapped electrons and trapped holes, respectively.

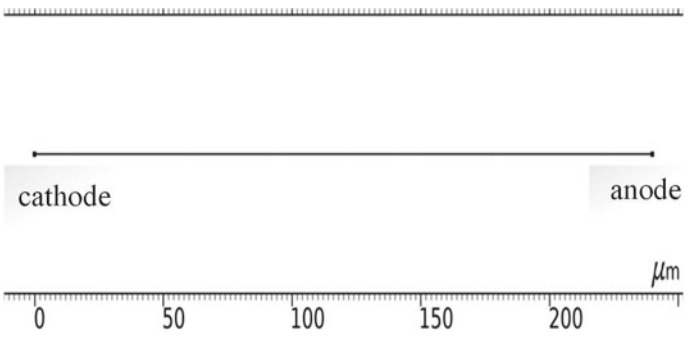

Fig. 2 One-dimensional finite element model of epoxy sample

2.3 Finite Element Compression Model of Epoxy Material

Figure 2 shows the one-dimensional geometric model of the epoxy flat sample in COMSOL.

The left end point is the cathode, and the right end point is the anode. The electrostatic field is coupled with the mass transfer field to simulate the charge transport process, and the transient charge density of four different carriers is calculated. Set the maximum unit length to 2.4 μm.

For macroscopic parameters such as electrode injection barrier and trap barrier, the measured data of our research group are combined. In order to reflect the influence of temperature and field strength on carrier mobility, jump conductance is used to describe the charge mobility [9] in the simulation, as shown in the following formula [8–11]:

$$\mu(x) = \exp\left(\frac{1.32 \times 10^{-5} \cdot |E| - 5715.5}{T}\right)/|E| \tag{6}$$

3 Simulation Results

3.1 Space Charge Distribution of Epoxy Materials at High Temperature

The following external applied electric field 40 kV/mm is taken as an example for analysis. In order to clearly reflect the change trend of space charge within two hours of pressurization, the space charge nephogram corresponding to 40–100 °C is drawn in Fig. 3.

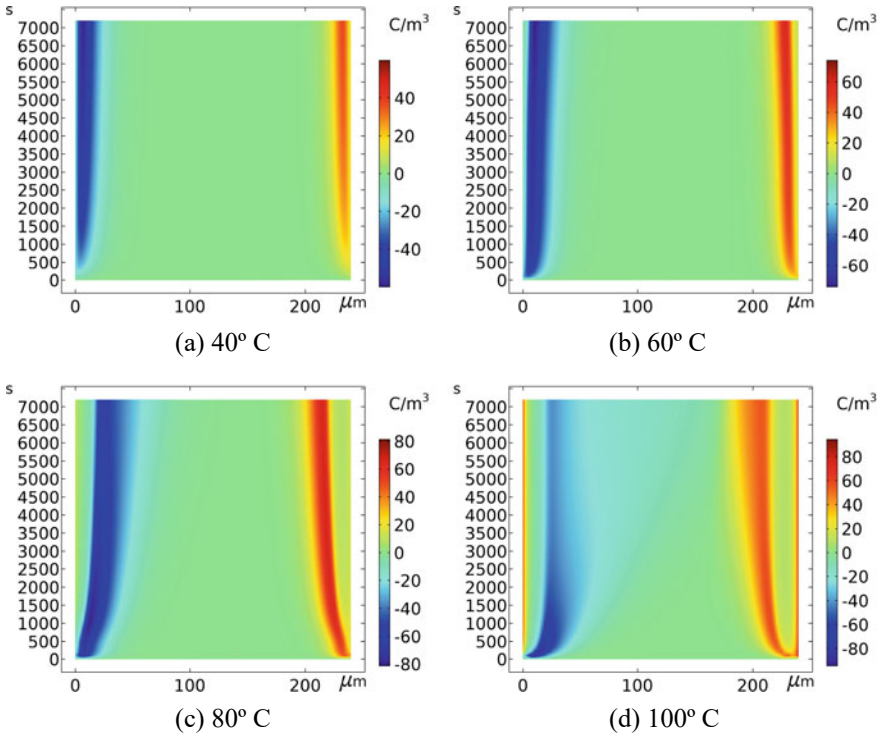

Fig. 3 Cloud map of space charge distribution at different temperatures under 40 kV/mm electric field

It can be seen from Fig. 3 that at 40–60 °C, there is a homopolar charge distribution. In the first 100 s, the charge accumulation speed at 60 °C is significantly faster than that at 40 °C. When the temperature is 80 °C, starting from 1500 s, it is about 0–5 μm near the cathode There was a less obvious accumulation of positive charges at m, the maximum positive charge density was 10.3 C/m^3, and then the positive charges were covered by negative charges.0–8 μm near cathode at 100 °C There is always an accumulation of heteropolar charges at m, and the maximum positive charge density is 50.8 C/m^3. At this time, the negative charge diffusion depth of the cathode also increases significantly.

In order to study the charge distribution at different temperatures at the same time, Fig. 4 shows the space charge distribution at different temperatures at four times in 100–7200 s.

At 100s, the curve trends at four temperatures are roughly the same, and the charge peak gradually moves toward the interior of the medium. It can be seen that the space charge injection and diffusion at 40 °C are not obvious, and the area with space charge density of 0 is 60–100 μm. Taking the cathode as an example, the charge peaks at 40–100 °C are about 8 C/m^3, 35 C/m^3, 68 C/m^{3}and 95 C/m^3 respectively, indicating that the increase of temperature promotes the charge accumulation near

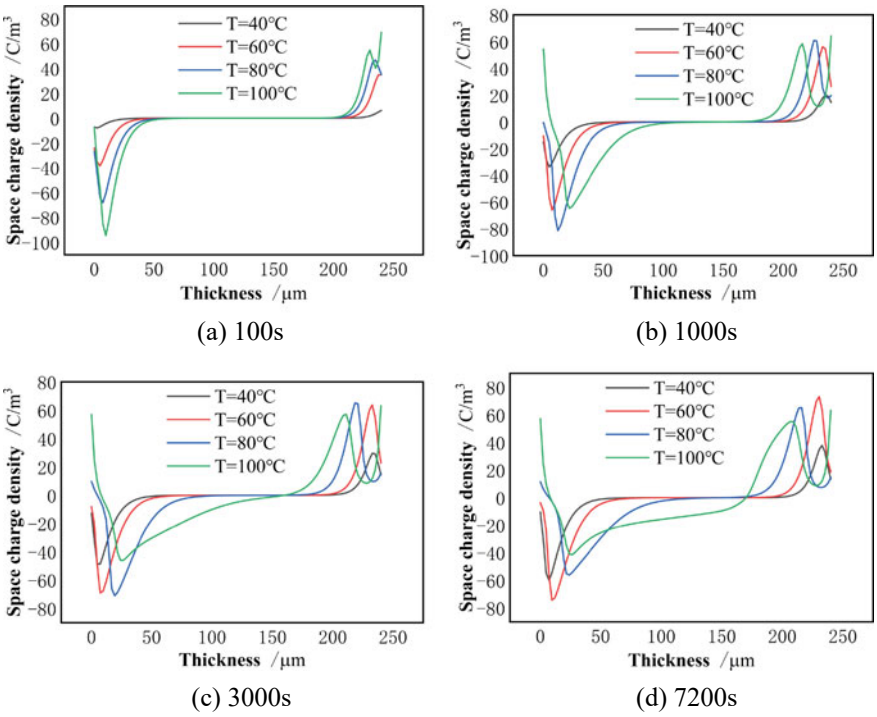

Fig. 4 Space charge distribution at the same time and at different temperatures under 40 kV/mm electric field

the two electrodes. In addition, the charge accumulation near the anode is always less than the cathode at the early stage of pressurization.

To further understand the transport process of different carriers in the medium, Fig. 5 shows four carrier distributions at different times at 80 °C.

At 100 s, the injection of free holes/electrons is obvious, but the number of carriers transported to their opposite sides is limited. The cathode free electron injection barrier is small, although it is easy to inject, the capture rate is greater than the free hole, making the overall negative charge accumulation greater than the positive charge. At 1000–3000 s, it can be seen that the contribution of trapped carriers to space charge is the highest. Taking 3000 s as an example, the average density of trapped holes/trapped electrons accounts for 65.19% and 87.2% of the average positive/negative accumulated charge density respectively; 0–8 at 7200 μs. The concentration of trapped holes at m is greater than that of trapped electrons, and the superposition of the two makes the cathode present positive charge accumulation.

For the cathode, when the temperature is $\leq$ 60 °C, a large number of electrons are trapped near the cathode after injection, leading to the accumulation of negative charges. At the same time, the migrated holes accumulate due to limited extraction, and are compounded with negative charges. The accumulation amount near the

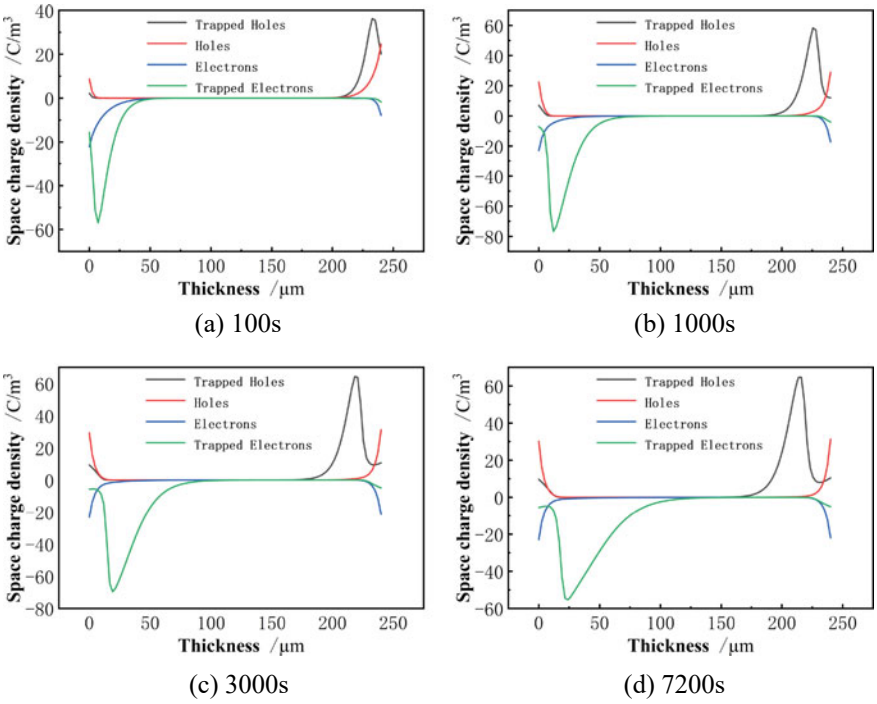

Fig. 5 Carrier distribution at different times at 80 °C

interface is the largest, so the recombination amount is also the largest. Therefore, the charge density close to the cathode interface is smaller than the internal charge density. Then the temperature rise promotes the process of trapping and recombination, which leads to the increase of free charge density (the charge migrated in the shallow trap) and the acceleration of transport rate. When the temperature is $\geq$ 80 °C, because the hole extraction ability is weak, and the injected holes are continuously transported, the hole transport rate is greater than the extraction rate, and a large number of holes accumulate near the cathode to form an accumulation of heteropolar charges. The electron extraction rate near the anode is always greater than the transport rate, maintaining the accumulation of homopolar charges. The electron injection barrier is smaller than the hole, which leads to the injection electron density is greater than the hole, so that the overall electron accumulation is greater than the hole.

3.2 *Electric Field Distribution of Epoxy Materials at High Temperature*

The diffusion degree and accumulation density of the charge at different temperatures are different. The distribution of the charge determines the distribution of the electric field, which reacts on the distribution of the charge. The two depend on each other and together determine the transport process of the space charge. Eq. (7) is the electric field distribution corresponding to the space charge. Figure 6 shows the electric field distribution at different temperatures.

$$E(x) = \frac{1}{\varepsilon_0 \varepsilon_r} \int_{x_0}^{x} \rho(x) \mathrm{d}x \tag{7}$$

When the voltage is applied for 100 s, the electric field distribution trend at different temperatures is basically the same, that is, the electric field distortion near

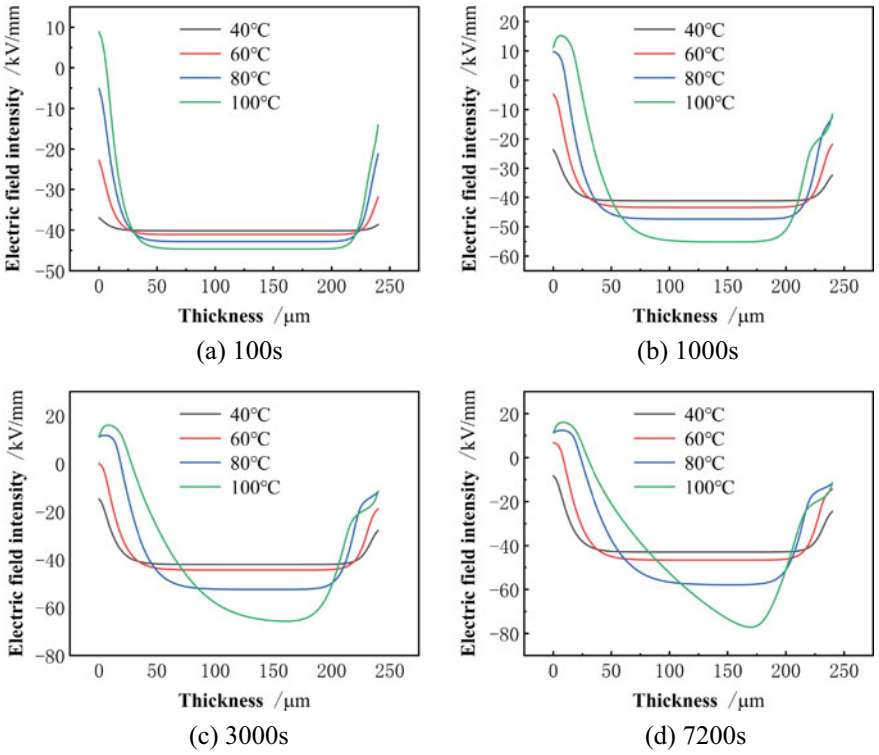

Fig. 6 External applied electric field is 40 kV/mm and internal electric field distribution at different temperatures

the two poles is serious and the distortion degree near the cathode is greater than that near the anode. The electric field in the middle is relatively uniform, indicating that the space charge injection in the sample is not obvious at this time, and the reason for the asymmetric distribution near the two poles is that the negative charge accumulation near the cathode is greater than the positive charge accumulation near the anode. At 1000 s, the distribution of electric field is similar to that at 100 s. The difference is that with the increase of time, the distortion of electric field intensity in the middle is more obvious, indicating that more homopolar charges accumulate in the sample. At 100 °C, the electric field near the cathode shows a short curve of first increasing and then decreasing, which corresponds to the process of positive charges accumulating at the cathode and being covered by negative charges. The transient accumulation of heteropolar charges enhances the edge electric field.

When the pressure is 3000 s, the field strength in the middle of the 80–100°C curve rises significantly, and when the temperature is greater than 80 °C, the place of the maximum electric field moves to the right and is close to the anode, which indicates that the negative charge diffusion is further deepened. The electric field distribution at 7200 s is basically similar to that at 3000 s.

To more intuitively describe the distortion degree of temperature to electric field distribution, it can be expressed by defining distortion factor C_d, which is defined as follows:

$$C_d = \frac{|E_{max} - E_a|}{|E_a|}| \tag{8}$$

where, E_{max} is the maximum electrical field in the model, and E_a is the average electrical field of the voltage.

The electric field distortion factor at different temperatures is plotted according to Eq. (8) as shown in Fig. 7, which shows the electric field distribution at different temperatures. The degree of electric field distortion is measured by the distortion factor. The greater the distortion factor value, the greater the distortion degree of corresponding field intensity.

We can be obtained from Fig. 7 that the electric field distortion at temperature $\leq$ 60 °C is significantly less than that at temperature $\geq$ 80 °C. At 60 °C, the electric field distortion factor at the end of pressurization is only 0.15, while at 80 and 100 °C, the electric field distortion factors reach 0.41 and 0.92 respectively. According to the expression of Schottky injection and jump conductance, high temperature conditions promote the injection and mobility of charges, accelerate the carrier transport rate, lead to the accumulation of heteropolar charges, significantly increase the field strength near the cathode, and finally further increase the degree of electric field distortion.

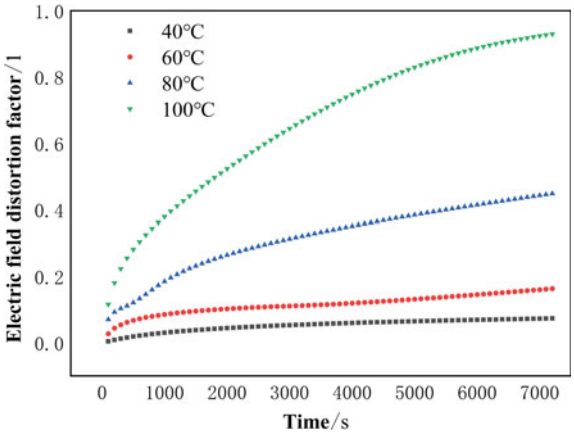

Fig. 7 Electric field distortion factors at different temperatures when the applied electric field is 40 kV/mm

4 Conclusion

In this paper, based on the bipolar charge transport process, and considering the limitation of carrier extraction, the finite element model of epoxy material is constructed in COMSOL, and the space charge numerical simulation under extreme operating conditions is carried out. The electric field distribution features and space charge features of epoxy material under high temperature conditions are obtained. The main research work is summarized as follows:

(1) The finite element model of electrostatic field coupled with material transfer field is constructed, and the relevant model parameters are modified.
(2) It is found that the diffusion depth of positive and negative charges is increasing and the area with zero charge density is gradually shrinking under the long-term action and temperature rise. When the temperature of the cathode is ≤ 60 °C, the charge density at the interface is less than the internal charge density, and when the temperature is ≥ 80 °C, the heteropolar charge accumulation is formed near the cathode.
(3) The contribution of trapped carriers to space charge is the highest at the later stage of pressurization. The degree of electric field distortion at temperature ≤ 60 °C is significantly less than that at temperature ≥ 80 °C. This is because the high temperature conditions promote the increase of charge injection and mobility, which accelerates the carrier transport rate. However, carrier extraction is limited leads to the accumulation of heteropolar charges, which greatly increases the field strength near the cathode, and finally shows that the degree of electric field distortion is further aggravated. With the increase of temperature, the maximum electric field moves to the right, and the electric field distortion is obvious when the temperature is ≥ 80 °C.

Acknowledgements This work is supported by the Gansu Provincial Science and Technology Commissioner Special Project (22CX8GA111) and Gansu Provincial Natural Science Foundation of China (21JR7RA237)

References

1. Qang W, Liao J, Tian H et al (2017) Egularity analysis of the temperature distribution of epoxy impregnated paper converter transformer bushings. Dielectr Electr Insul IEEE Trans 24(5):3254–3264
2. Ruijin L, Jiyu W, Yuan Y et al (2016) Review on characteristics of new cellulose insulating paper under converter transformers. Trans China Electrotechnical Soc 31(10):1–15 (in Chinese)
3. Gong J, Li Z, Liu X (2016) Space charge characteristics of alumina/epoxy resin composites and AC electric field aging under high temperature and humidity. Trans China Electrotechnical Soc 31(18):191–198 (in Chinese)
4. Ma Z, Yang L, Bhutta MS et al (2020) Effect of thickness on the space charge behavior and dc breakdown strength of cross-linked polyethylene insulation. IEEE Access 8:85552–85566
5. Li L, Zhang X, Jin H et al (2021) Study on the temperature distribution of composite insulator of UHV-DC line considering solar radiation
6. Li K, Zhang H, Jin H et al (2021) Space charge dynamic characteristics of epoxy material under extreme conditions
7. Morab S, Sundaram MM, Pivrikas A (2022) Time-dependent charge carrier transport with hall effect in organic semiconductors for Langevin and Non-Langevin systems. Nanomaterials 12(24):4414
8. Shao Y, Tu Y, Chen G et al (2021) Simulation of space charge characteristics of epoxy resin under pulse voltage. In: 22nd International symposium on high voltage engineering (ISH 2021). IET, pp 1520–1525
9. Zhong X, Zheng Y, Dang B et al, Polarity effect of polymer space charge distribution under DC electric field. Chin J Electr Eng 36(24):6693–6701 + 6922 (1016) (in Chinese)
10. Tian F, Hou C (2018) A trap regulated space charge suppression model for LDPE based nanocomposites by simulation and experiment. IEEE Trans Dielectr Electr Insul 25(6):2169–2177
11. Zhang H (2019) Study on space charge characteristics of epoxy composites for UHV DC bushings under polarity reversal. Xi'an Jiaotong University (in Chinese)

FEM Analysis of Electric Field Distribution Under Different Material Characteristics in Optical Fiber Insulator

Wenhao Lu, Jiuhui Zhao, Yanjie Cui, Yang Feng, Liang Liu, Shengtao Li, Wei Xiao, and Senlin Zhao

Abstract Optical fiber current transformer (OFCT) is widely used in flexible DC transmission to improve the ability of information perception of power grid, and optical fiber insulator is the key component of OFCT to provide insulation and protection. However, discharges in optical fiber insulator seriously affect the stable operation of the power system. Here, the effect of material characteristics of different parts on the electric field distribution in insulator is explored to figure out the inner discharge mechanism. A ± 400 kV optical fiber insulator 3D simulation model is constructed in COMSOL Multiphysics, and differences in the electric field distribution in the insulator are compared and analyzed by finite element method under different conductivity of materials. The results show that the conductivity of the fiber coating and filling compound significantly affects the electric filed at interfaces in the insulator flange sections. The semiconducting fiber coating results in a mismatched potential into the flange sections at both terminals, which further leads to a remarkable electric field distortion on the inner wall of fiber sheath at the interface between the sheath and coating layer. The maximum electric field at the interface is even up to 84.5 kV/mm. The electric field distortion also occurs at the interface between epoxy

W. Lu · Y. Cui
Electric Power Research Institute, CSG EHV Power Transmission Company, Guangzhou 510663, Guangdong, China

J. Zhao · Y. Feng (✉) · S. Li (✉)
State Key Laboratory of Electrical Insulation and Power Equipment, Xi'an Jiaotong University, Xi'an 710049, Shaanxi, China
e-mail: fengyang@xjtu.edu.cn

S. Li
e-mail: sli@mail.xjtu.edu.cn

L. Liu
NR Electric Power Electronics Co., Ltd., Changzhou 213100, Jiangsu, China

W. Xiao
Electric Power Research Institute, CSG, Guangzhou 510663, Guangdong, China

S. Zhao
Nanjing Nari-Relays Electric Co., Ltd, Nangjing 211122, Jiangsu, China

© Beijing Paike Culture Commu. Co., Ltd. 2024

X. Dong and L. Cai (eds.), *The Proceedings of 2023 4th International Symposium on Insulation and Discharge Computation for Power Equipment (IDCOMPU2023)*, Lecture Notes in Electrical Engineering 1102, https://doi.org/10.1007/978-981-99-7405-4_62

tube and filling compound when the conductivity of the filling compound increases. Therefore, the increases in conductivity of the fiber coating and filling compound leads to electric field distortion at interfaces, which can cause discharges in the optical fiber insulator.

Keywords Finite element simulation · Electric field · Optical fiber insulator · Conductivity

1 Introduction

Flexible high-voltage DC transmission based on modular multilevel converts has a broad application prospect in renewable energy power generation, long-distance power transmission and so on [1–4]. Flexible DC transmission requires higher sampling accuracy, response speed and dynamic range, which makes optical fiber current transformer (OFCT) widely used in various flexible DC transmissions because of its fast response speed and wide measurement range [5, 6].

Kunliulong project is the first ± 800 kV multi-terminal flexible DC transmission project in the whole world [7–10]. However, a large number of optical fiber current transformers failed due to the damage of optical fiber insulators. After carful dissection, it is found that the failure of the optical fiber insulator is derived from the internal discharges, especially at the interfaces between different materials in the metal flanges at high- and low-voltage terminals, which seriously threats the stable operation of the power system.

In order to improve the stability of the OFCT, it is urgent to explore the mechanism of discharges in the optical fiber insulator. In this work, the effect of material characteristics on the electric field distribution in the optical fiber insulator is systematically studied using finite element simulation method. As the conductivities of fiber coating and filling compound change, the fluctuations in the internal electric field distribution characteristics of the insulator are calculated and analyzed. The influence of material conductivity on the electric field distortion is then discussed to figure out the origin of discharges.

2 Methodology

2.1 3D Simulation Model of Optical Fiber Insulator

A ± 400 kV optical fiber insulator is utilized to study the effect of material characteristics on the electric field distribution. The 3D simulation model of the insulator is shown in Fig. 1. The optical fiber insulator is composed of silicone rubber shed, epoxy tube, filling compound and optical fiber unit from outside to inside. The optical fiber

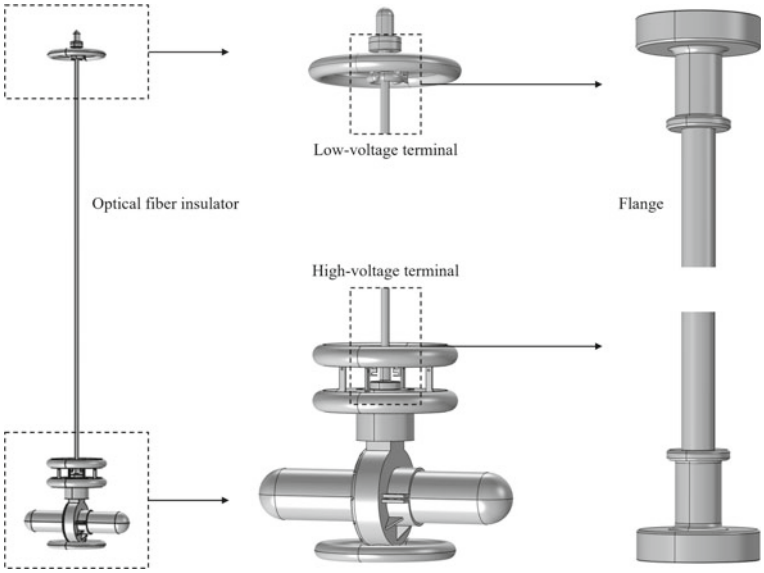

Fig. 1 3D simulation model of the optical fiber insulator

Table 1 Structures and electrical parameters of materials

Structure	Material	Conductivity (S/m)	Permittivity
Flange	Steel	1.00×10^{6}	1.00
Shed	Silicone rubber	3.57×10^{-14}	3.35
Epoxy tube	Epoxy resin	1.30×10^{-13}	4.92
Filling compound	Multicomponent mixture	1.00×10^{-13}	2.08
Optical fiber sheath	ETFE	1.33×10^{-15}	2.48
Coating layer	Semi-conductive coating	1.25×10^{-9}	36
Optical fiber core	Silica glass	1.00×10^{-14}	3.75

unit consists of the fiber sheath, coating layer and fiber core. Materials and electrical parameters of each structure are shown in Table 1. By dissecting the damaged optical fiber insulator, it is found that the discharge occurs in both high- and low-voltage flange terminals. Given that, our work is focused on the above-mentioned positions.

2.2 Calculation Principle

Electric field strength can be calculated from Maxwell's equations. Since the optical fiber insulator is operated under DC voltage, the simplified Maxwell's equations of constant current field are used, which can be expressed as follows,

$$\begin{cases} \nabla \cdot \boldsymbol{J} = Q \\ \boldsymbol{E} = -\nabla V \end{cases} \tag{1}$$

where $\boldsymbol{J}$ is current density vector, Q is quantity of charge, $\boldsymbol{E}$ is electric field strength vector, V is potential.

For isotropic media, the constitutive relations are as follows,

$$\begin{cases} \boldsymbol{J} = \sigma \boldsymbol{E} \\ \boldsymbol{D} = \varepsilon_0 \varepsilon_\mathrm{r} \boldsymbol{E} \end{cases} \tag{2}$$

where σ is conductivity, $\boldsymbol{D}$ is electric displacement vector, ε_0 is dielectric constant of vacuum, ε_r is relative dielectric constant of media.

These quantities must obey the principles followed with boundary conditions. The boundary of the simulation domain is electrically insulating, which can be expressed as follows,

$$\boldsymbol{n} \cdot \boldsymbol{J} = 0 \tag{3}$$

where $\boldsymbol{n}$ is normal vector.

Considering the operating conditions of OFCT, the metal flanges at the high-voltage terminal V_H and at the low-voltage terminal V_L are set to 400 kV and 0 kV, respectively.

$$\begin{cases} V_H = 400\,\mathrm{kV} \\ V_L = 0 \end{cases} \tag{4}$$

The geometric model is divided into free tetrahedral mesh cells for 3D finite element calculation based on the above equations and boundary conditions. The electric field distribution is obtained from electric potential by solving the partial differential equation for the three-dimension domain.

3 Results and Analysis

3.1 Distribution of Potential and Electric Field

Figure 2 shows the potential distribution at the terminals of the optical fiber insulator. It is found that the potentials on the silicone rubber, epoxy tube and filling compound synchronously increase when gradually approaching the high-voltage terminal. In the flange section, all potentials on these materials remain at 400 kV. However, the voltage in the potential distribution graph shows an obvious difference between the coating layer, fiber core and outlet of the fiber. It inevitably leads to a potential gradient on the fiber sheath. Similarly, the potential of the coating layer and fiber

core at the low-voltage terminal in the flange section is higher than that of the outlet parts. It also results in a potential gradient on the fiber sheath in the low-voltage terminal, which further produces a radial electric field strength.

The potentials of the filling compound and coating layer along the axial direction are extracted and shown in Fig. 3. It is found that the electric potentials on the filling compound and the coating layer remain consistent out of the flange sections, while the potential difference between them occurs near and in both flange sections. And the largest potential difference is observed in both flange sections. This is because the semiconducting fiber coating layer exhibits a slower change in potential compared with the insulating filling compound in both flange sections. Therefore, the conductivity of materials in the optical fiber insulator plays an important role in electric potential distribution.

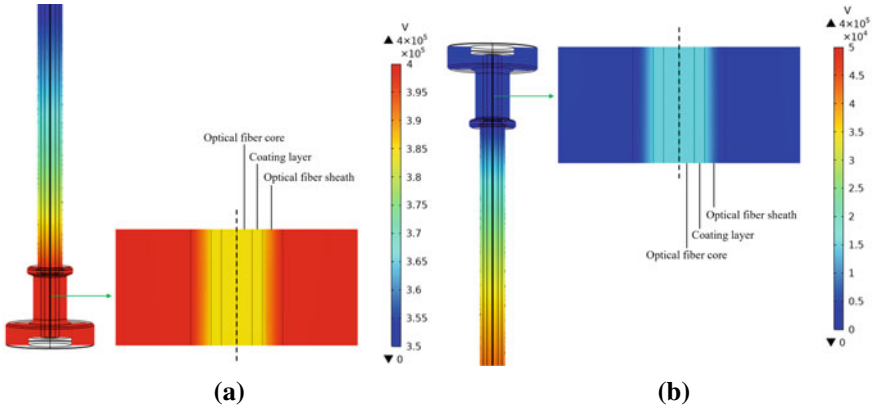

Fig. 2 Potential distribution at **a** high-voltage terminal and **b** low-voltage terminal

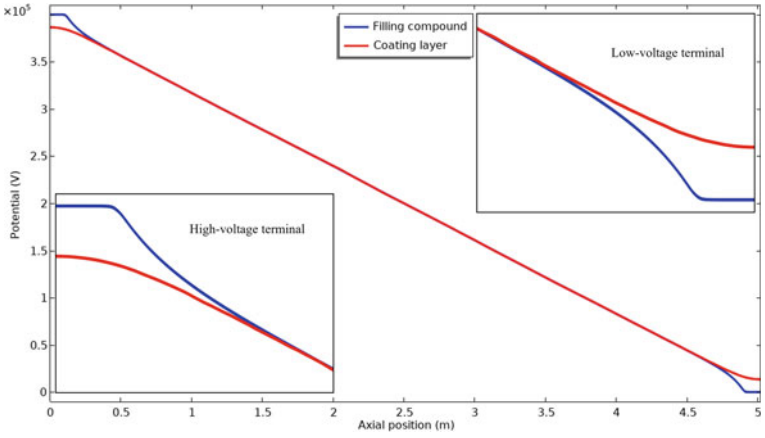

Fig. 3 The distribution of electric potential along the axial direction

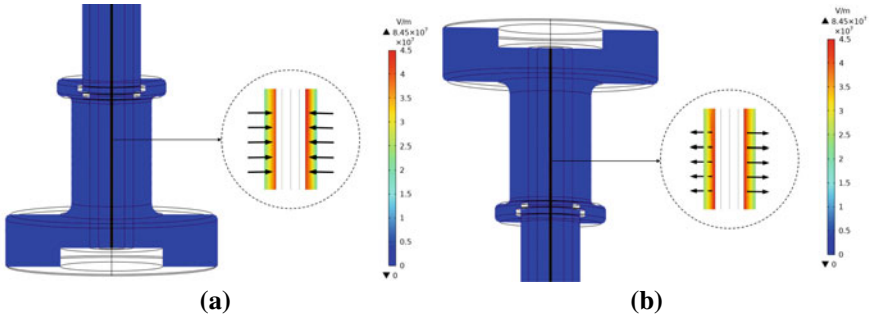

Fig. 4 Electric field distribution at **a** high-voltage terminal and **b** low-voltage terminal

Figure 4 shows the electric field distribution at high- and low-voltage terminals of the optical fiber insulator, respectively. An electric field distortion occurs in the fiber sheath and the highest electric field strength appears on the inner wall of fiber sheath at interfaces between the fiber sheath and coating layer. The direction of the electric field is dependent on terminals, where the electric fields at the high-voltage and low-voltage terminals are inward and outward, respectively. It is consistent with the calculation results of potentials. The maximum electric field strength in the fiber sheath is up to 84.5 kV/mm. It must be considered that the interfaces between the fiber sheath and coating layer should be taken into account as a critical part due to the large difference in conductivity for the fiber sheath and coating layer, where the order of magnitude is larger than 6.

The electric field for each component along the radial direction passing through the axis in the flange section is shown in Fig. 5. It is apparent that the epoxy tube and filling compound are not subjected to any radial electric field. The highest value of the electric field is localized in the fiber sheath, and the maximum value appears at the interface between the fiber sheath and coating layer. The high peak amplitude of the electric field is above 4×10^7 V/m. Therefore, the internal discharge mechanism of the optical fiber insulator can be illustrated. The electric field on the inner wall of the fiber sheath in the metal flange section is much larger than that around it, which is easy to trigger a discharge. Meanwhile, the multicomponent interface also can continuously accumulate space charges under the strong radial DC electric field, which will further promote the discharge. In order to further explore the influence of conductivity characteristics of materials on discharges, the changes in electric field distribution with the conductivity of the fiber coating and filling compound are calculated and analyzed.

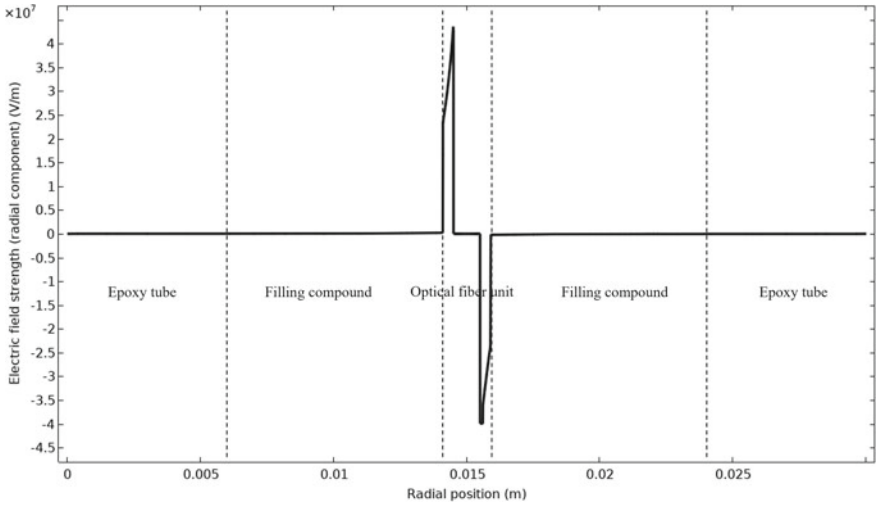

Fig. 5 Distribution of electric field strength along the radial direction

3.2 Variation of Electric Field Distribution with the Conductivity of Coating Layer

Figure 6 exhibits the change in the maximum electric field strength on the fiber sheath with the conductivity of coating layer. The calculation result indicates that the electric field magnitude is strongly dependent on the conductivity of fiber coating layer. When the conductivity ranges from 10^{-14} to 10^{-5} S/m, the maximum electric field strength varies by up to 4 orders of magnitude. The electric field distortion can be ignored when the conductivity is below 10^{-13} S/m. However, the maximum electric field strength sharply enhances as the conductivity increases and the maximum value on the fiber sheath finally reaches a limit value exceeding 1000 kV/mm.

3.3 Variation of Electric Field Distribution with the Conductivity of Filling Compound

Besides the fiber coating layer, the effect of the filling compound on the electric field distribution is also needed to be considered because its conductivity is sensitive to moisture. As expected, an electric field distortion is detected on the inner wall of the epoxy tube at the interfaces between the epoxy tube and filling compound, as shown in Fig. 7a. Figure 7b shows the change in the maximum electric field strength on the epoxy tube with the conductivity of filling compound. The result reveals that the electric field magnitude is also highly related to the conductivity of filling compound. The maximum electric field strength varies by around 3 orders of magnitude in the

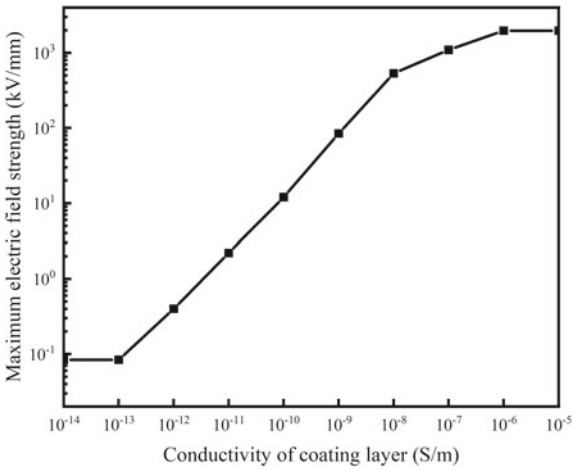

Fig. 6 The maximum electric field strength on the fiber sheath varies with the conductivity of coating layer

range of 10^{-14} to 10^{-6} S/m. The electric field distribution is almost uniform when the conductivity is below 10^{-13} S/m. Nevertheless, the maximum electric field strength significantly increases as the conductivity increases and the maximum value on the epoxy tube eventually reaches a stable value around 100 kV/mm. Therefore, both conductivities of the fiber coating layer and filling compound are important material characteristics on the electric field distribution. Given conductivities of the fiber coating layer and filling compound, it can be concluded that once the conductivity of the filling compound is higher than that of the coating layer, the electric field distortion in the insulator will be transferred from the fiber sheath to the epoxy tube, as illustrated in Fig. 7b.

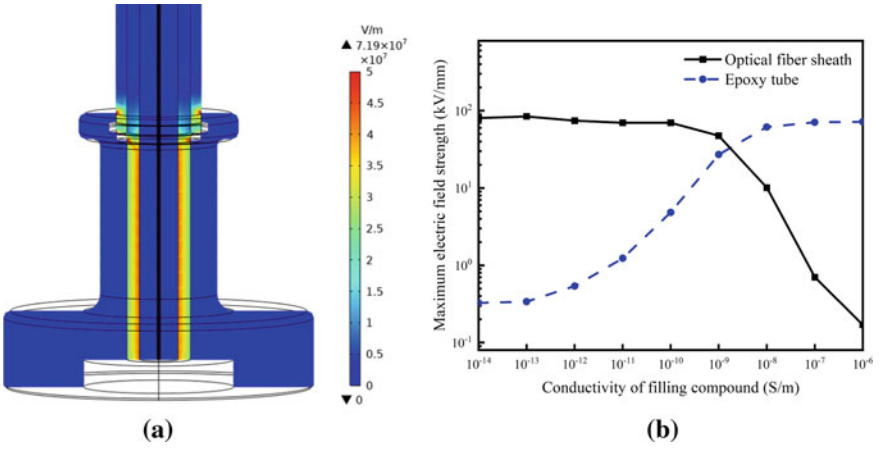

Fig. 7 **a** Electric field distortion on the inner wall of the epoxy tube and **b** the maximum electric field strength on the fiber sheath and the epoxy tube

4 Conclusion

The discharge mechanism of the optical fiber insulator is explored by discussing the effect of material characteristics on the electric field distribution through finite element simulation method. The results show the internal discharge is derived from the obvious electric field distortion at the interfaces between multicomponent in metal flange sections at both high- and low-voltage terminals. The difference in conductivity of internal materials results in mismatched electric potential, which further leads to a radial electric field. Under operating conditions, the electric fields on the inner wall of the fiber sheath and epoxy tube at interfaces can be strongly distorted as the conductivities of fiber coating layer and filling compound increase. Therefore, the conductivity of the materials plays a dominant role in electric field distortion and thus the discharges. It is necessary to keep the conductivity of materials in optical fiber insulators well matched. This work provides a theoretical basis for understanding and preventing the failure of OFCT.

Acknowledgements This work was supported by Electric Power Research Institute, CSG EHV Power Transmission Company, Guangzhou (0120002022030301SJ00028). It was also supported by State Key Laboratory of Electrical Insulation and Power Equipment, Xi'an Jiaotong University.

References

1. Zou C, Wei R, Feng J, Zhou Y (2022) Development status and application prospect of VSC-HVDC. South Power Syst Technol 16(3):1–7
2. Wang C, Chen W, Xu J, Li X, Liu W, Ma J (2022) Analysis of surplus power dissipation strategy of flexible DC transmission system based on energy dissipation resistance. In: 5th International conference on power and energy applications,. IEEE, Guangzhou, China, pp 464–468
3. Wang Q, Huang L, Ying F, Miao Y, Yan J, Liu Y (2021) Topology optimization of offshore DC transmission system based on small signal stability. In: International conference on power system technology. IEEE, Haikou, China, pp 990–994
4. Li Z, Song Q, An F, Zhao B, Yu Z, Zeng R (2021) Review on DC transmission systems for integrating large-scale offshore wind farms. Energy Convers Econ 2(1):1–14
5. Zhao J, Xu S, Wu B, Sun X (2022) Research on the performance of a fiber optical current transformer for high voltage filtering capacitor unbalanced current measurement. J Opt Technol 89(6):353–358
6. Liu C, Zhu X, Su H (2022) Research progress of high sensitivity all fiber optic current sensor. Laser Technology 46(2):175–181
7. Yang X, Zhao Y, Zhang S, Wang Q, Li Q, Chen Z, Liu X, Lu W (2021) Simulation study on inductive characteristics of 800 kV kunliulong DC line. High Voltage Apparatus 57(9):66–71
8. Li J, Zhu B, Guo Y, Liang Z, Wu H, Liu H (2021) The simulation of Kunliulong flexible dc project with single station operation and out of operation. In: Industrial and commercial power system Asia. IEEE, Chengdu, China, pp 1028–1034
9. Shu H, Zhao H, Zhang X, Dong H, Chen N, Bo Z (2021) Reliability analysis of main electrical connection for sending-end converter station in Kunliulong hybrid DC project of China. Autom Electric Power Syst 45(22):115–123

10. Zhou D, Lu Q, Zhou Y, Gu S, Peng W (2021) Multi-terminal DC line fault recovery with fault self-clearing and analysis of converter station online exit strategy. In: 5th Conference on energy internet and energy system integration. IEEE, Taiyuan, China, pp 859–863

Research on Electromagnetic Disturbance Intensity Distribution of Substation Based on Traveling Wave Antenna Theory

Ninghui He, Xutao Wu, Yifan Lang, Zijian Huang, Yaowen Wen, and Yangchun Cheng

Abstract The electromagnetic environment in AIS substations is complex and variable, the operating arc of isolation switch or lightning intrusion wave can generate extremely strong transient electromagnetic harassment, which seriously affects the performance of sensors. Therefore, analyzing the electromagnetic environment of substations is necessary to improve their anti-interference performance and ensure the safe and reliable operation of the power system. Firstly, based on the theory of traveling wave antenna, the theory of electromagnetic wave refraction and reflection, and the superposition principle, a calculation model of electromagnetic field radiated by transient current waves in complex high-voltage networks considering long conductors and metal shells of equipment is established in this paper; Then a typical 110 kV AIS substation model is simulated by the electromagnetic wave simulation software, and the electromagnetic field distribution at the installation location of common transformer equipment live detection and online monitoring sensors in the substation is analyzed under different transient disturbance scenarios. Based on the above research, the electromagnetic compatibility reliability test parameters of sensors have been clarified, and the installation method of sensors has been optimized to improve the anti-electromagnetic interference ability of sensors in the substation.

Keywords Traveling wave antenna theory · Electromagnetic field · Thunder wave · Switching impulse

N. He · X. Wu
Electric Power Research Institute of State Grid Ningxia Electric Power Co., Ltd., Yinchuan 750002, China

Y. Lang · Z. Huang · Y. Wen · Y. Cheng (✉)
Beijing Key Laboratory of High Voltage & EMC, North China Electric Power University, Beijing 102206, China
e-mail: langyf72@163.com

© Beijing Paike Culture Commu. Co., Ltd. 2024

X. Dong and L. Cai (eds.), *The Proceedings of 2023 4th International Symposium on Insulation and Discharge Computation for Power Equipment (IDCOMPU2023)*, Lecture Notes in Electrical Engineering 1102, https://doi.org/10.1007/978-981-99-7405-4_63

1 Introduction

The extremely strong transient electromagnetic interference in substations poses a huge threat to state sensing sensors, especially low-power smart sensors. Taking the electromagnetic interference generated by the action arc of the isolation switch as an example: during the operation of the high-voltage isolation switch, there will be dozens or even hundreds of times of arc extinguishing and burning at the switch fracture. Due to the influence of electromagnetic interference during the switch operation process, the electromagnetic working environment is harsh, and the reliability and anti-interference issues of the protection device become more prominent.

The Electric Power Research Institute of the United States has developed a measurement system for the electromagnetic environment of substations through on-site measurements of multiple substations, and obtained a large amount of electromagnetic steady-state and transient disturbance data inside the substations [1, 2]. Russell et al. [3] provided transient electromagnetic disturbance levels and obtained electromagnetic disturbance waveforms for a large number of AIS and GIS substations with isolation switch operations at 500 kV and below through on-site testing. Rao et al. [4, 5] studied the electromagnetic interference phenomenon during switch operation in GIS, and measured the induced current, voltage, and transient electric and magnetic fields generated by secondary equipment during switch operation in GIS substations with voltage levels of 230 and 500 kV. Zhang et al. [6–9] measured and analyzed the transient electromagnetic interference caused by switch operation in substations. The Electromagnetic Compatibility Laboratory of North China Electric Power University measured and analyzed the electromagnetic interference caused by the switch operation of smart component current transformer ports in 500 kV GIS [10]. Kong et al. [11] studied the transient electric field measurement method for switching operation of DC circuit breakers. Rao et al. [12] measured the power frequency electromagnetic field in 220 and 500 kV substations.

Based on the research mentioned above, this article conducts a theoretical analysis of the propagation of disturbance sources on long wires based on the theory of traveling wave antennas. And the electromagnetic wave refraction and reflection theory was used to explain the shielding effect of transformer and other substation devices on electromagnetic waves. On this basis, the distribution of electromagnetic disturbance intensity in the substation under the action of disconnector operation wave and lightning intrusion wave is analyzed through a typical 110 kV substation model,, and the electromagnetic intensity at the typical location where the sensor is installed is emphatically analyzed. The results obtained can lay a solid foundation for further research on the rational electromagnetic protection design of smart sensing equipment and the development of relevant detection standards.

2 Methods

2.1 Traveling Wave Antenna Theory

When a long wire is terminated with a matching resistor R_L, there are no reflected waves, and the current on the wire is a traveling wave. To simplify the analysis and ignore the influence of the bottom, the radiation of the vertical section of the wire and the attenuation of the current along the line are ignored. The simplified structure and coordinates of the long wire are shown in Fig. 1.

Assuming that the phase constant of the traveling wave propagation along the wire is equal to the phase constant k of the wave in free space, the current along the long wire can be expressed as:

$$I(z) = I_0 e^{-\mathrm{j}kz} \tag{1}$$

According to the superposition principle, the far field of a long wire can be obtained by superposition of the far field of each current element on it. According to the basic principles of microwave science, when $kr >> 1$ or $r >> \lambda$ The far field of the current source I (z) dz at z on the traveling wave length wire is as follows:

$$\mathrm{d}E_\theta = \mathrm{j}\frac{60\pi I_0}{\lambda r} sin\theta e^{-\mathrm{j}kz} e^{-\mathrm{j}k(r - z\cos\theta)} \mathrm{d}z \tag{2}$$

where r is the distance from the source point to the field point at z = 0.

The far-field of a row wavelength wire with a length of l is as follows:

$$\begin{aligned} E_\theta &= \int_0^l \mathrm{d}E_\theta = \mathrm{j}\frac{60\pi I_0}{\lambda r} sin\theta e^{-\mathrm{j}kr} \int_0^l e^{-\mathrm{j}kz(1-\cos\theta)} \mathrm{d}z \\ &= \frac{60 I_0}{r} e^{-\mathrm{j}kr} \frac{sin\theta}{1-\cos\theta} \sin\left[\frac{kl}{2}(1-\cos\theta)\right] e^{-\mathrm{j}\frac{kl}{2}(1-\cos\theta)} \end{aligned} \tag{3}$$

The direction function is as follows:

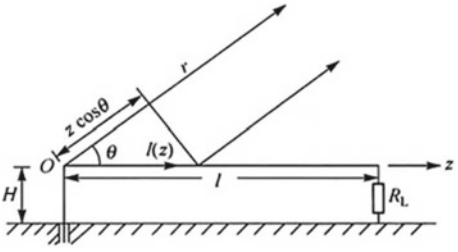

Fig. 1 Schematic diagram of line wavelength wire antenna

$$f(\theta) = \frac{sin\theta}{1-\cos\theta} \sin\left[\frac{kl}{2}(1-\cos\theta)\right] = \cot\frac{\theta}{2} \sin\left[\frac{kl}{2}(1-\cos\theta)\right] \quad (4)$$

2.2 *Theory of Electromagnetic Wave Refraction and Diffraction*

Reflection of electromagnetic waves on the surface of conductors. Electromagnetic waves undergo reflection and refraction at the interface of different media. The incident, reflected, and transmitted waves at the interface are related to the magnetic permeability of materials on both sides of the interface μ and dielectric constant ε. Any point source can be developed as an integral superposition of *TE* type and *TM* type z-direction plane wave spectrum, and the propagation of plane wave in plane layered composite media can be described by reflection coefficient and transmission coefficient. Theoretical analysis has shown that both TE and TM waves will undergo total reflection on the surface of an ideal conductor. Thus, the surface of the transformer oil tank forms a reflection wall for external electromagnetic waves.

Diffraction of electromagnetic waves on the surface of conductors. Diffraction of waves refers to the phenomenon of waves encountering obstacles, bypassing the edges of obstacles and entering geometric shadow areas during propagation. When geometrical optics rays encounter the discontinuity of an object, diffraction will occur. Keller proposed a new method for approximate calculation of high-frequency electromagnetic fields in 1957. He introduced a new diffracted ray to eliminate the discontinuity of the field on the shadow boundary of geometrical optics rays, and properly corrected the field in the shadow area, which is called geometric diffraction theory.

3 Simulation Modeling and Result Analysis

3.1 *Modeling*

A typical 110kV AIS substation was established by electromagnetic field simulation software, which includes the most basic components, such as lightning arresters, isolation switches, circuit breakers, voltage transformers, and transformers. All components are arranged with reference to ordinary AIS substations. The substation model used for simulation calculation is shown in Fig. 2.

Disturbance scenario of isolation switch operation wave. A single-phase (intermediate phase) standard operating wave of 250/2500 μs was applied to the isolation switch on the side away from the transformer. According to the requirements of

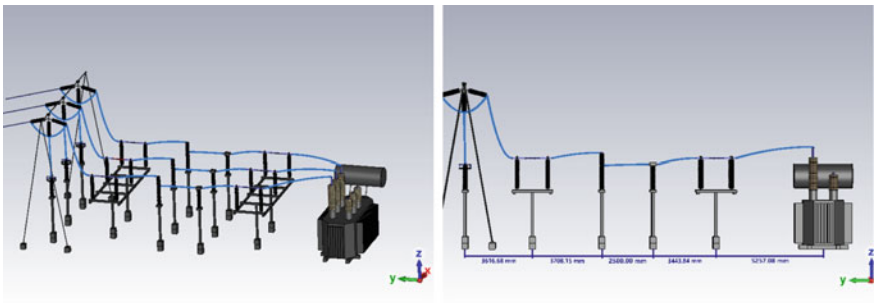

(a) Aerial view of the model. (b) Front view of the model.

Fig. 2 AIS substation model schematic diagram

the Electrical Equipment Manual for Electrical Engineering, the rated current of the isolation switch is around 600–1000 A. Therefore, a current wave with an amplitude of 1000 A is selected as the operating wave to simulate the electromagnetic interference experienced by the substation when the isolation switch operates. The waveform of the disturbance source is shown in Fig. 3.

The operation of isolation switches often accompanies the generation of arcs. In this simulation model, the commonly used arc model is used for the arc resistance. Its expression is as follows:

$$r(t) = R_0 \cdot e^{-t/\tau} + R_1 \tag{5}$$

where $R_0 \cdot e^{-t/\tau}$ is the arc resistance during the initial stage of discharge, R_0 is generally taken as 10^{12} Ω, and τ is generally taken as 1ns. R_1 is the arc resistance during the steady-state arcing stage, usually taken as 2–5 Ω.

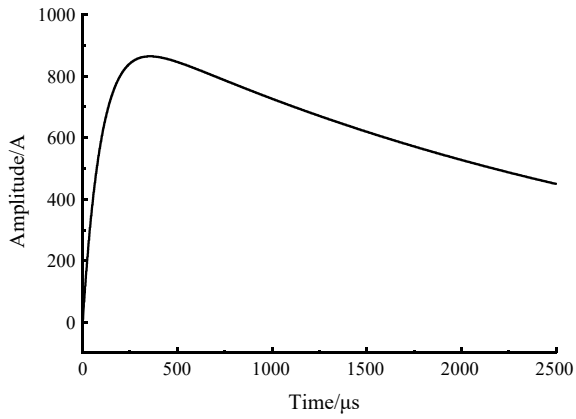

Fig. 3 Waveform of isolation switch operation wave

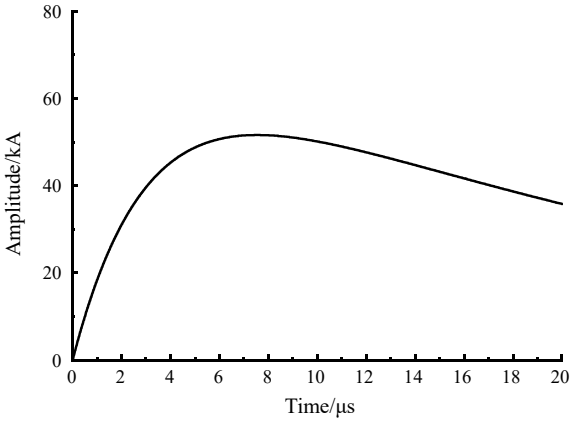

Fig. 4 Waveform of lightning wave

Disturbance scenario of lightning intrusion waves. Apply common lightning current wave 8/20 μs at the incoming line of the substation. The current amplitude value is 80 kA. The waveform of the disturbance source is shown in Fig. 4.

3.2 Propagation of Electromagnetic Waves in Substations Under the Influence of Disturbance Sources

The coupling effect of parallel long wires. When a disturbance source is coupled to a wire, the electromagnetic radiation field generated by the traveling waves on the wire overlaps with the original electromagnetic radiation field, causing changes to the original electromagnetic radiation field. The electromagnetic field at some positions is strengthened by the conduction of traveling waves on long wires. As shown in Fig. 5, the coupling effect of parallel long wires on disturbance sources.

Shielding of electromagnetic radiation by metal enclosures of electrical equipment. According to the analysis above, the metal casing of large electrical equipment such as transformers has a shielding effect. Figure 6 shows the shielding effect of the transformer on the disturbance source.

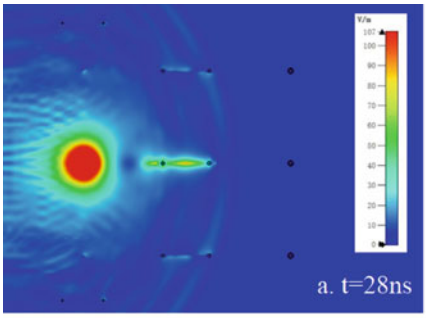

(a) t=28ns.

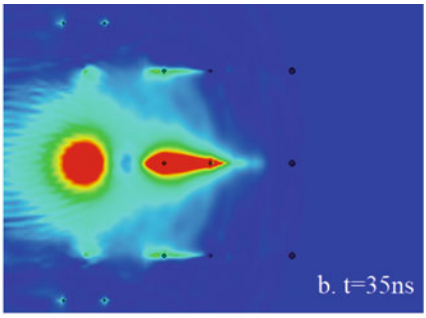

(b) t=35ns.

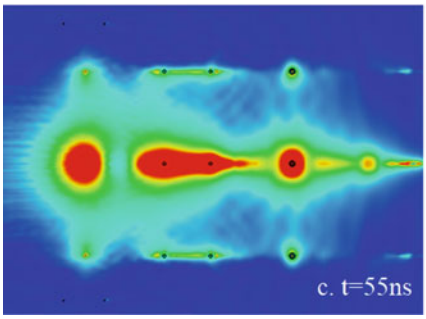

(c) t=55ns.

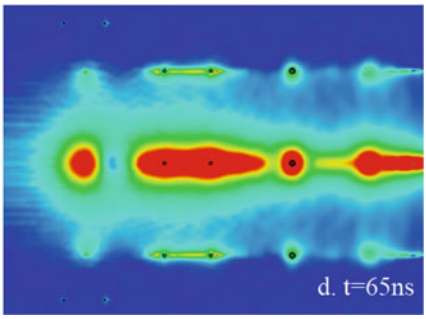

(d) t=65ns.

Fig. 5 Coupling of Parallel Long Wires to Disturbance Sources

3.3 Electromagnetic Disturbance Intensity Distribution

Electromagnetic disturbance intensity at the transformer bushing. In the research of transformer live detection, many sensors are often installed at the transformer bushing, thus it is necessary to analyze the electromagnetic interference intensity at the transformer bushing. Figure 7 shows the electromagnetic disturbance intensity at the transformer bushing.

Electromagnetic disturbance intensity around the transformer. Various detection devices are often installed around transformers, analyzing the electromagnetic interference intensity around transformers can help with the scientific arrangement of detection devices. Figure 8 shows the electromagnetic disturbance intensity around the transformer.

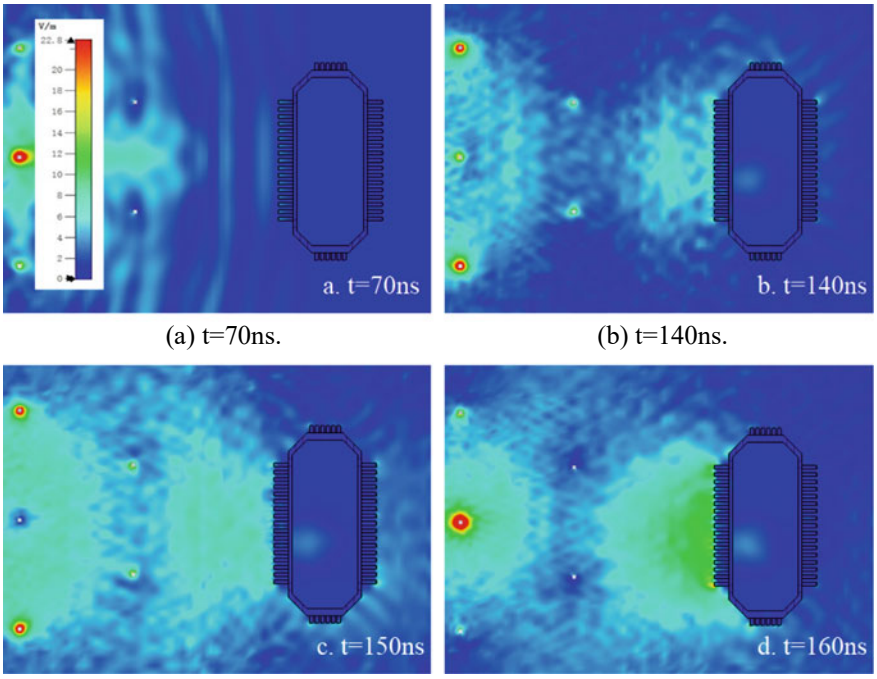

(a) t=70ns. (b) t=140ns.

(c) t=150ns. (d) t=160ns.

Fig. 6 Reflection and diffraction of electromagnetic disturbance by transformer shell

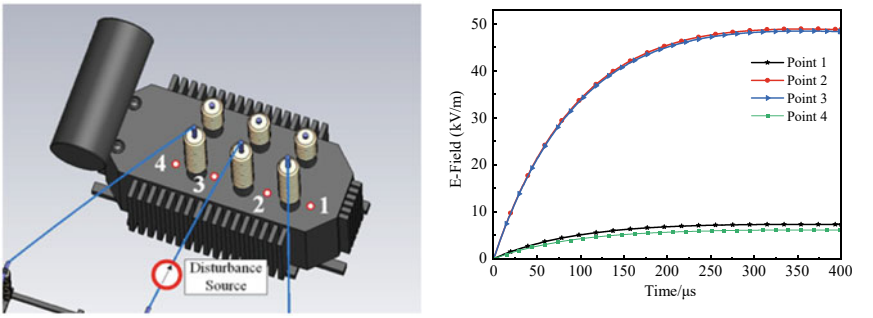

(a) Distribution of measurement points. (b) Distribution of Electric Field Intensity.

Fig. 7 Electromagnetic disturbance intensity at transformer bushing

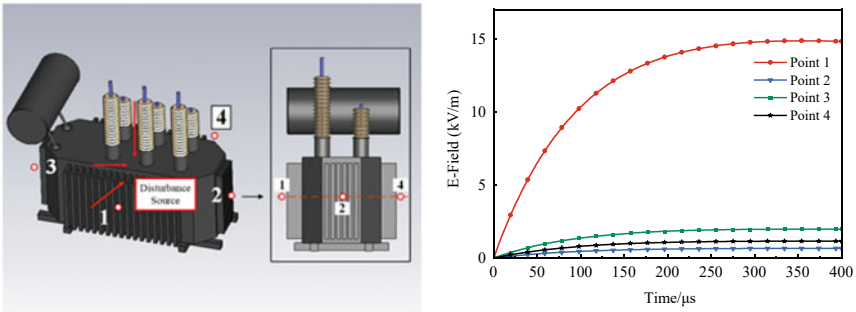

(a) Distribution of measurement points. (b) Distribution of Electric Field Intensity.

Fig. 8 Electromagnetic disturbance intensity around transformer

4 Conclusion

This article explains the propagation mode of transient electromagnetic disturbance sources in substations based on the theory of traveling wave antennas. The shielding effect of the metal shell of electrical equipment on electromagnetic radiation was explained through the reflection theory and diffraction theory of electromagnetic waves. Finally, a typical 110kV substation was established through electromagnetic simulation software. The propagation of transient disturbance source in substation under the action of disconnector operation wave and lightning wave is simulated, and the intensity distribution of electromagnetic disturbance in substation is given on this basis. This article provides a basis for subsequent research on electromagnetic interference protection of sensors in substations and the development of more practical electromagnetic compatibility reliability test parameters for sensors.

Acknowledgements This work is supported by the Ningxia Natural Science Foundation project (2021AAC03498).

References

1. Barrack CS, Siew WH, Pryor BM (1997) The measurement of fast transient electromagnetic interference within power system substations. In: Proceedings of the sixth international conference on developments in power system protection. IET, Nottingham, UK, pp 270–273
2. Wiggins CM, Wright SE (1991) Switching transient fields in substations. IEEE Trans Power Delivery 6(2):591–600
3. Thomas DE, Wiggins CM, Nickel FS et al (1989) Prediction of the electromagnetic field and current transients in power transmission and distribution systems. IEEE Trans Power Delivery 4(1):744–755
4. Rao MM, Thomas MJ, Singh BP (2007) Electromagnetic field emission from gas-to-air bushing in a GIS during switching operations. IEEE Trans Electromagn Compat 2(49):313–321

5. Rao MM, Rao TP, Ram SST et al (2008) Simulation of capacitively graded bushing for very fast transients generated in a GIS during switching operations. J Electrical Eng Technol 3(1):36–42
6. Zhang W (2003) Research on switching transient electromagnetic interference in substations. North China Electric Power University (in Chinese)
7. Li Q, Zhang W, Yang Z et al (2022) Analysis of the coupling characteristics of the spatial electromagnetic field of the substation on the cable of the power IOT sink node. South Power Syst Technol 16(07):92–100 (in Chinese)
8. Wang P, Zhang W, Yang Z et al (2022) Analysis of coupling mechanism of space electromagnetic field to wireless communication unit in substation. J North China Electric Power University (Natural Science Edition), 49(02):97–105 (in Chinese)
9. Fu S (2022) Research on spatial electromagnetic field distribution characteristics of switching operation in GIS substation. North China Electric Power University (in Chinese)
10. Liu X, Cui X, Wu F et al (2015) Measurement and analysis on electromagnetic disturbance of intelligent electronic device current transformer ports due to switching operations in a 500 kV Gas Insulated Substation. High Voltage Eng 41(05):1709–1718 (in Chinese))
11. Kong XX, Li Y, Liu L et al (2023) Transient electric field caused by the operation of the MMC and HVDC CB and its application in the condition monitoring. In: Proceedings of the CSEE, (2023-05-05), pp 1–12 (in Chinese)
12. Rao Z, Guo Q, Quan D et al (2004) Measurement of power frequency electric & magnetic field in 500 kV substation. High Voltage Eng 09:41–43 (in Chinese)

Numerical Calculation of Circulation Current in High Voltage Submarine Cable Grounded with Segmented Interconnection

Xi Qin, Wenjun Zhou, Ming Lü, Zhongjiang Chen, Lifeng Qiu, Chunshen Wang, and Shiyou Yang

Abstract In the operation of a single-core submarine cable, an alternating current in the cable will generate an alternating electromagnetic field, which results in induction voltages in the metal sheath and steel armor of the cable. When the metal sheaths and steel armors of the submarine cables are grounded at both ends with several connection points in the middle, the metal sheaths and steel armors will generate circulation currents, which will yield Joule losses, influencing the thermal safety of the cables. Consequently, it is essential to study the circulation current in high voltage submarine cables. In this point of view, an equivalent circuit model of the circulation current of the sheath and the armor is first established, and the circuit parameters in a typical laying condition are then calculated by using finite element method. The circulation currents for a case study are calculated. The numerical results show that the induced circulation current in the steel armor is apparently larger than that in the metal sheath, and both are proportional to the value of core current.

Keywords Submarine cable · Metal sheath · Steel armor · Circulation current · Inductance parameters

1 Introduction

With the rapid development of the economy in the coastal areas, the demand for submarine cables in engineering continues to increase [1–4]. Crosslinked polyethylene power cables have the advantages of low cost, safety and convenience, and take

X. Qin · W. Zhou · M. Lü · Z. Chen · L. Qiu
Zhejiang Huayun Electric Power Engineering Design & Consultation Co., Ltd, Hangzhou 310014, China

C. Wang (✉) · S. Yang
College of Electrical Engineering, Zhejiang University, Hangzhou 310027, China
e-mail: foreseer@qq.com

© Beijing Paike Culture Commu. Co., Ltd. 2024

X. Dong and L. Cai (eds.), *The Proceedings of 2023 4th International Symposium on Insulation and Discharge Computation for Power Equipment (IDCOMPU2023)*, Lecture Notes in Electrical Engineering 1102, https://doi.org/10.1007/978-981-99-7405-4_64

an increasingly important position in ocean power transmissions and transformations [3]. Generally, distinguished from overland power cables, it is necessary to install a metal armor layer on the submarine cables in order to ensure the mechanical strength of the cable. As the alternating current in the core conductor of a single core submarine cable will generate alternating electromagnetic fields around the cable, induced voltages will occur in the metal sheath and armor layer of the submarine cable. And a circulation current will be induced in the metal sheath and armor layer of the submarine cable under the condition that the metal sheath, armor layer, and the earth constitute a closed loop.

However, this special laying environment makes it impossible to use the cross-connected grounding for the metal sheath and sheath of the submarine cable [5]. Therefore, there are three common grounding modes for submarine cable in engineering applications. The first one is that the two ends are connected to each other and the middle is never short connected, that is, the metal sheaths and armor layers at both ends of the submarine cable are connected and grounded directly. The second one is the interconnected grounding at both ends and the short connection at the middle segment, that is, the metal sheaths and sheaths at both ends of the submarine cable are interconnected, and at the middle of the submarine cable, the metal sheaths and sheaths are connected in segments to achieve multi-point grounding, which is often used when the tolerance level of the outer insulation sheath of the submarine cable is lower than the induction voltage of the metal sheath. The third one is to connect the two ends to the ground and to use semi-conductive sheath, that is, to replace the insulation between the metal sheath and the sheath of the submarine cable with semi-conductive sheath while the metal sheath and the sheath at both ends of the submarine cable are interconnected [4]. Under the three common grounding modes of submarine cables mentioned above, large circulation currents will be induced on the metal sheaths and sheaths of submarine cables [6]. The circulation current not only produces enormous Joule loss, increases the temperature of submarine cables, accelerates the aging of submarine cables insulation, but also reduces the ampacity of a submarine cable [7–9]. Consequently, accurate calculation of the circulation currents of metal sheath and sheath of single-core submarine cable has vital theoretical significance and engineering application value.

In this point of view, this paper establishes the equivalent circuit model for the circulation current of the metal sheath and armor layer in a single-core submarine cable with interconnected grounding at both ends and short grounding at middle-interrogation and subsection. The calculation of inductance parameters of submarine cable is also discussed according to the theory of electromagnetic field. The submarine cable circulation under different load currents is simulated. The results of this study provide some theoretical guidance for the design and operation of submarine cable grounding.

2 Equivalent Circuit Model for Circulation Currents in a Submarine Cable

When the tolerance level of the outer insulation layer of the submarine cable is lower than the induction voltage of the metal sheath, the two-end grounding and interconnection of the middle segment are often used. The equivalent circuit of circulation currents is shown in Fig. 1 [4]. While the metal sheaths and steel armors at both ends of the submarine cable are interconnected, at the middle of the submarine cable, the metal sheaths and steel armors are connected in three sections. Therefore, Fig. 1 can be seen as three identical equivalent circuits connected, each of which consists of six circuits.

In Fig. 1, in the i th($i = 1, 2, 3$, the same hereinafter) equivalent circuit: $\dot{I}_{sji}$ and $\dot{I}_{aji}$ are the j th($j = 1,2,3$, the same hereinafter) phase metal sheath current and the armor current respectively; $\dot{U}_{sji}$ and $\dot{U}_{aji}$ are the j th phase metal sheath induced voltage and the armor induced voltage produced by the three-phase core conductor current respectively; $\dot{U}\prime_{sji}$ is the induced voltage produced by the current of the other two phases metal sheathes on the j th phase metal sheath; $\dot{U}\prime_{aji}$ is the j th phase armor induced voltage produced by three-phase metal sheath current; $\dot{U}''_{sji}$ is the j th phase sheath induced voltage produced by three-phase armor current; $\dot{U}''_{aji}$ is the induced voltage produced by the current of the other two phases armors on the j th phase armor; $Z_{sji} = R_{sji} + jX_{sji}$, $Z_{aji} = R_{aji} + jX_{aji}$ are the self-impedance of the j th phase metal sheath and armor; R_d and R_e are geodetic equivalent resistance and the grounding resistance of submarine cables, respectively.

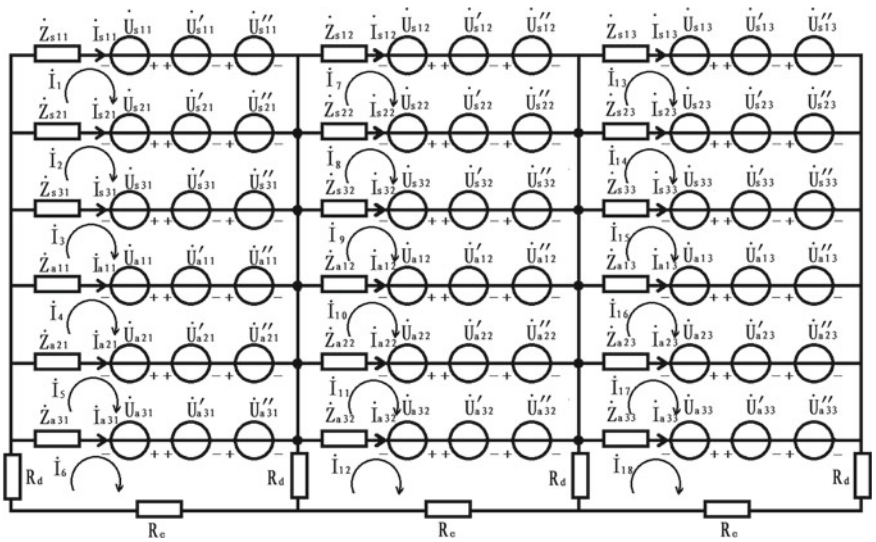

Fig. 1 Equivalent circuit for circulating current calculation in the mode of interconnected grounding at both ends and short grounding at the middle section

It is readily to derive the equations for the 18 circuits of Fig. 1 from electric circuit theory. For example, the equation set of the six circuits in the first component of the whole circuits is:

$$\begin{cases} \dot{U}_{s11} + \dot{U}'_{s21} + \dot{U}''_{s21} + \left(\dot{I}_2 - \dot{I}_1\right)(R_{s21} + jX_{s21}) = \\ \quad \dot{I}_1(R_{s11} + jX_{s11}) + \dot{U}'_{s11} + \dot{U}''_{s11} + \dot{U}_{s21} \\ \dot{U}_{s21} + \dot{U}'_{s31} + \dot{U}''_{s31} + \left(\dot{I}_3 - \dot{I}_2\right)(R_{s31} + jX_{s31}) = \\ \quad (I_2 - I_1)(R_{s21} + jX_{s21}) + \dot{U}'_{s21} + \dot{U}''_{s21} + \dot{U}_{s31} \\ \dot{U}_{s31} + \dot{U}'_{a11} + \dot{U}''_{a11} + \left(I_4 - \dot{I}_3\right)(R_{a11} + jX_{a11}) = \\ \quad \left(I_3 - \dot{I}_2\right)(R_{s31} + jX_{s31}) + \dot{U}'_{s31} + \dot{U}''_{s31} + \dot{U}_{a11} \end{cases} \tag{1}$$

$$\begin{cases} \dot{U}_{a11} + \dot{U}'_{a21} + \dot{U}''_{a21} + (I_5 - I_4)(R_{a21} + jX_{a21}) = \\ \quad (I_4 - I_3)(R_{a11} + jX_{a11}) + \dot{U}'_{a11} + \dot{U}''_{a11} + \dot{U}_{a21} \\ \dot{U}_{a21} + \dot{U}'_{a31} + \dot{U}''_{a31} + \left(I_6 - \dot{I}_5\right)(R_{a31} + jX_{a31}) = \\ \quad (I_5 - I_4)(R_{a21} + jX_{a21}) + \dot{U}'_{a21} + \dot{U}''_{a21} + \dot{U}_{a31} \\ \dot{U}_{a31} = (I_6 - I_5)(R_{a31} + jX_{a31}) + \dot{U}'_{a31} + \dot{U}''_{a31} + \\ \quad \left(I_6 - \dot{I}_{12}\right)R_d + I_6(R_d + R_e) \end{cases} \quad \text{(Continued 1)}$$

For the i th equivalent circuit in Fig. 1, the induced voltages of the three-phase line current generated on the metal sheath and armor layer of the submarine cable are:

$$\begin{cases} \dot{U}_{s1i} = -j\omega L_i\left(M_{c1-s1}\dot{I}_{c1} + M_{c2-s1}\dot{I}_{c2} + M_{c3-s1}\dot{I}_{c3}\right) \\ \dot{U}_{s2i} = -j\omega L_i\left(M_{c1-s2}\dot{I}_{c1} + M_{c2-s2}\dot{I}_{c2} + M_{c3-s2}\dot{I}_{c3}\right) \\ \dot{U}_{s3i} = -j\omega L_i\left(M_{c1-s3}\dot{I}_{c1} + M_{c2-s3}\dot{I}_{c2} + M_{c3-s3}\dot{I}_{c3}\right) \end{cases} \tag{2}$$

$$\begin{cases} \dot{U}_{a1i} = -j\omega L_i\left(M_{c1-a1}\dot{I}_{c1} + M_{c2-a1}\dot{I}_{c2} + M_{c3-a1}\dot{I}_{c3}\right) \\ \dot{U}_{a2i} = -j\omega L_i\left(M_{c1-a2}\dot{I}_{c1} + M_{c2-a2}\dot{I}_{c2} + M_{c3-a2}\dot{I}_{c3}\right) \\ \dot{U}_{s3i} = -j\omega L_i\left(M_{c1-a3}\dot{I}_{c1} + M_{c2-a3}\dot{I}_{c2} + M_{c3-a3}\dot{I}_{c3}\right) \end{cases} \tag{3}$$

where, $\dot{I}_{cj}$ is the core current of the j th phase submarine cable; L_i is the length of the equivalent circuit section of the ith submarine cable; M_{c1-a1}, M_{c2-a1}, M_{c3-a1} are the mutual inductance of unit length between the core conductor of each phase and the phase A armor layer of the submarine cable and the earth return; The same is for M_{c1-a2}, M_{c2-a2}, M_{c3-a2}, M_{c1-a3}, M_{c2-a3}, M_{c3-a3}; M_{c1-s1}, M_{c2-s1}, M_{c3-s1} are the mutual inductance of unit length between the core of each phase and the phase A metal sheath of the submarine cable and the earth circulation; The same is for M_{c1-s2}, M_{c2-s2}, M_{c3-s2}, M_{c1-s3}, M_{c2-s3}, M_{c3-s3}.

For the i th equivalent circuit in Fig. 1, the induced voltage generated by the current of the other two-phase metal sheaths on the metal sheaths and armor layers of submarine cables is:

$$\begin{cases} U'_{s1i} = -j\omega L_i\left(M_{s1-s2}\dot{I}_{s2i} + M_{s1-s3}\dot{I}_{s3i}\right) \\ U'_{s2i} = -j\omega L_i\left(M_{s1-s2}\dot{I}_{s1i} + M_{s2-s3}\dot{I}_{s3i}\right) \\ U'_{s3i} = -j\omega L_i\left(M_{s1-s3}\dot{I}_{s1i} + M_{s2-s3}\dot{I}_{s2i}\right) \end{cases} \tag{4}$$

$$\begin{cases} \dot{U}'_{a1i} = -j\omega L_i\left(M_{s1-a1}\dot{I}_{s1i} + M_{s2-a1}\dot{I}_{s2i} + M_{s3-a1}\dot{I}_{s3i}\right) \\ \dot{U}'_{a2i} = -j\omega L_i\left(M_{s1-a2}\dot{I}_{s1i} + M_{s2-a2}\dot{I}_{s2i} + M_{s3-a2}\dot{I}_{s3i}\right) \\ \dot{U}'_{a3i} = -j\omega L_i\left(M_{s1-a3}\dot{I}_{s1i} + M_{s2-a3}\dot{I}_{s2i} + M_{s3-a3}\dot{I}_{s3i}\right) \end{cases} \tag{5}$$

where, M_{s1-s2}, M_{s2-s3}, M_{s1-s3} are the mutual inductance of unit length between A-phase and B-phase, B-phase and C-phase, A-phase and C-phase submarine cable metal sheath and the earth return; M_{s1-a1}, M_{s2-a1}, M_{s3-a1} are the mutual inductance of unit length between the metal sheath of each phase submarine cable and the earth return to the armor layer of the A phase submarine cable; the same is for M_{s1-a2}, M_{s2-a2}, M_{s3-a2}, M_{s1-a3}, M_{s2-a3}, M_{s3-a3}.

For the first equivalent circuit in Fig. 1, the induced voltage generated by the armor current of three phases on the metal sheath and the armor layer of the submarine cable is:

$$\begin{cases} \dot{U}''_{s1i} = -j\omega L_i\left(M_{s1-a1}\dot{I}_{a1i} + M_{s1-a2}\dot{I}_{a2i} + M_{s1-a3}\dot{I}_{a3i}\right) \\ \dot{U}''_{s2i} = -j\omega L_i\left(M_{s2-a1}\dot{I}_{a1i} + M_{s2-a2}\dot{I}_{a2i} + M_{s2-a3}\dot{I}_{a3i}\right) \\ \dot{U}''_{s3i} = -j\omega L_i\left(M_{s3-a1}\dot{I}_{a1i} + M_{s3-a2}\dot{I}_{a2i} + M_{s3-a3}\dot{I}_{a3i}\right) \end{cases} \tag{6}$$

$$\begin{cases} \dot{U}''_{a1i} = -j\omega L_i\left(M_{a1-a2}\dot{I}_{a2i} + M_{a1-a3}\dot{I}_{a3i}\right) \\ \dot{U}''_{a2i} = -j\omega L_i\left(M_{a1-a2}\dot{I}_{a1i} + M_{a2-a3}\dot{I}_{a3i}\right) \\ \dot{U}''_{a3i} = -j\omega L_i\left(M_{a1-a3}\dot{I}_{a1i} + M_{a2-a3}\dot{I}_{a2i}\right) \end{cases} \tag{7}$$

where, M_{a1-a2}, M_{a2-a3}, M_{a1-a3} are the mutual inductance of unit length between A-phase and B-phase, B-phase and C-phase, A-phase and C-phase submarine cable armor layer and the earth return.

From Eqs. (1) to (7), the currents can be solved, and the circulation ones on the metal sheaths and sheaths of submarine cables are obtained.

To determine the parameters of the previous circuit model, the finite element method is used. For example, the mutual inductance, M_{ij}, of coil i and coil j are computed using

$$M_{ij} = \frac{2W_{ij}}{I_i I_j} = \frac{\iiint_V \mathbf{B}_i \cdot \mathbf{H}_j dV}{I_i I_j} \tag{8}$$

where, $\boldsymbol{B}_i$ is the magnetic flux density produced by current I_i of coil i, $\boldsymbol{H}_j$ is the magnetic strength of the magnetic field produced by current I_j of coil j.

In this paper, the magnetic field is calculated by the finite element method.

3 Numerical Examples

A three-phase single-core 110 kV submarine cable is selected as a case study. The parameters of three-phase single-core 110 kV submarine cable are listed in Table 1 [3].

3.1 Inductance Calculation

A two-dimensional solid model is developed for electromagnetic field computations, including three-phase submarine cable and reference conductor (earth). The diagram of the calculation model of the three-phase submarine cables is shown in Fig. 2. To calculate the mutual inductance and self-inductance of three-phase submarine cable, the core, metal sheath and armor of three-phase submarine cable are set as excitations, and the reference conductor (earth) is set as reference ground. Based on these conditions, the mutual inductance of the unit length between the three-phase metal sheath of the submarine cable and the earth circuit, the mutual inductance of unit length between the three-phase armor and the earth circuit, the mutual inductance of unit length between the three-phase core and the earth circuit to the metal sheath and the earth circuit, the mutual inductance of unit length between the three-phase core and the earth circuit to the armor and the earth circuit, and the mutual inductance of unit length between the three-phase core and the earth circuit to three-phase metal sheath and earth circuit mutual inductance to unit length of armor and earth circuit, three-phase metal sheath and earth circuit unit length self-inductance, three-phase armor and earth circuit unit length self-inductance are calculated, as given in Table 2.

Table 1 Parameters of three-phase single core 110 kV submarine cable

Component	Material	External diameter/mm
Conductor	Copper	37.5
Shielding layer of conductor	Semiconducting layer	40.9
Insulating layer	XLPE	72.9
Shielding layer of insulator	Semiconducting layer	75.3
Water blocking layer	Semiconducting layer	77.3
Metal sheath	Lead	83.3
Inner sheath	Polyethylene	92.3
Optical cable protection layer	Polyethylene	104.3
Optical cable protection cushion	Buffer tape	106.3
Armor layer	Copper	118.3
Outer layer	Polypropylene	127.3

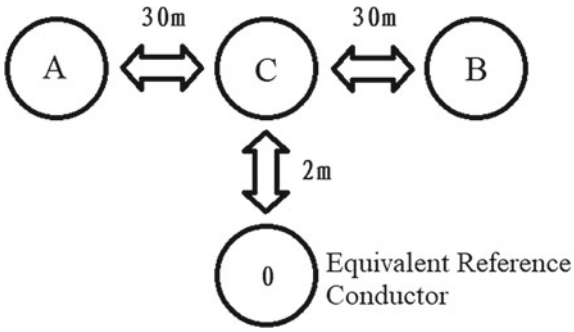

Fig. 2 Schematic diagram of solid model of three-phase submarine cable

Table 2 Inductance parameters of the equivalent circuit

M_{ij}/μH	$i = c1$	$i = c2$	$i = c3$	$i = s1$	$i = s1$	$i = s3$	$i = a1$	$i = a2$	$i = a3$
$j = c1$	2.479	0.740	1.147	2.482	0.740	1.147	2.482	0.740	1.147
$j = c2$	0.740	1.401	0.740	0.740	1.404	0.740	0.740	1.404	0.740
$j = c3$	1.147	0.740	2.482	1.147	0.740	2.485	1.147	0.740	2.485
$j = s1$	2.482	0.740	1.147	2.532	0.740	1.147	2.535	0.740	1.147
$j = s2$	0.740	1.404	0.740	0.740	1.455	0.740	0.740	1.457	0.740
$j = s3$	1.147	0.740	2.485	1.147	0.740	2.536	1.147	0.740	2.538
$j = a1$	2.482	0.740	1.147	2.535	0.740	1.147	2.738	0.740	1.147
$j = a2$	0.740	1.404	0.740	0.740	1.457	0.740	0.740	1.660	0.740
$j = a3$	1.147	0.740	2.485	1.147	0.740	2.538	1.147	0.740	2.742

3.2 Circulation Currents Under Different Load Currents

For the three-phase single-core submarine cable system with interconnected grounding at both ends and short connection at each section, the total length of the submarine cable segment is 10 km. The three-phase core current of submarine cable is balanced, and the effective value of core current is denoted by I_L. According to the previous model and method, the metal sheath and sheath circulation currents of submarine cable under different load currents are calculated.

Since $\dot{I}_{sj1}$, $\dot{I}_{sj2}$ and $\dot{I}_{sj3}$, $\dot{I}_{aj1}$, $\dot{I}_{aj2}$ and $\dot{I}_{aj3}$ are approximately equal in size, this means that $\dot{I}_{sj}$ of $\dot{I}_{sj1}$, $\dot{I}_{sj2}$ and $\dot{I}_{sj3}$ and $\dot{I}_{aj}$ of $\dot{I}_{aj1}$, $\dot{I}_{aj2}$ and $\dot{I}_{aj3}$ are used to represent the metal sheath and armor circulation current of submarine cables, respectively. The numerical results of metal sheath circulation current, induced loss and armor circulation current, induced loss corresponding to the three-phase submarine cable system are shown in Tables 3 and 4, respectively.

From Tables 2 and 3, it can be seen that in a three-phase single core submarine cable system with interconnected grounding at both ends and short connection in the middle section, the metal sheath and armor layer of the three-phase submarine cable have a large circulation current. At the same time, when the core current increases, the

Table 3 Circulation currents and induced loss of three-phase metal sheath of submarine cable

I_L/A	I_{s1}/A	Induced loss of sheath A/(W/m)	I_{s2}/A	Induced loss of sheath B/(W/m)	I_{s3}/A	Induced loss of sheath C/(W/m)
200	18.172	0.0608	18.205	0.0611	18.161	0.0608
400	36.343	0.2433	36.411	0.2442	36.323	0.2430
600	54.515	0.5475	54.616	0.5495	54.484	0.5468
800	72.687	0.9733	72.822	0.9768	72.646	0.9721
1000	90.858	1.5208	91.027	1.5263	90.807	1.5189

Table 4 Circulation current and induced loss of three-phase armor layer of submarine cable

I_L/A	I_{a1}/A	Induced loss of armor A/(W/m)	I_{a2}/A	Induced loss of armor B/(W/m)	I_{a3}/A	Induced loss of armor C/(W/m)
200	18.172	0.0608	18.205	0.0611	18.161	0.0608
400	36.343	0.2433	36.411	0.2442	36.323	0.2430
600	54.515	0.5475	54.616	0.5495	54.484	0.5468
800	72.687	0.9733	72.822	0.9768	72.646	0.9721
1000	90.858	1.5208	91.027	1.5263	90.807	1.5189

circulation current of the metal sheath and armor layer increases, and the circulation current of the metal sheath and armor layer changes in a positive proportion to the core current.

4 Conclusions

In order to study the magnitude and distribution of circulating current in the metal sheath and armor layer of submarine cables under different load currents, an equivalent circuit model of circulating currents in the metal sheath and armor layer of the cable is established for a three-phase single core submarine cable system with interconnected grounding at both ends and short connection in the middle section, and the calculation of model parameters is discussed. On this basis, the numerical analysis and calculation of the circulating current in the metal sheath and armor layer of a typical submarine cable under different load currents have been conducted, providing a reference for the grounding of submarine cables in engineering.

References

1. Shao S, Ma X, Feng R et al (2020) Review of researches on submarine cables at home and abroad. South Power Syst Technol 14(11):81–88 (in Chinese)

2. Huang X, Lei Z, Mei R et al (2022) Influence of high voltage AC single-core submarine cable grounding circuit resistance matching on metal sheath current distribution characteristics. Wire Cable 2022(10):42–47, 62 (in Chinese)
3. Zhang C et al (2017) Influence of grounding mode of 110 kV submarine cable on carrying capacity and circulation. Guangdong Electric Power 8:122–127 (in Chinese)
4. Liu Y, Xiao Y, Su Y et al (2018) Loss calculation and influence on ampacity of single-core AC submarine cable under different grounding modes. High Voltage Apparatus 54(10):56–62 (in Chinese)
5. Yu Y (2017) Analysis and treatment of circulation problems of 110kV submarine crosslinking cables. Electronic Test 2017(19):96–97, 108 (in Chinese)
6. Wang E, Zhang X, Liu H et al (2021) Research on submarine cable structure optimization based on the influence of sheath and armor circulation distribution on current carrying capacity. Power Syst Clean Energy 37(3):92–98 (in Chinese)
7. Xiong L, Chen Y, Jiao Y et al (2019) Study on the effect of cable group laying mode on temperature field distribution and cable ampacity. Energies 12(17):3397
8. Huang F, Li J (2017) Optimization research on ampacity of underground high voltage cable based on interior point method. IOP conference series-materials science and engineering, Changsha
9. Li L, Yong J, Xu W (2020) Single-sheath bonding—a new method to bond/ground cable sheaths. IEEE Trans Power Delivery 35(2):1065–1068

Short Circuit Electromagnetic Force Analysis of 500 kV Autotransformer Based on Field-Circuit Coupling

Zishi Yang, Chuang Liu, Qingjun Peng, Lilan Liu, Jianwei Cheng, Hang Yuan, Qingyu Wang, and Peng Liu

Abstract As transformer capacity and voltage levels continue to rise, the short-circuit resistance of transformers has become an important factor affecting the stability of the power grid. When a short-circuit fault occurs, the interaction of short-circuit current and leakage magnetic field will generate large electromagnetic forces in the winding, which will lead to winding deformation or even cause the transformer to withdraw from operation. Therefore, it is crucial to calibrate and analyze the short-circuit electromagnetic force of the winding. Currently, the short-circuit electromagnetic force is mainly studied using the traditional finite element analysis method. Combining the field-circuit coupling method with the traditional finite element method can more accurately simulate the circuit state during a short-circuit

Q. Peng
Electric Power Research Institute of CSG Yunnan Power Grid Corporation, Kunming 650032, Yunnan, China
e-mail: 13648716143@139.com

Z. Yang · C. Liu · L. Liu · H. Yuan (✉) · Q. Wang · P. Liu
State Key Laboratory of Electrical Insulated and Power Equipment, Xi'an Jiaotong University, Xi'an 710049, Shaanxi, China
e-mail: 675172784@qq.com

Z. Yang
e-mail: Yangzishi@stu.xjtu.edu.cn

C. Liu
e-mail: jackliu-7@qq.com

L. Liu
e-mail: lll2010041003@stu.xjtu.edu.cn

Q. Wang
e-mail: wqy.1991624@xjtu.edu.cn

P. Liu
e-mail: pengliu@mail.xjtu.edu.cn

J. Cheng
Electric Power Research Institute of CSG, Guangzhou 510063, Guangdong, China
e-mail: chengjw@csg.cn

© Beijing Paike Culture Commu. Co., Ltd. 2024

X. Dong and L. Cai (eds.), *The Proceedings of 2023 4th International Symposium on Insulation and Discharge Computation for Power Equipment (IDCOMPU2023)*, Lecture Notes in Electrical Engineering 1102, https://doi.org/10.1007/978-981-99-7405-4_65

fault and thus obtain a more accurate leakage magnetic field distribution. In this paper, the leakage magnetic field distribution of a 500 kV autotransformer is simulated and analyzed based on the field-circuit coupling method, and the short-circuit electromagnetic force distribution is obtained. At the same time, the case of axial offset of the winding is considered, and the effect of the offset on the short-circuit electromagnetic force distribution is compared and analyzed.

Keywords Autotransformer · Field-circuit coupling · Short circuit electromagnetic force · Finite elements method

1 Introduction

In recent years, with the gradual increase of the power grid and the continuous increase in voltage levels, external short-circuit shocks have become serious problems of power transformers [1, 2]. With the rise in system capacity and individual transformer capacity, the operation of transformers has become even more severe. A short-circuit current produces high magnetic field, resulting in high short-circuit electromagnetic force. If the transformer lacks sufficient ability of short-circuit resistance, this short-circuit force will destroy the winding, causing severe deformation of the coil and even causing the transformer as a whole to withdraw from operation, thus causing serious effects on the power system [3–5]. Therefore, for power companies, an accurate assessment of the short-circuit resistance of transformers is important for the healthy management of transformers and the stability of the power grid. The multi-physics simulation can simulate the leakage magnetic field and the forces on the winding under a variety of short-circuit fault conditions, thus effectively reducing the failure rate of the transformer and improving the stability of the equipment.

Li Debo et al. [6] analyze the structural force and pressure-acoustic fields of transformers based on multi-physics field simulations and obtains noise spectral profiles. In reference [7], the transformer winding deformation after a short-circuit fault was analyzed based on the finite element method, considering the non-linear elastic properties of the pre-stress and shims. In reference [8], two-dimensional axisymmetric modeling of the transformer winding based on magnetic-structural coupling was carried out to analyze the elastic–plastic deformation of the winding. In reference [9], a combination of flexural analysis methods considering initial defects and finite element methods was used to investigate the auxiliary instability of transformer windings with multiple short circuits. In reference [10], the field-circuit coupling method was combined with a three-dimensional finite element simulation method to obtain the leakage magnetic field distribution and current distribution patterns of a phase-shifted rectifier transformer. In reference [11], the transient waveforms of winding currents after the short-circuit faults were obtained using the field-path coupling method. Most of the existing studies use traditional finite element methods to simulate the physical field of windings under short-circuit, and relatively few studies consider the field-circuit coupling method. The basic principle of the field-circuit

coupling method is to simulate multiple physical fields inside the model and connect them with circuit parameters outside. Compared to traditional finite element methods, the field-circuit coupling method can simulate the actual fault situation more accurately, calculating the leakage magnetic field by electromagnetic induction and thus obtaining the time-domain distribution of the current.

Under the same capacity and voltage level, autotransformers are relatively smaller in size and require less material than independently wound transformers, and the losses of transformers are greatly reduced, easy to transport and install, and operate more efficiently [12, 13]. Due to the above-mentioned advantages, autotransformers are widely used in voltage classes of 500 kV and above. Due to the direct electrical connection between the primary and secondary sides of autotransformers, the short-circuit electromagnetic force on the winding of autotransformers are greater than those on independently wound transformers under the same short-circuit fault conditions. However, there are few simulation studies on the electromagnetic force of autotransformers, so it is essential to carry out relevant research. The field-circuit coupling method facilitates the intuitive connection between electricity and magnetism and has unique advantages in the analysis of autotransformers.

In this paper, the field-circuit coupling model is combined with the finite element multi-physics field simulation method to obtain the leakage magnetic field of a 500 kV autotransformer under a short-circuit fault and to analyze the short-circuit electromagnetic force distribution of the medium-voltage and high-voltage windings. The effect of winding offset on the leakage magnetic field distribution of the transformer and the winding force is also compared by considering the case of axial offset of the winding relative to the center position.

2 Simulation Model of the Transformer

2.1 Geometry Model

The actual structure of the transformer is complex, containing a core, winding, pad, brace, structural parts, oil tank, etc. Regarding the characteristics of short-circuit conditions, the following assumptions are declared in the analysis of the magnetic field. The eddy current demagnetizing effect of the wire and skin effect is not considered, the current density within the wire cake is considered to be uniformly distributed, and the winding copper wire conductivity is constant. The influence of the core puller, clamp, etc. on the leakage flux distribution in the oil tank is not considered. The geometry of the simulation model of the autotransformer is shown in Fig. 1.

In this paper, a 500 kV autotransformer is simulated and modeled. According to the actual magnetic circuit characteristics of this transformer, a two-dimensional axisymmetric finite element analysis can basically reflect the actual leakage field. The main parameters of the autotransformer are shown in Table 1.

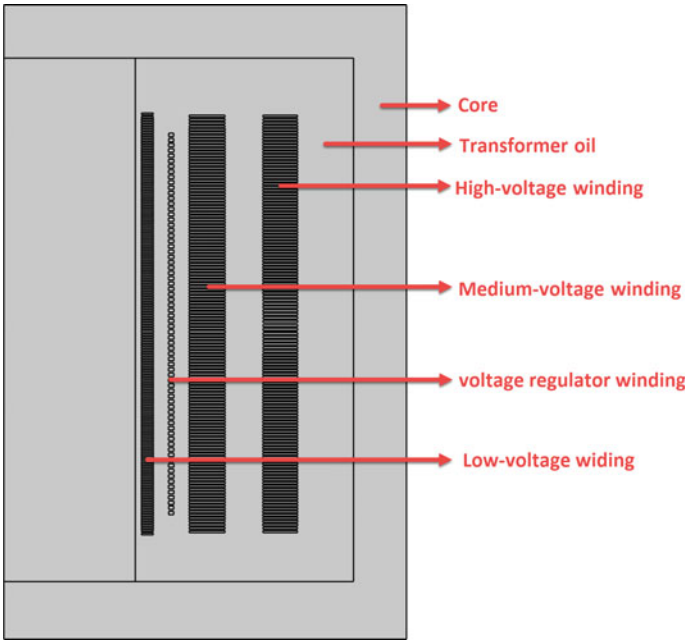

Fig. 1 Simulation model of an autotransformer

Table 1 Main parameters of a 500 kV autotransformer

Parameters	Low-voltage winding	Voltage regulator winding	Medium-voltage winding	High-voltage winding
Rated capacity/MVA	80	/	334	334
Rated voltage/kV	40.5	/	252	550
Number of turns	81	32	312	367
Inner radius/mm	649	778	875	1223
Outer radius/mm	704	800	1043	1385

2.2 The Field-Circuit Coupling Model

The "field-circuit coupling" method refers to the method in which the transformer is solved by finite element modeling inside the transformer and treated as a circuit element outside, which is connected to an equivalent closed circuit according to the respective circuit parameters. This method facilitates the solution of the electromagnetic field problem in case of a short circuit on one side of the winding and the simulation of the transient process with the help of an applied voltage source. When creating the transformer short-circuit model, a node of the line cake ground in the field is used as the node of the equivalent circuit to complete the circuit to achieve

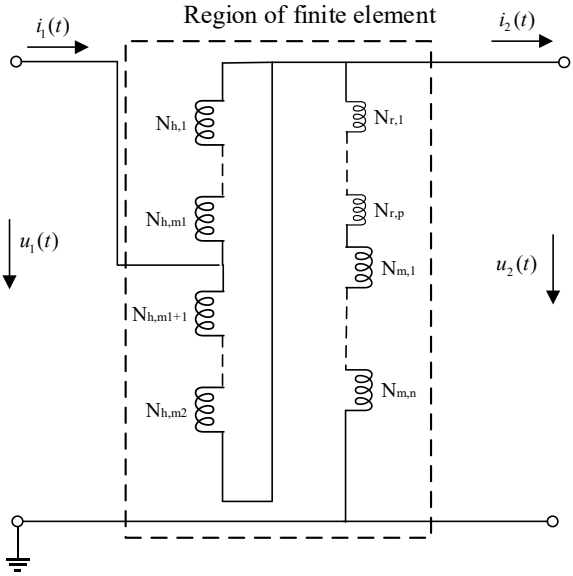

Fig. 2 Schematic diagram of field-circuit coupling model

coupling, while the line cake elements are connected in series with the supply voltage and load resistance to form an equivalent closed circuit. The schematic diagram of the field-circuit coupling for autotransformer high-mid operation is shown in Fig. 2. In the figure, $N_{h,1}$,…, $N_{h,m1}$,…,$N_{h,m2}$ are the number of turns per pie for the high voltage winding, $N_{m,1}$, $N_{m,2}$,…, $N_{m,n}$ are the number of turns per pie for the medium voltage winding, $N_{r,1}$, $N_{r,2}$,…, $N_{r,p}$ are the number of turns per pie for the regulating winding, where the HV winding is connected to the circuit in parallel.

3 Analysis of Leakage Magnetic Field and Electromagnetic Force

3.1 Distribution of Leakage Magnetic Field

In this paper, the transformer leakage magnetic field distribution at the peak moment of the current is obtained based on the field-circuit coupling method and the finite element method for a three-phase symmetric short-circuit failure during the high-medium operation mode of the transformer, as shown in Fig. 3. From the figure, the magnetic flux of the transformer is concentrated between the HV and MV windings with a peak value of 2.03 T, which is due to the opposite direction of transformer HV winding and MV winding currents during the high-medium operation mode, and the magnetic field is superimposed and enhanced at the location between the windings. From the magnetic line distribution, most of the magnetic lines are distributed in

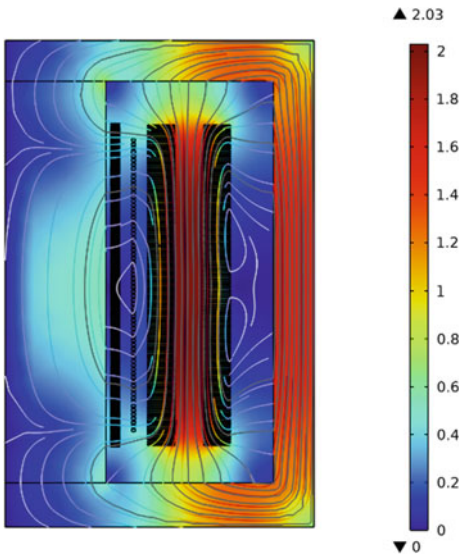

Fig. 3 Leakage magnetic field distribution of windings

the axial direction between the HVand MV windings, forming the axial magnetic density.

3.2 Distribution of Axial Electromagnetic Force

According to the magnetic field distribution, the axial short-circuit electromagnetic force distribution of the HV winding and the MV winding is calculated, as shown in Fig. 4. The axial force distributions of the HV and MV windings have similar trends, with the end of the winding subjected to a larger axial force, while the middle part is subjected to an axial electromagnetic force close to 0. This is due to the fact that the radial leakage magnetic density component shows a trend of high at both ends and low in the middle, and the axial force is determined by the distribution of the radial magnetic field.

3.3 Distribution of Radial Electromagnetic Force

The distribution of the radial electromagnetic force in the MV winding and the HV winding is shown in Fig. 5. The distribution of the radial force in the MV winding and the HV winding has a similar trend, but in the opposite direction. This is due to the fact that according to the principle of Lorentz force, in the case of opposite currents flowing through the MV and HV windings, the inner MV winding is

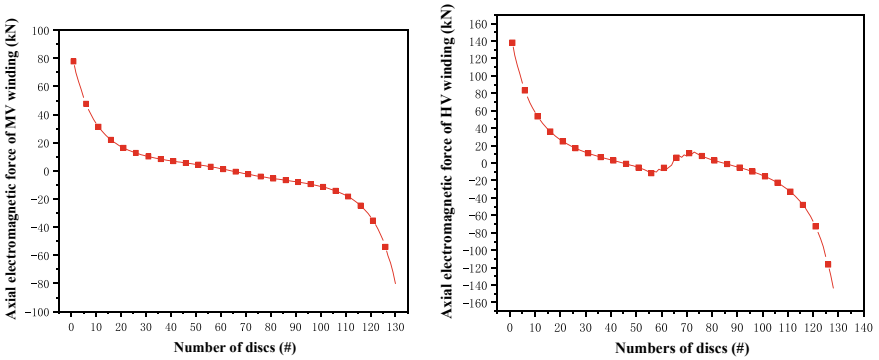

(a) MV winding (b) HV winding

Fig. 4 Distribution of axial electromagnetic force of MV winding and HV winding

influenced by the inward radiation electromagnetic force while the outer HV winding is influenced by the outward radiation electromagnetic force. For both windings, the radial electromagnetic force component in the middle of the winding is significantly larger than that in the end of the winding, because the axial component of the magnetic field determines the magnitude of the radial electromagnetic force. In the middle of the winding, most of the magnetic lines are distributed in the axial direction, and the axial component of the magnetic field is large; while at the end of the winding, the magnetic lines are shifted, and the radial component gradually increases, which leads to an increase in the amplitude of the radial force.

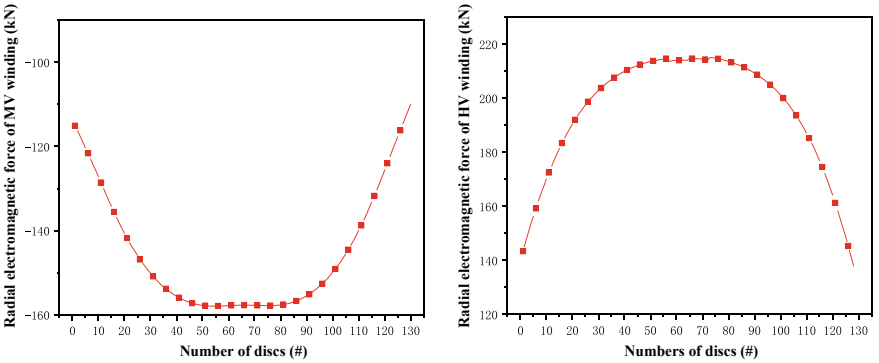

(a) MV winding (b) HV winding

Fig. 5 Distribution of radial electromagnetic force of MV winding and HV winding

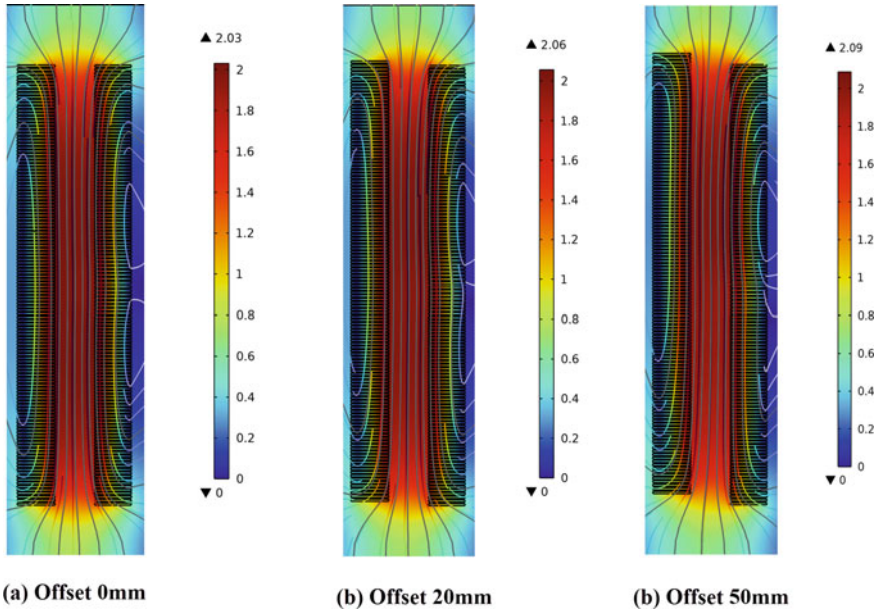

Fig. 6 Distribution of leakage magnetic field during winding excursions

4 Analysis of Leakage Magnetic Field and Electromagnetic Force During Winding Excursions

4.1 Distribution of Leakage Magnetic Field

Due to the uncertainties in the transformer manufacturing and assembly process, the transformer windings may experience offset relative to the center position, which may lead to significant changes in the electromagnetic force. In this paper, we consider the case where the MV winding is offset in the axial direction and analyze the leakage magnetic field, as shown in Fig. 6. Relative to the peak leakage field, the winding offset does not change the magnetic field distribution much, and the peak leakage field increases by about 0.06 T for an axial offset of 50 mm in the MV winding. But due to the change in the relative position of the winding, the electromagnetic force will change accordingly.

4.2 Distribution of Axial Electromagnetic Force

In this paper, simulation analysis is performed for a total of six cases where the medium-voltage winding is offset in the axially forward direction, and the winding

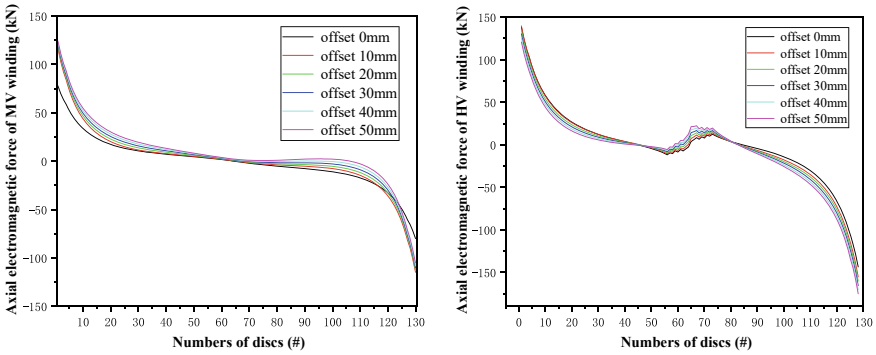

(a) MV winding (b) HV winding

Fig. 7 Distribution of axial electromagnetic force of MV and HV windings during excursions

offset is between 0 and 50 mm, as shown in Fig. 7. From the figures, it can be seen that for the end of the MV winding, the absolute value of the axial electromagnetic force increases after the offset occurs, which indicates that the force at the end of the winding is enhanced in the original direction. For the middle part of the MV winding, the axial electromagnetic force undergoes an overall small shift relative to the zero point as the offset increases due to its axial offset relative to the center position. The force in the middle of the HV winding is similar to that of the MV winding, and the axial electromagnetic force on the edge of the high-voltage winding decreases with increasing winding offset, but the change is relatively small.

4.3 Distribution of Radial Electromagnetic Force

The distribution of the radial force on the MV winding and the HV winding in the case of winding offset is shown in Fig. 8. The force of both after the occurrence of winding offset has changed significantly. For the medium-voltage winding and the HV winding, the absolute value of the electromagnetic force in the lower part of the winding decreases as the offset increases, while the absolute value of the electromagnetic force in the upper part of the winding increases. This is due to the change in the axial magnetic field caused by the offset of the MV winding, which leads to the imbalance of the forces in different parts of the winding.

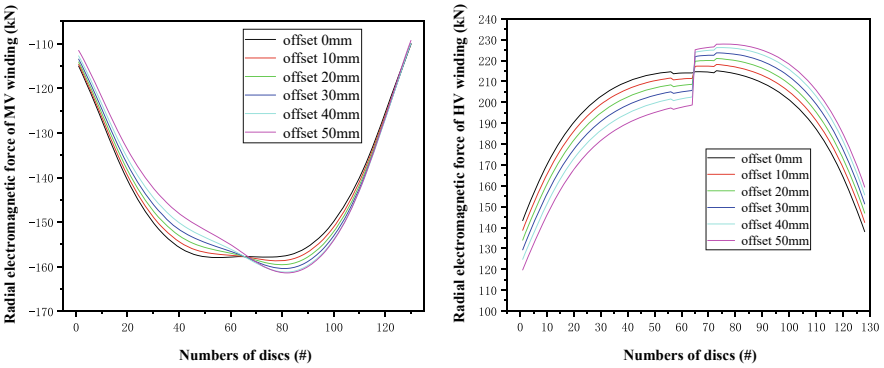

(a) MV winding (b) HV winding

Fig. 8 Distribution of radial electromagnetic force of high voltage winding during excursions

5 Conclusions

In this paper, based on the combination of field-path coupling and finite element method, a multi-physics field simulation is carried out for a 500 kV autotransformer to obtain the leakage magnetic field distribution during a short-circuit failure, and the electromagnetic force distribution of the winding is analyzed and calculated, and the electromagnetic force simulation is also carried out for the fault case of axial excursions of the MV winding, and the following conclusions are obtained.

(a) In the case of autotransformer high-mid operation and short circuit on the medium-voltage side, the leakage flux is mainly concentrated in the channel between the medium-voltage winding and the high-voltage winding with a peak value of 2.03 T. The axial short-circuit electromagnetic force of the MV winding and the HV winding shows a trend of high at the end and low at the middle, and has symmetry. The radial electromagnetic force of MV winding and HV winding tends to be low at the end and high at the middle, and the direction of the radial electromagnetic force of the two windings is opposite.

(b) After the axial offset of medium voltage winding, the change of the leakage field is relatively small, about 0.06T. With the increase of offset, the axial electromagnetic force in the middle of MV winding and HV winding has a small offset relative to the zero point, while the absolute value of axial electromagnetic force at the end of MV winding increases and the absolute value of radial electromagnetic force at the end of high voltage winding decreases. After the offset of the winding, the radial electromagnetic force of both MV winding and HV winding shows a trend of decreasing axial electromagnetic force at the lower part of the winding and increasing axial electromagnetic force at the upper part of the winding.

Acknowledgements This work was supported by the Science and Technology Project of CSG YNKJXM2021008.

References

1. Ge M et al (2019) Fault diagnosis of large capacity transformer after short line short circuit current surge. High Voltage Apparatus 55(5):62–68 (in Chinese)
2. Zhang B, Zhang F, Yao H (2020) Analysis and counter measure of transformer fault caused by continuous near zone short circuit. Transformer 57(6):81–84 (in Chinese)
3. Zhou X et al (2022) Comparative analysis of short circuit mechanical characteristics of transformer winding under different models. High Voltage Apparatus 58(01):148–154 (in Chinese)
4. Luo XX et al (2021) Research on short-circuit force of transformer winding with single-phase short-circuit and three-phase short-circuit. In: 11th international conference on power and energy systems (ICPES) 2021, pp 219–223
5. Oria C, Ortiz A, Ferreno D, Carrascal I, Fernandez I (2019) State-of-the-art review on the performance of cellulosic dielectric materials in power transformers: mechanical response and ageing. IEEE Trans Dielectr Electr Insul 26(3):939–954
6. Li DB, Li BY, Liu YY et al (2017) Multi-physics coupling analysis of power transformer vibration and noise. Guangdong Electric Power 30(06):115–119 (in Chinese)
7. Zhang HJ et al (2014) Dynamic deformation analysis of power transformer windings in Short-Circuit fault by FEM. IEEE Trans Appl Supercond 24(3):1–4
8. Wang X, Zhao ZG (2019) Research on elastoplastic deformation of transformer windings based on magnetic structure coupling field. Transformer 56(2):51–53 (in Chinese)
9. Zhang B, Li Y (2017) Radial instability of large transformer windings under multiple shock conditions. Trans China Electro-technical Soc 32(2):71–76 (in Chinese)
10. Zheng HB, Zhai JQ, Li Z et al (2016) Evaluation of radial short circuit withstand capability of inner windings of large power transformers. Power Syst Prot Control 44(22):154–158 (in Chinese)
11. Zhang JJ, Liu LR, Liu DS et al (2015) Method of simulating partial short circuit fault current of transformer coil with field circuit coupling. Trans China Electrotechnical Soc 30(20):65–70 (in Chinese)
12. Zhang Y et al (2018) A new nonlinear model of three-winding autotransformer. Power Syst Prot Control 46(23):45–51 (in Chinese)
13. Bruzzese C, Ruggeri E, Tcodori S, Zito D, Santini E (2016) Electromagnetic design and thermal analysis of phase shift autotransformers. In: International symposium on power electronics, electrical drives, automation and motion (SPEEDAM), pp 458–463

Simulation Study on Electric Field Characteristics of Spacer Under DC Superimposed Impulse Voltage

Zuodong Liang, Weijian Zhuang, Fangwei Liang, Xianhao Fan, Chuanyang Li, and Jinliang He

Abstract In HVDC GIL systems, the superimposed impulse voltage on the existing DC operating voltage poses a serious threat to electrical insulation. While the influence of DC superimposed impulse voltage has been widely studied through experimental methods, simulation studies have received comparatively little attention. In this paper, a multi-physics model is built to analyze the electric field characteristics of spacers under DC superimposed impulse voltage and investigates the influence of geometrical parameters on electric field distribution. Results indicate that a smaller ratio of inner diameter of enclosure to inner diameter of conductor and a larger insulation distance of spacer result in a smaller maximum electric field strength on the surface of spacers. This work provides valuable insights for the design of HVDC GIL.

Keywords HVDC GIL · DC superimposed impulse voltage · DC spacer · Multi-physics simulation

Z. Liang · W. Zhuang · F. Liang · X. Fan · C. Li · J. He (✉)
Department of Electrical Engineering, Tsinghua University, Beijing 100084, People's Republic of China
e-mail: hejl@tsinghua.edu.cn

Z. Liang
e-mail: lzd21@mails.tsinghua.edu.cn

W. Zhuang
e-mail: zhuangwj21@mails.tsinghua.edu.cn

F. Liang
e-mail: liangfangwei@tsinghua.edu.cn

X. Fan
e-mail: 1812301008@st.gxu.edu.cn

© Beijing Paike Culture Commu. Co., Ltd. 2024

X. Dong and L. Cai (eds.), *The Proceedings of 2023 4th International Symposium on Insulation and Discharge Computation for Power Equipment (IDCOMPU2023)*, Lecture Notes in Electrical Engineering 1102, https://doi.org/10.1007/978-981-99-7405-4_66

1 Introduction

HVDC gas insulated transmission line (GIL) has garnered increasing attention as a method for large-capacity power transmission in long-distance used in off-shore wind power stations, special regions of extreme environment and cities [1]. HVDC GIL employs high cross-section aluminum conductors and enclosure pipes, offering several advantages over traditional overhead lines or cables, including reduced electromagnetic interference, lower environmental impact, enhanced security, and decreased maintenance costs. Despite these advantages, HVDC GIL has yet to be applied in engineering due to challenges in its design and operation, particularly regarding DC superimposed impulse voltage (SI) [2–4]. DC SI, generated by switching operations or lightning strikes, can result in insulation breakdown or flashover on the spacer [5, 6].

The spacers support the conductor and maintain a uniform electric field in GIL. However, the accumulation of charge on the spacer surface can result in diminished insulation performance [7]. Previous research has demonstrated that the flashover voltage of spacer significantly decreases under DC SI. As the time of pre applied DC voltage increases, the flashover voltage of spacer further decreases under DC SI, and the smallest flashover voltage occurs when the polarity of the pre applied DC voltage is opposite to that of the impulse voltage [8–10]. Therefore, ensuring insulation performance of spacer under DC SI is a critical design requirement for HVDC GIL.

A multi-physics model of ± 800 kV DC GIL prototype is constructed, and the electric field characteristics under DC SI is analyzed based on finite element method in this paper. Relationship between the electric field strength under DC SI and the geometric structure of HVDC GIL is obtained. It is hopefully that the content of this paper can provide valuable insights for further design of HVDC GIL.

2 Simulations

2.1 Geometric Structure

The geometric structure of ± 800 kV DC GIL prototype is shown in Fig. 1, including SF_6 insulation gas, a spacer with a metal insert and a grounding ring, a conductor with shielding and a metal enclosure with particle traps. The detailed structures of the conductor and enclosure are ignored as they are equipotential bodies.

The diameter of conductor D_c changes from 130 to 200 mm when the diameter of enclosure D_e is 1100 mm. The main geometric parameters of three ± 800 kV DC GIL prototypes are shown in Table 1.

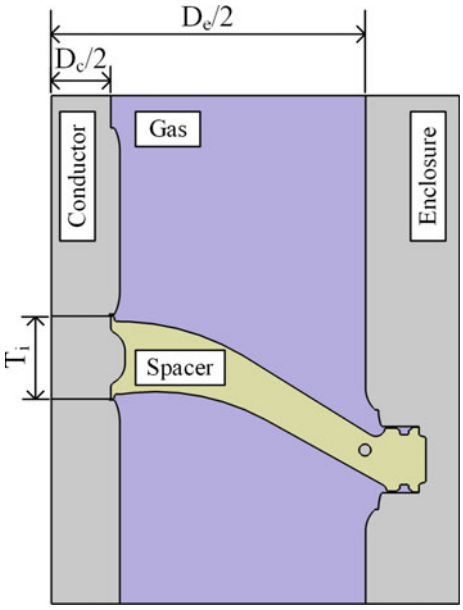

Fig. 1 The geometric structure of ± 800 kV DC GIL prototype

Table 1 The main geometric parameters of three ± 800 kV DC GIL prototypes

Name	D_c (mm)	D_e (mm)	T_i (mm)
A	130	1100	140
B	175	1100	140
C	200	1100	140

2.2 Multi-physics Model

Under DC voltage, free charge accumulates at the interface between the solid and gas. As shown in Fig. 2, the surface charge has three sources, including the gas side current J_{gn}, the solid side current J_{in} and the surface current J_s.

The charge accumulation on spacer surface is following (1), where ρ_S is the surface charge density. The gas side normal current density and the surface current density J_{gn} and J_s are calculated by (2) and (3), where $\boldsymbol{n}$ is the unit normal vector, κ_V is the volume electric conductance of the solid, κ_S is the surface electric conductance, $\boldsymbol{E}$ is the electric field, and $\boldsymbol{E}_\tau$ is the electric field's tangential component.

$$\partial \rho_S / \partial t = J_{in} - J_{gn} - J_s \tag{1}$$

$$J_{in} = n \cdot \kappa_V \boldsymbol{E} \tag{2}$$

$$J_s = \nabla \cdot (\kappa_S \boldsymbol{E}_\tau) \tag{3}$$

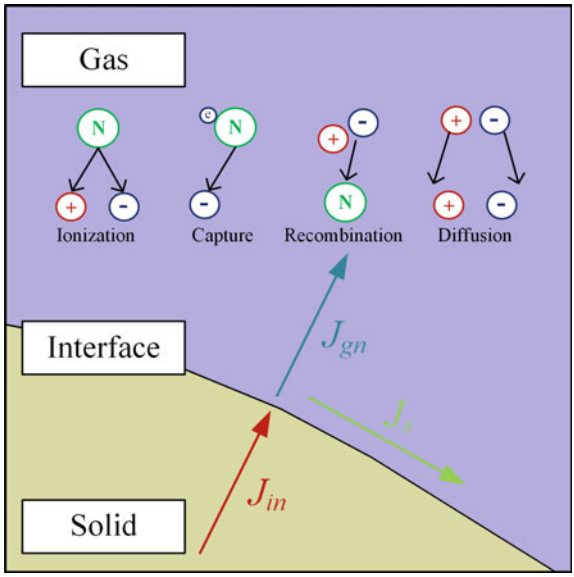

Fig. 2 Three sources of surface charge accumulation

The gaseous electrical conductance in SF_6 gas is the result of the ionization, capture, recombination and diffusion of positive and negative ions, and the gas side normal current density J_{gn} is calculated by (4) to (6), where N^+ and N^- are the positive and negative ions' numerical density, α^+ and α^- are the positive and negative ion mobility, D^+ and D^- are the positive and negative ions diffusion coefficient, k_r is the recombination rate, $\partial n_{IP}/\partial t$ is the generation rate of positive and negative ion-pair, and e is the elementary charge.

$$J_{gn} = ne \cdot [(\alpha^+ N^+ \boldsymbol{E} + \alpha^- N^- \boldsymbol{E}) - (D^+ \nabla N^+ - D^- \nabla N^-)] \tag{4}$$

$$\partial N^+/\partial t = D^+ \nabla^2 N^+ - N^+ N^- k_r - div\left(\alpha^+ N^+ \boldsymbol{E}\right) + \partial n_{IP}/\partial t \tag{5}$$

$$\partial N^-/\partial t = D^+ \nabla^2 N^- - N^+ N^- k_r - div\left(\alpha^- N^- \boldsymbol{E}\right) + \partial n_{IP}/\partial t \tag{6}$$

The multi-physics model is constructed in COMSOL software, and the electric potential on the center conductor φ_c and on the grounded enclosure φ_e are assigned with Dirichlet condition (7) and (8).

$$\varphi_c = U \tag{7}$$

$$\varphi_e = 0 \tag{8}$$

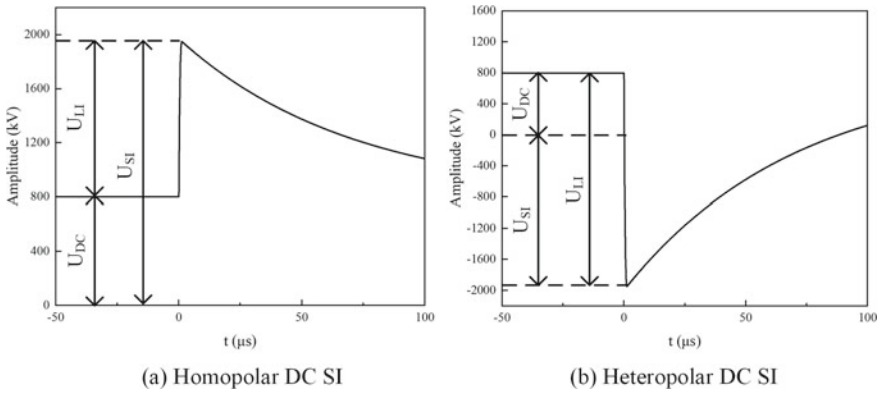

Fig. 3 Waveforms of DC SI

where U is the DC SI as shown in Fig. 3. The steady + 800 kV DC voltage is applied for 21,600 s, and then the applied voltage is changed to lighting impulse voltage with the amplitude of ± 1950 kV.

3 Results

3.1 Electric Field Distribution

The electric field distribution of three prototypes when steady + 800 kV DC voltage is applied for 21,600 s is shown in Fig. 4. With larger D_c, the insulation distance is relatively smaller. Thus, the peak value of electric field's tangential component on the spacer surface increases about 14.4% from prototype A to prototype C.

The electric field distribution of three prototypes at the peak of heteropolar DC SI is shown in Fig. 5. The maximum tangential electric field strength occurs on the concave of the spacers near to the conductor. Thus, the local geometric structure of spacers could have a relatively large impact on the local electric field. While the simulation results indicate that a larger ratio of D_e to D_i results in a larger peak value of tangential electric field strength on the spacer surface.

The electric field distribution of three prototypes at the peak of homopolar DC SI is shown in Fig. 6. Under homopolar DC SI, the peak value of tangential electric field strength slightly changes among three prototypes. It seems that the change of the ratio of D_e to D_i results in little difference of the electric field distribution under homopolar DC SI.

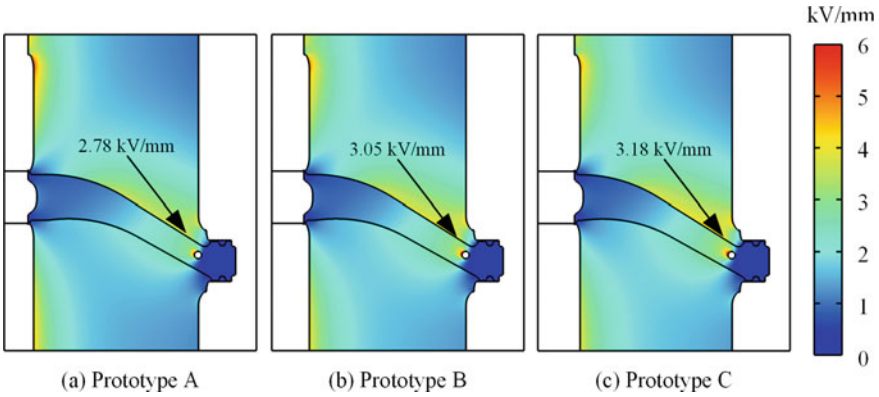

Fig. 4 DC electric field distribution at steady state

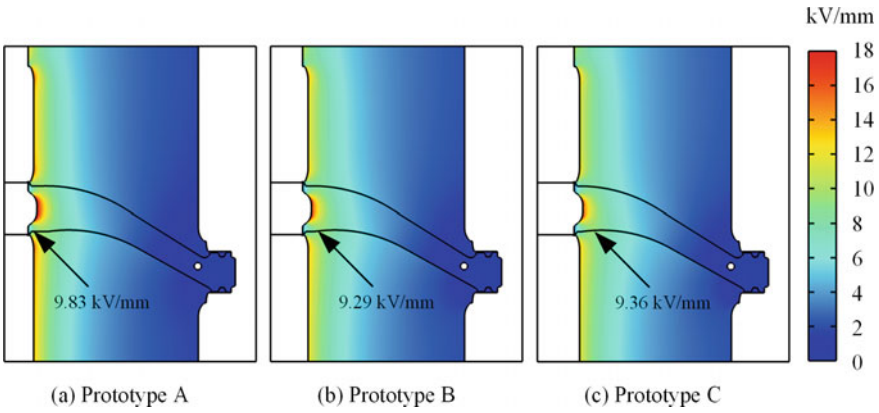

Fig. 5 Heteropolar DC SI electric field distribution

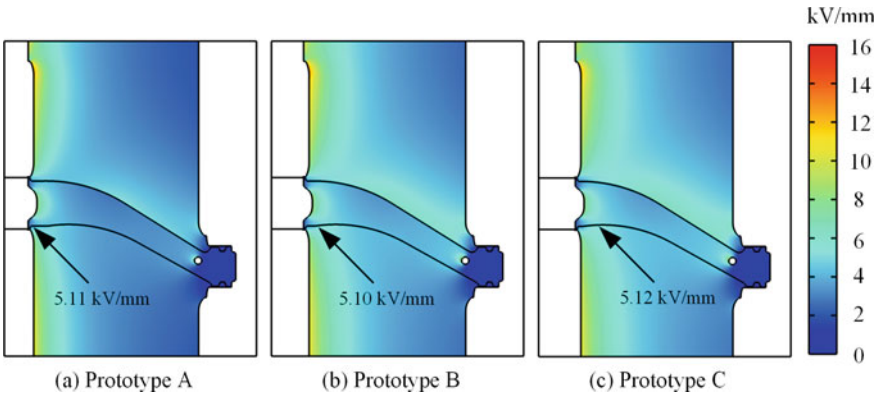

Fig. 6 Homopolar DC SI electric field distribution

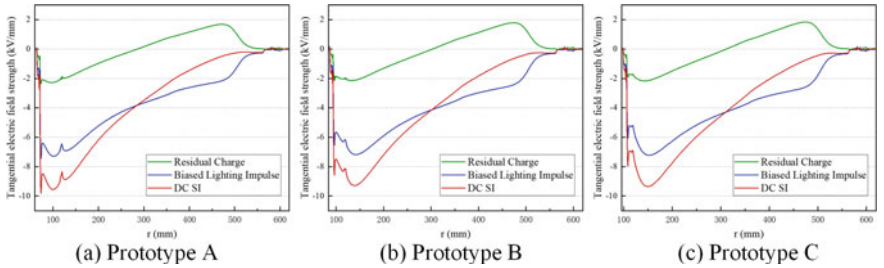

Fig. 7 The electric field's tangential component on the concave

3.2 Discussion

The electric field distribution of the HVDC GIL system under DC SI can be treated as a composition of the electric field distribution generated by the residual charge when the conductor is grounded and that under biased lighting impulse without the accumulated charge. The tangential electric field strength on the concave of three spacers is shown in Fig. 7. The electric field generated by the residual charge with grounded conductor changes little among three prototypes, while the electric field under biased lighting impulse differs a lot. Thus, the peak value of tangential electric field strength under DC SI mainly depends on that under biased lighting impulse, which increases when the ratio of D_e to D_i increases.

4 Conclusions

(1) In this paper, the electric field distribution of three ± 800 kV DC GIL prototypes is analyzed using finite element method. The simulation results show that the electric field distortion is most severe under heteropolar DC SI, and the tangential electric field strength reaches 9.83 kV/mm.
(2) The ratio of inner diameter of enclosure D_e to inner diameter of conductor D_c mainly determines the maximum tangential electric field strength under DC SI. A smaller ratio of D_e to D_c results in a smaller maximum electric field strength on the spacer surface.
(3) The electric field distribution of the HVDC GIL system under DC SI can be treated as a composition of the electric field distribution generated by the residual charge with grounded conductor and that under biased lighting impulse without the accumulated charge. The change of the ratio of D_e to D_c has little impact on the electric field generated by the residual charge, while it has relatively large impact on that under biased lighting impulse.

Acknowledgements This work was supported by the S&T Project of State Grid Corporation of China (SGTYHT/21-JS-223).

References

1. Li CY, Zhang CH, Lv JZ et al (2022) China's 10-year progress in DC gas-insulated equipment: from basic research to industry perspective. iEnergy 1(4):400–433
2. Hu Q, Li QM, Liu ZP, Liu H (2021) Impact analysis of charge accumulation on electric field distribution of DC GIL tri-post insulator under temperature gradients. Adv Technol Electr Eng Energy 40(7):20–27 (in Chinese)
3. Li CY, Zhu YJ, Zhi QY et al (2021) Dust figures as a way for mapping surface charge distribution—a review. IEEE Trans Dielectr Electr Insul 28:853–863
4. J t. Ma, Q G. Zhang, Z C. Wu et al.: Breakdown characteristics of particle-contaminated HVDC GIL under superimposed voltage of DC and impulse. IEEE Trans Dielectr Electr Insul 25(4), 1439–1447 (2018)
5. Gockenbach E (1978) Influence of pre-existing DC voltage on the breakdown performance of SF_6 under impulse voltage. In: Proceedings of the international symposium on gaseous dielectrics, pp 138–146
6. Ma JT, Zhang QG, You HY et al (2017) Study on insulation characteristics of GIS under combined voltage of DC and lightning impulse. IEEE Trans Dielectr Electr Insul 24(2):893–900
7. Liang ZD, Lin CJ, Liang FW et al (2022) Designing HVDC GIS/GIL spacer to suppress charge accumulation. High Voltage 7:645–651
8. Hasegawa T, Yamaji K, Hatano M et al (1996) DC dielectric characteristics and conception of insulation design for DC GIS. IEEE Trans Power Delivery 11(4):1776–1782
9. Okabe S, Ueta G, Utsumi T et al (2015) Insulation characteristics of GIS insulators under lightning impulse with DC voltage superimposed. IEEE Trans Dielectr Electr Insul 22(6):1–9
10. Ma JT, Zhang QG, Wu ZC et al (2017) Study on flashover characteristics of insulators in SF6 under combined voltage of DC and lightning impulse. Electr Insul Confer 62–65

Study on Cumulative Characteristics of Transformer Windings Based on Finite Element Simulation

Jun Liu, Kun Li, Xiaoqing Lin, Wenhao Ai, Xu Li, Shurong Xu, and Yong Gao

Abstract The study on cumulative characteristics of transformer windings is of great significance to improve the short-circuit withstand ability of power transformers. Current research on the cumulative characteristics of windings is nascent, with the impact of simulation modeling methods—including multiple short-circuit conditions—on these characteristics yet to be established. Therefore, the cumulative characteristics of windings are studied based on finite element simulation in this work. Firstly, we examine the simplified method of simulating multiple short-circuit impacts. Furthermore, we utilize a multi-physics coupling model to evaluate the effect of short-circuit current loading on the cumulative characteristics. The results demonstrate that the short circuit current under intermittent loading, considering the residual stress, is more consistent with the engineering practice than that under continuous loading. Our study of intermittent loading reveals that with an increase in short-circuit impacts, the equivalent stress under load diminishes gradually, suggesting a hardening phenomenon. Therefore, the winding shows stronger bending resistance with increased strain when the copper wire reaches the plastic stage. In addition, when the winding enters the hardening stage, the cumulative increase of the displacement and stress borne by the winding are reduced.

Keywords Cumulative characteristics · Finite element method (FEM) · Short-circuit fault · Power transformers

J. Liu · K. Li · S. Xu · Y. Gao
Guizhou Power Grid Co., Ltd. Electric Power Research Institute, Guiyang 550002, China

J. Liu · X. Lin · W. Ai · X. Li (✉)
College of Electrical & Information Engineering, Hunan University, Changsha 410082, China
e-mail: 15893818693@163.com

© Beijing Paike Culture Commu. Co., Ltd. 2024

X. Dong and L. Cai (eds.), *The Proceedings of 2023 4th International Symposium on Insulation and Discharge Computation for Power Equipment (IDCOMPU2023)*, Lecture Notes in Electrical Engineering 1102, https://doi.org/10.1007/978-981-99-7405-4_67

1 Introduction

The dynamic response of the winding structure is investigated through the analysis of electromagnetic and mechanical characteristics when subjected to the impact of a single high magnitude current [1, 2]. In practical production applications, power transformers encounter multiple short-circuit incidents, often involving multiple reclosures within a single accident. Consequently, the study of winding accumulation characteristics has received increasing attention. The accumulation characteristics of power transformer short-circuits can be categorized into thermal and force effects [3]. Within a short timeframe, the residual stresses arising from the short-circuit fault result in hidden cumulative losses that can significantly impact the power transformer. Thus, this paper primarily focuses on investigating the force effect of the winding.

Although advancements have been made in the manufacturing process of transformers, smaller short-circuit current shocks may not significantly affect transformer operation. However, as the number of short-circuits increases, winding damage or instability may occur even under the same short-circuit current shock [4, 5].

Currently, research on the cumulative characteristics of transformers during short-circuits is still in its early stages. Jiang S constructed a transformer segmentation model to study the leakage magnetic field, electrodynamic force, and cumulative deformation of windings under various operating conditions [6]. Li B developed a coupled electric–magnetic-structural field model for different short-circuit scenarios and analyzed the relationship between winding deformation and the number of short-circuits [3]. Yao et al. employed a two-dimensional finite element method to conduct a numerical simulation of a 220 kV oil-immersed transformer, utilizing Maxwell's system of equations and elastic–plastic mechanics theory [7].

Two simulation methods are commonly used to study the cumulative characteristics of winding deformation. The first method involves applying multiple repetitions of the same short-circuit shock in the simulation to explore the relationship between the number of short-circuit shocks and deformation, stress, and strain [7]. The second method assumes that each short-circuit shock produces a displacement of 5 mm and investigates the relationship between winding deformation size and maximum stress [6], examining whether stress changes abruptly with increasing deformation.

Furthermore, Lin et al. conducted multiple tests on the transformer under 100% short-circuit current conditions and observed an abrupt change in impedance as the number of short-circuits increased [8]. Li et al. analyzed the trends of copper changes and short-circuit force changes during accumulation after multiple instances of accumulated stress loading using test data [9]. Both short-circuit tests and numerical simulations were conducted to verify the cumulative characteristics of the short-circuit force effect.

In short, scholars have conducted simulation studies and experimental explorations of short-circuit accumulation characteristics. However, the influence of modeling methods, such as multiple short-circuit conditions in simulations, on the

results remains unclear. This paper focuses on studying the accumulation characteristics of windings from this perspective. Firstly, a simplified method of simulating multiple short-circuit shocks is investigated. Secondly, a coupled magnetic field-structural field analysis model is developed to compare and analyze the short-circuit current loading methods.

2 Multiple Short Circuit Impacts

2.1 Theoretical Analysis

The shape of a particular unit of the winding changes when it is subjected to an electromagnetic force, which can be calculated using the following equation [10]:

$$\varepsilon = \frac{F_j}{E} \tag{1}$$

$$\Delta L = \varepsilon \cdot L \tag{2}$$

where E is Young's modulus, F_j is the stress of a unit, ε is the strain of a unit; L is the length of a unit and ΔL is the length increased or decreased by the stress.

Hence, the deformation variable of a specific cell within the winding under M short-circuit shocks is denoted as [10]:

$$\Delta L = \sum_{m=1}^{M} \Delta L_m = \int \frac{F_j}{E} dL \tag{3}$$

where M is the number of shocks.

In the calculation of the cumulative properties of the winding, the Von Mises criterion, based on the concept of equivalent force-strain, is employed to assess whether the copper wire undergoes plastic deformation. Once the equivalent force and equivalent strain of the copper wire surpass this threshold, the material enters the yielding phase, in accordance with the principles of the fourth strength theory in material mechanics, known as the Von Mises criterion and can be described as [7]:

$$\sigma_e = \sqrt{\left[(\sigma_1 - \sigma_2)^2 + (\sigma_2 - \sigma_3)^2 + (\sigma_3 - \sigma_1)^2\right]/2} \tag{4}$$

$$\varepsilon_e = \sqrt{2/3 \times \left(\varepsilon_1^2 + \varepsilon_2^2 + \varepsilon_3^2\right)} \tag{5}$$

where, σ_1, σ_2, σ_3 are principal stresses; ε_1, ε_2, ε_3 are the principal strains; σ_e is equivalent stress; ε_e is equivalent strain.

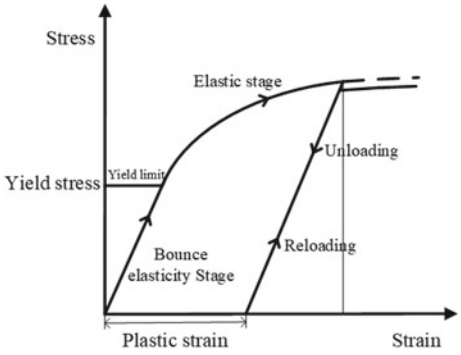

Fig. 1 Deformation properties of copper wire [11]

According to the mechanics of materials, the material deformation properties (stress–strain curve) of copper conductors are shown in Fig. 1 [11]. Before the loading stress surpasses the initial yield stress, the copper conductor undergoes elastic deformation, exhibiting a reversible response. However, once the loading stress exceeds the initial yield stress, the copper conductor enters the elastic–plastic deformation regime, where permanent deformation occurs. It should be noted that even after unloading the stress, the copper conductor does not fully recover its original shape, indicating the presence of residual deformation.

The value of the yield limit is called the initial yield stress, which is the stress to which the copper conductor is subjected when plastic strain first appears. When the copper conductor enters the plastic phase, the phenomenon of increasing strain and exhibiting stronger bending resistance is called hardening. In the elastic–plastic stage, the stress required increases with increasing strain, as shown in Fig. 1.

The effective strain ε_{eff} due to a short circuit is composed of a linear elastic component and a nonlinear plastic component, as shown in Eq. (6) [11]:

$$\varepsilon_{eff} = \varepsilon_{pe} + \frac{\sigma_{eff}}{E} \tag{6}$$

where ε_{pe} is effective plastic strain, that is, strain produced during the plastic stage; σ_{eff}/E is effective elastic strain, that is, strain produced during the linear elastic stage; σ_{eff} is effective stress; E is Young's modulus.

The stress–strain curve describing plastic phase is called the hardening function, as shown in Eq. (7) [11]:

$$\sigma_{\text{hard}} = \sigma_{\exp}\left(\varepsilon_{eff}\right) - \sigma_{ys} = \sigma_{\exp}\left(\varepsilon_{pe} + \frac{\sigma_{eff}}{E}\right) - \sigma_{ys} \tag{7}$$

where $\sigma_{\exp}$ is the fitting function of the stress–strain curve measured by the test; σ_{ys} is the initial yield stress.

As the quantity of short-circuit shocks increases, the plastic deformation gradually accumulates and the winding strength and stability decreases. The stress–strain curve of copper wire used in this paper is shown in Fig. 2.

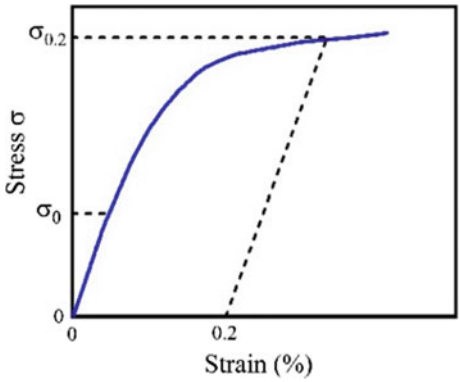

Fig. 2 The stress–strain curve of copper wire

2.2 Loading Simplification

To accurately simulate the cumulative characteristics of windings during a short circuit, a short-time multiple low-voltage symmetrical short-circuit shock, intentionally more severe than the actual scenario, is assumed in Fig. 3. The three windings are loaded with currents as depicted in Fig. 3a–c. This study focuses on analyzing the cumulative characteristics of stress and displacement on the windings, specifically examining the maximum force location on each winding. By investigating these cumulative characteristics, valuable insights can be gained regarding the response of the windings under such conditions.

To simplify the simulation process while ensuring the validity of the results, this paper conducts multiple short-circuit shock simulation tests utilizing the wave crest of the first half-period of the short circuit current. The objective is to investigate the cumulative characteristics of the transformer winding.

To effectively simulate the cumulative characteristics of the winding under multiple short-circuit current shocks, the continuous loading of short-circuit current shown in Fig. 3 is simplified to a loading and unloading process as illustrated in Fig. 4.

3 Establishment of Finite Element Model

A 220 kV oil-immersed three-winding transformer is studied with the parameters shown in Table 1.

In studying the cumulative characteristics of power transformers, the process of solving and coupling between the electromagnetic and structural fields is shown in Fig. 5 [12].

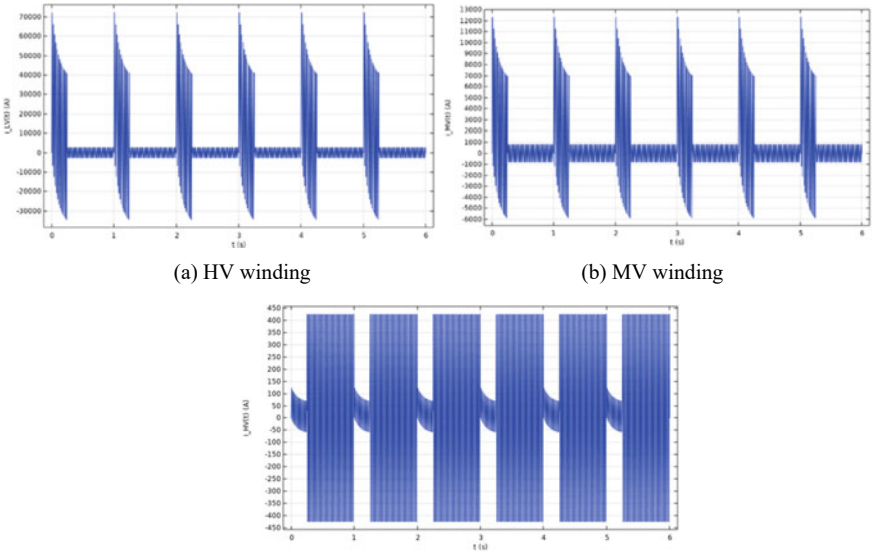

(a) HV winding

(b) MV winding

(c) LV winding

Fig. 3 The short circuit current on windings

Fig. 4 Simplified short-circuit current on windings

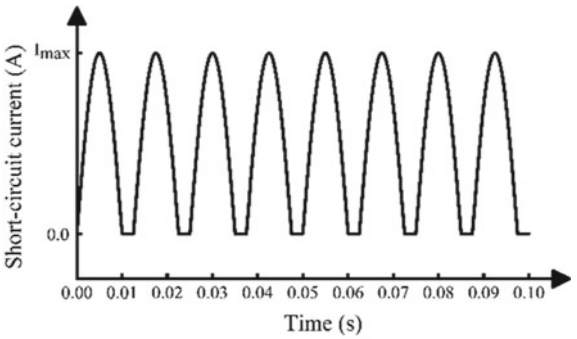

Table 1 The geometric parameters of the transformer

Parameters	Value
Low/Medium/High voltage rated capacity (MVA)	60/120/120
Low/Medium/High voltage rated current (A)	1979.5/602.5/314.9
Core radius (mm)	396
Center distance of iron core Column (mm)	2165
Compression height (mm)	1810
Inner diameter of LV/MV/HV winding (mm)	829/1035/1327
Outer diameter of LV/MV/HV winding (mm)	937/1191/1513

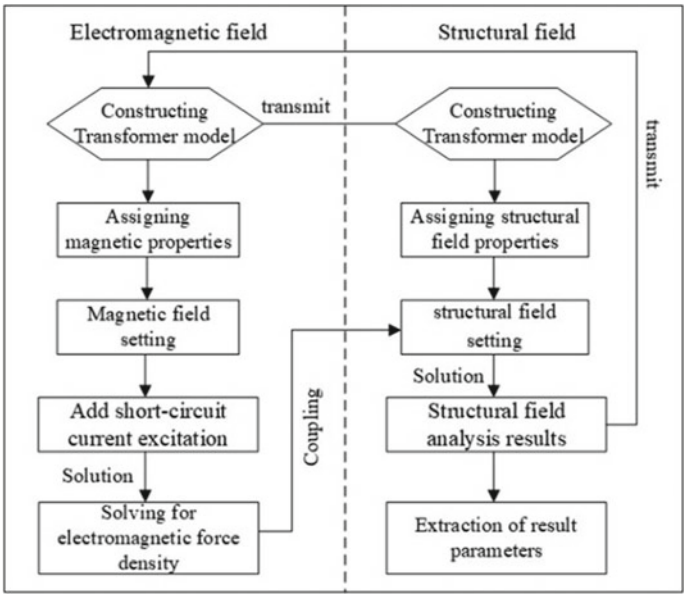

Fig. 5 Electromagnetic field-structural field coupling method

4 Study of Winding Accumulation Characteristics During Short Circuit

4.1 Continuous Loading Short Circuit Current

The short-circuit current shown in Fig. 4 is applied to the finite element model of a single-phase transformer. Specifically, the first peak of each winding is considered individually for the low-voltage symmetrical short-circuit shown in Fig. 3. The resulting accumulated displacement, stress, and plastic strain of the winding under multiple short-circuit current shocks are presented in Table 2. The simulation includes a total of five short-circuit current shocks.

The cumulative effects of stresses and displacements are plotted with the short circuit current as shown in Fig. 6. The loaded equivalent stress gradually decreases with the increase of the quantity of short-circuit shocks, verifying the existence of the hardening phenomenon. When the copper conductor enters the plastic stage, it shows stronger bending resistance with increasing strain. The residual stress and residual deformation keep accumulating and increasing: the cumulative increase of residual stress is about 10.4 MPa and the cumulative increase of residual displacement is about 0.51 mm.

Table 2 Cumulative summary of stress and displacement under continuous loading short-circuit current

Short-circuit impacts	1	2	3	4	5
Max stress (MPa)	82.3	81.2	80	79.5	78.8
Residual stress (MPa)	10.2	10.3	10.2	10.4	10.4
Max displacement (mm)	0.87	0.86	0.86	0.86	0.87
Residual displacement (mm)	0.51	0.51	0.51	0.52	0.52
Residual stress accumulation (MPa)	10.2	20.5	30.7	41.1	51.5
Residual displacement accumulation (mm)	0.51	1.02	1.53	2.05	2.57

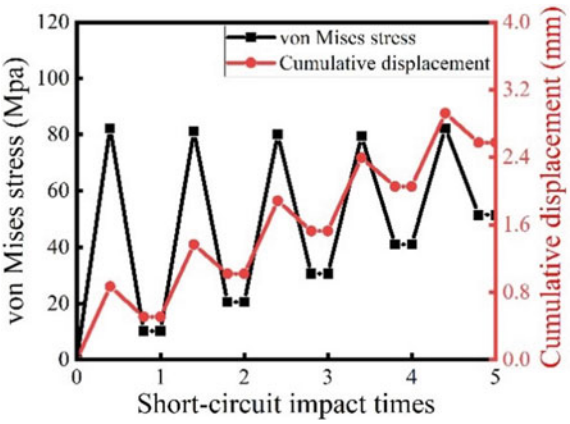

Fig. 6 Stress and displacement accumulation in winding of short circuit current under continuous loading

4.2 Intermittent Loading Short Circuit Current

The cumulative results after one short-circuit shock were obtained after loading the first cycle of 0.012 s of short-circuit current. In the subsequent studies with multiple short-circuit shocks, the latter cumulative simulation inherits the solution of the previous study and takes the residual stress into account the boundary conditions of the next structural field. The results of the first five simulations are shown in Table 3.

Plotting the results of Table 3 in Fig. 7, it can be obtained that: with the increase of the quantity of short-circuit shocks, the maximum pressure on the winding gradually decreases slightly with the increase of the quantity of short-circuit shocks, and the increase of the residual stress and accumulated displacement slows down, which is the cumulative characteristic of the winding hardening stage.

From the above two simulation methods, it can be seen that the accumulation trends of stress and displacement are basically the same, and the cumulative effects of windings during short circuit can be simulated by using continuous loading and intermittent loading of short circuit current. However, from the specific data analysis, it can be seen that, ignoring the simulation error, the residual stress and displacement generated by the continuously loaded short-circuit current are basically the same

Table 3 Cumulative summary of stress and displacement under intermittent loading short circuit current

Short-circuit impacts	1	2	3	4	5
Max stress (MPa)	82.3	80.6	79.3	78.5	77.9
Residual stress (MPa)	10.2	17.6	24.8	31.9	39.1
Max displacement (mm)	0.87	1.28	1.63	1.97	2.32
Residual displacement (mm)	0.51	0.89	1.26	1.62	1.98
Residual stress increase (MPa)	10.2	7.4	7.2	7.1	7.2
Residual displacement increase (mm)	0.51	0.38	0.37	0.36	0.37

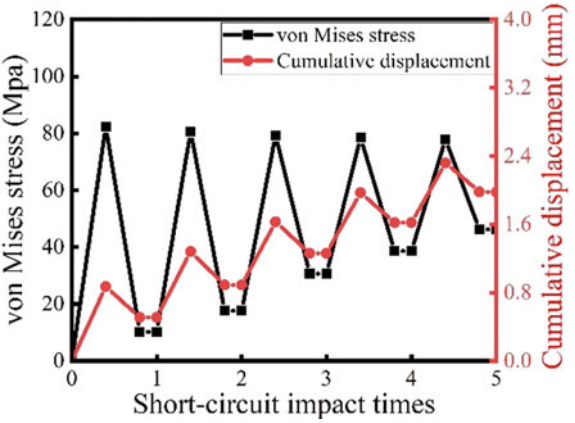

Fig. 7 Stress and displacement accumulation in winding of short circuit current under intermittent loading

each time, and the stress and displacement show linear accumulation characteristics, which is different from the actual operating experience. Furthermore, although the process of intermittent loading of short-circuit current is more tedious, requiring the residual stresses after each short-circuit shock to be added to the boundary conditions of the structural field and inheriting the previous solution to start the next simulation, this simulation method takes into account the internal damage to the winding caused by the previous short-circuit force and is more in line with the actual objective situation. Subsequently, the simulation results of intermittently loaded short-circuit current show that the cumulative increase in displacement and stress will be smaller when the winding enters the hardening phase, which is more realistic. Therefore, the comparative study in this paper can provide a reference for the subsequent simulation modeling of the cumulative characteristics of the winding.

5 Conclusion

This paper presents a comprehensive simulation study investigating the cumulative characteristics of windings subjected to multiple short circuit shocks. The study focuses on two main aspects. Firstly, the paper examines different simplification methods for simulating multiple short circuit shocks in order to identify the most appropriate approach. Secondly, a coupled magnetic field-structure field model is developed to analyze the loading method of short circuit current and assess its impact on the cumulative characteristics.

The simulation results reveal that intermittent loading of short circuit current and considering the influence of the residual stress from previous shocks yield simulation outcomes that are more consistent with real-world engineering scenarios compared to continuous loading of multiple short circuit current shocks. By studying intermittent loading of short circuit current, the cumulative characteristics of the winding are elucidated. As the quantity of short circuit shocks increases, the loading equivalent force gradually decreases, providing empirical evidence for the existence of the hardening phenomenon. Moreover, as the copper conductor enters the plastic stage, it exhibits enhanced resistance to bending as strain increases. Additionally, the study finds that when the material reaches the hardening stage, the cumulative increase in displacement and the stresses endured by the winding decrease.

These findings contribute to a better understanding of the behavior of windings under multiple short circuit shocks, providing valuable insights for the design and analysis of transformers in practical applications.

Acknowledgements This work was funded by Key Project of Guizhou Power Grid Company of China (066600GS62200006)

References

1. Fonseca WS, Lima DS, Lima AKF et al (2018) Analysis of structural behavior of transformer's winding under inrush current conditions. IEEE Trans Ind Appl 54(3):2285–2294
2. Taghikhani Z, Taghikhani MA, Gharehpetian GB (1999) Inrush current modeling of three-limb core-type power transformers based on efficient analytical-numerical hybrid method. Int J Electr Power Energy Syst 117:105694. Author F, Author S, Author T (1999) Book title, 2nd edn. Publisher, Location
3. Li B (2016) Mechanistic study on the cumulative effect of short-circuit shocks in power transformers. Huazhong University of Science and Technology, Wuhan (in Chinese)
4. Yu C-L (2020) A method for evaluating the electrodynamic capability of transformers against short-circuit currents based on finite element analysis. Xi'an University of Science and Technology, Xi'an (in Chinese)
5. Wang S, Zhang H, Wang S et al (2016) Cumulative deformation analysis for transformer winding under short-circuit fault using magnetic–structural coupling model. IEEE Trans Appl Supercond 26(7):0–5
6. Shan J (2012) Force analysis of power transformer winding deformation. North China Electric Power University, Beijing (in Chinese)

7. Yao S, Hao Z, Si J et al (2019) Dynamic deformation analysis of power transformer windings under multiple short-circuit impacts. In: 2019 IEEE 8th international conference on advanced power system automation and protection (APAP). IEEE, Xi'an, China, pp 1394–1397
8. Lin C, Li Y, Xiao X et al (2018) Equivalent model design and test for short circuit cumulative effect of EHV transformer. IOP Conf Ser Mater Sci Eng 452(4):042094
9. Li Z, Li L, Sun et al (2017) Accumulation effect test for power transformer short-circuit micro-deformation. Guangdong Electric Power 30(5):92–95 (in Chinese)
10. Wu W, Yu C (2020) Modeling and simulation of transformer winding accumulation deformation. J Xi'an Univ Sci Technol 40(2):336–341 + 368 (in Chinese)
11. Liu H (2017) Mechanics of materials, I 6th edn. Higher Education Press, Beijing (in Chinese)
12. Du J (2018) Research on dynamic stability analysis of power transformer windings based on cumulative effects. Shenyang University of Technology, Shenyang (in Chinese)

Study on Hydrophobic Mobility of Composite Insulators at Different Umbrella Skirt Positions

Yixian Fu, Xiangtao Song, Wei Wang, Feiyan Han, and Tianyang Li

Abstract Hydrophobicity and hydrophobicity migration, as important indicators for evaluating the aging degree of composite insulators and the operating condition of transmission lines, have significant research value. This article takes AC composite insulators with different years of grid operation in Shandong region as the research object. The static contact angle method is used to conduct artificial pollution experiments on the high, medium, and low voltage end skirts of composite insulators under different years of operation. Molecular dynamics software is used to simulate the adsorption effect of different substances in the pollution layer on siloxane molecules, and the microscopic mechanism of electric field on hydrophobic migration is studied. The results indicate that in the artificial pollution experiment, the hydrophobicity migration of the high and medium voltage ends is superior to that of the low voltage end. The adsorption of siloxane molecules on the surface of kaolin is the strongest. The greater the electric field intensity, the stronger the adsorption capacity.

Keywords Hydrophobicity · Hydrophobic mobility · Siloxane · Electric field

1 Introduction

Composite insulators are widely used in power systems due to their advantages of light weight and good pollution flashover resistance that glass and porcelain insulators do not possess [1]. The excellent pollution flashover resistance of composite insulators is related to the good hydrophobicity and hydrophobicity migration of the

Y. Fu · X. Song · W. Wang
State Grid Shandong Electric Power Company Ultra High Voltage Company, Jinan, China

F. Han (✉) · T. Li
College of Electrical and Electronic Engineering, Shandong University of Technology Zibo, Zibo, China
e-mail: 494910380@qq.com

© Beijing Paike Culture Commu. Co., Ltd. 2024

X. Dong and L. Cai (eds.), *The Proceedings of 2023 4th International Symposium on Insulation and Discharge Computation for Power Equipment (IDCOMPU2023)*, Lecture Notes in Electrical Engineering 1102, https://doi.org/10.1007/978-981-99-7405-4_68

silicone rubber material used [2]. However, after years of operation, the aging of silicone rubber materials and the accumulation of dirt on the surface of insulators have reduced or lost their hydrophobicity, leading to a significant decrease in their pollution resistance [3]. The hydrophobicity of the composite insulator after contamination still has a high flashover voltage, effectively suppressing the occurrence of pollution flashover accidents. At present, research suggests that the hydrophobicity and migration of silicone rubber are due to the presence of non crosslinked hydrophobic small molecule polysiloxanes in the silicone rubber material, which can migrate to the surface fouling layer and obtain hydrophobicity from the surface fouling layer [4]. Therefore, the hydrophobicity migration and hydrophobicity of composite insulators that have been in operation for many years are of great research significance as indicators for insulator status detection and aging degree evaluation.

At present, there are many studies on the mechanism of hydrophobic migration. Scholars at home and abroad generally believe that hydrophobic migration is the process by which the fouling layer obtains small molecules of siloxane in silicone rubber [3]. Reference [4] conducted hydrophobic material transfer experiments by setting different temperatures in a constant temperature chamber to study the effect of temperature on hydrophobic migration. It was concluded that the higher the temperature, the better the hydrophobic migration. Reference [5] studied the hydrophobic migration process of insulator strings coated with RTV anti pollution flashover coating running near different pollution sources. It was found that the hydrophobic migration on the surface of coated insulators became worse and slower with increasing service life. Reference [6] studied the hydrophobicity changes of silicone rubber material for composite insulator umbrella skirts under strong AC corona action. The conclusion is drawn that an appropriate amount of pollution layer is beneficial for the silicone rubber umbrella skirt of composite insulators to resist corona aging. Moreover, after corona action, due to the migration of hydrophobic small molecule siloxanes within the silicone rubber material, the surface hydrophobicity can be restored to a near initial state in a short period of time, whether in a clean or dirty state. Reference [7] conducted hydrophobicity tests under natural pollution and after removal of pollution, as well as hydrophobicity migration tests after artificial coating. The research results indicate that the hydrophobicity of the high-voltage and low-voltage ends of DC composite insulators is generally worse than that of the middle, and the hydrophobicity distribution along the string shows an inverted U-shaped shape. Umbrella skirts with poor hydrophobicity and migration are more commonly found near the high and low voltage ends. Reference [8] conducted a systematic hydrophobicity migration test using the static contact angle method. The research results showed that the edge of the insulator umbrella skirt had the worst hydrophobicity migration, while the root had the best hydrophobicity migration. The hydrophobicity migration of insulators in different directions also varied. In the case of natural pollution, there is a lot of research on the hydrophobicity of composite insulators, but there is relatively little research on hydrophobicity migration [9–11]. There is limited research on the adsorption effect of the dirty layer on hydrophobicity and hydrophobicity migration. There is limited research

on the micro mechanisms of hydrophobicity and hydrophobicity migration through molecular dynamicsubsequent paragraphs, however, are indented.

This article takes AC composite insulators with different years of grid operation in Shandong region as the research object. In order to study the hydrophobicity migration performance of composite insulators with different positions of umbrella skirts under different operating years, manual contamination and hydrophobicity migration tests were conducted. In order to further study the hydrophobicity and hydrophobicity migration mechanism of insulator contamination layer, the adsorption capacity of contamination types in the contamination layer was first simulated through the molecular dynamics software Materials Studio, and then the substances with the strongest adsorption capacity among the pollutants were selected through the radial distribution function and binding energy indicators, and the effects of electric field strength and temperature on the adsorption capacity were studied. The adsorption capacity of kaolin to siloxane molecules was analyzed according to binding energy, and the mechanism of temperature and electric field on hydrophobicity and hydrophobicity migration was explored. The hydrophobicity and hydrophobicity migration tests, as reasonable reference indicators, can provide guidance for the operation status detection and aging degree judgment of AC composite insulators in Shandong region of China.

2 Test Method and Result Analysis

2.1 Test Sample

The test samples used in the experiment were all taken from AC 220 kV transmission line insulators from different manufacturers operating on site in Shandong region. The selected samples were composite insulators with different years of operation in different regions. Although the surface of the umbrella skirt had some degree of fouling and powdering, it still maintained good hydrophobicity. The sample type is FXBW-220/100. For the operational composite insulators sampled for inspection, the umbrella skirts at the high voltage end, medium voltage end, and low voltage end are taken for analysis, and detailed information is shown in Table 1.

In order to test the hydrophobicity and migration of composite insulators, a large umbrella skirt was cut along the interface between the umbrella skirt and the sheath to form a test piece. Take a large umbrella skirt at the high, medium, and low voltage ends, and evenly take 5 test points from the root to the edge on each 1/4 round small test piece, taking the average value.

Table 1 Basic information of composite insulator samples

Insulator number	Service life/year	Manufacturer	Operating area	Voltage level (kV)
A	1	a	Coastal zone	220
B	9	b	Farmland area	220
C	9	b	Farmland area	220
D	10	c	Coastal zone	220
E	11	b	Farmland area	220
F	14	c	Farmland area	220
G	14	c	Coastal zone	220
H	15	b	Coastal zone	220
I	16	c	Farmland area	220
J	17	b	Farmland area	220

Fig. 1 Static contact angle measurement

(a) Hydrophobic surface **(b) Hydrophilic surface**

2.2 Test Method

Clean and pre-treat the surface sample with anhydrous ethanol and deionized water. After drying, place it in a dust-proof container and store it under laboratory conditions for at least 24 h. Conduct coating pre-treatment on the sample and test the surface hydrophobicity migration according to the standard DL/T 376-2019. Add 21 g of sodium chloride powder and 242 g of kaolin solution per liter of water, and then place it in a soaking tank. Soak the pretreated sample in the soaking tank. Maintain the laboratory environment temperature at around 22 °C and relative humidity between 50 and 60% [12]. Measure and record the surface hydrophobicity of the test sample at regular intervals, and observe the hydrophobicity migration of each composite insulator at the high, medium, and low voltage ends. The hydrophobicity migration time is 96 h. Use a static contact angle measuring instrument to collect static contact angle data for the test samples before and after the experiment (Fig. 1).

2.3 Analysis of Test Results

In order to study the effect of different positions of umbrella skirts on the hydrophobicity migration performance of composite insulators, manual contamination and hydrophobicity migration tests were conducted. The hydrophobicity migration results of 10 strings of composite insulators with different operating years at the

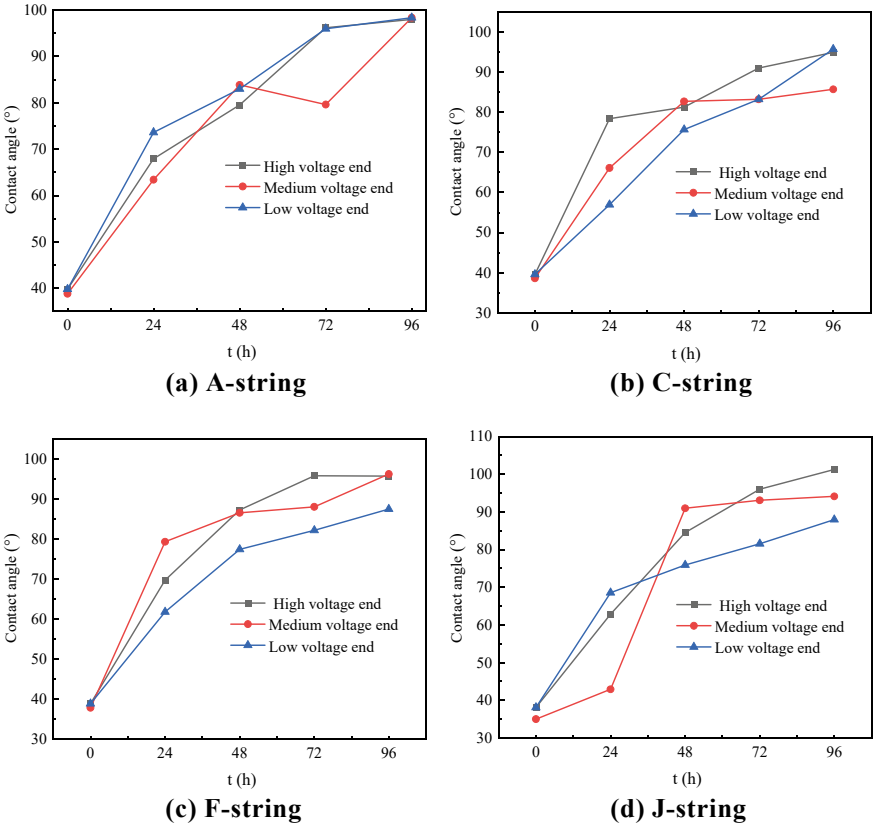

Fig. 2 Hydrophobicity migration curve at different positions of umbrella skirt

high, medium, and low voltage ends of each string of umbrella skirt are shown in Fig. 2.

Overall, the A and C string insulators with shorter operating years are less affected by the position of the umbrella skirt, while the F and J string insulators with longer operating years are more affected by the position of the umbrella skirt. This shows that the degree of hydrophobic migration at the high and medium voltage ends is generally higher than that at the low voltage end.

The mechanism of the influence of umbrella skirt position on hydrophobicity migration is as follows. Insulators with short service life have a low probability and proportion of corona and arc discharge, and the surface of silicone rubber produces fewer small molecules. The influence of electric field strength on hydrophobicity migration is small. However, insulators with long service life are more likely to have corona and arc discharge, and the high discharge probability at the high-voltage end is more likely to damage the chemical bond inside the umbrella skirt, resulting in

more small siloxane molecules. The concentration of siloxane molecules at the high-pressure end is at a high level, which is influenced by the concentration difference inside and outside the umbrella skirt. The degree and speed of hydrophobic migration at the high-pressure end are at a high level. Secondly, the ability of the dirt layer to adsorb siloxanes increases with the increase of electric field strength. The adsorption capacity of the pollution layer generally leads to a higher degree of hydrophobic migration at the high and medium pressure ends than at the low pressure ends. Furthermore, the temperature at the high voltage end continuously increases due to corona and arc discharge, leading to an increase in molecular migration speed, resulting in a generally higher degree of hydrophobic migration at the high and medium voltage ends than at the low voltage ends. In order to further verify the impact of the above reasons on hydrophobic migration, simulation analysis will be conducted in the following text.

3 Simulation Analysis of Adsorption Capacity

Some scholars have conducted extensive research on the effects of corona and arc discharge on the hydrophobicity characteristics of insulators. However, there is limited research on the influence of electric field and temperature on the adsorption effect of the pollution layer, which leads to differences in hydrophobicity characteristics. This article focuses on simulating the influence of electric field and temperature on the hydrophobicity characteristics of insulators. Regardless of the influence of siloxane concentration, fix the number of siloxanes in the simulation. Soluble substances are greatly affected by relative humidity, while insoluble substances are less affected by relative humidity. Simulation focuses on studying the adsorption effect of insoluble substances on siloxanes.

3.1 Interface Model Simulation

The molecular dynamics simulation method is used to study the adsorption of siloxane on the surface of insoluble substances. The simulation software uses Materials Studio, and the force field uses COMPASS force field. The simulation time is 50 ps, totaling 50,000 steps. The GUIP/Dreiding module is selected for simulation, with a simulation temperature of 20 °C. The interface model simulation diagram of four molecular structures at 293 K is shown in Fig. 3.

In order to further investigate the adsorption of small molecule siloxanes on the surfaces of various insoluble substances, this article analyzed the results and parameters of molecular dynamics simulations. The adsorption energy E_{ads} can be used to study the adsorption capacity of various insoluble surfaces for small molecule siloxanes. The surface areas of each simulation system are different. In order to unify

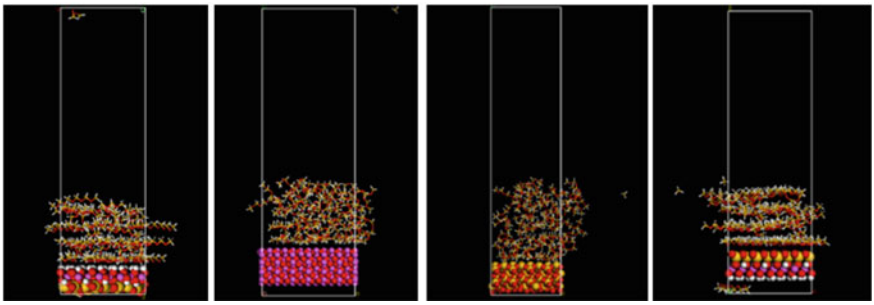

(a) Al-O surface-LWM (b)Al_2O_3-LWM (c) SiO_2-LWM (d) Si-Osurface-LWM

Fig. 3 Interface model simulation diagram

Table 2 Calculation results of "siloxane surface" binding energy

Solid surface	Kaolin Al-O surface	Al_2O_3	SiO_2	Kaolin Si–O surface
E_{ads} (kcal/mol)	− 9692.08	− 328.92	− 118.65	− 9460.8
$S_{surface}$ (Å^2)	754.97	706.10	502.87	754.97
E'_{ads} (cal/m^2)	− 2.1317	− 0.0774	− 0.0392	− 2.0808

the quantitative standard, the adsorption of the system is measured by the binding energy E'_{ads} per unit surface area.

E_{ads} is the adsorption energy between siloxane molecules and the surface in the system; When E_{ads} is negative, siloxane molecules can adsorb on the solid surface, and the greater the absolute value, the stronger the adsorption effect; When E_{ads} is positive, it indicates that they are mutually exclusive, meaning that siloxane molecules cannot adsorb on the surface. From Table 2, it can be seen that for the adsorption energy of siloxane molecules on the unit surface, kaolin has the highest, followed by Al_2O_3 surface, SiO_2 surface has the smallest, and siloxane molecules have the strongest adsorption effect on the surface of kaolin.

3.2 The Effect of Electric Field on Adsorption Capacity

The migration of hydrophobicity in artificial pollution experiments exhibits a certain pattern due to different positions of umbrella skirts. In order to study the reasons for the occurrence of the above laws, it is of great significance to simulate the influence of electric fields on the adsorption capacity of insoluble pollutants in the pollution layer.

Based on the electric field distribution of 220 kV composite insulators in the literature, the electric field strengths at the high, medium, and low voltage ends were selected to be 5.3kV/cm, 0.66kV/cm, and 0.14kV/cm, respectively. When studying

Table 3 Calculation results of binding energy of different electric fields

Solid surface	High voltage end	Medium voltage end	Low voltage end	No electric field
E_{ads} (kcal/mol)	− 9692.08	− 328.92	− 118.65	− 9460.8
$S_{surface}$ (Å^2)	754.97	706.10	502.87	754.97
E'_{ads} (cal/m^2)	− 2.1317	− 0.0774	− 0.0392	− 2.0808

the influence of electric field on the adsorption capacity of insoluble pollutants in the pollution layer, molecular simulation was set to a temperature of 20 °C (293K) at room temperature; The air pressure is standard atmospheric pressure (0.1 MPa); The integration step size is 0.1 fs; The number of iterations is 100000; The total simulation duration is 100 ps; The simulation module is GULP/Dreiding. The simulation selects the Si–O surface of kaolin, and the calculation results of binding energy under different electric fields are shown in Table 3.

From Table 3, it can be seen that the adsorption energy of siloxane molecules on a unit surface at different umbrella skirt positions is as follows: high voltage end > medium voltage end > low voltage end > no electric field.

The adsorption of siloxane by the fouling layer increases with the increase of electric field strength, and the content of siloxane in the fouling layer also increases. The hydrophobicity of the fouling layer is enhanced, and the migration degree of siloxane is increased. The degree and speed of hydrophobic migration at the high and medium voltage ends are superior to those at the low voltage end.

4 Conclusion

The degree and speed of hydrophobic migration at the high and medium voltage ends of composite insulators are superior to those at the low voltage end. Due to the influence of electric field intensity on the adsorption capacity of siloxane molecules, the concentration of siloxane molecules on the surface of kaolin is as follows: high voltage end > medium voltage end > low voltage end. The simulation verified the law of hydrophobic migration at different positions of the umbrella skirt from a microscopic perspective.

Acknowledgements This work was supported by the Science and Technology Project of State Grid Shandong Electric Power Company Entitled “Research and application of lean evaluation technology for aging performance of synthetic insulators” (Grant: 520618220001).

References

1. Peng J, Liu Y, Peng W, Liu Z, Zhang C (2021) Study on hydrophobicity of umbrella sleeve material for hard composite insulator. Trans China Electrotechnical Soc 36(S1):14–21 (in Chinese)
2. Huang Z, Peng X, Wang Z, Chen L, Fang P (2018) Study on small molecular siloxane in operating composite insulator. High Voltage Eng 44(09):2822–2827 (in Chinese)
3. Chen G (2020) Study on hydrophobic material transfer and its characteristics of superhydrophobic antifouling flashover material. Huazhong University of Science and Technology (in Chinese)
4. Lei L, Lin M, Wang Y, Wang W, Fu Z, Huang S, Huang D (2021) Experimental study on the influence of iron oxide on hydrophobic migration characteristics of room temperature vulcanized silicone rubber. Power Grid Technol 45(02):833–839 (in Chinese)
5. Jia Z, Li T, Chen C, Yang C, Chen R, Lin C (2014) Operation characteristics of room temperature vulcanized silicone rubber anti pollution flashover coating in Guangdong. High Voltage Technol 40(07) 1963–1969 (in Chinese)
6. Zhu Y, Yu J, Liu J, Liu C, Zhang D, Fang J (2019) Effect of AC Corona on hydrophobicity of silicone rubber umbrella skirt of composite insulator. Electric Power Sci Eng 35(02):33–37 (in Chinese)
7. Yang C, Wu M, He J, Wang Y, Dong Y, Zhang C, Jia Z, Chen C (2014) Hydrophobicity distribution law of operating DC composite insulators. Power Grid Technol 38(06):1650–1656 (in Chinese)
8. Jia Z, Yang C, Wang X, Wang Z, Zhicheng G, Yu X (2015) Aging characteristics of composite insulators based on hydrophobic migration test. High Voltage Technol 41(06):1907–1914 (in Chinese)
9. Shi J, Dong H, Quan Y, Chen C, Yan S (2020) Evaluation of thermoplastic polyolefin materials for the hard shed of composite insulators. J Appl Polym Sci 137(36)
10. Tian Y, Yuan Z, Huang X, Liu C, Li S, Lu D (2020)High-efficiency enhancement of the surface weatherability and electrical and mechanical properties of a cycloaliphatic epoxy-based hybrid nanocomposite via reaction-induced organic functional groups. Prog Org Coat 148
11. Meng X, Peng G, Niu K, Wang X, Mei H, Wang L (2022) Characteristics of Small-molecule migration of silicone rubber insulator in electrical power systems. Polymers 14(13)
12. Li M, Cao B, Liu Y, Wang L (2022) Novel micro-capsule-doped insulating material with hydrophobicity transfer capability triggered by creepage discharge. High Voltage 7(5)